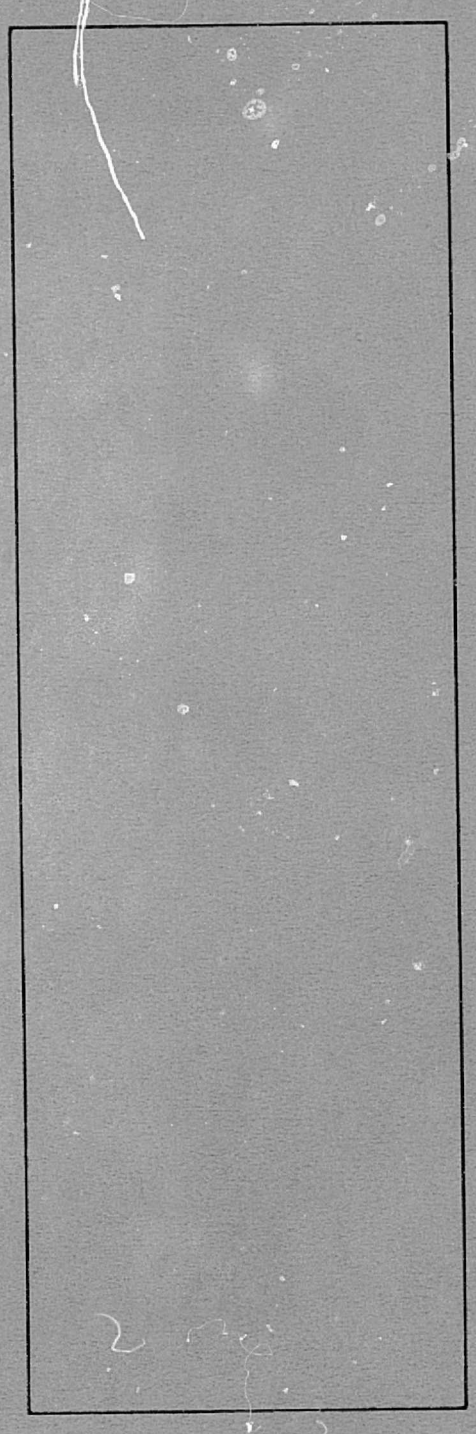

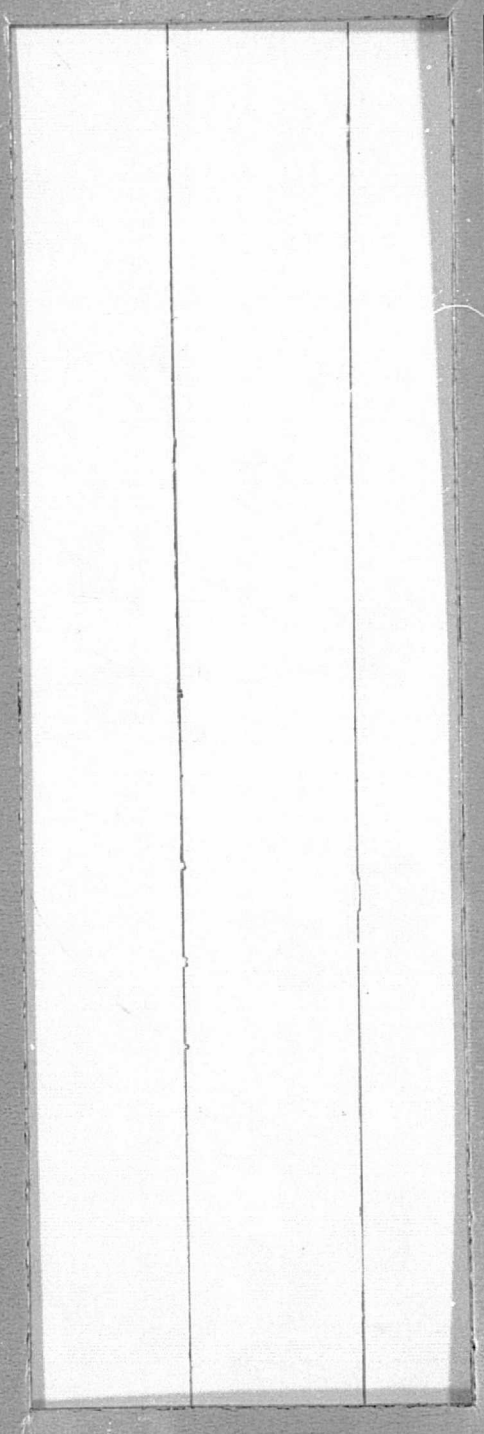

Bendix

Guidance Systems Division

THE
BENDIX
CORPORATION

GUIDANCE SYSTEMS
DIVISION

ANALYTICAL STUDY OF INSIDE-OUT GIMBAL DYNAMICS

FINAL REPORT
VOLUME I

ANALYTICAL STUDY OF
INSIDE-OUT/COINCIDENT
GIMBAL DYNAMICS

SEPTEMBER 1976

CONTRACT NAS8-31629

PREPARED FOR:

GEORGE C. MARSHALL
SPACE FLIGHT CENTER
MARSHALL SPACE
FLIGHT CENTER,
ALABAMA 35812

Prepared by:

S. Calvin Rybák
Program Manager
Energy, Environment, and
Technology Office

Approved by:

M. Brown
Technical Director
Energy, Environment, and
Technology Office

S. Seeb
Director of Engineering
Guidance Systems Division

FOREWORD

This Final Report is submitted in accordance with the requirements of Contract No. NAS8-31629, "Analytical Study of Inside-Out Gimbal Dynamics."

This report consists of two volumes:

Volume I - Analytical Study of Inside-Out/ Coincident Gimbal Dynamics

Volume II - Appendix

CONTENTS

		Page
Foreword.		ii
Contents.		iii
1.	INTRODUCTION.	1-1
2.	MODEL DESCRIPTION	2-1
2.1	IOG Mathematical Model.	2-2
2.1.1	Translational Equations of Motion	2-2
2.1.2	Rotational Equations of Motion.	2-7
2.1.3	Computational Scheme for Updating $_3T_2$	2-12
2.1.4	Specification of Gimbal Wire Torques.	2-16
2.2	Offset Gimbal Mathematical Model.	2-19
2.2.1	Translational Equations of Motion	2-19
2.2.2	Rotational Equations of Motion.	2-24
2.2.3	Derivation of Gimbal Torques.	2-56
2.3	IOG Stability Model	2-58
3.	IOG SYSTEM STABILITY ANALYSIS	3-1
3.1	System Stability as a Function of Telescope Look Angle for Nominal System Parameters	3-1
3.2	System Stability as a Function of Control Loop Bandwidth Variations.	3-2
3.3	System Stability as a Function of Telescope Mass and Inertia Variations.	3-3
3.4	System Stability as a Function of Pedestal Mass and Inertia Variations.	3-3
3.5	System Stability as a Function of Sensor and Actuator Variations	3-3
3.6	System Stability as a Function of Variations in Suspension Characteristics.	3-4
3.7	System Stability as a Function of Geometrical Variations.	3-4
4.	IOG LINEAR SYSTEM PERFORMANCE	4-1
4.1	IOG Pointing Performance.	4-1
4.1.1	IOG Pointing Performance as a Function of Location Within the Orbiter Cargo Bay	4-1
4.1.2	IOG Pointing Performance as a Function of Variation in Suspension Damping	4-2
4.1.3	IOG Pointing Performance as a Function of Pedestal Mass and Inertia Variations	4-3

CONTENTS (Continued)

		Page
4.1.4	IOG Pointing Performance as a Function of Telescope Mass and Inertia Variations	4-5
4.2	IOG Earth Tracking Performance.	4-8
5.	IOG LIMIT CYCLE ANALYSIS AND NONLINEAR PERFORMANCE.	5-1
5.1	Describing Function Analysis of IOG System. . . .	5-1
5.1.1	IOG Wire Torque Characteristics	5-1
5.1.2	IOG Equations of Motion	5-2
5.1.3	Planar Limit Cycle Analysis	5-10
5.2	Nonlinear IOG Performance Characteristics	5-23
6.	DERIVATION OF SUSPENSION CHARACTERISTICS FOR COINCIDENT GIMBAL SYSTEM CONFIGURATION.	6-1
6.1	Derivation of Linear and Rotational Stiffness and Damping Coefficients for the Coincident Gimbal Suspension System	6-1
6.2	Inherent Relationships Between Suspension Parameters for the Coincident Gimbal System	6-7
6.3	Comparison of Coincident Gimbal Suspension System with Square Based Suspension System	6-9
7.	COINCIDENT GIMBAL SYSTEM PERFORMANCE.	7-1
7.1	Coincident Gimbal Pointing Performance.	7-1
7.2	Coincident Gimbal Earth Tracking Performance. . .	7-2
7.3	Coincident Gimbal Raster Scanning Performance . .	7-3
7.4	Pointing Performance with Modified Suspension Characteristics	7-4
7.5	Coincident Gimbal Earth Tracking Performance with Recommended Suspension Parameters	7-7
8.	ANALYSIS OF EARTH TRACKING PROFILES	8-1
8.1	Derivation of Earth Tracking Profiles	8-1
8.2	Comparison Between Actual Earth Tracking Profiles and the Hyperbolic Approximations	8-7
8.3	Approximate Relationship Between Peak Angular Acceleration and Orbital Altitude	8-10
8.4	Approximate Relationships Between Peak Rate of Change of Acceleration and Orbital Altitude . .	8-10
9.	COINCIDENT GIMBAL SYSTEM EARTH POINT TRACKING PERFORMANCE.	9-1
9.1	Estimated Torque Required to Perform Earth Point Tracking.	9-1

CONTENTS (Continued)

		Page
9.2	Payload Mass Characteristics That Can Be Accommodated by the IPS in the Earth Point Tracking Mode for Various Orbital Altitudes.	9-4
9.3	Peak Tracking Error Incurred During Earth Point Tracking.	9-7
9.4	Pedestal Rotations, Translations and Isolator Elongations Incurred During Earth Point Tracking	9-7
9.5	Techniques for Improving Telescope Tracking Accuracy During Earth Point Tracking.	9-9
10.	INSTRUMENT POINTING SYSTEM (IPS) NOISE ANALYSIS . .	10-1
10.1	Separate Rate Plus Position Sensor Implementation	10-1
10.1.1	Pointing Error Due to Position Sensor Noise . .	10-1
10.1.2	Angular Error Due to Rate Gyro Noise Assuming Separate Rate and Position Sensors.	10-4
10.1.3	Angular Error Due to Torquer Noise.	10-5
10.1.4	Torquer Range Used Due to Position Sensor Noise	10-5
10.1.5	Torquer Range Used Due to Rate Gyro Noise Assuming Separate Rate and Position Sensors . .	10-9
10.1.6	Computation of Optimum Pointing Control Loop Bandwidth for Separate Rate Plus Position Sensor Implementation	10-10
10.2	Rate Gyro Hold Sensor Implementation.	10-11
10.2.1	Pointing Error Due to Rate Gyro and Position Noise	10-11
10.2.2	Torque Noise Due to Rate Gyro Noise for Rate Gyro Hold Sensor Implementation	10-15
10.2.3	Pointing Accuracies and Update Frequencies Involved When Using the LDG 540 Gyro in a Rate Gyro Hold Mode.	10-17
10.3	Derived Rate Sensor Implementation.	10-19
10.3.1	Angular Error Due to Position Noise for Derived Rate Sensor Implementation.	10-19
10.3.2	Torque Noise Due to Position Noise for the Derived Rate Sensor Implementation.	10-20
10.3.3	Computation of Optimum Loop Bandwidth for Derived Rate Sensor Implementation.	10-22
10.3.4	Criteria for Choosing Between Derived Rate and Separate Rate Plus Position Sensor Implementations	10-23
10.3.5	Criteria for Choosing Between Rate Gyro Hold and Derived Rate Sensor Implementations . . .	10-23
10.4	Summary and Recommendations	10-24

CONTENTS (Continued)

		Page
11.	SUMMARY AND CONCLUSIONS	11-1
12.	RECOMMENDED FUTURE EFFORT	12-1

Figure

2-1	IOG Schematic Diagram	2-63
2-2	Wire Torques	2-64
2-3	Offset Gimbal System Configuration	2-65
4-1	Crew Motion Disturbance Profile	4-10
4-2	Peak x-Axis Pointing Error vs Telescope Look Angle as a Function of IOG Location in the Cargo Bay	4-11
4-3	Peak y-Axis Pointing Error vs Telescope Look Angle as a Function of IOG Location in the Cargo Bay	4-12
4-4	Peak Telescope Pointing Error vs Telescope Look Angle as a Function of Suspension Damping Characteristics	4-13
4-5	Telescope x-Axis Pointing Error	4-14
4-6	Telescope y-Axis Pointing Error	4-14
4-7	Telescope z-Axis Pointing Error	4-15
4-8	Telescope x-Axis Rate Error	4-15
4-9	Telescope y-Axis Rate Error	4-16
4-10	Telescope z-Axis Rate Error	4-16
4-11	Pedestal x-Axis Angular Rotation	4-17
4-12	Pedestal y-Axis Angular Rotation	4-17
4-13	Pedestal z-Axis Rotation	4-18
4-14	Pedestal x-Axis Rate	4-18
4-15	Pedestal y-Axis Rate	4-19
4-16	Pedestal z-Axis Rate	4-19
4-17	Pedestal x-Axis CM Translation	4-20
4-18	Pedestal y-Axis CM Translation	4-20
4-19	Pedestal z-Axis CM Translation	4-21
4-20	Pedestal x-Axis CM Velocity	4-21
4-21	Pedestal y-Axis CM Velocity	4-22
4-22	Pedestal z-Axis CM Velocity	4-22
4-23	x-Axis Control Torque	4-23
4-24	y-Axis Control Torque	4-23
4-25	z-Axis Control Torque	4-24
4-26	Telescope x-Axis Pointing Error	4-25
4-27	Telescope y-Axis Pointing Error	4-25
4-28	Telescope z-Axis Pointing Error	4-26
4-29	Telescope x-Axis Rate Error	4-26

CONTENTS (Continued)

		Page
4-30	Telescope y-Axis Rate Error	4-27
4-31	Telescope z-Axis Rate Error	4-27
4-32	Pedestal x-Axis Rotation.	4-28
4-33	Pedestal y-Axis Rotation.	4-28
4-34	Pedestal z-Axis Rotation.	4-29
4-35	Pedestal x-Axis Rate.	4-29
4-36	Pedestal y-Axis Rate.	4-30
4-37	Pedestal z-Axis Rate.	4-30
4-38	Pedestal x-Axis CM Translation.	4-31
4-39	Pedestal y-Axis CM Translation.	4-31
4-40	Pedestal z-Axis CM Translation.	4-32
4-41	Pedestal x-Axis CM Velocity	4-32
4-42	Pedestal y-Axis CM Velocity	4-33
4-43	Pedestal z-Axis CM Velocity	4-33
4-44	x-Axis Control Torque	4-34
4-45	y-Axis Control Torque	4-34
4-46	z-Axis Control Torque	4-35
4-47	Telescope x-Axis Pointing Error	4-36
4-48	Telescope y-Axis Pointing Error	4-36
4-49	Telescope z-Axis Pointing Error	4-37
4-50	Telescope x-Axis Rate Error	4-37
4-51	Telescope y-Axis Rate Error	4-38
4-52	Telescope z-Axis Rate Error	4-38
4-53	Pedestal x-Axis Rotation.	4-39
4-54	Pedestal y-Axis Rotation.	4-39
4-55	Pedestal z-Axis Rotation.	4-40
4-56	Pedestal x-Axis Rate.	4-40
4-57	Pedestal y-Axis Rate.	4-41
4-58	Pedestal z-Axis Rate.	4-41
4-59	Pedestal x-Axis CM Translation.	4-42
4-60	Pedestal y-Axis CM Translation.	4-42
4-61	Pedestal z-Axis CM Translation.	4-43
4-62	Pedestal x-Axis CM Velocity	4-43
4-63	Pedestal y-Axis CM Velocity	4-44
4-64	Pedestal z-Axis CM Velocity	4-44
4-65	x-Axis Control Torque	4-45
4-66	y-Axis Control Torque	4-45
4-67	z-Axis Control Torque	4-46
4-68	Peak Pointing Error as a Function of Pedestal Mass and Inertia Variations.	4-47
4-69	Peak Pointing Error for Small Telescope Nominal Suspension Parameters	4-48

CONTENTS (Continued)

		Page
5-1	IOG Wire Torque Characteristics	5-24
5-2	Alternate Representation of IOG Wire Torque Characteristic.	5-25
5-3	Telescope y-Axis Pointing Error	5-26
5-4	Telescope y-Axis Rate Error	5-26
5-5	Pedestal y-Axis Rotation.	5-27
5-6	Pedestal y-Axis Rate.	5-27
5-7	Pedestal x-Axis CM Translation.	5-28
5-8	Pedestal z-Axis CM Translation.	5-28
5-9	Pedestal x-Axis CM Velocity	5-29
5-10	Pedestal z-Axis CM Velocity	5-29
5-11	y-Axis Control Torque	5-30
5-12	Telescope y-Axis Pointing Error	5-31
5-13	Telescope y-Axis Rate Error	5-31
5-14	Pedestal y-Axis Rotation.	5-32
5-15	Pedestal y-Axis Rate.	5-32
5-16	Pedestal x-Axis CM Translation.	5-33
5-17	Pedestal z-Axis CM Translation.	5-33
5-18	Pedestal x-Axis CM Velocity	5-34
5-19	Pedestal z-Axis CM Velocity	5-34
5-20	y-Axis Control Torque	5-35
6-1	Skewed Spring Suspension System	6-11
6-2	Geometrical Relationship Between Suspension Parameters.	6-12
7-1	Telescope x-Axis Pointing Error	7-8
7-2	Telescope y-Axis Pointing Error	7-8
7-3	Telescope z-Axis Pointing Error	7-9
7-4	Telescope x-Axis Rate Error	7-9
7-5	Telescope y-Axis Rate Error	7-10
7-6	Telescope z-Axis Rate Error	7-10
7-7	Pedestal x-Axis Rotation.	7-11
7-8	Pedestal y-Axis Rotation.	7-11
7-9	Pedestal z-Axis Rotation.	7-12
7-10	Pedestal x-Axis Rate.	7-12
7-11	Pedestal y-Axis Rate.	7-13
7-12	Pedestal z-Axis Rate.	7-13
7-13	Pedestal x-Axis CM Translation.	7-14
7-14	Pedestal y-Axis CM Translation.	7-14
7-15	Pedestal z-Axis CM Translation.	7-15
7-16	Pedestal x-Axis CM Rate	7-15
7-17	Pedestal y-Axis CM Rate	7-16
7-18	Pedestal z-Axis CM Rate	7-16
7-19	x-Axis Control Torque	7-17
7-20	y-Axis Control Torque	7-17

CONTENTS

		Page
7-21	z-Axis Control Torque	7-18
7-22	Telescope x-Axis Pointing Error	7-19
7-23	Telescope y-Axis Pointing Error	7-19
7-24	Telescope z-Axis Pointing Error	7-20
7-25	Telescope x-Axis Rate Error	7-20
7-26	Telescope y-Axis Rate Error	7-21
7-27	Telescope z-Axis Rate Error	7-21
7-28	Pedestal x-Axis Rotation.	7-22
7-29	Pedestal y-Axis Rotation.	7-22
7-30	Pedestal z-Axis Rotation.	7-23
7-31	Pedestal x-Axis Rate.	7-23
7-32	Pedestal y-Axis Rate.	7-24
7-33	Pedestal z-Axis Rate.	7-24
7-34	Pedestal x-Axis CM Translation.	7-25
7-35	Pedestal y-Axis CM Translation.	7-25
7-36	Pedestal z-Axis CM Translation.	7-26
7-37	Pedestal x-Axis CM Velocity	7-26
7-38	Pedestal y-Axis CM Velocity	7-27
7-39	Pedestal z-Axis CM Velocity	7-27
7-40	x-Axis Control Torque	7-28
7-41	y-Axis Control Torque	7-28
7-42	z-Axis Control Torque	7-29
7-43	Telescope x-Axis Pointing Error	7-30
7-44	Telescope y-Axis Pointing Error	7-30
7-45	Telescope z-Axis Pointing Error	7-31
7-46	Telescope x-Axis Rate Error	7-31
7-47	Telescope y-Axis Rate Error	7-32
7-48	Telescope z-Axis Rate Error	7-32
7-49	Pedestal x-Axis Rotation.	7-33
7-50	Pedestal y-Axis Rotation.	7-33
7-51	Pedestal z-Axis Rotation.	7-34
7-52	Pedestal x-Axis Rate.	7-34
7-53	Pedestal y-Axis Rate.	7-35
7-54	Pedestal z-Axis Rate.	7-35
7-55	Pedestal x-Axis CM Translation.	7-36
7-56	Pedestal y-Axis CM Translation.	7-36
7-57	Pedestal z-Axis CM Translation.	7-37
7-58	Pedestal x-Axis CM Velocity	7-37
7-59	Pedestal y-Axis CM Velocity	7-38
7-60	Pedestal z-Axis CM Velocity	7-38
7-61	x-Axis Control Torque	7-39
7-62	y-Axis Control Torque	7-39

CONTENTS (Continued)

		Page
7-63	z-Axis Control Torque	7-40
7-64	Telescope x-Axis Tracking Error	7-41
7-65	Telescope y-Axis Tracking Error	7-41
7-66	Telescope z-Axis Tracking Error	7-42
7-67	Telescope x-Axis Tracking Rate Error	7-42
7-68	Telescope y-Axis Tracking Rate Error	7-43
7-69	Telescope z-Axis Tracking Rate Error	7-43
7-70	Pedestal x-Axis Rotation	7-44
7-71	Pedestal y-Axis Rotation	7-44
7-72	Pedestal z-Axis Rotation	7-45
7-73	Pedestal x-Axis Rate	7-45
7-74	Pedestal y-Axis Rate	7-46
7-75	Pedestal z-Axis Rate	7-46
7-76	Pedestal x-Axis CM Translation	7-47
7-77	Pedestal y-Axis CM Translation	7-47
7-78	Pedestal z-Axis CM Translation	7-48
7-79	Pedestal x-Axis CM Velocity	7-48
7-80	Pedestal y-Axis CM Velocity	7-49
7-81	Pedestal z-Axis CM Velocity	7-49
7-82	x-Axis Control Torque	7-50
7-83	y-Axis Control Torque	7-50
7-84	z-Axis Control Torque	7-51
7-85	X-UV (Soft X-Ray) Spectroheliograph	7-52
7-86	Raster Scan Command Profiles	7-52
7-87	Telescope y-Axis Peak Pointing Error vs x and y Linear Suspension Stiffness	7-53
7-88	Telescope Peak Pointing Error vs Linear Suspension Stiffness	7-54
7-89	Telescope x-Axis Pointing Error	7-55
7-90	Telescope y-Axis Pointing Error	7-55
7-91	Telescope z-Axis Pointing Error	7-56
7-92	Telescope x-Axis Rate Error	7-56
7-93	Telescope y-Axis Rate Error	7-57
7-94	Telescope z-Axis Rate Error	7-57
7-95	Pedestal x-Axis Rotation	7-58
7-96	Pedestal y-Axis Rotation	7-58
7-97	Pedestal z-Axis Rotation	7-59
7-98	Pedestal x-Axis Rate	7-59
7-99	Pedestal y-Axis Rate	7-60
7-100	Pedestal z-Axis Rate	7-60
7-101	Pedestal x-Axis CM Translation	7-61
7-102	Pedestal y-Axis CM Translation	7-61

CONTENTS (Continued)

		Page
7-103	Pedestal z-Axis CM Translation.	7-62
7-104	Pedestal x-Axis CM Velocity	7-62
7-105	Pedestal y-Axis CM Velocity	7-63
7-106	Pedestal z-Axis CM Velocity	7-63
7-107	x-Axis Control Torque	7-64
7-108	y-Axis Control Torque	7-64
7-109	z-Axis Control Torque	7-65
7-110	Telescope x-Axis Pointing Error	7-66
7-111	Telescope y-Axis Pointing Error	7-66
7-112	Telescope z-Axis Pointing Error	7-67
7-113	Telescope x-Axis Rate Error	7-67
7-114	Telescope y-Axis Rate Error	7-68
7-115	Telescope z-Axis Rate Error	7-68
7-116	Pedestal x-Axis Rotation.	7-69
7-117	Pedestal y-Axis Rotation.	7-69
7-118	Pedestal z-Axis Rotation.	7-70
7-119	Pedestal x-Axis Rate.	7-70
7-120	Pedestal y-Axis Rate.	7-71
7-121	Pedestal z-Axis Rate.	7-71
7-122	Pedestal x-Axis CM Translation.	7-72
7-123	Pedestal y-Axis CM Translation.	7-72
7-124	Pedestal z-Axis CM Translation.	7-73
7-125	Pedestal x-Axis CM Velocity	7-73
7-126	Pedestal y-Axis CM Velocity	7-74
7-127	Pedestal z-Axis CM Velocity	7-74
7-128	x-Axis Control Torque	7-75
7-129	y-Axis Control Torque	7-75
7-130	z-Axis Control Torque	7-76
7-131	Telescope x-Axis Pointing Error	7-77
7-132	Telescope y-Axis Pointing Error	7-77
7-133	Telescope z-Axis Pointing Error	7-78
7-134	Telescope x-Axis Rate Error	7-78
7-135	Telescope y-Axis Rate Error	7-79
7-136	Telescope z-Axis Rate Error	7-79
7-137	Pedestal x-Axis Rotation.	7-80
7-138	Pedestal y-Axis Rotation.	7-80
7-139	Pedestal z-Axis Rotation.	7-81
7-140	Pedestal x-Axis Rate.	7-81
7-141	Pedestal y-Axis Rate.	7-82
7-142	Pedestal z-Axis Rate.	7-82
7-143	Pedestal x-Axis CM Translation.	7-83
7-144	Pedestal y-Axis CM Translation.	7-83

CONTENTS (Continued)

		Page
7-145	Pedestal z-Axis CM Translation.	7-84
7-146	Pedestal x-Axis CM Velocity	7-84
7-147	Pedestal y-Axis CM Velocity	7-85
7-148	Pedestal z-Axis CM Velocity	7-85
7-149	x-Axis Control Torque	7-86
7-150	y-Axis Control Torque	7-86
7-151	z-Axis Control Torque	7-87
7-152	Telescope x-Axis Tracking Error	7-88
7-153	Telescope y-Axis Tracking Error	7-88
7-154	Telescope z-Axis Tracking Error	7-89
7-155	Telescope x-Axis Tracking Rate Error.	7-89
7-156	Telescope y-Axis Tracking Rate Error.	7-90
7-157	Telescope z-Axis Tracking Rate Error.	7-90
7-158	Pedestal x-Axis Rotation.	7-91
7-159	Pedestal y-Axis Rotation.	7-91
7-160	Pedestal z-Axis Rotation.	7-92
7-161	Pedestal x-Axis Rate.	7-92
7-162	Pedestal y-Axis Rate.	7-93
7-163	Pedestal z-Axis Rate.	7-93
7-164	Pedestal x-Axis CM Translation.	7-94
7-165	Pedestal y-Axis CM Translation.	7-94
7-166	Pedestal z-Axis CM Translation.	7-95
7-167	Pedestal x-Axis CM Velocity	7-95
7-168	Pedestal y-Axis CM Velocity	7-96
7-169	Pedestal z-Axis CM Velocity	7-96
7-170	x-Axis Control Torque	7-97
7-171	y-Axis Control Torque	7-97
7-172	z-Axis Control Torque	7-98
8-1	Schematic of Vehicle in Earth Orbit	8-14
8-2	Planar Schematic of Vehicle in Earth Orbit. . . .	8-15
8-3	Peak Angular Acceleration vs Orbital Altitude . . .	8-16
8-4	Peak Rate of Change of Acceleration vs Orbital Altitude.	8-17
9-1	Telescope x-Axis Tracking Error	9-12
9-2	Telescope y-Axis Tracking Error	9-12
9-3	Telescope z-Axis Tracking Error	9-13
9-4	Telescope x-Axis Tracking Rate Error.	9-13
9-5	Telescope y-Axis Tracking Rate Error.	9-14
9-6	Telescope z-Axis Tracking Rate Error.	9-14
9-7	Pedestal x-Axis Rotation.	9-15
9-8	Pedestal y-Axis Rotation.	9-15
9-9	Pedestal z-Axis Rotation.	9-16
9-10	Pedestal z-Axis Rate.	9-16

CONTENTS (Continued)

		Page
9-11	Pedestal y-Axis Rate.	9-17
9-12	Pedestal z-Axis Rate.	9-17
9-13	Pedestal x-Axis CM Translation.	9-18
9-14	Pedestal y-Axis CM Translation.	9-18
9-15	Pedestal z-Axis CM Translation.	9-19
9-16	Pedestal x-Axis CM Velocity	9-19
9-17	Pedestal y-Axis CM Velocity	9-20
9-18	Pedestal z-Axis CM Velocity	9-20
9-19	x-Axis Control Torque	9-21
9-20	y-Axis Control Torque	9-21
9-21	z-Axis Control Torque	9-22
9-22	Telescope x-Axis Tracking Error	9-23
9-23	Telescope y-Axis Tracking Error	9-23
9-24	Telescope z-Axis Tracking Error	9-24
9-25	Telescope x-Axis Tracking Rate.	9-24
9-26	Telescope y-Axis Tracking Rate Error.	9-25
9-27	Telescope z-Axis Tracking Rate Error.	9-25
9-28	Pedestal x-Axis Rotation.	9-26
9-29	Pedestal y-Axis Rotation.	9-26
9-30	Pedestal z-Axis Rotation.	9-27
9-31	Pedestal x-Axis Rate.	9-27
9-32	Pedestal y-Axis Rate.	9-28
9-33	Pedestal z-Axis Rate.	9-28
9-34	Pedestal x-Axis CM Translation.	9-29
9-35	Pedestal y-Axis CM Translation.	9-29
9-36	Pedestal z-Axis CM Translation.	9-30
9-37	Pedestal x-Axis CM Velocity	9-30
9-38	Pedestal y-Axis CM Velocity	9-31
9-39	Pedestal z-Axis CM Velocity	9-31
9-40	x-Axis Control Torque	9-32
9-41	y-Axis Control Torque	9-32
9-42	z-Axis Control Torque	9-33
9-43	Telescope y-Axis Tracking Error	9-34
9-44	Telescope y-Axis Tracking Rate Error.	9-34
9-45	Pedestal y-Axis Rotation.	9-35
9-46	Pedestal y-Axis Rate.	9-35
9-47	Pedestal x-Axis CM Translation.	9-36
9-48	Pedestal z-Axis CM Translation.	9-36
9-49	Pedestal x-Axis CM Velocity	9-37
9-50	Pedestal z-Axis CM Velocity	9-37
9-51	y-Axis Control Torque	9-38
9-52	Telescope Pointing Error vs Suspension Stiffness for 2 Hz Pointing Control Loop Bandwidth. . . .	9-39

CONTENTS (Continued)

		Page
9-53	Telescope Inertia vs Orbital Altitude	9-40
9-54	Orbital Altitude (Km)	9-41
9-55	Telescope x-Axis Tracking Error	9-42
9-56	Telescope y-Axis Tracking Error	9-42
9-57	Telescope z-Axis Tracking Error	9-43
9-58	Telescope x-Axis Tracking Rate Error.	9-43
9-59	Telescope y-Axis Tracking Rate Error.	9-44
9-60	Telescope z-Axis Tracking Rate Error.	9-44
9-61	Pedestal x-Axis Rotation.	9-45
9-62	Pedestal y-Axis Rotation.	9-45
9-63	Pedestal z-Axis Rotation.	9-46
9-64	Pedestal x-Axis Rate.	9-46
9-65	Pedestal y-Axis Rate.	9-47
9-66	Pedestal z-Axis Rate.	9-47
9-67	Pedestal x-Axis CM Translation.	9-48
9-68	Pedestal y-Axis CM Translation.	9-48
9-69	Pedestal z-Axis CM Translation.	9-49
9-70	Pedestal x-Axis CM Velocity	9-49
9-71	Pedestal y-Axis CM Velocity	9-50
9-72	Pedestal z-Axis CM Velocity	9-50
9-73	x-Axis Control Torque	9-51
9-74	y-Axis Control Torque	9-51
9-75	z-Axis Control Torque	9-52
10-1	Simplified Block Diagram of the IPS for Separate Rate Plus Position Sensor Implementation.	10-26
10-2	Contour for Noise Integral Evaluation	10-27
10-3	Simplified Block Diagram of the IPS with Rate Gyro Noise	10-28
10-4	Simplified Block Diagram of the IPS with Torquer Noise Input	10-29
10-5	Noise Torque Due to Position Sensor Noise (Equation 10-38).	10-30
10-6	Comparison of Position Sensor Noise Equivalent Angle Requirements from Pointing Stability and Torque Noise Viewpoints (Equations 10-40, 10-41).	10-31
10-7	IPS Loop Bandwidth for Which Position Sensor Noise Equivalent Angle Requirements are Equal from Both Pointing Stability and Torquer Noise Viewpoints (Equation 10-42).	10-32
10-8	Torquer Noise Resulting from Allowable Rate Gyro Noise Considering Stability Only (Equation 10-48)	10-33

CONTENTS (Concluded)

		Page
10-9	Comparison of Rate Sensor Equivalent Rate Error Requirements from Pointing Stability and Torque Noise Viewpoints (Equations 10-50, 10-51)	10-34
10-10	IPS Loop Bandwidth for Which Noise Equivalent Rate Error Requirements are Equal from Both Pointing Stability and Torquer Noise Viewpoints (Equation 10-52).	10-35
10-11	Simplified Block Diagram for Rate Gyro Hold Sensor Implementation.	10-36
10-12	Analog Rate Gyro Update Loop.	10-37
10-13	Modified Analog Rate Gyro Update Loop	10-37
10-14	Simplified Block Diagram of IOG Control Loop Using Derived Rate Sensor Implementation.	10-38
10-15	Noise Torque Due to Position Sensor Noise from Pointing Stability Viewpoint Only	10-39
10-16	Comparison of Position Sensor Noise Equivalent Angle Requirements from Pointing Stability and Torque Noise Viewpoints (Equations 10-119, 10-120)	10-40
10-17	IPS Loop Bandwidth for Which Position Sensor Noise Equivalent Angle Requirements are Equal from Both Pointing Stability and Torquer Range Utilization Viewpoints.	10-41

Table

2-1	IOG Parameters.	2-18
3-1	Summary of IOG Stability Studies.	3-6
4-1	Legend for Computer Plots	4-4
5-1	Limit Cycle Amplitude for Zero Telescope Look Angle	5-16
5-2	Limit Cycle Amplitude for 40° Telescope Look Angle.	5-22
7-1	Recommended Suspension Parameters	7-6
8-1	Peak Angular Acceleration as a Function of Orbital Altitude.	8-11
8-2	Peak Rate of Change of Acceleration	8-13
9-1	Telescope Tracking Error Mass and Inertia Characteristics That Can be Accommodated by the IPS During Earth Point Tracking	9-6
9-2	Peak Pedestal Rotations and CM Translations Incurred During Earth Point Tracking.	9-8

1. INTRODUCTION

Examination of candidate experiments projected for the joint European/American Spacelab program indicates that a considerable number of these require pointing stabilities of $\pm$ 1 arc-second or better which far exceeds the pointing stability capability of the Shuttle Orbiter. In addition, a number of experiments require accurate slewing, i.e., to within $\pm$ 1 arc-second of a defined trajectory, in order to track a point on Earth with great precision. It is, therefore, clear that a pointing system is needed in order to meet Spacelab experiment requirements. To this end, the European Space Agency (ESA) under the auspices of their ESTEC branch, working in conjunction with Dornier Systems, is developing an Instrument Pointing System (IPS) which is projected to meet Spacelab experiment requirements. The IPS being developed is a three axis gimballed system which mates with the back end of a prospective payload resulting in a large mass offset (i.e., distance between telescope C.M. and gimbal intersection point). The effects of the large mass offset are counteracted by a suspension system which isolates the IPS from disturbances such as man motion, RCS thruster firings, etc., that arise in the orbiter. The Bendix Corporation, under contract to Marshall Spaceflight Center, has been conducting studies on the IPS for the past year. The objective of these studies is to determine the performance capabilities of the IPS in order to aid NASA in their support of the ESA IPS design by making the findings of the study available in a timely manner. Modifications that would result in overall improved IPS performance could be then incorporated in the IPS design in a cost effective manner resulting in an experiment pointing system that will meet the broadest possible experiment requirements.

This report describes the study results obtained to date on the performance capabilities and limitations of the IPS as presently conceived by ESTEC and offers some suggestions of design modifications that if implemented will result in overall improved IPS performance. Since the design and configuration of the IPS has been modified over the period of time this study has been performed, a portion of the study has been performed with the Inside-Out Gimbal (IOG) configuration which was subsequently updated to the present Coincident Gimbal System configuration. However, due to the similarity of the two systems, the results obtained for the IOG also apply to the Coincident Gimbal System.

This report consists of two volumes. The first, which is the main body of the report, describes the analyses and simulations performed during the course of the study and the conclusions and recommendations resulting from these investigations. The second volume, which is an appendix to the main body of this report, presents all of the eigenvalue data obtained upon which the results of the IPS system stability analysis presented in section 3.0 are based. In addition, Coincident Gimbal earth point tracking time histories that were not included in the main body of the report are presented in the appendix.

2. MODEL DESCRIPTION

Two mathematical models describing two types of Instrument Pointing System (IPS) configurations were developed in the course of the study. The types of IPS for which mathematical models were developed are the Inside-Out Gimbal (IOG) and the Offset Gimbal System configurations. Only the IOG model was computer implemented since the Offset Gimbal System configuration was eliminated from contention as being a viable system configuration.

The IOG model is a large angle nonlinear model consisting of three bodies. One body represents the shuttle orbiter and pallet, the second represents the IOG pedestal, and the third represents the instrument plus the inner (i.e., inertial) gimbal upon which the instrument mounts. Features of the model include:

a. Full strapdown equations of motion describing the relative orientation between pedestal and instrument.

b. Nonlinear Euler terms due to telescope rotation.

c. Full six degree of freedom suspension dynamics between pallet and Coincident Gimbal pedestal.

d. Complete representation of gimbal wire torques.

e. Small and large angle tracking capability.

f. Sensor and actuator dynamics.

The Offset Gimbal math model is a large angle nonlinear model consisting of eight bodies. One body represents the shuttle orbiter and pallet, six bodies are used to represent the Offset Gimbal System configuration, and one body represents the instrument. Features of the mathematical formulation are:

a. Offset gimbal flexibility characterization including flexible interface between inertially stable gimbal and instrument.

b. Full strapdown equations of motion.

c. Nonlinear Euler terms due to various body rotations.

f. Capability of mounting sensors on inertial gimbal or or instrument.

In addition, a linear stability model was developed for the Coincident Gimbal by formulating the system "A" matrix and obtaining the corresponding system eigenvalues. This model was used extensively to determine the stability boundaries of the coincident gimbal system configuration to control system and geometric parameter variations.

2.1 IOG Mathematical Model - The sections that follow will outline the derivation of the mathematical model used to determine IOG pointing and slewing performance.

2.1.1 Translational Equations of Motion - Referring to figure 2-1, the following translational equations of motion can be written for the system depicted.

$$F_{1e}+F_{c12}=m_1\ddot{\rho}_1 \tag{2-1}$$

$$F_{2e}-F_{c12}+F_H=m_2\ddot{\rho}_2 \tag{2-2}$$

$$F_{3e}-F_H=m_3\ddot{\rho}_3 \tag{2-3}$$

$$\sum_{j=1}^{3} F_{je}=M\ddot{\rho}_o;\ M=(m_1+m_2+m_3) \tag{2-4}$$

where:

$F_{je}(j=1,2,3)$ = external forces applied to bodies 1 thru 6 respectively

F_{c12} = compliance force between bodies 1 and 2,

F_H = hinge force between bodies 2 and 3

$m_j(j=1,2,3)$ = mass of bodies 1 thru 3

$\rho_j(j=1,2,3)$ = distance from origin of arbitrary inertial coordinate frame to center of mass of bodies 1 thru 3

ρ_o = distance from origin of arbitrary inertial coordinate frame to the composite center of mass of the system shown in figure 2-1.

Additionally, from the geometry shown in figure 2-1 we have

$$\rho_1=\rho_o+R_1 \tag{2-5}$$

$$\rho_2=\rho_o+R_2 \tag{2-6}$$

$$\rho_3=\rho_o+R_3 \tag{2-7}$$

where:

R_j (j=1,2,3) = distance from composite center of mass to the center of mass of bodies 1 thru 3

From the definition of the composite system center of mass

$$m_1R_1+m_2R_2+m_3R_3=0 \tag{2-8}$$

Also from geometrical considerations

$$R_2=R_1+R_{120}+\varepsilon_{12} \tag{2-9}$$

$$R_3=R_1+R_{120}+\varepsilon_{12}+r_1+r_2 \tag{2-10}$$

where:

R_{120} = inertially fixed vector directed from the CM of body 1 to body 2 when the system is in an unstressed state

ε_{12} = relative linear displacement between bodies 1 and 2 measured with respect to R_{120}

r_1 = distance from CM of body 2 to gimbal hinge point

r_2 = distance from gimbal hinge point to CM of body 3

Substituting equations (2-9) and (2-10) into equation (2-8) and solving for R_1 yields

$$R_1=-\frac{1}{M}\left[(m_2+m_3)(R_{120}+\varepsilon_{12})+m_3(r_1+r_2)\right] \tag{2-11}$$

Substituting equations (2-7), (2-11), and (2-4) into equation (2-3) and solving for the hinge force yields

$$F_H = \frac{1}{M}\left[(m_1+m_2)F_{3e} - m_3(F_{1e}+F_{2e}) - m_1 m_3 \ddot{\varepsilon}_{12} - m_3(m_1+m_2)(\ddot{r}_1+\ddot{r}_2)\right] \qquad (2\text{-}12)$$

The compliance force between bodies 1 and 2 of the k^{th} isolator can be written as

$$F_{c12k} = K_{12}\cdot\varepsilon_{12} + D_{12}\cdot\dot{\varepsilon}_{12} + K_{12}\cdot\left[(\beta^{12}_{k2}-\beta^{12}_{k20}) - (\beta^{12}_{k1}-\beta^{12}_{k10})\right] + D_{12}\cdot\left[\dot{\beta}^{12}_{k2}-\dot{\beta}^{12}_{k1}\right] \qquad (2\text{-}13)$$

where:

$\beta^{12}_{k1}(k=1,\ldots,4)$ = distance from CM of body 1 to the k^{th} lumped spring damper between bodies 1 and 2 on the body 1 side of the k^{th} spring damper system. This vector is fixed in body 1.

$\beta^{12}_{k2}(k=1,\ldots,4)$ = distance from CM of body 2 to the k^{th} lumped spring damper between bodies 1 and 2 on the body 2 side of the k^{th} spring damper system. This vector is fixed in body 2.

$\beta^{12}_{k10}(k=1,\ldots,4)$ = value of β^{12}_{k1} when system is unstressed.

$\beta^{12}_{k20}(k=1,\ldots,4)$ = value of β^{12}_{k2} when system is unstressed.

K_{12} = spring constant between bodies 1 and 2.

D_{12} = damping constant of spring damper between bodies 1 and 2.

The damping and spring constants are defined as diagonal matrices in the following manner

$$K_{12} = \mathrm{diag}\left[K_{12x}; K_{12y}; K_{12z}\right] \qquad (2\text{-}14)$$

$$D_{12} = \mathrm{diag}\left[D_{12x}; D_{12y}; D_{12z}\right] \qquad (2\text{-}15)$$

For small angular rotations of bodies 1 and 2 the following relations apply

$$\beta_{k1}^{12}=\beta_{k10}^{12}+\theta_1 x\beta_{k10}^{12} \tag{2-16}$$

$$\beta_{k2}^{12}=\beta_{k20}^{12}+\theta_2 x\beta_{k20}^{12} \tag{2-17}$$

$$\dot{\beta}_{k1}^{12}=\omega_1 x\beta_{k10}^{12} \tag{2-18}$$

$$\dot{\beta}_{k2}^{12}=\omega_2 x\beta_{k20}^{12} \tag{2-19}$$

In addition

$$\beta_{k10}^{12}=R_{120}+R_{E20}+\alpha_{k20}^{12} \tag{2-20}$$

$$\beta_{k20}^{12}=R_{E20}+\alpha_{k20}^{12} \tag{2-21}$$

where:

θ_1 = angular rotation of body 1

θ_2 = angular rotation of body 2

ω_1 = angular rate of body 1

ω_2 = angular rate of body 2

R_{E20} = inertial vector equal to the distance from CM of body 2 to center of elasticity of spring damper system between bodies 1 and 2 when the system is unstressed

$\alpha_{k20}^{12}(k=1,\ldots,4)$ = inertial vector equal to the distance from the center of elasticity of the spring damper system between bodies 1 and 2 to the k^{th} spring damper of that system.

Substituting equations (2-16) thru (2-21) into equation (2-13) and rearranging terms yields

$$F_{c12k}=K_{12}\cdot\left[\varepsilon_{12}+(\theta_2-\theta_1)xR_{E20}-\theta_1xR_{120}+(\theta_2-\theta_1)x\alpha_{k20}^{12}\right]$$
$$+D_{12}\cdot\left[\dot{\varepsilon}_{12}+(\omega_2-\omega_1)xR_{E20}+(\omega_2-\omega_1)x\alpha_{k20}^{12}-\omega_1xR_{120}\right] \qquad (2-22)$$

However

$$F_{c12}=\sum_{k=1}^{4}F_{c12k} \qquad (2-23)$$

Substituting equation (2-22) into equation (2-23) and performing the indicated summations yields

$$F_{c12}=K_{12}\cdot\left[4\varepsilon_{12}+4(\theta_2-\theta_1)xR_{E20}-4\theta_1xR_{120}+(\theta_2-\theta_1)x\sum_{k=1}^{4}\alpha_{k20}^{12}\right] \qquad (2-24)$$

$$+D_{12}\cdot\left[4\dot{\varepsilon}_{12}+4(\omega_2-\omega_1)xR_{E20}-4\omega_1xR_{120}+(\omega_2-\omega_1)x\sum_{k=1}^{4}\alpha_{k20}^{12}\right] \qquad (2-25)$$

However, by the definition of center of elasticity

$$\sum_{k=1}^{4}\alpha_{K20}^{12}=0 \qquad (2-26)$$

Therefore

$$F_{c12}=4K_{12}\cdot\left[\varepsilon_{12}+(\theta_2-\theta_1)xR_{E20}-\theta_1xR_{120}\right]$$
$$+4D_{12}\cdot\left[\dot{\varepsilon}_{12}+(\omega_2-\omega_1)xR_{E20}-\omega_1xR_{120}\right]$$

A force equation will be required in order to solve for ε_{12}. This equation is obtained by substituting equations (2-26), (2-11) and (2-5) into equation (2-1) which results in

$$\frac{m_2+m_3}{M} F_{1e} - \frac{m_1}{M}(F_{2e}+F_{3e}) = -\left[\frac{m_1}{M}(m_2+m_3)\ddot{\varepsilon}_{12}+4D\cdot\dot{\varepsilon}_{12}+4K_{12}\cdot\varepsilon_{12}\right]$$

$$+4D_{12}\cdot\left[(\omega_1-\omega_2)xR_{E20}+\omega_1xR_{120}\right]+4K_{12}\cdot\left[(\theta_1-\theta_2)xR_{E20}+\theta_1xR_{120}\right]$$

$$-\frac{m_1m_3}{M}(\ddot{r}_1+\ddot{r}_2) \qquad (2-27)$$

2.1.2 Rotational Equations of Motion - The following paragraphs will develop the rotational equations of motion of the system depicted in figure 2-1. In this development it will be assumed that the coordinate frames of bodies 1 and 2 are aligned. However, the coordinate frame of body 3 can be at an arbitrary orientation with respect to bodies 1 and 2.

Body 1 - The rotational equation of motion for body 1 can be written as

$$T_{1e}+R_{11}xF_{1e}+\sum_{k=1}^{4}\beta_{k1}^{12}xF_{c12k}=\frac{d}{dt}(J_1\cdot\omega_1)$$

Substituting equations (2-16), (2-20) and (2-22) into equation (2-28) and doing the indicated summation eliminating second order terms yields

$$T_{1e}+R_{11}xF_{1e}=\frac{d}{dt}(J_1\cdot\omega_1)+d_{12}\cdot(\omega_1-\omega_2)+k_{12}\cdot(\theta_1-\theta_2)$$

$$+4(R_{120}+R_{E20})x\left\{D_{12}\cdot\left[(\omega_1-\omega_2)xR_{E20}+\omega_1xR_{120}\right]\right.$$

$$\left.+K_{12}\cdot\left[(\theta_1-\theta_2)xR_{E20}+\theta_1xR_{120}\right]\right\}-4(R_{120}+R_{E20})x\left[D_{12}\cdot\dot{\varepsilon}_{12}+K_{12}\cdot\varepsilon_{12}\right] \qquad (2-29)$$

where

$$k_{12}=\text{diag}\{4K_{12z}(\alpha^{12}_{120y})^2;4K_{12z}(\alpha^{12}_{120x})^2;4[K_{12y}(\alpha^{12}_{120x})^2+K_{12x}(\alpha^{12}_{120y})^2]\}$$

$$d_{12}=\text{diag}\{4D_{12z}(\alpha^{12}_{120y})^2;4D_{12z}(\alpha^{12}_{120x})^2;4[K_{12z}\ \alpha^{12}_{120x})^2+D_{12x}(\alpha^{12}_{120y})^2]\}$$

$T_{je}(j=1,2,3)$= External torque acting on j^{th} body

Body 2 - The rotational equation of motion for body 2 can be written as

$$T^2_{WT}+T_{2e}-T^2_H+R_{22}xF_{2e}-\sum_{k=1}^{4}\beta^{12}_{k2}xF_{c12k}+r_1xF_H=\frac{d}{dt}(J_2\cdot\omega_2) \qquad (2\text{-}30)$$

Substituting equations (2-12), (2-17), (2-21), and (2-22) into equation (2-30) and eliminating second order terms gives

$$T^2_{WT}+T_{2e}+R_{22}xF_{2e}+\frac{(m_1+m_2)}{M}r_1xF^2_{3e}-\frac{m_3}{M}r_1x(F_{1e}+F_{2e})=\frac{d}{dt}(J_2\cdot\omega_2)+d_{12}\cdot(\omega_2-\omega_1)$$

$$+k_{12}\cdot(\theta_2-\theta_1)+4R_{E20}x\left\{D_{12}\cdot\left[(\omega_2-\omega_1)xR_{E20}-\omega_1xR_{120}\right]+K_{12}\cdot\left[(\theta_2-\theta_1)xR_{E20}-\theta_1xR_{120}\right]\right\}$$

$$+\frac{m_1m_3}{M}r_1x\ddot{\varepsilon}_{12}+4R_{E20}x\left[D_{12}\cdot\dot{\varepsilon}_{12}+K_{12}\cdot\varepsilon_{12}\right]+\frac{m_3(m_1+m_2)}{M}r_1(\ddot{r}_1x\ddot{r}^2_2)+T^2_H \qquad (2\text{-}31)$$

where:

F^2_{3e} = external force acting on body 3 written in body 2 coordinates

T^2_H = hinge torque acting on bodies 2 and 3 written in body 2 coordinates

T^2_{WT}= wire torques applied to body 2 written in body 2 coordinates

r^2_2 = distance from hinge point to CM of body 3 written in body 2 coordinates

Body 3 - The rotational equation of motion for body 3 can be expressed as

$$-T^3_{WT}+T_H+T_{3e}+R_{33}xF_{3e}+r_2xF_H=\frac{d}{dt}(J_3\cdot\omega_3) \tag{2-32}$$

Substituting equation (144) into equation (154) yields

$$-T^3_{WT}+T_{3e}+R_{33}xF_{3e}+\frac{(m_1+m_2)}{M}r_2xF_{3e}-\frac{m_3}{M}r_2x(F^3_{1e}+F^3_{2e})=\frac{d}{dt}(J_3\cdot\omega_3)$$

$$-T_H+\frac{m_1m_3}{M}r_2x\ddot{\varepsilon}^3_{12}+\frac{m_3(m_1+m_2)}{M}r_2x(\ddot{r}^3_1+\ddot{r}_2) \tag{2-33}$$

where:

T^3_{WT} = wire torques applied to body 3 written in body 3 coordinates

F^3_{1e}, F^3_{2e} = external force acting on bodies 1 and 2, respectively, written in body 3 coordinates

ω_3 = angular rate of body 3

r_1 = distance from CM of body 2 to hinge point, written in body 3 coordinates

Rewriting equations (2-27), (2-29), (2-31), and (2-33) in matrix form yields

$$\begin{aligned}
&T_{1e}+\bar{R}_{11}\cdot F_{1e}=J_1\cdot\dot{\omega}_1+d_{12}\cdot(\omega_1-\omega_2)+k_{12}\cdot(\theta_1-\theta_2)\\
&-4(\bar{R}_{120}+\bar{R}_{E20})\cdot\left\{D_{12}\cdot\left[\bar{R}_{E20}\cdot(\omega_1-\omega_2)+\bar{R}_{120}\cdot\omega_1\right]\right.\\
&\left.+K_{12}\cdot\left[\bar{R}_{E20}\cdot(\theta_1-\theta_2)+\bar{R}_{120}\cdot\theta_1\right]\right\}\\
&-4(\bar{R}_{120}+\bar{R}_{E20})\cdot\left[D_{12}\cdot\dot{\varepsilon}_{12}+K_{12}\cdot c_{12}\right]
\end{aligned} \tag{2-34}$$

$$T_{2e}+\bar{R}_{22}\cdot F_{2e}+\frac{m_1+m_2}{M}\bar{r}_1\cdot {}_2T_3\cdot F_{3e}-\frac{m_3}{M}\bar{r}_1\cdot(F_{1e}+F_{2e})=J_2^*\cdot\dot{\omega}_2+d_{12}\cdot(\omega_2-\omega_1)$$
$$+k_{12}\cdot(\theta_2-\theta_1)-4\bar{R}_{E20}\cdot\left\{D_{12}\cdot\left[\bar{R}_{E20}\cdot(\omega_2-\omega_1)-\bar{R}_{120}\cdot\omega_1\right]+K_{12}\cdot\left[\bar{R}_{E20}\cdot(\theta_2-\theta_1)-R_{120}\cdot\theta_1\right]\right\}$$
$$+\frac{m_1m_3}{M}\bar{r}_1\cdot\ddot{\varepsilon}_{12}+4\bar{R}_{E20}\cdot\left[D_{12}\cdot\dot{\varepsilon}_{12}+K_{12}\cdot\varepsilon_{12}\right]-\frac{m_3(m_1+m_2)}{M}\bar{r}_1\cdot\left\{{}_2T_3\cdot\left[\bar{r}_2\cdot\dot{\omega}_3+\bar{\omega}_3\cdot(\bar{r}_2\cdot\omega_3)\right]\right\}$$
$$+{}_2T_3\cdot T_H \qquad (2\text{-}35)$$

$$T_{3e}+\bar{R}_{33}\cdot F_{3e}+\frac{m_1+m_2}{M}\bar{r}_2\cdot F_{3e}-\frac{m_3}{M}\bar{r}_2\cdot {}_2T_3^{-1}\cdot(F_{1e}+F_{2e})=J_3^*\cdot\dot{\omega}_3+\bar{\omega}_3\cdot\left[J_3^*\cdot\omega_3\right]$$
$$+\frac{m_1m_3}{M}\bar{r}_2\cdot\left[{}_2T_3^{-1}\cdot\ddot{\varepsilon}_{12}\right]-\frac{m_3(m_1+m_2)}{M}\bar{r}_2\cdot\left[{}_2T_3^{-1}\cdot\bar{r}_1\cdot\dot{\omega}_2\right]-T_H \qquad (2\text{-}36)$$

$$\frac{m_2+m_3}{M}F_{1e}-\frac{m_1}{M}(F_{2e}+{}_2T_3\cdot F_{3e})=-\left[\frac{m_1}{M}(m_2+m_3)\ddot{\varepsilon}_{12}+4D_{12}\cdot\dot{\varepsilon}_{12}+4K_{12}\cdot\varepsilon_{12}\right]$$
$$-4D_{12}\cdot\left[\bar{R}_{E20}\cdot(\omega_1-\omega_2)+\bar{R}_{120}\cdot\omega_1\right]-4K_{12}\cdot\left[\bar{R}_{E20}\cdot(\theta_1-\theta_2)+\bar{R}_{120}\cdot\theta_1\right]+\frac{m_1m_3}{M}(\bar{r}_1\cdot\dot{\omega}_2)$$
$$+\frac{m_1m_3}{M}\left\{{}_2T_3\cdot\left[\bar{r}_2\cdot\dot{\omega}_3+\bar{\omega}_3\cdot(\bar{r}_2\cdot\omega_3)\right]\right\} \qquad (2\text{-}37)$$

where:

$$J_2^*=\mathrm{diag}\left[J_{2x};J_{2y};J_{2z}\right]+\frac{m_3(m_1+m_2)}{M}\begin{bmatrix}(r_{1y}^2+R_{1z}^2) & -r_{1x}r_{1y} & -r_{1x}r_{1z}\\ -r_{1x}r_{1y} & (r_{1x}^2+R_{1z}^2) & -r_{1y}r_{1z}\\ -r_{1x}r_{1z} & -r_{1y}r_{1z} & (r_{1x}^2+r_{1y}^2)\end{bmatrix} \qquad (2\text{-}38)$$

$$J_3^*=\mathrm{diag}\left[J_{3x};J_{3y};J_{3z}\right]+\frac{m_3(m_1+m_2)}{M}\begin{bmatrix}(r_{2y}^2+r_{2z}^2) & -r_{2x}r_{2y} & -r_{2x}r_{2z}\\ -r_{2x}r_{2y} & (r_{2x}^2+r_{2z}^2) & -r_{2y}r_{2z}\\ -r_{2x}r_{2z} & -r_{2y}r_{2z} & (r_{2x}^2+r_{2y}^2)\end{bmatrix} \qquad (2\text{-}39)$$

$$\bar{\omega}_3=\begin{bmatrix}0 & -\omega_{3z} & \omega_{3y}\\ \omega_{3z} & 0 & -\omega_{3x}\\ -\omega_{3y} & \omega_{3x} & 0\end{bmatrix} \qquad (2\text{-}40)$$

and ${}_2T_3$ is the transformation from body 3 to body 2 coordinates and is equal to

$$ {}_2T_3 = \begin{bmatrix} a_{11} & a_{12} & a_{13} \\ a_{21} & a_{22} & a_{23} \\ a_{31} & a_{32} & a_{33} \end{bmatrix} \tag{2-41} $$

$$ {}_2T_3^{-1} = {}_3T_2 = \begin{bmatrix} a_{11} & a_{21} & a_{31} \\ a_{12} & a_{22} & a_{32} \\ a_{13} & a_{23} & a_{33} \end{bmatrix} \tag{2-42} $$

An assumption inherent in equations (2-34) thru (2-37) is that the nonlinear Euler, centrifugal and Coriolis terms are negligible for bodies 1 and 2. Equations (2-34) thru (2-37) form the complete set of equations of motion of the system shown in figure 2-1.

It now becomes necessary to define the control torques T_H and the computation scheme for updating ${}_2T_3$. The control torques are given by

$$ T_H = -\left[\frac{\omega_{nT}}{s+\omega_{nT}}\right]\left[\frac{\omega_{ns}^2}{s^2+2\zeta_s\omega_{ns}s+\omega_{ns}^2}\right]\left[K_R \cdot\omega_3^* + K_P \cdot\theta_3^* + K_I \cdot\frac{\theta_3^*}{s}\right] \tag{2-43} $$

and

$$ \omega_3^* = (\omega_3 - \omega_{3c}) \tag{2-44} $$

$$ \theta_3^* = (\theta_3 - \theta_{3c}) \tag{2-45} $$

$$ \theta_{3c} = \int_0^t \omega_{3c}\,dt \tag{2-46} $$

where:

$$ K_R = \text{diag}\left[K_{Rx}\ ; K_{Ry}\ ; K_{Rz}\right] \tag{2-47} $$

$$ K_P = \text{diag}\left[K_{Px}\ ; K_{Py}\ ; K_{Pz}\right] \tag{2-48} $$

$$K_I = \text{diag}\left[K_{Ix} ; K_{Iy} ; K_{Iz}\right] \tag{2-49}$$

where

K_R = system rate gain $\frac{n\text{-}m}{rad/sec}$

K_P = system position gain $\frac{n\text{-}m}{rad}$

K_I = system integral gain $\frac{n\text{-}m}{sec}$

ω_{3c} = rate command vector

θ_{3c} = angular position command

$\frac{1}{\omega_{nT}}$ = gimbal torquer time constant

ω_{ns} = rate gyro natural frequency

ζ_s = rate gyro damping ratio

2.1.3 Computational Scheme for Updating ${}_3T_2$ - In order to complete the equations of motion given in equations (2-34) thru (2-37), a method for computationally updating the transformation from body 3 to body 2 coordinates must be specified. Since the effects of gimbal wire torques is to be evaluated in the course of the study it will be convenient to express ${}_3T_2$ in terms of modified Euler angles and update the transformation by integration of Euler rate equations. In this manner, the Euler angles and rates will always be known, which will be convenient for computing wire torques and gimbal friction which depend functionally on Euler angles and rates. In addition, none of the gimbal angles approach $\pi/2$ rad (90 degrees) which eliminates the singularity problem encountered when Euler angles are used as the strapdown computation algorithm.

In order to properly compute the transformation between bodies 2 and 3 coordinates the rotation sequence between the bodies must be specified. For the IPS that rotation sequence is z, y, x when going from body 2 to body 3. In addition, since bodies 2 and 3 rotate independently of each other relative Euler angles and rates

which are a function of these rotations must be computed in order to properly specify the transformation. Equations (2-50) thru (2-52) specify the transformation matrices going from body 2 to body 3.

$$\begin{bmatrix} X_o \\ Y_o \\ Z_o \end{bmatrix} = \begin{bmatrix} \cos\theta_z & \sin\theta_z & 0 \\ -\sin\theta_z & \cos\theta_z & 0 \\ 0 & 0 & 1 \end{bmatrix} \begin{bmatrix} X_b \\ Y_b \\ Z_b \end{bmatrix} \tag{2-50}$$

$$\begin{bmatrix} X_m \\ Y_m \\ Z_m \end{bmatrix} = \begin{bmatrix} 1 & 0 & 0 \\ 0 & \cos\phi_x & \sin\phi_x \\ 0 & -\sin\phi_x & \cos\phi_x \end{bmatrix} \begin{bmatrix} X_o \\ Y_o \\ Z_o \end{bmatrix} \tag{2-51}$$

$$\begin{bmatrix} X_i \\ Y_i \\ Z_i \end{bmatrix} = \begin{bmatrix} \cos\psi_y & 0 & -\sin\psi_y \\ 0 & 1 & 0 \\ \sin\psi_y & 0 & \cos\psi_y \end{bmatrix} \begin{bmatrix} X_m \\ Y_m \\ Z_m \end{bmatrix} \tag{2-52}$$

where

X_b, Y_b, Z_b = x,y, and z axis of the pedestal fixed coordinate frame

X_o, Y_o, Z_o = x,y, and z axes of the outer gimbal

X_m, Y_m, Z_m = x,y, and z axes of the middle gimbal

X_i, Y_i, Z_i = x,y, and z axes of the inner or inertial gimbal

θ_z = relative rotation of outer gimbal about the z axis

ϕ_x = relative rotation of the middle gimbal about the x axis

ψ_y = relative rotation of the inner gimbal about the y axis

However

$$\left.\begin{aligned} \theta_z &= \theta_{3z} - \theta_{2z} \\ \varphi_x &= \varphi_{3x} - \varphi_{2x} \\ \psi_y &= \psi_{3y} - \psi_{2y} \end{aligned}\right\} \qquad (2\text{-}53)$$

where

$\theta_{kz}(k=2,3)$ = Euler angle about the z axis due to the k^{th} body inertial rotation

$\phi_{kx}(k=2,3)$ = Euler angle about the x axis due to the k^{th} body inertial rotation

$\psi_{ky}(k=2,3)$ = Euler angle about the y axis due to the k^{th} body inertial rotation

The telescope (i.e., body 3) inertial rate written in terms of Euler rates are given by

$$\begin{bmatrix} \omega_{3x} \\ \omega_{3y} \\ \omega_{3z} \end{bmatrix} = \begin{bmatrix} \cos\psi_y & 0 & -\sin\psi_y \\ 0 & 1 & 0 \\ \sin\psi_y & 0 & \cos\psi_y \end{bmatrix} \begin{bmatrix} 1 & 0 & 0 \\ 0 & \cos\varphi_x & \sin\varphi_x \\ 0 & -\sin\varphi_x & \cos\varphi_x \end{bmatrix} \begin{bmatrix} \dot{\varphi}_{3x} \\ 0 \\ \dot{\theta}_{3z} \end{bmatrix} + \begin{bmatrix} 0 \\ \dot{\psi}_{3y} \\ 0 \end{bmatrix} \qquad (2\text{-}54)$$

Expanding equation (2-54) yields

$$\begin{bmatrix} \omega_{3x} \\ \omega_{3y} \\ \omega_{3z} \end{bmatrix} = \begin{bmatrix} -\cos\varphi_x \sin\psi_y & \cos\psi_y & 0 \\ \sin\varphi_x & 0 & 1 \\ \cos\varphi_x \cos\psi_y & \sin\psi_y & 0 \end{bmatrix} \begin{bmatrix} \dot{\theta}_{3z} \\ \dot{\varphi}_{3x} \\ \dot{\psi}_{3y} \end{bmatrix} \qquad (2\text{-}55)$$

Solving equation (2-55) for the Euler rates gives

$$\begin{bmatrix} \dot{\theta}_{3z} \\ \dot{\psi}_{3x} \\ \dot{\psi}_{3y} \end{bmatrix} = \begin{bmatrix} -\sec\varphi_x \sin\psi_y & 0 & \sec\varphi_x \cos\psi_y \\ \cos\psi_y & 0 & \sin\psi_y \\ \tan\varphi_x \sin\psi_y & 1 & -\tan\varphi_x \cos\psi_y \end{bmatrix} \begin{bmatrix} \omega_{3x} \\ \omega_{3y} \\ \omega_{3z} \end{bmatrix} \qquad (2\text{-}56)$$

The pedestal (i.e., body 2) inertial rates written in terms of Euler rates are given by

$$\begin{bmatrix} \omega_{2x} \\ \omega_{2y} \\ \omega_{2z} \end{bmatrix} = \begin{bmatrix} \cos\theta_z & -\sin\theta_z & 0 \\ \sin\theta_z & \cos\theta_z & 0 \\ 0 & 0 & 1 \end{bmatrix} \begin{bmatrix} 1 & 0 & 0 \\ 0 & \cos\varphi_x & -\sin\varphi_x \\ 0 & \sin\varphi_x & \cos\varphi_x \end{bmatrix} \begin{bmatrix} \dot{\psi}_{2x} \\ \dot{\psi}_{2y} \\ 0 \end{bmatrix} + \begin{bmatrix} 0 \\ 0 \\ \dot{\theta}_{2z} \end{bmatrix} \qquad (2\text{-}57)$$

Expanding and simplifying equation (2-57) gives

$$\begin{bmatrix} \omega_{2x} \\ \omega_{2y} \\ \omega_{2z} \end{bmatrix} = \begin{bmatrix} 0 & \cos\theta_z & -\sin\theta_z \cos\varphi_x \\ 0 & \sin\theta_z & \cos\theta_z \cos\varphi_x \\ 1 & 0 & \sin\varphi_x \end{bmatrix} \begin{bmatrix} \dot{\theta}_{2z} \\ \dot{\psi}_{2x} \\ \dot{\psi}_{2y} \end{bmatrix} \qquad (2\text{-}58)$$

Solving equation (2-58) for the Euler rates due to body 2 gives

$$\begin{bmatrix} \dot{\theta}_{2z} \\ \dot{\psi}_{2x} \\ \dot{\psi}_{2y} \end{bmatrix} = \begin{bmatrix} \sin\theta_z \tan\varphi_x & -\cos\theta_z \tan\varphi_x & 1 \\ \cos\theta_z & \sin\theta_z & 0 \\ -\sin\theta_z \sec\varphi_x & \cos\theta_z \sec\varphi_x & 0 \end{bmatrix} \begin{bmatrix} \omega_{2x} \\ \omega_{2y} \\ \omega_{2z} \end{bmatrix} \qquad (2\text{-}59)$$

The relative Euler rates are obtained by differentiating equation (2-53) and substituting equations (2-56) and (2-59) into the results which yields

$$\left.\begin{aligned}
\dot{\theta}_z &= \omega_{3z}\sec\varphi_x\cos\psi_y - \omega_{3x}\sec\varphi_x\sin\psi_y - (\omega_{2x}\tan\varphi_x\sin\theta_z + \omega_{2y}\tan\varphi_x\cos\theta_z + \omega_{2z}) \\
\dot{\varphi}_x &= \omega_{3x}\cos\psi_y + \omega_{3z}\sin\psi_y - (\omega_{2x}\cos\theta_z + \omega_{2y}\sin\theta_z) \\
\dot{\psi}_y &= \omega_{3x}\tan\varphi_x\sin\psi_y + \omega_{3y} - \omega_{3z}\tan\varphi_x\cos\psi_y - (\omega_{2y}\sec\varphi_x\cos\theta_z - \omega_{2x}\sec\varphi_x\sin\theta_z)
\end{aligned}\right\} \quad (2\text{-}60)$$

The transformation from body 3 to body 2 is given by

$$ {}_2T_3 = \begin{bmatrix} \cos\theta_z & -\sin\theta_z & 0 \\ \sin\theta_z & \cos\theta_z & 0 \\ 0 & 0 & 1 \end{bmatrix} \begin{bmatrix} 1 & 0 & 0 \\ 0 & \cos\varphi_x & -\sin\varphi_x \\ 0 & \sin\varphi_x & \cos\varphi_x \end{bmatrix} \begin{bmatrix} \cos\psi_y & 0 & \sin\psi_y \\ 0 & 1 & 0 \\ -\sin\psi_y & 0 & \cos\psi_y \end{bmatrix} \quad (2\text{-}61)$$

Expanding equation (2-61) yields

$$ {}_2T_3 = \begin{bmatrix} \cos\theta_z\cos\psi_y - \sin\theta_z\sin\varphi_x\sin\psi_y & -\sin\theta_z\cos\varphi_x & \cos\theta_z\sin\psi_y - \sin\theta_z\sin\varphi_x\cos\psi_y \\ \sin\theta_z\cos\psi_y + \cos\theta_z\sin\varphi_x\sin\psi_y & \cos\theta_z\cos\varphi_x & \sin\theta_z\sin\psi_y - \cos\theta_z\sin\varphi_x\cos\psi_y \\ -\cos\varphi_x\sin\psi_y & \sin\varphi_x & \cos\varphi_x\cos\psi_y \end{bmatrix} \quad (2\text{-}62)$$

2.1.4 Specification of Gimbal Wire Torques - The gimbal wire torque characteristic is shown in figure 2-2, where

$T_{\theta z}$ = Wire torque due to relative Euler rotation about the z axis (n-m)

$T_{\phi x}$ = Wire torque due to relative Euler rotation about the x axis (n-m)

$T_{\psi y}$ = Wire torque due to relative Euler rotation about the y axis (n-m)

K_{WT} = Wire torque slope $(\frac{n-m}{rad})$

H_{WT} = Jump in wire torque characteristic when relative Euler rate changes sign (n-m)

Using the transformations given in equations (2-50) thru (2-52) the wire torques acting on body 3 (i.e., the telescope) can be written as

$$\begin{bmatrix} T_{WT3x} \\ T_{WT3y} \\ T_{WT3z} \end{bmatrix} = \begin{bmatrix} \cos\psi_y & 0 & -\sin\psi_y \\ 0 & 1 & 0 \\ \sin\psi_y & 0 & \cos\psi_y \end{bmatrix} \begin{bmatrix} 1 & 0 & 0 \\ 0 & \cos\varphi_x & \sin\varphi_x \\ 0 & -\sin\varphi_x & \cos\varphi_x \end{bmatrix} \begin{bmatrix} -T_{\varphi_x} \\ 0 \\ -T_{\theta z} \end{bmatrix} + \begin{bmatrix} 0 \\ -T_{\psi_y} \\ 0 \end{bmatrix} \qquad (2\text{-}63)$$

Expanding equation (2-63) and rearranging terms yields

$$\begin{bmatrix} T_{WT3x} \\ T_{WT3y} \\ T_{WT3z} \end{bmatrix} = \begin{bmatrix} -\cos\varphi_x \sin\psi_y & \cos\psi_y & 0 \\ \sin\varphi_x & 0 & 1 \\ \cos\varphi_x \cos\psi_y & \sin\psi_y & 0 \end{bmatrix} \begin{bmatrix} -T_{\theta z} \\ -T_{\varphi_x} \\ -T_{\psi_y} \end{bmatrix} \qquad (2\text{-}64)$$

Similarly the wire torques acting on body 2, i.e., the IOG pedestal are given by

$$\begin{bmatrix} T_{WT2x} \\ T_{WT2y} \\ T_{WT2z} \end{bmatrix} = \begin{bmatrix} 0 & \cos\theta_z & -\sin\theta_z \cos\varphi_x \\ 0 & \sin\theta_z & \cos\theta_z \cos\varphi_x \\ 1 & 0 & \sin\varphi_x \end{bmatrix} \begin{bmatrix} T_{\theta z} \\ T_{\varphi_x} \\ T_{\psi_y} \end{bmatrix} \qquad (2\text{-}65)$$

Equation (2-64) and (2-65) combined with equations (2-34), (2-35), (2-36), (2-37), (2-43), (2-60), and (2-62) form the complete mathematical model of the IOG.

Table 2-1 lists a baseline set of parameters for the IOG.

Table 2-1. IOG Parameters

$m_1=8.054\times10^4$ kg	$D_{12x}=D_{12y}=D_{12z}=59.93$ n-sec/m
$m_2=1.95\times10^2$ kg	$K_{12x}=K_{12y}=K_{12z}=125$ n/m
$m_3=2.683\times10^3$ kg	$d_{12x}=14.96$ (n-m-sec)/rad
$J_{1x}=1.551\times10^6$ kg-m^2	$d_{12y}=14.96$ (n-m-sec)/rad
$J_{1y}=6.953\times10^6$ kg-m^2	$d_{12z}=29.92$ (n-m-sec)/rad
$J_{1z}=7.543\times10^6$ kg-m^2	$k_{12x}=31.25$ n-m/rad
$J_{2x}=50$ kg-m^2	$k_{12y}=31.25$ n-m/rad
$J_{2y}=50$ kg-m^2	$k_{12z}=62.5$ n-m/rad
$J_{2z}=50$ kg-m^2	$K_{R3x}=2.214\times10^4$ (n-m-sec)/rad
$J_{3x}=2.903\times10^3$ kg-m^2	$K_{R3y}=1.972\times10^4$ (n-m-sec)/rad
$J_{3y}=2.648\times10^3$ kg-m^2	$K_{R3z}=2.47\times10^4$ (n-m-sec)/rad
$J_{3z}=2.605\times10^3$ kg-m^2	$K_{P3x}=7.856\times10^4$ n-m/rad
$R_{11}=15\ \hat{1}_x+4.7\times10^{-2}\ \hat{1}_z$ m	$K_{P3y}=7.00\times10^4$ n-m/rad
$R_{E20}=0.375\ \hat{1}_z$ m	$K_{P3z}=8.764\times10^4$ n-m/rad
$r_1=0.375\ \hat{1}_z$ m	$K_{I3x}=1.24\times10^5$ n-m/sec
$r_2=1.689\ \hat{1}_z$ m	$K_{I3y}=1.105\times10^5$ n-m/sec
$R_{120}=-4.72\ \hat{1}_x-1.579\ \hat{1}_z$ m	$K_{I3z}=1.384\times10^5$ n-m/sec
	$W_{nT}=125.7$ rad/sec
	$W_{ns}=163.4$ rad/sec
	$\zeta_s=0.5$

2.2 Offset Gimbal Mathematical Model - The sections that follow will outline the derivation of the mathematical model for the offset gimbal system configuration. Figure 2-3 is a schematic representation of the offset gimbal for which the mathematical model described below is derived.

2.2.1 Translational Equations of Motion - Referring to figure 2-3, the following translational equations of motion apply

$$F_{1e} + F_{C12} = m_1 \ddot{\rho}_1 \tag{2-66}$$

$$F_{2e} - F_{C12} + F_{H23} = m_2 \ddot{\rho}_2 \tag{2-67}$$

$$F_{3e} - F_{H23} + F_{I34} = m_3 \ddot{\rho}_3 \tag{2-68}$$

$$F_{4e} - F_{I34} + F_{H45} = m_4 \ddot{\rho}_4 \tag{2-69}$$

$$F_{5e} - F_{H45} + F_{I56} = m_5 \ddot{\rho}_5 \tag{2-70}$$

$$F_{6e} - F_{I56} + F_{H67} = m_6 \ddot{\rho}_6 \tag{2-71}$$

$$F_{7e} - F_{H67} + F_{I78} = m_7 \ddot{\rho}_7 \tag{2-72}$$

$$F_{8e} - F_{I78} = m_8 \ddot{\rho}_8 \tag{2-73}$$

$$\sum_{j=1}^{8} F_{je} = M \ddot{\rho}_o \tag{2-74}$$

$$\sum_{j=1}^{8} m_j = M \tag{2-75}$$

where

$F_{je}(j=1,\ldots,8)$ = External forces acting on bodies 1 thru 8

$\rho_j(j=1,\ldots,8)$ = Location of CM of bodies 1 thru 8 with respect to some arbitrary inertial reference frame

$m_j(j=1,\ldots,8)$ = Mass of bodies 1 thru 8

F_{C12} = Suspension force between bodies 1 and 2

$F_{H23}; F_{H45}; F_{H67}$ = Hinge forces between bodies 2&3, 4&5, and 6&7 respectively

ρ_o = Location of system composite CM

$F_{I34}; F_{I56}; F_{I78}$ = Interface forces acting between bodies 3&4, 5&6, and 7&8

From the geometry shown in figure (2-3) the following relationships apply

$$\rho_1 = \rho_o + R_1 \tag{2-76}$$

$$\rho_2 = \rho_o + R_2 \tag{2-77}$$

$$\rho_3 = \rho_o + R_3 \tag{2-78}$$

$$\rho_4 = \rho_o + R_4 \tag{2-79}$$

$$\rho_5 = \rho_o + R_5 \tag{2-80}$$

$$\rho_6 = \rho_o + R_6 \tag{2-81}$$

$$\rho_7 = \rho_o + R_7 \tag{2-82}$$

$$\rho_8 = \rho_o + R_8 \tag{2-83}$$

$$R_2 = R_1 + R_{120} + \epsilon_{12} \tag{2-84}$$

$$R_3 = R_1 + R_{120} + \epsilon_{12} + r_1 + r_2 \tag{2-85}$$

$$R_4 = R_1 + R_{120} + \epsilon_{12} + r_1 + r_2 + r_3 + r_4 \tag{2-86}$$

$$R_5 = R_1 + R_{120} + \epsilon_{12} + r_1 + r_2 + r_3 + r_4 + r_5 + r_6 \tag{2-87}$$

$$R_6 = R_1 + R_{120} + \epsilon_{12} + r_1 + r_2 + r_3 + r_4 + r_5 + r_6 + r_7 + r_8 \tag{2-88}$$

$$R_7 = R_1 + R_{120} + \epsilon_{12} + r_1 + r_2 + r_3 + r_4 + r_5 + r_6 + r_7 + r_8 + r_9 + r_{10} \tag{2-89}$$

$$R_8 = R_1 + R_{120} + \epsilon_{12} + r_1 + r_2 + r_3 + r_4 + r_5 + r_6 + r_7 + r_8 + r_9 + r_{10} + r_{11} + r_{12} \tag{2-90}$$

where

R_{120} = Inertial vector corresponding to the location of body with respect to body at the start of the problem with the isolators in an undeformed state.

From the definition of the center of mass the following applies

$$\sum_{j=1}^{8} m_j R_j = 0 \tag{2-91}$$

which results in

$$R_1 = -\frac{1}{m_1}\sum_{j=2} m_j R_j \tag{2-92}$$

Substituting equations (2-83) thru (2-90) into equation (2-92), rearranging terms and solving for R_1 gives

$$R_1 = \frac{1}{M}\Big[(m_2+m_3+m_4+m_5+m_6+m_7+m_8)(R_{120}+\epsilon_{12}) + (m_3+m_4+m_5+m_6+m_7+m_8)(r_1+r_2)$$
$$+(m_4+m_5+m_6+m_7+m_8)(r_3+r_4) + (m_5+m_6+m_7+m_8)(r_5+r_6)$$
$$+(m_6+m_7+m_8)(r_7+r_8) + (m_7+m_8)(r_9+r_{10}) + m_8(r_{11}+r_{12})\Big] \tag{2-93}$$

Substituting equations (2-84) thru (2-90), and (2-93 into equations (2-76) thru (2-83) differentiating and using the relationship

$$\ddot{\rho}_o = \frac{1}{M}\sum_{j=1}^{8} F_{je} \tag{2-94}$$

results in

$$\ddot{\rho}_1 = \frac{1}{M}\sum_{j=1}^{8} F_{je} - \frac{1}{M}\Big[\ddot{\epsilon}_{12}\sum_{j=2}^{8} m_j + (\ddot{r}_1+\ddot{r}_2)\sum_{j=3}^{8} m_j + (\ddot{r}_3+\ddot{r}_4)\sum_{j=4}^{8} m_j$$
$$+(\ddot{r}_5+\ddot{r}_6)\sum_{j=5}^{8} m_j + (\ddot{r}_7+\ddot{r}_8)\sum_{j=6}^{8} m_j + (\ddot{r}_9+\ddot{r}_{10})(m_7+m_8) + (\ddot{r}_{11}+\ddot{r}_{12})m_8\Big] \tag{2-95}$$

$$\ddot{\rho}_2 = \frac{1}{M}\sum_{j=1}^{8} F_{je} + \frac{m_1}{M}\ddot{\epsilon}_{12} - \frac{1}{M}\Big[(\ddot{r}_1+\ddot{r}_2)\sum_{j=3}^{8} m_j + (\ddot{r}_3+\ddot{r}_4)\sum_{j=5}^{8} m_j$$

$$+(\ddot{r}_5+\ddot{r}_6)\sum_{j=7}^{8} m_j + (\ddot{r}_7+\ddot{r}_8)\sum_{j=9}^{8} m_j + (\ddot{r}_9+\ddot{r}_{10})(m_7+m_8) + (\ddot{r}_{11}+\ddot{r}_{12})m_8\Big] \qquad (2\text{-}96)$$

$$\ddot{\rho}_3 = \frac{1}{M}\sum_{j=1}^{8} F_{je} + \frac{m_1}{M}\ddot{\epsilon}_{12} + \frac{m_1+m_2}{M}(\ddot{r}_1+\ddot{r}_2) - \frac{1}{M}\Big[(\ddot{r}_3+\ddot{r}_4)\sum_{j=5}^{8} m_j$$

$$+(\ddot{r}_5+\ddot{r}_6)\sum_{j=7}^{8} m_j + (\ddot{r}_7+\ddot{r}_8)\sum_{j=9}^{8} m_j + (\ddot{r}_9+\ddot{r}_{10})(m_7+m_8) + (\ddot{r}_{11}+\ddot{r}_{12})m_8\Big] \qquad (2\text{-}97)$$

$$\ddot{\rho}_4 = \frac{1}{M}\sum_{j=1}^{8} F_{je} + \frac{m_1}{M}\ddot{\epsilon}_{12} + \frac{m_1+m_2}{M}(\ddot{r}_1+\ddot{r}_2) + \frac{1}{M}(\ddot{r}_3+\ddot{r}_4)\sum_{j=1}^{3} m_j$$

$$-\frac{1}{M}\Big[(\ddot{r}_5+\ddot{r}_6)\sum_{j=5}^{8} m_j + (\ddot{r}_7+\ddot{r}_8)\sum_{j=9}^{8} m_j + (\ddot{r}_9+\ddot{r}_{10})(m_7+m_8) + (\ddot{r}_{11}+\ddot{r}_{12})m_8\Big] \qquad (2\text{-}98)$$

$$\ddot{\rho}_5 = \frac{1}{M}\sum_{j=1}^{8} F_{je} + \frac{1}{M}\Big[m_1\ddot{\epsilon}_{12} + (m_1+m_2)(\ddot{r}_1+\ddot{r}_2) + (\ddot{r}_3+\ddot{r}_4)\sum_{j=1}^{3} m_j + (\ddot{r}_5+\ddot{r}_6)\sum_{j=1}^{4} m_j\Big]$$

$$-\frac{1}{M}\Big[(\ddot{r}_7+\ddot{r}_8)\sum_{j=6}^{8} m_j + (\ddot{r}_9+\ddot{r}_{10})(m_7+m_8) + (\ddot{r}_{11}+\ddot{r}_{12})m_8\Big] \qquad (2\text{-}99)$$

$$\ddot{\rho}_6 = \frac{1}{M}\sum_{j=1}^{8} F_{je} + \frac{1}{M}\Big[m_1\ddot{\epsilon}_{12} + (m_1+m_2)(\ddot{r}_1+\ddot{r}_2) + (\ddot{r}_3+\ddot{r}_4)\sum_{j=1}^{3} m_j + (\ddot{r}_5+\ddot{r}_6)\sum_{j=1}^{4} m_j$$

$$+(\ddot{r}_7+\ddot{r}_8)\sum_{j=1}^{5} m_j - \frac{1}{M}\Big[(m_7+m_8)(\ddot{r}_9+\ddot{r}_{10}) + m_9(\ddot{r}_{11}+\ddot{r}_{12}) \qquad (2\text{-}100)$$

$$\ddot{\rho}_7 = \frac{1}{M}\sum_{j=1}^{8} F_{je} + \frac{1}{M}\Big[m_1\ddot{\epsilon}_{12} + (m_1+m_2)(\ddot{r}_1+\ddot{r}_2) + (\ddot{r}_3+\ddot{r}_4)\sum_{j=1}^{3} m_j + (\ddot{r}_5+\ddot{r}_6)\sum_{j=1}^{4} m_j$$

$$+(\ddot{r}_7+\ddot{r}_8)\sum_{j=1}^{5} m_j + (\ddot{r}_9+\ddot{r}_{10})\sum_{j=1}^{6} m_j\Big] - \frac{m_8}{M}(\ddot{r}_{11}+\ddot{r}_{12}) \qquad (2\text{-}101)$$

$$\ddot{\rho}_8 = \frac{1}{M}\sum_{j=1}^{8} F_{je} + \frac{1}{M}\Big[m_1\ddot{\epsilon}_{12} + (m_1+m_2)(\ddot{r}_1+\ddot{r}_2) + (\ddot{r}_3+\ddot{r}_4)\sum_{j=1}^{3} m_j + (\ddot{r}_5+\ddot{r}_6)\sum_{j=1}^{4} m_j$$

$$+(\ddot{r}_7+\ddot{r}_8)\sum_{j=1}^{5} m_j + (\ddot{r}_9+\ddot{r}_{10})\sum_{j=1}^{6} m_j + (\ddot{r}_{11}+\ddot{r}_{12})\sum_{j=1}^{7} m_j\Big] \qquad (2\text{-}102)$$

Substituting equation (2-102) into equation (2-73) and rearranging terms gives

$$F_{I78} = \frac{1}{M}\left(F_{Be}\sum_{j=1}^{7} m_j - m_8\sum_{j=1}^{7} F_{je}\right) - \frac{m_8}{M}\left[m_1\ddot{\varepsilon}_{12} + (m_1+m_2)(\ddot{r}_1+\ddot{r}_2) + (\ddot{r}_3+\ddot{r}_4)\sum_{j=1}^{3} m_j\right.$$

$$\left. + (\ddot{r}_5+\ddot{r}_6)\sum_{j=1}^{4} m_j + (\ddot{r}_7+\ddot{r}_8)\sum_{j=1}^{5} m_j + (\ddot{r}_9+\ddot{r}_{10})\sum_{j=1}^{6} m_j + (\ddot{r}_{11}+\ddot{r}_{12})\sum_{j=1}^{7} m_j\right] \qquad (2\text{-}103)$$

Substituting equations (2-101) and (2-103) into equation (2-72) yields

$$F_{H67} = \frac{1}{M}\left[(F_{Be}+F_{7e})\sum_{j=1}^{6} m_j - (m_7+m_8)\sum_{i=1}^{6} F_{je}\right] - \frac{m_7+m_8}{M}\left[m_1\ddot{\varepsilon}_{12} + (m_1+m_2)(\ddot{r}_1+\ddot{r}_2)\right.$$

$$\left. + (\ddot{r}_3+\ddot{r}_4)\sum_{j=1}^{3} m_j + (\ddot{r}_5+\ddot{r}_6)\sum_{j=1}^{4} m_j + (\ddot{r}_7+\ddot{r}_8)\sum_{j=1}^{5} m_j + (\ddot{r}_9+\ddot{r}_{10})\sum_{j=1}^{6} m_j\right] - \frac{m_8}{M}(\ddot{r}_{11}+\ddot{r}_{12})\sum_{j=1}^{6} m_j \qquad (2\text{-}104)$$

Substituting equations (2-104) and (2-100) into equation (2-71) yields

$$F_{I56} = \frac{1}{M}\left[\sum_{j=1}^{5} m_j\sum_{j=6}^{8} F_{je} - \sum_{j=6}^{8} m_j\sum_{j=1}^{5} F_{je}\right] - \frac{1}{M}\left\{\left(\sum_{j=6}^{8} m_j\right)\left[m_1\ddot{\varepsilon}_{12} + (m_1+m_2)(\ddot{r}_1+\ddot{r}_2) + (\ddot{r}_3+\ddot{r}_4)\sum_{j=1}^{3} m_j\right.\right.$$

$$\left.\left. + (\ddot{r}_5+\ddot{r}_6)\sum_{j=1}^{4} m_j + (\ddot{r}_7+\ddot{r}_8)\sum_{j=1}^{5} m_j\right] + \left(\sum_{j=1}^{5} m_j\right)\left[(m_7+m_8)(\ddot{r}_9+\ddot{r}_{10}) + m_8(\ddot{r}_{11}+\ddot{r}_{12})\right]\right\} \qquad (2\text{-}105)$$

Substituting equations (2-99) and (2-105) into equation (2-70) gives

$$F_{H45} = \frac{1}{M}\left[\sum_{j=1}^{5} m_j\sum_{j=5}^{8} F_{je} - \sum_{j=5}^{8} m_j\sum_{j=1}^{4} F_{je}\right] - \frac{1}{M}\left\{\left(\sum_{j=5}^{8} m_j\right)\left[m_1\ddot{\varepsilon}_{12} + (m_1+m_2)(\ddot{r}_1+\ddot{r}_2) + (\ddot{r}_3+\ddot{r}_4)\sum_{j=1}^{3} m_j\right.\right.$$

$$\left.\left. + (\ddot{r}_5+\ddot{r}_6)\sum_{j=1}^{4} m_j\right] + \left(\sum_{j=1}^{4} m_j\right)\left[(\ddot{r}_7+\ddot{r}_8)\sum_{j=6}^{8} m_j + (m_7+m_8)(\ddot{r}_9+\ddot{r}_{10}) + m_8(\ddot{r}_{11}+\ddot{r}_{12})\right]\right\} \qquad (2\text{-}106)$$

Substituting equations (2-98) and (2-106) into equation (2-69) yields

$$F_{I34} = \frac{1}{M}\left[\sum_{j=1}^{3} m_j\sum_{j=4}^{8} F_{je} - \sum_{j=4}^{8} m_j\sum_{j=1}^{3} F_{je}\right] - \frac{1}{M}\left\{\left(\sum_{j=4}^{8} m_j\right)\left[m_1\ddot{\varepsilon}_{12} + (m_1+m_2)(\ddot{r}_1+\ddot{r}_2) + (\ddot{r}_3+\ddot{r}_4)\sum_{j=1}^{3} m_j\right]\right.$$

$$\left. + \left(\sum_{j=1}^{3} m_j\right)\left[(\ddot{r}_5+\ddot{r}_6)\sum_{j=5}^{8} m_j + (\ddot{r}_7+\ddot{r}_8)\sum_{j=6}^{8} m_j + (m_7+m_8)(\ddot{r}_9+\ddot{r}_{10}) + m_8(\ddot{r}_{11}+\ddot{r}_{12})\right]\right\} \qquad (2\text{-}107)$$

Substituting equations (2-97) and (2-107) into equation (2-68) results in

$$F_{H23} = \frac{1}{M}\left[(m_1+m_2)\sum_{j=3}^{8} F_{je} - (F_{j1}+F_{j2})\sum_{j=3}^{8} m_j\right] - \frac{1}{M}\left\{\left(\sum_{j=3}^{8} m_j\right)\left[m_1\ddot{\varepsilon}_{12} + (m_1+m_2)(\ddot{r}_1+\ddot{r}_2)\right]\right.$$

$$\left. + (m_1+m_2)\left[(\ddot{r}_3+\ddot{r}_4)\sum_{j=4}^{8} m_j + (\ddot{r}_5+\ddot{r}_6)\sum_{j=5}^{8} m_j + (\ddot{r}_7+\ddot{r}_8)\sum_{j=6}^{8} m_j + (m_7+m_8)(\ddot{r}_9+\ddot{r}_{10}) + m_8(\ddot{r}_{11}+\ddot{r}_{12})\right]\right\} \qquad (2\text{-}108)$$

The Suspension Force F_{C12} can be derived in exactly the same manner as described in section 2.1.1 and is given in equation (2-26) which is repeated here for convenience

$$F_{C12} = 4D\cdot\dot{\epsilon}_{12} + 4D\cdot[(\omega_2-\omega_1)\times R_{E20}] - 4D\cdot(\omega_1\times R_{120}) + 4K\cdot\epsilon_{12} + 4K\cdot[(\theta_2-\theta_1)\times R_{E20}] - 4K\cdot(\theta_1\times R_{120}) \quad (2\text{-}26)$$

2.2.2 Rotational Equations of Motion - Referring to figure 2-3, the following rotational equations of motion apply for the 8 bodies depicted

$$T_{1e} + R_{11}\times F_{1e} + \sum_{k=1}^{4}\beta_{k1}^{12}\times F_{C12k} = \frac{d}{dt}(J_1\cdot\omega_1) \quad (2\text{-}109)$$

$$T_{2e} + T_{23f} + T_{23WT} + R_{22}\times F_{2e} - \sum_{k=1}^{4}\beta_{k2}^{12}\times F_{C12k} + r_1\times F_{H23} - {}_3M_2^c|_2 = \frac{d}{dt}(J_2\cdot\omega_2) + T_{\alpha 2} \quad (2\text{-}110)$$

$$T_{3e} - T_{23f} - T_{23WT} + R_{33}\times F_{3e} + r_2\times F_{H23} + r_3\times F_{I34} + {}_3M_2^c|_3 = \frac{d}{dt}(J_3\cdot\omega_3) + d_{34}\cdot(\omega_3-\omega_4) + k_{34}\cdot(\theta_3-\theta_4) - T_{\alpha 2} \quad (2\text{-}111)$$

$$T_{4e} + T_{45f} + T_{45WT} + R_{44}\times F_{4e} + r_4\times F_{I34} + r_5\times F_{H45} - {}_4M_4^c|_4 = \frac{d}{dt}(J_4\cdot\omega_4) + d_{34}\cdot(\omega_4-\omega_3) + k_{34}\cdot(\theta_4-\theta_3) + T_{\beta x} \quad (2\text{-}112)$$

$$T_{5e} - T_{45f} - T_{45WT} + R_{55}\times F_{5e} + r_6\times F_{H45} + r_7\times F_{I56} - {}_4M_4^c|_5 = \frac{d}{dt}(J_5\cdot\omega_5) + d_{56}\cdot(\omega_5-\omega_6) + k_{56}\cdot(\theta_5-\theta_6) - T_{\beta x} \quad (2\text{-}113)$$

$$T_{6e} + T_{67f} + T_{67WT} + R_{66}\times F_{6e} + r_8\times F_{I56} + r_9\times F_{H67} - {}_7M_4^c|_6 = \frac{d}{dt}(J_6\cdot\omega_6) + d_{56}\cdot(\omega_6-\omega_5) + k_{56}\cdot(\theta_6-\theta_5) + T_{\beta y} \quad (2\text{-}114)$$

$$T_{7e} - T_{67f} - T_{67WT} + R_{77}\times F_{7e} + r_{10}\times F_{H67} + r_{11}\times F_{I78} + {}_7M_4^c|_7 = \frac{d}{dt}(J_7\cdot\omega_7) + d_{78}\cdot(\omega_7-\omega_8) + k_{78}\cdot(\theta_7-\theta_8) - T_{\beta y} \quad (2\text{-}115)$$

$$T_{8e} + R_{88}\times F_{8e} + r_{12}\times F_{I78} = \frac{d}{dt}(J_8\cdot\omega_8) + d_{78}\cdot(\omega_8-\omega_7) + k_{78}\cdot(\theta_8-\theta_7) \quad (2\text{-}116)$$

where

β_{k1}^{12}, F_{C12k}, F_{H23}; F_{I34}, F_{H45}, F_{H67} and F_{I78} are defined in sections 2.2.1 and 2.1.1

$R_{jj}(j=1,\ldots 8)$ = Distance from CM to the applied external force for the jth body

$T_{23f};T_{45f};T_{67f}$ = Frictional torques between bodies 2&3, 4&5, and 6&7 respectively

$J_j(j=1,\ldots,8)$ = Inertia tensor of jth body

$T_{23WT}; T_{45WT}; T_{67WT}$ = Wire torques between bodies 2&3, 4&5, and 6&7 respectively

${}_3M_2^c|_2$ = Constraint torque applied by body 2 on body 3 written in body 2 coordinates

${}_3M_2^c|_3$ = Constraint torque applied by body 2 on body 3 written in body 3 coordinates

${}_5M_4^c|_5$ = Constraint torque applied by body 4 on body 5 written in body 4 coordinates

${}_5M_4^c|_5$ = Constraint torque applied by body 4 on body 5 written in body 5 coordinates

${}_7M_6^c|_6$ = Constraint torque applied by body 6 on body 7 written in body 6 coordinates

${}_7M_6^c|_7$ = Constraint torque applied by body 6 on body 7 written in body 7 coordinates

$T_{\alpha z}, T_{\beta x}, T_{\gamma y}$ = Gimbal torques applied by the gimbal torque motors about the α_z, β_x, and γ_y axes respectively

In order to obtain a complete set of equations of motion for the offset gimbal system a translational equation of motion is required to be added to equations (2-109) thru (2-116). Equation (2-67) will be used to fulfill this requirement and is repeated here for convenience

$$F_{23} - F_{C12} + F_{H23} = M_2 \ddot{\rho}_2 \qquad (2\text{-}67)$$

Equations (2-68) and (2-109) thru (2-116) form a complete set of equations of motion for the Offset Gimbal system configuration.

Substituting equations (2-13), (2-16) thru (2-21), (2-26), and (2-103) thru (2-108) doing the indicated inertial time differentiations, summations, simplifying, rearranging terms, and putting the equations in matrix format yields the following set of system equations of motion, all of which use the following convention for the mass summations:

$$m_{jk} = \sum_{i=j}^{k} m_i \qquad \begin{cases} j = 1, & k = 2,3,\cdots 7 \\ k = 8, & j = 2,3,\cdots 7 \end{cases} \qquad (2\text{-}117)$$

$$T_{1e} + \bar{R}_{11} \cdot F_{1e} = J_1 \cdot \omega_1 + d \cdot (\omega_1 - \omega_2) + k \cdot (\theta_1 - \theta_2) - 4(\bar{R}_{120} + \bar{R}_{E20}) \cdot \{D \cdot [\bar{R}_{E20} \cdot (\omega_1 - \omega_2) + \bar{R}_{120} \cdot \omega_1]$$
$$+ K \cdot [\bar{R}_{E20} \cdot (\theta_1 - \theta_2) + \bar{R}_{120} \cdot \theta_1]\} - 4(\bar{R}_{120} + \bar{R}_{E20}) \cdot (D \cdot \dot{\epsilon}_{12} + K \cdot \epsilon_{12}) + \bar{\omega}_1 \cdot (J_1 \cdot \omega_1) \qquad (2\text{-}118)$$

$$T_{2e} + T_{23fz} + T_{23WTz} + \bar{R}_{22} \cdot F_{2e} + \frac{1}{M} \bar{r}_1 \cdot \left(m_{12} \sum_{j=3}^{8} F_{je} - m_{38} \sum_{j=1}^{2} F_{je}\right) - {}_3M_2^c \Big|_2^{XY} =$$
$$\left(J_2 - \frac{1}{M} m_{12} m_{38} \bar{r}_1 \cdot \bar{r}_1\right) \cdot \dot{\omega}_2 + d \cdot (\omega_2 - \omega_1) + k \cdot (\theta_2 - \theta_1) - 4\bar{R}_{E20} \cdot \{D \cdot [\bar{R}_{E20} \cdot (\omega_2 - \omega_1) - \bar{R}_{120} \cdot \omega_1]$$
$$+ K \cdot [\bar{R}_{E20} \cdot (\theta_2 - \theta_1) - \bar{R}_{120} \cdot \theta_1]\} - \frac{1}{M}\{m_{12}[\bar{r}_1 \cdot (m_{38}\bar{r}_2 + m_{48}\bar{r}_3) \cdot \dot{\omega}_3 + \bar{r}_1 \cdot (m_{48}\bar{r}_4 + m_{58}\bar{r}_5) \cdot \dot{\omega}_4$$
$$+ \bar{r}_1 \cdot (m_{58}\bar{r}_6 + m_{68}\bar{r}_7) \cdot \dot{\omega}_5 + \bar{r}_1 \cdot (m_{68}\bar{r}_8 + m_{78}\bar{r}_9) \cdot \dot{\omega}_6 + \bar{r}_1 \cdot (m_{78}\bar{r}_{10} + m_8 \bar{r}_{11}) \cdot \dot{\omega}_7 + m_8 \bar{r}_1 \cdot \bar{r}_{12} \cdot \dot{\omega}_8]\}$$
$$+ \frac{1}{M} m_{38} m_1 \bar{r}_1 \cdot \ddot{\epsilon}_{12} + 4\bar{R}_{E20} \cdot (D \cdot \dot{\epsilon}_{12} + K \cdot \epsilon_{12}) + T_{\alpha z} + \bar{\omega}_2 \cdot (J_2 \cdot \omega_2) - \frac{1}{M}\{m_{38} m_{12} \bar{r}_1 \cdot \bar{\omega}_2 \cdot (\bar{r}_1 \cdot \omega_2)$$
$$+ m_{12}[\bar{r}_1 \cdot [m_{38}\bar{\omega}_3 \cdot (\bar{r}_2 \cdot \omega_3) + m_{48}\bar{\omega}_3 \cdot (\bar{r}_2 \cdot \omega_3)] + \bar{r}_1 \cdot [m_{48}\bar{\omega}_4 \cdot (\bar{r}_4 \cdot \omega_4) + m_{58}\bar{\omega}_4 \cdot (\bar{r}_5 \cdot \omega_4)]$$
$$+ \bar{r}_1 \cdot [m_{58}\bar{\omega}_5 \cdot (\bar{r}_6 \cdot \omega_5) + m_{68}\bar{\omega}_5 \cdot (\bar{r}_7 \cdot \omega_5)] + \bar{r}_1 \cdot [m_{68}\bar{\omega}_6 \cdot (\bar{r}_8 \cdot \omega_6) + m_{78}\bar{\omega}_6 \cdot (\bar{r}_9 \cdot \omega_6)]$$
$$+ \bar{r}_1 \cdot [m_{78}\bar{\omega}_7 \cdot (\bar{r}_{10} \cdot \omega_7) + m_8 \bar{\omega}_7 \cdot (\bar{r}_{11} \cdot \omega_7)] + m_8 \bar{r}_1 \cdot \bar{\omega}_8 \cdot (\bar{r}_1 \cdot \omega_8)]\}$$
$$+ \frac{m_1}{M} m_{38} \bar{r}_1 \cdot [\dot{\bar{\omega}}_2 \cdot \epsilon_{12} + 2\bar{\omega}_2 \cdot \dot{\epsilon}_{12} + \bar{\omega}_2 \cdot (\bar{\omega}_2 \cdot \epsilon_{12})] \qquad (2\text{-}119)$$

$$T_{3e} - T_{23fz} - T_{23WTz} + \bar{R}_{33} \cdot F_{3e} + \frac{1}{M}\left[\bar{r}_1 \cdot \left(m_{12} \sum_{j=3}^{8} F_{je} - m_{38} \sum_{j=1}^{2} F_{je}\right) + \bar{r}_3 \cdot \left(m_{13} \cdot \sum_{j=4}^{8} F_{je} - m_{48} \sum_{j=1}^{3} F_{je}\right)\right] + {}_3M_2^c \Big|_3^{XY} =$$
$$\left\{J_3 - \frac{1}{M}\left[m_{12}(m_{38}\bar{r}_2 + m_{48}\bar{r}_3) \cdot \bar{r}_2 + m_{48}(m_{12}\bar{r}_2 + m_{13}\bar{r}_3) \cdot \bar{r}_3\right]\right\} \cdot \dot{\omega}_3 + d_{34} \cdot (\omega_3 - \omega_4) + k_{34} \cdot (\theta_3 - \theta_4)$$
$$- \frac{1}{M}\{m_{12}(m_{38}\bar{r}_2 + m_{48}\bar{r}_3) \cdot \bar{r}_1 \cdot \dot{\omega}_2 + (m_{12}\bar{r}_2 + m_{13}\bar{r}_3) \cdot [(m_{48}\bar{r}_4 + m_{58}\bar{r}_5) \cdot \dot{\omega}_4 + (m_{58}\bar{r}_6 + m_{68}\bar{r}_7) \cdot \dot{\omega}_5$$
$$+ (m_{68}\bar{r}_8 + m_{78}\bar{r}_9) \cdot \dot{\omega}_6 + (m_{78}\bar{r}_{10} + m_8 \bar{r}_{11}) \cdot \dot{\omega}_7 + m_8 \bar{r}_{12} \cdot \dot{\omega}_8]\} + \frac{m_1}{M}(m_{38}\bar{r}_2 + m_{48}\bar{r}_3) \cdot \ddot{\epsilon}_{12} - T_{\alpha z}$$
$$+ \bar{\omega}_3 \cdot (J \cdot \omega_3) - \frac{1}{M}\{m_{12}(m_{38}\bar{r}_2 + m_{48}\bar{r}_3) \cdot \bar{\omega}_2 \cdot (\bar{r}_1 \cdot \omega_2) + m_{12}(m_{38}\bar{r}_2 + m_{48}\bar{r}_3) \cdot \bar{\omega}_3 \cdot (\bar{r}_2 \cdot \omega_3)$$
$$+ m_{48}(m_{12}\bar{r}_2 + m_{13}\bar{r}_3) \cdot \bar{\omega}_3 \cdot (\bar{r}_3 \cdot \omega_3) + (m_{12}\bar{r}_2 + m_{13}\bar{r}_3) \cdot [m_{48}\bar{\omega}_4 \cdot (\bar{r}_4 \cdot \omega_4) + m_{58}\bar{\omega}_4 \cdot (\bar{r}_5 \cdot \omega_4)$$
$$+ m_{58}\bar{\omega}_5 \cdot (\bar{r}_4 \cdot \omega_5) + m_{68}\bar{\omega}_5 \cdot (\bar{r}_7 \cdot \omega_5) + m_{68}\bar{\omega}_6 \cdot (\bar{r}_8 \cdot \omega_6) + m_{78}\bar{\omega}_6 \cdot (\bar{r}_9 \cdot \omega_6) + m_{78}\bar{\omega}_7 \cdot (\bar{r}_{10} \cdot \bar{\omega}_7)$$
$$+ m_8 \bar{\omega}_7 \cdot (\bar{r}_{11} \cdot \omega_7) + m_8 \bar{\omega}_8 \cdot (\bar{r}_{12} \cdot \omega_8)]\} + \frac{m_1}{M}(m_{38}\bar{r}_2 + m_{48}\bar{r}_3) \cdot [\dot{\bar{\omega}}_2 \cdot \epsilon_{12} + 2\bar{\omega}_2 \cdot \dot{\epsilon}_{12} + \bar{\omega}_2 \cdot (\bar{\omega}_2 \cdot \epsilon_{12})]$$

(2-120)

$$T_{4e} + T_{45fx} + T_{45WTx} + \bar{R}_{44} \cdot F_{4e} + \frac{1}{M}\left[\bar{r}_4 \cdot \left(m_{13}\sum_{j=4}^{8} F_{je} - m_{48}\sum_{j=1}^{3} F_{je}\right) + \bar{r}_5 \cdot \left(m_{14}\sum_{j=5}^{8} F_{je} - m_{58}\sum_{j=1}^{4} F_{je}\right)\right] - {}_5M_4^c\Big|_4^{yz} =$$

$$\left\{J_4 - \frac{1}{M}\left[m_{13}(m_{48}\bar{r}_4 + m_{58}\bar{r}_5)\cdot\bar{r}_4 + m_{58}(m_{13}\bar{r}_4 + m_{14}\bar{r}_5)\cdot\bar{r}_5\right]\right\}\cdot\dot{\omega}_4 + d_{34}(\omega_4 - \omega_3) + k_{34}\cdot(\theta_4 - \theta_3)$$

$$-\frac{1}{M}\left\{m_{12}(m_{48}\bar{r}_4 + m_{58}\bar{r}_5)\cdot\bar{r}_1\cdot\dot{\omega}_2 + \left[m_{12}(m_{48}\bar{r}_4 + m_{58}\bar{r}_5)\cdot\bar{r}_2 + m_{13}(m_{48}\bar{r}_4 + m_{58}\bar{r}_5)\cdot\bar{r}_3\right]\cdot\dot{\omega}_3\right.$$

$$\left. + (m_{13}\bar{r}_4 + m_{14}\bar{r}_5)\cdot\left[(m_{58}\bar{r}_6 + m_{68}\bar{r}_7)\cdot\dot{\omega}_5 + (m_{68}\bar{r}_8 + m_{78}\bar{r}_9)\cdot\dot{\omega}_6 + (m_{78}\bar{r}_{10} + m_8\bar{r}_{11})\cdot\dot{\omega}_7 + m_8\bar{r}_{12}\cdot\dot{\omega}_8\right]\right\}$$

$$+\frac{m_1}{M}(m_{48}\bar{r}_4 + m_{58}\bar{r}_5)\cdot\ddot{\epsilon}_{12} + T_{\beta x} - \frac{1}{M}\left\{(m_{48}\bar{r}_4 + m_{58}\bar{r}_5)\cdot\left[m_{12}\left[\bar{\omega}_2\cdot(\bar{r}_1\cdot\omega_2) + \bar{\omega}_3\cdot(\bar{r}_2\cdot\omega_3)\right]\right.\right.$$

$$\left. + m_{13}\left[\bar{\omega}_3\cdot(\bar{r}_3\cdot\omega_3) + \bar{\omega}_4\cdot(\bar{r}_4\cdot\omega_4)\right]\right\} + (m_{13}\bar{r}_4 + m_{14}\bar{r}_5)\cdot\left[m_{58}\left[\bar{\omega}_4\cdot(\bar{r}_5\cdot\omega_4) + \bar{\omega}_5\cdot(\bar{r}_6\cdot\omega_5)\right]\right.$$

$$\left.\left. + m_{68}\left[\bar{\omega}_5\cdot(\bar{r}_7\cdot\omega_5) + \bar{\omega}_6\cdot(\bar{r}_8\cdot\omega_6)\right] + m_{78}\left[\bar{\omega}_6\cdot(\bar{r}_9\cdot\omega_6) + \bar{\omega}_7\cdot(\bar{r}_{10}\cdot\omega_7)\right] + m_8\left[\bar{\omega}_7\cdot(\bar{r}_{11}\cdot\omega_7) + \bar{\omega}_8\cdot(\bar{r}_{12}\cdot\omega_8)\right]\right]\right\}$$

$$+\frac{m_1}{M}(m_{48}\bar{r}_4 + m_{58}\bar{r}_5)\cdot\left[\dot{\bar{\omega}}_2\cdot\epsilon_{12} + 2\bar{\omega}_2\cdot\dot{\epsilon}_{12} + \bar{\omega}_2\cdot(\bar{\omega}_2\cdot\epsilon_{12})\right] + \bar{\omega}_4\cdot(J_4\cdot\omega_4) \qquad (2\text{-}121)$$

$$T_{5e} - T_{45fx} - T_{45WTx} + \bar{R}_{55}\cdot F_{5e} + \frac{1}{M}\left[\bar{r}_6\cdot\left(m_{14}\sum_{j=5}^{8} F_{je} - m_{58}\sum_{j=1}^{4} F_{je}\right) + \bar{r}_7\cdot\left(m_{15}\sum_{j=6}^{8} F_{je} - m_{68}\sum_{j=1}^{5} F_{je}\right)\right] + {}_5M_4^c\Big|_5^{yz} =$$

$$\left\{J_5 - \frac{1}{M}\left[m_{14}(m_{58}\bar{r}_6 + m_{68}\bar{r}_7)\cdot\bar{r}_6 + m_{68}(m_{14}\bar{r}_6 + m_{15}\bar{r}_7)\cdot\bar{r}_7\right]\right\}\cdot\dot{\omega}_5 + d_{56}(\omega_5 - \omega_6) + k_{56}\cdot(\theta_5 - \theta_6)$$

$$-\frac{1}{M}\left\{(m_{58}\bar{r}_6 + m_{68}\bar{r}_7)\cdot\left[m_{12}\bar{r}_1\cdot\dot{\omega}_2 + (m_{12}\bar{r}_2 + m_{13}\bar{r}_3)\cdot\dot{\omega}_3 + (m_{13}\bar{r}_4 + m_{14}\bar{r}_5)\cdot\dot{\omega}_4\right]\right.$$

$$\left. + (m_{14}\bar{r}_6 + m_{15}\bar{r}_7)\cdot\left[(m_{68}\bar{r}_8 + m_{78}\bar{r}_9)\cdot\dot{\omega}_6 + (m_{78}\bar{r}_{10} + m_8\bar{r}_{11})\cdot\dot{\omega}_7 + m_8\bar{r}_{12}\cdot\dot{\omega}_8\right]\right\}$$

$$+\frac{m_1}{M}(m_{58}\bar{r}_6 + m_{68}\bar{r}_7)\cdot\ddot{\epsilon}_{12} - T_{\beta x} + \bar{\omega}_5\cdot(J\cdot\omega_5) - \frac{1}{M}\left\{(m_{58}\bar{r}_6 + m_{68}\bar{r}_7)\cdot\left[m_{12}\left[\bar{\omega}_2\cdot(\bar{r}_1\cdot\omega_2)\right.\right.\right.$$

$$\left. + \bar{\omega}_3\cdot(\bar{r}_2\cdot\omega_3)\right] + m_{13}\left[\bar{\omega}_3\cdot(\bar{r}_3\cdot\omega_3) + \bar{\omega}_4\cdot(\bar{r}_4\cdot\omega_4)\right] + m_{14}\left[\bar{\omega}_4\cdot(\bar{r}_5\cdot\omega_4) + \bar{\omega}_5\cdot(\bar{r}_6\cdot\omega_6)\right]\Big)$$

$$+ (m_{14}\bar{r}_6 + m_{15}\bar{r}_7)\cdot\left[m_{68}\left[\bar{\omega}_5\cdot(\bar{r}_7\cdot\omega_5) + \bar{\omega}_6\cdot(\bar{r}_8\cdot\omega_6)\right] + m_{78}\left[\bar{\omega}_6\cdot(\bar{r}_9\cdot\omega_6) + \bar{\omega}_7\cdot(\bar{r}_{10}\cdot\omega_7)\right]\right.$$

$$\left.\left. + m_8\left[\bar{\omega}_7\cdot(\bar{r}_{11}\cdot\omega_7) + \bar{\omega}_8\cdot(\bar{r}_{12}\cdot\omega_8)\right]\right]\right\} + \frac{m_1}{M}(m_{58}\bar{r}_6 + m_{68}\bar{r}_7)\cdot\left[\dot{\bar{\omega}}_2\cdot\epsilon_{12} + 2\bar{\omega}_2\cdot\dot{\epsilon}_{12} + \bar{\omega}_2\cdot(\bar{\omega}_2\cdot\epsilon_{12})\right]$$

(2-122)

$$T_{6e} + T_{67F_y} + T_{67WT_y} + \bar{R}_{66}\cdot F_{6e} + \frac{1}{M}\left[\bar{r}_8\cdot\left(m_{15}\sum_{j=6}^{8}F_{je} - m_{68}\sum_{j=1}^{5}F_{je}\right) + \bar{r}_9\cdot\left(m_{16}\sum_{j=7}^{8}F_{je} - m_{78}\sum_{j=1}^{6}F_{je}\right)\right] - {}_7M_6^c\Big|_6^{xz} =$$

$$\left\{J_6 - \frac{1}{M}\left[m_{15}\left(m_{68}\bar{r}_8 + m_{78}\bar{r}_9\right)\cdot\bar{r}_8 + m_{78}\left(m_{15}\bar{r}_8 + m_{16}\bar{r}_9\right)\cdot\bar{r}_9\right]\right\}\cdot\dot{\omega}_6 + d_{56}\cdot(\omega_6 - \omega_5) + k_{56}\cdot(\theta_6 - \theta_5)$$

$$- \frac{1}{M}\left\{\left(m_{68}\bar{r}_8 + m_{78}\bar{r}_9\right)\cdot\left[m_{12}\bar{r}_1\cdot\omega_2 + \left(m_{12}\bar{r}_2 + m_{13}\bar{r}_3\right)\cdot\dot{\omega}_3 + \left(m_{13}\bar{r}_4 + m_{14}\bar{r}_5\right)\cdot\dot{\omega}_4 + \left(m_{14}\bar{r}_6 + m_{15}\bar{r}_7\right)\cdot\dot{\omega}_5\right]\right.$$

$$\left. + \left(m_{15}\bar{r}_8 + m_{16}\bar{r}_9\right)\cdot\left[\left(m_{78}\bar{r}_{10} + m_8\bar{r}_{11}\right)\cdot\dot{\omega}_7 + m_8\bar{r}_{12}\cdot\dot{\omega}_8\right]\right\} + \frac{m_1}{M}\left(m_{68}\bar{r}_8 + m_{78}\bar{r}_9\right)\cdot\ddot{\varepsilon}_{12} + T_{6y} + \bar{\omega}_6\cdot(J\cdot\omega_6)$$

$$- \frac{1}{M}\left\{\left(m_{68}\bar{r}_8 + m_{78}\bar{r}_9\right)\cdot\left\{m_{12}\left[\bar{\omega}_2\cdot(\bar{r}_1\cdot\omega_2) + \bar{\omega}_3\cdot(\bar{r}_2\cdot\omega_3)\right] + m_{13}\left[\bar{\omega}_3\cdot(\bar{r}_3\cdot\omega_3) + \bar{\omega}_4\cdot(\bar{r}_4\cdot\omega_4)\right]\right.\right.$$

$$\left.\left. + m_{14}\left[\bar{\omega}_4\cdot(\bar{r}_5\cdot\omega_4) + \bar{\omega}_5\cdot(\bar{r}_6\cdot\omega_5)\right] + m_{15}\left[\bar{\omega}_5\cdot(\bar{r}_7\cdot\omega_5) + \bar{\omega}_6\cdot(\bar{r}_8\cdot\omega_6)\right]\right\}$$

$$+ \left(m_{15}\bar{r}_8 + m_{16}\bar{r}_9\right)\cdot\left\{m_{78}\left[\bar{\omega}_6\cdot(\bar{r}_9\cdot\omega_6) + \bar{\omega}_7\cdot(\bar{r}_{10}\cdot\omega_7)\right] + m_8\left[\bar{\omega}_7\cdot(\bar{r}_{11}\cdot\omega_7) + \bar{\omega}_8\cdot(\bar{r}_{12}\cdot\omega_8)\right]\right\}\Big\}$$

$$+ \frac{m_1}{M}\left(m_{68}\bar{r}_8 + m_{78}\bar{r}_9\right)\cdot\left[\dot{\bar{\omega}}_2\cdot\epsilon_{12} + 2\bar{\omega}_2\cdot\dot{\epsilon}_{12} + \bar{\omega}_2\cdot(\bar{\omega}_2\cdot\epsilon_{12})\right] \qquad (2\text{-}123)$$

$$T_{7e} - T_{67F_y} - T_{67WT_y} + \bar{R}_{77}\cdot F_{7e} + \frac{1}{M}\left[\bar{r}_{10}\cdot\left(m_{16}\sum_{j=7}^{8}F_{je} - m_{78}\sum_{j=1}^{6}F_{je}\right) + \bar{r}_{11}\cdot\left(m_{17}F_{8e} - m_8\sum_{j=1}^{7}F_{je}\right)\right] + {}_7M_6^c\Big|_7^{xz} =$$

$$\left\{J_7 - \frac{1}{M}\left[m_{16}\left(m_{78}\bar{r}_{10} + m_8\bar{r}_{11}\right)\cdot\bar{r}_{10} + m_8\left(m_{15}\bar{r}_{10} + m_{17}\bar{r}_{11}\right)\cdot\bar{r}_{11}\right]\right\}\cdot\dot{\omega}_7 + d_{78}\cdot(\omega_7 - \omega_8) + k_{78}\cdot(\theta_7 - \theta_8)$$

$$- \frac{1}{M}\left\{\left(m_{78}\bar{r}_{10} + m_8\bar{r}_{11}\right)\cdot\left[m_{12}\bar{r}_1\cdot\dot{\omega}_2 + \left(m_{12}\bar{r}_2 + m_{13}\bar{r}_3\right)\cdot\dot{\omega}_3 + \left(m_{13}\bar{r}_4 + m_{14}\bar{r}_5\right)\cdot\dot{\omega}_4 + \left(m_{14}\bar{r}_6 + m_{15}\bar{r}_7\right)\cdot\dot{\omega}_5\right.\right.$$

$$\left.\left. + \left(m_{15}\bar{r}_8 + m_{16}\bar{r}_9\right)\cdot\dot{\omega}_6\right] + m_8\left(m_{16}\bar{r}_{10} + m_{17}\bar{r}_{11}\right)\cdot\bar{r}_{12}\cdot\dot{\omega}_8\right\} + \frac{m_1}{M}\left(m_{78}\bar{r}_{10} + m_8\bar{r}_{11}\right)\cdot\ddot{\varepsilon}_{12} - T_{8y} + \bar{\omega}_7\cdot(J_7\cdot\omega_7)$$

$$- \frac{1}{M}\left\{\left(m_{78}\bar{r}_{10} + m_8\bar{r}_{11}\right)\cdot\left\{m_{12}\left[\bar{\omega}_2\cdot(\bar{r}_1\cdot\omega_2) + \bar{\omega}_3\cdot(\bar{r}_2\cdot\omega_3)\right] + m_{13}\left[\bar{\omega}_3\cdot(\bar{r}_3\cdot\omega_3) + \bar{\omega}_4\cdot(\bar{r}_4\cdot\omega_4)\right]\right.\right.$$

$$+ m_{14}\left[\bar{\omega}_4\cdot(\bar{r}_5\cdot\omega_4) + \bar{\omega}_5\cdot(\bar{r}_6\cdot\omega_5)\right] + m_{15}\left[\bar{\omega}_5\cdot(\bar{r}_7\cdot\omega_5) + \bar{\omega}_6\cdot(\bar{r}_8\cdot\omega_6)\right]$$

$$\left.\left. + m_{16}\left[\bar{\omega}_6\cdot(\bar{r}_9\cdot\omega_6) + \bar{\omega}_7\cdot(\bar{r}_{10}\cdot\omega_7)\right]\right) + m_8\left(m_{16}\bar{r}_{10} + m_{17}\bar{r}_{11}\right)\cdot\left[\bar{\omega}_7\cdot(\bar{r}_{11}\cdot\omega_7) + \bar{\omega}_8\cdot(\bar{r}_{12}\cdot\omega_8)\right]\right\}$$

$$+ \frac{m_1}{M}\left(m_{78}\bar{r}_{10} + m_8\bar{r}_{11}\right)\cdot\left[\dot{\bar{\omega}}_2\cdot\epsilon_{12} + 2\bar{\omega}_2\cdot\dot{\epsilon}_{12} + \bar{\omega}_2\cdot(\bar{\omega}_2\cdot\epsilon_{12})\right] \qquad (2\text{-}124)$$

$$T_{8e} + \bar{R}_{88} \cdot F_{8e} + \frac{1}{M}\left[\bar{r}_{12} \cdot \left(m_{17} F_{8e} - m_8 \sum_{j=1}^{7} F_{je}\right)\right] = \left[J_8 - \frac{m_8}{M} m_{17} \bar{r}_{12} \cdot \bar{r}_{12}\right] \cdot \dot{\omega}_8 + d_{78} \cdot (\omega_8 - \omega_7)$$

$$+ k_{78}(\theta_8 - \theta_7) - \frac{m_8}{M}\left\{\bar{r}_{12} \cdot \left[m_{12} \bar{r}_1 \cdot \dot{\omega}_2 + (m_{12} \bar{r}_2 + m_{13} \bar{r}_3) \cdot \dot{\omega}_3 + (m_{13} \bar{r}_4 + m_{14} \bar{r}_5) \cdot \dot{\omega}_4\right.\right.$$

$$\left.\left. + (m_{14} \bar{r}_6 + m_{15} \bar{r}_7) \cdot \dot{\omega}_5 + (m_{15} \bar{r}_8 + m_{16} \bar{r}_9) \cdot \dot{\omega}_6 + (m_{16} \bar{r}_{10} + m_{17} \bar{r}_{11}) \cdot \dot{\omega}_7\right]\right\} + \frac{m_8}{M} m_1 \bar{r}_{12} \cdot \ddot{\epsilon}_{12}$$

$$+ \bar{\omega}_8 \cdot (J_8 \cdot \omega_8) - \frac{m_8}{M}\left\{m_{12} \bar{r}_{12} \cdot \left[\bar{\omega}_1 \cdot (\bar{r}_1 \cdot \omega_1) + \bar{\omega}_2 \cdot (\bar{r}_2 \cdot \omega_2)\right] + m_{13} \bar{r}_{12} \cdot \left[\bar{\omega}_3 \cdot (\bar{r}_3 \cdot \omega_3) + \bar{\omega}_4 \cdot (\bar{r}_4 \cdot \omega_4)\right]\right.$$

$$+ m_{14} \bar{r}_{12} \cdot \left[\bar{\omega}_4 \cdot (\bar{r}_5 \cdot \omega_4) + \bar{\omega}_5 \cdot (\bar{r}_6 \cdot \omega_5)\right] + m_{15} \bar{r}_{12} \cdot \left[\bar{\omega}_5 \cdot (\bar{r}_7 \cdot \omega_5) + \bar{\omega}_6 \cdot (\bar{r}_8 \cdot \omega_6)\right]$$

$$\left. + m_{16} \bar{r}_{12} \cdot \left[\bar{\omega}_6 \cdot (\bar{r}_9 \cdot \omega_6) + \bar{\omega}_7 \cdot (\bar{r}_{10} \cdot \omega_7)\right] + m_{17} \bar{r}_{12} \cdot \left[\bar{\omega}_7 \cdot (\bar{r}_{11} \cdot \omega_7) + \bar{\omega}_8 \cdot (\bar{r}_{12} \cdot \omega_8)\right]\right\}$$

$$+ \frac{m_8}{M} m_1 \bar{r}_{12}\left[\dot{\bar{\omega}}_2 \cdot \epsilon_{12} + 2\bar{\omega}_2 \cdot \dot{\epsilon}_{12} + \bar{\omega}_2 \cdot (\bar{\omega}_2 \cdot \epsilon_{12})\right] \qquad (2\text{-}125)$$

$$\frac{1}{M}\left(m_1 \sum_{j=2}^{8} F_{je} - m_{28} F_{1e}\right) = \frac{m_1}{M} m_{28} \ddot{\epsilon}_{12} + 4D \cdot \dot{\epsilon}_{12} + 4K \cdot \epsilon_{12} - \frac{m_1}{M}\left[m_{38} \bar{r}_1 \cdot \dot{\omega}_2 + (m_{38} \bar{r}_2 + m_{48} \bar{r}_3) \cdot \dot{\omega}_3\right.$$

$$+ (m_{48} \bar{r}_4 + m_{58} \bar{r}_5) \cdot \dot{\omega}_4 + (m_{58} \bar{r}_6 + m_{68} \bar{r}_7) \cdot \dot{\omega}_5 + (m_{68} \bar{r}_8 + m_{78} \bar{r}_9) \cdot \dot{\omega}_6 + (m_{78} \bar{r}_{10} + m_8 \bar{r}_{11}) \cdot \dot{\omega}_7$$

$$\left. + m_8 \bar{r}_{12} \cdot \dot{\omega}_8\right] - 4D \cdot \left[\bar{R}_{E20} \cdot (\omega_2 - \omega_1)\right] + 4D \cdot \bar{R}_{120} \cdot \omega_1 - 4K \cdot \left[\bar{R}_{E20} \cdot (\theta_2 - \theta_1)\right] + 4K \cdot \bar{R}_{120} \cdot \theta_1$$

$$- \frac{m_8}{M}\left\{m_{38}\left[\bar{\omega}_2 \cdot (\bar{r}_1 \cdot \omega_2) + \bar{\omega}_3 \cdot (\bar{r}_2 \cdot \omega_3)\right] + m_{48}\left[\bar{\omega}_3 \cdot (\bar{r}_3 \cdot \omega_3) + \bar{\omega}_4 \cdot (\bar{r}_4 \cdot \omega_4)\right]\right.$$

$$+ m_{58}\left[\bar{\omega}_4 \cdot (\bar{r}_5 \cdot \omega_4) + \bar{\omega}_5 \cdot (\bar{r}_6 \cdot \omega_5)\right] + m_{68}\left[\bar{\omega}_5 \cdot (\bar{r}_7 \cdot \omega_5) + \bar{\omega}_6 \cdot (\bar{r}_8 \cdot \omega_6)\right]$$

$$\left. + m_{78}\left[\bar{\omega}_6 \cdot (\bar{r}_9 \cdot \omega_6) + \bar{\omega}_7 \cdot (\bar{r}_{10} \cdot \omega_7)\right] + m_8\left[\bar{\omega}_7 \cdot (\bar{r}_{11} \cdot \omega_7) + \bar{\omega}_8 \cdot (\bar{r}_{12} \cdot \omega_8\right]\right\} \qquad (2\text{-}126)$$

where

$${}_3M_2^c\Big|_2^{x,y}$$ = Constraint torque applied by body 2 on body 3 about the x and y axes written in body 2 coordinates

$${}_3M_2^c\Big|_3^{x,y}$$ = Constraint torque applied by body 2 on body 3 about the x and y axes written on body 3 coordinates

$${}_5M_4^c\Big|_4^{y,z}$$ = Constraint torque applied by body 4 on body 5 about the y and z axes written in body 4 coordinates

$${}_5M_4^c\Big|_5^{y,z}$$ = Constraint torque applied by body 4 on body 5 about the y and z axes written in body 5 coordinates

$${}_7M_6^c\Big|_6^{x,z}$$ = Constraint torque applied by body 6 on body 7 about the x and z axes written in body 6 coordinates

$${}_7M_6^c\Big|_7^{x,z}$$ = Constraint torque applied by body 6 on body 7 about the x and z axes written in body 7 coordinates

The definition of the various matrices indicated in equations (2-118) thru (2-126) is given at the end of this section.

The reason the constraint torques only appear about two axes reflects that each of the gimbals have a single rotational degree of freedom. In addition, the gimbal friction and wire torques only act about the axis of the respective gimbal rotational degree of freedom as indicated in the above equations.

Inserting the gimbal constraints, the following relationships result:

$$\dot{\omega}_3 = {}_3T_2^{*T} \cdot \dot{\omega}_2 + \begin{bmatrix} 0 \\ 0 \\ \dot{\omega}_{3z} \end{bmatrix} \tag{2-127}$$

$$\omega_3 = {}_3T_2^{*T} \cdot \omega_2 + \begin{bmatrix} 0 \\ 0 \\ \omega_{3z} \end{bmatrix} \tag{2-128}$$

$$\dot{\omega}_5 = {}_5T_4^{*T} \cdot \dot{\omega}_4 + \begin{bmatrix} \dot{\omega}_{5x} \\ 0 \\ 0 \end{bmatrix} \tag{2-129}$$

$$\omega_5 = {}_5T_4^{*T} \cdot \omega_4 + \begin{bmatrix} \omega_{5x} \\ 0 \\ 0 \end{bmatrix} \tag{2-130}$$

$$\dot{\omega}_7 = {}_7T_6^{*T} \cdot \dot{\omega}_6 + \begin{bmatrix} 0 \\ \dot{\omega}_{7y} \\ 0 \end{bmatrix} \tag{2-131}$$

$$\omega_7 = {}_7T_6^{*T} \cdot \omega_6 + \begin{bmatrix} 0 \\ \omega_{7y} \\ 0 \end{bmatrix} \tag{2-132}$$

$${}_3M_2^c|_2 = {}_2T_3^* \cdot {}_3M_2^c|_3 = {}_3T_2^{*T} \cdot {}_3M_2^c|_3 \tag{2-133}$$

$${}_5M_4^c|_4 = {}_4T_5^* \cdot {}_5M_4^c|_5 = {}_5T_4^{*T} \cdot {}_5M_4^c|_5 \tag{2-134}$$

$${}_7M_6^c|_6 = {}_6T_7^* \cdot {}_7M_6^c|_7 = {}_7T_6^{*T} \cdot {}_7M_6^c|_7 \tag{2-135}$$

$$ {}_3T_2 = \begin{bmatrix} \cos\alpha_z & \sin\alpha_z & 0 \\ -\sin\alpha_z & \cos\alpha_z & 0 \\ 0 & 0 & 1 \end{bmatrix} \tag{2-136} $$

$$ {}_3T_2^* = \begin{bmatrix} \cos\alpha_z & \sin\alpha_z & 0 \\ -\sin\alpha_z & \cos\alpha_z & 0 \\ 0 & 0 & 0 \end{bmatrix} \tag{2-137} $$

$$ {}_5T_4 = \begin{bmatrix} 1 & 0 & 0 \\ 0 & \cos\beta_x & \sin\beta_x \\ 0 & -\sin\beta_x & \cos\beta_x \end{bmatrix} \tag{2-138} $$

$$ {}_5T_4^* = \begin{bmatrix} 0 & 0 & 0 \\ 0 & \cos\beta_x & \sin\beta_x \\ 0 & -\sin\beta_x & \cos\beta_x \end{bmatrix} \tag{2-139} $$

$$ {}_7T_6 = \begin{bmatrix} \cos\gamma_y & 0 & -\sin\gamma_y \\ 0 & 1 & 0 \\ \sin\gamma_y & 0 & \cos\gamma_y \end{bmatrix} \tag{2-140} $$

$$ {}_7T_6^* = \begin{bmatrix} \cos\gamma_y & 0 & -\sin\gamma_y \\ 0 & 0 & 0 \\ \sin\gamma_y & 0 & \cos\gamma_y \end{bmatrix} \tag{2-141} $$

$$ \alpha_z = \theta_{3z} - \theta_{2z} \tag{2-142} $$

$$ \beta_x = \theta_{5x} - \theta_{4x} \tag{2-143} $$

$$ \gamma_z = \theta_{7y} - \theta_{6y} \tag{2-144} $$

$$ \dot{\alpha}_z = \omega_{3z} - \omega_{2z} \tag{2-145} $$

$$ \dot{\beta}_x = \omega_{5x} - \omega_{4x} \tag{2-146} $$

$$ \dot{\gamma}_y = \omega_{7y} - \omega_{6y} \tag{2-147} $$

Equations (2-146) thru (2-147) are used to compute the relative orientations of the various bodies or they form the strapdown equations of motion.

In order to complete the equation of motion development for the offset gimbal system configuration, the constraint torques must be eliminated from equations (2-119) thru (2-124).

The constraint torques may be eliminated by solving equations (2-120), (2-122), and (2-124) for these torques which only act about two axes. Hence the constraint torques are given by the expressions that follow:

$$
{}_3M_2^c\Big|_2^{xy} = {}_3T_2^{*T}\cdot\Bigg\{\Big(J_3 - \frac{1}{M}\Big[m_{12}\left(m_{38}\bar{r}_2 + m_{48}\bar{r}_1\right)\cdot\bar{r}_2 + m_{48}\left(m_{12}\bar{r}_2 + m_{13}\bar{r}_3\right)\cdot\bar{r}_3\Big]\Big)\cdot\left({}_3T_2^{*}\cdot\dot{\omega}_2 + \begin{bmatrix}0\\0\\\dot{\omega}_{3z}\end{bmatrix}\right)
$$

$$
+ d_{34}\cdot\left({}_3T_2^{*}\cdot\omega_2 + \begin{bmatrix}0\\0\\\omega_{3z}\end{bmatrix} - \omega_4\right) + k_{34}\cdot\left({}_3T_2^{*}\cdot\theta_2 + \begin{bmatrix}0\\0\\\theta_{3z}\end{bmatrix} - \theta_4\right) - \frac{1}{M}\Big\{m_{12}\left(m_{38}\bar{r}_2 + m_{48}\bar{r}_3\right)\cdot{}_3T_2\cdot\bar{r}_1\cdot\dot{\omega}_2
$$

$$
+ \left(m_{12}\bar{r}_2 + m_{13}\bar{r}_3\right)\cdot\Big[\left(m_{48}\bar{r}_4 + m_{58}\bar{r}_5\right)\cdot\dot{\omega}_4 + {}_5T_4^{T}\cdot\left(m_{58}\bar{r}_6 + m_{68}\bar{r}_7\right)\cdot\left({}_5T_4^{*}\cdot\dot{\omega}_4 + \begin{bmatrix}\dot{\omega}_{5x}\\0\\0\end{bmatrix}\right)
$$

$$
+ {}_5T_4^{T}\cdot\left(m_{68}\bar{r}_8 + m_{78}\bar{r}_9\right)\cdot\dot{\omega}_6 + {}_5T_4^{T}\cdot{}_7T_6^{T}\left(m_{78}\bar{r}_{10} + m_8\bar{r}_{11}\right)\cdot\left({}_7T_6^{*}\dot{\omega}_6 + \begin{bmatrix}0\\\dot{\omega}_{7y}\\0\end{bmatrix}\right)
$$

$$
+ m_8\,{}_5T_4^{T}\cdot{}_7T_6^{T}\cdot\bar{r}_{12}\cdot\dot{\omega}_8\Big]\Big\} + \frac{m_1}{M}\left(m_{38}\bar{r}_2 + m_{48}\bar{r}_3\right)\cdot{}_3T_2\cdot\dot{\epsilon}_{12} - \Big\{T_{3e} + \bar{R}_{33}\cdot F_{3e}
$$

$$
+ \frac{1}{M}\Big[\bar{r}_2\cdot\Big[m_{12}\Big(F_{3e} + F_{4e} + {}_5T_4^{T}\cdot\left(F_{5e} + F_{6e}\right) + {}_5T_4^{T}\cdot{}_7T_6^{T}\cdot\left(F_{7e} + F_{8e}\right)\Big) - m_{38}\,{}_3T_2\cdot\left(F_{1e} + F_{2e}\right)\Big]
$$

$$
+ \bar{r}_3\cdot\Big[m_{13}\Big(F_{4e} + {}_5T_4^{T}\cdot\left(F_{5e} + F_{6e}\right) + {}_5T_4^{T}\cdot{}_7T_6^{T}\cdot\left(F_{7e} + F_{8e}\right)\Big) - m_{48}\Big({}_3T_2\cdot\left(F_{1e} + F_{2e}\right) + F_{3e}\Big)\Big]\Big]\Big\}
$$

(2-148)

$$
{}_5M_4^c\big|_4^{yz} = {}_5T_4^{*T}\left\{\left[J_5 - \frac{1}{M}\left[m_{14}\left(m_{58}\bar{r}_6 + m_{68}\bar{r}_7\right)\cdot\bar{r}_6 + m_{68}\left(m_{14}\bar{r}_5 + m_{15}\bar{r}_7\right)\cdot\bar{r}_7\right]\right]\cdot\left({}_5T_4^{*}\cdot\dot{\omega}_4 + \begin{bmatrix}\dot{\omega}_{5x}\\0\\0\end{bmatrix}\right)\right.
$$

$$
+ d_{56}\cdot\left({}_5T_4^{*}\cdot\omega_4 + \begin{bmatrix}\omega_{5x}\\0\\0\end{bmatrix} - \omega_6\right) + k_{56}\cdot\left({}_5T_4^{*}\cdot\theta_4 + \begin{bmatrix}\theta_{5x}\\0\\0\end{bmatrix} - \theta_6\right) - \frac{1}{M}\left[\left(m_{58}\bar{r}_6 + m_{68}\bar{r}_7\right)\cdot\left[m_{12}\,{}_5T_4\cdot{}_3T_2\cdot\bar{r}_1\cdot\dot{\omega}_2\right.\right.
$$

$$
\left.+ {}_5T_4\cdot\left(m_{12}\bar{r}_2 + m_{13}\bar{r}_3\right)\cdot\left({}_3T_2^{*}\cdot\dot{\omega}_2 + \begin{bmatrix}0\\0\\\dot{\omega}_{3z}\end{bmatrix}\right) + {}_5T_4\cdot\left(m_{13}\bar{r}_4 + m_{14}\bar{r}_5\right)\cdot\dot{\omega}_4\right]
$$

$$
+ \left(m_{14}\bar{r}_6 + m_{15}\bar{r}_7\right)\cdot\left[\left(m_{68}\bar{r}_8 + m_{78}\bar{r}_7\right)\cdot\dot{\omega}_{\cdot} + {}_7T_6^{T}\cdot\left(m_{78}\bar{r}_{10} + m_8\bar{r}_{11}\right)\cdot\left({}_7T_6^{*}\cdot\dot{\omega}_6 + \begin{bmatrix}0\\\dot{\omega}_{7y}\\0\end{bmatrix}\right)\right.
$$

$$
\left.\left. + m_8\,{}_7T_6^{T}\cdot\bar{r}_{12}\cdot\dot{\omega}_8\right]\right] + \frac{m_1}{M}\left(m_{58}\bar{r}_6 + m_{68}\bar{r}_7\right)\cdot{}_5T_4\cdot{}_3T_2\cdot\ddot{\epsilon}_{12} \quad - \left[T_{5e} + \bar{R}_{55}\cdot F_{5e}\right.
$$

$$
+ \frac{1}{M}\left[\bar{r}_6\cdot\left[m_{14}\left(F_{5e} + F_{6e} + {}_7T_6^{T}\cdot\left(F_{7e} + F_{8e}\right)\right) - m_{58}\left({}_5T_4\cdot{}_3T_2\cdot\left(F_{1e} + F_{2e}\right) + {}_5T_4\cdot\left(F_{3e} + F_{4e}\right)\right)\right]\right.
$$

$$
\left.\left.\left.+ \bar{r}_7\cdot\left[m_{15}\left(F_{6e} + {}_7T_6^{T}\cdot\left(F_{7e} + F_{8e}\right)\right) - m_{68}\left({}_5T_4\cdot{}_3T_2\cdot\left(F_{1e} + F_{2e}\right) + {}_5T_4\left(F_{3e} + F_{4e}\right) + F_{5e}\right)\right]\right]\right]\right\}
$$

(2-149)

$$
{}_7M_6^c\big|_6^{xz} = {}_7T_6^{*T}\cdot\Big\{\Big[J_7 - \frac{1}{M}\Big[m_{16}(m_{78}\bar{r}_{10}+m_8\bar{r}_{11})\circ\bar{r}_{10} + m_8(m_{16}\bar{r}_{10}+m_{17}\bar{r}_{11})\cdot\bar{r}_{11}\Big]\cdot({}_7T_6^*\cdot\dot{\omega}_6 + \begin{bmatrix}0\\ \dot{\omega}_{7y}\\ 0\end{bmatrix}\Big)
$$

$$
+ d_{78}\cdot({}_7T_6^*\cdot\omega_6 + \begin{bmatrix}0\\ \omega_{7y}\\ 0\end{bmatrix} - \omega_8) + k_{78}\cdot({}_7T_6^*\cdot\theta_6 + \begin{bmatrix}0\\ \theta_{7y}\\ 0\end{bmatrix} - \theta_8) - \frac{1}{M}\Big[(m_{78}\bar{r}_{10}+m_8\bar{r}_{11})\cdot\Big[m_{12}\,{}_7T_6\cdot{}_5T_4\cdot{}_3T_2\cdot\bar{r}_1\cdot\dot{\omega}_2
$$

$$
+ {}_7T_6\cdot{}_5T_4\cdot(m_{12}\bar{r}_2+m_{13}\bar{r}_3)\cdot({}_3T_2^*\cdot\dot{\omega}_2 + \begin{bmatrix}0\\ 0\\ \dot{\omega}_{3z}\end{bmatrix}) + {}_7T_6\cdot{}_5T_4\cdot(m_{13}\bar{r}_4+m_{14}\bar{r}_5)\cdot\dot{\omega}_4
$$

$$
+ {}_7T_6\cdot(m_{14}\bar{r}_6+m_{15}\bar{r}_7)\cdot({}_5T_4^*\cdot\dot{\omega}_4 + \begin{bmatrix}\dot{\omega}_{5x}\\ 0\\ 0\end{bmatrix}) + {}_7T_6\cdot(m_{15}\bar{r}_8+m_{16}\bar{r}_9)\cdot\dot{\omega}_6\Big] + m_8(m_{16}\bar{r}_{10}+m_{17}\bar{r}_{11})\cdot\bar{r}_{12}\cdot\dot{\omega}_8\Big]
$$

$$
+ \frac{m_1}{M}(m_{78}\bar{r}_{10}+m_8\bar{r}_{11})\cdot{}_7T_6\cdot{}_5T_4\cdot{}_3T_2\cdot\ddot{\epsilon}_{12} - \Big[T_{7e} + \bar{R}_{77}\cdot F_{7e} + \frac{1}{M}\Big[\bar{r}_{10}\cdot\Big[m_{16}(F_{7e}+F_{8e})
$$

$$
- m_{78}\Big({}_7T_6\cdot{}_5T_4\cdot{}_3T_2\cdot(F_{1e}+F_{2e}) + {}_7T_6\cdot{}_5T_4\cdot(F_{3e}+F_{4e}) + {}_7T_6\cdot(F_{5e}+F_{6e})\Big)\Big]
$$

$$
+ \bar{r}_{11}\cdot\Big[m_{17}F_{8e} - m_8\Big({}_7T_6\cdot{}_5T_4\cdot{}_3T_2\cdot(F_{1e}+F_{2e}) + {}_7T_6\cdot{}_5T_4\cdot(F_{3e}+F_{4e}) + {}_7T_6\cdot(F_{5e}+F_{6e}) + F_{7e}\Big)\Big]\Big]\Big]\Big\}
$$

(2-150)

It should be noted that in the derivation of the gimbal constraint torques only the linear terms were considered, and everything that follows from this point on considers only the linear terms of the equations of motion.

Substitution of equations (2-148),(2-149), and (2-150) into equations (2-119), (2-121), and (2-123) respectively results in a set of system equations that can be written in the following manner:

$$A_{11} \cdot \dot{\omega}_1 = a_{11} \cdot \omega_1 + a_{12} \cdot \theta_1 + a_{13} \cdot \omega_2 + a_{14} \cdot \theta_2 + a_{15} \cdot \dot{\epsilon}_{12} + a_{16} \cdot \epsilon_{12} + D_1 \qquad (2\text{-}151)$$

$$B_{11} \cdot \dot{\omega}_2 + B_{12} \cdot \dot{\omega}_{3z} + B_{13} \cdot \dot{\omega}_4 + B_{14} \cdot \dot{\omega}_{5x} + B_{15} \cdot \dot{\omega}_6 + B_{16} \cdot \dot{\omega}_{7y} + B_{17} \cdot \dot{\omega}_8 + B_{18} \cdot \ddot{\epsilon}_{12} = b_{11} \cdot \omega_1$$
$$+ b_{12} \cdot \theta_1 + b_{13} \cdot \omega_2 + b_{14} \cdot \theta_2 + b_{15} \cdot \omega_4 + b_{16} \cdot \theta_4 + b_{17} \cdot \dot{\epsilon}_{12} + b_{18} \cdot \epsilon_{12} + b_{19} T_{\alpha z} + D_2 \qquad (2\text{-}152)$$

$$B_{21} \cdot \dot{\omega}_2 + B_{22} \cdot \dot{\omega}_{3z} + B_{23} \cdot \dot{\omega}_4 + B_{24} \cdot \dot{\omega}_{5x} + B_{25} \cdot \dot{\omega}_6 + B_{26} \cdot \dot{\omega}_{7y} + B_{27} \cdot \dot{\omega}_8 + B_{28} \cdot \ddot{\epsilon}_{12} = b_{21} \cdot \omega_{3z}$$
$$+ b_{22} \cdot \theta_{3z} + b_{23} \cdot \omega_4 + b_{24} \cdot \theta_4 + b_{25} T_{\alpha z} + D_3 \qquad (2\text{-}153)$$

$$B_{31} \cdot \dot{\omega}_2 + B_{32} \cdot \dot{\omega}_{3z} + B_{33} \cdot \dot{\omega}_4 + B_{34} \cdot \dot{\omega}_{5x} + B_{35} \cdot \dot{\omega}_6 + B_{36} \cdot \dot{\omega}_{7y} + B_{37} \cdot \dot{\omega}_8 + B_{38} \cdot \ddot{\epsilon}_{12} = b_{31} \cdot \omega_2$$
$$+ b_{32} \cdot \theta_2 + b_{33} \cdot \omega_{3z} + b_{34} \cdot \theta_{3z} + b_{35} \cdot \omega_4 + b_{36} \cdot \theta_4 + b_{37} \cdot \omega_6 + b_{38} \cdot \theta_6 + b_{39} T_{\beta x} + D_4 \qquad (2\text{-}154)$$

$$B_{41} \cdot \dot{\omega}_2 + B_{42} \cdot \dot{\omega}_{3z} + B_{43} \cdot \dot{\omega}_4 + B_{44} \cdot \dot{\omega}_{5x} + B_{45} \cdot \dot{\omega}_6 + B_{46} \cdot \dot{\omega}_{7y} + B_{47} \cdot \dot{\omega}_8 + B_{48} \cdot \ddot{\epsilon}_{12} = b_{41} \omega_{5x}$$
$$+ b_{42} \cdot \theta_{5x} + b_{43} \cdot \omega_6 + b_{44} \cdot \theta_6 + b_{45} T_{\beta x} + D_5 \qquad (2\text{-}155)$$

$$B_{51} \cdot \dot{\omega}_2 + B_{52} \cdot \dot{\omega}_{3z} + B_{53} \cdot \dot{\omega}_4 + B_{54} \cdot \dot{\omega}_{5x} + B_{55} \cdot \dot{\omega}_6 + B_{56} \cdot \dot{\omega}_{7y} + B_{57} \cdot \dot{\omega}_8 + B_{58} \cdot \ddot{\epsilon}_{12} = b_{51} \cdot \omega_4$$
$$+ b_{52} \cdot \theta_4 + b_{53} \cdot \omega_{5x} + b_{54} \cdot \theta_{5x} + b_{55} \cdot \omega_6 + b_{56} \cdot \theta_6 + b_{57} \cdot \omega_8 + b_{58} \cdot \theta_8 + b_{59} T_{\gamma y} + D_6 \qquad (2\text{-}156)$$

$$B_{61} \cdot \dot{\omega}_2 + B_{62} \cdot \dot{\omega}_{3z} + B_{63} \cdot \dot{\omega}_4 + B_{64} \cdot \dot{\omega}_{5x} + B_{65} \cdot \dot{\omega}_6 + B_{66} \cdot \dot{\omega}_{7y} + B_{67} \cdot \dot{\omega}_8 + B_{68} \cdot \ddot{\epsilon}_{12} = b_{61} \cdot \omega_{7y}$$
$$+ b_{62} \cdot \theta_{7y} + b_{63} \cdot \omega_8 + b_{64} \cdot \theta_8 + b_{65} T_{\gamma y} + D_7 \qquad (2\text{-}157)$$

$$B_{71} \cdot \dot{\omega}_2 + B_{72} \cdot \dot{\omega}_{3z} + B_{73} \cdot \dot{\omega}_4 + B_{74} \cdot \dot{\omega}_{5x} + B_{75} \cdot \dot{\omega}_6 + B_{76} \cdot \dot{\omega}_{7y} + B_{77} \cdot \dot{\omega}_8 + B_{78} \cdot \ddot{\epsilon}_{12} = b_{71} \cdot \omega_6$$
$$+ b_{72} \cdot \theta_6 + b_{73} \cdot \omega_{7y} + b_{74} \cdot \theta_{7y} + b_{75} \cdot \omega_8 + b_{76} \cdot \theta_8 + D_8 \qquad (2\text{-}158)$$

$$B_{81} \cdot \dot{\omega}_2 + B_{82} \cdot \dot{\omega}_{3z} + B_{83} \cdot \dot{\omega}_4 + B_{84} \cdot \dot{\omega}_{5x} + B_{85} \cdot \dot{\omega}_6 + B_{86} \cdot \dot{\omega}_{7y} + B_{87} \cdot \dot{\omega}_8 + B_{88} \cdot \ddot{\epsilon}_{12} = b_{81} \cdot \omega_1$$
$$+ b_{82} \cdot \theta_1 + b_{83} \cdot \omega_2 + b_{84} \cdot \theta_2 + b_{85} \cdot \dot{\epsilon}_{12} + b_{86} \cdot \epsilon_{12} + D_9 \qquad (2\text{-}159)$$

where

$$A_{11} = J_1 \tag{2-160}$$

$$a_{11} = 4(\bar{R}_{120} + \bar{R}_{E20}) \cdot D \cdot (\bar{R}_{120} + \bar{R}_{E20}) - d \tag{2-161}$$

$$a_{12} = 4(\bar{R}_{120} + \bar{R}_{E20}) \cdot K \cdot (\bar{R}_{120} + \bar{R}_{E20}) - k \tag{2-162}$$

$$a_{13} = d - 4(\bar{R}_{120} + \bar{R}_{E20}) \cdot D \cdot \bar{R}_{E20} \tag{2-163}$$

$$a_{14} = k - 4(\bar{R}_{120} + \bar{R}_{E20}) \cdot K \cdot \bar{R}_{E20} \tag{2-164}$$

$$a_{15} = 4(\bar{R}_{120} + \bar{R}_{E20}) \cdot D \tag{2-165}$$

$$a_{16} = 4(\bar{R}_{120} + \bar{R}_{E20}) \cdot K \tag{2-166}$$

$$B_{11} = J_2 + {}_3T_2^{*T} \cdot J_3 \cdot {}_3T_2^{*} - \frac{1}{M}\Big\{ m_{12} m_{38} \bar{r}_1 \cdot \bar{r}_1 + m_{12} \bar{r}_1 \cdot {}_3T_2^{T} \cdot (m_{38} \bar{r}_2 + m_{48} \bar{r}_3) \cdot {}_3T_2^{*}$$
$$+ {}_3T_2^{*T} \cdot \left[m_{12} (m_{38} \bar{r}_2 + m_{48} \bar{r}_3) \cdot \bar{r}_2 + m_{48} (m_{12} \bar{r}_2 + m_{13} \bar{r}_3) \cdot \bar{r}_3 \right] \cdot {}_3T_2^{*}$$
$$+ {}_3T_2^{*T} \cdot \left[m_{12} (m_{38} \bar{r}_2 + m_{48} \bar{r}_3) \cdot \bar{r}_3 \right] \cdot {}_3T_2 \cdot \bar{r}_1 \Big\} \qquad (2\text{-}167)$$

$$B_{12} = -\frac{1}{M}\Big\{ {}_3T_2^{*T} \cdot \left[m_{12} (m_{38} \bar{r}_2 + m_{48} \bar{r}_3) \cdot r_2 |_{3C} + m_{48} (m_{12} \bar{r}_2 + m_{13} \bar{r}_3) \cdot \bar{r}_3 |_{3C} \right]$$
$$+ m_{12} \bar{r}_1 \cdot {}_3T_2^{T} \cdot (m_{38} \bar{r}_2 |_{3C} + m_{48} \bar{r}_3 |_{3C}) \Big\} \qquad (2\text{-}168)$$

$$B_{13} = -\frac{1}{M}\Big\{ m_{12} \left[\bar{r}_1 \cdot {}_3T_2 \cdot (m_{48} \bar{r}_4 + m_{58} \bar{r}_5) + \bar{r}_1 \cdot {}_3T_2^{T} \cdot {}_5T_4^{T} \cdot (m_{58} \bar{r}_6 + m_{68} \bar{r}_7) \cdot {}_5T_4^{*} \right]$$
$$+ {}_3T_2^{T} \cdot \Big\{ (m_{12} \bar{r}_2 + m_{13} \bar{r}_3) \cdot \left[m_{48} \bar{r}_4 + m_{58} \bar{r}_5 + {}_5T_4^{T} \cdot (m_{58} \bar{r}_6 + m_{68} \bar{r}_7) \cdot {}_5T_4^{*} \right] \Big\} \Big\} \qquad (2\text{-}169)$$

$$B_{14} = -\frac{1}{M}\Big[m_{12} \bar{r}_1 \cdot {}_3T_2^{T} \cdot {}_5T_4^{T} \cdot (m_{58} \bar{r}_6 |_{1C} + m_{68} \bar{r}_7 |_{1C})$$
$$+ {}_3T_2^{*T} \cdot (m_{12} \bar{r}_2 + m_{13} \bar{r}_3) \cdot {}_5T_4^{T} \cdot (m_{58} \bar{r}_6 |_{1C} + m_{68} \bar{r}_7 |_{1C}) \Big] \qquad (2\text{-}170)$$

$$B_{15} = -\frac{1}{M}\Big\{ m_{12} \left[\bar{r}_1 \cdot {}_3T_2^{T} \cdot {}_5T_4^{T} \cdot (m_{68} \bar{r}_8 + m_{78} \bar{r}_9) + \bar{r}_1 \cdot {}_3T_2^{T} \cdot {}_5T_4^{T} \cdot {}_7T_6^{T} \cdot (m_{78} \bar{r}_{10} + m_8 \bar{r}_{11}) \cdot {}_7T_6^{*} \right.$$
$$\left. + {}_3T_2^{*T} \cdot (m_{12} \bar{r}_2 + m_{13} \bar{r}_3) \cdot \left[{}_5T_4 \cdot (m_{68} \bar{r}_8 + m_{78} \bar{r}_9) + {}_5T_4 \cdot {}_7T_6 \cdot (m_{78} \bar{r}_{10} + m_8 \bar{r}_{11}) \cdot {}_7T_6^{*} \right] \right\} \qquad (2\text{-}171)$$

$$B_{16} = -\frac{1}{M}\Big[m_{12} \bar{r}_1 \cdot {}_3T_2^{T} \cdot {}_5T_4^{T} \cdot {}_7T_6^{T} \cdot (m_{78} \bar{r}_{10} |_{2C} + m_8 \bar{r}_{11} |_{2C})$$
$$+ {}_3T_2^{*T} \cdot (m_{12} \bar{r}_2 + m_{13} \bar{r}_3) \cdot {}_5T_4^{T} \cdot {}_7T_6^{T} \cdot (m_{78} \bar{r}_{10} |_{2C} + m_8 \bar{r}_{11} |_{2C}) \Big] \qquad (2\text{-}172)$$

$$B_{17} = -\frac{m_8}{M}\Big[m_{12} \bar{r}_1 \cdot {}_3T_2^{T} \cdot {}_5T_4^{T} \cdot {}_7T_6^{T} \cdot \bar{r}_{12} + {}_3T_2^{*T} \cdot (m_{12} \bar{r}_2 + m_{13} \bar{r}_3) \cdot {}_5T_4^{T} \cdot {}_7T_6^{T} \cdot \bar{r}_{12} \Big] \qquad (2\text{-}173)$$

$$B_{18} = \frac{m_1}{M}\Big[m_{12} \bar{r}_1 + {}_3T_2^{*T} \cdot (m_{38} \bar{r}_2 + m_{48} \bar{r}_3) \cdot {}_3T_2 \qquad (2\text{-}174)$$

$$B_{21} = -\frac{1}{M}\left[m_{12}\left(m_{38}\bar{r}_2|_{3R} + m_{48}\bar{r}_3|_{3R}\right)\cdot {}_3T_2\cdot\bar{r}_1 + m_{12}\left(m_{38}\bar{r}_2|_{3R} + m_{48}\bar{r}_3|_{3R}\right)\cdot\bar{r}_2\cdot {}_3T_2^* + m_{48}\left(m_{12}\bar{r}_2|_{3R} + m_{13}\bar{r}_3|_{3R}\right)\cdot\bar{r}_3\cdot {}_3T_2^*\right] \quad (2\text{-}175)$$

$$B_{22} = J_{3z} - \frac{1}{M}\left[m_{12}\left(m_{38}\bar{r}_2|_{3R} + m_{48}\bar{r}_3|_{3R}\right)\cdot\bar{r}_2|_{3C} + m_{48}\left(m_{12}\bar{r}_2|_{3R} + m_{13}\bar{r}_3|_{3R}\right)\cdot\bar{r}_3|_{3C}\right] \quad (2\text{-}176)$$

$$B_{23} = -\frac{1}{M}\left(m_{12}\bar{r}_2|_{3R} + m_{13}\bar{r}_3|_{3R}\right)\cdot\left[m_{48}\bar{r}_4 + m_{58}\bar{r}_5 + {}_5T_4\circ\left(m_{58}\bar{r}_6 + m_{68}\bar{r}_7\right)\cdot {}_5T_4^*\right] \quad (2\text{-}177)$$

$$B_{24} = -\frac{1}{M}\left(m_{12}\bar{r}_2|_{3R} + m_{13}\bar{r}_3|_{3R}\right)\cdot {}_5T_4^T\cdot\left(m_{58}\bar{r}_5|_{1C} + m_{68}\bar{r}_7|_{1C}\right) \quad (2\text{-}178)$$

$$B_{25} = -\frac{1}{M}\left(m_{12}\bar{r}_2|_{3R} + m_{13}\bar{r}_3|_{3R}\right)\cdot\left[{}_5T_4^T\cdot\left(m_{48}\bar{r}_8 + m_{78}\bar{r}_9\right) + {}_5T_4^T\cdot {}_7T_6^T\cdot\left(m_{78}\bar{r}_{10} + m_8\bar{r}_{11}\right)\cdot {}_7T_6^* \quad (2\text{-}179)$$

$$B_{26} = -\frac{1}{M}\left(m_{12}\bar{r}_2|_{3R} + m_{13}\bar{r}_3|_{3R}\right)\cdot {}_5T_4^T\cdot {}_7T_6^T\cdot\left(m_{78}\bar{r}_{10}|_{2C} + m_8\bar{r}_{11}|_{2C}\right) \quad (2\text{-}180)$$

$$B_{27} = -\frac{m_8}{M}\left(m_{12}\bar{r}_2|_{3R} + m_{13}\bar{r}_3|_{3R}\right)\cdot {}_5T_4^T\circ {}_7T_6^T\cdot\bar{r}_{12} \quad (2\text{-}181)$$

$$B_{28} = \frac{m_1}{M}\left(m_{12}\bar{r}_2|_{3R} + m_{13}\bar{r}_3|_{3R}\right)\cdot {}_3T_2 \quad (2\text{-}182)$$

$$B_{31} = -\frac{1}{M}\Big\{ m_{12}\left(m_{48}\bar{r}_4 + m_{58}\bar{r}_5\right)\cdot {}_3T_2\cdot\bar{r}_1 + \left(m_{48}\bar{r}_4 + m_{58}\bar{r}_5\right)\cdot\left(m_{12}\bar{r}_2 + m_{13}\bar{r}_3\right)\cdot {}_3T_2^{*}$$
$$+ {}_5T_4^{*T}\cdot\left(m_{58}\bar{r}_6 + m_{68}\bar{r}_7\right)\cdot\left[m_{12}\cdot {}_5T_4\cdot {}_3T_2\cdot\bar{r}_1 + {}_5T_4\cdot\left(m_{12}\bar{r}_2 + m_{13}\bar{r}_3\right)\cdot {}_3T_2^{*}\right]\Big\} \qquad (2\text{-}183)$$

$$B_{32} = -\frac{1}{M}\Big[m_{12}\left(m_{48}\bar{r}_4 + m_{58}\bar{r}_5\right)\cdot\bar{r}_2|_{3C} + m_{13}\left(m_{48}\bar{r}_4 + m_{58}\bar{r}_5\right)\cdot\bar{r}_3|_{3C}$$
$$+ {}_5T_4^{*T}\cdot\left(m_{58}\bar{r}_6 + m_{68}\bar{r}_7\right)\cdot {}_5T_4\cdot\left(m_{12}\bar{r}_2|_{3C} + m_{13}\bar{r}_3|_{3C}\right)\Big] \qquad (2\text{-}184)$$

$$B_{33} = J_4 + {}_5T_4^{*T}\cdot J_5\cdot {}_5T_4^{*} - \frac{1}{M}\Big[m_{13}\left(m_{48}\bar{r}_4 + m_{58}\bar{r}_5\right)\cdot\bar{r}_4 + m_{58}\left(m_{13}\bar{r}_4 + m_{14}\bar{r}_5\right)\cdot\bar{r}_5$$
$$+ {}_5T_4^{*T}\cdot\Big[m_{14}\left(m_{58}\bar{r}_6 + m_{68}\bar{r}_7\right)\cdot\bar{r}_6 + m_{68}\left(m_{14}\bar{r}_6 + m_{15}\bar{r}_7\right)\cdot\bar{r}_7\Big]\cdot {}_5T_4^{*}$$
$$+ {}_5T_4^{*T}\cdot\left(m_{58}\bar{r}_6 + m_{68}\bar{r}_7\right)\cdot {}_5T_4\cdot\left(m_{13}\bar{r}_4 + m_{14}\bar{r}_5\right)$$
$$+ \left(m_{13}\bar{r}_4 + m_{14}\bar{r}_5\right)\cdot {}_5T_4^{T}\cdot\left(m_{58}\bar{r}_6 + m_{68}\bar{r}_7\right)\cdot {}_5T_4^{*} \qquad (2\text{-}185)$$

$$B_{34} = -\frac{1}{M}\Big\{ {}_5T_4^{*T}\cdot\Big[m_{14}\left(m_{58}\bar{r}_6 + m_{68}\bar{r}_7\right)\cdot\bar{r}_5|_{1C} + m_{68}\left(m_{14}\bar{r}_6 + m_{15}\bar{r}_7\right)\cdot\bar{r}_7|_{1C}\Big]$$
$$+ \left(m_{13}\bar{r}_4 + m_{14}\bar{r}_5\right)\cdot {}_5T_4^{T}\cdot\left(m_{58}\bar{r}_6|_{1C} + m_{68}\bar{r}_7|_{1C}\right)\Big\} \qquad (2\text{-}186)$$

$$B_{35} = -\frac{1}{M}\Big\{\left(m_{13}\bar{r}_4 + m_{14}\bar{r}_5\right)\cdot\Big[{}_5T_4^{T}\cdot\left(m_{68}\bar{r}_8 + m_{78}\bar{r}_9\right) + {}_5T_4^{T}\cdot {}_7T_6^{T}\cdot\left(m_{78}\bar{r}_{10} + m_8\bar{r}_{11}\right)\cdot {}_7T_6^{*}\Big]$$
$$+ {}_5T_4^{*T}\cdot\left(m_{14}\bar{r}_6 + m_{15}\bar{r}_7\right)\cdot\Big[m_{68}\bar{r}_8 + m_{78}\bar{r}_9 + {}_7T_6^{T}\cdot\left(m_{78}\bar{r}_{10} + m_8\bar{r}_{11}\right)\cdot {}_7T_6^{*}\Big]\Big\} \qquad (2\text{-}187)$$

$$B_{36} = -\frac{1}{M}\Big[\left(m_{13}\bar{r}_4 + m_{14}\bar{r}_5\right)\cdot {}_5T_4^{T}\cdot {}_7T_6^{T}\cdot\left(m_{78}\bar{r}_{10}|_{2C} + m_8 r_{11}|_{2C}\right)$$
$$+ {}_5T_4^{*T}\cdot\left(m_{14}\bar{r}_6 + m_{15}\bar{r}_7\right)\cdot {}_7T_6^{T}\cdot\left(m_{78}\bar{r}_{10}|_{2C} + m_8 r_{11}|_{2C}\right)\Big] \qquad (2\text{-}188)$$

$$B_{37} = -\frac{m_8}{M}\Big[\left(m_{13}\bar{r}_4 + m_{14}\bar{r}_5\right)\cdot {}_5T_4^{T}\cdot {}_7T_6^{T}\cdot\bar{r}_{12} + {}_5T_4^{*T}\cdot\left(m_{14}\bar{r}_6 + m_{15}\bar{r}_7\right)\cdot {}_7T_6^{T}\cdot\bar{r}_{12}\Big] \qquad (2\text{-}189)$$

$$B_{38} = \frac{m_1}{M}\Big[\left(m_{48}\bar{r}_4 + m_{58}\bar{r}_5\right)\cdot {}_3T_2 + {}_5T_4^{*T}\cdot\left(m_{58}\bar{r}_6 + m_{68}\bar{r}_7\right)\cdot {}_5T_4\cdot {}_3T_2 \qquad (2\text{-}190)$$

$$B_{41} = -\frac{1}{M}\left(m_{58}\bar{r}_6|_{1R} + m_{68}\bar{r}_7|_{1R}\right)\cdot\left[{}_5T_4\cdot{}_3T_2\cdot\bar{r}_1 + {}_5T_4\cdot\left(m_{12}\bar{r}_2 + m_{13}\bar{r}_3\right)\cdot{}_3T_2^*\right] \tag{2-191}$$

$$B_{42} = -\frac{1}{M}\left(m_{58}\bar{r}_6|_{1R} + m_{68}\bar{r}_7|_{1R}\right)\cdot{}_5T_4\cdot\left(m_{12}\bar{r}_2|_{3C} + m_{13}\bar{r}_3|_{3C}\right) \tag{2-192}$$

$$B_{43} = -\frac{1}{M}\left[\left(m_{58}\bar{r}_6|_{1R} + m_{68}\bar{r}_7|_{1R}\right)\cdot{}_5T_4\cdot\left(m_{13}\bar{r}_4 + m_{14}\bar{r}_5\right) + m_{14}\left(m_{58}\bar{r}_6|_{1R} + m_{68}\bar{r}_7|_{1R}\right)\cdot\bar{r}_6\cdot{}_5T_4^*\right.$$
$$\left. + m_{68}\left(m_{14}\bar{r}_6|_{1R} + m_{15}\bar{r}_7|_{1R}\right)\cdot\bar{r}_7\cdot{}_5T_4^*\right] \tag{2-193}$$

$$B_{44} = J_{5x} - \frac{1}{M}\left[m_{14}\left(m_{58}\bar{r}_6|_{1R} + m_{68}\bar{r}_7|_{1R}\right)\cdot\bar{r}_6|_{1C} + m_{68}\left(m_{14}\bar{r}_6|_{1R} + m_{15}\bar{r}_7|_{1R}\right)\cdot\bar{r}_7|_{1C}\right] \tag{2-194}$$

$$B_{45} = -\frac{1}{M}\left(m_{14}\bar{r}_6|_{1R} + m_{15}\bar{r}_7|_{1R}\right)\cdot\left[m_{68}\bar{r}_8 + m_{78}\bar{r}_9 + {}_7T_6^T\cdot\left(m_{78}\bar{r}_{10} + m_8\bar{r}_{11}\right)\cdot{}_7T_6^*\right] \tag{2-195}$$

$$B_{46} = -\frac{1}{M}\left(m_{14}\bar{r}_6|_{1R} + m_{15}\bar{r}_7|_{1R}\right)\cdot{}_7T_6^T\cdot\left(m_{78}\bar{r}_{10}|_{2C} + m_8\bar{r}_{11}|_{2C}\right) \tag{2-196}$$

$$B_{47} = -\frac{m_8}{M}\left(m_{14}\bar{r}_6|_{1R} + m_{15}\bar{r}_7|_{1R}\right)\cdot{}_7T_6^T\cdot\bar{r}_{12} \tag{2-197}$$

$$B_{48} = \frac{m_1}{M}\left(m_{58}\bar{r}_6|_{1R} + m_{68}\bar{r}_7|_{1R}\right)\cdot{}_5T_4\cdot{}_3T_2 \tag{2-198}$$

$$B_{51} = -\frac{1}{M}\Big\{ m_{12}\left(m_{68}\bar{r}_8 + m_{78}\bar{r}_9\right)\cdot {}_5T_4\cdot {}_3T_2\cdot \bar{r}_1 + {}_7T_6^*\cdot\left(m_{78}\bar{r}_{10} + m_8\bar{r}_{11}\right)\cdot\Big[m_{12}\,{}_7T_6\cdot {}_5T_4\cdot {}_3T_2\cdot \bar{r}_1$$
$$+ {}_7T_6\cdot {}_5T_4\cdot\left(m_{12}\bar{r}_2 + m_{13}\bar{r}_3\right)\cdot {}_3T_2^*\Big] + \left(m_{68}\bar{r}_8 + m_{78}\bar{r}_9\right)\cdot {}_5T_4\cdot\left(m_{12}\bar{r}_2 + m_{13}\bar{r}_3\right)\cdot {}_3T_2^*\Big\} \qquad (2\text{-}199)$$

$$B_{52} = -\frac{1}{M}\Big[\left(m_{68}\bar{r}_8 + m_{78}\bar{r}_9\right)\cdot {}_5T_4\cdot\left(m_{12}\bar{r}_2|_{3C} + m_{13}\bar{r}_3|_{3C}\right)$$
$$+ {}_7T_6^{*T}\cdot\left(m_{78}\bar{r}_{10} + m_8\bar{r}_{11}\right)\cdot {}_7T_6\cdot {}_5T_4\cdot\left(m_{12}\bar{r}_2|_{3C} + m_{13}\bar{r}_3|_{3C}\right)\Big] \qquad (2\text{-}200)$$

$$B_{53} = -\frac{1}{M}\Big\{\left(m_{68}\bar{r}_8 + m_{78}\bar{r}_9\right)\cdot\Big[{}_5T_4\cdot\left(m_{13}\bar{r}_4 + m_{14}\bar{r}_5\right) + \left(m_{14}\bar{r}_6 + m_{15}\bar{r}_7\right)\cdot {}_5T_4^*\Big]$$
$$+ {}_7T_6^{*T}\cdot\left(m_{78}\bar{r}_{10} + m_8\bar{r}_{11}\right)\cdot\Big[{}_7T_6\cdot {}_5T_4\cdot\left(m_{13}\bar{r}_4 + m_{14}\bar{r}_5\right) + {}_7T_6\cdot\left(m_{14}\bar{r}_6 + m_{15}\bar{r}_7\right)\cdot {}_5T_4^*\Big]\Big\} \qquad (2\text{-}201)$$

$$B_{54} = -\frac{1}{M}\Big[\left(m_{68}\bar{r}_8 + m_{78}\bar{r}_9\right)\cdot\left(m_{14}\bar{r}_6|_{1C} + m_{15}\bar{r}_7|_{1C}\right)$$
$$+ {}_7T_6^{*T}\cdot\left(m_{78}\bar{r}_{10} + m_8\bar{r}_{11}\right)\cdot {}_7T_6\cdot\left(m_{14}\bar{r}_6|_{1C} + m_{15}\bar{r}_7|_{1C}\right)\Big] \qquad (2\text{-}202)$$

$$B_{55} = J_6 + {}_7T_6^{*T}\cdot J_7\cdot {}_7T_6^* - \frac{1}{M}\Big\{ m_{15}\left(m_{68}\bar{r}_8 + m_{78}\bar{r}_9\right)\cdot\bar{r}_8 + m_{78}\left(m_{15}\bar{r}_8 + m_{16}\bar{r}_9\right)\cdot\bar{r}_9$$
$$+\left(m_{15}\bar{r}_8 + m_{16}\bar{r}_9\right)\cdot {}_7T_6^T\cdot\left(m_{78}\bar{r}_{10} + m_8\bar{r}_{11}\right)\cdot {}_7T_6^* + {}_7T_6^{*T}\cdot\left(m_{78}\bar{r}_{10} + m_8\bar{r}_{11}\right)\cdot\Big[m_{16}\bar{r}_{10}\cdot {}_7T_6^*$$
$$+ {}_7T_6\cdot\left(m_{15}\bar{r}_8 + m_{16}\bar{r}_9\right)\Big] + {}_7T_6^{*T}\cdot m_8\left(m_{16}\bar{r}_{10} + m_{17}\bar{r}_{11}\right)\cdot\bar{r}_{11}\cdot {}_7T_6^*\Big\} \qquad (2\text{-}203)$$

$$B_{56} = -\frac{1}{M}\Big\{\left(m_{15}\bar{r}_8 + m_{16}\bar{r}_9\right)\cdot {}_7T_6^T\cdot\left(m_{78}\bar{r}_{10}|_{2C} + m_8\bar{r}_{11}|_{2C}\right)$$
$$+ {}_7T_6^{*T}\cdot\Big[m_{16}\left(m_{78}\bar{r}_{10} + m_8\bar{r}_{11}\right)\cdot\bar{r}_{10}|_{2C} + m_8\left(m_{16}\bar{r}_{10} + m_{17}\bar{r}_{11}\right)\cdot\bar{r}_{11}|_{1C}\Big]\Big\} \qquad (2\text{-}204)$$

$$B_{57} = -\frac{m_8}{M}\Big[\left(m_{15}\bar{r}_8 + m_{16}\bar{r}_9\right)\cdot {}_7T_6^T\cdot\bar{r}_{12} + {}_7T_6^{*T}\cdot\left(m_{16}\bar{r}_{10} + m_{17}\bar{r}_{11}\right)\cdot\bar{r}_{12}\Big] \qquad (2\text{-}205)$$

$$B_{58} = \frac{m_1}{M}\Big[\left(m_{68}\bar{r}_8 + m_{78}\bar{r}_9\right)\cdot {}_5T_4\cdot {}_3T_2 + {}_7T_6^{*T}\cdot\left(m_{78}\bar{r}_{10} + m_8\bar{r}_{11}\right)\cdot {}_7T_6\cdot {}_5T_4\cdot {}_3T_2\Big] \qquad (2\text{-}206)$$

$$B_{61} = -\frac{1}{M}\left(m_{78}\bar{r}_{10}|_{2R} + m_8\bar{r}_{11}|_{2R}\right)\cdot {}_7T_6\cdot {}_5T_4\cdot\left[m_{12}\,{}_3T_2\cdot\bar{r}_1 + \left(m_{12}\bar{r}_2 + m_{13}\bar{r}_3\right)\cdot {}_3T_2^*\right] \tag{2-207}$$

$$B_{62} = -\frac{1}{M}\left(m_{78}\bar{r}_{10}|_{2R} + m_8\bar{r}_{11}|_{2R}\right)\cdot {}_7T_6\cdot {}_5T_4\cdot\left(m_{12}\bar{r}_2|_{3C} + m_{13}\bar{r}_3|_{3C}\right) \tag{2-208}$$

$$B_{63} = -\frac{1}{M}\left(m_{78}\bar{r}_{10}|_{2R} + m_8\bar{r}_{11}|_{2R}\right)\cdot {}_7T_6\cdot\left[{}_5T_4\cdot\left(m_{13}\bar{r}_4 + m_{14}\bar{r}_5\right) + \left(m_{14}\bar{r}_6 + m_{15}\bar{r}_7\right)\cdot {}_5T_4^*\right] \tag{2-209}$$

$$B_{64} = -\frac{1}{M}\left(m_{78}\bar{r}_{10}|_{2R} + m_8\bar{r}_{11}|_{2R}\right)\cdot {}_7T_6\cdot\left(m_{14}\bar{r}_6|_{1C} + m_{15}\bar{r}_7|_{1C}\right) \tag{2-210}$$

$$B_{65} = -\frac{1}{M}\Big\{\left(m_{78}\bar{r}_{10}|_{2R} + m_8\bar{r}_{11}|_{2R}\right)\cdot\left[m_{16}\bar{r}_{10}\cdot {}_7T_6^* + {}_7T_6\cdot\left(m_{15}\bar{r}_8 + m_{16}\bar{r}_9\right)\right] + m_8\left(m_{16}\bar{r}_{10}|_{2R} + m_{17}\bar{r}_{11}|_{2R}\right)\cdot\bar{r}_{11}\cdot {}_7T_6^*\Big\} \tag{2-211}$$

$$B_{66} = J_{7y} - \frac{1}{M}\left[m_{16}\left(m_{78}\bar{r}_{10}|_{2R} + m_8\bar{r}_{11}|_{2R}\right)\cdot\bar{r}_{10}|_{2C} + m_8\left(m_{16}\bar{r}_{10}|_{2R} + m_{17}\bar{r}_{11}|_{1R}\right)\cdot\bar{r}_{11}|_{2C}\right] \tag{2-212}$$

$$B_{67} = -\frac{m_8}{M}\left(m_{16}r_{10}|_{2R} + m_{17}r_{11}|_{2R}\right)\cdot\bar{r}_{12} \tag{2-213}$$

$$B_{68} = \frac{m_1}{M}\left(m_{78}\bar{r}_{10}|_{2R} + m_8\bar{r}_{11}|_{2R}\right)\cdot {}_7T_6\cdot {}_5T_4\cdot {}_3T_2 \tag{2-214}$$

$$B_{71} = -\frac{m_8}{M}\bar{r}_{12}\cdot {}_7T_6\cdot {}_5T_4\cdot\left[m_{12}\,{}_3T_2\cdot\bar{r}_1 + \left(m_{12}\bar{r}_2 + m_{13}\bar{r}_3\right)\cdot {}_3T_2^*\right] \tag{2-215}$$

$$B_{72} = -\frac{m_8}{M}\bar{r}_{12}\cdot {}_7T_6\cdot {}_5T_4\cdot\left(m_{12}\bar{r}_2|_{3C} + m_{13}\bar{r}_3|_{3C}\right) \tag{2-216}$$

$$B_{73} = -\frac{m_8}{M}\bar{r}_{12}\cdot {}_7T_6\cdot\left[{}_5T_4\left(m_{13}\bar{r}_4 + m_{14}\bar{r}_5\right) + \left(m_{14}\bar{r}_6 + m_{15}\bar{r}_7\right)\cdot {}_5T_4^*\right] \tag{2-217}$$

$$B_{74} = -\frac{m_8}{M}\bar{r}_{12}\cdot {}_7T_6\cdot\left(m_{14}\bar{r}_6|_{1C} + m_{15}\bar{r}_7|_{1C}\right) \tag{2-218}$$

$$B_{75} = -\frac{m_8}{M}\,\bar{r}_{12}\cdot\left[{}_7T_6\cdot(m_{15}\bar{r}_8 + m_{16}\bar{r}_7) + (m_{16}\bar{r}_{10} + m_{17}\bar{r}_{11})\cdot{}_7T_6^{*}\right] \tag{2-219}$$

$$B_{76} = -\frac{m_8}{M}\,\bar{r}_{12}\cdot\left(m_{16}\bar{r}_{10}|_{2c} + m_{17}\bar{r}_{11}|_{2c}\right) \tag{2-220}$$

$$B_{77} = J_8 - \frac{m_8}{M}\,m_{17}\,\bar{r}_{12}\cdot\bar{r}_{12} \tag{2-221}$$

$$B_{78} = \frac{m_1 m_8}{M}\,\bar{r}_{12}\cdot{}_7T_6\cdot{}_5T_4\cdot{}_3T_2 \tag{2-222}$$

$$B_{81} = -\frac{m_1}{M}\left[m_{38}\bar{r}_3 + {}_3T_2^{T}\cdot\left(m_{38}\bar{r}_2 + m_{48}\bar{r}_3\right)\cdot{}_3T_2^{*}\right] \tag{2-223}$$

$$B_{82} = -\frac{m_1}{M}\,{}_3T_2^{T}\cdot\left(m_{38}\bar{r}_2|_{3c} + m_{48}\bar{r}_3|_{3c}\right) \tag{2-224}$$

$$B_{83} = -\frac{m_1}{M}\,{}_3T_2^{T}\cdot\left[m_{48}\bar{r}_4 + m_{58}\bar{r}_5 + {}_5T_4^{T}\cdot\left(m_{58}\bar{r}_6 + m_{68}\bar{r}_7\right)\cdot{}_5T_4^{*}\right] \tag{2-225}$$

$$B_{84} = -\frac{m_1}{M}\,{}_3T_2^{T}\cdot{}_5T_4^{T}\cdot\left(m_{48}\bar{r}_4|_{4c} + m_{58}\bar{r}_5|_{4c}\right) \tag{2-226}$$

$$B_{85} = -\frac{m_1}{M}\,{}_3T_2^{T}\cdot{}_5T_4^{T}\cdot\left[m_{48}\bar{r}_8 + m_{78}\bar{r}_7 + {}_7T_6^{T}\cdot\left(m_{78}\bar{r}_{10} + m_8\bar{r}_{11}\right)\right] \tag{2-227}$$

$$B_{86} = -\frac{m_1}{M}\,{}_3T_2^{T}\cdot{}_5T_4^{T}\cdot{}_7T_6^{T}\cdot\left(m_{78}\bar{r}_{10}|_{2c} + m_8\bar{r}_{11}|_{2c}\right) \tag{2-228}$$

$$B_{87} = -\frac{m_1 m_8}{M}\,{}_3T_2^{T}\cdot{}_5T_4^{T}\cdot{}_7T_6^{T}\cdot\bar{r}_{12} \tag{2-229}$$

$$B_{88} = \frac{m_1}{M}\,m_{28}\,I \tag{2-230}$$

$$b_{11} = d - 4\bar{R}_{E20} \cdot D \cdot (\bar{R}_{120} + \bar{R}_{E20}) \tag{2-231}$$

$$b_{12} = k - 4\bar{R}_{E20} \cdot K \cdot (\bar{R}_{120} + \bar{R}_{E20}) \tag{2-232}$$

$$b_{13} = -({}_3T_2^{*T} \cdot d_{34} \cdot {}_3T_2^{*} + d) + 4\bar{R}_{E20} \cdot D \cdot \bar{R}_{E20} \tag{2-233}$$

$$b_{14} = -({}_3T_2^{*T} \cdot k_{34} \cdot {}_3T_2^{*} + k) + 4\bar{R}_{E20} \cdot K \cdot \bar{R}_{E20} \tag{2-234}$$

$$b_{15} = {}_3T_2^{*T} \cdot d_{34} \tag{2-235}$$

$$b_{16} = {}_3T_2^{*T} \cdot k_{34} \tag{2-236}$$

$$b_{17} = -4\bar{R}_{E20} \cdot D \tag{2-237}$$

$$b_{18} = -4\bar{R}_{E20} \cdot K \tag{2-238}$$

$$b_{19} = [0 \quad 0 \quad -1]^T \tag{2-239}$$

$$b_{21} = -d_{34z} \tag{2-240}$$

$$b_{22} = -k_{34z} \tag{2-241}$$

$$b_{23} = d_{34}|_{3R} \tag{2-242}$$

$$b_{24} = k_{34}|_{3R} \tag{2-243}$$

$$b_{25} = 1 \tag{2-244}$$

$$b_{11} = d - 4\bar{R}_{E20} \cdot D \cdot (\bar{R}_{120} + \bar{R}_{E20}) \tag{2-231}$$

$$b_{12} = k - 4\bar{R}_{E20} \cdot K \cdot (\bar{R}_{120} + \bar{R}_{E20}) \tag{2-232}$$

$$b_{13} = -({}_3T_2^{*T} \cdot d_{34} \cdot {}_3T_2^{*} + d) + 4\bar{R}_{E20} \cdot D \cdot \bar{R}_{E20} \tag{2-233}$$

$$b_{14} = -({}_3T_2^{*T} \cdot k_{34} \cdot {}_3T_2^{*} + k) + 4\bar{R}_{E20} \cdot K \cdot \bar{R}_{E20} \tag{2-234}$$

$$b_{15} = {}_3T_2^{*T} \cdot d_{34} \tag{2-235}$$

$$b_{16} = {}_3T_2^{*T} \cdot k_{34} \tag{2-236}$$

$$b_{17} = -4\bar{R}_{E20} \cdot D \tag{2-237}$$

$$b_{18} = -4\bar{R}_{E20} \cdot K \tag{2-238}$$

$$b_{19} = [0 \quad 0 \quad -1]^T \tag{2-239}$$

$$b_{21} = -d_{34\pm} \tag{2-240}$$

$$b_{22} = -k_{34\pm} \tag{2-241}$$

$$b_{23} = d_{34} I_{3R} \tag{2-242}$$

$$b_{24} = k_{34} I_{3R} \tag{2-243}$$

$$b_{25} = 1 \tag{2-244}$$

$$b_{31} = d_{34} \cdot {}_3T_2^* \tag{2-245}$$

$$b_{32} = k_{34} \cdot {}_3T_2^* \tag{2-246}$$

$$b_{33} = d_{34}|_{3C} \tag{2-247}$$

$$b_{34} = k_{34}|_{3C} \tag{2-248}$$

$$b_{35} = -\left(d_{34} + {}_5T_4^{*T} \cdot d_{56} \cdot {}_5T_4^*\right) \tag{2-249}$$

$$b_{36} = -\left(k_{34} + {}_5T_4^{*T} \cdot k_{56} \cdot {}_5T_4^*\right) \tag{2-250}$$

$$b_{37} = {}_5T_4^{*T} \cdot d_{56} \tag{2-251}$$

$$b_{38} = {}_5T_4^{*T} \cdot k_{56} \tag{2-252}$$

$$b_{39} = \begin{bmatrix} -1 & 0 & 0 \end{bmatrix}^T \tag{2-253}$$

$$b_{41} = -d_{56x} \tag{2-254}$$

$$b_{42} = -k_{56x} \tag{2-255}$$

$$b_{43} = d_{56}|_{1R} \tag{2-256}$$

$$b_{44} = k_{56}|_{1R} \tag{2-257}$$

$$b_{45} = 1 \tag{2-258}$$

$$b_{31} = d_{34} \circ {}_3T_2^* \tag{2-245}$$

$$b_{32} = k_{34} \circ {}_3T_2^* \tag{2-246}$$

$$b_{33} = d_{34}|_{3C} \tag{2-247}$$

$$b_{34} = k_{34}|_{3C} \tag{2-248}$$

$$b_{35} = -\left(d_{34} + {}_5T_4^{*T} \circ d_{56} \circ {}_5T_4^*\right) \tag{2-249}$$

$$b_{36} = -\left(k_{34} + {}_5T_4^{*T} \circ k_{56} \circ {}_5T_4^*\right) \tag{2-250}$$

$$b_{37} = {}_5T_4^{*T} \circ d_{56} \tag{2-251}$$

$$b_{38} = {}_5T_4^{*T} \circ k_{56} \tag{2-252}$$

$$b_{39} = \begin{bmatrix} -1 & 0 & 0 \end{bmatrix}^T \tag{2-253}$$

$$b_{41} = -d_{56x} \tag{2-254}$$

$$b_{42} = -k_{56x} \tag{2-255}$$

$$b_{43} = d_{56}|_{1R} \tag{2-256}$$

$$b_{44} = k_{56}|_{1R} \tag{2-257}$$

$$b_{45} = 1 \tag{2-258}$$

$$b_{51} = d_{56} \cdot {}_5T_4^* \tag{2-259}$$

$$b_{52} = k_{56} \cdot {}_5T_4^* \tag{2-260}$$

$$b_{53} = d_{56}|_{1C} \tag{2-261}$$

$$b_{54} = k_{56}|_{1C} \tag{2-262}$$

$$b_{55} = -({}_7T_6^{*T} \cdot d_{78} \cdot {}_7T_6^* + d_{56}) \tag{2-263}$$

$$b_{56} = -({}_7T_6^{*T} \cdot k_{78} \cdot {}_7T_6^* + k_{56}) \tag{2-264}$$

$$b_{57} = {}_7T_6^{*T} \cdot d_{78} \tag{2-265}$$

$$b_{58} = {}_7T_6^{T} \cdot k_{78} \tag{2-266}$$

$$b_{59} = [0 \quad -1 \quad 0]^T \tag{2-267}$$

$$b_{61} = -d_{78y} \tag{2-268}$$

$$b_{62} = -k_{78y} \tag{2-269}$$

$$b_{63} = d_{78}|_{2R} \tag{2-270}$$

$$b_{64} = k_{78}|_{2R} \tag{2-271}$$

$$b_{65} = 1 \tag{2-272}$$

$$b_{51} = d_{56} \cdot {}_5T_4^* \tag{2-259}$$

$$b_{52} = k_{56} \cdot {}_5T_4^* \tag{2-260}$$

$$b_{53} = d_{56}|_{1C} \tag{2-261}$$

$$b_{54} = k_{56}|_{1C} \tag{2-262}$$

$$b_{55} = -({}_7T_6^{*T} \cdot d_{78} \cdot {}_7T_6^* + d_{56}) \tag{2-263}$$

$$b_{56} = -({}_7T_6^{*T} \cdot k_{78} \cdot {}_7T_6^* + k_{56}) \tag{2-264}$$

$$b_{57} = {}_7T_6^{*T} \cdot d_{78} \tag{2-265}$$

$$b_{58} = {}_7T_6^{T} \cdot k_{78} \tag{2-266}$$

$$b_{59} = [0 \quad -1 \quad 0]^T \tag{2-267}$$

$$b_{61} = -d_{78y} \tag{2-268}$$

$$b_{62} = -k_{78y} \tag{2-269}$$

$$b_{63} = d_{78}|_{2R} \tag{2-270}$$

$$b_{64} = k_{78}|_{2R} \tag{2-271}$$

$$b_{65} = 1 \tag{2-272}$$

$$b_{71} = d_{78} \cdot {}_7T_6^* \tag{2-273}$$

$$b_{72} = k_{78} \cdot {}_7T_6^* \tag{2-274}$$

$$b_{73} = d_{78} l_{2C} \tag{2-275}$$

$$b_{74} = k_{78} l_{2C} \tag{2-276}$$

$$b_{75} = -d_{78} \tag{2-277}$$

$$b_{76} = -k_{78} \tag{2-278}$$

$$b_{81} = -4D \cdot (\bar{R}_{12o} + \bar{R}_{12o}) \tag{2-279}$$

$$b_{82} = -4K \cdot (\bar{R}_{12o} + \bar{R}_{12o}) \tag{2-280}$$

$$b_{83} = 4D \cdot \bar{R}_{E2o} \tag{2-281}$$

$$b_{84} = 4K \cdot \bar{R}_{E2o} \tag{2-282}$$

$$b_{85} = -4D \tag{2-283}$$

$$b_{86} = -4K \tag{2-284}$$

$$D_i = T_{ie} + \bar{R}_{ii} \cdot F_{ie} \tag{2-285}$$

$$D_2 = T_{2e} + T_{23fz} + T_{23WTz} + \bar{R}_{22}\cdot F_{2e} + {}_3T_2^{*T}\cdot(T_{3e} + \bar{R}_{33}\cdot F_{3e}) - \frac{1}{M}\{(m_{38}\bar{r}_1 + m_{38}\,{}_3T_2^{*T}\cdot\bar{r}_2\cdot{}_3T_2$$
$$+ m_{48}\,{}_3T_2^{*T}\cdot\bar{r}_3\cdot{}_3T_2)\cdot(F_{1e}+F_{2e}) - (m_{12}\bar{r}_1\cdot{}_3T_2^{T} + m_{12}\,{}_3T_2^{*T}\cdot\bar{r}_2 - m_{48}\,{}_3T_2^{*T}\cdot\bar{r}_3)\cdot F_{3e}$$
$$-(m_{12}\bar{r}_1\cdot{}_3T_2^{T} + m_{12}\,{}_3T_2^{*T}\cdot\bar{r}_2 + m_{13}\,{}_3T_2^{*T}\cdot\bar{r}_3)\cdot[F_{4e} + {}_5T_4\cdot(F_{5e}+F_{6e}) + {}_5T_4\cdot{}_7T_6\cdot(F_{7e}+F_{8e})]\} \quad (2\text{-}286)$$

$$D_3 = T_{3ez} - T_{23fz} - T_{23WTz} + \bar{R}_{33}|_{3R}\cdot F_{3e} - \frac{1}{M}\{(m_{38}\bar{r}_2|_{3R} - m_{48}\bar{r}_3|_{3R})\cdot{}_3T_2\cdot(F_{1e}+F_{2e})$$
$$-(m_{12}\bar{r}_2|_{3R} - m_{48}\bar{r}_3|_{3R})\cdot F_{3e} - (m_{12}\bar{r}_2|_{3R} + m_{13}\bar{r}_3|_{3R})\cdot[F_{4e} + {}_5T_4\cdot(F_{5e}+F_{6e}) + {}_5T_4\cdot{}_7T_6\cdot(F_{7e}+F_{8e})]\} \quad (2\text{-}287)$$

$$D_4 = T_{4e} + T_{45fx} + T_{45WTx} + \bar{R}_{44}\cdot F_{4e} + {}_5T_4^{*T}\cdot(T_{5e} + \bar{R}_{55}\cdot F_{5e}) - \frac{1}{M}\{[(m_{48}\bar{r}_4 + m_{58}\bar{r}_5 + m_{58}\,{}_5T_4^{*T}\cdot\bar{r}_6\cdot{}_5T_4$$
$$+ m_{68}\,{}_5T_4^{*T}\cdot\bar{r}_7\cdot{}_5T_4)\cdot[{}_3T_2\cdot(F_{1e}+F_{2e}) + F_{3e}] - (m_{13}\bar{r}_4 - m_{58}\bar{r}_5 - m_{58}\,{}_5T_4^{*T}\cdot\bar{r}_6\cdot{}_5T_4 - m_{68}\,{}_5T_4^{*T}\cdot\bar{r}_7\cdot{}_5T_4)\cdot F_{4e}$$
$$-(m_{13}\bar{r}_4\cdot{}_5T_4^{T} + m_{14}\bar{r}_5\cdot{}_5T_4^{T} + m_{14}\,{}_5T_4^{*T}\cdot\bar{r}_6 + m_{15}\,{}_5T_4^{*T}\cdot\bar{r}_7)\cdot[F_{6e} + {}_7T_6^{T}\cdot(F_{7e}+F_{8e})]\} \quad (2\text{-}288)$$

$$D_5 = T_{5ex} - T_{45fx} - T_{45WTx} + \bar{R}_{55}|_{1R}\cdot F_{5e} - \frac{1}{M}\{(m_{58}\bar{r}_6|_{1R} + m_{68}\bar{r}_7|_{1R})\cdot[{}_5T_4\cdot{}_3T_2\cdot(F_{1e}+F_{2e}) + {}_5T_4\cdot(F_{3e}+F_{4e})]$$
$$-(m_{14}\bar{r}_6|_{1R} - m_{68}\bar{r}_7|_{1R})\cdot F_{5e} - (m_{14}\bar{r}_6|_{1R} + m_{15}\bar{r}_7|_{1R})\cdot[F_{6e} + {}_7T_6^{T}\cdot(F_{7e}+F_{8e})]\} \quad (2\text{-}289)$$

$$D_6 = T_{6e} + T_{67fy} + T_{67WTy} + \bar{R}_{66}\cdot F_{6e} + {}_7T_6^{*T}\cdot(T_{7e} + \bar{R}_{77}\cdot F_{7e}) - \frac{1}{M}\{[m_{68}\bar{r}_8 + m_{78}\bar{r}_9$$
$$+ {}_7T_5^{*T}\cdot(m_{78}\bar{r}_{10} + m_8\bar{r}_{11})\cdot{}_7T_6]\cdot[{}_5T_4\cdot{}_3T_2\cdot(F_{1e}+F_{2e}) + {}_5T_4\cdot(F_{3e}+F_{4e}) + F_{5e}]$$
$$-[m_{15}\bar{r}_8 - m_{78}\bar{r}_9 - {}_7T_6^{*T}\cdot(m_{78}\bar{r}_{10} + m_8\bar{r}_{11})\cdot{}_7T_6]\cdot F_{6e} - [(m_{15}\bar{r}_8 + m_{16}\bar{r}_9)\cdot{}_7T_6^{T}$$
$$+ {}_7T_6^{*T}\cdot(m_{16}\bar{r}_{10} - m_8\bar{r}_{11})]\cdot F_{7e} - [(m_{15}\bar{r}_8 + m_{16}\bar{r}_9)\cdot{}_7T_6^{T} + {}_7T_6^{*T}\cdot(m_{16}\bar{r}_{10} + m_{17}\bar{r}_{11})]\cdot F_{8e}\} \quad (2\text{-}290)$$

$$D_7 = T_{7ey} - T_{67fy} - T_{67WTy} + \bar{R}_{77}|_{2R}\cdot F_{7e} - \frac{1}{M}\{(m_{78}\bar{r}_{10}|_{2R} + m_8\bar{r}_{11}|_{2R})\cdot[{}_7T_6\cdot{}_5T_4\cdot{}_3T_2\cdot(F_{1e}+F_{2e})$$
$$+ {}_7T_6\cdot{}_5T_4\cdot(F_{3e}+F_{4e}) + {}_7T_6\cdot(F_{5e}+F_{6e})] - (m_{16}\bar{r}_{10}|_{2R} - m_8\bar{r}_{11}|_{2R})\cdot F_{7e}$$
$$-(m_{16}\bar{r}_{10}|_{2R} + m_{17}\bar{r}_{11}|_{2R})\cdot F_{8e}\} \quad (2\text{-}291)$$

$$D_8 = T_{8e} + \bar{R}_{88}\cdot F_{8e} - \frac{1}{M}\{m_8\bar{r}_{12}\cdot[{}_7T_6\cdot{}_5T_4\cdot{}_3T_2\cdot(F_{1e}+F_{2e}) + {}_7T_6\cdot{}_5T_4\cdot(F_{3e}+F_{4e}) + {}_7T_6\cdot(F_{5e}+F_{6e})$$
$$+ \bar{r}_{12}\cdot F_{7e}] - m_{17}\bar{r}_{12}\cdot F_{8e}\} \quad (2\text{-}292)$$

$$D_q = -\frac{1}{M}\left\{ m_{22} F_{1e} - m_1 \left[F_{2e} + {}_3T_2^T \cdot (F_{3e} + F_{4e}) + {}_3T_2^T \cdot {}_5T_4^T \cdot (F_{5e} + F_{6e}) + {}_3T_2^T \cdot {}_5T_4^T \cdot {}_7T_6^T \cdot (F_{7e} + F_{8e}) \right] \right\} \quad (2\text{-}293)$$

$$\bar{r}_i = \begin{bmatrix} 0 & -r_{iz} & r_{iy} \\ r_{iz} & 0 & -r_{ix} \\ -r_{iy} & r_{ix} & 0 \end{bmatrix} \qquad i = 1, 2, \cdots 12 \qquad (2\text{-}294)$$

$$\bar{R}_{120} = \begin{bmatrix} 0 & -R_{120z} & R_{120y} \\ R_{120z} & 0 & -R_{120x} \\ -R_{120y} & R_{120x} & 0 \end{bmatrix} \qquad (2\text{-}295)$$

$$\bar{R}_{E20} = \begin{bmatrix} 0 & -R_{E20z} & R_{E20y} \\ R_{E20z} & 0 & -R_{E20x} \\ -R_{E20y} & R_{E20x} & 0 \end{bmatrix} \qquad (2\text{-}296)$$

$$d = \mathrm{diag}\{d_x, d_y, d_z\} \qquad (2\text{-}297)$$

$$k = \mathrm{diag}\{k_x, k_y, k_z\} \qquad (2\text{-}298)$$

$$D = \mathrm{diag}\{D_x, D_y, D_z\} \qquad (2\text{-}299)$$

$$K = \mathrm{diag}\{K_x, K_y, K_z\} \qquad (2\text{-}300)$$

$$d_{34} = \mathrm{diag}\{d_{34x}, d_{34y}, d_{34z}\} \qquad (2\text{-}301)$$

$$k_{34} = \mathrm{diag}\{k_{34x}, k_{34y}, k_{34z}\} \qquad (2\text{-}302)$$

$$d_{56} = \mathrm{diag}\{d_{56x}, d_{56y}, d_{56z}\} \qquad (2\text{-}303)$$

$$k_{56} = \mathrm{diag}\{k_{56x}, k_{56y}, k_{56z}\} \qquad (2\text{-}304)$$

$$d_{78} = \text{diag}\{d_{78x}, d_{78y}, d_{78z}\} \tag{2-305}$$

$$k_{78} = \text{diag}\{k_{78x}, k_{78y}, k_{78z}\} \tag{2-306}$$

$$d_{34}|_{3R} = [0 \quad 0 \quad d_{34z}] \tag{2-307}$$

$$k_{34}|_{3R} = [0 \quad 0 \quad k_{34z}] \tag{2-308}$$

$$d_{34}|_{3C} = \begin{bmatrix} 0 \\ 0 \\ d_{34z} \end{bmatrix} \tag{2-309}$$

$$k_{34}|_{3C} = \begin{bmatrix} 0 \\ 0 \\ k_{34z} \end{bmatrix} \tag{2-310}$$

$$d_{56}|_{1R} = [d_{56x} \quad 0 \quad 0] \tag{2-311}$$

$$k_{56}|_{1R} = [k_{56x} \quad 0 \quad 0] \tag{2-312}$$

$$d_{56}|_{1C} = \begin{bmatrix} d_{56x} \\ 0 \\ 0 \end{bmatrix} \tag{2-313}$$

$$k_{56}|_{1C} = \begin{bmatrix} k_{56x} \\ 0 \\ 0 \end{bmatrix} \tag{2-314}$$

$$d_{78}|_{2R} = [0 \quad d_{78y} \quad 0] \tag{2-315}$$

$$k_{78}|_{2R} = [0 \quad k_{78y} \quad 0] \tag{2-316}$$

$$d_{78}|_{2c} = \begin{bmatrix} 0 \\ d_{78y} \\ 0 \end{bmatrix} \tag{2-317}$$

$$k_{78}|_{2c} = \begin{bmatrix} 0 \\ k_{78y} \\ 0 \end{bmatrix} \tag{2-318}$$

$$J_k = \text{diag}\{J_{kx}, J_{ky}, J_{kz}\} \qquad k = 1, 2 \cdots 8 \tag{2-319}$$

$$\bar{r}_2|_{3c} = \begin{bmatrix} r_{2y} \\ -r_{2x} \\ 0 \end{bmatrix} \tag{2-320}$$

$$\bar{r}_3|_{3c} = \begin{bmatrix} r_{3y} \\ -r_{3x} \\ 0 \end{bmatrix} \tag{2-321}$$

$$\bar{r}_6|_{1c} = \begin{bmatrix} 0 \\ r_{6z} \\ -r_{6y} \end{bmatrix} \tag{2-322}$$

$$\bar{r}_7|_{1c} = \begin{bmatrix} 0 \\ r_{7z} \\ -r_{7y} \end{bmatrix} \tag{2-323}$$

$$\bar{r}_{10}|_{2C} = \begin{bmatrix} -r_{10z} \\ 0 \\ r_{10x} \end{bmatrix} \tag{2-324}$$

$$\bar{r}_{11}|_{2C} = \begin{bmatrix} -r_{11z} \\ 0 \\ r_{11x} \end{bmatrix} \tag{2-325}$$

$$\bar{r}_{2}|_{3R} = \begin{bmatrix} -r_{2y} & r_{2x} & 0 \end{bmatrix} \tag{2-326}$$

$$\bar{r}_{3}|_{3R} = \begin{bmatrix} -r_{3y} & r_{3x} & 0 \end{bmatrix} \tag{2-327}$$

$$\bar{r}_{6}|_{1R} = \begin{bmatrix} 0 & -r_{6z} & r_{6y} \end{bmatrix} \tag{2-328}$$

$$\bar{r}_{7}|_{1R} = \begin{bmatrix} 0 & -r_{7z} & r_{7y} \end{bmatrix} \tag{2-329}$$

$$\bar{r}_{10}|_{2R} = \begin{bmatrix} r_{10z} & 0 & -r_{10x} \end{bmatrix} \tag{2-330}$$

$$\bar{r}_{11}|_{2R} = \begin{bmatrix} r_{11z} & 0 & -r_{11x} \end{bmatrix} \tag{2-331}$$

$$\underline{I} = \begin{bmatrix} 1 & 0 & 0 \\ 0 & 1 & 0 \\ 0 & 0 & 1 \end{bmatrix} \tag{2-332}$$

$$\dot{\omega}_1 = \begin{bmatrix} \dot{\omega}_{1x} \\ \dot{\omega}_{1y} \\ \dot{\omega}_{1z} \end{bmatrix} \tag{2-333}$$

$$\omega_1 = \begin{bmatrix} \omega_{1x} \\ \omega_{2x} \\ \omega_{3x} \end{bmatrix} \tag{2-334}$$

$$\dot{\omega}_2 = \begin{bmatrix} \dot{\omega}_{2x} \\ \dot{\omega}_{2y} \\ \dot{\omega}_{2z} \end{bmatrix} \qquad (2\text{-}335)$$

$$\dot{\omega}_4 = \begin{bmatrix} \dot{\omega}_{4x} \\ \dot{\omega}_{4y} \\ \dot{\omega}_{4z} \end{bmatrix} \qquad (2\text{-}336)$$

$$\omega_4 = \begin{bmatrix} \omega_{4x} \\ \omega_{4y} \\ \omega_{4z} \end{bmatrix} \qquad (2\text{-}337)$$

$$\dot{\omega}_6 = \begin{bmatrix} \dot{\omega}_{6x} \\ \dot{\omega}_{6y} \\ \dot{\omega}_{6z} \end{bmatrix} \qquad (2\text{-}338)$$

$$\omega_6 = \begin{bmatrix} \omega_{6x} \\ \omega_{6y} \\ \omega_{6z} \end{bmatrix} \qquad (2\text{-}339)$$

$$\dot{\omega}_8 = \begin{bmatrix} \dot{\omega}_{8x} \\ \dot{\omega}_{8y} \\ \dot{\omega}_{8z} \end{bmatrix} \qquad (2\text{-}340)$$

$$\omega_8 = \begin{bmatrix} \omega_{8x} \\ \omega_{8y} \\ \omega_{8z} \end{bmatrix} \qquad (2\text{-}341)$$

$$\ddot{\varepsilon}_{12} = \begin{bmatrix} \ddot{\varepsilon}_{12x} \\ \ddot{\varepsilon}_{12y} \\ \ddot{\varepsilon}_{12z} \end{bmatrix} \tag{2-342}$$

$$\dot{\varepsilon}_{12} = \begin{bmatrix} \dot{\varepsilon}_{12x} \\ \dot{\varepsilon}_{12y} \\ \dot{\varepsilon}_{12z} \end{bmatrix} \tag{2-343}$$

$$\varepsilon_{12} = \begin{bmatrix} \varepsilon_{12x} \\ \varepsilon_{12y} \\ \varepsilon_{12z} \end{bmatrix} \tag{2-344}$$

$$\theta_1 = \begin{bmatrix} \theta_{1x} \\ \theta_{1y} \\ \theta_{1z} \end{bmatrix} \tag{2-345}$$

$$\theta_2 = \begin{bmatrix} \theta_{2x} \\ \theta_{2y} \\ \theta_{2z} \end{bmatrix} \tag{2-346}$$

$$\theta_4 = \begin{bmatrix} \theta_{4x} \\ \theta_{4y} \\ \theta_{4z} \end{bmatrix} \tag{2-347}$$

$$\theta_6 = \begin{bmatrix} \theta_{6x} \\ \theta_{6y} \\ \theta_{6z} \end{bmatrix} \tag{2-348}$$

$$\Theta_g = \begin{bmatrix} \Theta_{gx} \\ \Theta_{gy} \\ \Theta_{gz} \end{bmatrix} \tag{2-349}$$

2.2.3 Derivation of Gimbal Torques - In order to complete the mathematical model for the Offset Gimbal, the gimbal torque equations must be specified. Using the transformations shown in equations (2-136), (2-138) and (2-140) the desired control torque can be written in terms of the gimbal torque in the following manner:

$$T_c = \begin{bmatrix} \cos\gamma_y & 0 & -\sin\gamma_y \cos\beta_x \\ 0 & 1 & \sin\beta_x \\ \sin\gamma_y & 0 & \cos\gamma_y \cos\beta_x \end{bmatrix} \begin{bmatrix} T_{\beta xc} \\ T_{\gamma yc} \\ T_{\alpha zc} \end{bmatrix} \tag{2-350}$$

Solving equation (2-350) for the gimbal torques gives

$$\begin{bmatrix} T_{\beta xc} \\ T_{\gamma yc} \\ T_{\alpha zc} \end{bmatrix} = \begin{bmatrix} \cos\gamma_y & 0 & \sin\gamma_y \\ \tan\beta_x \sin\gamma_y & 1 & -\tan\beta_x \cos\gamma_y \\ -\sec\beta_x \sin\gamma_y & 0 & \sec\beta_x \cos\gamma_y \end{bmatrix} \begin{bmatrix} T_{cx} \\ T_{cy} \\ T_{cz} \end{bmatrix} = \Omega \cdot T_c \tag{2-351}$$

where

$T_{\beta xc}; T_{\gamma yc}; T_{\alpha zc}$ = Gimbal torque commands to the $\beta_x, \gamma_y, \alpha_z$ gimbal axes respectively.

$T_{cx}; T_{cy}; T_{cz}$ = Desired Control Torques

The gimbal command torques are related to the actual generated torque by the following expression:

$$\begin{bmatrix} T_{\beta x} \\ T_{\gamma y} \\ T_{\alpha z} \end{bmatrix} = \frac{\omega_{nT}}{s + \omega_{nT}} \begin{bmatrix} T_{\beta xc} \\ T_{\gamma yc} \\ T_{\alpha zc} \end{bmatrix} \tag{2-352}$$

where

$1/\omega_{nt}$ = Gimbal torquer time constant

The control torques can have two possible expressions depending on the location of the control sensors. For the first configuration assume that the sensors are located on body 8 (i.e., the telescope) and that the sensor is a rate gyro. For a controller that uses rate, position and integral of position the control torque command can be written as

$$T_C = \frac{-\omega_{nS}^2}{S^2 + 2\zeta_S \omega_{nS} S + \omega_{nS}^2} \left[K_R \cdot \omega_8 + K_p \cdot \theta_8 + K_I \cdot \frac{\theta_8}{S} \right] \tag{2-353}$$

Substituting equation (2-353) into equation (2-351) yields

$$\begin{bmatrix} T_{\beta xc} \\ T_{\gamma yc} \\ T_{\alpha zc} \end{bmatrix} = \frac{-\omega_{nS}^2}{S^2 + 2\zeta_S \omega_{nS} S + \omega_{nS}^2} \Omega \cdot \left[K_R \cdot \omega_8 + K_p \cdot \theta_8 + K_I \cdot \frac{\theta_8}{S} \right] \tag{2-354}$$

Substituting equation (2-354) into equation (2-352) gives

$$\begin{bmatrix} T_{\beta x} \\ T_{\gamma y} \\ T_{\alpha z} \end{bmatrix} = \frac{-\omega_{nT} \omega_{nS}^2}{(S + \omega_{nT})(S^2 + 2\zeta_S \omega_{nS} S + \omega_{nS}^2)} \Omega \cdot \left[K_R \cdot \omega_8 + K_p \cdot \theta_8 + K_I \cdot \frac{\theta_8}{S} \right] \tag{2-355}$$

The second configuration assumes that the sensors are on body 7. Using a similar development, the gimbal control torques can be written as:

$$\begin{bmatrix} T_{\beta x} \\ T_{\gamma y} \\ T_{\alpha z} \end{bmatrix} = \frac{-\omega_{nT} \omega_{nS}^2}{(S + \omega_{nT})(S^2 + 2\zeta_S \omega_{nS} S + \omega_{nS}^2)} \Omega \cdot \left\{ K_R \cdot \left({}_7T_6^* \cdot \omega_6 + \begin{bmatrix} 0 \\ \omega_{7y} \\ 0 \end{bmatrix} \right) + K_p \cdot \left({}_7T_6^* \cdot \theta_6 + \begin{bmatrix} 0 \\ \theta_{7y} \\ 0 \end{bmatrix} \right) + K_I \cdot \left({}_7T_6^* \cdot \frac{\theta_6}{S} + \begin{bmatrix} 0 \\ \frac{\theta_{7y}}{S} \\ 0 \end{bmatrix} \right) \right\} \tag{2-356}$$

where

$K_R = \text{diag}[K_{Rx}, K_{Ry}, K_{Rz}]$ system rate gain

$K_p = \text{diag}[K_{px}, K_{py}, K_{pz}]$ system position gain

$K_I = \text{diag}[K_{Ix}, K_{Iy}, K_{Iz}]$ system integral gain

ω_{ns} = gyro natural frequency

ζ_s = gyro damping ratio

2.3 IOG Stability Model - In order to aid in the determination of IOG system stability in an efficient and cost effective manner, a stability model for the IOG was developed. The stability model employed determined the roots of the system characteristic equation as a function of parameter variations by determining the eigenvalues of the system "A" matrix. To determine the system "A" matrix equations (2-34) through (2-37) can be rewritten excluding nonlinear terms and disturbances in the following manner:

$$\dot{\omega}_1 = a_{11}\cdot\omega_1 + a_{12}\cdot\omega_2 + a_{14}\cdot\dot{\epsilon}_{12} + a_{15}\cdot\theta_1 + a_{16}\cdot\theta_2 + a_{18}\cdot\epsilon_{12} \qquad (2\text{-}357)$$

$$B_{11}\cdot\dot{\omega}_2 + B_{12}\cdot\dot{\omega}_3 + B_{13}\cdot\ddot{\epsilon}_{12} = a_{21}\omega_1 + a_{22}\cdot\omega_2 + a_{24}\cdot\dot{\epsilon}_{12} + a_{25}\cdot\theta_1 + a_{26}\cdot\theta_2 + a_{28}\cdot\epsilon_{12} + a_{2,12}\cdot T_H \qquad (2\text{-}358)$$

$$B_{21}\cdot\dot{\omega}_2 + B_{22}\cdot\dot{\omega}_3 + B_{23}\cdot\ddot{\epsilon}_{12} = a_{3,12}\,T_H \qquad (2\text{-}359)$$

$$B_{31}\cdot\dot{\omega}_2 + B_{32}\cdot\dot{\omega}_3 + B_{33}\cdot\ddot{\epsilon}_{12} = a_{41}\cdot\omega_1 + a_{42}\cdot\omega_2 + a_{44}\cdot\dot{\epsilon}_{12} + a_{45}\cdot\theta_1 + a_{46}\cdot\theta_2 + a_{48}\cdot\epsilon_{12} \qquad (2\text{-}360)$$

$$\dddot{T}_H = a_{10,3}\cdot\omega_3 + a_{10,7}\cdot\theta_3 + a_{10,9}\cdot\theta_3^{\Sigma} + a_{10,10}\cdot\ddot{T}_H + a_{10,11}\cdot\dot{T}_H + a_{10,12}\cdot T_H \qquad (2\text{-}361)$$

Choosing the system state vector shown in equation (2-362)

$$\left[\omega_1 \quad \omega_2 \quad \omega_3 \quad \dot{\epsilon}_{12} \quad \theta_1 \quad \theta_2 \quad \theta_3 \quad \epsilon_{12} \quad \theta_3^{\Sigma} \quad \ddot{T}_H \quad \dot{T}_H \quad T_H\right]^T \qquad (2\text{-}362)$$

The system quations can be written in the following manner

$$\begin{bmatrix} \dot{\omega}_1 \\ \dot{\omega}_2 \\ \dot{\omega}_3 \\ \ddot{\epsilon}_{12} \\ \dot{\theta}_1 \\ \dot{\theta}_2 \\ \dot{\theta}_3 \\ \dot{\epsilon}_{12} \\ \dot{\theta}_3^I \\ \dddot{T}_H \\ \ddot{T}_H \\ \dot{T}_H \end{bmatrix} = \begin{bmatrix} a_{11} & a_{12} & 0 & a_{14} & a_{15} & a_{16} & 0 & a_{18} & 0 & 0 & 0 & 0 \\ & & & & & B^{-1}\ a & & & & & & \\ & & & & & (9\times9)\ (9\times36) & & & & & & \\ I & 0 & 0 & 0 & 0 & 0 & 0 & 0 & 0 & 0 & 0 & 0 \\ 0 & I & 0 & 0 & 0 & 0 & 0 & 0 & 0 & 0 & 0 & 0 \\ 0 & 0 & I & 0 & 0 & 0 & 0 & 0 & 0 & 0 & 0 & 0 \\ 0 & 0 & 0 & I & 0 & 0 & 0 & 0 & 0 & 0 & 0 & 0 \\ 0 & 0 & 0 & 0 & 0 & 0 & I & 0 & 0 & 0 & 0 & 0 \\ 0 & 0 & a_{10,3} & 0 & 0 & 0 & a_{10,7} & 0 & a_{10,9} & a_{10,10} & a_{10,11} & a_{10,12} \\ 0 & 0 & 0 & 0 & 0 & 0 & 0 & 0 & 0 & I & 0 & 0 \\ 0 & 0 & 0 & 0 & 0 & 0 & 0 & 0 & 0 & 0 & I & 0 \end{bmatrix} \begin{bmatrix} \omega_1 \\ \omega_2 \\ \omega_3 \\ \dot{\epsilon}_{12} \\ \theta_1 \\ \theta_2 \\ \theta_3 \\ \epsilon_{12} \\ \theta_{3I} \\ \ddot{T}_H \\ \dot{T}_H \\ T_H \end{bmatrix} \qquad (2\text{-}363)$$

where

$$B = \begin{bmatrix} B_{11} & B_{12} & B_{13} \\ B_{21} & B_{22} & B_{23} \\ B_{31} & B_{32} & B_{33} \end{bmatrix} \qquad (2\text{-}364)$$

$$a = \begin{bmatrix} a_{21} & a_{22} & 0 & a_{24} & a_{25} & a_{26} & 0 & a_{28} & 0 & 0 & 0 & a_{2,12} \\ 0 & 0 & 0 & 0 & 0 & 0 & 0 & 0 & 0 & 0 & 0 & a_{3,12} \\ a_{41} & a_{42} & 0 & a_{44} & a_{45} & a_{46} & 0 & a_{48} & 0 & 0 & 0 & a_{9,12} \end{bmatrix} \qquad (2\text{-}365)$$

and

$$a_{11} = J_1^{-1} \cdot [-d + 4(\bar{R}_{120} + \bar{R}_{E20}) \cdot D \cdot (\bar{R}_{120} + \bar{R}_{E20})] \quad (2\text{-}366)$$

$$a_{12} = J_1^{-1} \cdot [d - 4(\bar{R}_{120} + \bar{R}_{E20}) \cdot D \cdot \bar{R}_{E20}] \quad (2\text{-}367)$$

$$a_{14} = J^{-1} \cdot 4(\bar{R}_{120} + \bar{R}_{E20}) \cdot D \quad (2\text{-}368)$$

$$a_{15} = J^{-1} \cdot [-k + 4(\bar{R}_{120} + \bar{R}_{E20}) \cdot K \cdot (\bar{R}_{120} + \bar{R}_{E20})] \quad (2\text{-}369)$$

$$a_{16} = J^{-1} \cdot [k - 4(\bar{R}_{120} + \bar{R}_{E20}) \cdot K \cdot \bar{R}_{E20}] \quad (2\text{-}370)$$

$$a_{18} = J^{-1} \cdot 4(\bar{R}_{120} + \bar{R}_{E20}) \cdot K \quad (2\text{-}371)$$

$$a_{21} = d - 4\bar{R}_{E20} \cdot D \cdot (\bar{R}_{120} + \bar{R}_{E20}) \quad (2\text{-}372)$$

$$a_{22} = -d + 4\bar{R}_{E20} \cdot D \cdot \bar{R}_{E20} \quad (2\text{-}373)$$

$$a_{24} = -4\bar{R}_{E20} \cdot D \quad (2\text{-}374)$$

$$a_{25} = k - 4\bar{R}_{E20} \cdot K \cdot (\bar{R}_{120} + \bar{R}_{E20}) \quad (2\text{-}375)$$

$$a_{26} = -k + 4\bar{R}_{E20} \cdot K \cdot \bar{R}_{E20} \quad (2\text{-}376)$$

$$a_{28} = -4\bar{R}_{E20} \cdot K \quad (2\text{-}377)$$

$$a_{2,12} = -{}_2T_3 \quad (2\text{-}378)$$

$$a_{3,12} = I \quad (2\text{-}379)$$

$$a_{41} = 4D \cdot (\bar{R}_{120} + \bar{R}_{E20}) \quad (2\text{-}380)$$

$$a_{42} = -4D \cdot \bar{R}_{E20} \quad (2\text{-}381)$$

$$a_{44} = 4D \quad (2\text{-}382)$$

$$a_{45} = 4K \cdot (\bar{R}_{120} + \bar{R}_{E20}) \quad (2\text{-}383)$$

$$a_{46} = -4K \cdot \bar{R}_{E20} \quad (2\text{-}384)$$

$$a_{47} = 4K \quad (2\text{-}385)$$

$$a_{10,3} = -\omega_{nT}\omega_{nS}^2 K_R \tag{2-386}$$

$$a_{10,7} = -\omega_{nT}\omega_{nS}^2 K_P \tag{2-387}$$

$$a_{10,9} = -\omega_{nT}\omega_{nS}^2 K_I \tag{2-388}$$

$$a_{10,10} = -(2\zeta_S\omega_{nS} + \omega_{nT})\, I \tag{2-389}$$

$$a_{10,11} = -(\omega_{nS}^2 + 2\zeta_S\omega_{nS}\omega_{nT})\, I \tag{2-390}$$

$$a_{10,12} = -\omega_{nS}^2\,\omega_{nT}\, I \tag{2-391}$$

$$B_{11} = J_2^* \tag{2-392}$$

$$B_{12} = -\frac{m_3}{M}(m_1+m_2)\,\bar{r}_1 \cdot {}_2T_3 \cdot \bar{r}_2 \tag{2-393}$$

$$B_{13} = \frac{m_3}{M} m_1 \bar{r}_1 \tag{2-394}$$

$$B_{21} = -\frac{m_3}{M}(m_1+m_2)\,\bar{r}_2 \cdot {}_3T_2 \cdot \bar{r}_1 \tag{2-395}$$

$$B_{22} = J_3^* \tag{2-396}$$

$$B_{23} = \frac{m_3}{M} m_1 \bar{r}_2 \circ {}_3T_2 \tag{2-397}$$

$$B_{31} = \frac{m_3}{M} m_1 \bar{r}_1 \tag{2-398}$$

$$B_{32} = \frac{m_3}{M}\,{}_2T_3 \circ \bar{r}_2 \tag{2-399}$$

$$B_{33} = -\frac{m_1}{m}(m_2+m_3)\, I \tag{2-400}$$

$$I = \mathrm{diag}\{1,\ 1,\ 1\} \tag{2-401}$$

$$\theta_3^I = \int_0^t \theta_3\, dt \tag{2-402}$$

Eigenvalues of the system "A" matrix as defined by equation (2-363) were compared to those obtained from a reduced "A" matrix which assumes infinite mass and inertia for the shuttle. This reduced "A" matrix can be essentially obtained by deleting the 1st and 5th rows and 1st and 5th columns of the "A" matrix defined in equation (2-363). The eigenvalues for the reduced "A" matrix matched almost exactly with those obtained for the complete system except for the absence of the roots associated with shuttle modes of response. Hence, the reduced "A" matrix was used in all of the stability studies performed.

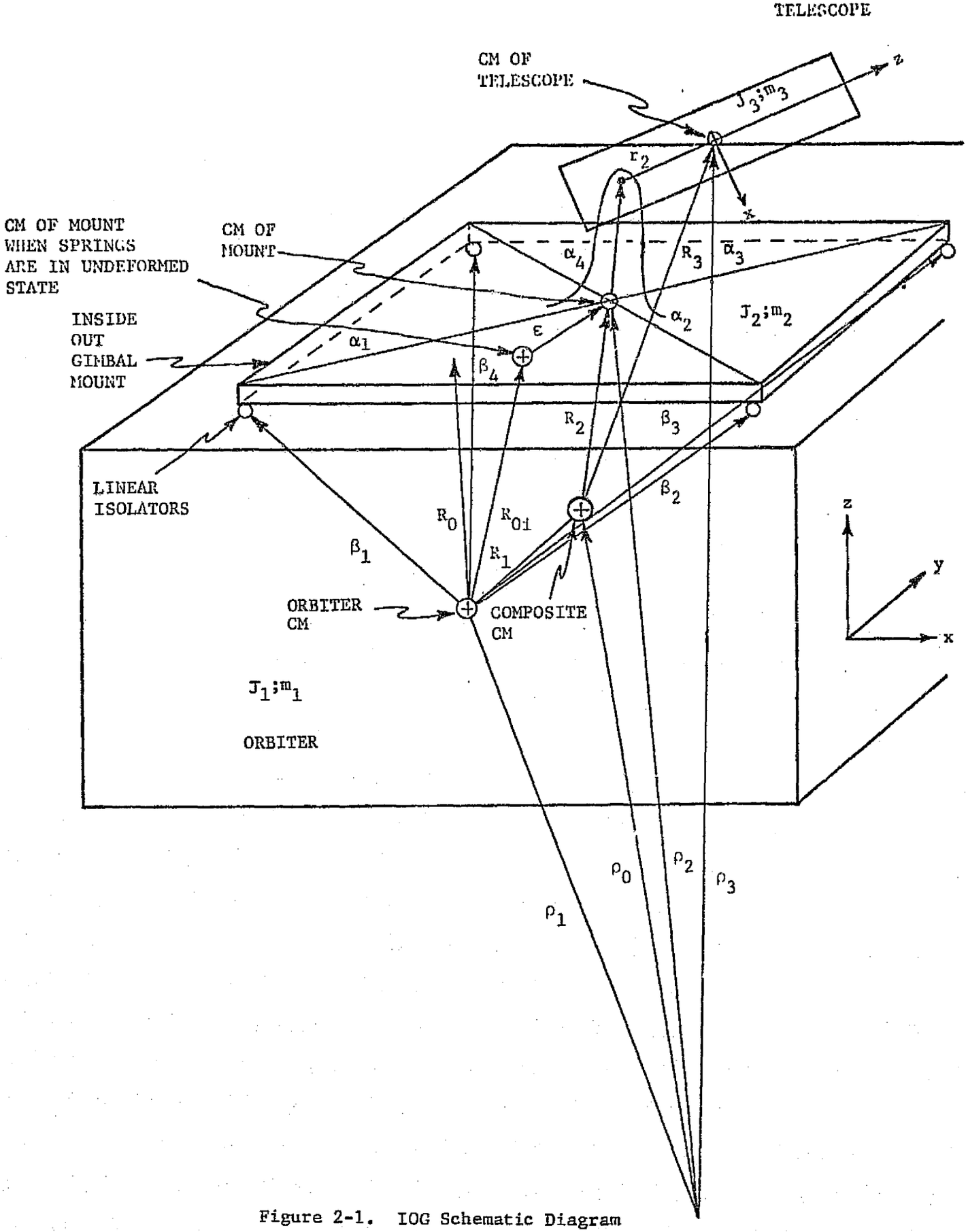

Figure 2-1. IOG Schematic Diagram

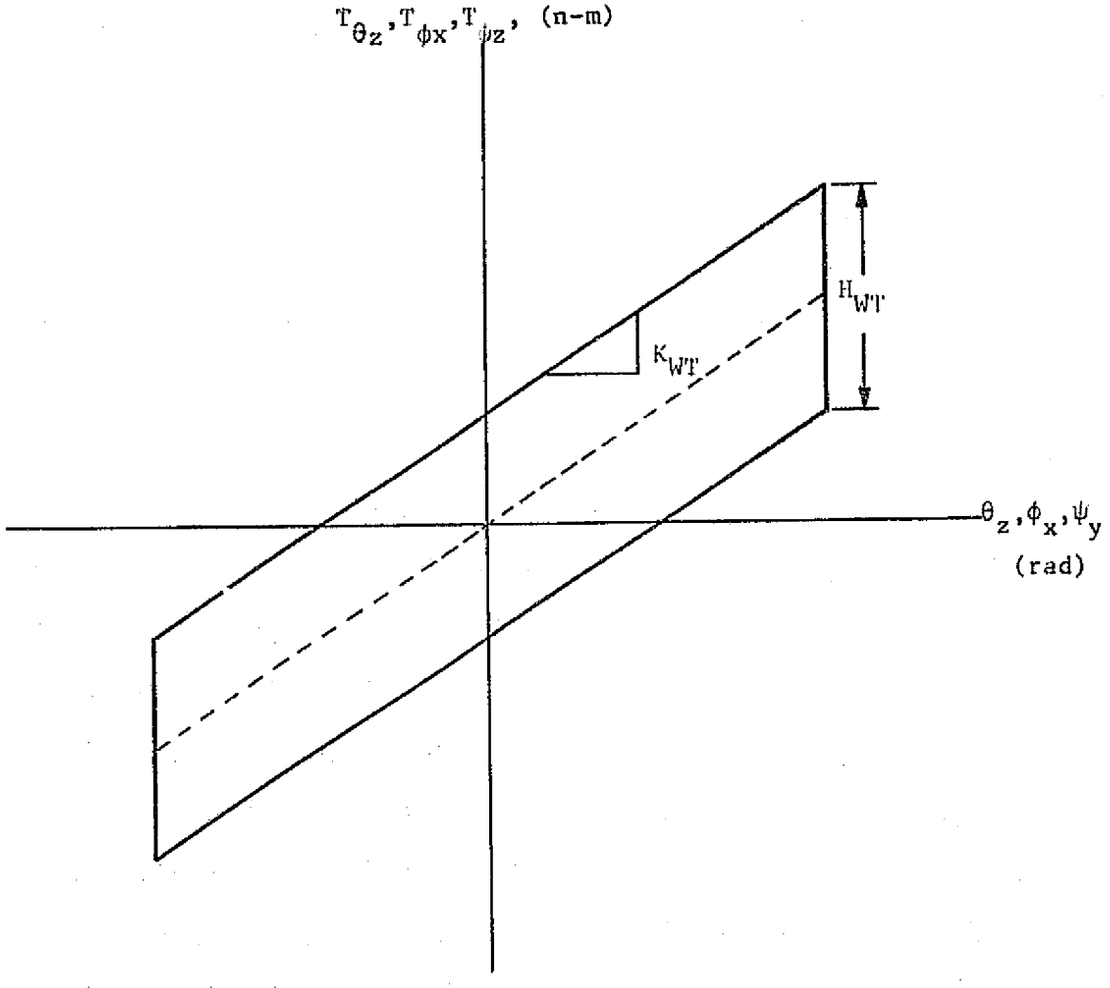

Figure 2-2. Wire Torques

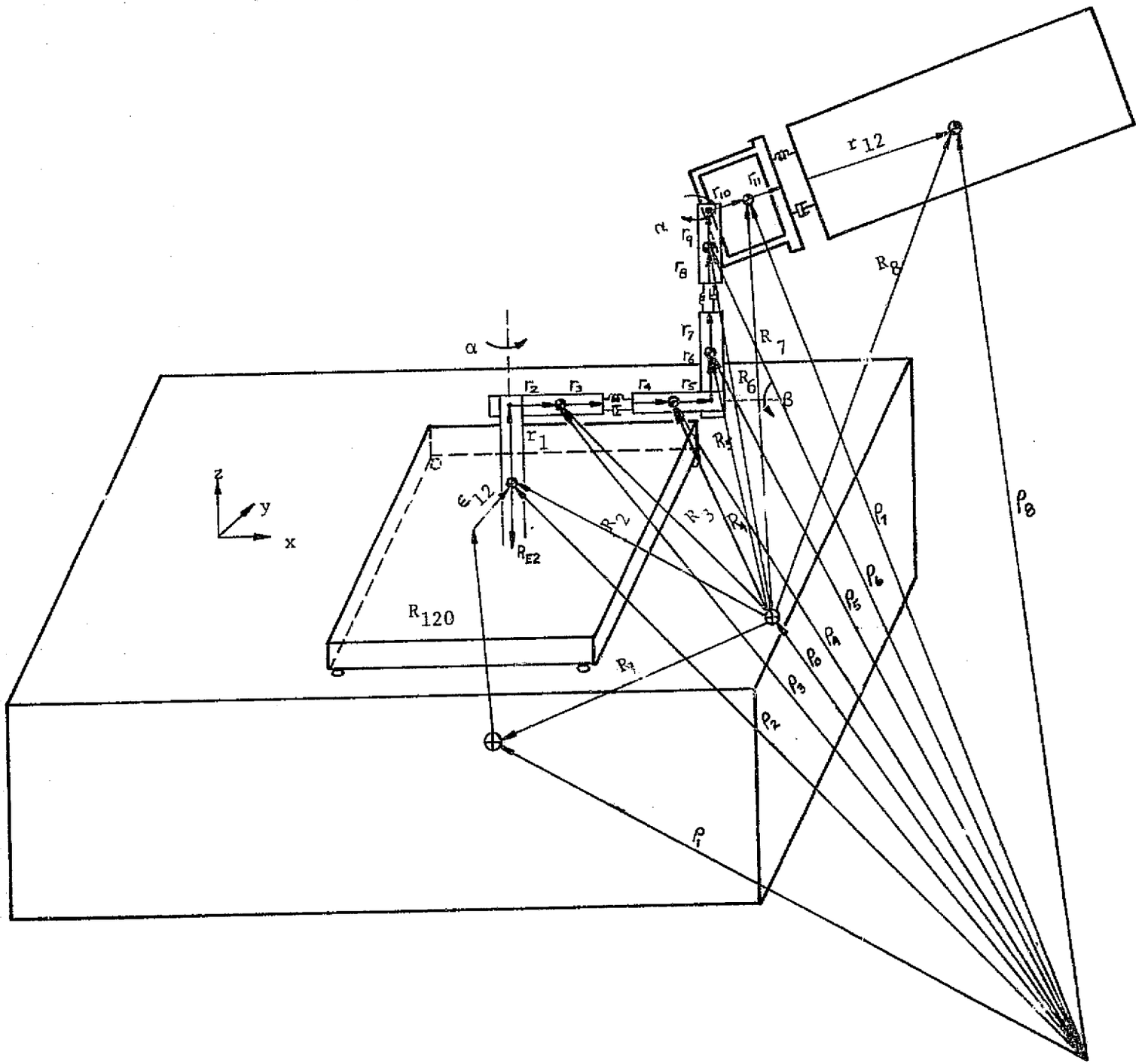

Figure 2-3. Offset Gimbal System Configuration

3. IOG SYSTEM STABILITY ANALYSIS

The following sections will describe the IOG system stability analyses that were performed during the course of the study. The stability studies performed included the following:

a. System stability as a Function of Telescope Look Angle for Nominal System Parameters.

b. System Stability as a Function of Control Loop Bandwidth Variations.

c. System Stability as a Function of Telescope Mass and Inertia Variations for Nominal Control Loop Bandwidths

d. System Stability as a Function of Pedestal Mass and Inertia Variations.

e. System Stability as a Function of Variations in Sensor and Actuator Characteristics.

f. System Stability as a Function of Geometrical Variations.

The nominal system bandwidth that has been used throughout this study is 2 Hz defined as the point where the transfer function from disturbance torque to command torque is down 3 db. Although running higher loop bandwidths would reduce system pointing errors due to disturbances originating in the orbiter, it is felt that from considerations of system stability in the presence of structural flexibility and system noise, using loop bandwidths that are appreciably higher than 2 Hz is not advisable. In addition, the nominal suspension parameters used are based on achieving a pointing stability of $\pm$ 1 arc-second in the presence of crew motion disturbances. The nominal suspension parameters are listed in table 2-1. A detailed discussion of the stability studies performed is presented in the sections that follow. All of the eigenvalue data obtained during this study phase is shown in the Appendix volume which accompanies this report.

3.1 System Stability as a Function of Telescope Look Angle For Nominal System Parameters - For the nominal system as described in table 2-1, the telescope was rotated about the y-axis and the system eigenvalues were determined at various different look angles. The look angle is defined to be zero when the telescope is pointing straight up out of the orbiter cargo bay and 90 degrees when the telescope is in the cargo bay with its z-axis parallel to the orbiter x-axis and is positive directed aft. The telescope look

angle was varied between zero degree and 90 degrees for which the resulting eigenvalues were all in the left half plan thus verifying system stability for the nominal parameters.

3.2 System Stability as a Function of Control Loop Bandwidth Variations - For the nominal system described in table 2-1, the pointing control loop bandwidth was varied and the resulting system eigenvalues determined as a function of these variations. The control loop bandwidth was varied between zero and 10 times the nominal loop bandwidth (i.e., 0 and 20 Hz) for telescope look angles varying between zero and 90 degrees. The results of these parameterizations are the following.

a. All of the system characteristic roots were stable when the loop was opened, i.e., the control loop bandwidth was zero.

b. At 1/10 nominal loop bandwidth (i.e., 0.2 Hz) the system was stable for telescope look angles varying between zero and 40 degrees. For telescope look angles between 60 and 90 degrees, the system was unstable showing an unstable root of $1.79 \times 10^{-3} \pm j.095$ at 60 degrees and $1.48 \times 10^{-3} \pm j.1295$ at 90 degrees. These roots describe the interaction between translation of the pedestal along the z-axis and telescope rotation about the y-axis.

c. At 1/5 nominal loop bandwidth (i.e., 0.4 Hz) the system was stable for telescope look angles between zero and 60 degrees. However, the system was unstable at 90 degrees exhibiting an eigenvalue of $2.88 \times 10^{-3} \pm j.385$.

d. The system was stable for loop bandwidths varying between 1/2 and four times (i.e., 1 and 8 Hz) nominal loop bandwidth for all telescope look angles between zero and 90 degrees.

e. For loop bandwidths of six times nominal the system was unstable for telescope look angles between zero and 10 degrees with one set of actuator poles crossing into the right half plane. For look angles between 20 and 90 degrees, the system was stable.

f. At ten times nominal loop bandwidth the system was unstable for all telescope look angles with three sets of actuator poles crossing to the right half plane for telescope look angles between zero and 60 degrees and one set of actuator poles crossing into the right half plane for a telescope look angle of 90 degrees.

3.3 System Stability as a Function of Telescope Mass and Inertia Variations - For the nominal system described in table 2-1, system stability was determined as a function of telescope mass and inertia variations. The telescope mass and inertia were varied concurrently in the same proportion which ranged from one hundredth to five times the nominal values shown in table 2-1. During these variations the pointing control loop bandwidth was continually adjusted to maintain a control loop bandwidth of 2 Hz. All other parameters were maintained at their nominal values. The results indicate that the system was stable for all values of telescope mass and inertia considered for telescope look angle ranging between zero and 60 degrees.

3.4 System Stability as a Function of Pedestal Mass and Inertia Variations - For the nominal system described in table 2-1, system stability was determined as a function of IOG pedestal and inertia variations. The pedestal mass and inertia were varied concurrently in the same proportion which ranged between one tenth to 10 times the nominal values indicated in table 2-1. These variations were conducted for zero and 60 degree telescope look angles. The results of these studies indicated that the system was stable for all variations made.

3.5 System Stability as a Function of Sensor and Actuator Variations - For the nominal system described in table 2-1, system stability was determined as a function variation in sensor and actuator characteristics. The gimbal torquer (modeled as a first order lag) time constants were varied from 20 to two times their nominal values (i.e., from .1591 to 1.591×10^{-2} sec). The rate gyros (which were modeled as second order transfer functions) natural frequencies were varied from one one-twentieth to one half times their nominal values (i.e., from 8.17 to 81.7 rad/sec) and damping ratio was varied from one hundredth to 0.6 times their nominal values (i.e., 0.005 to 0.3). The results of these studies were the following:

a. The system was stable for the range of gimbal torquer variations investigated for telescope look angles between zero and sixty degrees.

b. System was unstable when the gyro damping ratio was 0.01 or below and was stable when the sensor damping was 0.05 (i.e., one-tenth nominal) or greater for telescope look angles between zero and sixty degrees.

c. System was unstable when the gyro natural frequency was 16.34 rad/sec or below and was stable for gyro natural frequencies of 32.68 rad/sec or greater for telescope look angles varying between zero and 60 degrees.

These results indicate that system stability is not a sensitive function of variations in sensor and actuator characteristics.

3.6 System Stability as a Function of Variations in Suspension Characteristics - For the nominal system described in table 2-1, system stability was determined as a function of variations in suspension damping and linear stiffness. The suspension damping and stiffness were first varied together from one-tenth to 20 times the nominal values shown in table 2-1. Then with the suspension stiffness set at nominal values, suspension damping was varied from zero to one-half nominal. The results of these studies are outlined below:

a. The system was stable when suspension stiffness and damping were varied together over the range indicated above for telescope look angles between zero and sixty degrees.

b. The system was unstable for all telescope look angles when suspension damping was set to zero.

c. With suspension damping set at one-hundredth the nominal values shown in table 2-1 keeping the stiffness at their nominal values, the system was stable for telescope look angles between zero and 60 degrees. For a ninety degree telescope look angle, the system was unstable. The above was also true when suspension damping was set at one-fiftieth nominal.

d. The system was stable for telescope look angles between zero and 90 degrees when suspension damping was one-tenth nominal or greater.

These results indicate that system stability is not a sensitive function of variations in suspension characteristics.

3.7 System Stability as a Function of Geometrical Variations - For the nominal system described in table 2-1, system stability was determined as a function of geometrical variations. These variations included the following:

a. Telescope CM was moved in the x,y plane, r_2 (i.e., along the telescope transverse axes) between the nominal value of zero to two meters along the x and y axes.

b. The distance of the telescope CM with respect to the gimbal hinge point, r_2, was varied from the nominal value of 1.689 meters to 168.9 meters.

c. The location of the gimbal hinge point with respect to the pedestal CM, r_1, was varied along the x and y pedestal axes between the nominal value of zero to 0.375 meters.

d. The variations described in items a and c above, were performed concurrently.

The results of these studies are described below:

a. When the telescope CM was moved along the transverse axes of the telescope (i.e., x and y axes) the system was stable for offset values along the x and y axes of as much as two meters for telescope look angles varying between zero and 60 degrees.

b. When the distance of the telescope CM with respect to the gimbal hinge point, r_2, was 84.55 meters or less, the system was stable for zero telescope look angle. However, for telescope look angles of 60 degrees, the distance of the telescope CM with respect to the gimbal hinge point had to be kept to 33.78 meters or below for the system to be stable.

c. The system was stable for variations in the location of the gimbal hinge point with respect to the CM of the pedestal r_1, along the x and y axes of as much as 0.375 meters which corresponds to the distance that the gimbal hinge point is above the pedestal CM (i.e., distance along the z-axis) for telescope look angles between zero and 60 degrees.

d. The system was unstable when the concurrent values of r_1 and r_2 were

$$r_1 = .375\ \hat{i}_x - .375\ \hat{i}_y + .375\ \hat{i}_z \text{ meters}$$

$$r_2 = -1.5\ \hat{i}_x + 1.5\ \hat{i}_y + 1.689\ \hat{i}_z \text{ meters}$$

for a telescope look angle of zero degrees. When the telescope look angle was 60 degrees, the system was stable for the above conditions.

These results indicate that system stability is not very sensitive to realistic geometric variations that will reasonably be encountered.

A summary of the results obtained in the IOG stability studies performed and described above is given in table 3-1.

Table 3-1. Summary of IOG Stability Studies

Study Performed	Parameters Varied	Range of Variation	Results
System stability as a function of suspension damping for various telescope look angles 2 Hz control loop bandwidth	Suspension linear (D) and angular (d) damping coefficient Telescope look angle (θ)	$0 \leq D \leq$ 0.5 nominal $0 \leq d \leq$ 0.5 nominal $0 \leq \theta \leq 90°$	• For zero damping coefficient system was unstable for all telescope look angles. • For 1/100 nominal damping system was stable for look angles of 60° or less. • Unstable for telescope look angle of 90°. • System stable for all telescope look angles for 1/10 nominal suspension damping
System stability as a function of suspension characteristics keeping damping ratio constant. Telescope look angle 60° 2 Hz control loop bandwidth	Suspension linear (K) and angular (k) stiffness. Suspension linear (D) and angular (d) damping coefficient	0.1 nom $\leq K \leq$ 20 nom 0.1 nom $\leq k \leq$ 20 nom 0.1 nom $\leq D \leq$ 20 nom 0.1 nom $\leq d \leq$ 20 nom	• All conditions examined were stable.
System stability as a function of pedestal mass and inertia variations Telescope look angle 60° 2 Hz control loop bandwidth	Pedestal mass (m_2) Pedestal inertia (J_2)	0.1 nom $\leq m_2 \leq$ 10 nom 0.1 nom $\leq J_2 \leq$ 10 nom	• All conditions examined were stable.

Table 3-1. Summary of IOG Stability Studies (Continued)

Study Performed	Parameters Varied	Range of Variation	Results
System stability as a function of sensor damping ratio for various telescope look angles. 2 Hz control loop bandwidth	Sensor damping ratio (ζ_s) Telescope look angle (θ)	0.01 nom $\leq \zeta_s \leq$ nom $0 \leq \theta \leq 60°$	• System unstable for sensor damping ratio less than .05 which is 1/10 the nominal damping ratio. This was true for all look angles considered.
System stability as a function of sensor natural frequency for various telescope look angles. Sensor damping ratio 0.5 2 Hz control loop bandwidth	Sensor natural frequency (ω_{ns}) Telescope look angle (θ)	0.05 nom $\leq \omega_{ns} \leq$ nom $0 \leq \theta \leq 60°$	• System unstable for sensor natural frequency less than 1/5 nominal (i.e. 32.68 rad/sec). This was true for all telescope look angles considered.
System stability as a function of actuator band width for various telescope look angles. 2 Hz control loop bandwidth	Actuator bandwidth (ω_{nT}) Telescope look angle (θ)	0.05 nom $\leq \omega_{nT} \leq$ nom $0 \leq \theta \leq 60°$	• All conditions examined were stable.

Table 3-1. Summary of IOG Stability Studies (Continued)

Study Performed	Parameters Varied	Range of Variation	Results
System stability margins as a function of geometric variations for various telescope look angles. 2 Hz control loop bandwidth	Distance from pedestal CM to gimbal hinge point (r_1) Distance from gimbal hinge point to telescope CM (r_2) Telescope look angle	$-.375 \leq r_{1x} \leq .375$ $-.375 \leq r_{1y} \leq .375$ $r_{1z} = .375$ (nom) $-2.0 \leq r_{2x} \leq 0$ $0 \leq r_{2y} \leq 2.0$ $1.689 \leq r_{2z} \leq 168.9$ $0 \leq \theta \leq 60°$	• System stable for separate variations in r_1 for all conditions considered. • There were only two conditions examined for this parameterization $r_1 = -.375\hat{i}_x + .375\hat{i}_y + .375\hat{i}_z$; $\theta = 0°, 60°$ $r_1 = .375\hat{i}_1 - .375\hat{i}_y + .375\hat{i}_z$; $\theta = 0°$ • System was unstable for $r_1 = .375\hat{i}_z$ (nom) $r_2 \leq 85\hat{i}_z$; $\theta = 0$ $r_2 \leq 33.78\hat{i}_z$; $\theta = 60°$ • System was stable for nominal r_1 and nominal r_{2z} (i.e. 1.689) for the total range of parameterization of r_{2x}, r_{2y} and θ. • System was unstable for the following condition $r_1 = .375\hat{i}_x - .375\hat{i}_y + .375\hat{i}_z$ $r_2 = 1.5\hat{i}_x + 1.5\hat{i}_y + 1.689\hat{i}_z$ $\theta = 0°$ When the telescope angle was equal to 60° the system was stable for the above geometric conditions.

Table 3-1. Summary of IOG Stability Studies (Concluded)

Study Performed	Parameters Varied	Range of Variation	Results
System stability as a function of control loop bandwidth for various telescope look angles	Control loop bandwidth (f_n) Telescope look angle (θ)	$0 \leq f_n \leq$ 20 Hz $0 \leq \theta \leq$ 90°	• System was unstable for control loop bandwidths of .2Hz (1/10 nominal) or below when telescope look angles were 60 and 90 degrees. • System was unstable for control loop bandwidths .4Hz (1/5 nominal) or below when the telescope look angle was 90 degrees. • System was stable for all telescope look angles for $1Hz \leq f_n \leq 4Hz$ and unstable for $f_n \geq 6Hz$.
System stability as a function of telescope mass and inertia variations for various telescope look angles	Telescope mass (m_3) Telescope inertia (J_3) Telescope look angle θ	.01 nom $\leq m_3 \leq$ 5 nom .01 nom $\leq J_3 \leq$ 5 nom $0 \leq \theta \leq$ 60°	• All conditions examined were stable.

4. IOG LINEAR SYSTEM PERFORMANCE

The sections that follow describe the pointing performance of the IOG for nominal conditions and as a function of various system parameterizations which include the following:

a. Location of the IOG with respect to the orbiter.

b. Variation of suspension damping characteristics.

c. Variation of pedestal mass and inertia.

d. Variation of telescope mass and inertia.

In the performance of the system parameterization studies outlined below, a nominal set of system parameters were employed which are given in table 2-1. These parameters result in a 2Hz pointing control loop bandwidth defined as the point where the magnitude of the ratio of control torque to disturbance torque is down 3 db. Any deviations from these parameters will be expressedly noted in the discussion that follows. The crew motion disturbance force profile that was employed throughout the pointing performance studies is shown in figure 4-1.

IOG nonlinear system performance will be described in section 5.0.

Earth tracking performance of the IOG for the nominal system given in table 2-1 will also be described in the sections that follow.

4.1 IOG Pointing Performance

4.1.1 IOG Pointing Performance as a Function of Location Within the Orbiter Cargo Bay - The nominal parameters given in table 2-1 position the IOG as far forward in the orbiter cargo bay as possible. In order to position the IOG as far back in the cargo bay as is feasible, the baseline parameters shown in table 2-1 are modified in the following manner.

$$R_{120} = 4.18\ \hat{i}_x - 1.579\ \hat{i}_z \text{ m}$$

System responses under the influence of crew motion disturbances, applied along all three vehicle axes simultaneously, were taken for various telescope look angles for both positions of the IOG within the cargo bay. The peak pointing error incurred for the x and y telescope axes as a function of telescope look

angle for both IOG positions within the cargo bay are shown in figures 4-2 and 4-3. Examination of these figures indicate that pointing errors incurred when the IOG is mounted forward in the cargo bay far exceed those that result when the IOG is mounted in the rear of the cargo bay. The reason for this behavior is the following. When the IOG is mounted in a forward position the orbiter rotations and translations that occur due to the crew motion disturbance add to give the net linear motion of the IOG hinge point which is the primary disturbance input to the telescope. However, when the IOG is mounted in the rear of the cargo bay the orbiter translatory and rotary motions subtract to give the net translation of the of the gimbal hinge point thus resulting in a greatly reduced disturbance input to the telescope which in turn results in small pointing errors. It is for this reason that the baseline system parameters were defined so that the IOG is in a forward position in all of the ensuing response studies.

4.1.2 IOG Pointing Performance as a Function of Variation in Suspension Damping - System time response studies were performed for various telescope look angles as a function of suspension damping characteristics. The suspension damping was varied over a wide range of values and the effect on peak pointing error for a reduction in suspension damping of an order of magnitude is summarized in figure 4-4. The parameter values that result in a factor of ten reduction in suspension damping are given below.

$$D_x = D_y = D_z = 5.993 \ \frac{\text{n-sec}}{\text{m}}$$

$$d_x = d_y = 1.496 \text{ n-m-sec}$$

$$d_z = 2.992 \text{ n-m-sec}$$

Examination of figure 4-4 indicates that suspension damping has very little effect on system pointing performance when varied (i.e., reduced) by an order of magnitude. However, suspension damping should not be reduced by much more than an order of magnitude if adequate system stability margins are to be maintained. In addition, the linear mode of system oscillation is not damped by the control loop and only damps out by virtue of the damping in the suspension system. The nominal suspension damping coefficients are chosen such that a damping ratio of a tenth is achieved for the linear mode when considering all of the mass above the suspension point.

Figures 4-5 thru 4-25 show the IOG system response for nominal parameters in the presence of the crew motion disturbance shown in figure 4-1 applied simultaneously along the x,y, and z axes of the shuttle orbiter, for a telescope look angle of zero degrees. The legend that is employed in these plots and all subsequent plots shown in this report is given in table 4-1.

The symbols employed in table 4-1 are the same as those used in the mathematical model derivation outlined in section 2.1 and are defined in that section. It should be noted that when ω_{3c} and θ_{3c} are equal to zero, which they are in the case of stellar pointing, ω_3^* and θ_3^* are identically equal to ω_3 and θ_3 the angular rates and rotations of body 3. Figures 4-26 thru 4-46 show the IOG system response for nominal parameters with a crew motion disturbance applied simultaneously along all three orbiter axes for a telescope look angle of 0.6981 rad (40 degrees) while figures 4-47 thru 4-67 show IOG response for the same set of conditions but with a telescope look angle of 1.047 rad (60 degrees).

4.1.3 IOG Pointing Performance as a Function of Pedestal Mass and Inertia Variations - Time response studies were performed for various telescope look angles as a function of pedestal mass and inertia variation. The pedestal mass and inertia was varied by an order of magnitude about nominal (i.e., in both directions) with both the mass and inertia varying concurrently by the same ratio from nominal. The parameters that were modified from the nominal set shown in table 2-1 in order to accomplish the desired pedestal mass and inertia variation are given below:

$m_2 = 19.5$ Kg
$J_{2x} = J_{2y} = J_{2z} = 5$ Kg-m^2 — One tenth nominal pedestal mass and inertia

$m_2 = 1950$ Kg
$J_{2x} = J_{2y} = J_{2z} = 500$ Kg-m^2 — Ten times nominal pedestal mass and inertia

The results obtained from these time response studies are summarized in figure 4-68. Examination of this figure indicates that variations in pedestal mass and inertia by an order of magnitude from nominal does not have a marked effect on pointing performance. It can be seen that when the pedestal mass and inertia

Table 4-1. Legend for Computer Plots

THTXST = $\theta^*_{3x} = \theta_{3x} - \theta_{3xc}$	EPS12X = ε_{12x}
THTYST = $\theta^*_{3y} = \theta_{3y} - \theta_{3yc}$	EPS12Y = ε_{12y}
THTZST = $\theta^*_{3z} = \theta_{3z} - \theta_{3zc}$	EPS12Z = ε_{12z}
OMGXST = $\omega^*_{3x} = \omega_{3x} - \omega_{3xc}$	EPS12XDT = $\dot{\varepsilon}_{12x}$
OMGYST = $\omega^*_{3y} = \omega_{3y} - \omega_{3yc}$	EPS12YDT = $\dot{\varepsilon}_{12y}$
OMGZST = $\omega^*_{3z} = \omega_{3z} - \omega_{3zc}$	EPS12ZDT = $\dot{\varepsilon}_{12z}$
THETA2X = θ_{2x}	THTXC = T_{Hx}
THETA2Y = θ_{2y}	THTYC = T_{Hy}
THETA2Z = θ_{2z}	THTZC = T_{Hz}
OMEGA2X = ω_{2x}	
OMEGA2Y = ω_{2y}	
OMEGA2Z = ω_{2z}	

is reduced by an order of magnitude the x-axis pointing performance improves while the y-axis performance is unchanged. When the pedestal mass and inertia are increased by an order of magnitude the x-axis pointing errors increase while the y-axis errors decrease. This is to be expected since the suspension does not act primarily as a classical passive isolator in reducing errors in the x, y plane. It accomplishes that function by allowing the hinge point to translate "via" pedestal rotation about an appropriate axis in the x,y plane whose center of rotation is between the pedestal CM and the plane defined by the attach point of the individual isolators to the pedestal base plate. The rotation of the pedestal takes place due to the geometrical properties of the IOG and the influence of the telescope control torques which react back on the pedestal. Hence, as the pedestal mass and inertia decrease the speed with which the pedestal rotation in the x,y plane occurs with its accompanying hinge point translation increases thus reducing the disturbance input to the telescope, which results in improved pointing accuracy. When the pedestal mass and inertia are increased, the rotation of the pedestal in the x,y plane occurs at a slower rate which results in larger net hinge point accelerations thus increasing the disturbance input to the telescope which results in larger system pointing errors. For y-axis disturbances, the IOG suspension acts primarily as a classical passive isolator. Hence as the pedestal mass and inertia is increased the system pointing performance improves since the isolation natural frequency is lowered. However, it is seen that there was virtually no effect on the y-axis pointing error when the pedestal mass and inertia was reduced by a factor of ten. The reason for this is that the mass that is used to compute the linear suspension natural frequency in the "y" direction is a composite mass that is a function of the pedestal and telescope masses and the pointing control loop bandwidth. For the nominal pedestal mass and inertia the composite mass which determines suspension natural frequency is primarily determined by the telescope mass and the pointing control loop bandwidth. Hence reducing pedestal mass and inertia has virtually no effect on the y axis pointing error. This effect will be further demonstrated by the results obtained when the suspension linear stiffnesses in the x and y directions are increased while the rotational stiffness about the x and y axes are held constant.

4.1.4 IOG Pointing Performance as a Function of Telescope Mass and Inertia Variations - Pointing performance studies were performed using a small telescope defined in Dornier technical report IPS-TN-025-041. The mass properties of this telescope given in the above report are

$m = 290$ Kg

$J_x = J_y = 50$ Kg-m^2

$J_z = 35$ Kg-m^2

Distance from the Base of Telescope to C.M. = $1.5\ \hat{i}_z$ m

When these parameters are combined with the IOG stable mounting gimbal the following are the parameters that have been modified from the nominal set shown in Table 2-1.

$m_3 = 583$ Kg

$J_{3x} = 309.5$ Kg-m^2

$J_{3y} = 334.5$ Kg-m^2

$J_{3z} = 110$ Kg-m^2

$r_2 = 0.9346\ \hat{i}_z$ m

$K_R = \text{diag}\ [3.032\text{x}10^3;\ 3.277\text{x}10^3;\ 1.078\text{x}10^3]$ n-m-sec

$K_P = \text{diag}\ [1.076\text{x}10^4;\ 1.163\text{x}10^4;\ 3.824\text{x}10^3]$ n-m/rad

$K_I = \text{diag}\ [1.698\text{x}10^4;\ 1.835\text{x}10^4;\ 6.035\text{x}10^3]\ \frac{\text{n-m}}{\text{sec}}$

where a 2 Hz pointing control loop bandwidth was maintained for the small telescope.

The results of the pointing performance studies are summarized in figure 4-69. Examination of figure 4-69 indicates that the pointing error has increased by approximately a factor of five over those for the baseline telescope for both the x and y axes. This is not surprising since the loop bandwidth was maintained at 2 Hz for the small telescope and hence one might expect that the pointing error for the small telescope could be approximately derived from those incurred for the baseline telescope using the following relationship.

C.2

$$\theta_{\varepsilon i}|_s = \frac{r_2|_s}{r_2|_{nom}} \times \frac{J_{3i}|_{nom}}{J_{3i}|_s} \times \theta_{\varepsilon i}|_{nom} \qquad (4\text{-}1)$$

where

$r_2|_s$ = Distance from hinge point to telescope CM for small telescope

$r_2|_{nom}$ = Distance from hinge point to telescope CM for baseline telescope

$J_{3i}|_{nom}$ = Moment of Inertia of the nominal telescope plus the IOG stable mounting gimbal about the i^{th} axis $i = x,y$

$J_{3i}|_s$ = Moment of Inertia of the small telescope plus IOG stable mounting gimbal about the i^{th} axis $i = x,y$

$\theta_{\varepsilon i}|_{nom}$ = Pointing error incurred by the nominal telescope about the i^{th} axis $i = x,y$

$\theta_{\varepsilon i}|_s$ = Pointing error incurred by the small telescope about the i^{th} axis $i = x,y$

Substituting the appropriate parameter values in equation (4-1) and evaluating results in

$$\theta_{\varepsilon x}|_s = 5.19\theta_{\varepsilon x}|_{nom}$$

$$\theta_{\varepsilon y}|_s = 4.38\theta_{\varepsilon y}|_{nom} \qquad (4\text{-}2)$$

It is seen that equation (4-2) gives approximately a factor of five increase in pointing error for the small telescope over that incurred by the large telescope which is in good agreement with the simulation results.

In order to achieve performance similar to that achieved for the baseline telescope (i.e., between 0.5 and 0.6 arc-second) the suspension stiffness had to be reduced by a factor of five. These results indicate the strong possibility that one set of IOG suspension parameters will not yield sub arc-second pointing performance over the spectrum of payloads that are being considered for IOG stabilization. It is probable that two or perhaps three different suspension system characteristics will be required to yield sub arc-second pointing and tracking performance over the payload set being considered.

4.2 IOG Earth Tracking Performance - The earth point tracking performance of the baseline system defined in table 2-1 was determined for a 438 KM orbit. Both angular rate and position commands to the telescope pointing control system were used simultaneously to accomplish earth tracking. These profiles are given in equations (4-3) and (4-4).

$$\theta_c(5) = 1.136 \tanh[\frac{372-t}{65}] \qquad (4-3)$$

$$\omega_c(t) = -1.748\text{x}10^{-2}\text{sech}^2[\frac{372-t}{65}] \qquad (4-4)$$

The profiles shown in equations (4-3) and (4-4) are actually approximations to those derived in section 8, however, they are "good" approximations as indicated in that section and hence yield representative system performance when they are employed.

The results of the earth tracking studies for the nominal system indicate that the system tracking error was 0.86 arc-second peak which is within the desired tracking performance of $\pm$1 arc-second with an accompanying peak control torque of 5.33 n-m which is within the 20 n-m gimbal torquer capability. However, the pedestal rotation about the y axis θ_{2y} was 0.249 rad (14.27 deg) and the pedestal translations were $9.92\text{x}10^{-2}$m (3.906 in) and $4.39\text{x}10^{-3}$ (.1728 in) along the x and y axes respectively. These values resulted in isolator elongations of 2.60 in along their longitudinal axes. These values of pedestal rotations, translations and isolator elongations are well beyond the IOG suspension design limits and hence the nominal suspension system cannot accommodate the nominal payload for earth tracking from a 438 KM orbit. It should be noted that the situation becomes worse as the orbital altitude is decreased (see section 9) and the ensuing pedestal rotation translations and isolator elongations will increase further. It is, therefore, evident that if the IOG is to accommodate payloads in the 200 Kg class the suspension parameters must be modified, consistant with pointing performance requirements, to reduce pedestal rotations and translations. A possible approach to this problem would be to increase the suspension linear stiffness along the x and y axes and to increase the rotational stiffness about the x and y axes keeping the linear stiffness along the z axis at the nominal value shown in table 2-1. The rationale behind this approach is that the isolator does not act as a classical isolator along the x and y axes, hence, increasing the linear stiffness along these axes will have little effect

on the telescope pointing error incurred about these axes due to disturbance as originating in the orbiter (e.g., crew motion). Increasing the rotational stiffness about the x and y axes will increase the pointing error incurred about the x axis due to orbiter disturances, however, the pointing errors presently obtained with the nominal system about the x axis is small enough (i.e., 0.1 arc-second) to allow an increase in this error while still meeting the overall pointing stability requirement of ± 1 arc-second. A more detailed discussion of this subject and the results of the approach outlined above will be given in section 7.0.

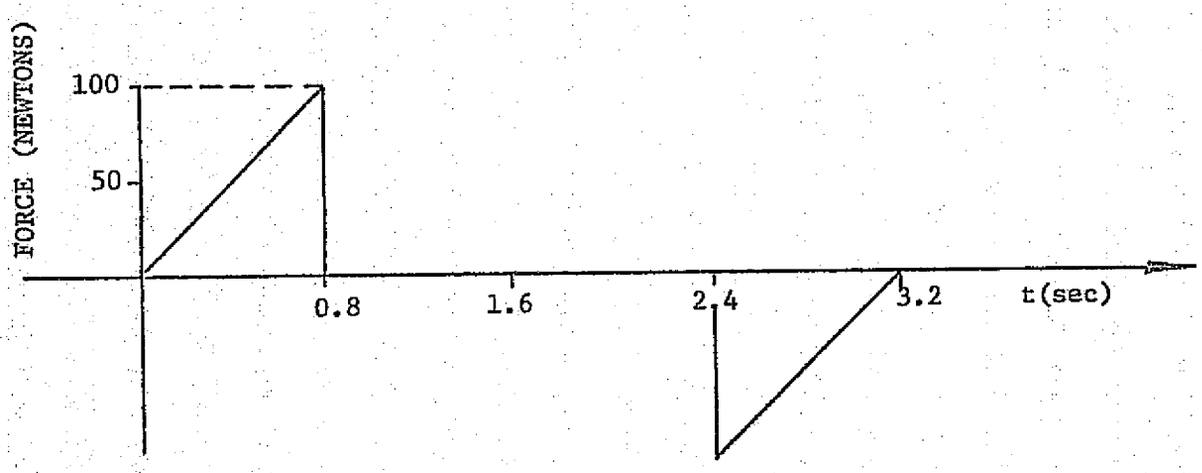

Figure 4-1. Crew Motion Disturbance Profile

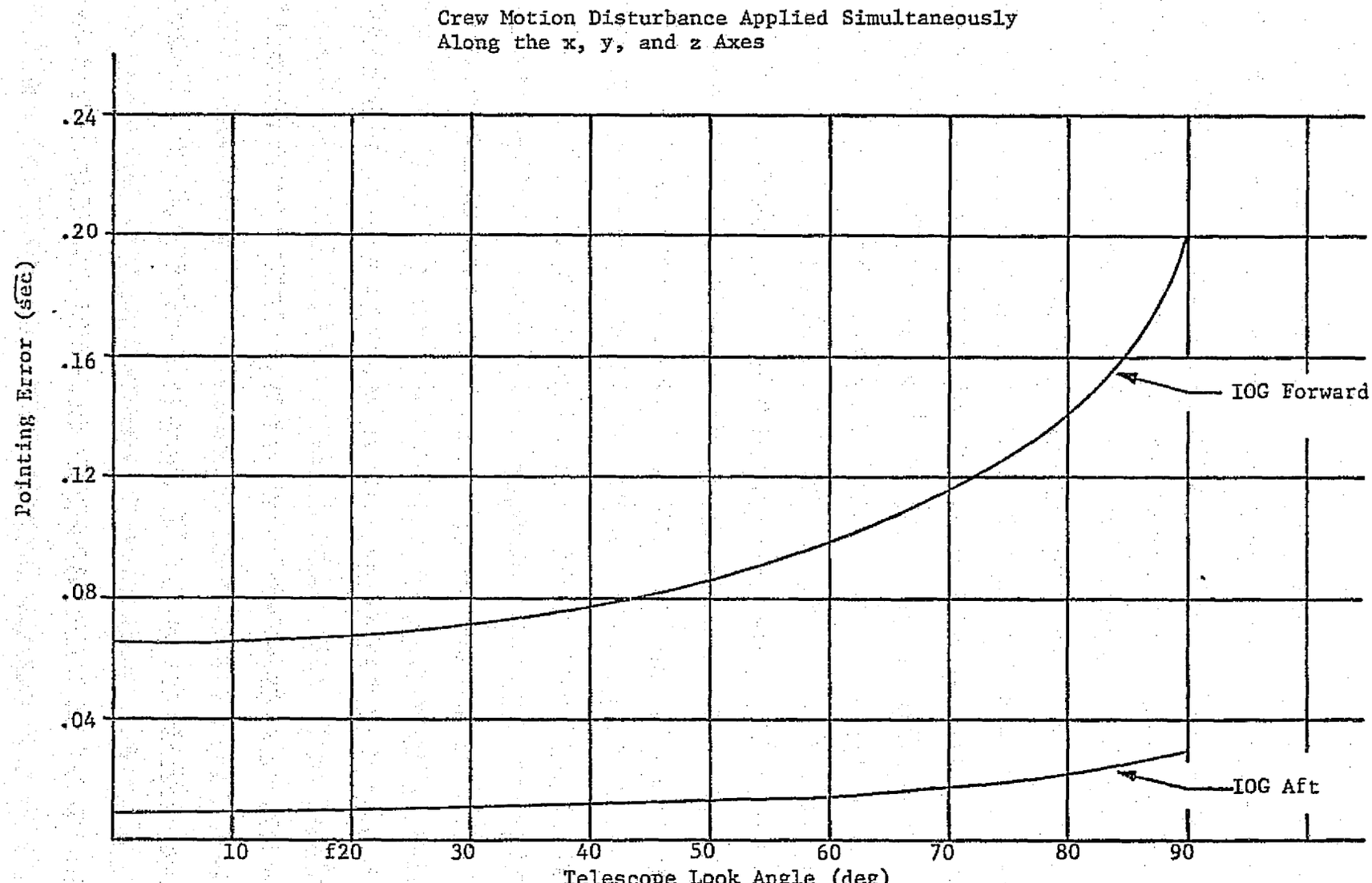

Figure 4-2. Peak x-Axis Pointing Error vs Telescope Look Angle as a Function of IOG Location in the Cargo Bay

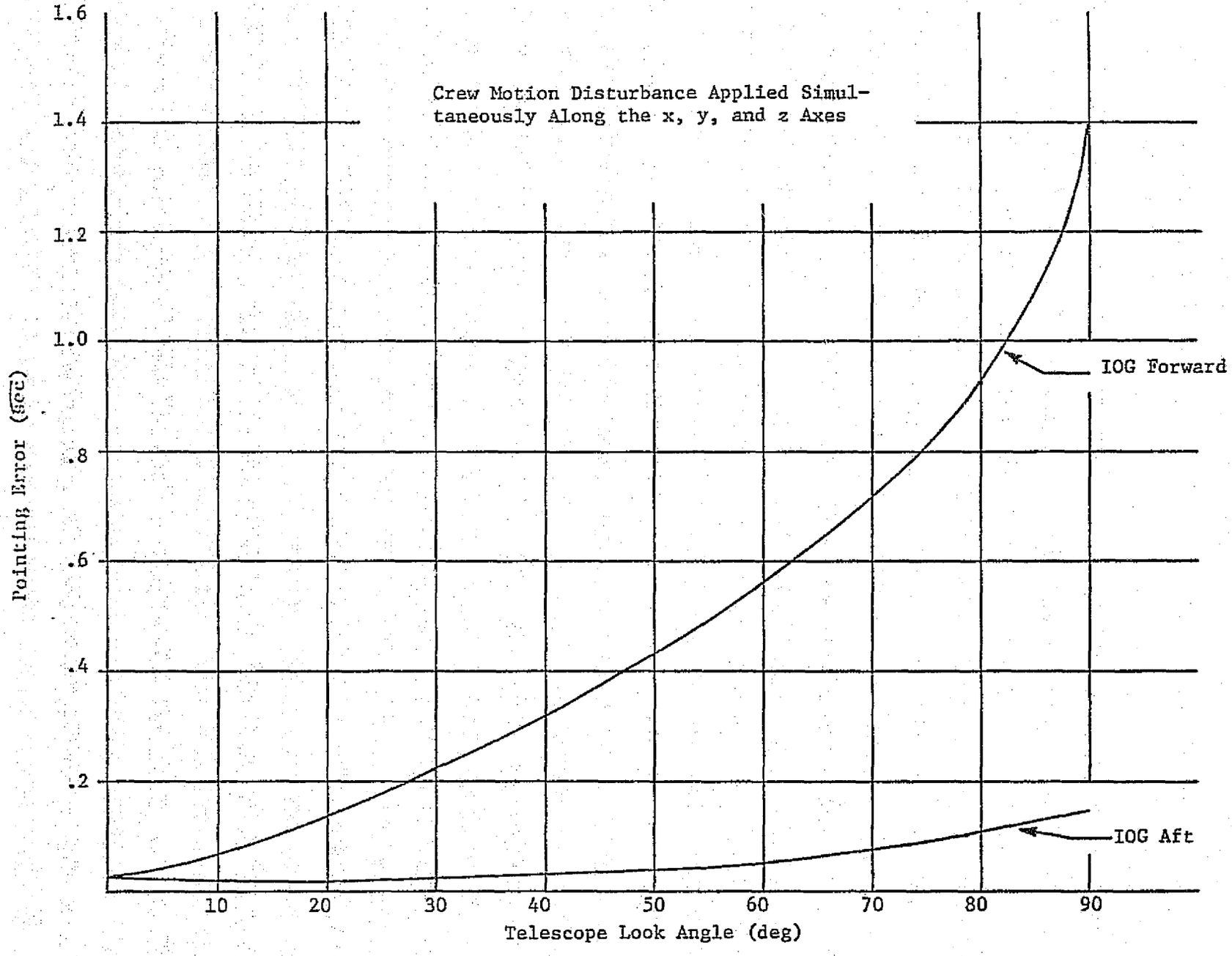

Figure 4-3. Peak y-Axis Pointing Error vs Telescope Look Angle as a Function of IOG Location in the Cargo Bay

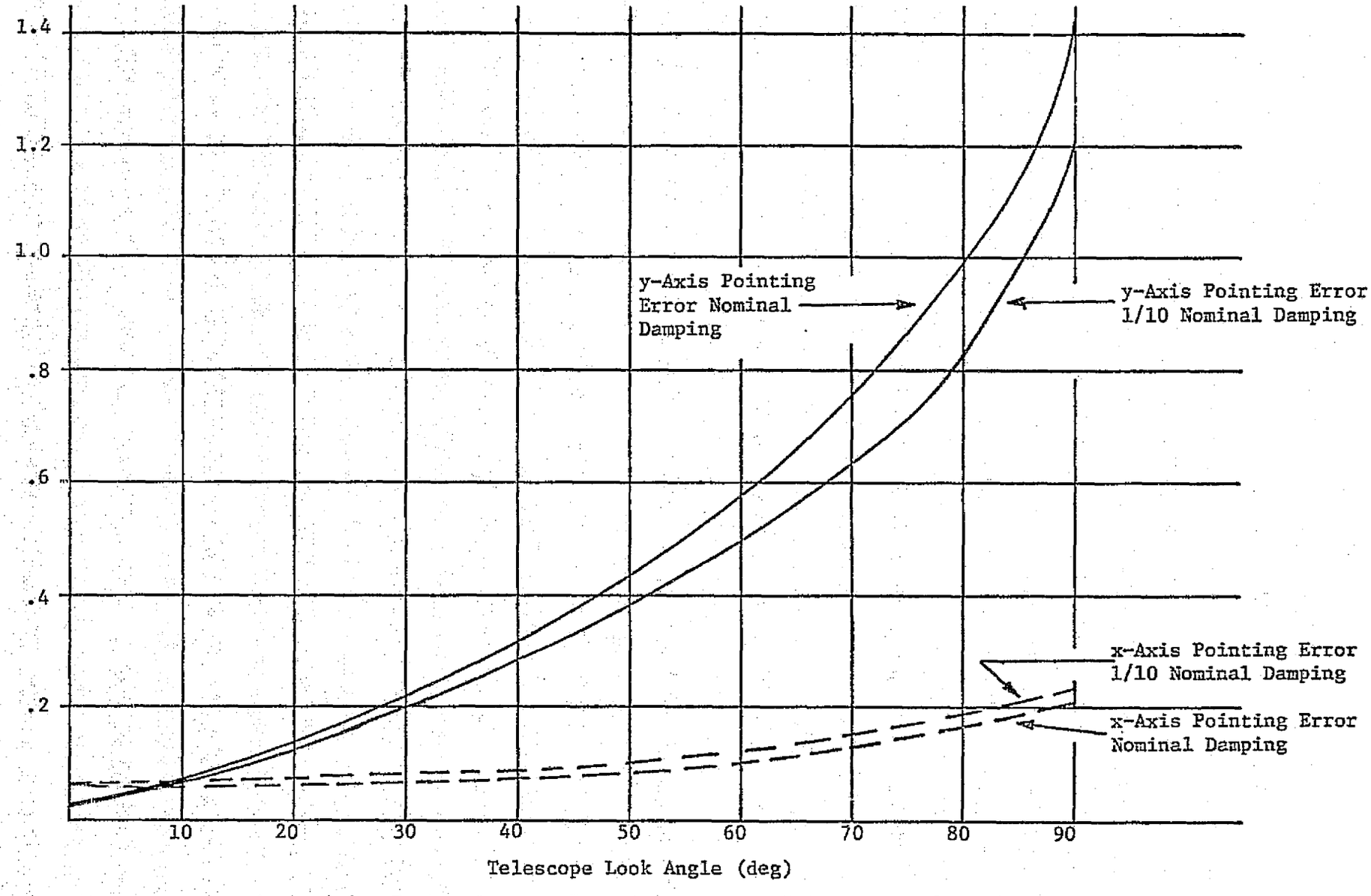

Figure 4-4. Peak Telescope Pointing Error vs Telescope Look Angle as a Function of Suspension Damping Characteristics

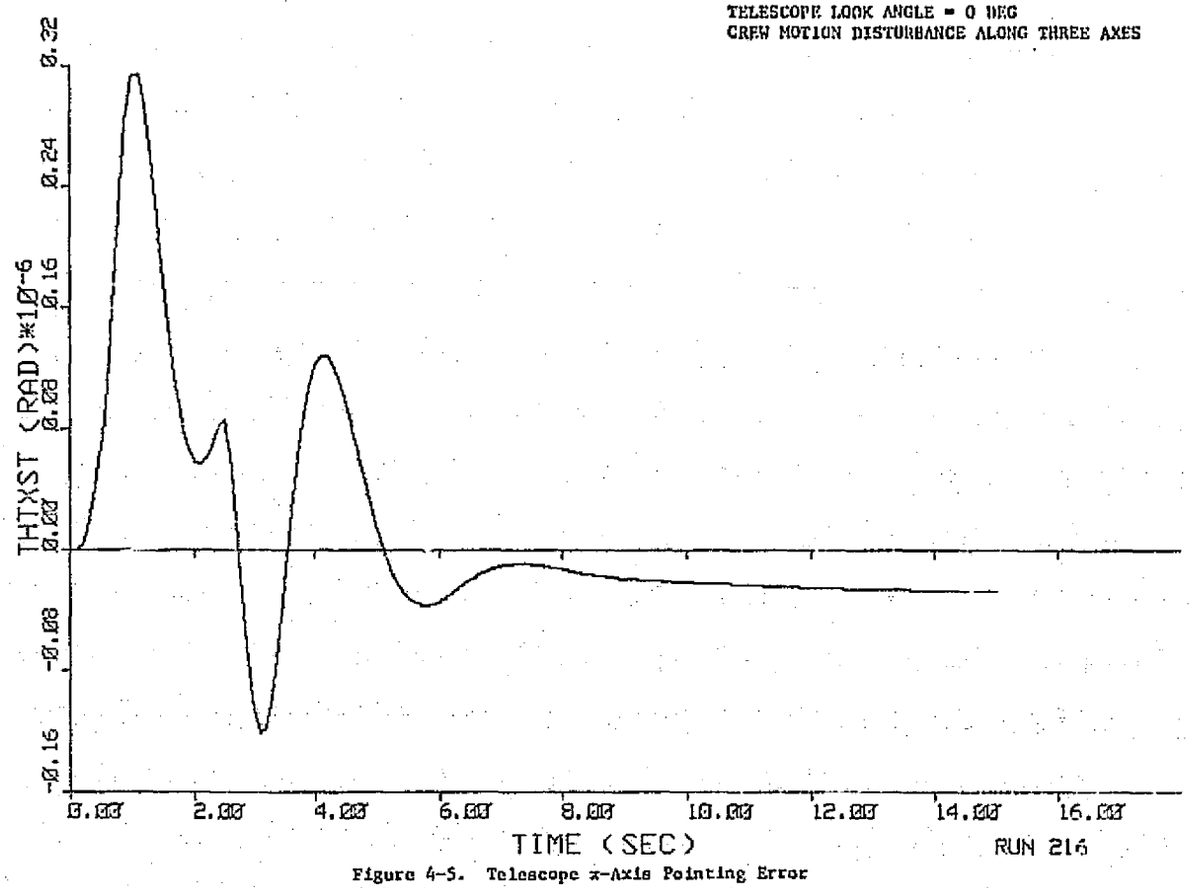

Figure 4-5. Telescope x-Axis Pointing Error

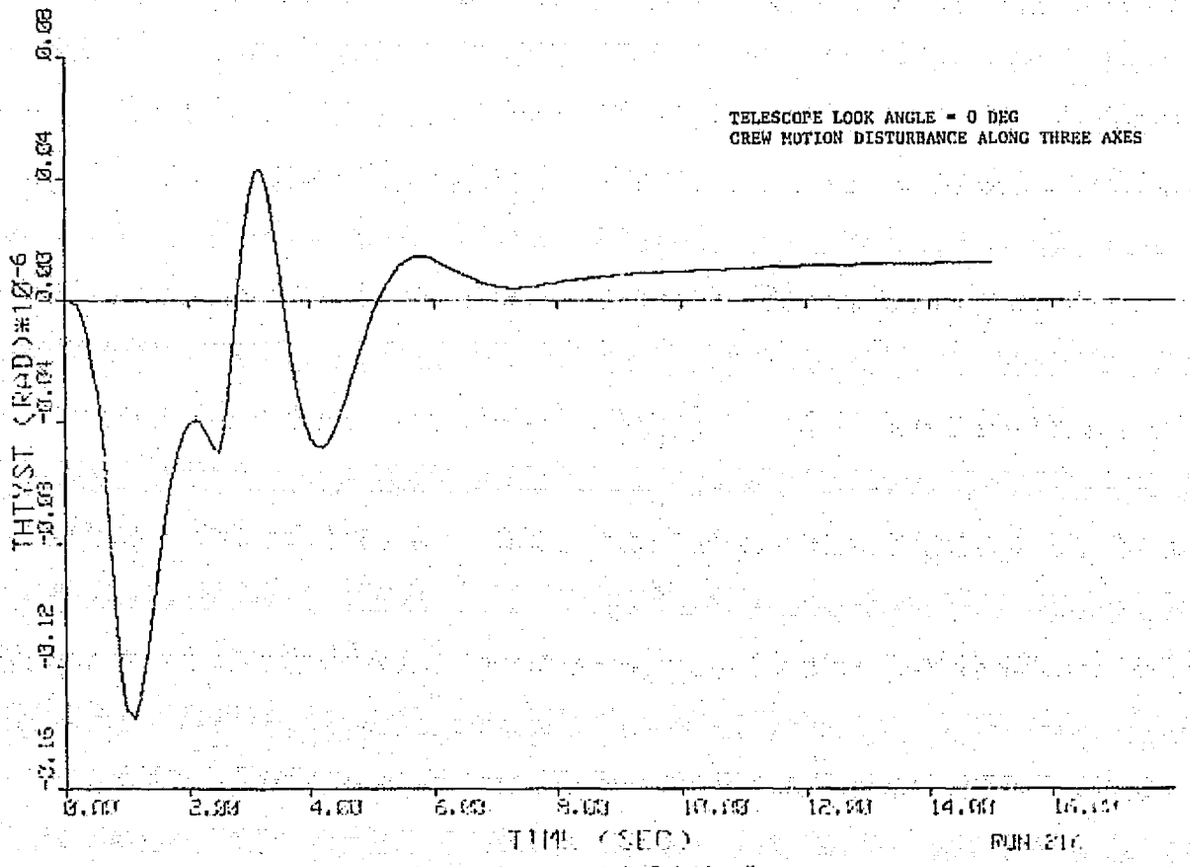

Figure 4-6. Telescope y-Axis Pointing Error

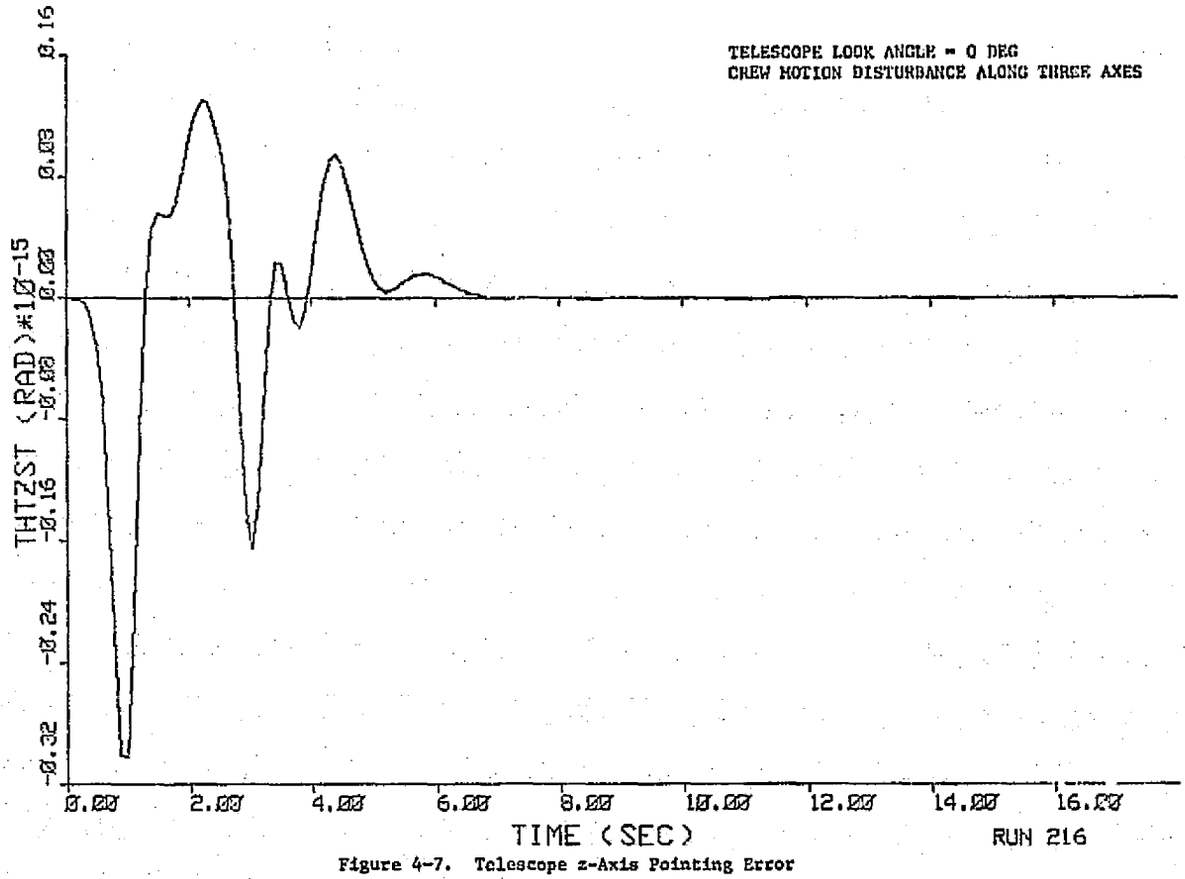

Figure 4-7. Telescope z-Axis Pointing Error

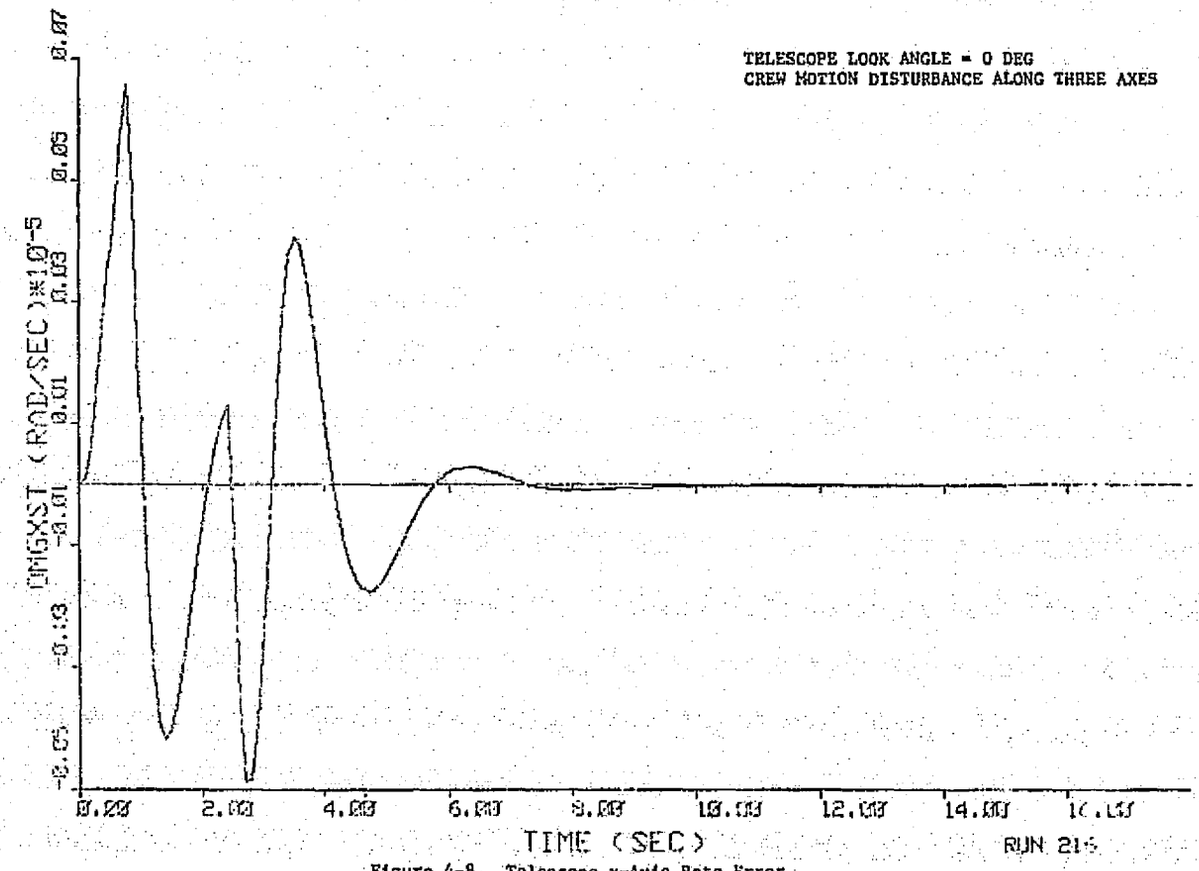

Figure 4-8. Telescope x-Axis Rate Error

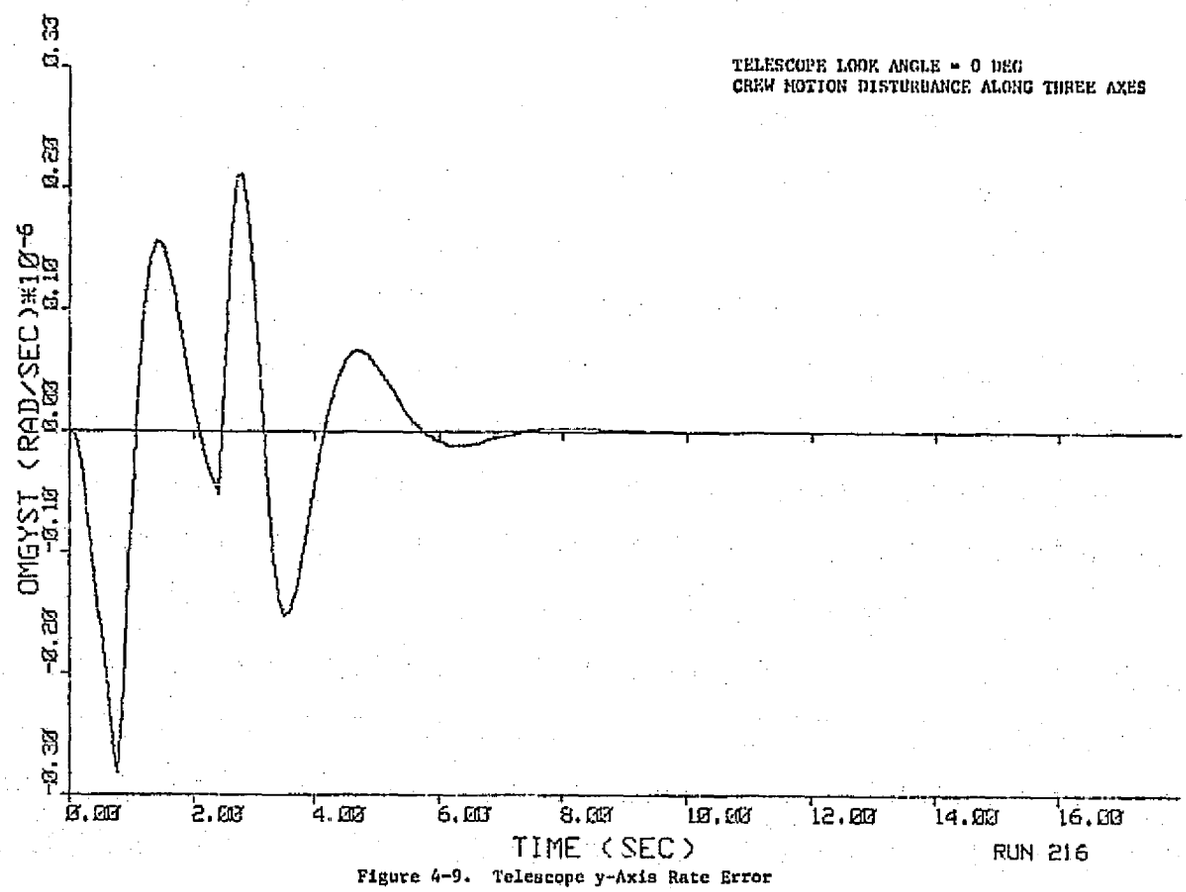

Figure 4-9. Telescope y-Axis Rate Error

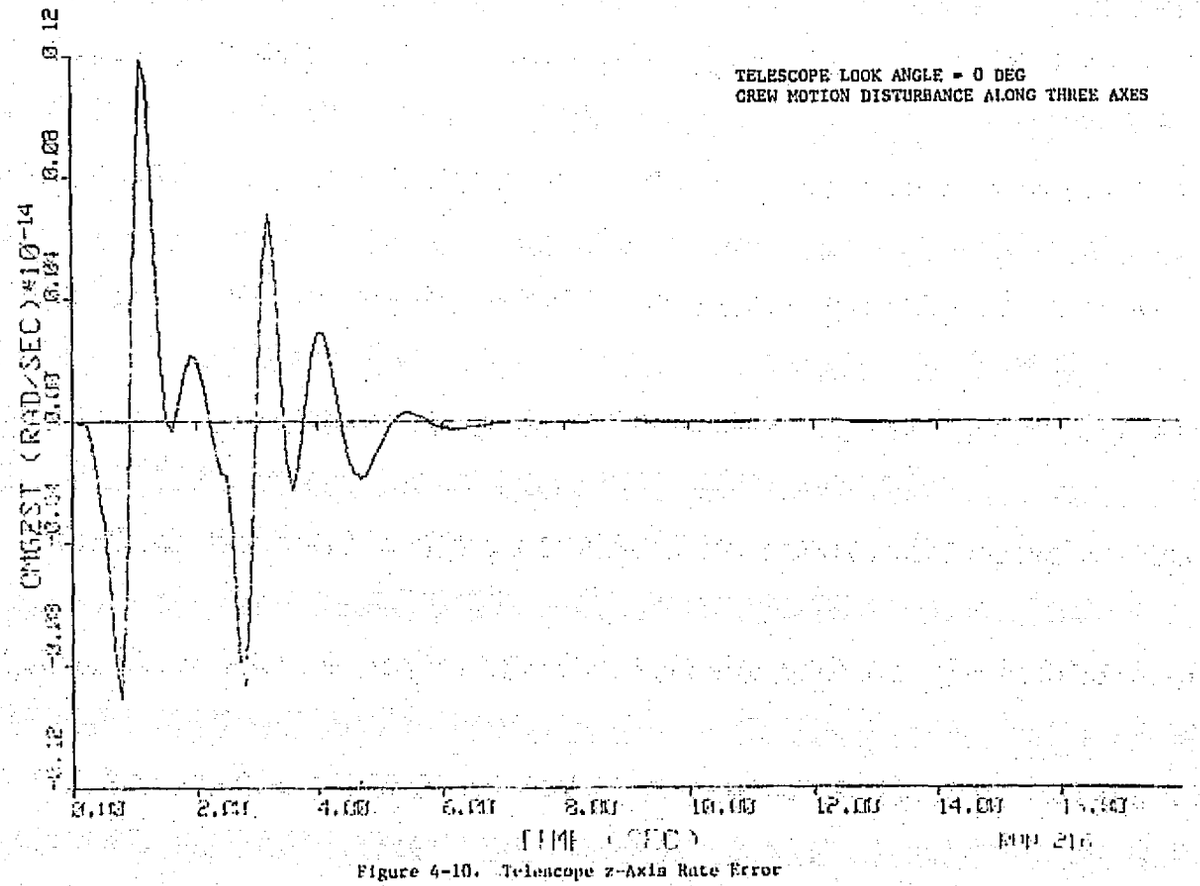

Figure 4-10. Telescope z-Axis Rate Error

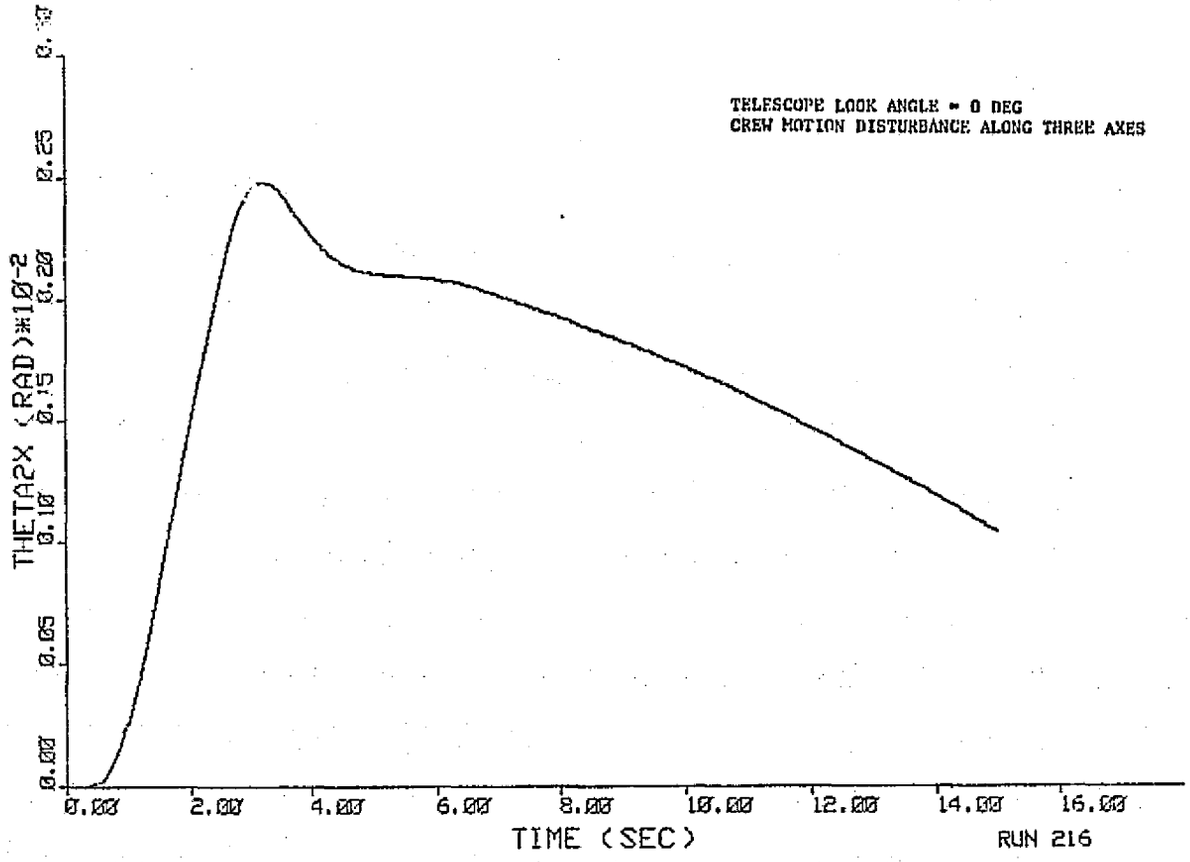

Figure 4-11. Pedestal x-Axis Angular Rotation

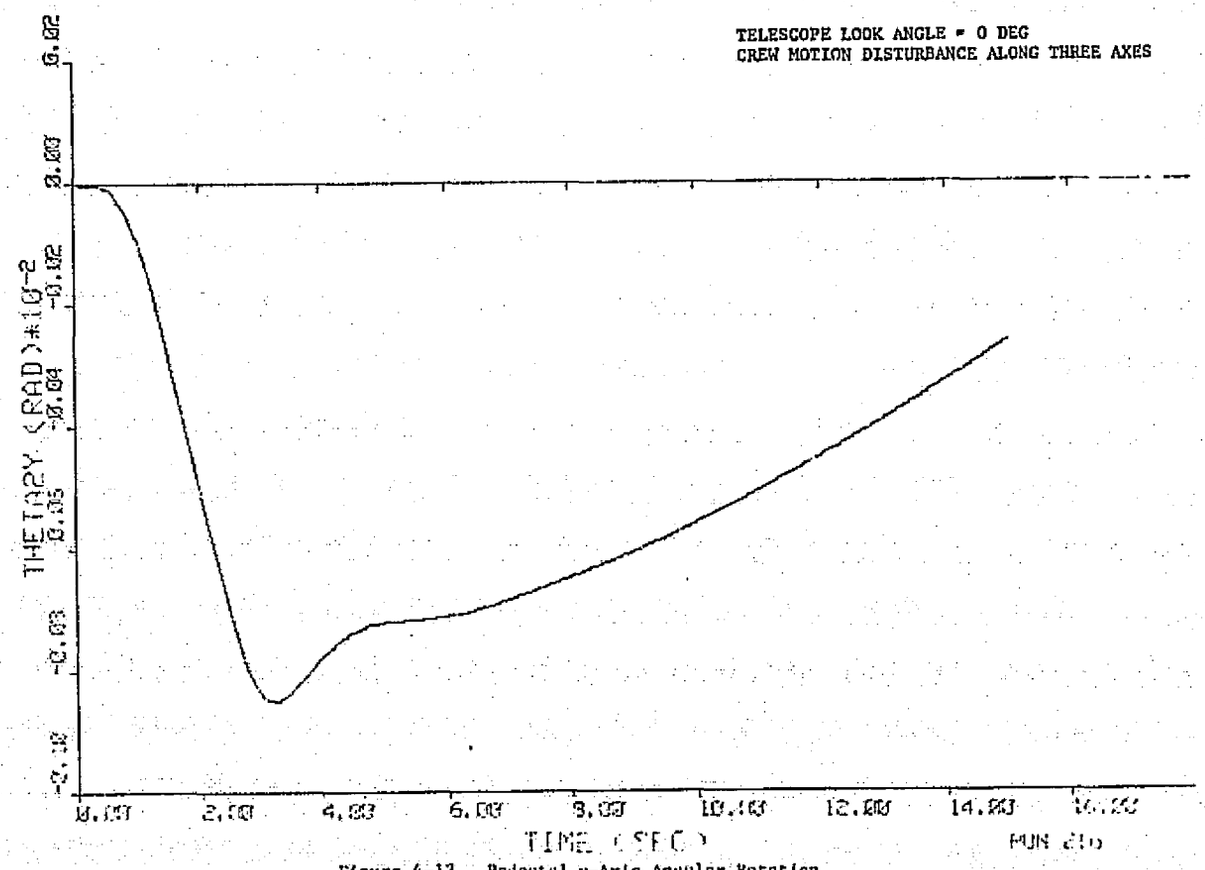

Figure 4-12. Pedestal y-Axis Angular Rotation

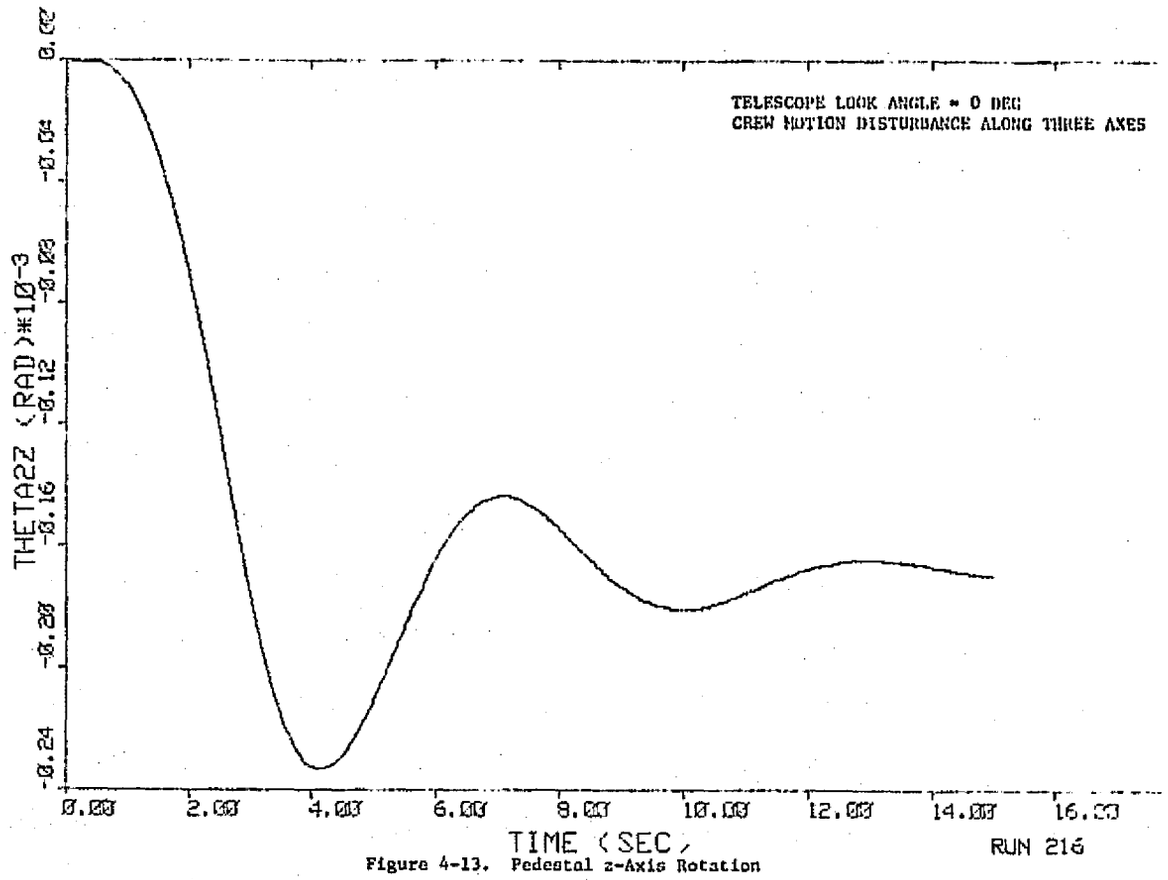

Figure 4-13. Pedestal z-Axis Rotation

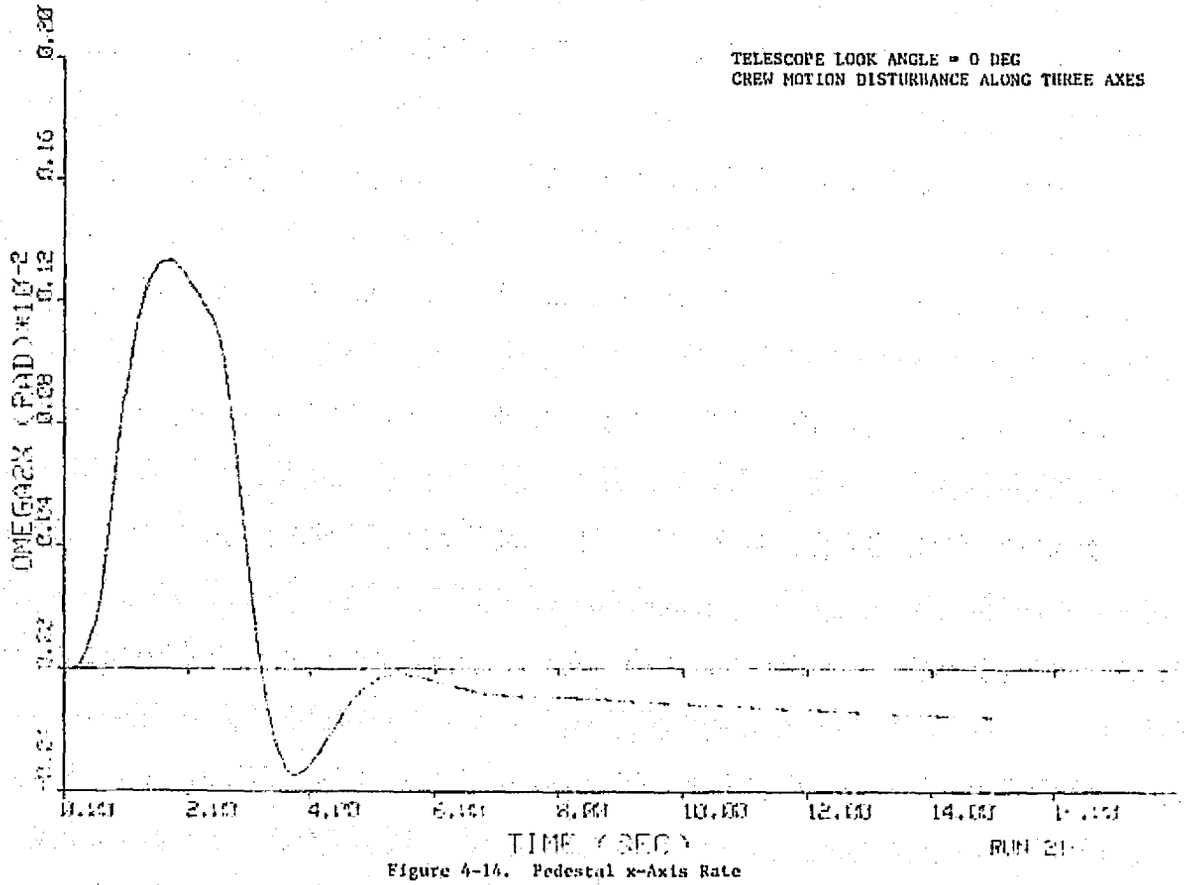

Figure 4-14. Pedestal x-Axis Rate

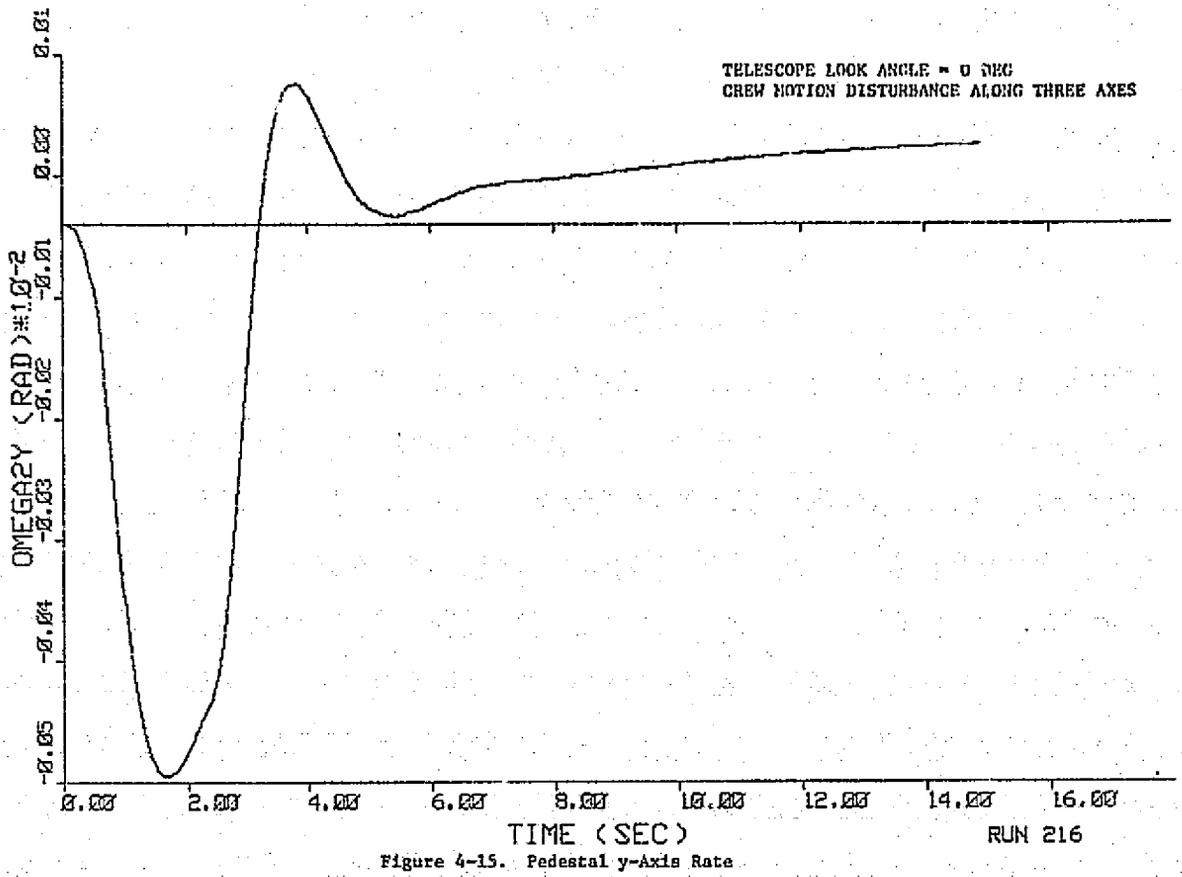

Figure 4-15. Pedestal y-Axis Rate

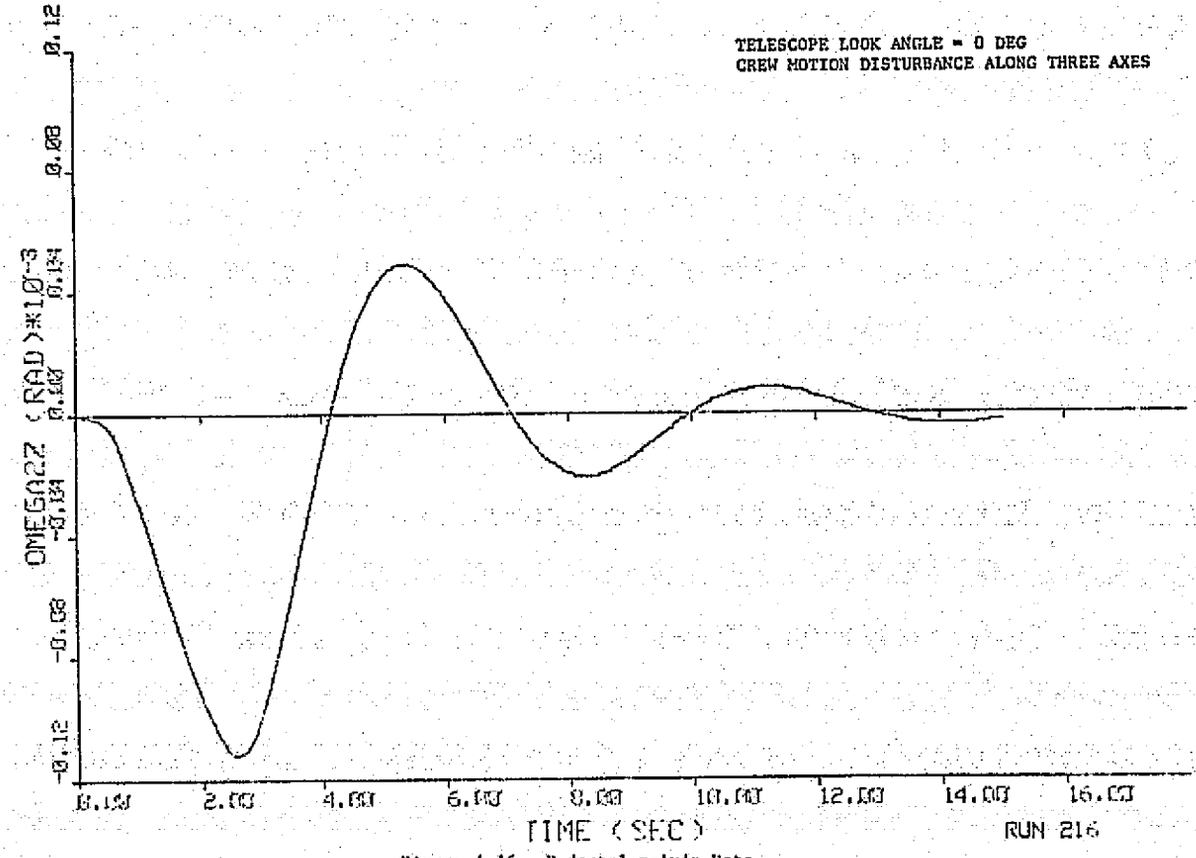

Figure 4-16. Pedestal z-Axis Rate

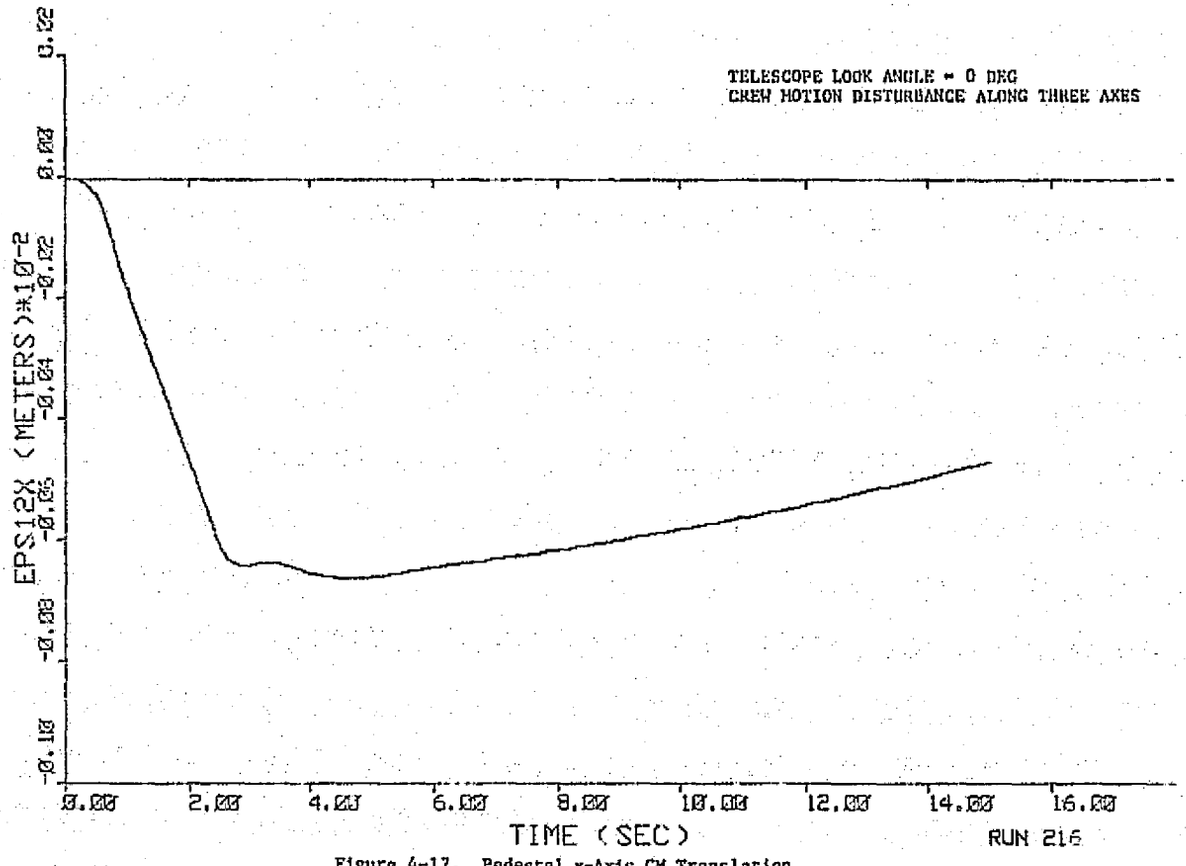

Figure 4-17. Pedestal x-Axis CM Translation

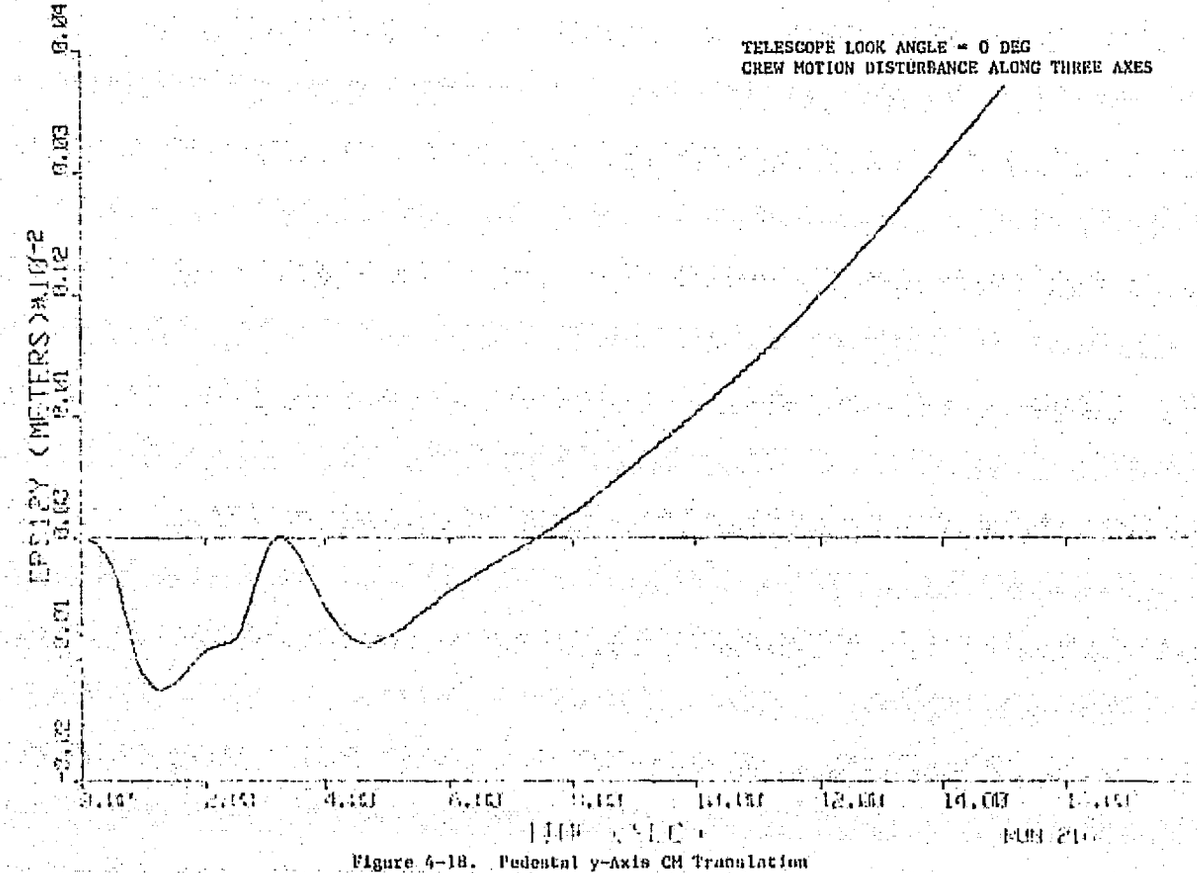

Figure 4-18. Pedestal y-Axis CM Translation

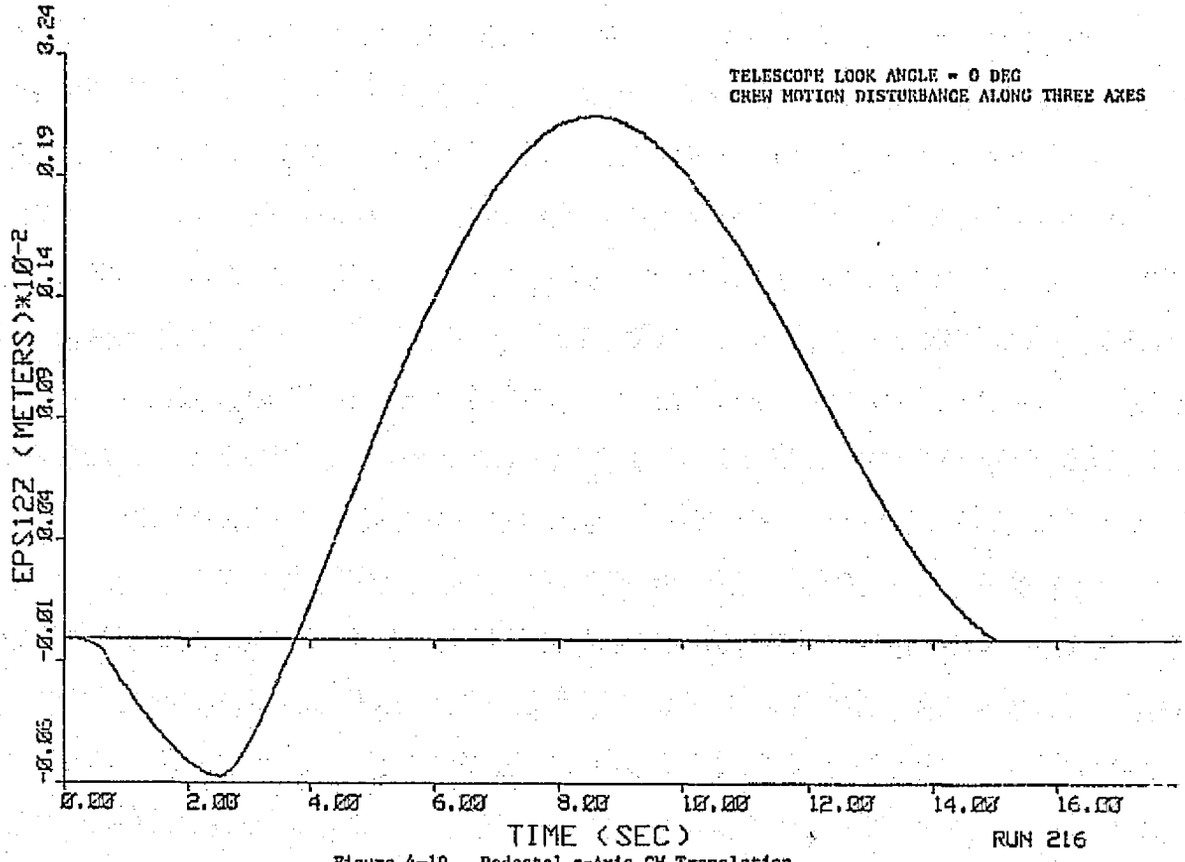

Figure 4-19. Pedestal z-Axis CM Translation

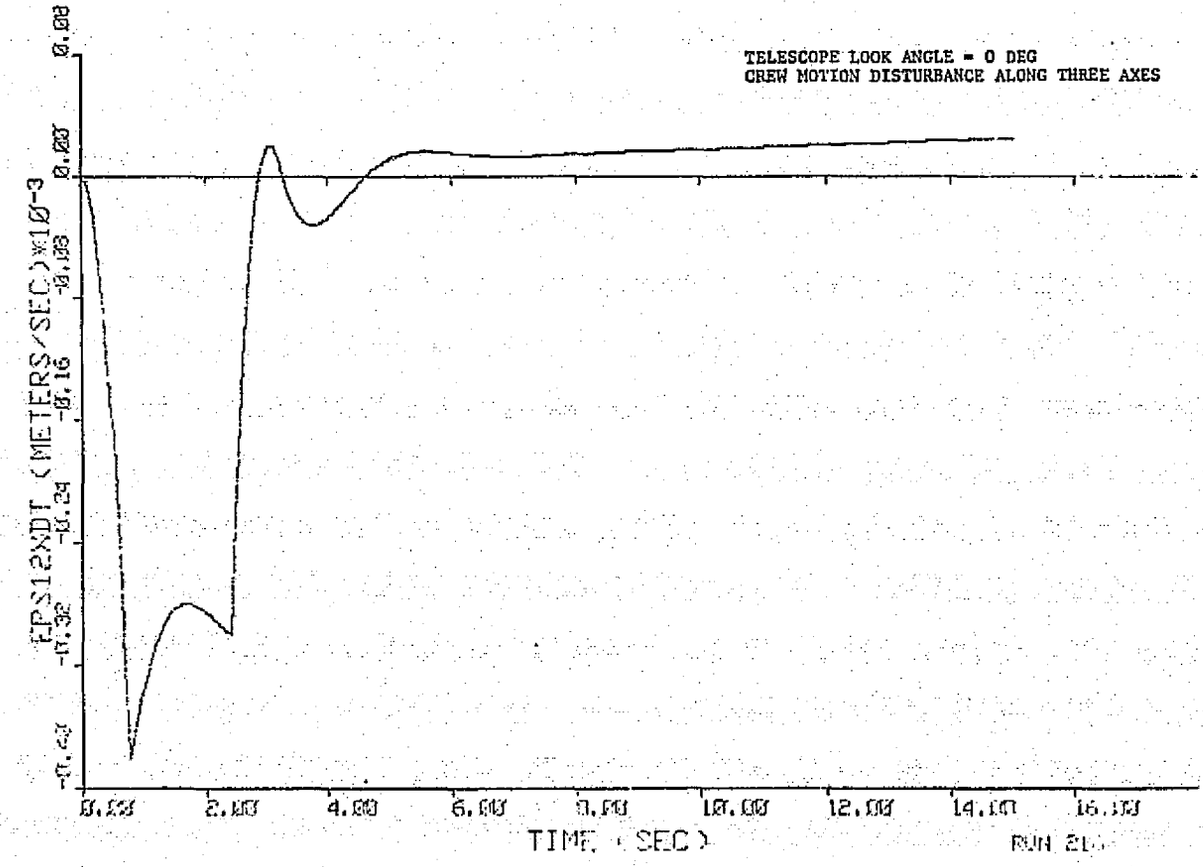

Figure 4-20. Pedestal x-Axis CM Velocity

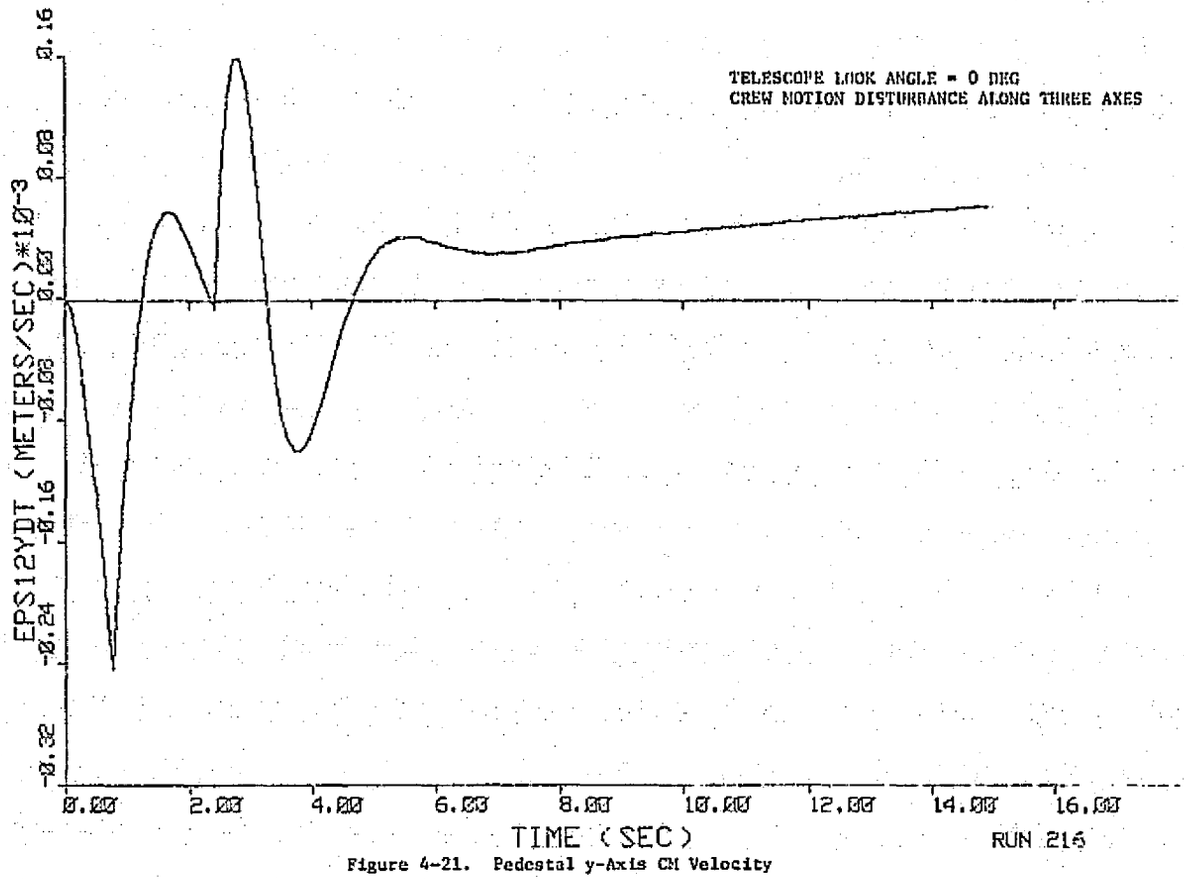

Figure 4-21. Pedestal y-Axis CM Velocity

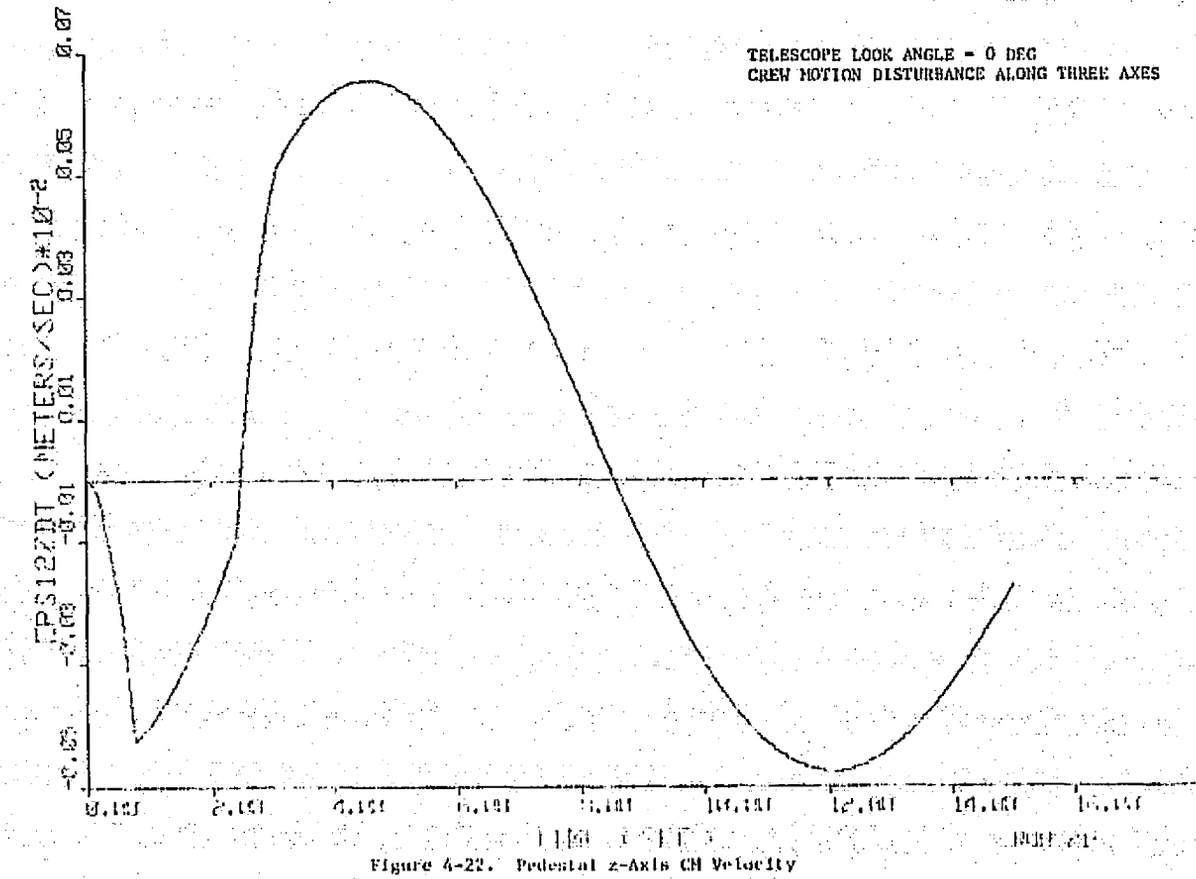

Figure 4-22. Pedestal z-Axis CM Velocity

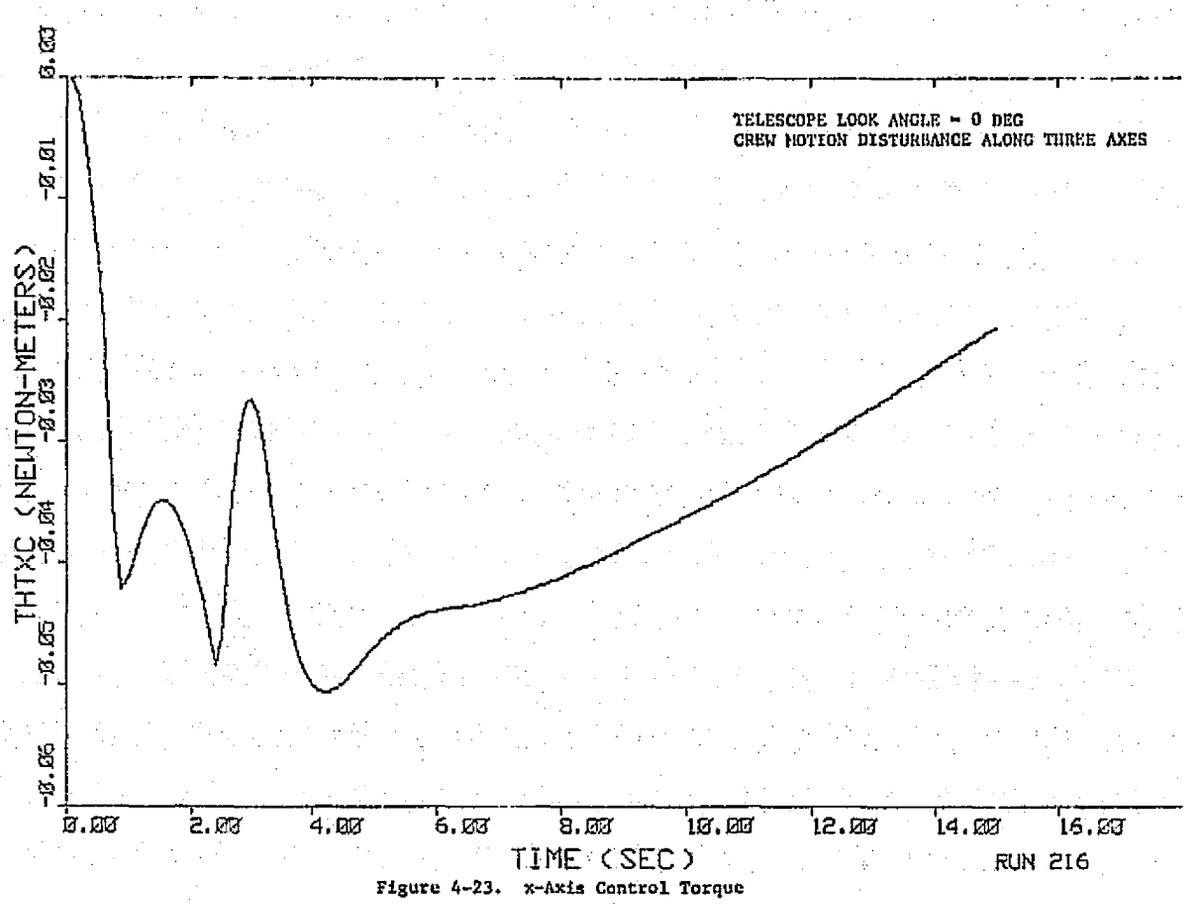

Figure 4-23. x-Axis Control Torque

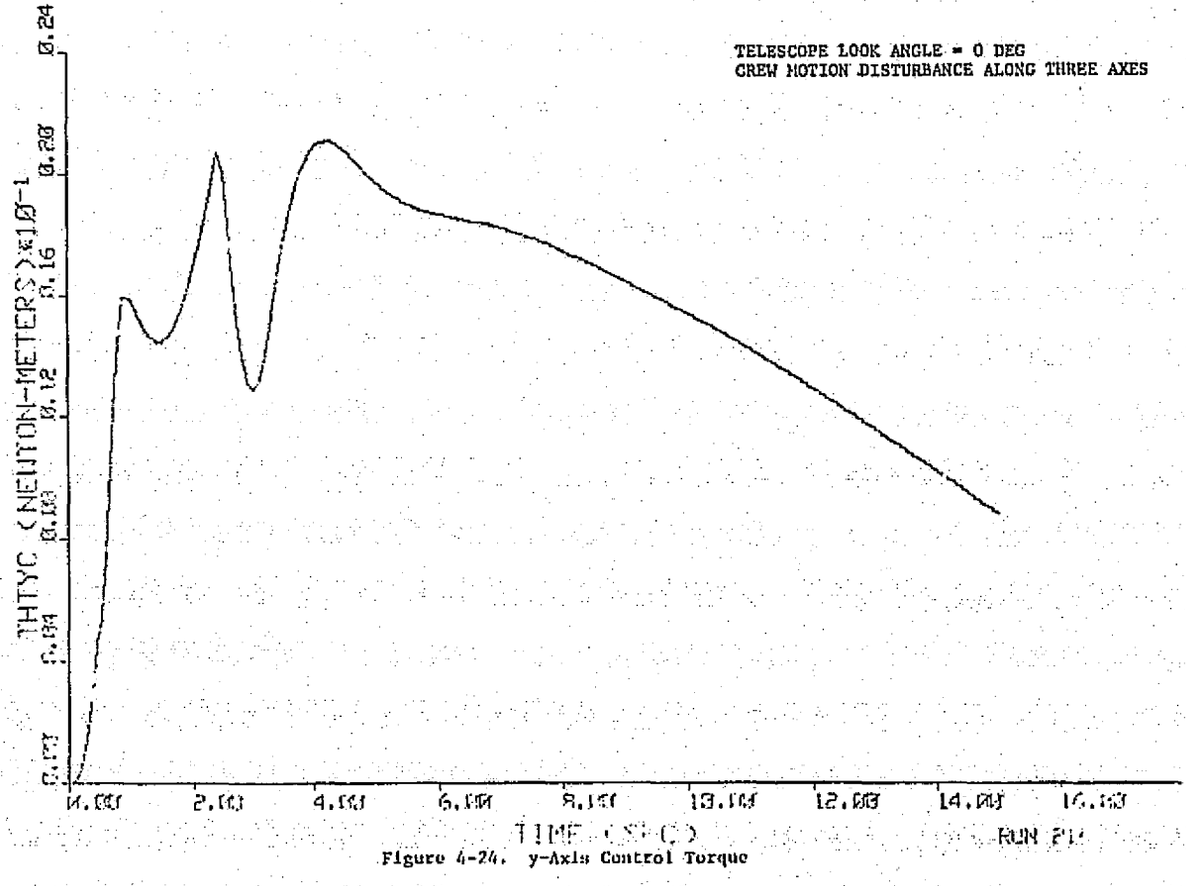

Figure 4-24. y-Axis Control Torque

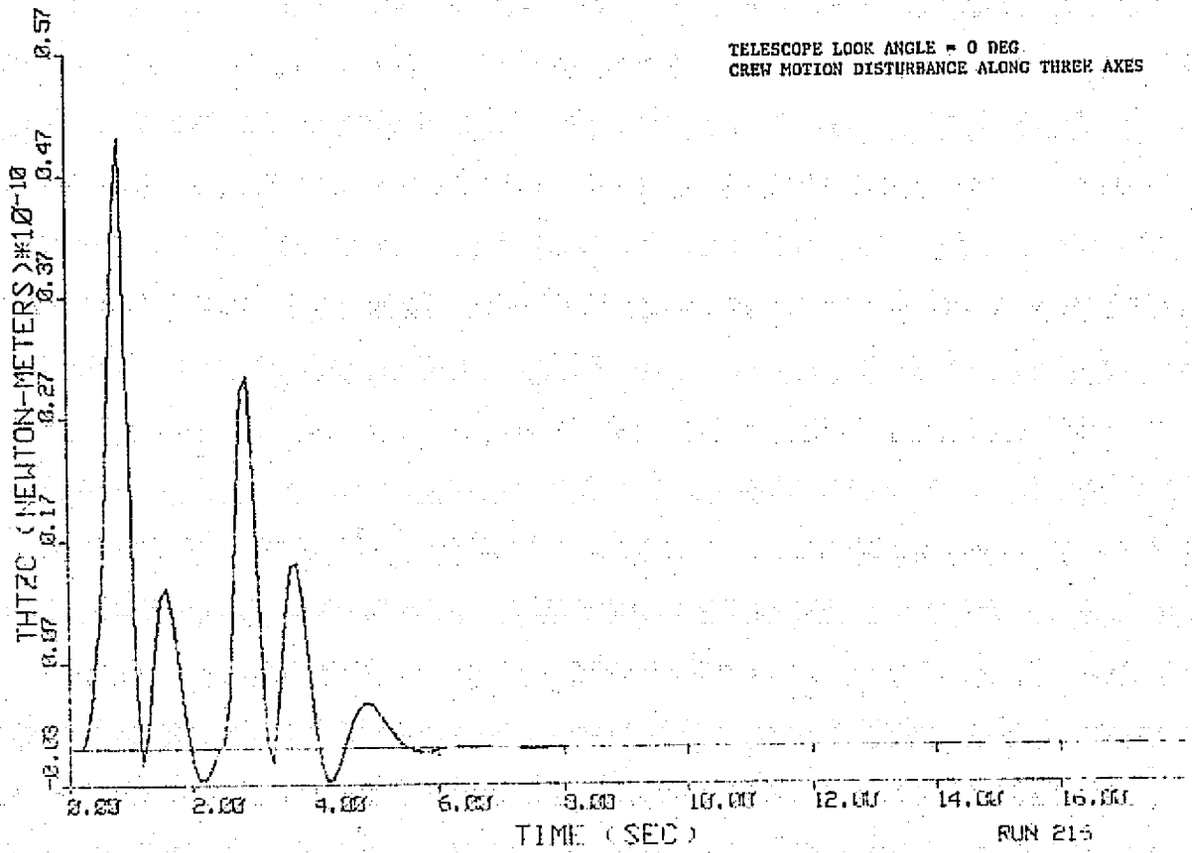

Figure 4-25. z-Axis Control Torque

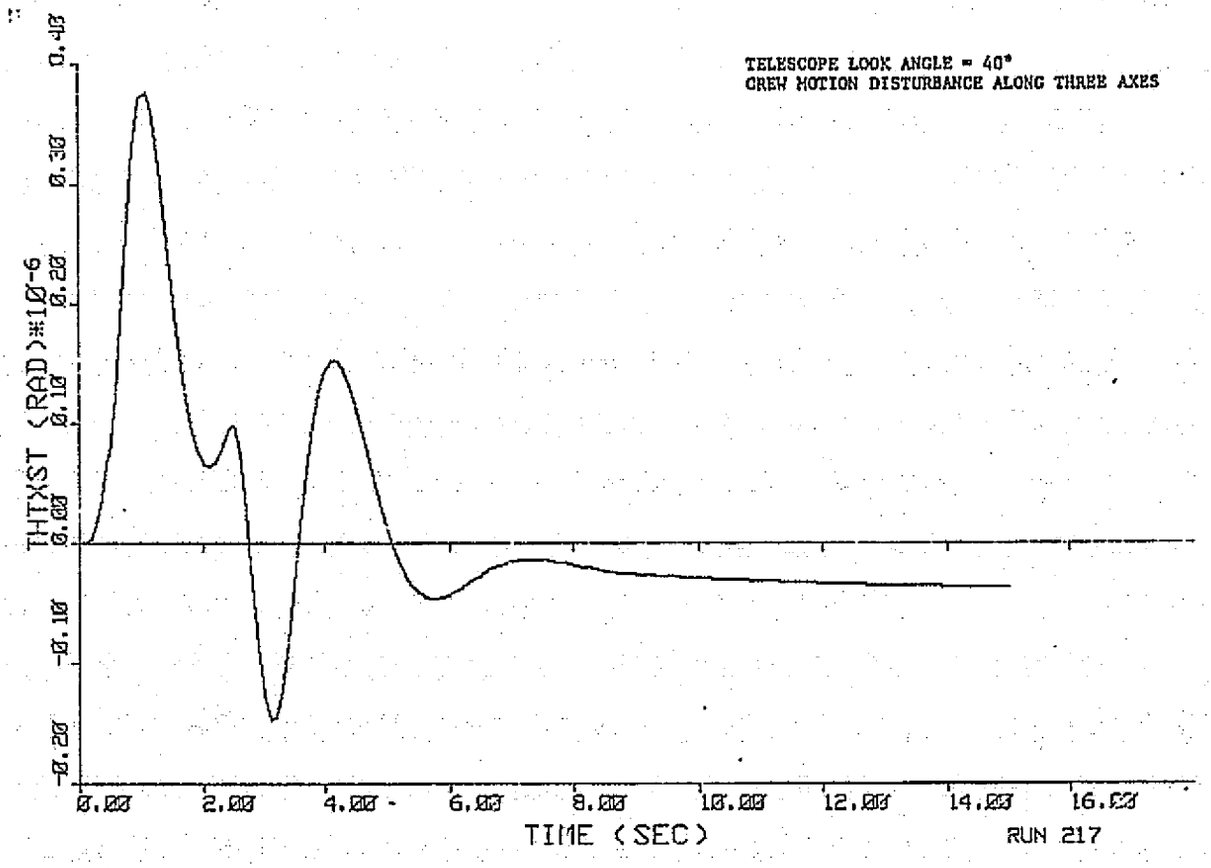

Figure 4-26. Telescope x-Axis Pointing Error

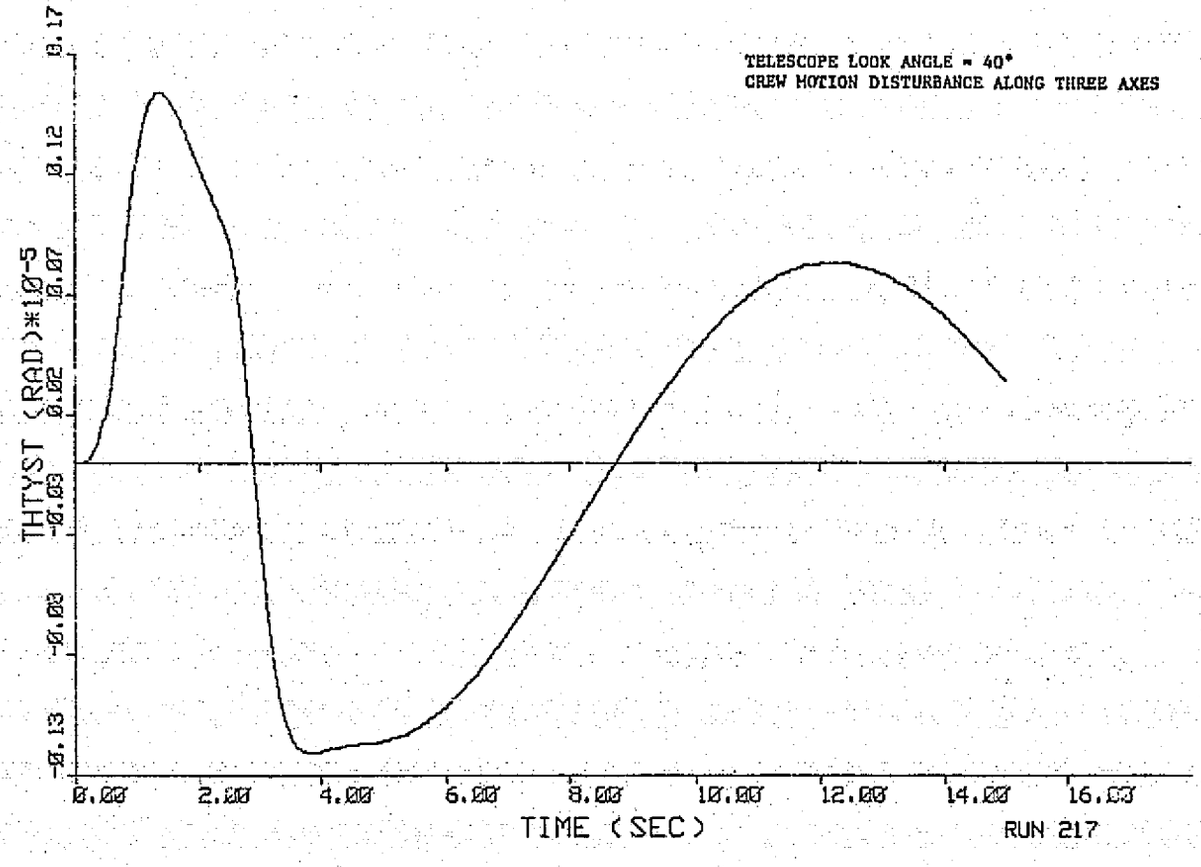

Figure 4-27. Telescope y-Axis Pointing Error

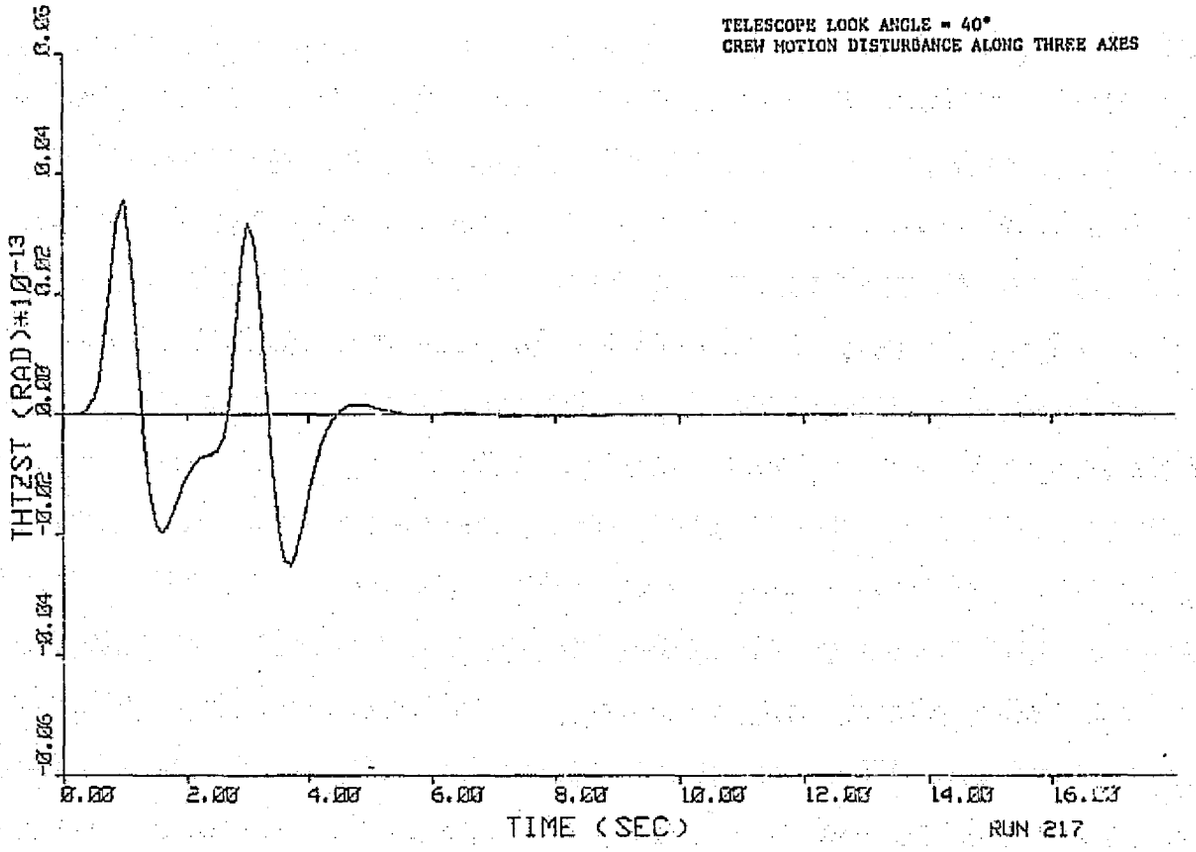

Figure 4-28. Telescope z-Axis Pointing Error

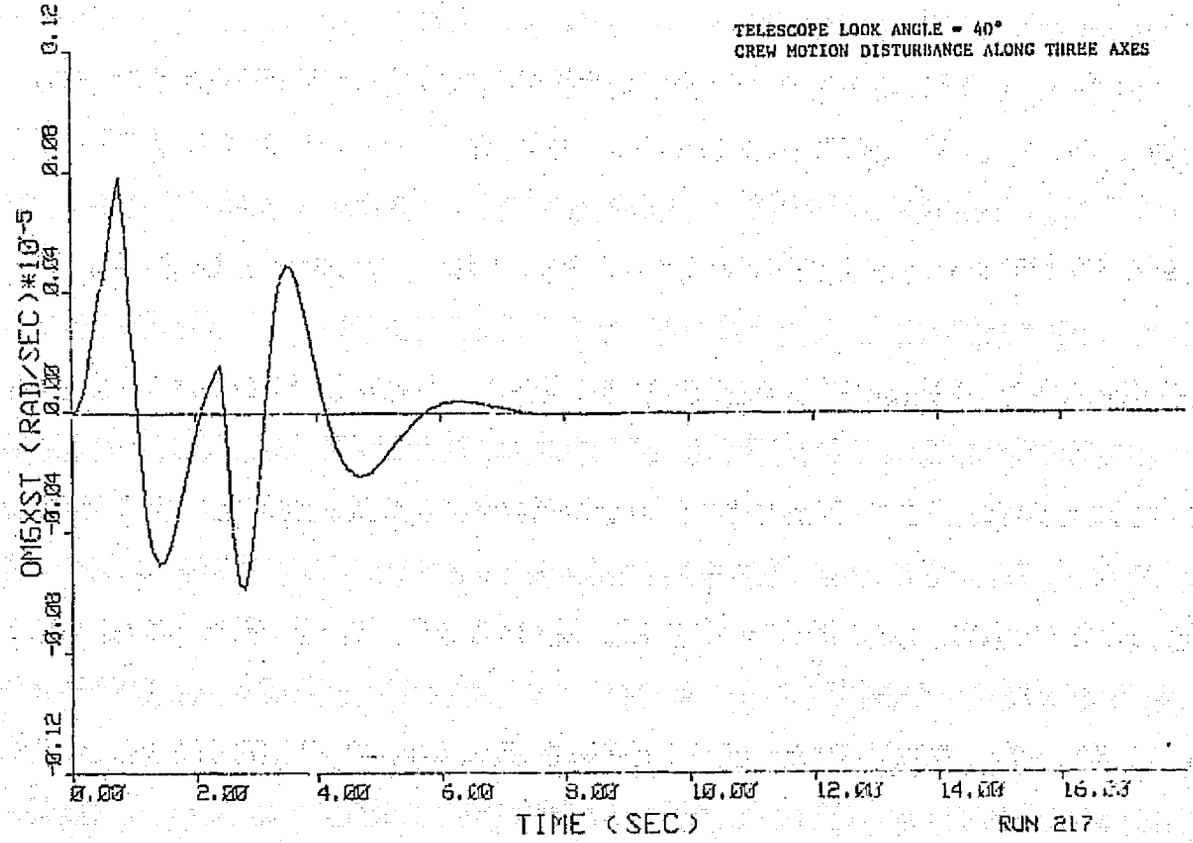

Figure 4-29. Telescope x-Axis Rate Error

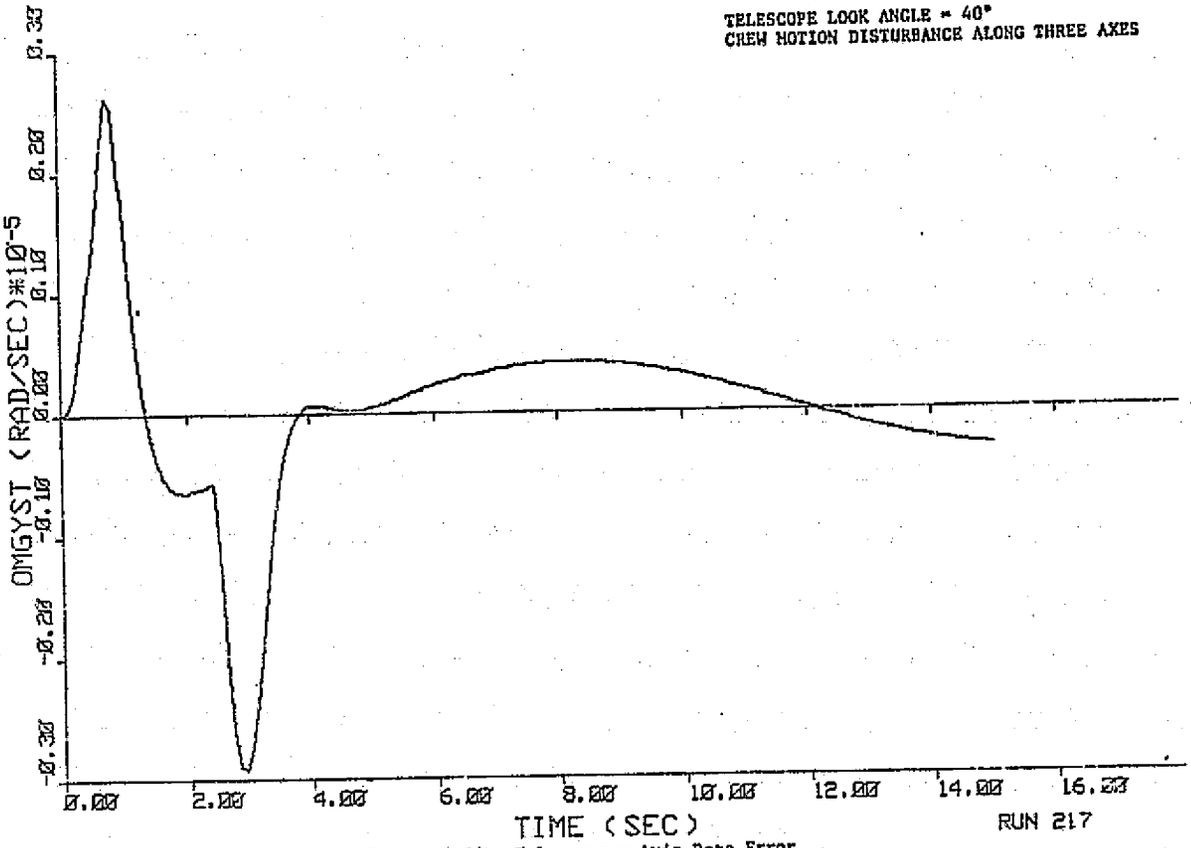

Figure 4-30. Telescope y-Axis Rate Error

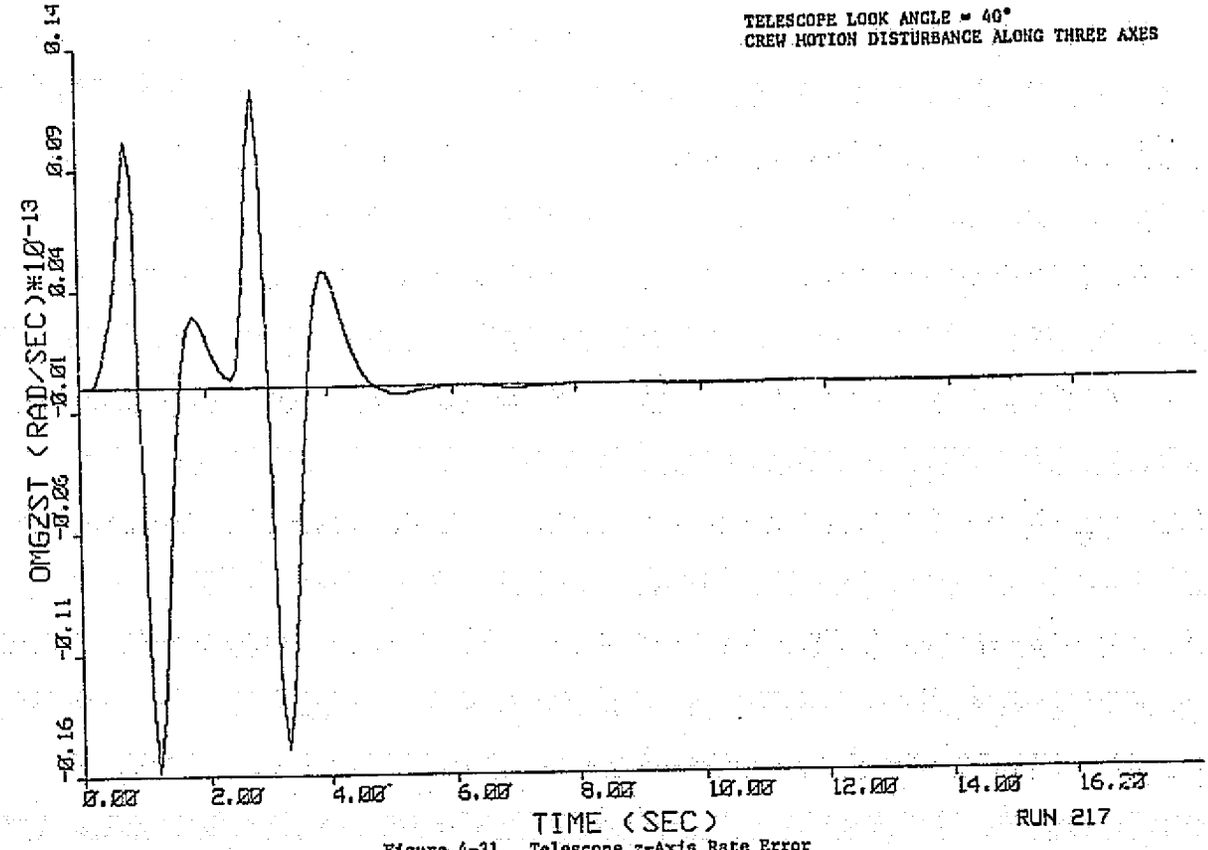

Figure 4-31. Telescope z-Axis Rate Error

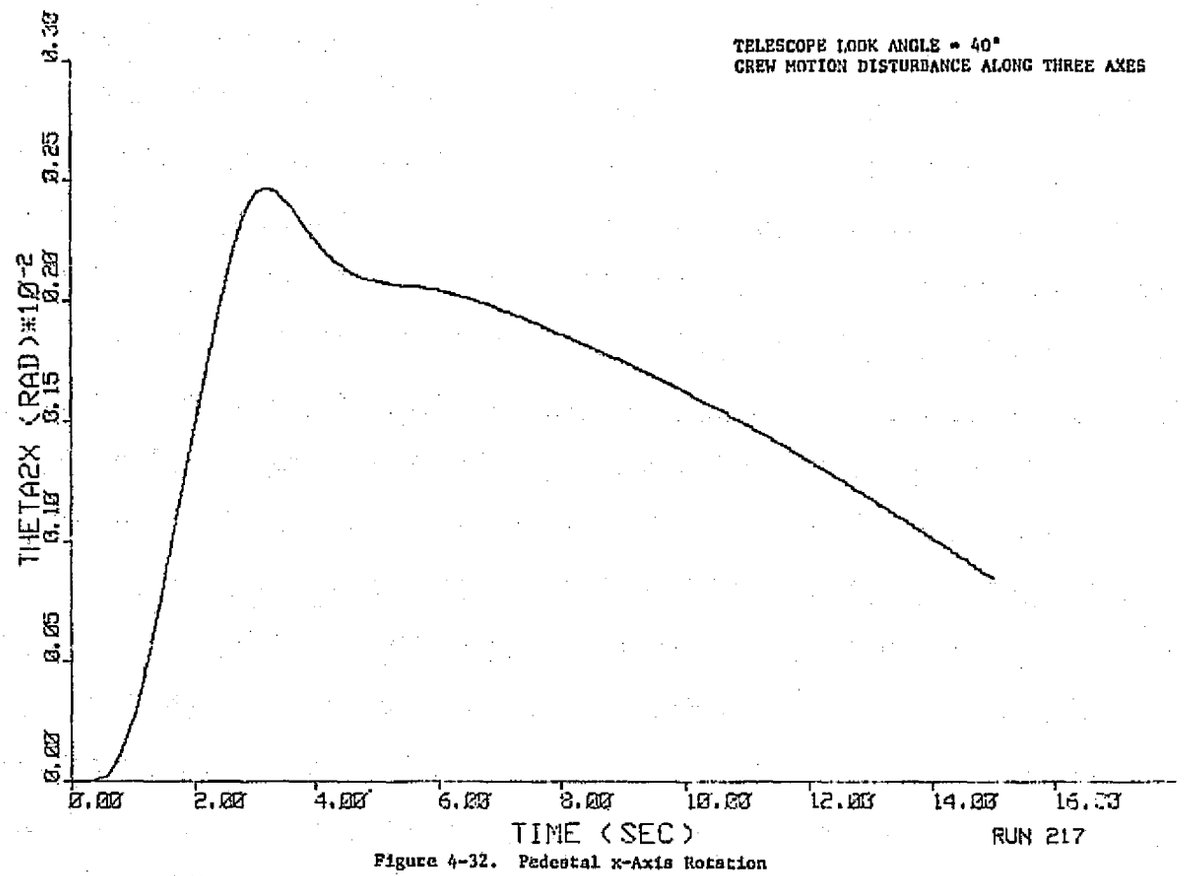

Figure 4-32. Pedestal x-Axis Rotation

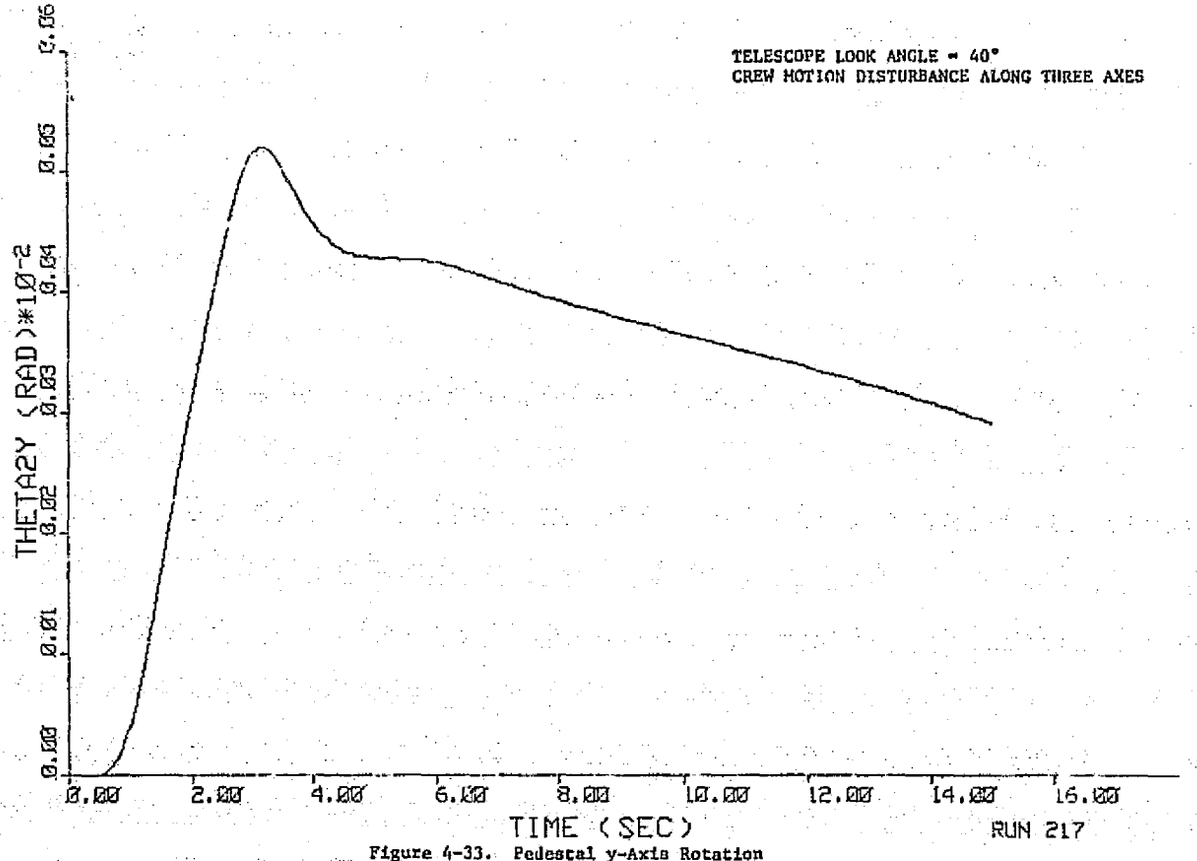

Figure 4-33. Pedestal y-Axis Rotation

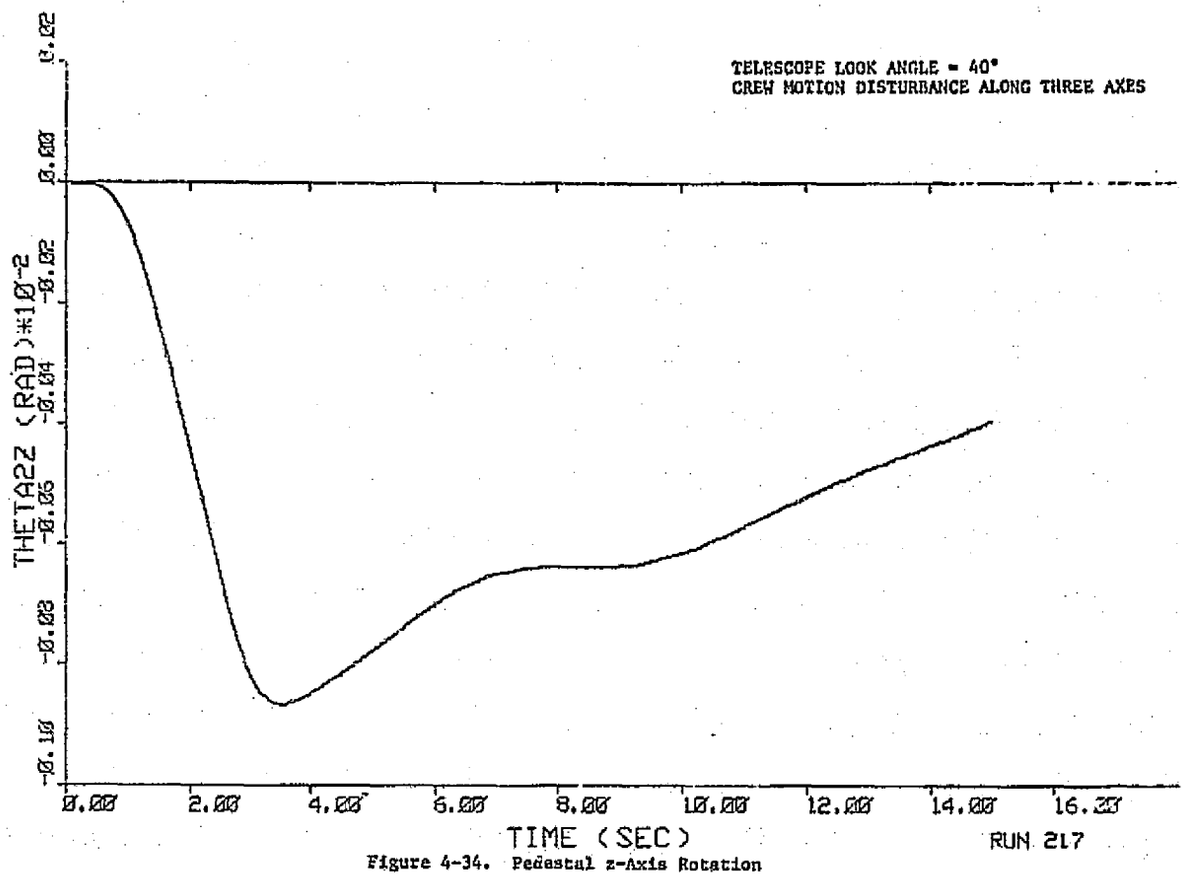

Figure 4-34. Pedestal z-Axis Rotation

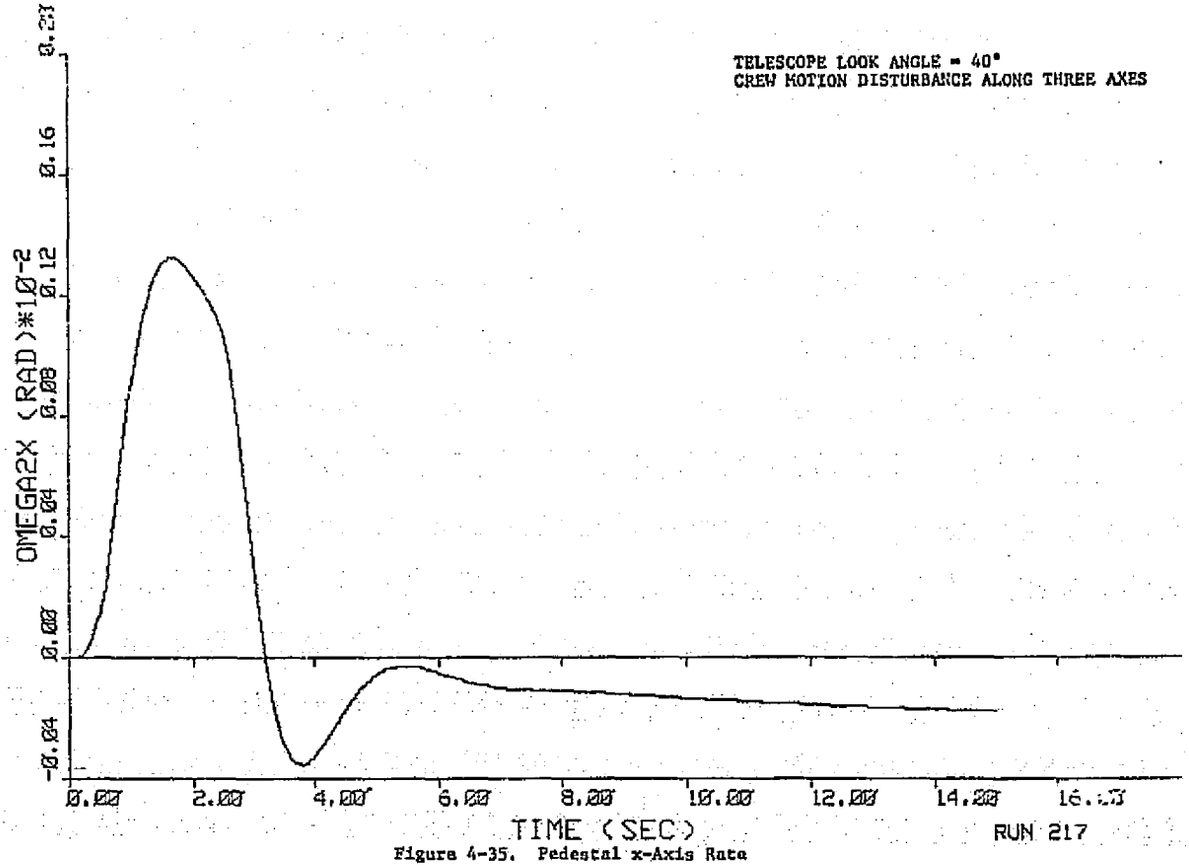

Figure 4-35. Pedestal x-Axis Rate

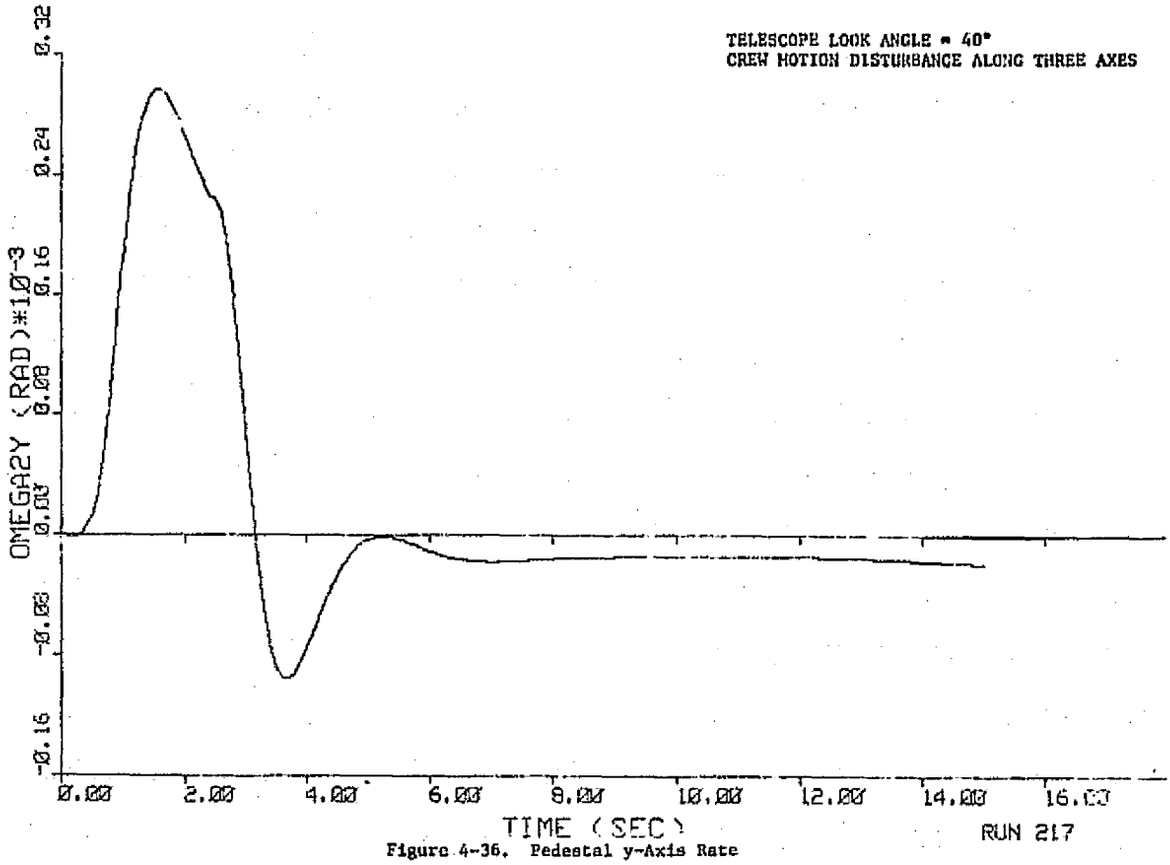

Figure 4-36. Pedestal y-Axis Rate

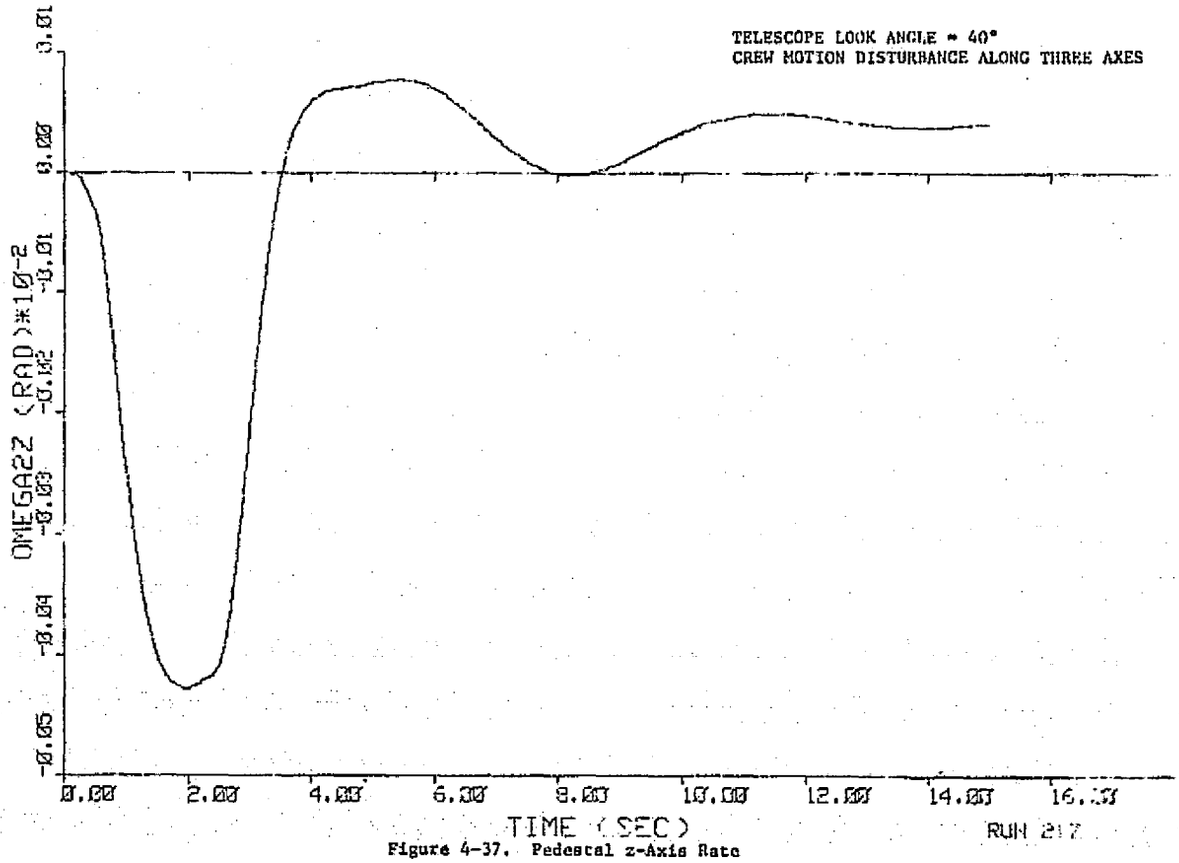

Figure 4-37. Pedestal z-Axis Rate

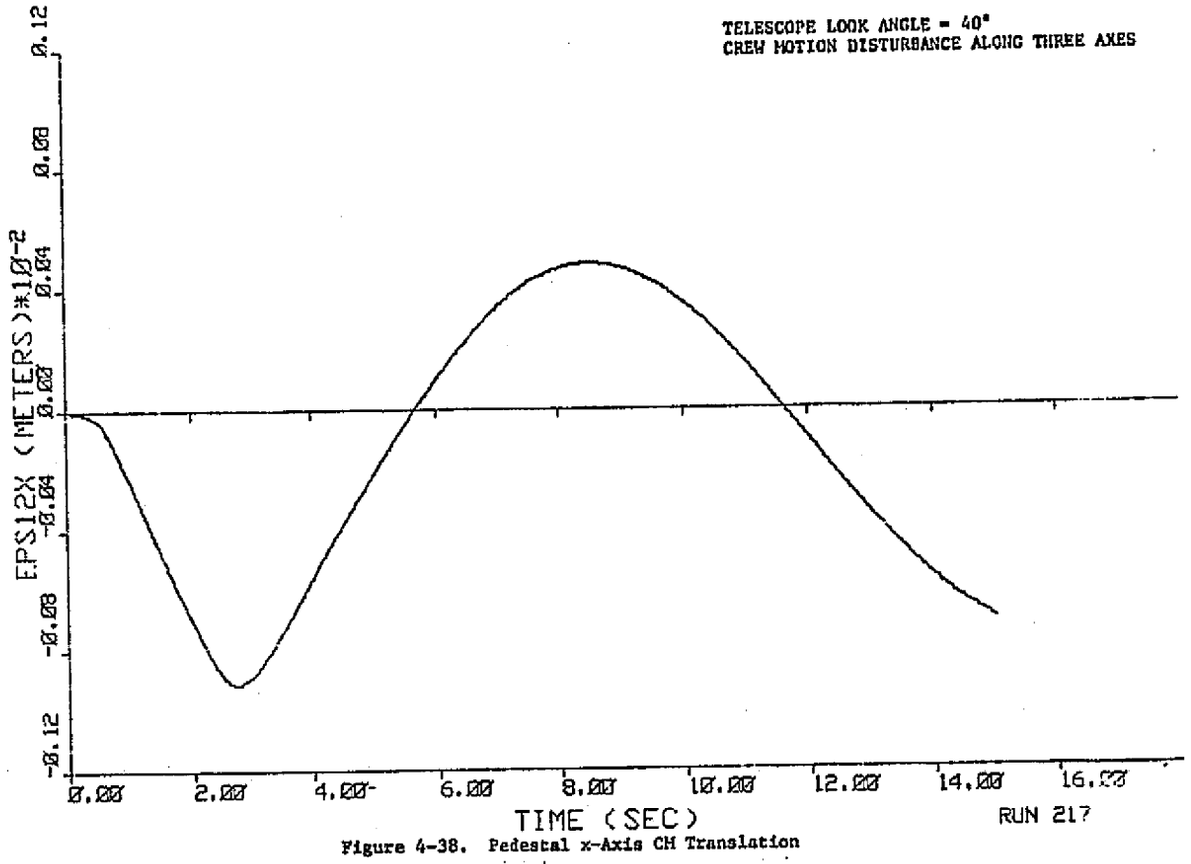

Figure 4-38. Pedestal x-Axis CM Translation

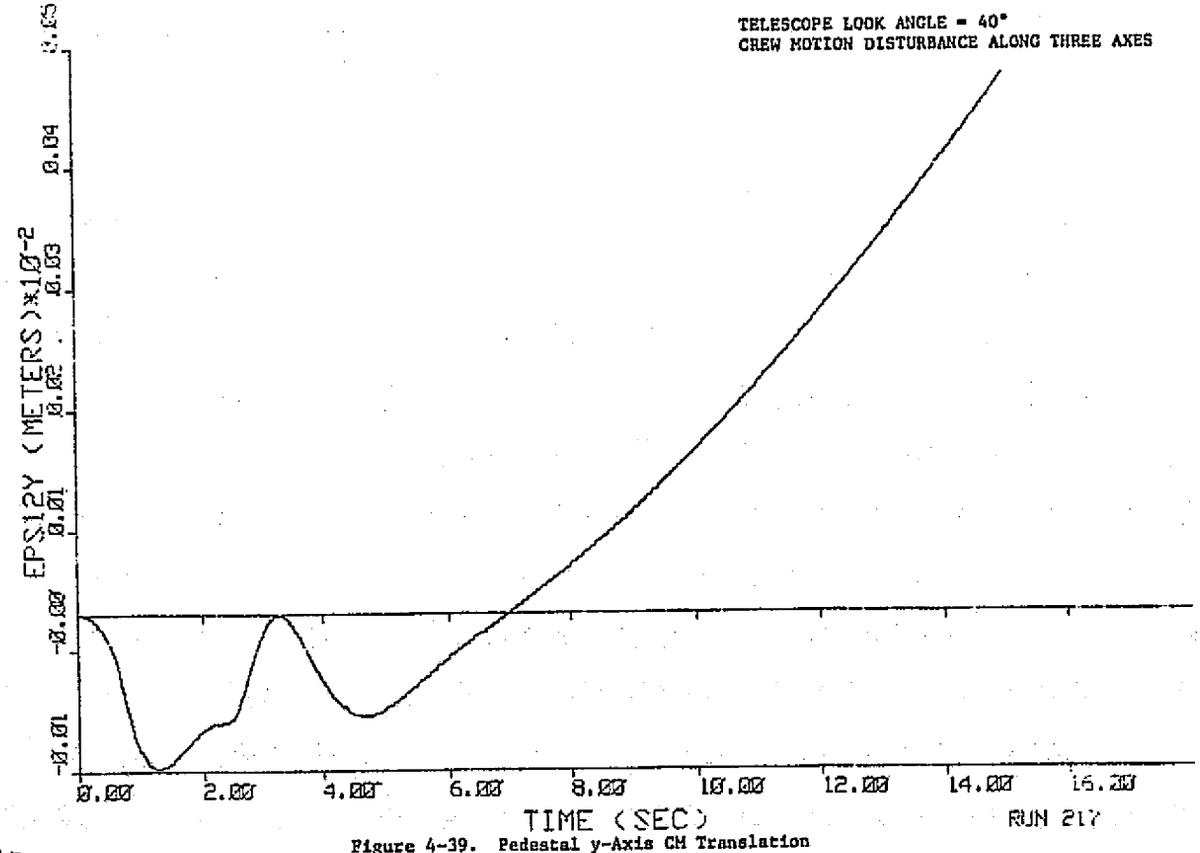

Figure 4-39. Pedestal y-Axis CM Translation

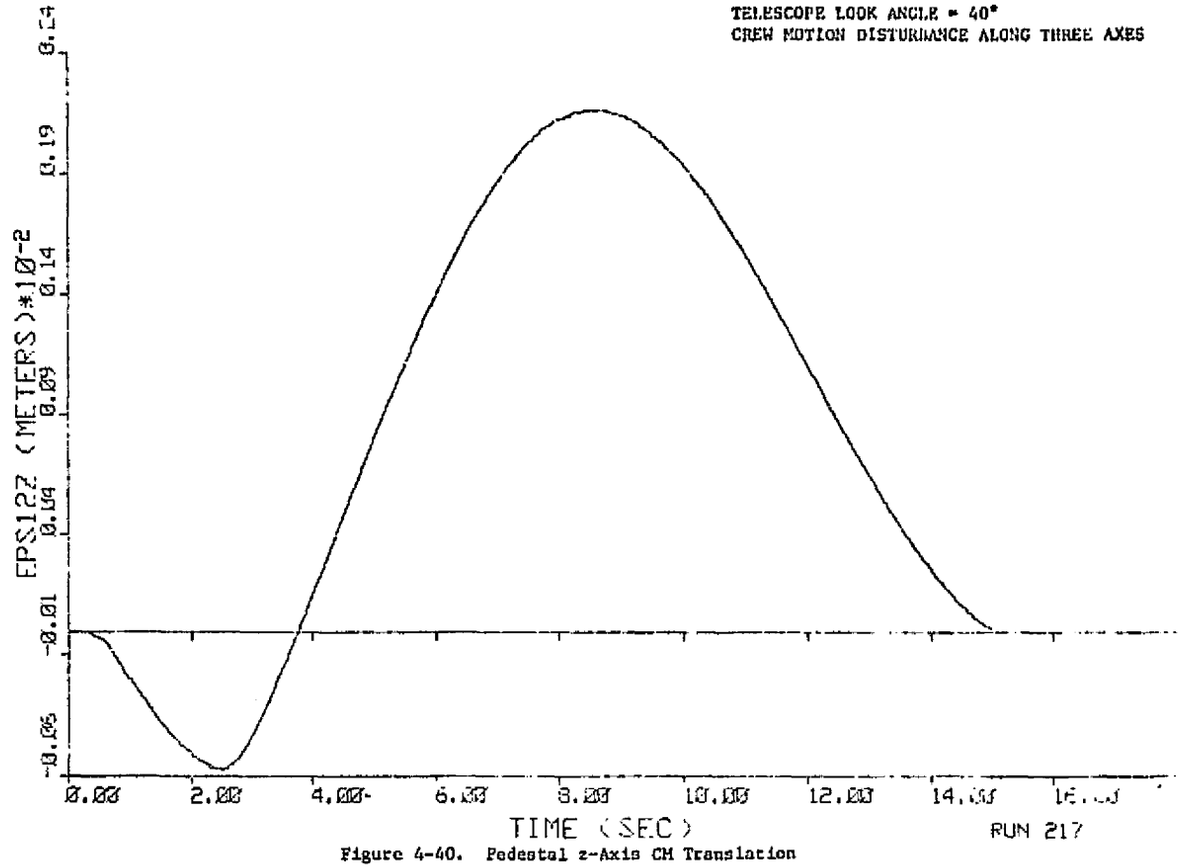

Figure 4-40. Pedestal z-Axis CM Translation

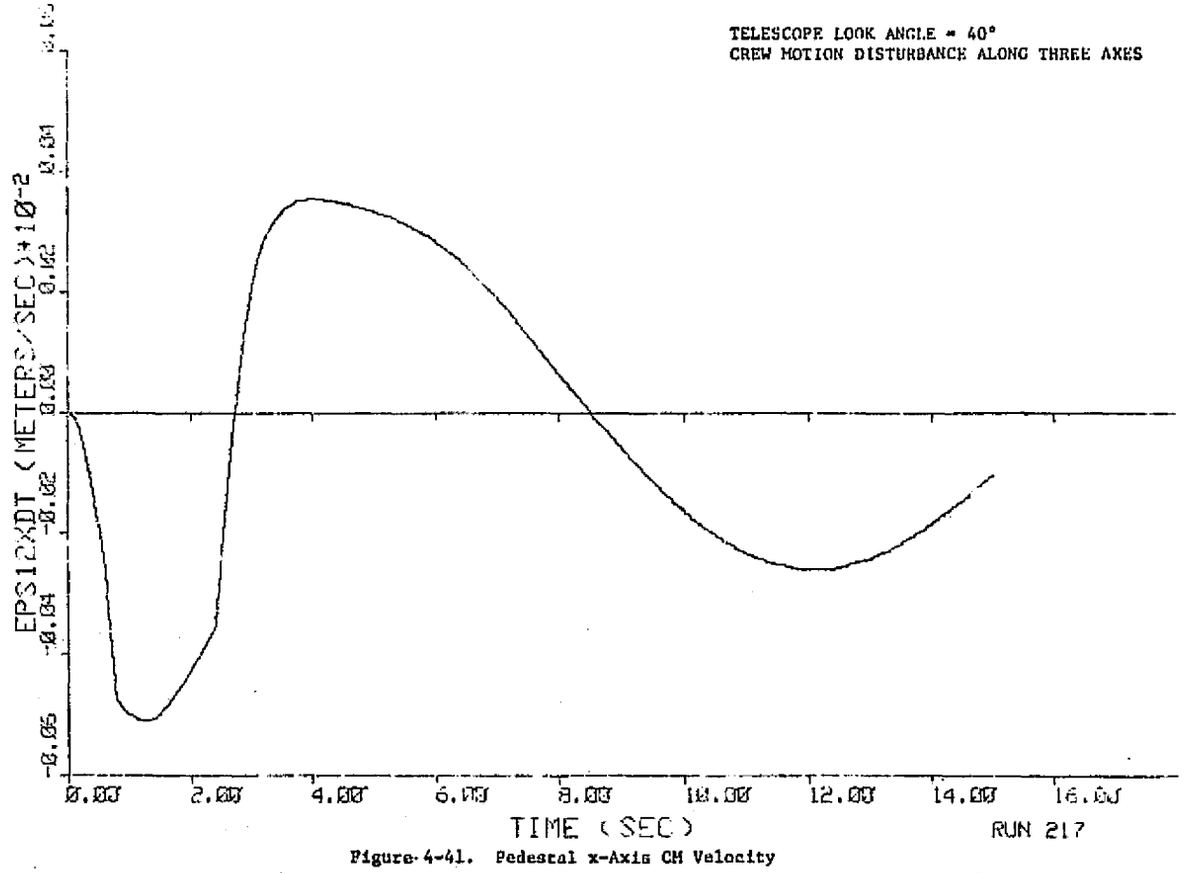

Figure 4-41. Pedestal x-Axis CM Velocity

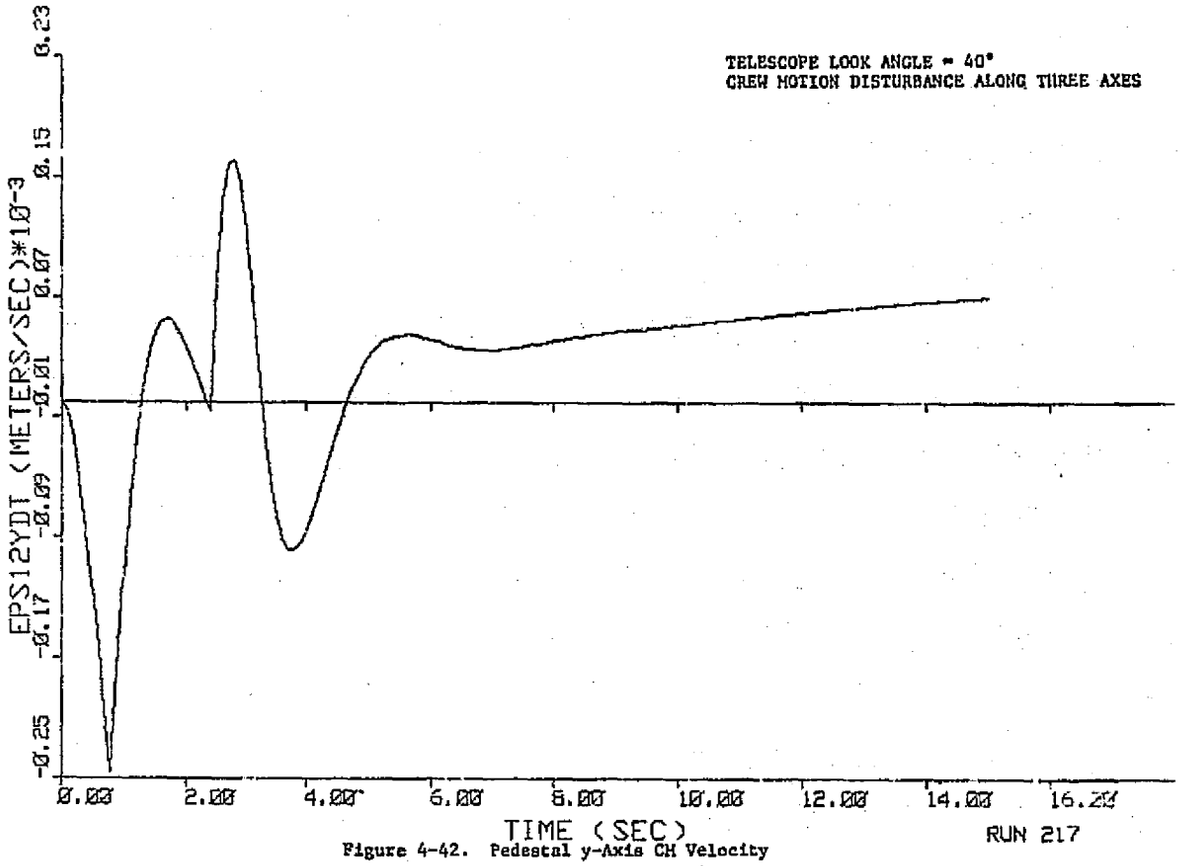

Figure 4-42. Pedestal y-Axis CH Velocity

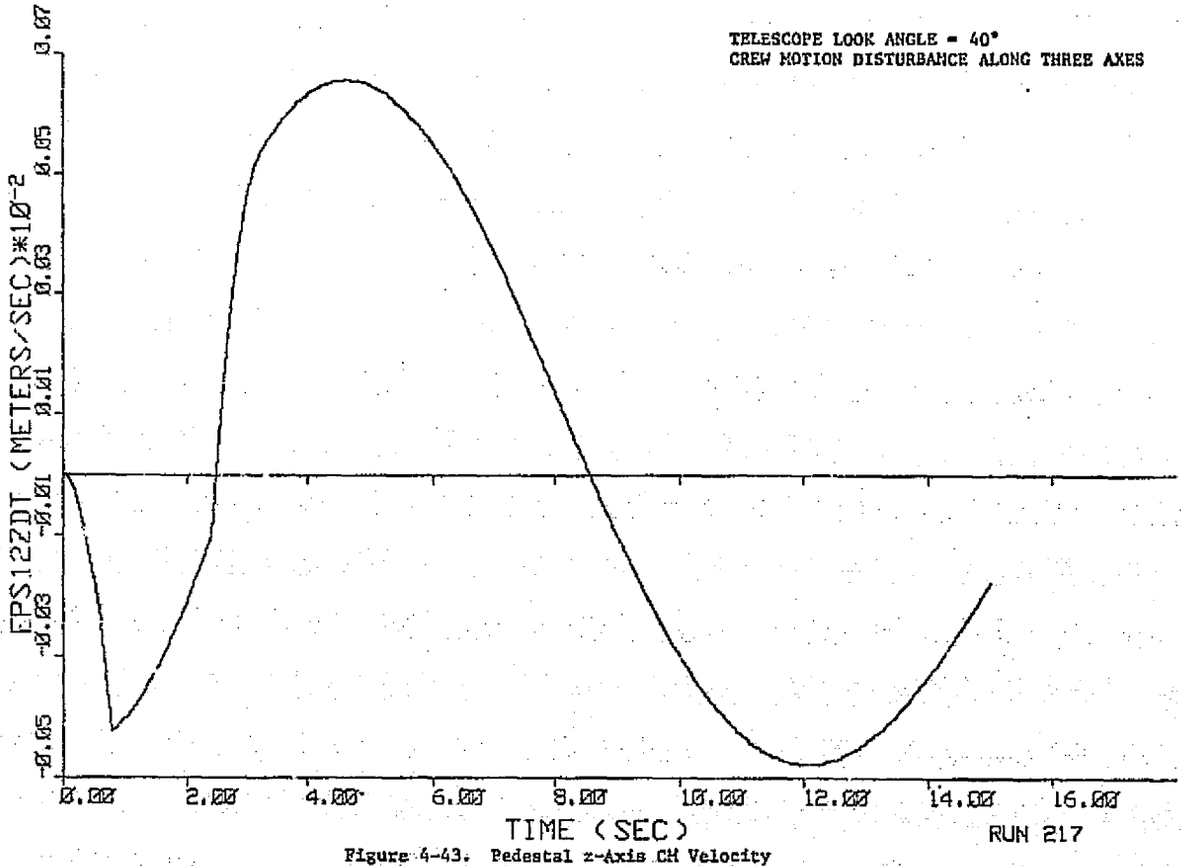

Figure 4-43. Pedestal z-Axis CH Velocity

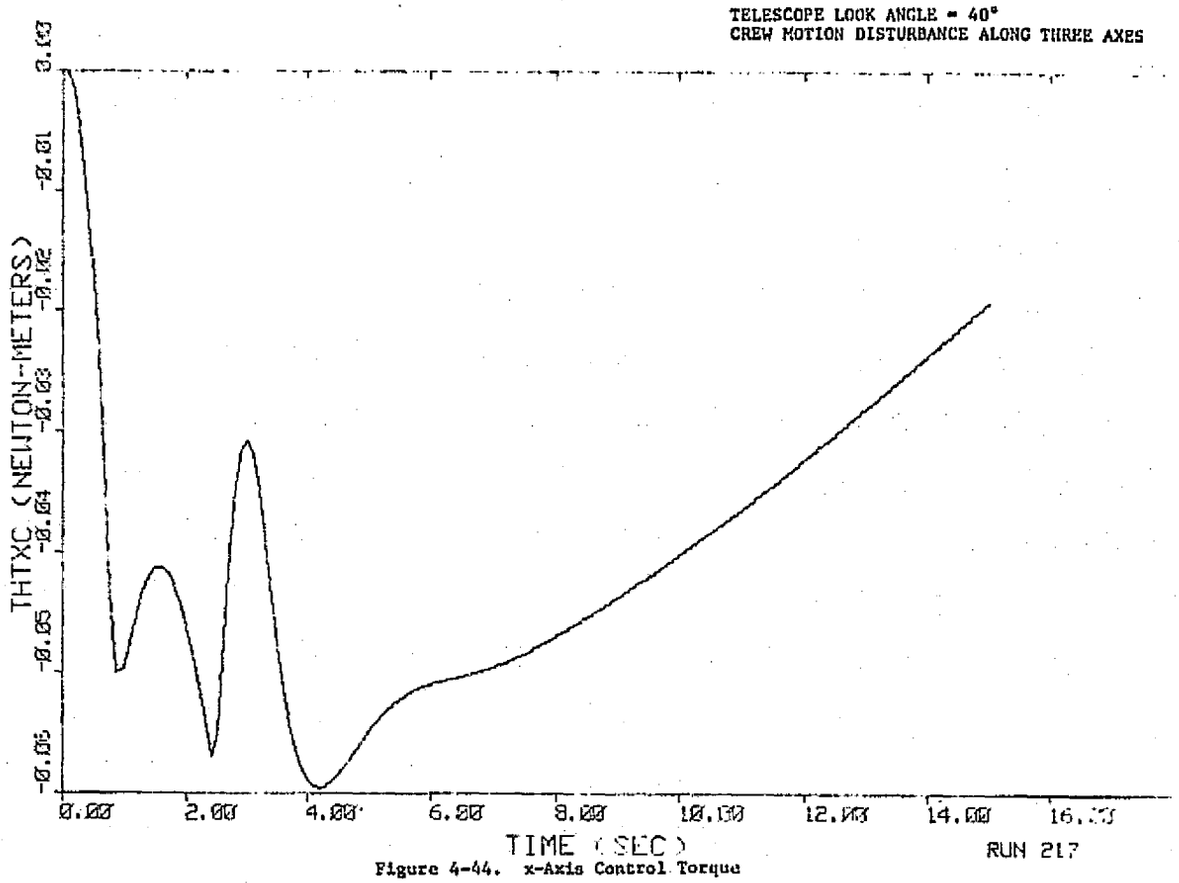

Figure 4-44. x-Axis Control Torque

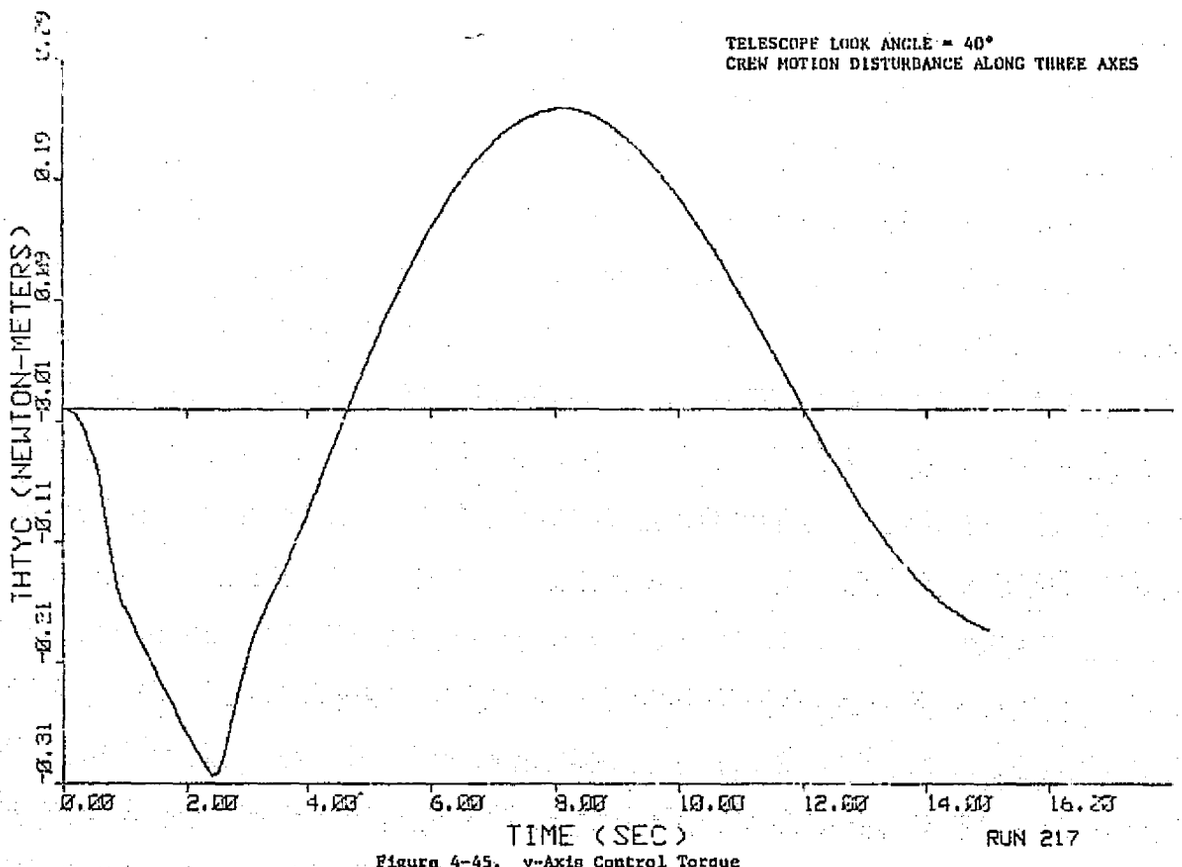

Figure 4-45. y-Axis Control Torque

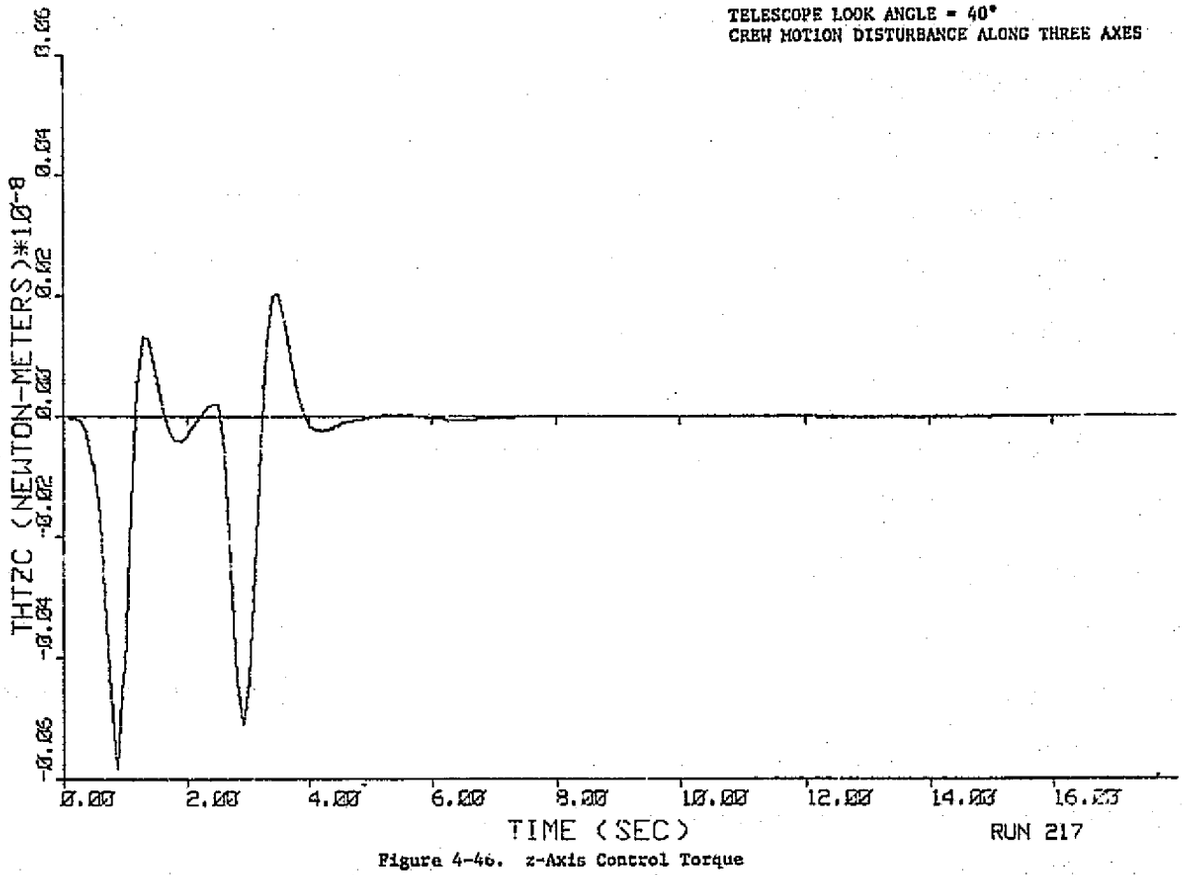

Figure 4-46. z-Axis Control Torque

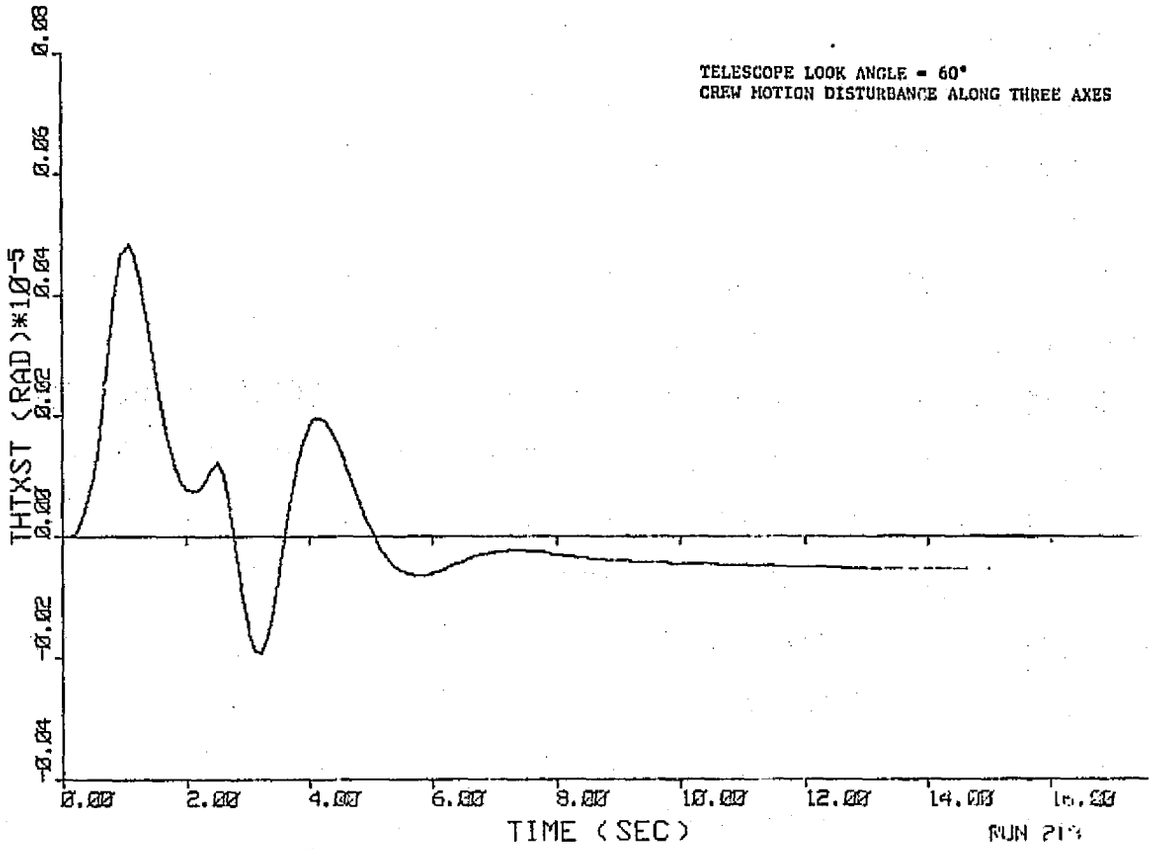

Figure 4-47. Telescope x-Axis Pointing Error

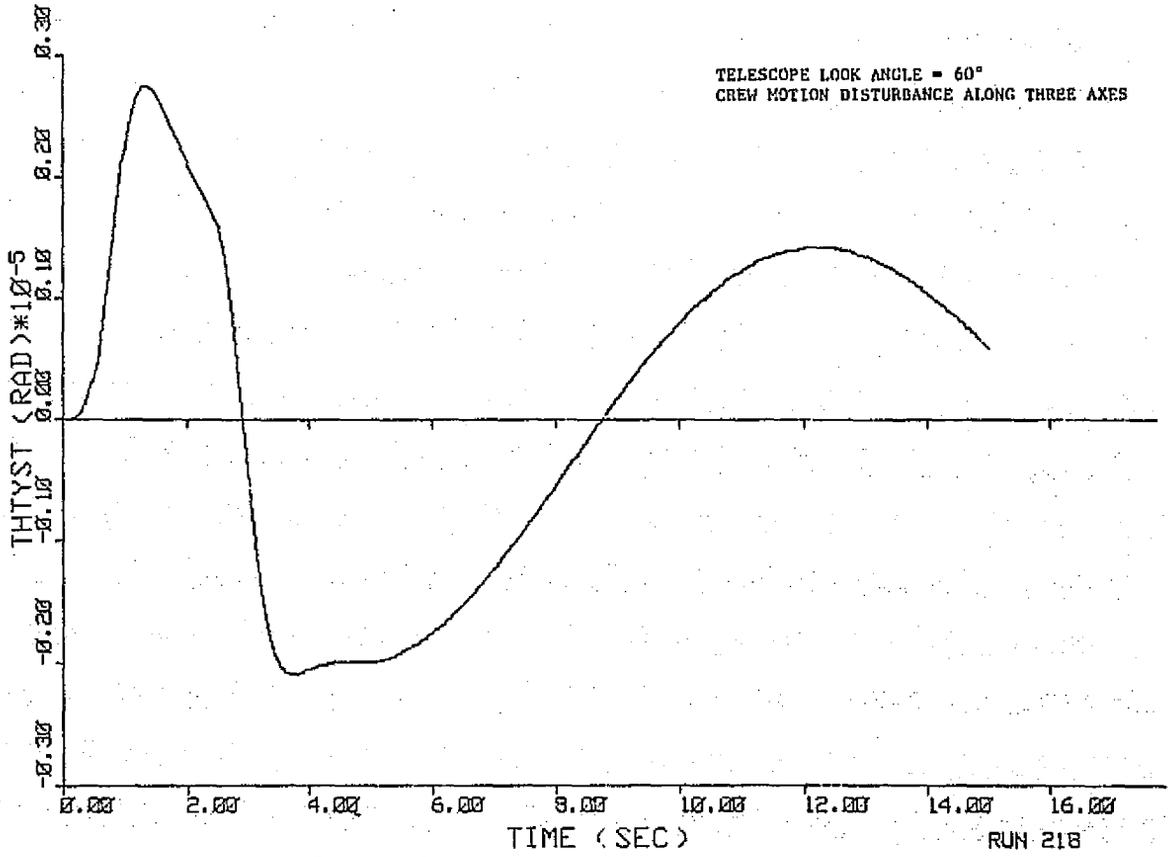

Figure 4-48. Telescope y-Axis Pointing Error

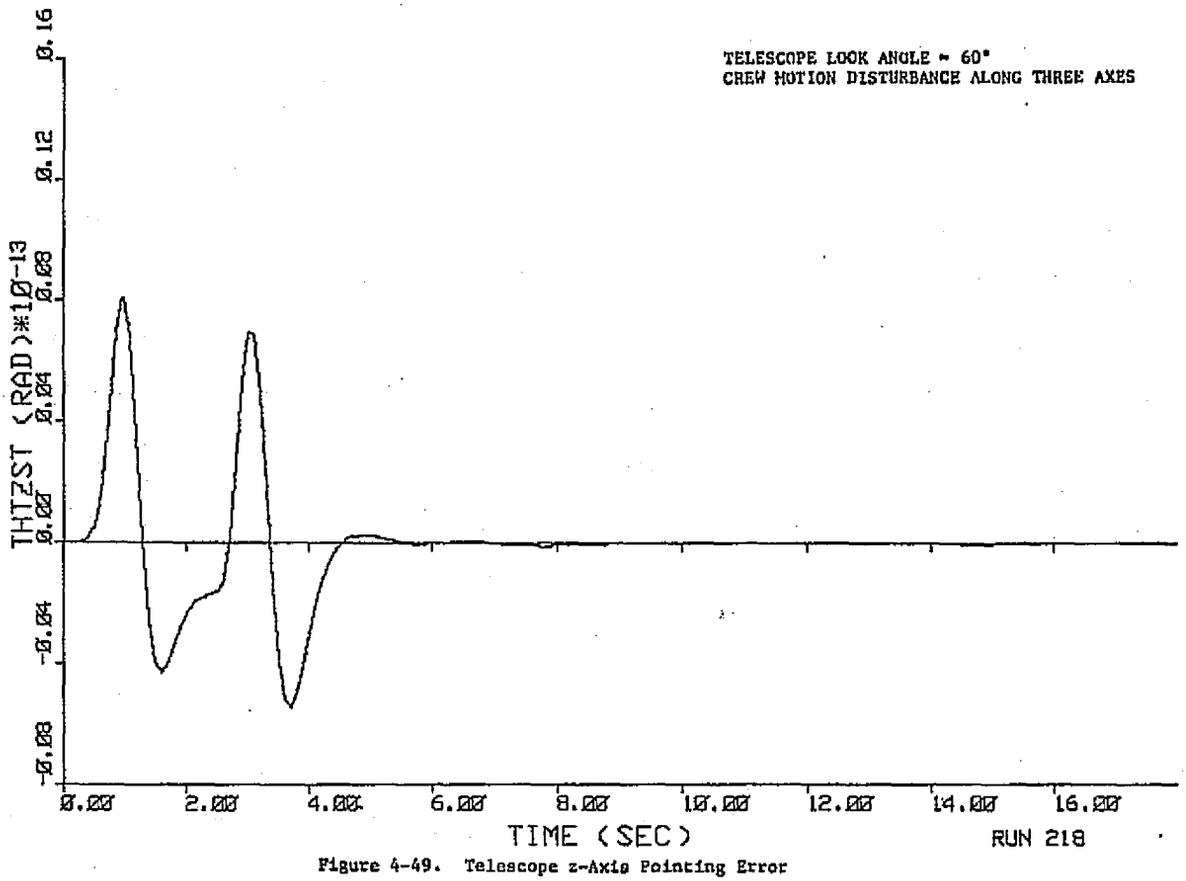

Figure 4-49. Telescope z-Axis Pointing Error

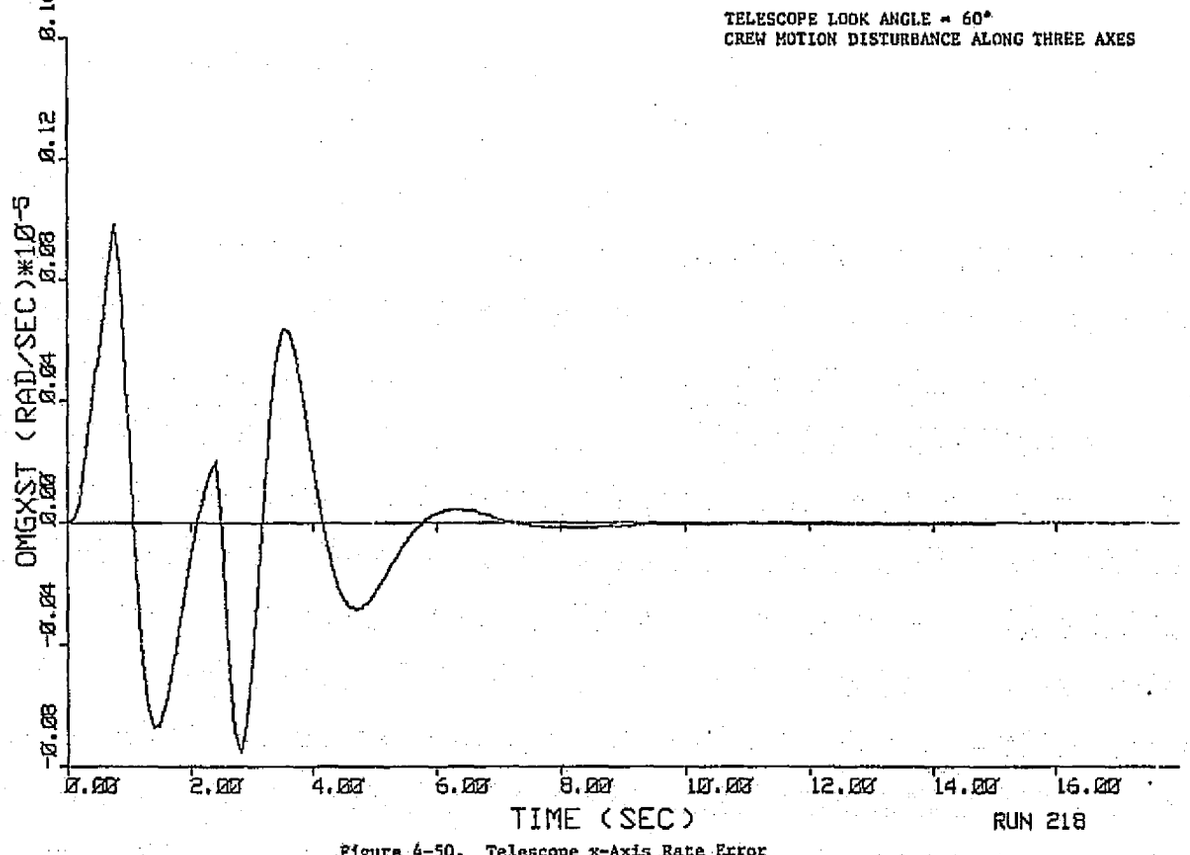

Figure 4-50. Telescope x-Axis Rate Error

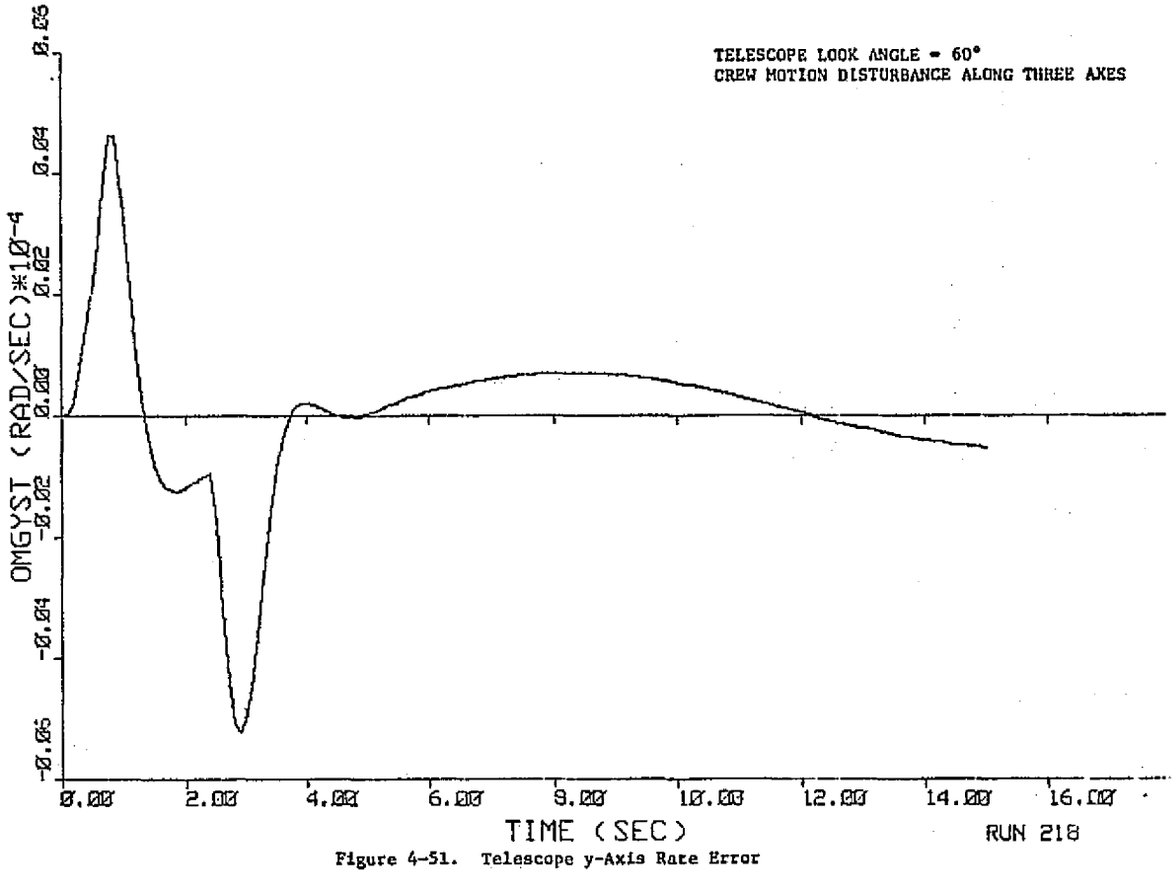

Figure 4-51. Telescope y-Axis Rate Error

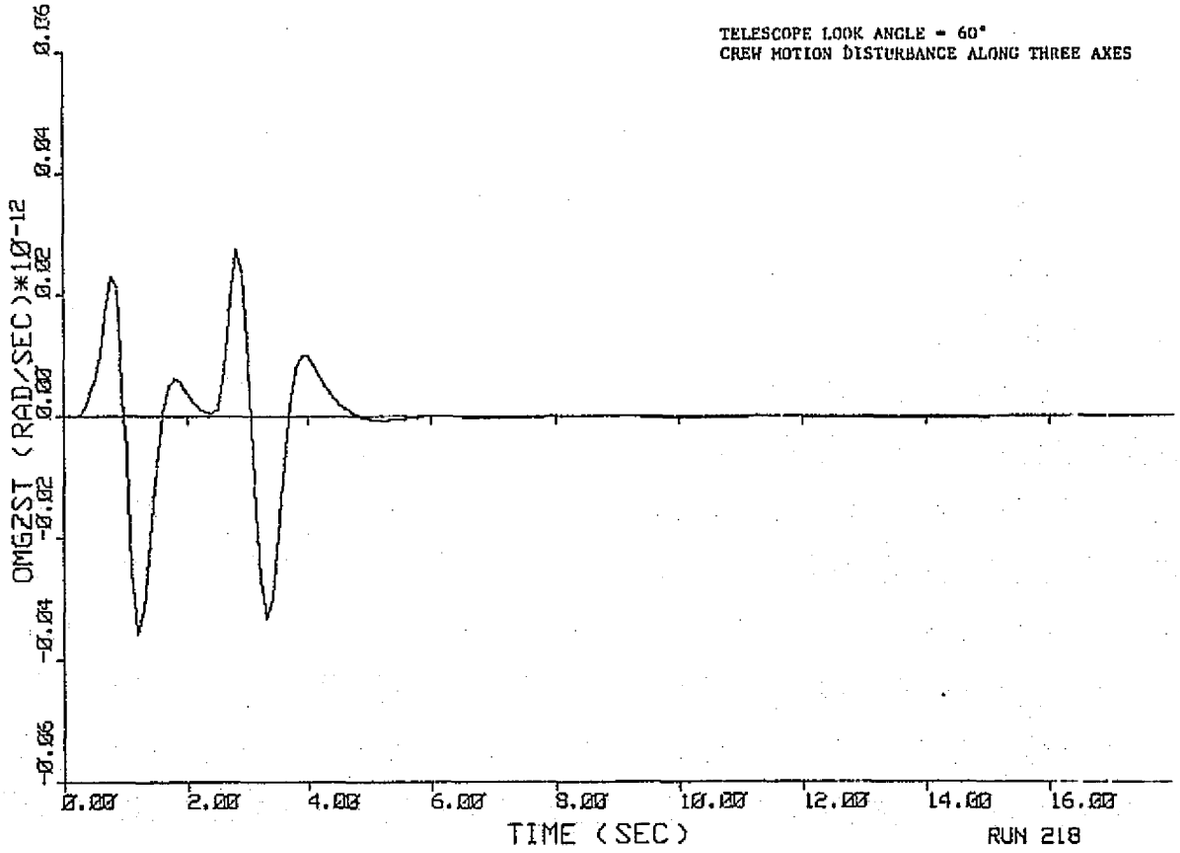

Figure 4-52. Telescope z-Axis Rate Error

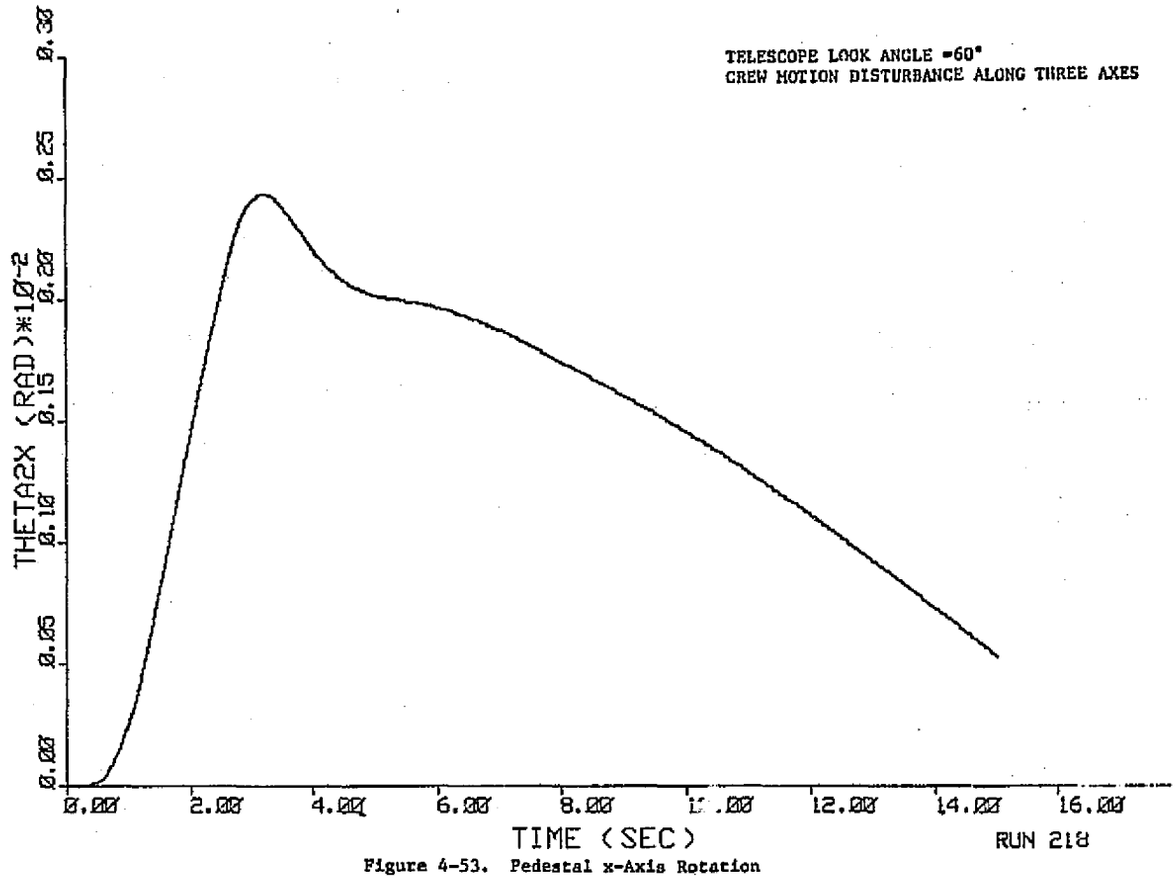

Figure 4-53. Pedestal x-Axis Rotation

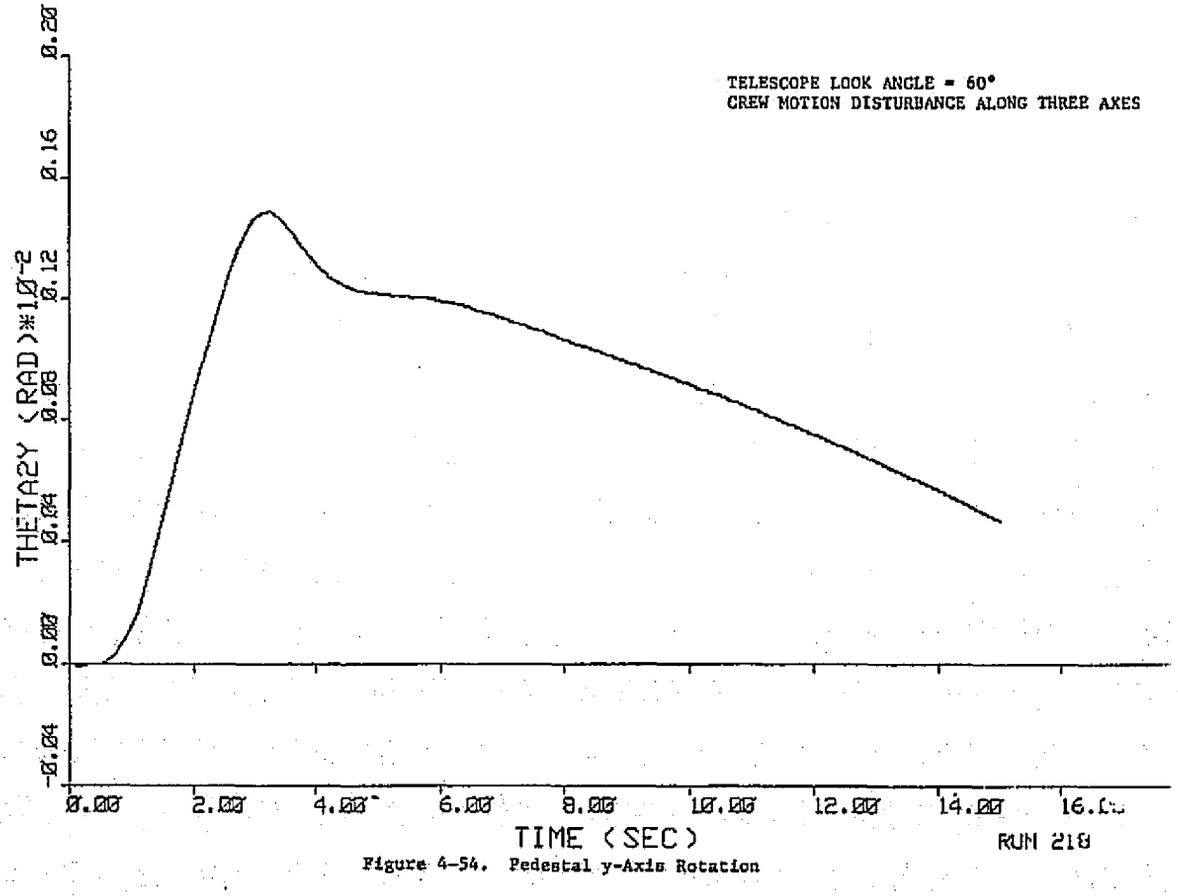

Figure 4-54. Pedestal y-Axis Rotation

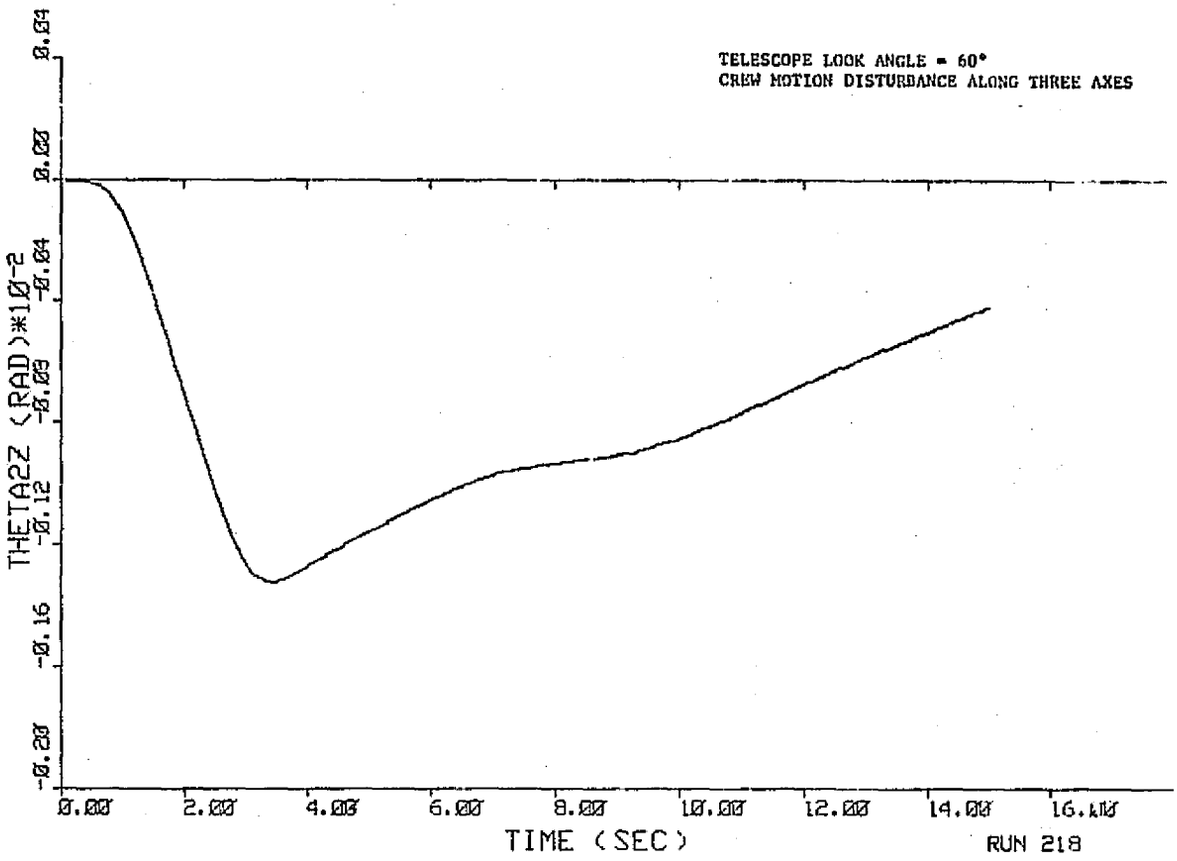

Figure 4-55. Pedestal z-Axis Rotation

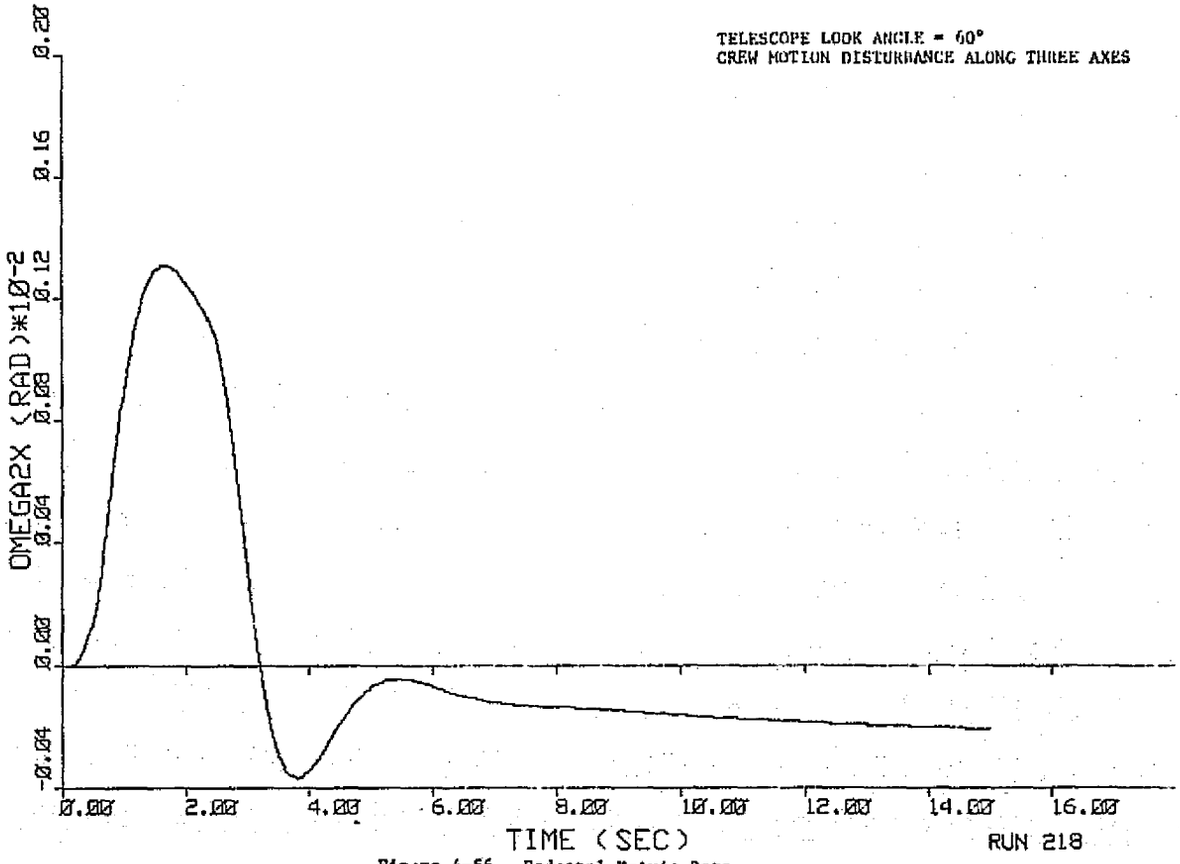

Figure 4-56. Pedestal X-Axis Rate

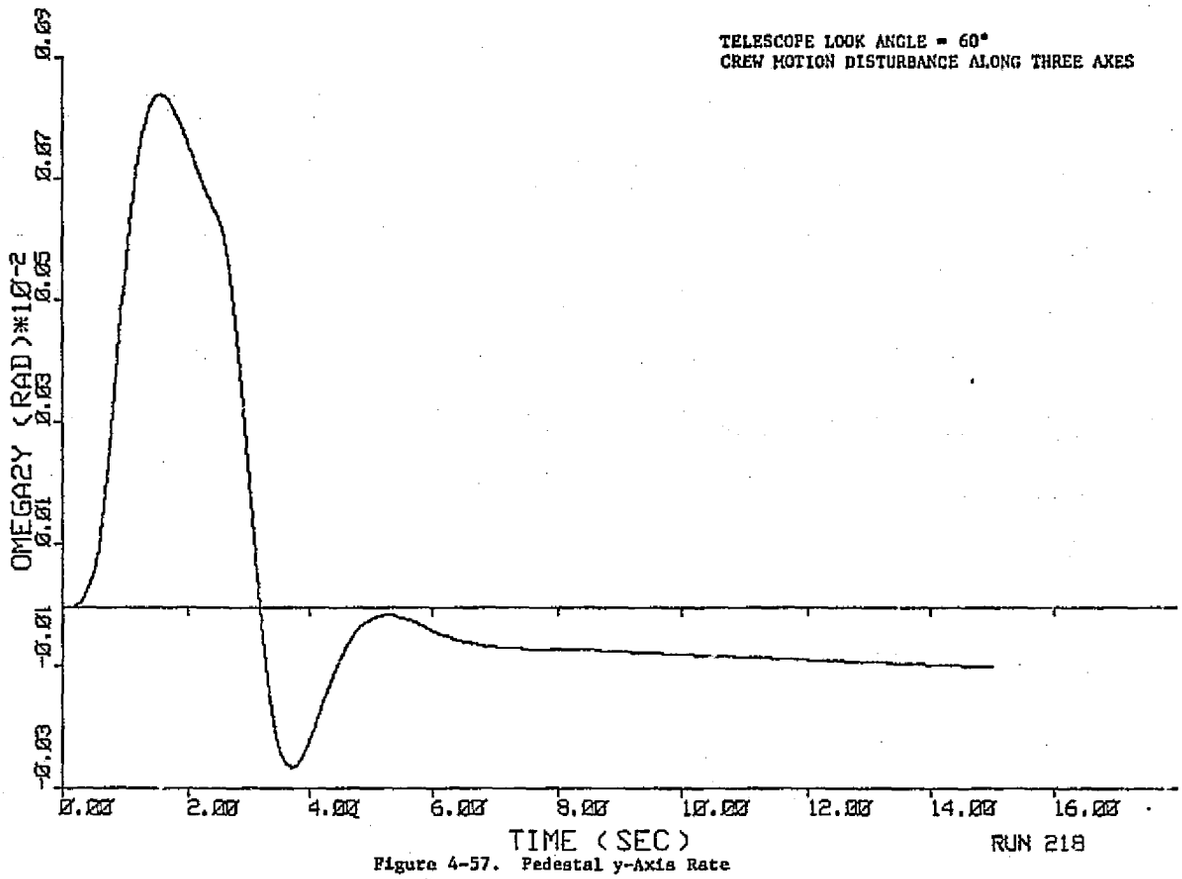

Figure 4-57. Pedestal y-Axis Rate

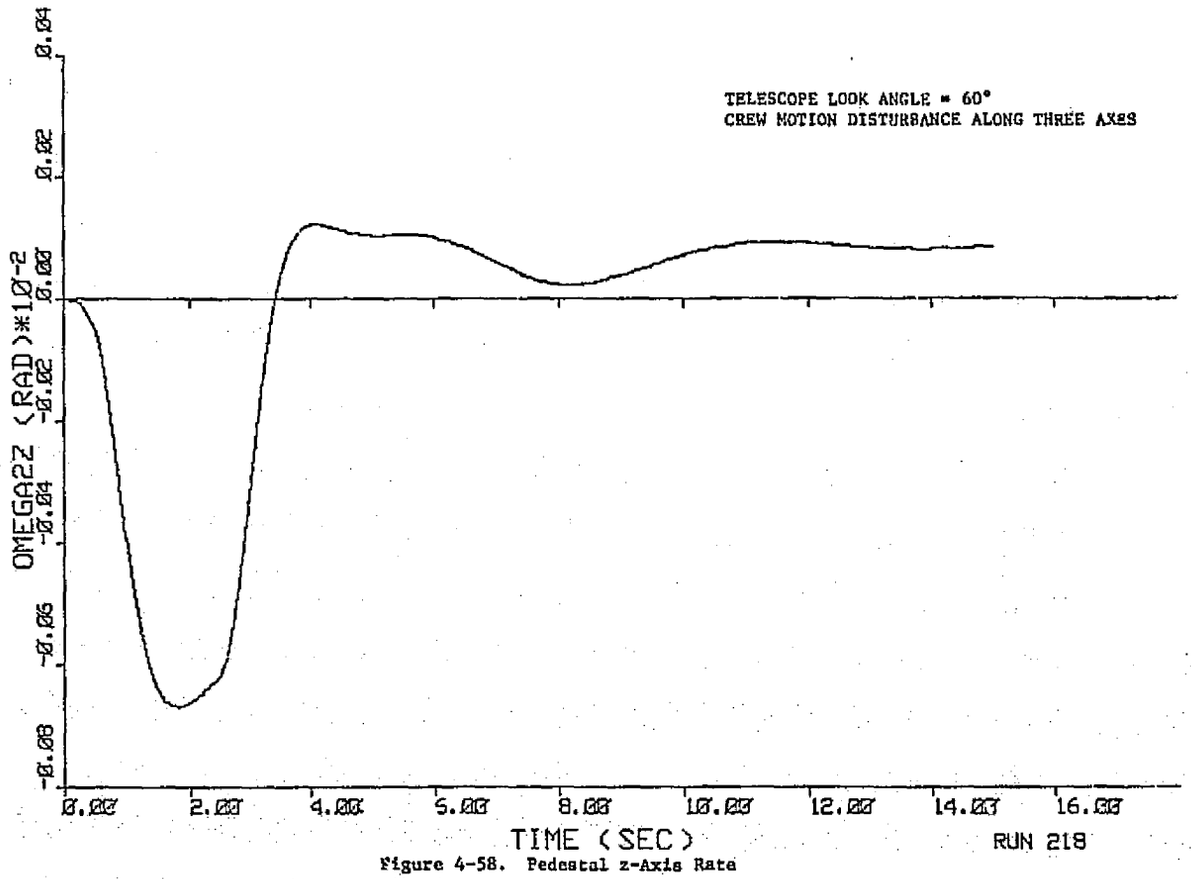

Figure 4-58. Pedestal z-Axis Rate

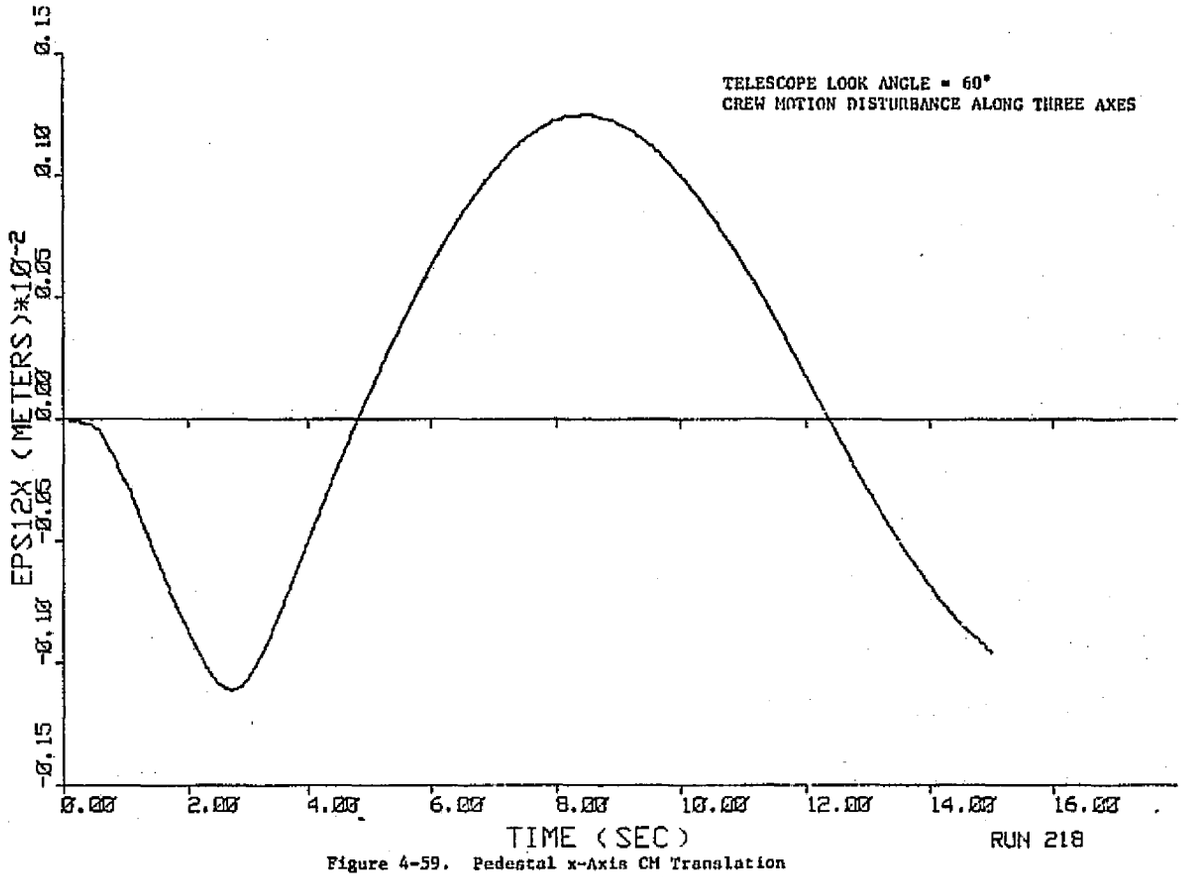

Figure 4-59. Pedestal x-Axis CM Translation

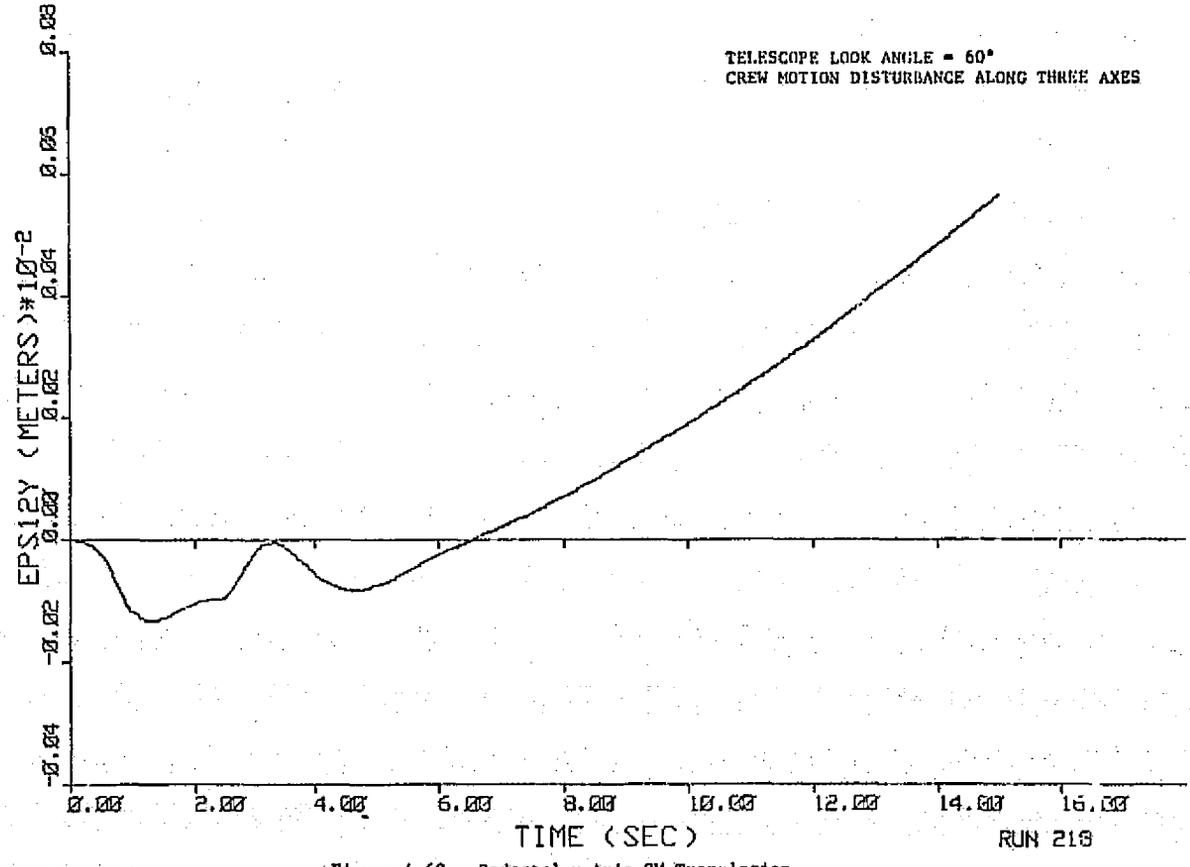

Figure 4-60. Pedestal y-Axis CM Translation

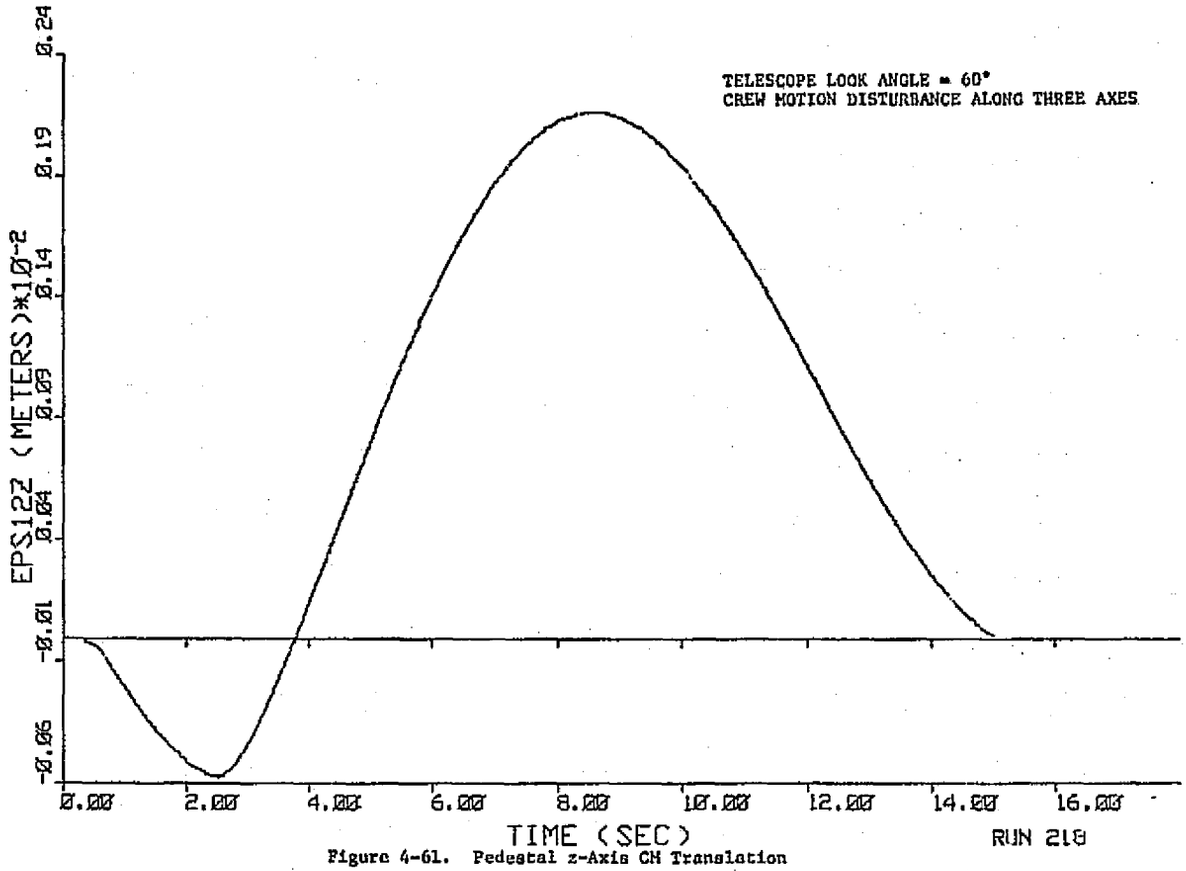

Figure 4-61. Pedestal z-Axis CM Translation

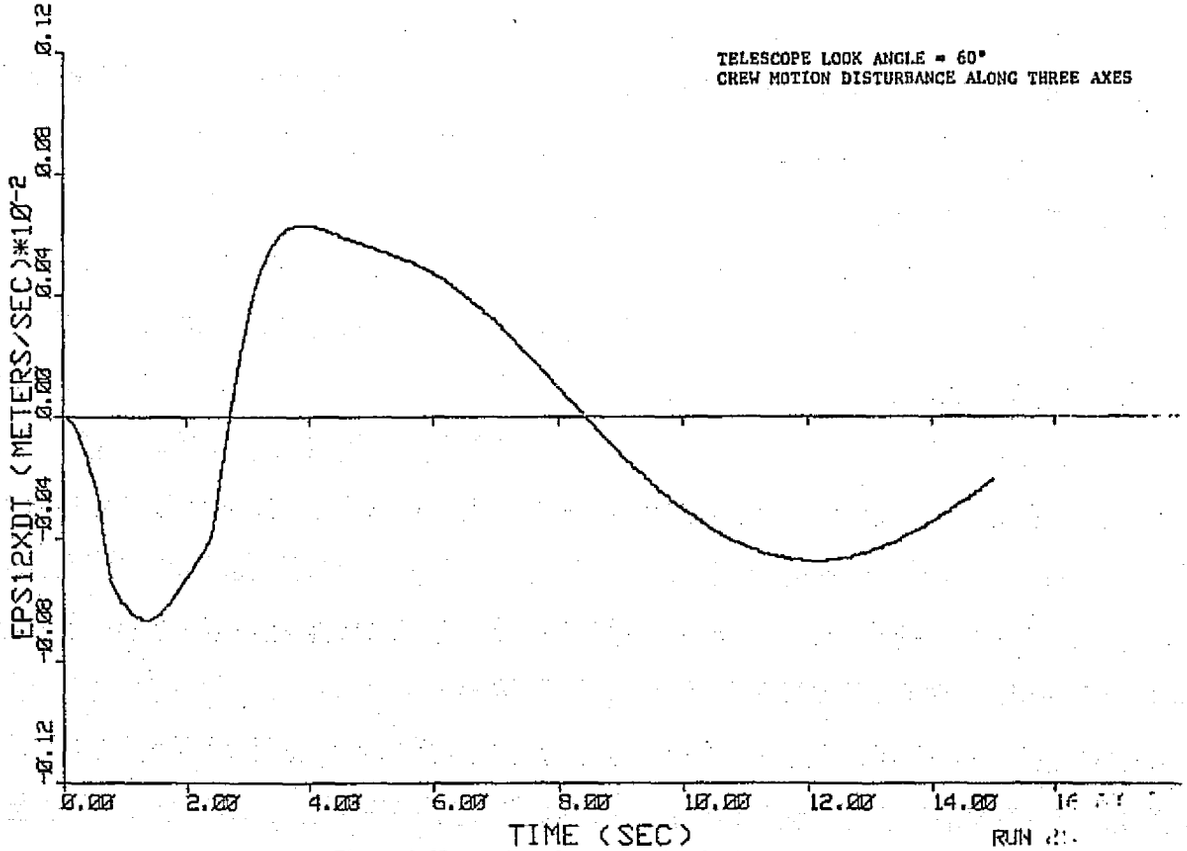

Figure 4-62. Pedestal x-Axis CM Velocity

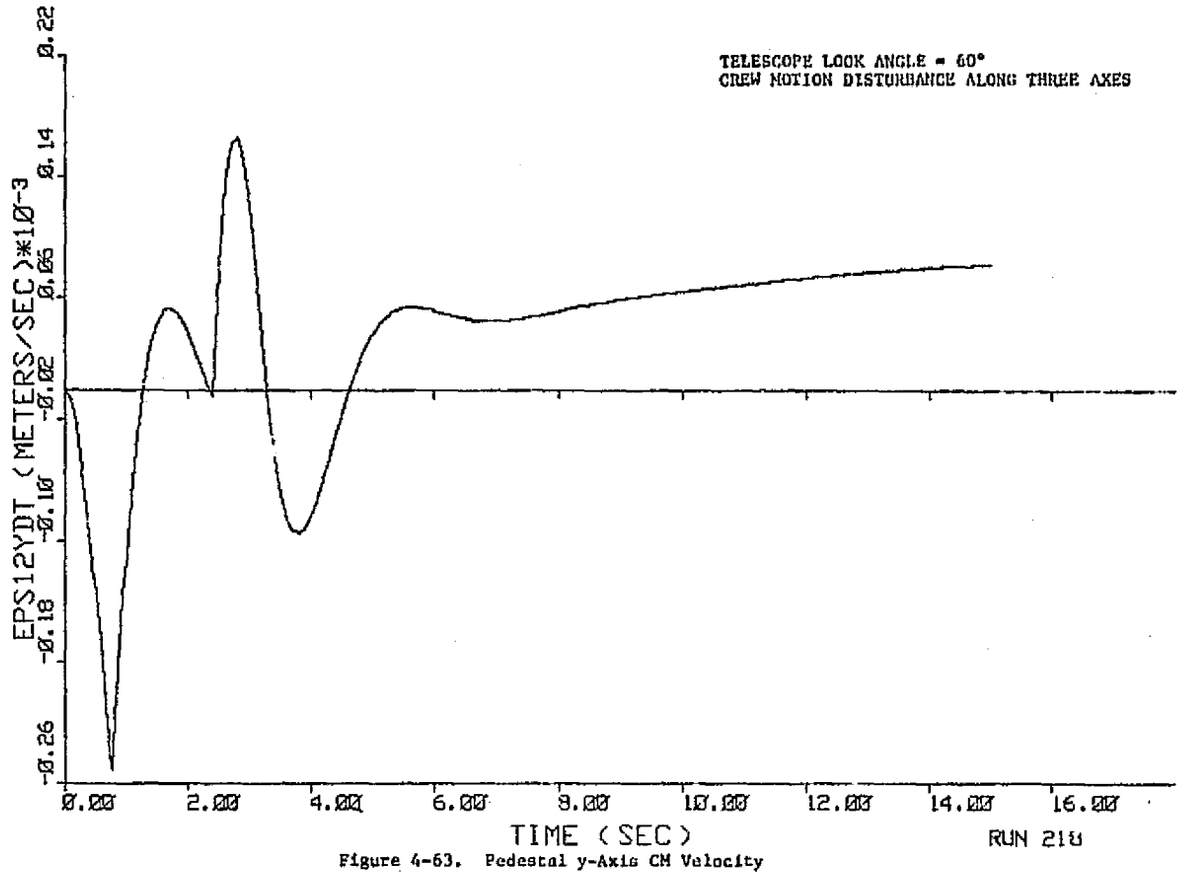

Figure 4-63. Pedestal y-Axis CM Velocity

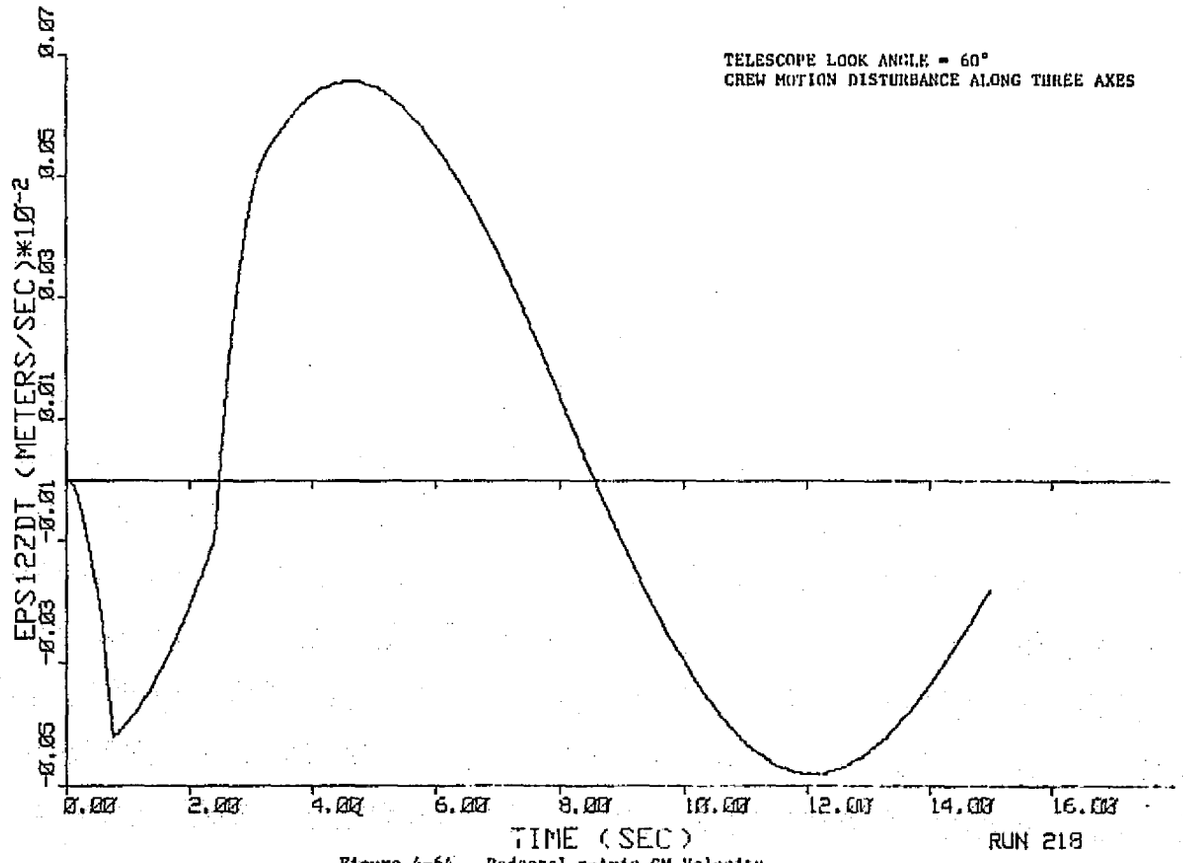

Figure 4-64. Pedestal z-Axis CM Velocity

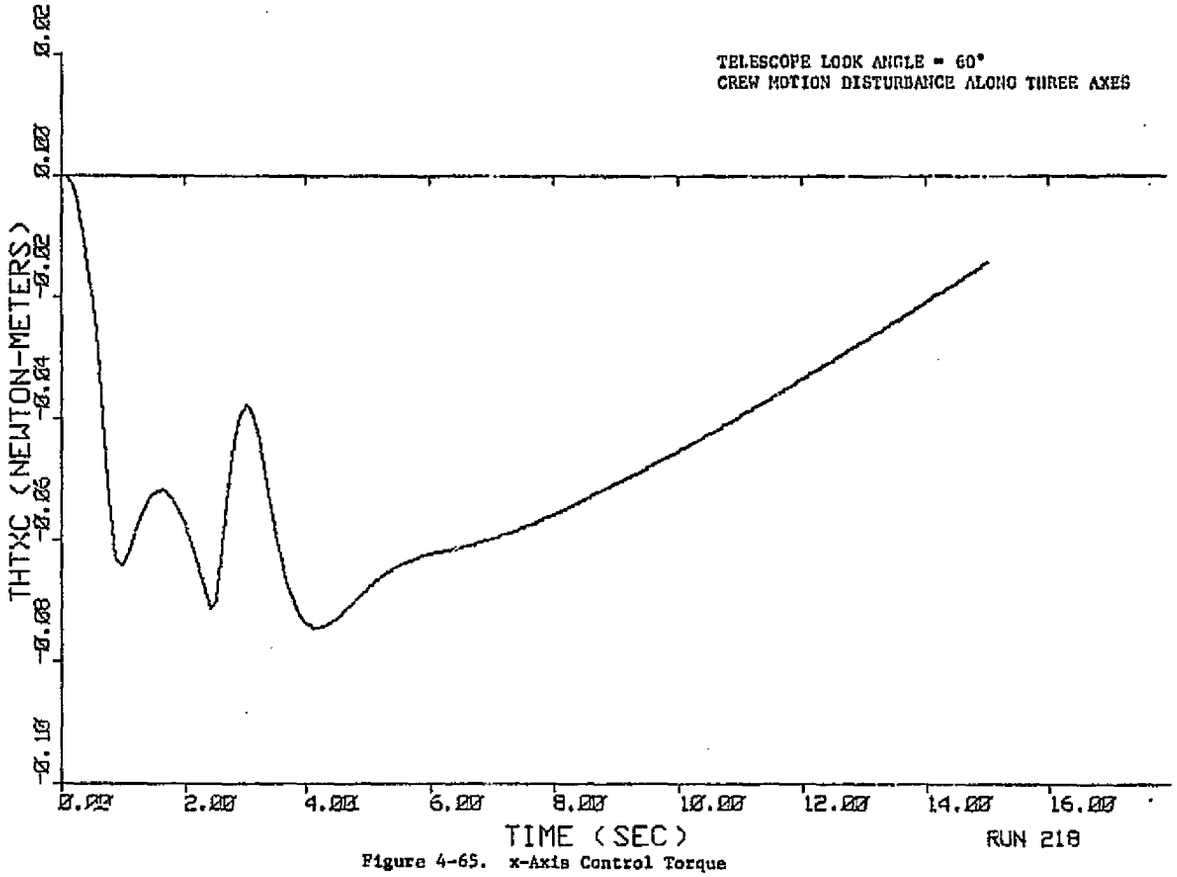

Figure 4-65. x-Axis Control Torque

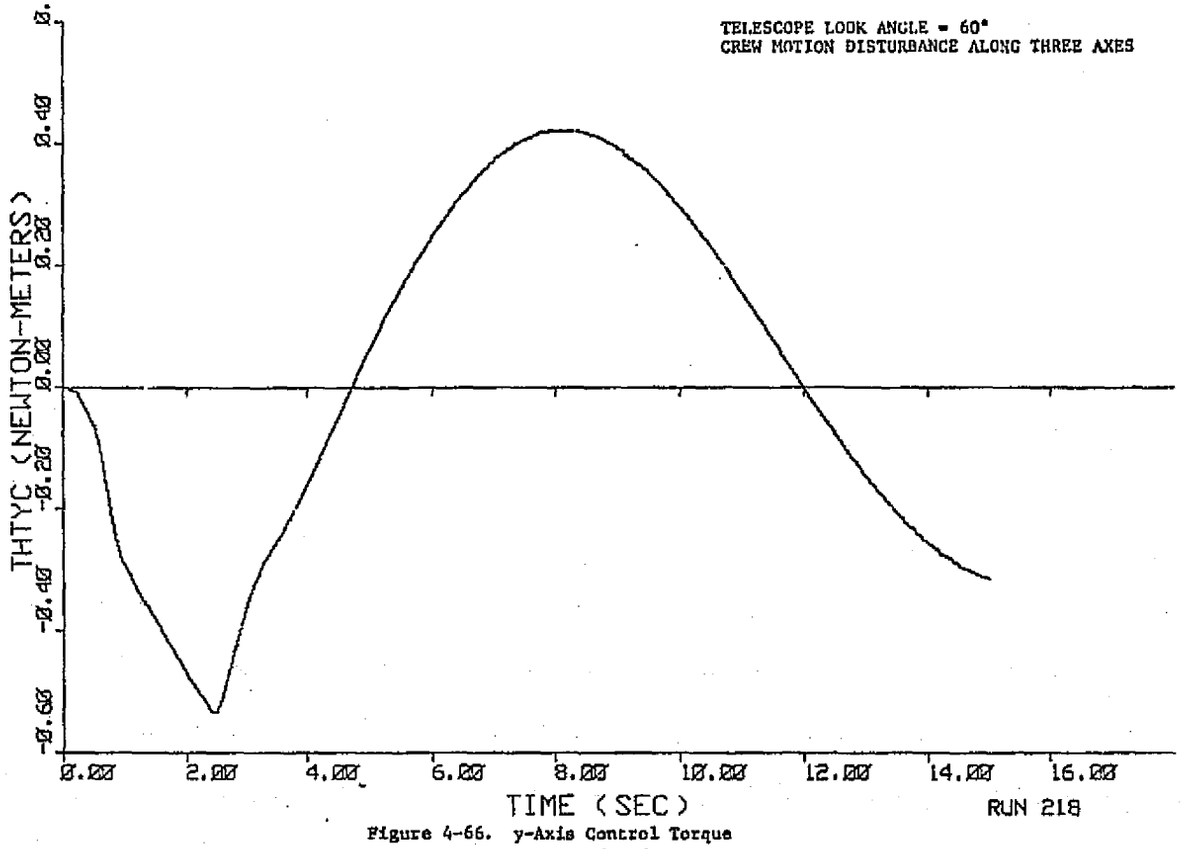

Figure 4-66. y-Axis Control Torque

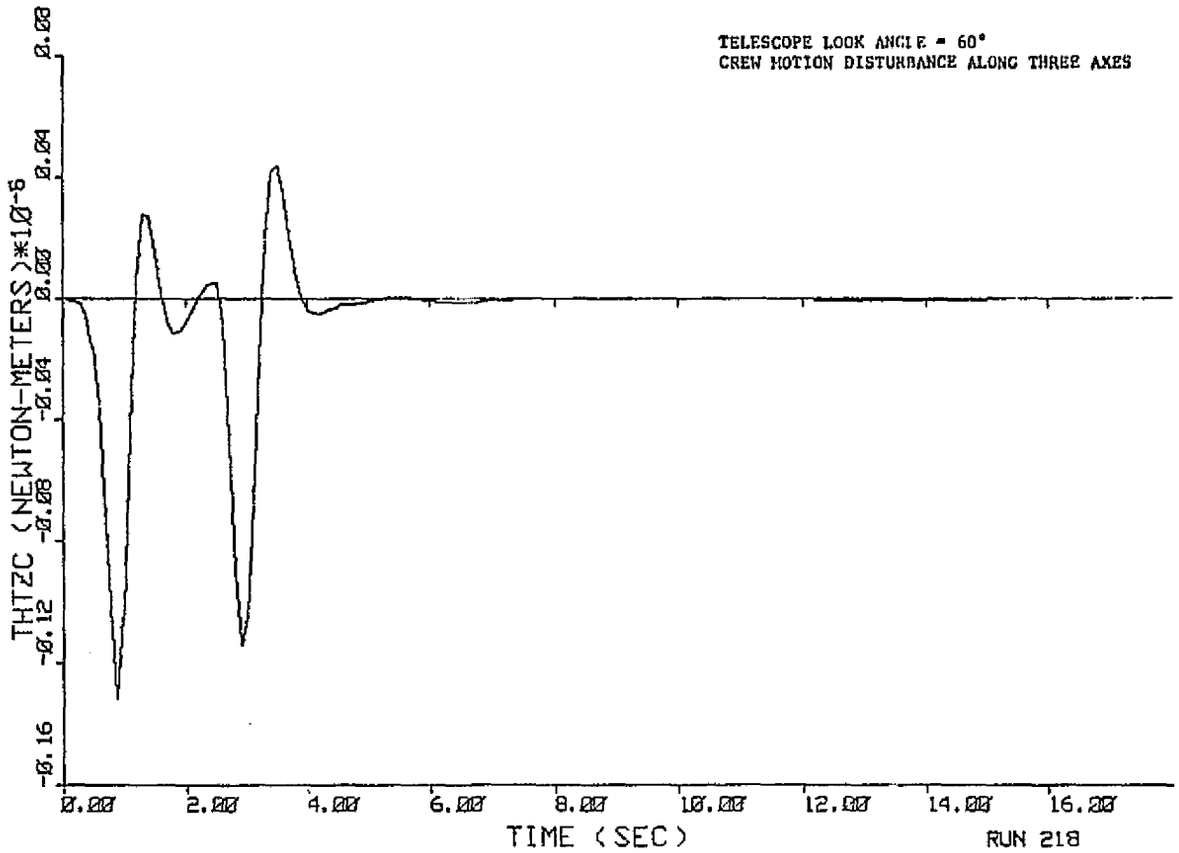

Figure 4-67. z-Axis Control Torque

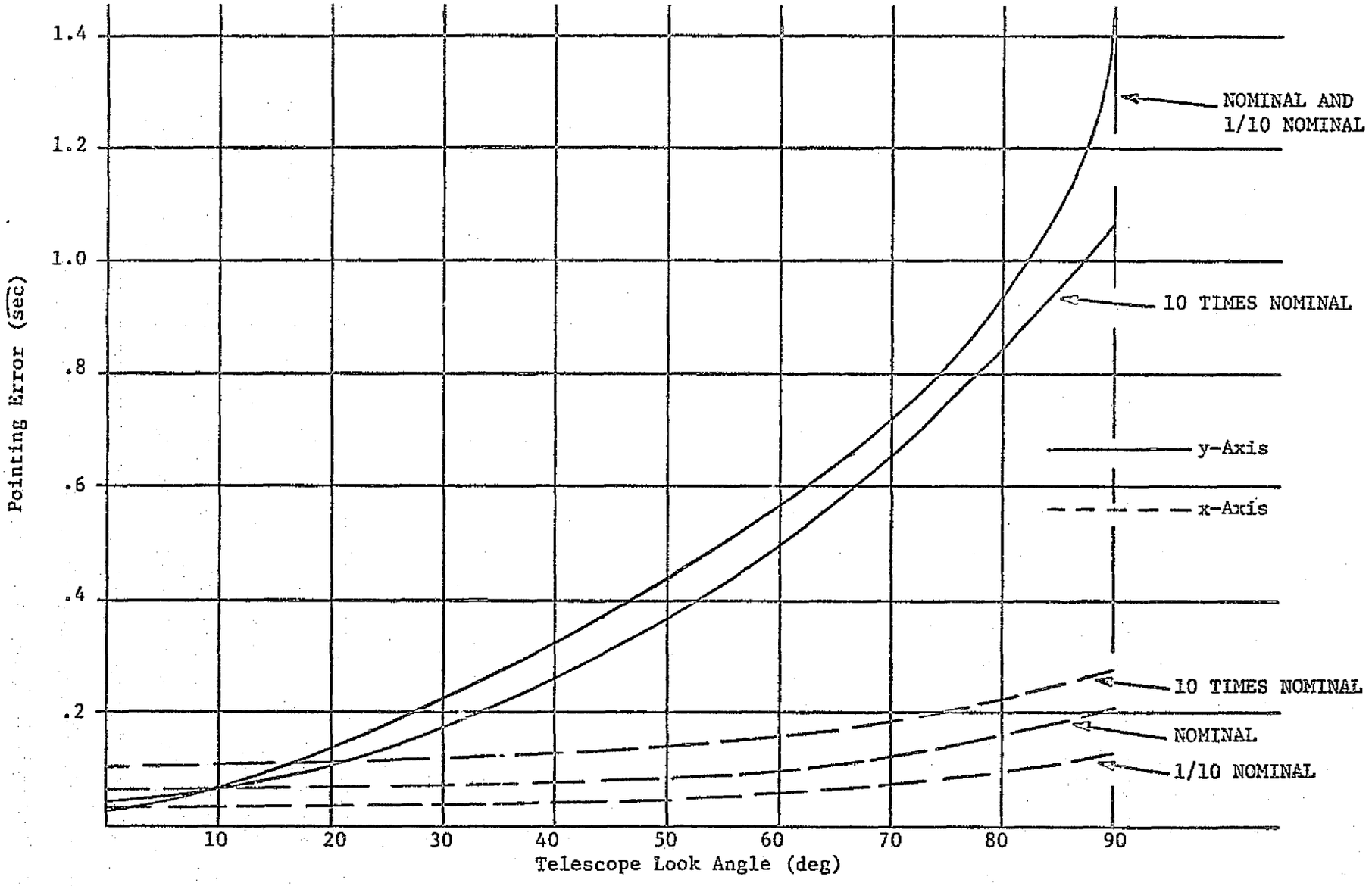

Figure 4-68. Peak Pointing Error as a Function of Pedestal Mass and Inertia Variations

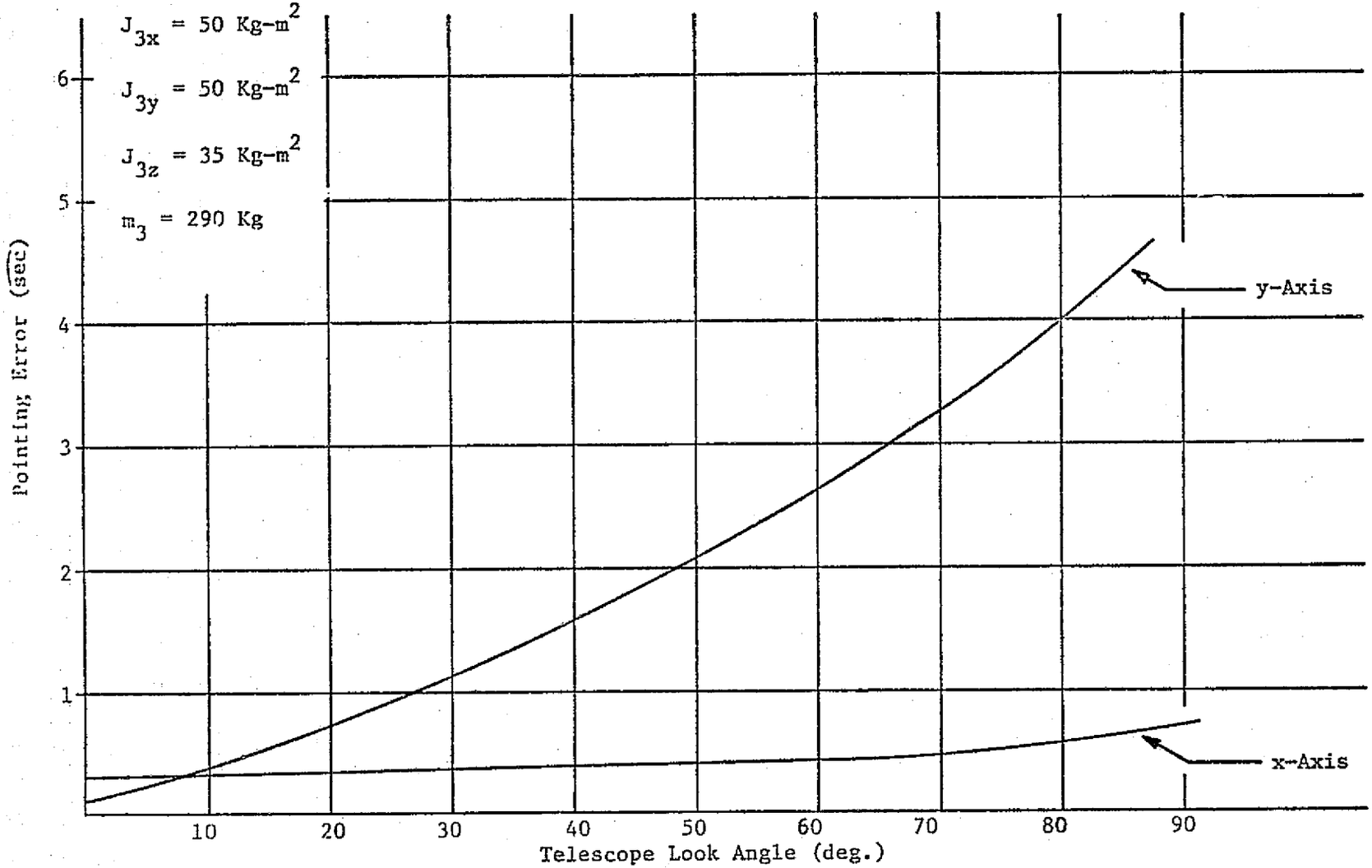

Figure 4-69. Peak Pointing Error for Small Telescope Nominal Suspension Parameters

5. IOG LIMIT CYCLE ANALYSIS AND NONLINEAR PERFORMANCE

The sections that follow describe a limit cycle analysis using describing function techniques for the IOG, under the influence of gimbal wire torques. Results obtained from this analysis are presented and compared to those obtained from the three axis IOG time simulation which gives a better understanding of the limit cycle phenomena observed and provides a cross-check to the time simulation.

The three body (i.e., Shuttle, IOG pedestal, IOG inner gimbal/telescope combination) three axis IOG equations of motion described in section 2.1 were reduced to a two body system consisting of the IOG pedestal and IOG gimbal/telescope combination. The analysis technique presented is three axis handling the three gimbal wire torque nonlinearities simultaneously for arbitrary telescope look angles. In order to facilitate numerical computation these equations were subsequently simplified by only considering planar motion and gimbal wire torques about the y axis of the IOG. The planar motions considered had the following degrees-of-freedom: 1) Rotation about the IOG pedestal y-axis; 2) rotation about the y axis of the IOG inner gimbal/telescope combination; 3) pedestal translation along the x axis; 4) pedestal translation along the z axis. IOG system limit cycle behavior was quantitatively investigated for telescope look angles of zero and 40 degrees and subsequently compared to results obtained from the time simulation. In addition, time response plots for various wire torque characteristics for a telescope look angle of 40 degrees are presented.

5.1 Describing Function Analysis of IOG System

5.1.1 IOG Wire Torque Characteristics - The wire torque characteristic employed in this analysis shown in figure 2-2 is repeated here for convenience.

As described in the December 5, 1975 bimonthly report of NASA Contract Number NAS8-31570 titled, "Research Study on IPS Digital Controller Design," the wire torque characteristic shown in figure 5-1 can be reduced as shown in figure 5-2.

The form of the wire torque characteristic shown in figure 5-2 is easier to handle analytically and will be used throughout this analysis.

5.1.2 IOG Equations of Motion - The equations of motion for the IOG, considering the system as three bodies consisting of the shuttle, IOG pedestal, and IOG inner gimbal/telescope assembly are derived in section 2.1. The final equations of motion given in section 2.1 are repeated here for convenience.

$$T_{1e}+\bar{R}_{11}\cdot F_{1e} = J_1\cdot\dot{\omega}_1+d\cdot(\omega_1-\omega_2)+k\cdot(\theta_1+\theta_2)-4(\bar{R}_{120}+\bar{R}_{E20})\cdot\{D\cdot[\bar{R}_{E20}\cdot(\omega_1-\omega_2)+\bar{R}_{120}\cdot\omega_1]+K\cdot[\bar{R}_{E20}\cdot(\theta_1-\theta_2)+\bar{R}_{120}\cdot\theta_1]\}-4(\bar{R}_{120}+\bar{R}_{E20})\cdot[D\cdot\dot{\varepsilon}+K\cdot\varepsilon] \quad (5\text{-}1)$$

$$T_{2e}+\bar{R}_{22}\cdot F_{2e}+\frac{m_1+m_2}{M}\bar{r}_1\cdot{}_2T_3\cdot F_{3e}-\frac{m_3}{M}\bar{r}_1\cdot(F_{1e}+F_{2e})+T_{WT}|_2=J_2^*\cdot\dot{\omega}_2+d\cdot(\omega_2-\omega_1)+k\cdot(\theta_2-\theta_1)$$
$$-4\bar{R}_{E20}\cdot\{D\cdot[\bar{R}_{E20}\cdot(\omega_2-\omega_1)-\bar{R}_{120}\cdot\omega_1]+K\cdot[\bar{R}_{E20}\cdot(\theta_2-\theta_1)-\bar{R}_{120}\cdot\theta_1]\}+\frac{m_1m_3}{M}\bar{r}_1\cdot\ddot{\varepsilon}$$
$$+4\bar{R}_{E20}\cdot[D\cdot\dot{\varepsilon}+K\cdot\varepsilon]-\frac{m_3(m_1+m_2)}{M}\bar{r}_1\cdot[{}_2T_3\cdot(\bar{r}_2\cdot\dot{\omega}_3+\bar{\omega}_3\cdot[\bar{r}_2\cdot\omega_3])]+{}_2T_3\cdot T_H \quad (5\text{-}2)$$

$$T_{3e}+R_{33}\cdot F_{3e}+\frac{(m_1+m_2)}{M}\bar{r}_2\cdot F_{3e}-\frac{m_3}{M}\bar{r}_2\cdot{}_3T_2\cdot(F_{1e}+F_{2e})-T_{WT}|_3 = J_3^*\cdot\dot{\omega}_3+\bar{\omega}_3\cdot[J_3^*\cdot\omega_3]$$
$$+\frac{m_1m_3}{M}\bar{r}_2\cdot[{}_3T_2\cdot\ddot{\varepsilon}]-\frac{m_3(m_1+m_2)}{M}\bar{r}_2\cdot[{}_3T_2\cdot\bar{r}_1\cdot\dot{\omega}_2]-T_H \quad (5\text{-}3)$$

$$-(\frac{m_2+m_3}{M})F_{1e}+\frac{m_1}{M}(F_{2e}+{}_2T_3\cdot F_{3e})=+[\frac{m_1}{M}(m_2+m_3)\ddot{\varepsilon}+4D\cdot\dot{\varepsilon}+4K\cdot\varepsilon]+4D\cdot[\bar{R}_{E20}\cdot(\omega_1-\omega_2)$$
$$+\bar{R}_{120}\cdot\omega_1]+4K\cdot[\bar{R}_{E20}\cdot(\theta_1-\theta_2)+\bar{R}_{120}\cdot\theta_1]-\frac{m_1m_3}{M}(\bar{r}_1\cdot\dot{\omega}_2)-\frac{m_1m_3}{M}[{}_2T_3\cdot(\bar{r}_2\cdot\dot{\omega}_3+\bar{\omega}_3\cdot[\bar{r}_2\cdot\omega_3])] \quad (5\text{-}4)$$

where

$T_{WT}|_2$ = Wire torques written in body 2 coordinates

$T_{WT}|_3$ = Wire torques written in body 3 coordinates

${}_3T_2 = {}_2T_3^{-1}$ = Transformation between bodies two and three

The "12" subscript used in the derivation shown in section 2.1 is dropped here, for convenience.

Since the shuttle mass and inertia far exceeds that of the IOG and the telescope, the above equations can be simplified by taking the limit as the shuttle mass and inertia (i.e., m_1 and J_1) approach infinity. This results in the following set of equations

$$T_{2e}+R_{22}\cdot F_{2e}+\bar{r}_1\cdot {}_2T_3\cdot F_{3e}+T_{WT}\big|_2 = J_2^*\cdot\omega_2+d\cdot\omega_2+k\cdot\theta_2\ 4\bar{R}_{E20}\cdot\{D\cdot\bar{R}_{E20}\cdot\omega_2+K\cdot\bar{R}_{E20}\cdot\theta_2\}$$

$$+m_3\bar{r}_1\cdot\ddot{\varepsilon}+4\bar{R}_{E20}\cdot[D\cdot\dot{\varepsilon}+K\cdot\varepsilon]-m_3\bar{r}_1\cdot[{}_2T_3\cdot\bar{r}_2\cdot\dot{\omega}_3]+{}_2T_3\cdot T_H \qquad (5\text{-}5)$$

$$T_{3e}+(\bar{R}_{33}+\bar{r}_2)\cdot F_{3e}-T_{WT}\big|_3 = J_3^*\cdot\dot{\omega}_3+m_3\bar{r}_2\cdot[{}_3T_2\cdot\ddot{\varepsilon}]-m_3\bar{r}_2\cdot[{}_3T_2\cdot\bar{r}_1\cdot\dot{\omega}_2]-T_H \qquad (5\text{-}6)$$

$$F_{2e}+{}_2T_3\cdot F_{3e} = (m_2+m_3)\ddot{\varepsilon}+4D\cdot\dot{\varepsilon}+4K\cdot\varepsilon-4D\cdot\bar{R}_{E20}\cdot\omega_2-4K\cdot\bar{R}_{E20}\cdot\theta_2-m_3\bar{r}_1\cdot\dot{\omega}_2$$

$$-m_3[{}_2T_3\cdot\bar{r}_2\cdot\dot{\omega}_3] \qquad (5\text{-}7)$$

where the nonlinear terms shown in equations (5-2) through (5-4) eliminated.

In order to make use of the wire torque characteristics shown in figure 5-2, the equation of motion for the IOG must be written in terms of relative accelerations, rates, and angle between the pedestal and the telescope (i.e., between bodies 2 and 3). This is accomplished by making the following substitution

$$\begin{aligned}
\dot{\omega}_3 &= {}_3T_2\cdot\dot{\omega}_2+\ddot{\gamma}\\
\dot{\omega}_3 &= {}_3T_2\cdot\omega_2+\dot{\gamma}\\
\theta_3 &= {}_3T_2\cdot\theta_2+\gamma\\
\theta_3^I &= {}_3T_2\cdot\theta_2^I+\gamma^I
\end{aligned} \qquad (5\text{-}8)$$

Substituting equation (5-8) into equations (5-5) through (5-7) gives

$$T_{2e}+R_{22}\cdot F_{2e}+\bar{r}_1\cdot {}_2T_3\cdot F_{3e}+T_{WT}|_2 = (J_2^*-m_3\bar{r}_1\cdot {}_2T_3\cdot\bar{r}_2\cdot {}_3T_2)\cdot\dot{\omega}_2$$
$$+(d-4\bar{R}_{E20}\cdot D\cdot\bar{R}_{E20}-{}_2T_3\cdot K_R\cdot {}_3T_2)\cdot\omega_2+(k-4\bar{R}_{E20}\cdot K\cdot\bar{R}_{E20}-{}_2T_3\cdot K_p\cdot {}_3T_2)\cdot\theta_2$$
$$-[{}_2T_3\cdot K_I\cdot {}_3T_2]\cdot\theta_2^I-[m_3\bar{r}_1\cdot {}_2T_3\cdot\bar{r}_2]\cdot\ddot{\gamma}-{}_2T_3\cdot[K_R\cdot\dot{\gamma}+K_p\cdot\gamma+K_I\cdot\gamma^I]$$
$$+m_3\bar{r}_1\cdot\ddot{\varepsilon}+4\bar{R}_{E20}\cdot[D\cdot\dot{\varepsilon}+K\cdot\varepsilon] \qquad (5\text{-}9)$$

$$T_{3e}+(\bar{R}_{33}+\bar{r}_2)\cdot F_{3e}-T_{WT}|_3=(J_3^*\cdot {}_3T_2-m_3\bar{r}_2\cdot {}_3T_2\cdot\bar{r}_1)\cdot\dot{\omega}_2+K_R\cdot {}_3T_2\cdot\omega_2+K_p\cdot {}_3T_2\cdot\theta_2$$
$$+K_I\cdot {}_3T_2\cdot\theta_2^I+J_3^*\cdot\ddot{\gamma}+K_R\cdot\dot{\gamma}+K_p\cdot\gamma+K_I\cdot\gamma^I+m_3\bar{r}_2\cdot[{}_3T_2]\cdot\ddot{\varepsilon} \qquad (5\text{-}10)$$

$$F_{2e}+{}_2T_3\cdot F_{3e}= -(m_3\bar{r}_1+m_{32}{}_2T_3\cdot\bar{r}_2\cdot {}_3T_2)\cdot\dot{\omega}_2-4D\cdot\bar{R}_{E20}\cdot\omega_2-4K\cdot\bar{R}_{E20}\cdot\theta_2-[m_{32}{}_2T_3\cdot\bar{r}_2]\cdot\ddot{\gamma}$$
$$+(m_2+m_3)\ddot{\varepsilon}+4D\cdot\dot{\varepsilon}+4K\cdot\varepsilon \qquad (5\text{-}11)$$

The relative angle, rate, and acceleration (i.e, γ, $\dot{\gamma}$, and $\ddot{\gamma}$) are written in telescope (body "3") coordinates. However, these quantities should be written in terms of the relative Euler angles between the IOG pedestal and telescope (i.e., bodies "2" and "3") since this will be required if single input describing functions are to be employed in the description of the gimbal wire torques.

The rotation sequence between the IOG pedestal and the telescope is z, x, y. Defining these rotations as θ_z, ϕ_x, ψ_y respectively, the relative rate $\dot{\gamma}$ can be written as:

$$\begin{bmatrix}\dot{\gamma}_x\\ \dot{\gamma}_y\\ \dot{\gamma}_z\end{bmatrix} = \begin{bmatrix}-\sin\psi_y\cos\phi_x & \cos\psi_y & 0\\ \sin\phi_x & 0 & 1\\ \cos\phi_x\cos\psi_y & \sin\psi_y & 0\end{bmatrix}\begin{bmatrix}\dot{\theta}_z\\ \dot{\phi}_x\\ \dot{\psi}_y\end{bmatrix} \qquad (5\text{-}12)$$

or

$$\dot{\gamma} = A \cdot \dot{\Omega} \tag{5-13}$$

The gimbal wire torque $T_{WT}|_2$ and $T_{WT}|_3$ respectively can be written as

$$\begin{bmatrix} T_{WT2x} \\ T_{WT2y} \\ T_{WT2z} \end{bmatrix} = \begin{bmatrix} 0 & \cos\theta_z & -\sin\theta_z\cos\phi_x \\ 0 & \sin\theta_z & \cos\theta_z\cos\phi_x \\ 1 & 0 & \sin\phi_x \end{bmatrix} \begin{bmatrix} T_{\theta z} \\ T_{\phi x} \\ T_{\psi y} \end{bmatrix} \tag{5-14}$$

or

$$T_{WT}|_2 = B \cdot T_{\theta,\phi,\psi} \tag{5-15}$$

$$\begin{bmatrix} T_{WT3x} \\ T_{WT3y} \\ T_{WT3z} \end{bmatrix} = \begin{bmatrix} -\sin\psi_y\cos\phi_x & \cos\psi_y & 0 \\ \sin\phi_x & 0 & 1 \\ \cos\phi_x\cos\psi_y & \sin\psi_y & 0 \end{bmatrix} \begin{bmatrix} T_{\theta z} \\ T_{\phi x} \\ T_{\psi y} \end{bmatrix} \tag{5-16}$$

or

$$T_{WT}|_3 = A \cdot T_{\theta,\phi,\psi} \tag{5-17}$$

As a consequence of the nonlinearity breakdown shown in section 5.2.1 the gimbal wire torques $T_{\theta,\phi,\psi}$ can be written as

$$T_{\theta,\phi,\psi} = N \cdot \dot{\Omega} + K_{WT} \cdot \Omega \tag{5-18}$$

where

N = the describing function of the switch shown in figure 2

K_{WT} = the wire torque slope (linear) shown in figure 2

and

$$N = \text{diag}\,[N_{\theta z},\ N_{\phi x},\ N_{\psi y}] \tag{5-19}$$

$$K_{WT} = \text{diag}\,[K_{WT\theta z},\ K_{WT\phi x},\ K_{WT\psi y}] \tag{5-20}$$

Substituting equations (5-13), (5-15), (5-17) and (5-18) into equations (5-9) through (5-11) the following results

$$T_{2e}+R_{22}\cdot F_{2e}+\bar{r}_1\cdot {}_2T_3\cdot F_{3e} = (J_2^*-m_3\bar{r}_1\cdot {}_2T_3\cdot\bar{r}_2\cdot {}_3T_2)\cdot\dot{\omega}_2+(d-4\bar{R}_{E20}\cdot D\cdot\bar{R}_{E20}-{}_2T_3\cdot K_R\cdot {}_3T_2)\cdot\omega_2$$

$$+(k-4\bar{R}_{E20}\cdot K\cdot\bar{R}_{E20}-{}_2T_3\cdot K_p\cdot {}_3T_2)\cdot\theta_2-[{}_2T_3\cdot K_I\cdot {}_3T_2]\cdot\theta_2^I-[m_3\bar{r}_1\cdot {}_2T_3\cdot\bar{r}_2\cdot A]\cdot\ddot{\Omega}$$

$$-{}_2T_3\cdot[K_R\cdot A\cdot\dot{\Omega}+K_p\cdot A\cdot\Omega+K_I\cdot A\cdot\Omega^I]-B\cdot N\cdot\dot{\Omega}-B\cdot K_{WT}\cdot\Omega+m_3\bar{r}_1\cdot\ddot{\varepsilon}\cdot$$

$$+4\bar{R}_{E20}\cdot[D\cdot\dot{\varepsilon}+K\cdot\varepsilon] \tag{5-21}$$

$$T_{3e}+(\bar{R}_{33}+\bar{r}_2)\cdot F_{3e} = (J_3^*\cdot {}_3T_2-m_3\bar{r}_2\cdot {}_3T_2\cdot\bar{r}_1)\cdot\dot{\omega}_2+K_R\cdot {}_3T_2\cdot\omega_2+K_p\cdot {}_3T_2\cdot\theta_2$$

$$+K_I\cdot {}_3T_2\cdot\theta_2^I+J_3^*\cdot A\cdot\ddot{\Omega}+[K_R\cdot A+A\cdot N]\cdot\dot{\Omega}+[K_p\cdot A+A\cdot K_{WT}]\cdot\Omega+K_I\cdot A\cdot\Omega^I+m_3\bar{r}_2\cdot {}_3T_2\cdot\ddot{\varepsilon} \tag{5-22}$$

$$F_{2e}+{}_2T_3\cdot F_{3e} = -(m_3\bar{r}_1+m_{32}{}_2T_3\cdot\bar{r}_2\cdot {}_3T_2)\cdot\dot{\omega}_2-4D\cdot\bar{R}_{E20}\cdot\omega_2-4K\cdot\bar{R}_{E20}\cdot\theta_2-m_{32}{}_2T_3\cdot\bar{r}_2\cdot A\cdot\ddot{\Omega}$$

$$+(m_2+m_3)\ddot{\varepsilon}+4D\cdot\dot{\varepsilon}+4K\cdot\varepsilon \tag{5-23}$$

It should be noted that in the derivation of equations (5-21) through (5-23) the "A" and "B" matrices were considered to be constant. In fact "${}_3T_2$" and "${}_2T_3$" are also considered constant if the system is to be linear where a describing function analysis on the gimbal torque nonlinearity can be conducted. These approximations are valid since the limit cycle amplitude incurred is generally "small" and the transformations can be considered constant.

The system equations derived above (excluding disturbances) can be written in the following form

$$C_{11}\cdot\dot{\omega}_2+C_{12}\cdot\ddot{\Omega}+C_{13}\cdot\ddot{\varepsilon} = a_{11}\cdot\omega_2+a_{12}\cdot\theta_2+a_{13}\cdot\theta_2^I+a_{14}\cdot\dot{\Omega}+a_{15}\cdot\Omega+a_{16}\cdot\Omega^I$$

$$+a_{17}\cdot\dot{\varepsilon}+a_{18}\cdot\varepsilon \qquad (5\text{-}24)$$

$$C_{21}\cdot\dot{\omega}_2+C_{22}\cdot\ddot{\Omega}+C_{23}\cdot\ddot{\varepsilon} = a_{21}\cdot\omega_2+a_{22}\cdot\theta_2+a_{23}\cdot\theta_2^I+a_{24}\cdot\dot{\Omega}+a_{25}\cdot\Omega+a_{26}\cdot\Omega^I \qquad (5\text{-}25)$$

$$C_{31}\cdot\dot{\omega}_2+C_{32}\cdot\ddot{\Omega}+C_{33}\cdot\ddot{\varepsilon} = a_{31}\cdot\omega_2+a_{32}\cdot\theta_2+a_{33}\cdot\dot{\varepsilon}+a_{34}\cdot\varepsilon \qquad (5\text{-}26)$$

The system "a" matrix can now be written as

$$\begin{vmatrix} \dot{\omega}_2 \\ \ddot{\Omega} \\ \ddot{\varepsilon} \\ \dot{\theta}_2 \\ \dot{\Omega} \\ \dot{\varepsilon} \\ \dot{\theta}_2^I \\ \dot{\Omega}^I \end{vmatrix} = \begin{vmatrix} & & & C^{-1}_{9x9}\cdot a_{9x24} & & & & \\ \hline 1 & 0 & 0 & 0 & 0 & 0 & 0 & 0 \\ 0 & 1 & 0 & 0 & 0 & 0 & 0 & 0 \\ 0 & 0 & 1 & 0 & 0 & 0 & 0 & 0 \\ 0 & 0 & 0 & 1 & 0 & 0 & 0 & 0 \\ 0 & 0 & 0 & 0 & 1 & 0 & 0 & 0 \end{vmatrix} \begin{vmatrix} \omega_2 \\ \dot{\Omega} \\ \dot{\varepsilon} \\ \theta_2 \\ \Omega \\ \varepsilon \\ \theta_2^I \\ \Omega^I \end{vmatrix} \qquad (5\text{-}27)$$

where

$$C_{11} = (J_2^* - m_3\bar{r}_1\cdot{}^2T_3\cdot\bar{r}_2\cdot{}^3T_2)$$

$$C_{12} = -m_3\bar{r}_1\cdot{}^2T_3\cdot\bar{r}_2\cdot A$$

$$C_{13} = m_3\bar{r}_1$$

$$C_{21} = (J_3^* \cdot {}_3T_2 - m_3 \bar{r}_2 \cdot {}_3T_2 \cdot \bar{\bar{r}}_1)$$

$$C_{22} = J_3^* \cdot A$$

$$C_{23} = m_3 \bar{r}_2 \cdot {}_3T_2$$

$$C_{31} = -(m_3 \bar{r}_1 + m_{32} {}_3T_3 \cdot \bar{r}_2 \cdot {}_3T_2)$$

$$C_{32} = m_{32} {}_3T_3 \cdot \bar{r}_2 \cdot A$$

$$C_{33} = (m_2 + m_3) I$$

$$a_{11} = (4\bar{R}_{E20} \cdot D \cdot R_{E20} + {}_2T_3 \cdot K_R \cdot {}_3T_2 - d)$$

$$a_{12} = (4\bar{R}_{E20} \cdot K \cdot R_{E20} + {}_2T_3 \cdot K_p \cdot {}_3T_2 - k)$$

$$a_{13} = {}_2T_3 \cdot K_I \cdot {}_3T_2$$

$$a_{14} = ({}_2T_3 \cdot K_R \cdot A + B \cdot N)$$

$$a_{15} = ({}_2T_3 \cdot K_p \cdot A + B \cdot K_{WT})$$

$$a_{16} = {}_2T_3 \cdot K_I \cdot A$$

$$a_{17} = -4\bar{R}_{E20} \cdot D$$

$$a_{18} = -4\bar{R}_{E20} \cdot K$$

$$a_{21} = -K_R \cdot {}_3T_2$$

$$a_{22} = -K_p \cdot {}_3T_2$$

$$a_{23} = -K_I \cdot {}_3T_2$$

$$a_{24} = -(K_R \cdot A + A \cdot N)$$

$$a_{25} = -(K_p \cdot A + A \cdot K_{WT})$$

$$a_{26} = -K_I \cdot A$$

$$a_{31} = 4D \cdot \bar{R}_{E20}$$

$$a_{32} = 4K \cdot \bar{R}_{E20}$$

$$a_{33} = -4D$$

$$a_{34} = -4K$$

$$J_2^* = \text{diag}\,[J_{2x}, J_{2y}, J_{2z}] + m_3 \begin{bmatrix} (r_{1y}^2 + r_{1z}^2) & -r_{1x}r_{1y} & -r_{1x}r_{1z} \\ -r_{1x}r_{1y} & (r_{1x}^2 + r_{1z}^2) & -r_{1y}r_{1z} \\ -r_{1x}r_{1z} & -r_{1y}r_{1z} & (r_{1x}^2 + r_{1y}^2) \end{bmatrix}$$

$$J_3^* = \text{diag}\,[J_{3x}, J_{3y}, J_{3z}] + m_3 \begin{bmatrix} (r_{2y}^2 + r_{2z}^2) & -r_{2x}r_{2y} & -r_{2x}r_{2z} \\ -r_{2x}r_{2y} & (r_{2x}^2 + r_{2y}^2) & -r_{2y}r_{2z} \\ -r_{2x}r_{2z} & -r_{2y}r_{2z} & (r_{2x}^2 + r_{2y}^2) \end{bmatrix}$$

The describing functions $N_{\theta z}$, $N_{\phi x}$, and $N_{\psi y}$ is given by

$$N_{\theta z} = \frac{4H_{WT}}{\pi \dot{\theta}_z}$$

$$N_{\phi x} = \frac{4H_{WT}}{\pi \dot{\psi}_x} \qquad (5\text{-}28)$$

$$N_{\psi y} \quad \frac{4H_{WT}}{\pi \dot{\psi}_y}$$

The system "a" matrix given in equation (5-27) can be used to generate three axis root loci as a function of variations in the describing function amplitude N. The condition for a limit cycle to exist will be for those values of N for which there are poles on the "jω" axis. The stability of the limit cycle can be easily established by noting whether the root locus crosses from the left half to the right half plane or vice-versa as a function of describing function amplitude variation in the vicinity of a particular pole on the "jω" axis. If the locus goes from the left hand plane to right half as the describing function is increased the limit cycle is stable if the opposite occurs then the limit cycle is unstable. It should be noted, however, that in the above

derivation it was implicitly assumed that a single sinusoidal input is sufficient to characterize the input to each of the gimbal wire torque nonlinearities. This assumption has proved to be adequate when analyzing IOG planar motion as described in the sections that follow. The adequacy of the assumption when all three gimbal nonlinearities are present with the telescope at an arbitrary angle with respect to the IOG pedestal which cross couples the IOG axes still remains to be demonstrated. This demonstration will come when the analytical results obtained from the root locus approach described above are compared with simulation results obtained from the time simulation.

Examination of equations (5-21) through (5-23) indicates that the limit cycle characteristics do not depend on K_{WT} since it is generally much smaller than K_p.

5.1.3 Planar Limit Cycle Analysis - Equations (5-21) through (5-23) which describe three dimensional motion of the IOG can be reduced to planar motion which consider the following degrees of freedom ω_{2y}, ψ_y, ε_x, and ε_z. These simplified equations are listed below.

$$T_{2ey}+R_{22}\cdot F_{2e}|_y+\bar{r}_1\cdot {}_2T_3\cdot F_{3e}|_y = (J_{2y}+m_3r_{1z}^2+m_3r_{1z}r_{2z}\cos\psi_{yo})\dot{\omega}_{2y}$$

$$+(d_y+4D_xR_{E20z}^2-K_{Ry})\omega_{2y}+(k_y+4K_xR_{E20z}^2-K_{py})\theta_{2y}-K_{Iy}\theta_{2y}^I+m_3r_{1z}r_{2z}\cos\psi_{yo}\ddot{\psi}_y$$

$$-(K_{Ry}+N_{\psi y})\dot{\psi}_y-(K_{py}+K_{WT\psi y})\psi_y-K_{Iy}\psi_y^I+m_3r_{1z}\ddot{\varepsilon}_x+4R_{E20}D_x\dot{\varepsilon}_x+4R_{E20z}K_x\varepsilon_x \qquad (5\text{-}29)$$

$$T_{3ey}+(R_{33}+\bar{r}_2)\cdot F_{3e}|_y = (J_{3y}+m_3r_{2z}^2+m_3r_{1z}r_{2z}\cos\psi_{yo})\dot{\omega}_{2y}+K_{Ry}\omega_{2y}+K_{py}\theta_{2y}$$

$$+K_{Iy}\theta_{2y}^I+(J_{3y}+m_3r_{2z}^2)\ddot{\psi}_y+(K_{Ry}+N_{\psi y})\dot{\psi}_y+(K_{py}+K_{WT\psi y})\psi_y+K_{Iy}\psi_y^I+m_3r_{2z}\cos\psi_{yo}\ddot{\varepsilon}_x$$

$$-m_3r_{2z}\sin\psi_{yo}\ddot{\varepsilon}_z \qquad (5\text{-}30)$$

$$F_{2e}|_x+{}_2T_3\cdot F_{3e}|_x = (m_3r_{1z}+m_3r_{2z}\cos\psi_{yo})\dot{\omega}_{2y}+4D_xR_{E20z}\omega_{2y}+4K_xR_{E20z}\theta_{2y}$$

$$+m_3r_{2z}\cos\psi_{yo}\ddot{\psi}_y+(m_2+m_3)\ddot{\varepsilon}_x+4D_x\dot{\varepsilon}_x+4K_x\varepsilon_x \qquad (5\text{-}31)$$

$$F_{2e}|_z + {}_2T_3 \cdot F_{3e}|_z = -m_3 r_{2z} \sin\psi_{yo} \dot{\omega}_{2y} - m_3 r_{2z} \sin\psi_{yo} \ddot{\psi}_y + (m_2+m_3)\ddot{\varepsilon}_z + 4D_z \dot{\varepsilon}_z + 4K_z \varepsilon_z \quad (5\text{-}32)$$

Taking the laplace transform of equations (5-29) through (5-32) gives the following:

$$T_{2ey} + R_{22} \cdot F_{2e}|_y + \bar{r}_1 \cdot {}_2T_3 \cdot F_{3e}|_y = \{(J_{2y} + m_3 r_{1z}^2 + m_3 r_{1z} r_{2z} \cos\psi_{yo}) S^2 + (d_y + 4D_x R_{E20z}^2 - K_{Ry}) S$$

$$+ (K_y + 4K_x R_{E20z}^2 - K_{py}) - \frac{K_{Iy}}{S} \} \theta_{2y} + \{m_3 r_{1z} r_{2z} \cos\psi_{yo} S^2 - (K_{Ry} + N_{\psi y}) S - (K_{py} + K_{WT\psi y}) - \frac{K_{Iy}}{S} \} \psi_y$$

$$+ \{m_3 r_{1z} S^2 + 4R_{E20z} D_x S + 4R_{E20z} K_x\} \varepsilon_x \quad (5\text{-}33)$$

$$T_{3ey} + (\bar{R}_{33} + \bar{r}_2) \cdot F_{3e}|_y = \{(J_{3y} + m_3 r_{2z}^2 + m_3 r_{1z} r_{2z} \cos\psi_{yo}) S^2 + K_{Ry} S + K_{py} + \frac{K_{Iy}}{S} \} \theta_{2y}$$

$$+ \{(J_{3y} + m_3 r_{2z}^2) S^2 + (K_{Ry} + N_{\psi y}) S + (K_{py} + K_{WT\psi y}) - \frac{K_{Iy}}{S} \} \psi_y + m_3 r_{2z} \cos\psi_{yo} S^2 \varepsilon_x - m_3 r_{2z} \sin\psi_{yo} S^2 \varepsilon_z$$

(5-34)

$$F_{2ex} + {}_2T_3 \cdot F_{3e}|_x = \{(m_3 r_{1z} + m_3 r_{2z} \cos\psi_{yo}) S^2 + 4D_x R_{E20z} S + 4K_x R_{E20z}\} \theta_{2y}$$

$$+ m_3 r_{2z} \cos\psi_{yo} S^2 \psi_y + \{(m_2+m_3) S^2 + 4D_x S + 4K_x\} \varepsilon_x \quad (5\text{-}35)$$

$$F_{2ez} + {}_2T_3 \cdot F_{2e}|_z = -m_3 r_{2z} \sin\psi_{yo} S^2 \theta_{2y} - m_3 r_{2z} \sin\psi_{yo} S^2 \psi_y + \{(m_2+m_3) S^2 + 4D_z S + 4K_z\} \varepsilon_z \quad (5\text{-}36)$$

The system characteristic equation is given by

$$\Delta = \det \begin{vmatrix} a_1 & a_2^N & a_3 & 0 \\ a_4 & a_5^N & a_6 & a_7 \\ a_8 & a_6 & a_9 & 0 \\ a_7 & a_7 & 0 & a_9 \end{vmatrix} \quad (5\text{-}37)$$

Expanding equation (5-37) yields

$$\Delta = a_7 \begin{vmatrix} a_1 & a_2^N & a_3 \\ a_8 & a_6 & a_9 \\ a_7 & a_7 & 0 \end{vmatrix} + a_9 \begin{vmatrix} a_1 & a_2^N & a_3 \\ a_4 & a_5^N & a_6 \\ a_8 & a_6 & a_9 \end{vmatrix} \tag{5-38}$$

which can be further expanded to

$$\Delta = a_2^N[a_7^2 a_9 + a_9(a_6 a_8 - a_4 a_9)] + a_5^N a_9(a_1 a_9 - a_3 a_8) + a_3 a_7^2(a_8 - a_6) + a_6 a_9(a_3 a_4 - a_1 a_6) - a_1 a_7^2 a_9 \tag{5-39}$$

and

$$a_1 = (J_{2y} + m_3 r_{1z}^2 + m_3 r_{1z} r_{2z} \cos\psi_{yo}) S^2 + (d_y + 4D_x R_{E20}^2 - K_{Ry}) S + (k_y + 4K_x R_{E20}^2 - K_{py}) - \frac{K_{Iy}}{S}$$

$$a_2^N = m_3 r_{1z} r_{2z} \cos\psi_{yo} S^2 - (K_{Ry} + N_{\psi y}) S - (K_{py} + K_{WT\psi y}) - \frac{K_{Iy}}{S}$$

$$a_3 = m_3 r_{1z} S^2 + 4R_{E20z} D_x S + 4R_{E20z} K_x$$

$$a_4 = (J_{3y} + m_3 r_{2z}^2 + m_3 r_{1z} r_{2z} \cos\psi_{yo}) S^2 + K_{Ry} S + K_{py} + \frac{K_{Iy}}{S}$$

$$a_5^N = (J_{3y} + m_3 r_{2z}^2) S^2 + (K_{Ry} + N_{\psi y}) S + (K_{py} + K_{WT\psi y}) + \frac{K_{Iy}}{S} \tag{5-40}$$

$$a_6 = m_3 r_{2z} \cos\psi_{yo} S^2$$

$$a_7 = -m_3 r_{xy} \sin\psi_{yo} S^2$$

$$a_8 = (m_3 r_{1z} + m_3 r_{2z} \cos\psi_{yo}) S^2 + 4D_x R_{E20z} S + 4K_x R_{E20z}$$

$$a_9 = (m_2 + m_3) S^2 + 4D_x S + 4K_x$$

For the system presently under consideration the following parameter values apply:

$m_2 = 195$ Kg

$m_3 = 2.683 \times 10^3$ Kg

$J_{2y} = 50$ Kg-m^2

$J_{3y} = 2.648 \times 10^3$ Kg-m^2

$r_{1z} = .375$ m

$r_{2z} = 1.689$ m

$R_{E20z} = -.375$ m

$d_y = 14.96 \frac{\text{n-m-sec}}{\text{rad}}$

$k_y = 31.25 \frac{\text{n-m}}{\text{rad}}$

$D_x = 59.93 \frac{\text{n-sec}}{\text{m}}$

$K_x = 125 \frac{\text{n}}{\text{m}}$

$K_{Ry} = 1.972 \times 10^4 \frac{\text{n-m-sec}}{\text{rad}}$

$K_{py} = 7.00 \times 10^4 \frac{\text{n-m}}{\text{rad}}$

$K_{Iy} = 1.105 \times 10^5 \frac{\text{n-m}}{\text{sec}}$

5.1.3.1 Limit Cycles for Zero Telescope Look Angles - Assuming $K_{WT\psi y} = 25 \frac{\text{n-m}}{\text{rad}}$ and $\psi_{yo} = 0$ the following results upon substitution of the system parameter values into equation (5-40).

$$a_1 = 2.12664\times10^3 S^2 - 1.96713\times10^4 S - 6.98984\times10^4 - \frac{1.105\times10^5}{S}$$

$$a_2^N = 1.69935\times10^3 S^2 - (1.972\times10^4 + N_{\psi y})S - (7.0025\times10^4) - \frac{1.105\times10^5}{S}$$

$$a_3 = 1.00613\times10^3 S^2 - 89.895S - 187.5 \qquad (5\text{-}41)$$

$$a_4 = 1.20012\times10^4 S^2 + (1.972\times10^4)S + (7.00\times10^4) + \frac{1.105\times10^5}{S}$$

$$a_5^N = 1.03019\times10^4 S^2 + (1.972\times10^4 + N_{\psi y})S + (7.0025\times10^4) + \frac{1.105\times10^5}{S}$$

$$a_6 = 4.53159\times10^3 S^2$$

$$a_7 = 0$$

$$a_8 = 5.53771\times10^3 S^2 - 89.895S - 187.5$$

$$a_9 = 2.878\times10^3 S^2 + 239.72S + 500$$

Substituting equation (5-41) into equation (5-39) and evaluating the expression yields:

$$\Delta = 6.5039\times10^8 S^7 + 1.5783\times10^{10} S^6 + 7.283\times10^{10} S^5 + 2.2356\times10^{11} S^4 + 3.57909\times10^{11} S^3$$
$$+ 2.87111\times10^{11} S^2 + 2.6\times10^9 S + 1.7\times10^9 + N_{\psi y} S^2 [9.99371\times10^6 S^4 + 4.8795\times10^6 S^3 + 9.437\times10^6 S^2$$
$$+ 1.4\times10^4 S + 1.56\times10^4] = 0 \qquad (5\text{-}42)$$

Rearranging the terms in equation (5-42) gives

$$\frac{S^2[9.99371\times10^6 S^4 + 4.8795\times10^6 S^3 + 9.437\times10^6 S^2 + 1.4\times10^4 S + 1.56\times10^4]}{(6.5039\times10^8 S^7 + 1.5783\times10^{10} S^6 + 7.283\times10^{10} S^5 + 2.2356\times10^{11} S^4 + 3.57909\times10^{11} S^3} = -\frac{1}{N_{\psi y}}$$
$$+ 2.87111\times10^{11} S^2 + 2.6\times10^9 S + 1.7\times10^9) \qquad (5\text{-}43)$$

Substituting $S=j\omega$ into equation (5-43) results in

$$\frac{\omega^2\{(9.99371\times10^6\omega^4 - 9.437\times10^6\omega^2 + 1.56\times10^4) + j(-4.8795\times10^6\omega^3 + 1.4\times10^4\omega)\}}{[-1.5783\times10^{10}\omega^6 + 2.2356\times10^{11}\omega^4 - 2.87111\times10^{11}\omega^2 + 1.7\times10^9]} = \frac{1}{N_{\psi y}}$$
$$+ j[-6.5039\times10^8\omega^7 + 7.283\times10^{10}\omega^5 - 3.57909\times10^{11}\omega^3 + 2.6\times10^9\omega] \qquad (5\text{-}44)$$

In order for equation (5-44) to be valid the imaginary part must be equal to zero. Rationalizing equation (5-44) results in the following necessary condition.

$$\omega^{10}-1.01075\text{x}10^{2}\omega^{8}+4.88179\text{x}10^{2}\omega^{6}-3.07797\text{x}10^{2}\omega^{4}+2.7393\omega^{2}-2.57854\text{x}10^{-3} = 0 \quad (5\text{-}45)$$

Solving equation (5-45) for ω gives

$$\omega = \pm.03271$$

$$\omega = \pm.08914$$

$$\omega = \pm.8564 \quad (5\text{-}46)$$

$$\omega = \pm2.0756$$

$$\omega = \pm9.7992$$

In order to determine whether all of the solutions for ω given in equation (5-46) are possible limit cycle points, the various solutions will have to be inserted into the real part of equation (5-44), given in equation (5-47), the results evaluated and shown to be positive

$$\text{Real Part} = \omega^{2}\{(9.99371\text{x}10^{6}\omega^{4}-9.437\text{x}10^{6}\omega^{2}+1.56\text{x}10^{4}) (-1.5783\text{x}10^{10}\omega^{6}+2.2356\text{x}10^{11}\omega^{4}-2.87111\text{x}10^{11}\omega^{2}+1.7\text{x}10^{9}) +(-4.8795\text{x}10^{6}\omega^{3}+1.4\text{x}10^{4}\omega) (-6.5039\text{x}10^{8}\omega^{7}+7.283\text{x}10^{10}\omega^{5}-3.57909\text{x}10^{11}\omega^{3}+2.6\text{x}10^{9}\omega)\}$$
$$\overline{(-1.5783\text{x}10^{10}\omega^{6}+2.2356\text{x}10^{11}\omega^{4}-2.87111\text{x}10^{11}\omega^{2}+1.7\text{x}10^{9})^{2}+(-6.5039\text{x}10^{8}\omega^{7} +7.283\text{x}10^{10}\omega^{5}-3.57909\text{x}10^{11}\omega^{3}+2.6\text{x}10^{9}\omega)^{2}} \quad (5\text{-}47)$$

When the above procedure is followed the solution of ω=9.7992 rad/sec is not a possible limit cycle point while all the others are..

The amplitude of the predicted limit cycles can be obtained by substitution of the predicted limit cycle frequency into the "real part" given in equation (5-47) and solving the following

$$\text{Real Part } (\omega_{\text{L.S.}}) = \frac{1}{N_{\psi y}} \quad (5\text{-}48)$$

Following this procedure the amplitude of the predicted limit cycles are shown in table 5-1.

Table 5-1. Limit Cycle Amplitude for Zero Telescope Look Angle

LIMIT CYCLE FREQUENCY (Hz)	RELATIVE RATE ($\dot{\psi}_y$) LIMIT CYCLE AMPLITUDE (rad/sec)	RELATIVE ANGLE (ψ_y) LIMIT CYCLE AMPLITUDE (rad)
5.206×10^{-3}	5.393×10^{-9}	1.649×10^{-7}
1.419×10^{-2}	1.048×10^{-6}	1.176×10^{-5}
0.136	2.054×10^{-5}	2.398×10^{-5}
0.33	4.809×10^{-4}	2.317×10^{-5}

One last piece of information to be determined is the stability of the limit cycle points that have been computed above. In order to ascertain limit cycle stability an analytical procedure outlined in a text titled "Multiple-Input Describing Functions and Nonlinear System Design" by A. Gelb and W. E. VanderVelde, is employed. This procedure requires that "jω" be substituted for "S" in equation (5-42) and the resultant expression be written in terms of real and imaginery parts as follows

$$\Delta = U(\dot{\psi}_y,\omega)+jV(\dot{\psi}_y,\omega) = 0 \qquad (5\text{-}49)$$

In order for a stable limit cycle to exist the following condition must be met

$$\left(\frac{\partial U}{\partial \dot{\psi}_y}_{\omega=\omega_{L.S.}}\right)\left(\frac{\partial V}{\partial \omega}_{\omega=\omega_{L.S.}}\right)-\left(\frac{\partial U}{\partial \omega}_{\omega=\omega_{L.S.}}\right)\left(\frac{\partial V}{\partial \dot{\psi}_y}_{\omega=\omega_{L.S.}}\right) > 0 \qquad (5\text{-}50)$$

Performing the above outlined operations and computing the partial derivatives indicated in equation (5-50) gives

$$\frac{\partial U}{\partial \dot{\psi}_y} = \frac{N_{\psi y}}{\dot{\psi}_y}\left[9.99371\text{x}10^{6}\omega^{6}-9.437\text{x}10^{6}\omega^{4}+1.56\text{x}10^{4}\omega^{2}\right]$$

$$\frac{\partial V}{\partial \dot{\psi}_y} = \frac{N_{\psi y}}{\dot{\psi}_y}\left[-4.8795\text{x}10^{6}\omega^{5}+1.4\text{x}10^{4}\omega^{3}\right]$$

$$\frac{\partial U}{\partial \omega} = -6(1.5783\text{x}10^{10}+9.99371\text{x}10^{6}N_{\psi y})\omega^{5}+4(2.2356\text{x}10^{11}+9.437\text{x}10^{6}N_{\psi y})\omega^{3} \qquad (5\text{-}51)$$
$$-2(2.87111\text{x}10^{11}+1.56\text{x}10^{4}N_{\psi y})\omega$$

$$\frac{\partial V}{\partial \omega} = -7(6.5039\text{x}10^{8})\omega^{6}+5(7.283\text{x}10^{10}+4.8795N_{\psi y})\omega^{4}$$
$$-3(3.57909\text{x}10^{11}+1.4\text{x}10^{4}N_{\psi y})\omega^{2}+2.6\text{x}10^{9}$$

Applying the stability criterion of equation (5-50) shows that the limit cycles occurring at $5.206\text{x}10^{-3}$ and 0.136 Hz are unstable while those occurring at $1.419\text{x}10^{-2}$ and 0.33 Hz are stable.

The actual limit cycles observed on the IOG time simulation for zero telescope look angle was at a frequency of 0.3229 Hz and the amplitudes of the relative rate and angle were $6.375\text{x}10^{-4}$ $\frac{\text{rad}}{\text{sec}}$ and $3.142\text{x}10^{-4}$ rad respectively. This is in close agreement with the limit cycle frequency and amplitude predicted via the analysis outlined above. However, a limit cycle at approximately 0.014 Hz that is predicted by the analysis was never observed on the actual time simulation. The reason for this is the finite bite size and sampling frequency that is employed in the simulation. The limit cycle amplitudes due to the sampled data effects were approximately a factor 60 larger than the level of limit cycle predicted at 0.014 Hz by the anlaysis. Hence the system cannot sustain this low amplitude limit cycle oscillation and goes into the limit cycle condition dictated by the sampled data effects.

In addition, the analysis described above indicates that the limit cycle frequency is independent of both wire torque jump and wire torque slope while limit cycle amplitude is directly proportional to wire torque jump. Both these effects have been verified on the IOG time simulation.

5.1.3.2 Limit Cycles for 40° Telescope Look Angle - Substituting the parameters listed in section 5.1.3 with $\psi_{yo} = 40°$ and $K_{WT\psi y} =$ 25 n-m/rad into equation (5-40) the following results.

$$a_1 = 1.72907\text{x}10^3S^2-1.96713\text{x}10^4S-6.98984\text{x}10^4-\frac{1.105\text{x}10^5}{S}$$

$$a_2^N = 1.30177\text{x}10^3S^2-(1.972\text{x}10^4+N_{\psi y})S-(7.0025\text{x}10^4)-\frac{1.105\text{x}10^5}{S}$$

$$a_3 = 1.00613\text{x}10^3S^2-89.895S-187.5$$

$$a_4 = 1.16036\text{x}10^4S^2+1.972\text{x}10^4S+7\text{x}10^4+\frac{1.105\text{x}10^5}{S}$$

$$a_5^N = 1.03019\text{x}10^4S^2+(1.972\text{x}10^4+N_{\psi y})S+(7.0025\text{x}10^4)+\frac{1.105\text{x}10^5}{S} \qquad (5\text{-}52)$$

$$a_6 = 3.4714\times10^{3}s^{2}$$

$$a_7 = -2.91285\times10^{3}s^{2}$$

$$a_8 = 4.47752\times10^{3}s^{2}-89.895s-187.5$$

$$a_9 = 2.878\times10^{3}s^{2}+239.72s+500$$

Substituting equation (5-52) into equation (5-39) and evaluating yields

$$\Delta = 1.91726\times10^{12}s^{8}+3.22055\times10^{13}s^{7}+1.66498\times10^{14}s^{6}+5.05956\times10^{14}s^{5}+8.46079\times10^{14}s^{4}$$
$$+8.49024\times10^{14}s^{3}+2.01736\times10^{14}s^{2}+1.27138\times10^{14}s+1.7\times10^{12}+\frac{8.7\times10^{11}}{s}$$
$$+N_{\psi y}[2.83152\times10^{10}s^{7}+1.4278\times10^{10}s^{6}+3.0781\times10^{10}s^{5}+4.19\times10^{9}s^{4}+4.369\times10^{9}s^{3}$$
$$+1.1\times10^{7}s^{2}+7.8\times10^{6}s] = 0 \qquad (5-53)$$

Rearranging terms gives

$$\frac{2.83152\times10^{10}s^{8}+1.4278\times10^{10}s^{7}+3.0781\times10^{10}s^{6}\ 4.19\times10^{9}s^{5}+4.369\times10^{9}s^{4}+1.1\times10^{7}s^{3}+7.8\times10^{6}s^{2}}{1.91726\times10^{12}s^{9}+3.22055\times10^{13}s^{8}+1.66498\times10^{14}s^{7}+5.05956\times10^{14}s^{6}+8.46079\times10^{14}s^{5}}$$
$$+8.49024\times10^{14}s^{4}+2.01736\times10^{14}s^{3}+1.27138\times10^{14}s^{2}+1.7\times10^{12}s+8.7\times10^{11} \qquad = -\frac{1}{N_{\psi y}}$$

(5-54)

Substituting $s=j\omega$ into equation (5-54) results in

$$\frac{+\omega^{2}[(-2.83152\times10^{10}\omega^{6}+3.0781\times10^{10}\omega^{4}-4.369\times10^{9}\omega^{2}+7.8\times10^{6})+j(1.4278\times10^{10}\omega^{5}-4.19\times10^{9}\omega^{3}+1.1\times10^{7}\omega)]}{(3.22055\times10^{13}\omega^{8}-5.05956\times10^{14}\omega^{6}+8.49024\times10^{14}\omega^{4}1.27138\times10^{14}\omega^{2}+8.7\times10^{11})+j(1.91726\times10^{12}\omega^{9}-1.66498\times10^{14}\omega^{7}+8.46079\times10^{14}\omega^{5}-2.01736\times10^{14}\omega^{3}+1.7\times10^{12}\omega)} = +\frac{1}{N_{\psi y}}$$

(5-55)

In order for equation (5-55) to be valid the imaginary part of the left hand of the equation must be equal to zero. This leads to the following constraint equation as a necessary condition for system limit cycles.

$$\omega^{14}-79.4585\omega^{12}+400.298\omega^{10}-335.99\omega^{8}+84.3163\omega^{6}-7.10739\omega^{4}+7.28899\times10^{-2}\omega^{2}$$
$$-6.79713\times10^{-5} = 0 \qquad (5\text{-}56)$$

Solving equation (5-56) results in the following

$$\omega = \pm.103175$$
$$= \pm.032185$$
$$= -.416312\pm j.04158$$
$$= +.416312\pm j.04158 \qquad (5\text{-}57)$$
$$= \pm 2.0887$$
$$= \pm.78875$$
$$= \pm 8.6092$$

In order to determine if each of the possible solutions shown in equation (5-51) are possible limit cycle points they each must be substituted into the real part of equation (5-55) and the result shown to be positive. The real part of equation (5-55) is given by equation (5-58).

$$\text{Real Part} = \omega^{2}\{(-2.83152\times10^{10}\omega^{6}+3.0781\times10^{10}\omega^{4}-4.369\times10^{9}\omega^{2}+7.8\times10^{6})$$
$$(3.22055\times10^{13}\omega^{8}-5.05956\times10^{14}\omega^{6}+8.49024\times10^{14}\omega^{4}-1.27138\times10^{14}\omega^{2}+8.7\times10^{11})$$
$$+(1.4278\times10^{10}\omega^{5}-4.19\times10^{9}\omega^{3}+1.1\times10^{7}\omega)(1.91726\times10^{12}\omega^{9}-1.66498\times10^{14}\omega^{7}$$
$$+8.46079\times10^{14}\omega^{5}-2.01736\times10^{14}\omega^{3}+1.7\times10^{12}\omega)$$
$$\frac{}{(3.22055\times10^{13}\omega^{8}-5.05956\times10^{14}\omega^{6}+8.49024\times10^{14}\omega^{4}-1.27138\times10^{14}\omega^{2}+8.7\times10^{11})^{2}}$$
$$+(1.91726\times10^{12}\omega^{9}-1.66498\times10^{14}\omega^{7}+8.46079\times10^{14}\omega^{5}-2.01736\times10^{14}\omega^{3}+1.7\times10^{12}\omega)^{2}$$
$$(5\text{-}58)$$

Substitution of the possible limit cycle frequencies shown in equation (5-57) into equation (5-58) reveals that the solution for "ω" of 8.6092 rad/sec cannot be a limit cycle point. Following the same procedure as outlined in section 5.1.3.1 the amplitude of the various possible limit cycles are given in table 5-2.

The stability of the limit cycle points computed above is determined in the same manner as outlined in section 5.1.3.1. The partial derivatives required to evaluate limit cycle stability are given in equation (5-59).

$$\frac{\partial U}{\partial \dot{\psi}_y} = \frac{N_{\psi y}}{\dot{\psi}_y}[-2.83152\text{x}10^{10}\omega^8+3.0781\text{x}10^{10}\omega^6-4.369\text{x}10^{9}\omega^4+7.8\text{x}10^{6}\omega^2]$$

$$\frac{\partial V}{\partial \dot{\psi}_y} = \frac{N_{\psi y}}{\dot{\psi}_y}[1.4278\text{x}10^{10}\omega^7-4.19\text{x}10^{9}\omega^5+1.1\text{x}10^{7}\omega^3] \qquad (5\text{-}59)$$

$$\frac{\partial U}{\partial \omega} = 8(3.22055\text{x}10^{13}+2.83152\text{x}10^{10}N_{\psi y})\omega^7-6(5.05956\text{x}10^{14}+3.0781\text{x}10^{10}N_{\psi y})\omega^5$$

$$+4(8.49024\text{x}10^{14}+4.369\text{x}10^{9}N_{\psi y})\omega^3-2(1.27138\text{x}10^{14}+7.8\text{x}10^{6}N_{\psi y})\omega$$

$$\frac{\partial V}{\partial \omega} = 9(1.91726\text{x}10^{12})\omega^8-7(1.66498\text{x}10^{14}+1.4278\text{x}10^{10}N_{\psi y})\omega^6$$

$$+5(8.46079\text{x}10^{14}+4.19\text{x}10^{9}N_{\psi y})\omega^4-3(2.01736\text{x}10^{14}+1.1\text{x}10^{7}N_{\psi y})\omega^2+1.7\text{x}10^{12}$$

Applying the limit cycle stability criteria shows that the limit cycle points at $5.122\text{x}10^{-3}$ and 0.126 Hz are unstable while the limit cycle points at $1.642\text{x}10^{-2}$ and 0.332 Hz are stable.

The limit cycle observed on the IOG time simulation (see section 5.2) was at 0.3226 Hz and the amplitudes of the relative rate ($\dot{\psi}_y$) and relative angle (ψ_y) were $7.998\text{x}10^{-4}$ rad/sec and $3.946\text{x}10^{-4}$ rad respectively.

The stable limit cycle at approximately 0.16 Hz predicted by the analysis was not observed on the time simulation for the reason outlined in section 5.3.1.1. It can be seen from these results that the limit cycle frequencies are hardly affected by telescope

Table 5-2. Limit Cycle Amplitude for 40° Telescope Look Angle

LIMIT CYCLE FREQUENCY (Hz)	RELATIVE RATE ($\dot{\psi}_y$) LIMIT CYCLE AMPLITUDE (rad/sec)	RELATIVE ANGLE (ψ_y) LIMIT CYCLE AMPLITUDE (rad)
5.122×10^{-3}	5.901×10^{-9}	1.833×10^{-7}
1.642×10^{-2}	1.232×10^{-6}	1.194×10^{-5}
0.126	1.417×10^{-5}	1.797×10^{-5}
0.332	6.693×10^{-4}	3.204×10^{-4}

look angle while the limit cycle amplitudes are slightly affected by the telescope look angle. In addition, if 1 arc-second total pointing stability is desired from the IOG and 20 percent of this budget is allocated for wire torques the jump in the wire torque characteristic should not exceed 0.05 n-m. For the small telescope described in section 4.1.4 the jump in the wire torque characteristic should not exceed 0.01 n-m if the same ground rules are followed.

5.2 Nonlinear IOG Performance Characteristics - Figures 5-3 to figure 5-11 show IOG system time response for a 40 degree telescope look angle for a jump in wire torque characteristic H_{WT} = 1 n-m and a wire torque slope of $K_{WT\psi y} = 25 \frac{n-m}{rad}$. Figures 5-12 to 5-20 indicate IOG time response for a 40 degree telescope look angle with H_{WT} = 0.5 n-m and $K_{WT\psi y}$ = 25 n-m/rad. The legend used in these figures is explained in table 4-1. Examination of these figures indicate that the telescope y axis limit cycle pointing error is directly proportional to the jump H_{WT} in the wire torque characteristic as implied in section 5.1.3.2. The transients that are observed at the start of the run are due to an initial wire torque of 17.45 n-m which is applied to the telescope when it is rotated to a forty degree look angle. Similarly it is seen that the y axis control torque limit cycles about this point since the control system must produce a torque equal and opposite to the average applied wire torque. In addition due to the geometry of the IOG and the fact that the telescope was only rotated about the y axis results in zero rotational motion of the telescope about the x and z axes, zero rotational motion of the pedestal about the x and z axes, zero translational motion of the pedestal CM along the y axis, and a control torque only being applied to the telescope y axis.

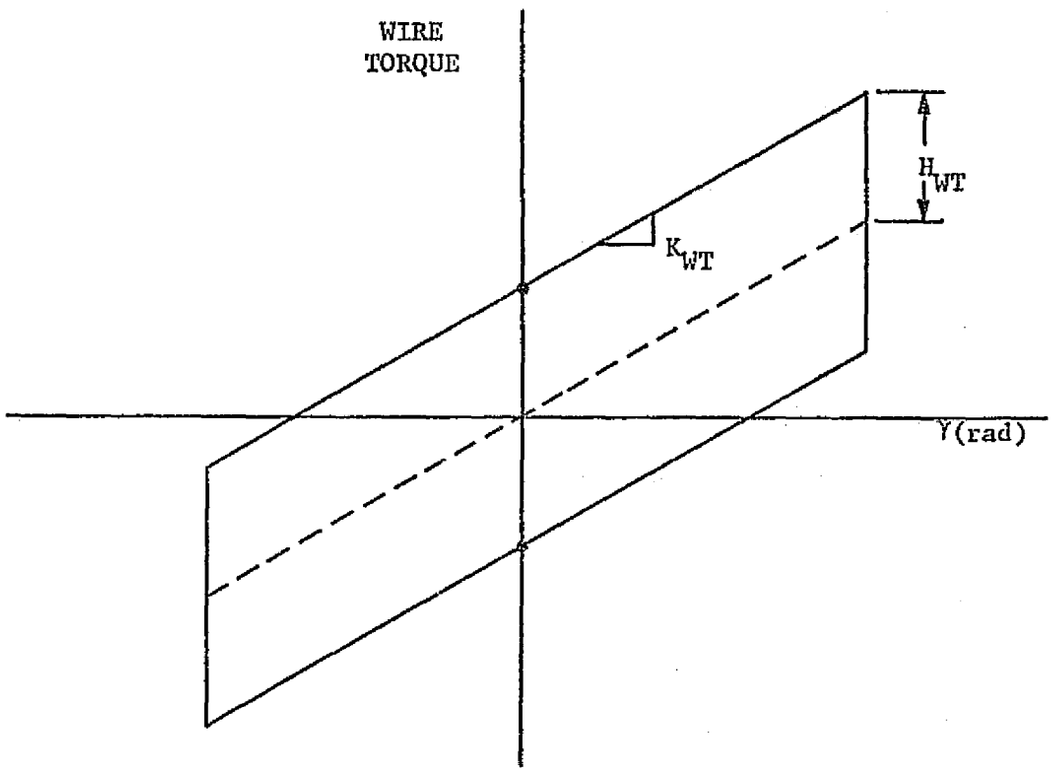

Figure 5-1. IOG Wire Torque Characteristics

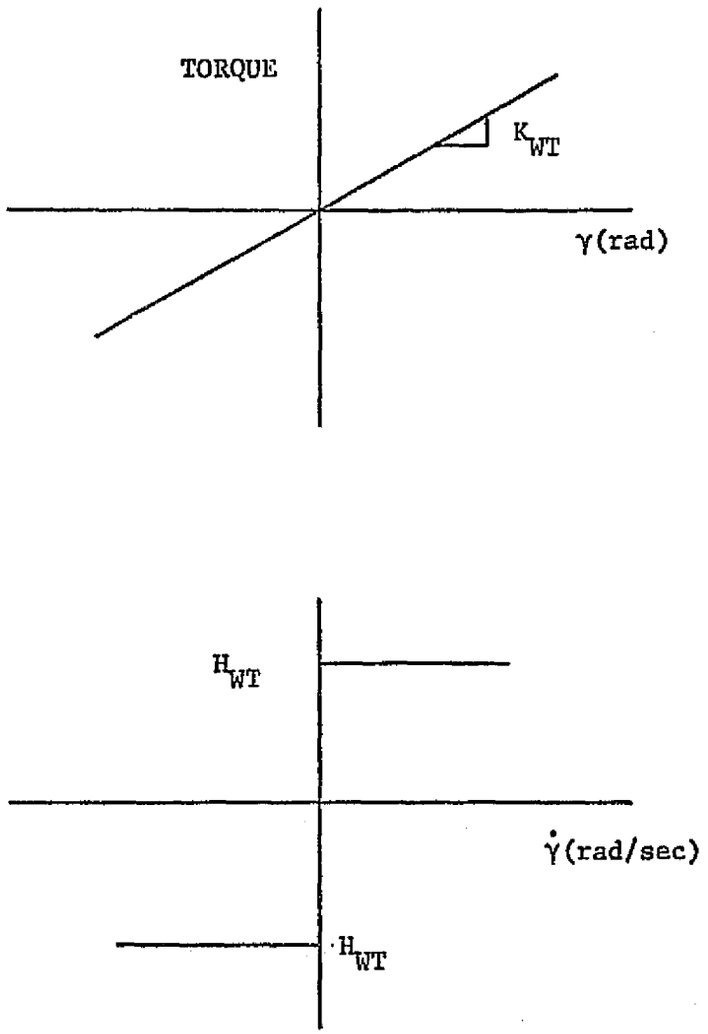

Figure 5-2. Alternate Representation of IOG Wire Torque Characteristic

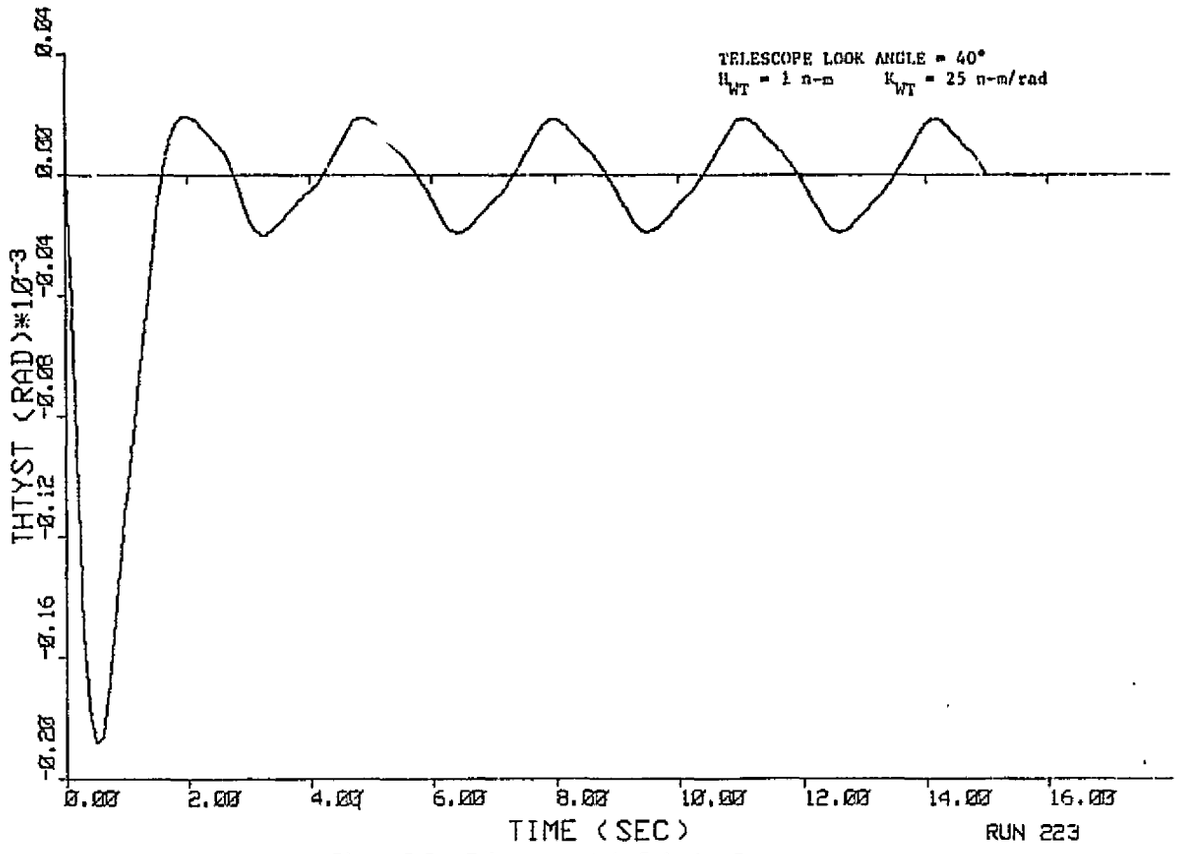

Figure 5-3. Telescope y-Axis Pointing Error

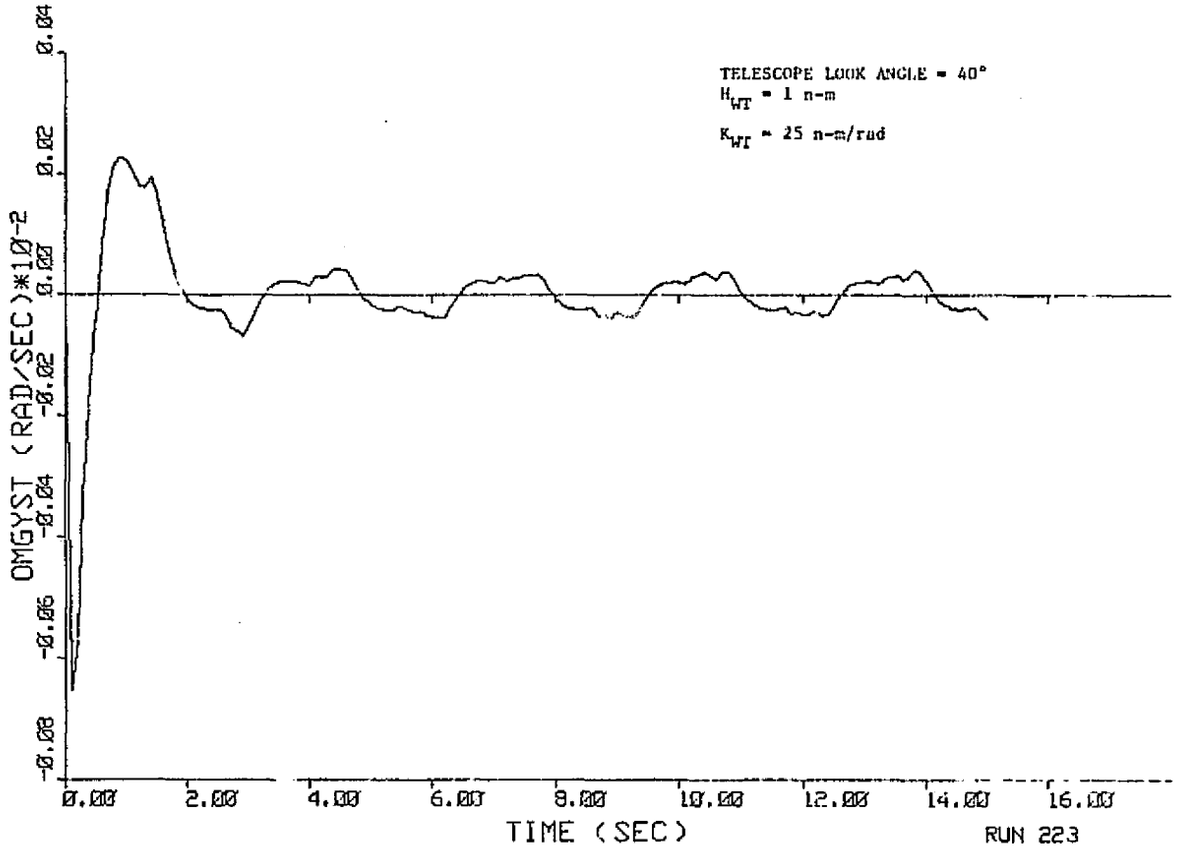

Figure 5-4. Telescope y-Axis Rate Error

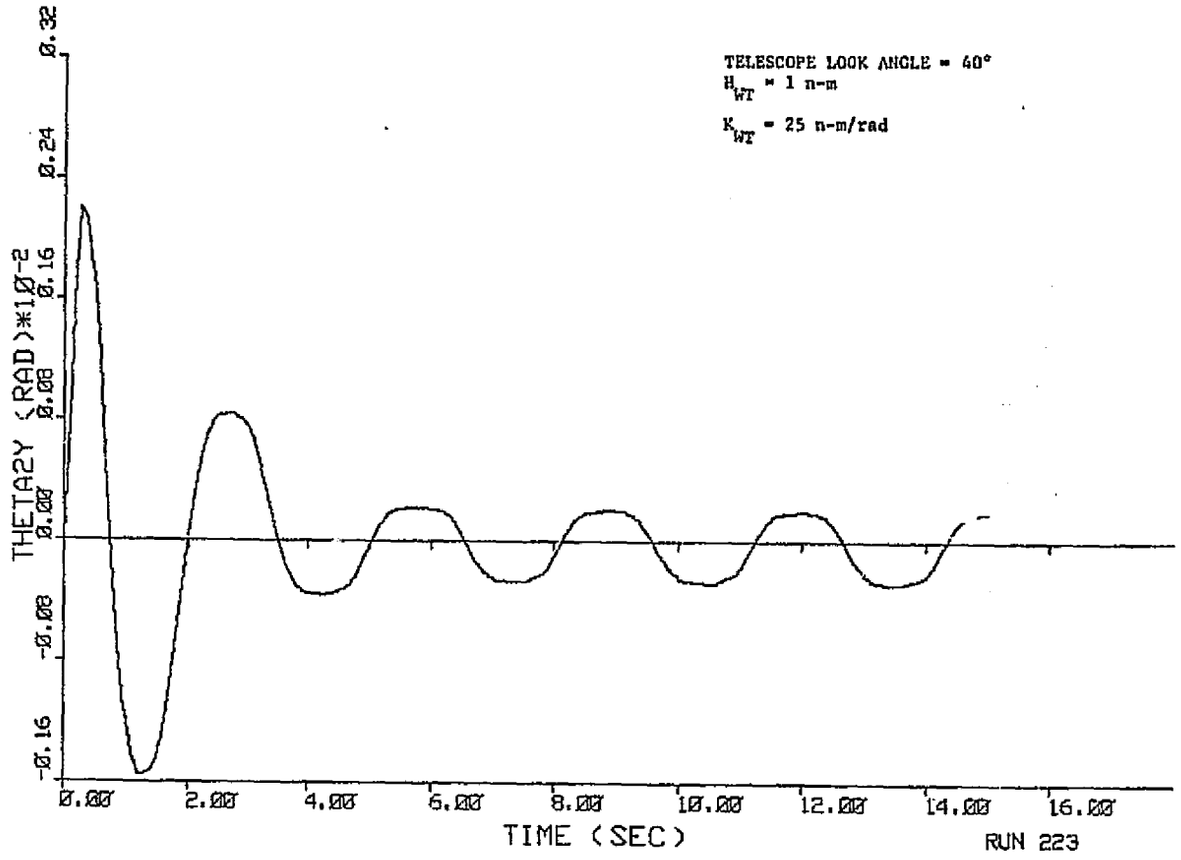

Figure 5-5. Pedestal y-Axis Rotation

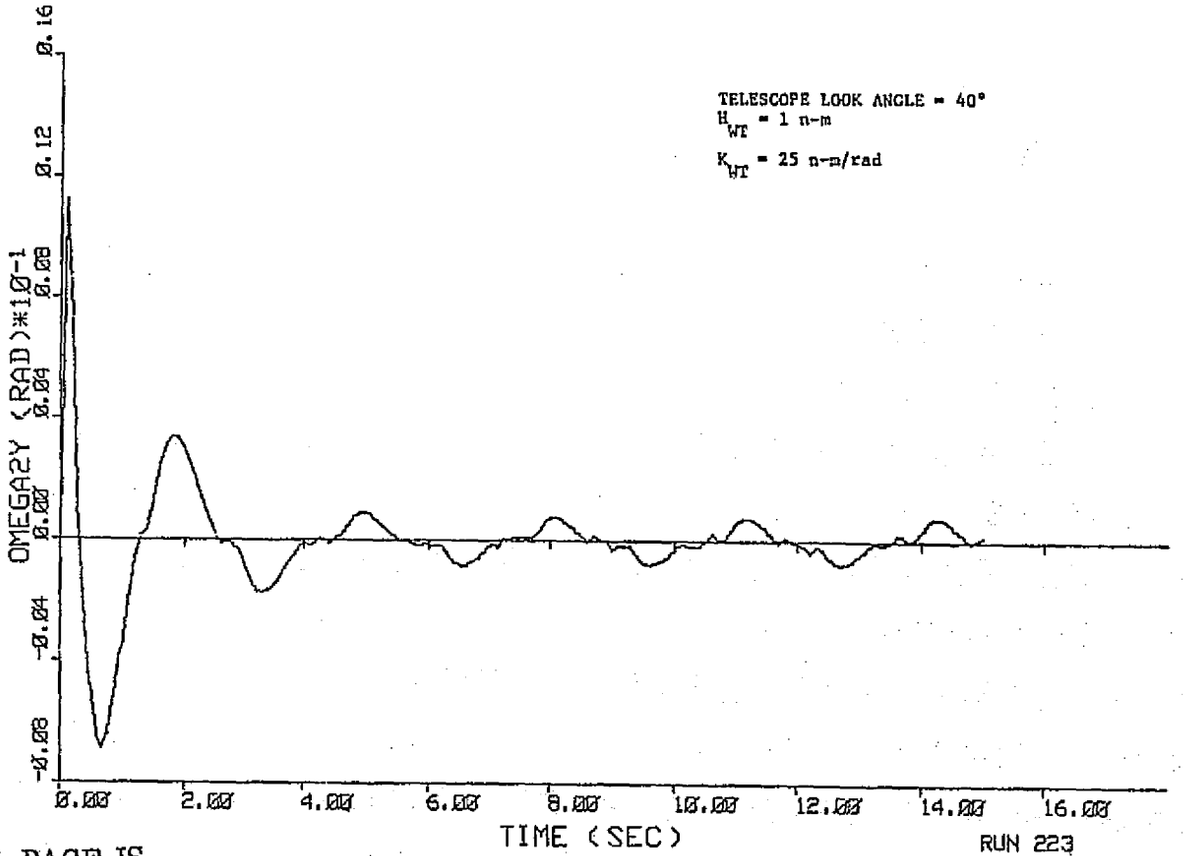

Figure 5-6. Pedestal y-Axis Rate

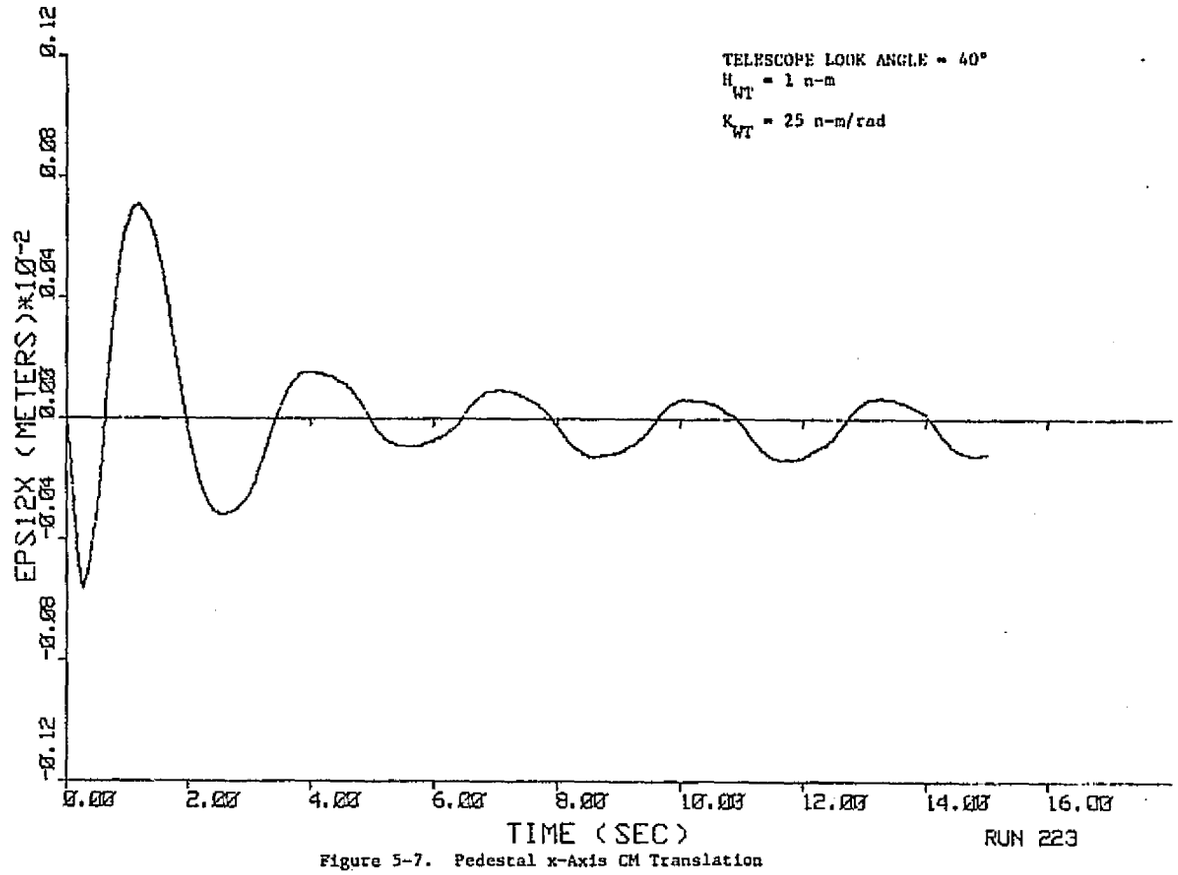

Figure 5-7. Pedestal x-Axis CM Translation

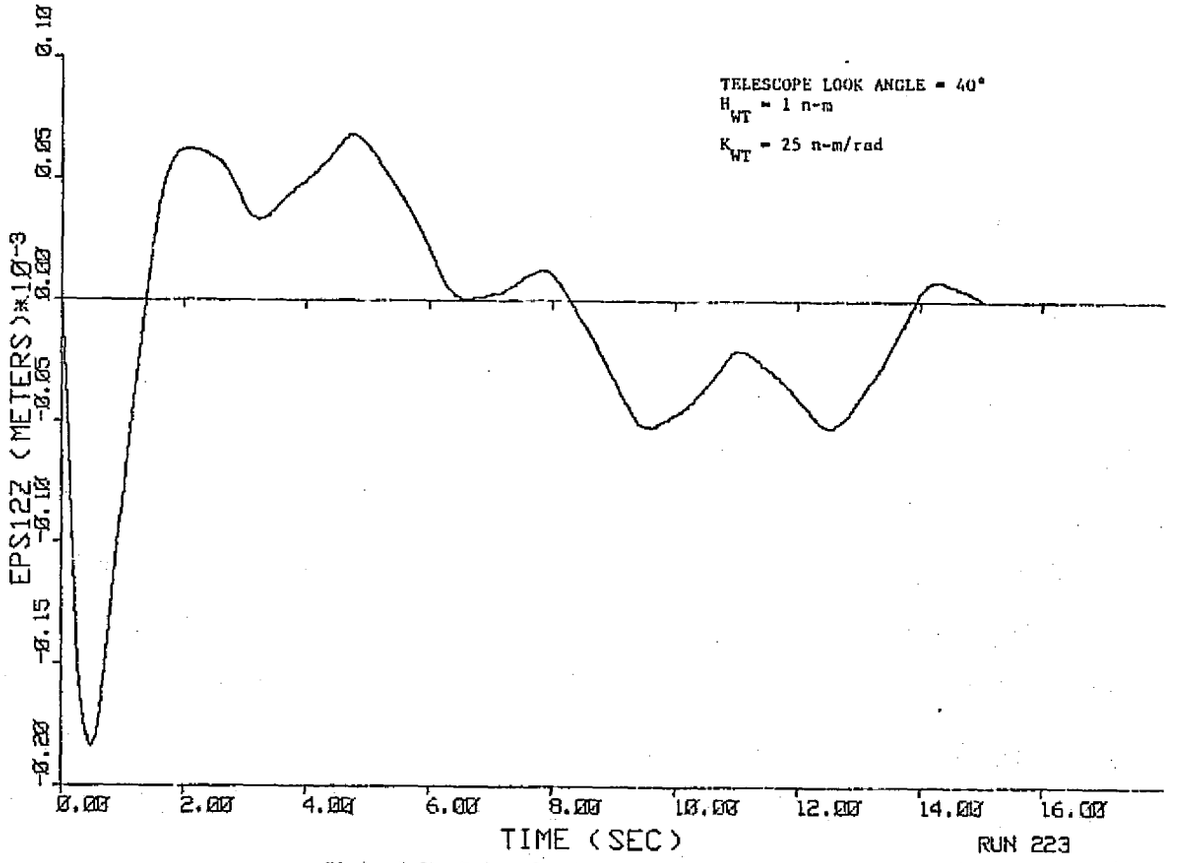

Figure 5-8. Pedestal z-Axis CM Translation

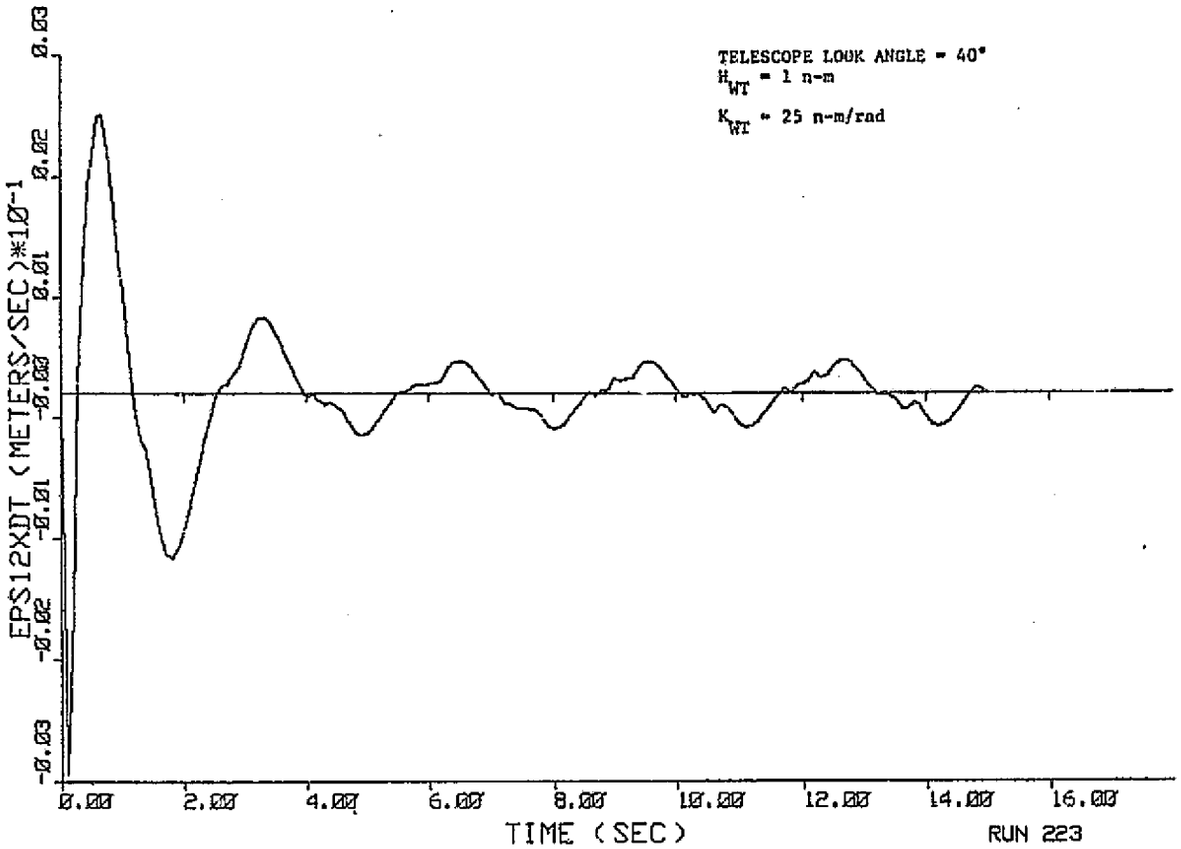

Figure 5-9. Pedestal x-Axis CM Velocity

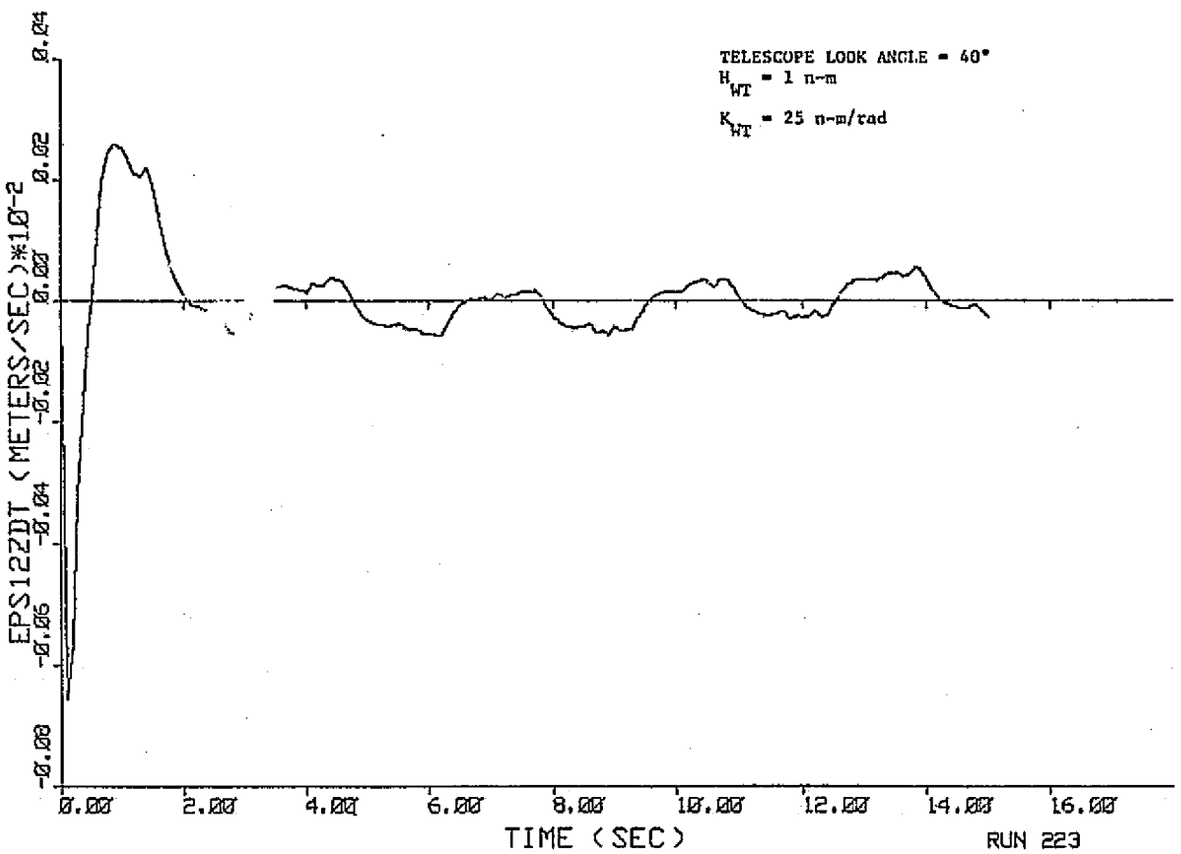

Figure 5-10. Pedestal z-Axis CM Velocity

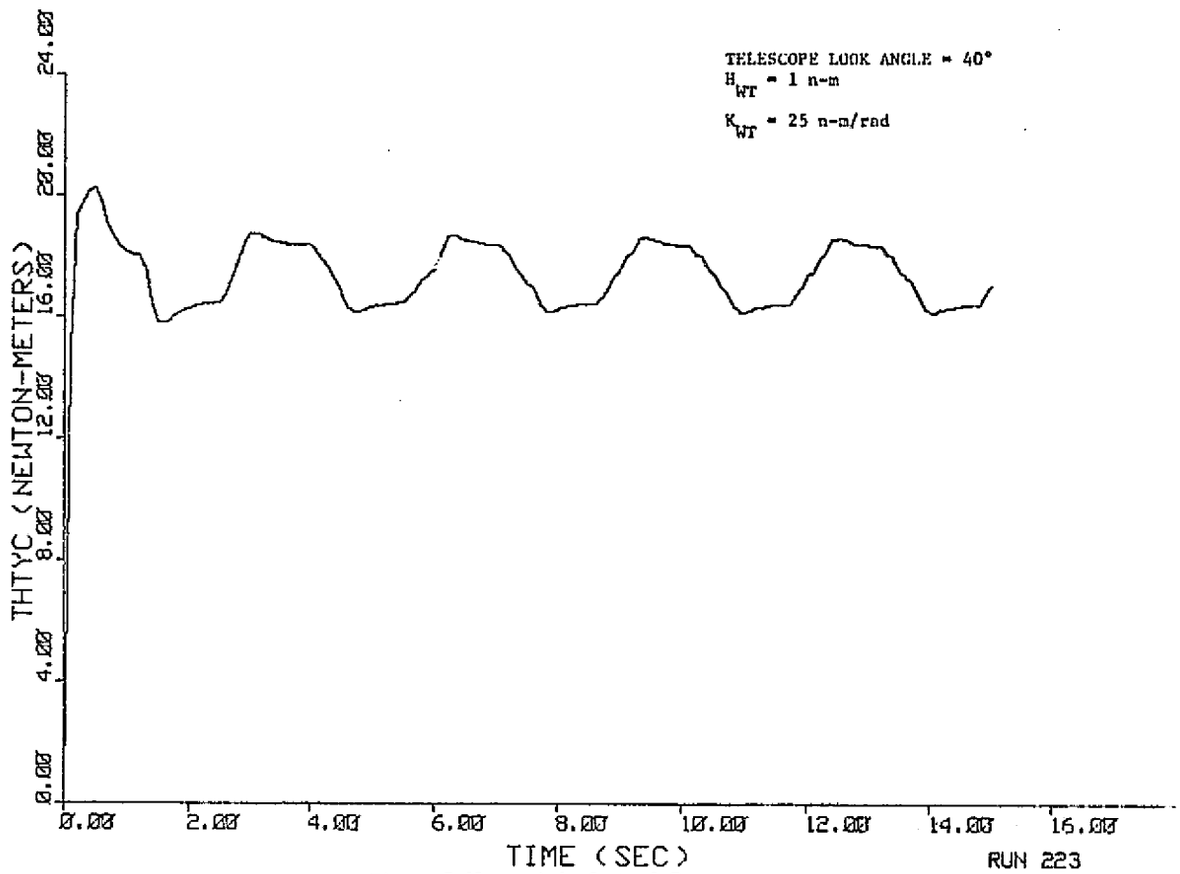

Figure 5-11. y-Axis Control Torque

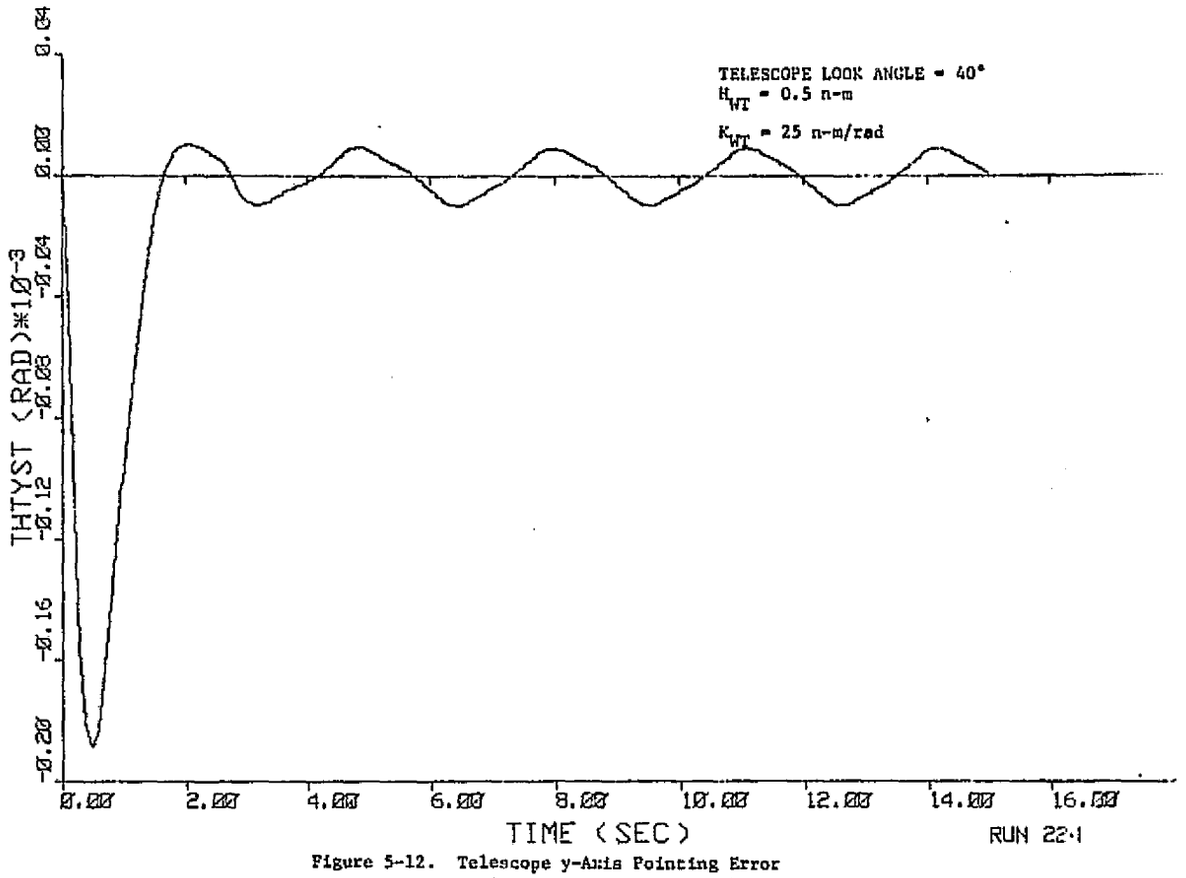

Figure 5-12. Telescope y-Axis Pointing Error

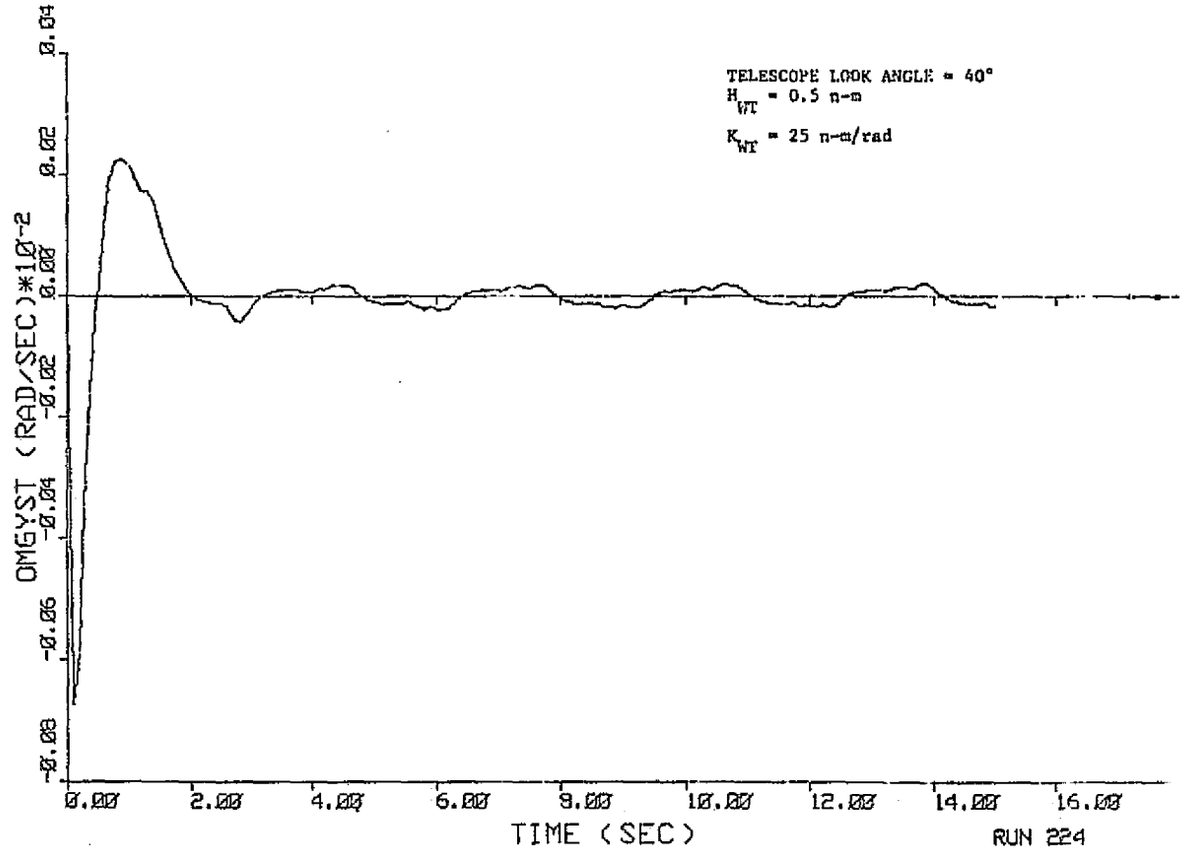

Figure 5-13. Telescope y-Axis Rate Error

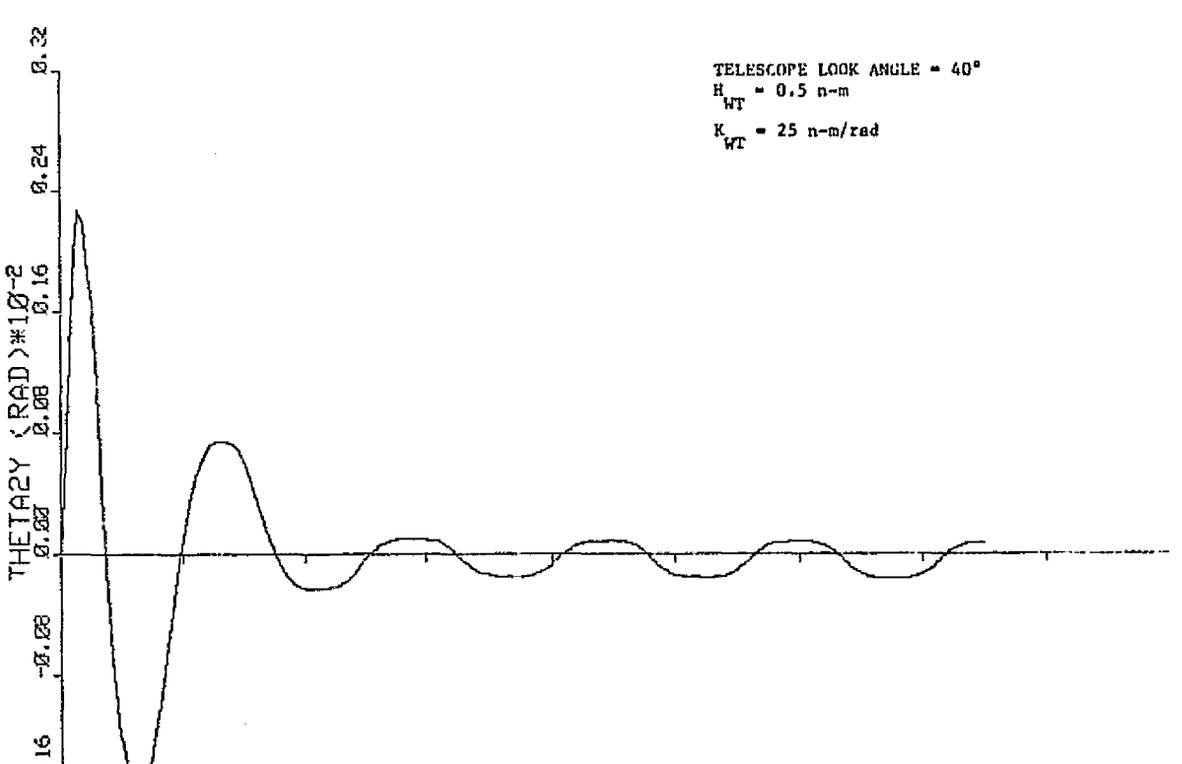

Figure 5-14. Pedestal y-Axis Rotation

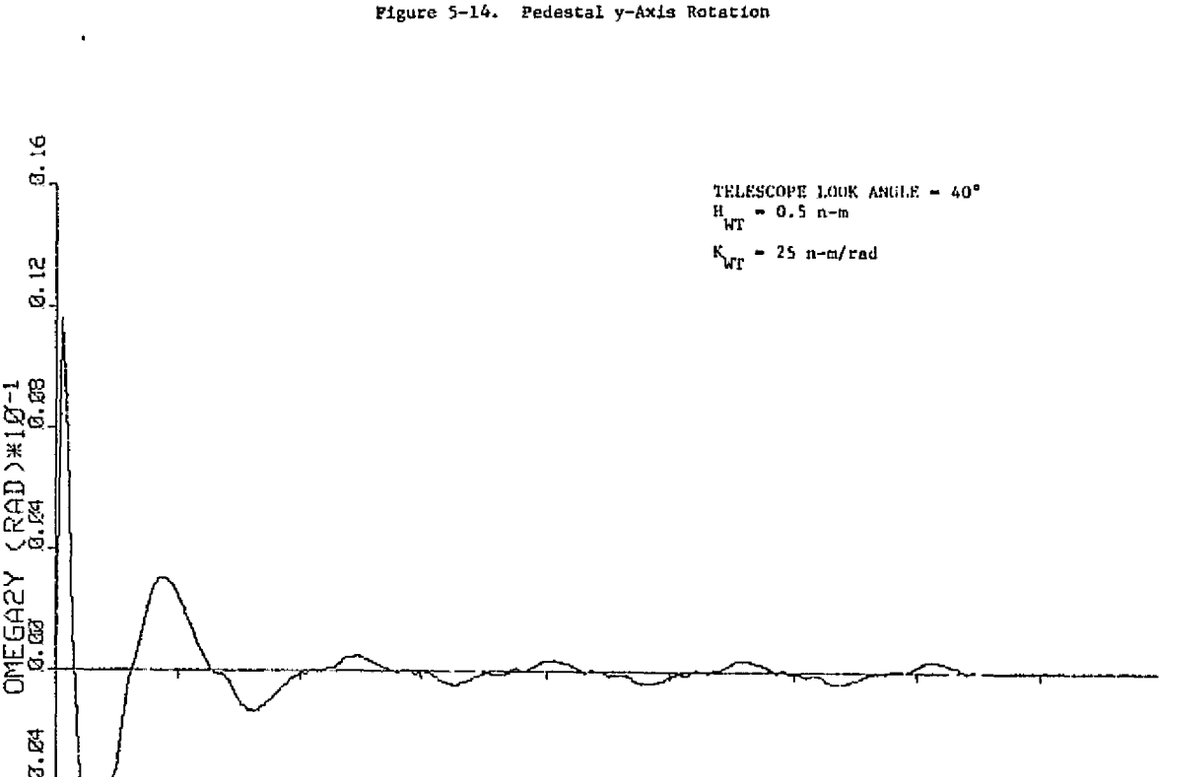

Figure 5-15. Pedestal y-Axis Rate

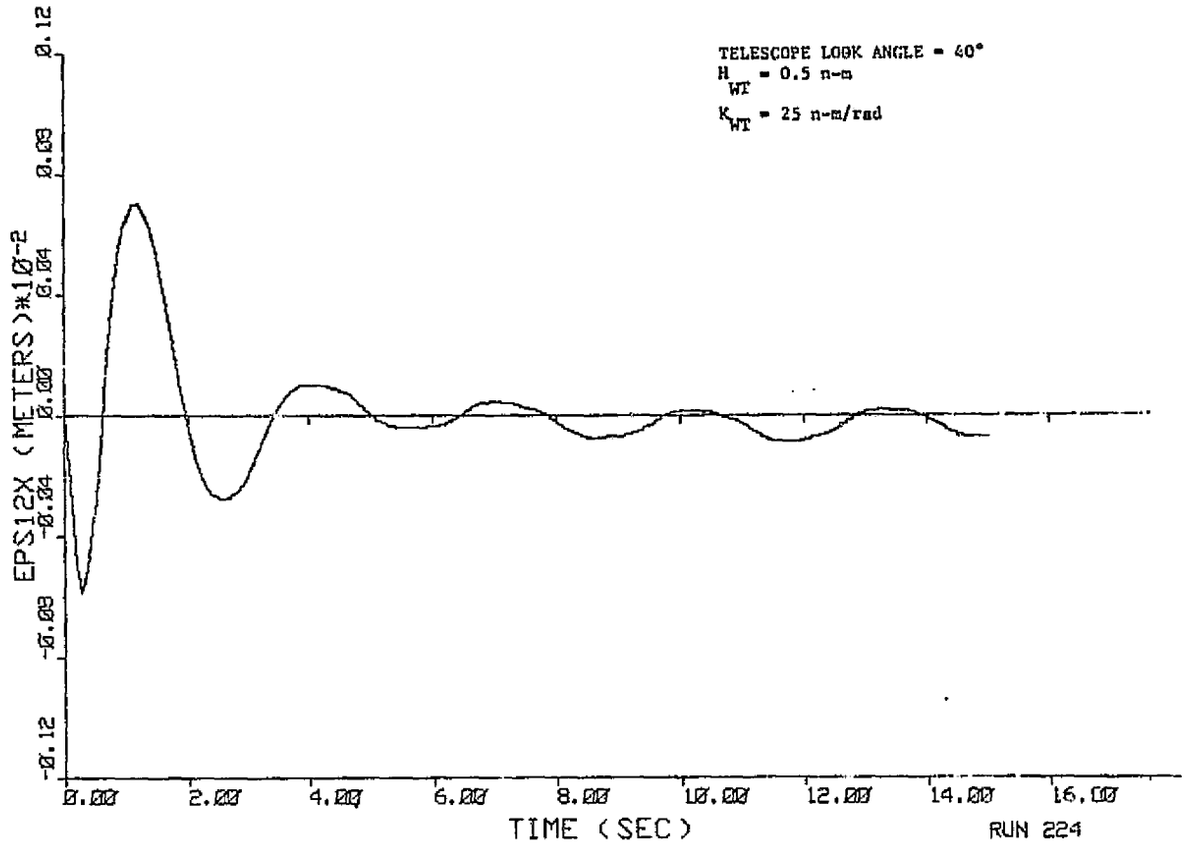

Figure 5-16. Pedestal x-Axis CM Translation

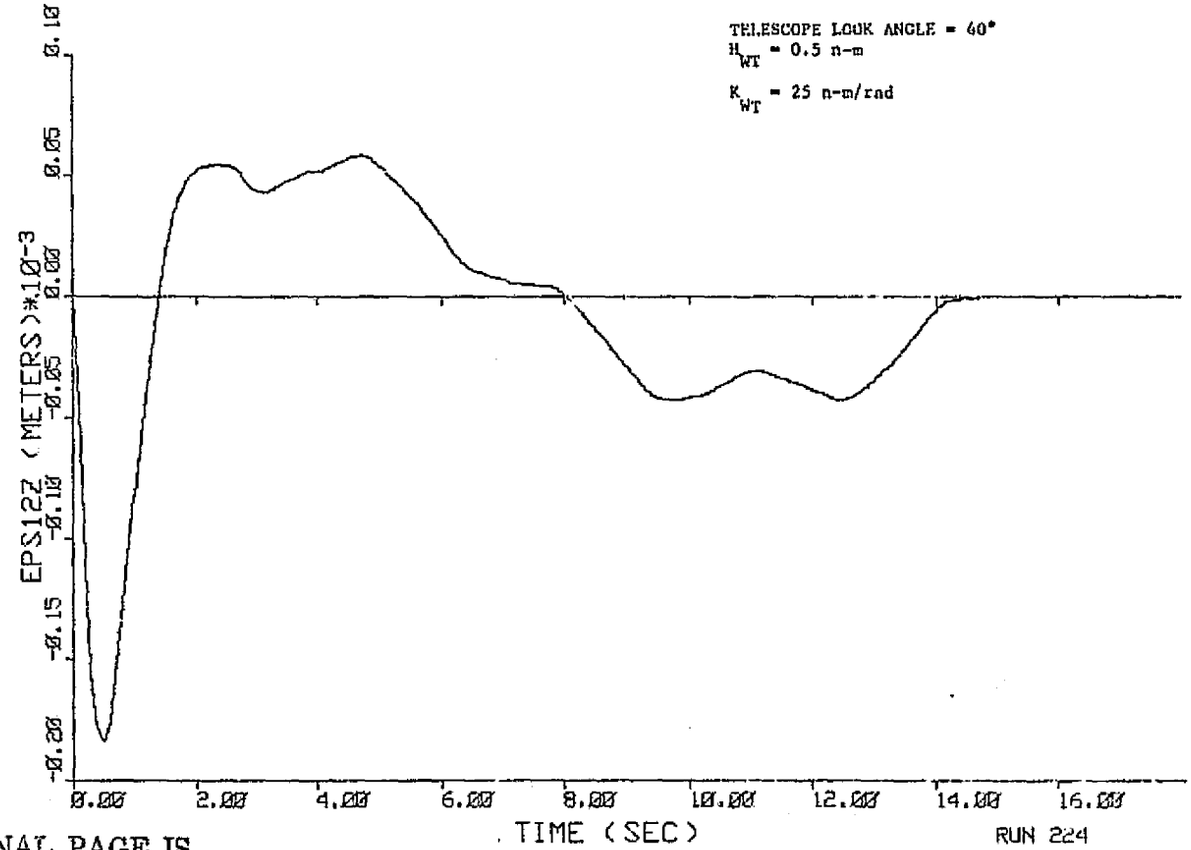

Figure 5-17. Pedestal z-Axis CM Translation

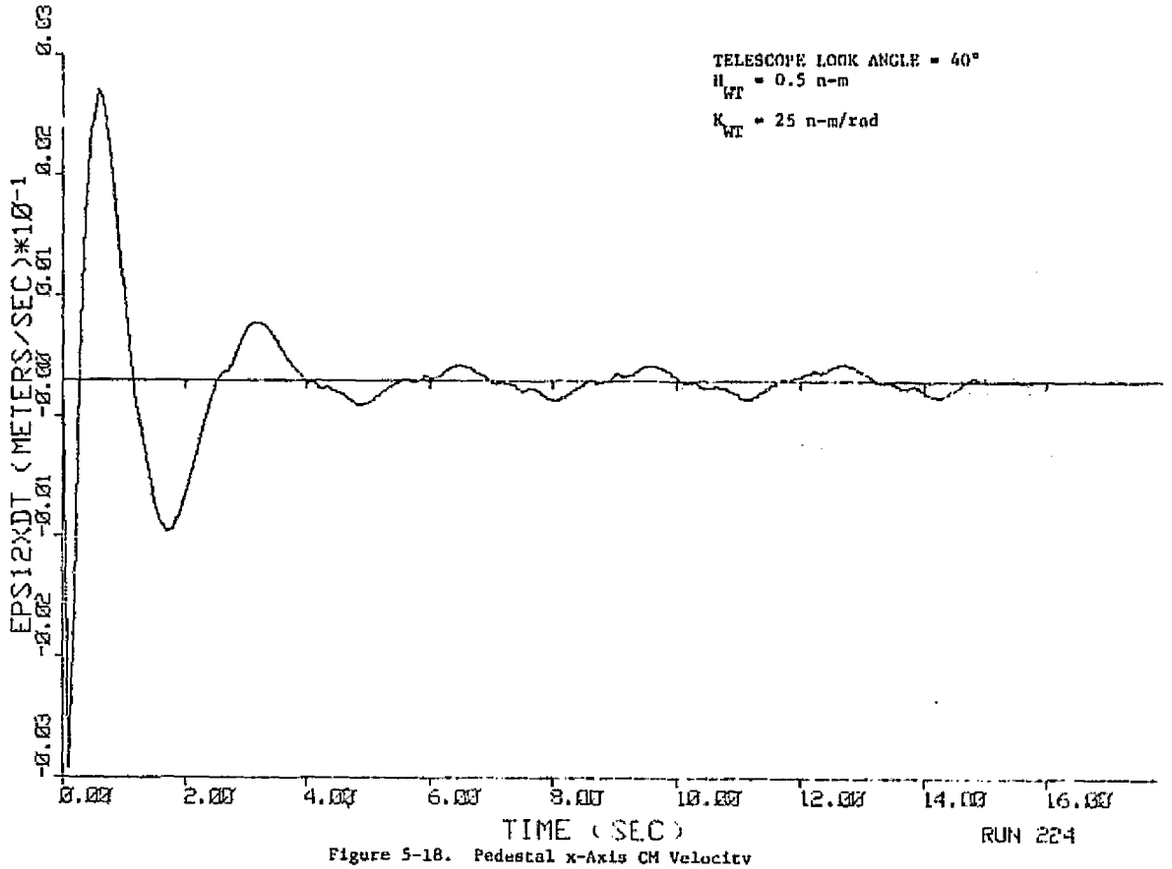

Figure 5-18. Pedestal x-Axis CM Velocity

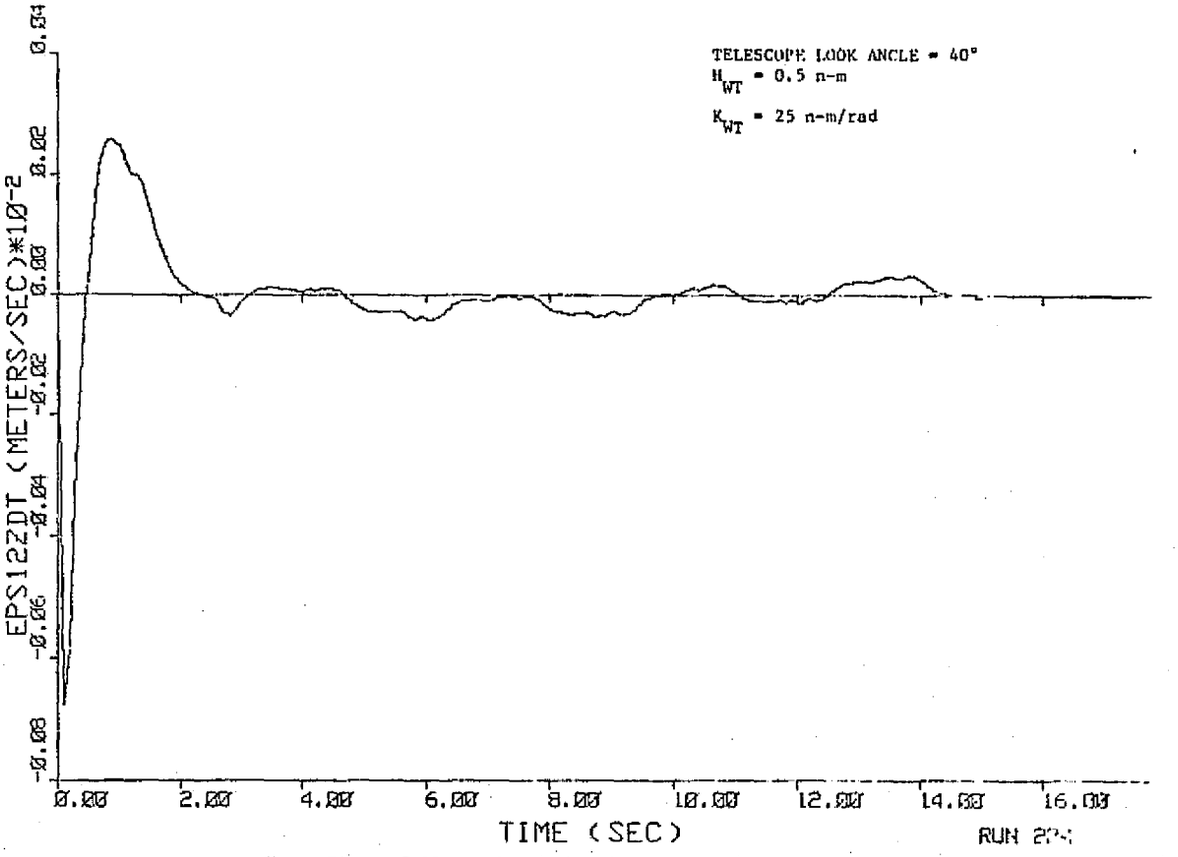

Figure 5-19. Pedestal z-Axis CM Velocity

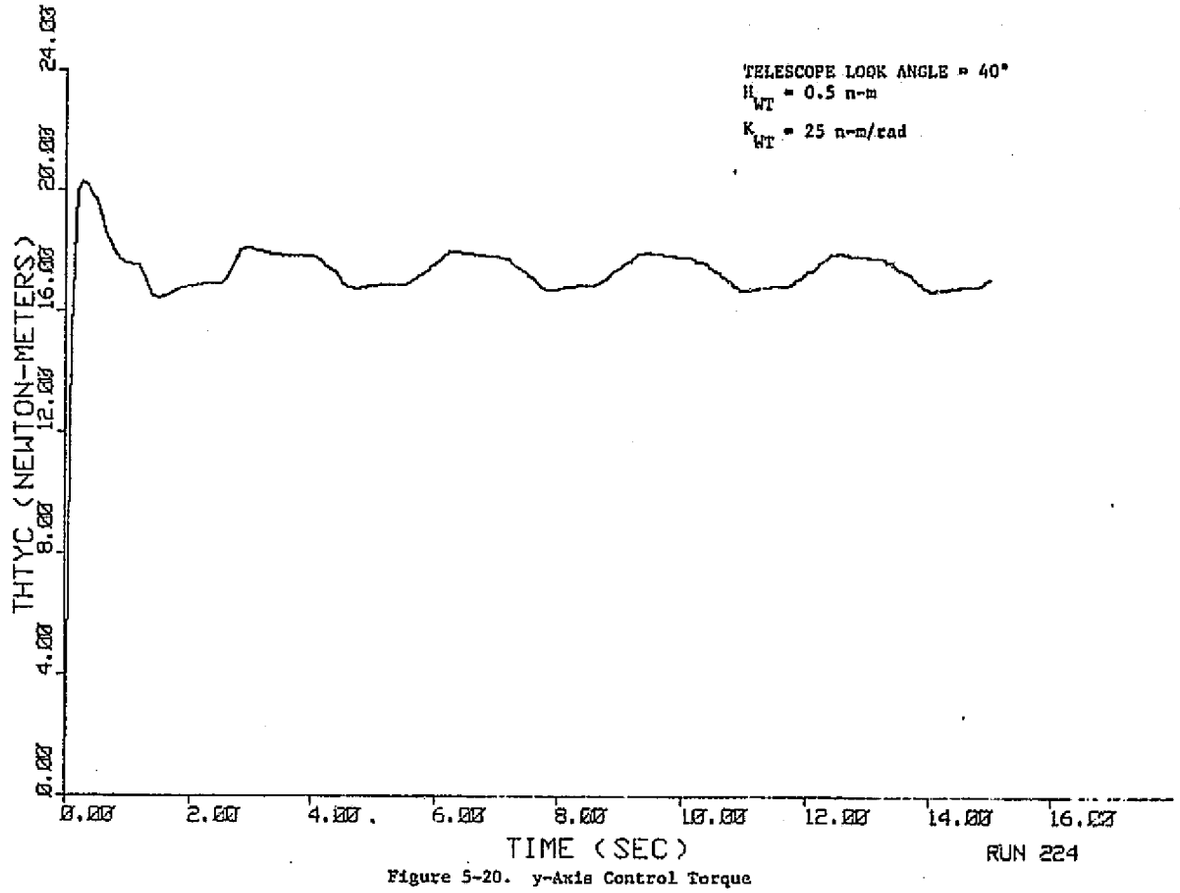

Figure 5-20. y-Axis Control Torque

6. DERIVATION OF SUSPENSION CHARACTERISTICS FOR COINCIDENT GIMBAL SYSTEM CONFIGURATION

The European Space Agency (ESA) in conjunction with Dornier Systems has recently modified the design of the IOG to the Coincident Gimbal System configuration. The most significant change between the IOG and the Coincident Gimbal is the configuration of the suspension system. The IOG had a square base pedestal with a four point suspension system consisting of a set of isolators at each corner of the pedestal. The pedestal for the Coincident Gimbal is circular with three sets of skewed isolators located on the periphery of the circle separated from each other by 120 degrees. Each of the isolator sets consist of two spring dampers skewed with respect to each other as shown in figure 6-1. In the sections that follow the coincident gimbal suspension linear and rotational stiffness and linear and rotational damping coefficients are derived as a function of individual spring stiffness, damping, and spring slew angle. In the derivation it is assumed that all of the springs have equal stiffness and damping characteristics along their respective axial directions.

In addition, suspension system relationships inherent in the Coincident Gimbal design are derived and a comparison is made with the IOG four point suspension.

6.1 Derivation of Linear and Rotational Stiffness and Damping Coefficients for the Coincident Gimbal Suspension System

The geometric configuration of the proposed Coincident Gimbal skewed spring suspension system is shown in figure 6-1.

Examination of figure 6-1 indicates that three spring damper assemblies are positioned 120 degrees apart around the periphery of a circle of radius R. Each assembly contains two springs that are canted at an angle α with respect to the plate (i.e., Coincident Gimbal pedestal) to which they are attached.

The force that is applied by the j^{th} spring can be written as

$$F_{sj} = K[|r_{oj}+\varepsilon|-|r_{oj}|]\frac{r_{oj}+\varepsilon}{|r_{oj}+\varepsilon|} \qquad (6\text{-}1)$$

where

K = Axial spring stiffness (n/m)

r_{oj} = Unstressed spring length

ε = Spring elongation (i.e., translation of pedestal C.M.)

Equation (6-1) can be written as

$$F_{sj} = K\{[(r_{oxj}+\varepsilon_x)^2+(r_{oyj}+\varepsilon_y)^2+(r_{ozj}+\varepsilon_z)^2]^{1/2}-[r_{oxj}^2+r_{oyj}^2+r_{0zj}^2]^{1/2}\}$$
$$\frac{}{[(r_{oxj}+\varepsilon_x)^2+(r_{oyj}+\varepsilon_y)^2+(r_{ozj}+\varepsilon_z)^2]^{1/2}}$$

$$x\ \{(r_{oxj}+\varepsilon_x)\hat{i}_x+(r_{oyj}+\varepsilon_y)\hat{i}_y+(r_{ozj}+\varepsilon_z)\hat{i}_z \qquad (6\text{-}2)$$

Equation (6-2) can be written as

$$F_{sj} = K\left[1-\frac{[r_{oxj}^2+r_{oyj}^2+r^2{}_{ozj}]^{1/2}}{[(r_{oxj}+\varepsilon_x)^2+(r_{oyj}+\varepsilon_y)^2+(r_{ozj}+\varepsilon_z)^2]^{1/2}}\right]\{(r_{oxj}+\varepsilon_x)\hat{i}_x+(r_{oyj}+\varepsilon_y)\hat{i}_y$$
$$+(r_{0zj}+\varepsilon_z)\hat{i}_z\} \qquad (6\text{-}3)$$

Expanding equation (6-3) and eliminating second order terms (i.e., $|\varepsilon|<<1$) results in

$$F_{sj}\approx K\{1-\frac{1}{[1+2\frac{(r_{oxj}\varepsilon_x+r_{oyj}\varepsilon_y+r_{ozj}\varepsilon_z)}{r_{oxj}^2+r_{oyj}^2+r_{ozj}^2}]^{1/2}}\}\{(r_{oxj}+\varepsilon_x)\hat{i}_x+(r_{oyj}+\varepsilon_y)\hat{i}+(r_{ozj}+\varepsilon_z)\hat{i}_z\} \qquad (6\text{-}4)$$

Making use of the expansion of $\frac{1}{(1+x)^{1/2}}$ where $x<<1$ equation (6-4) can be written as

$$F_{sj}\approx K\frac{(r_{oxj}\varepsilon_x+r_{oyj}\varepsilon_y+r_{ozj}\varepsilon_z)}{r_{oxj}^2+r_{oyj}^2+r_{ozj}^2}\{(r_{oxj}+\varepsilon_x)\hat{i}_x+(r_{oyj}+\varepsilon_y)\hat{i}_y+(r_{ozj}+\varepsilon_z)\hat{i}_z\} \qquad (6\text{-}5)$$

Eliminating second order terms from equation (6-5) gives

$$F_{sj}=\frac{K}{r_{oxj}^2+r_{oyj}^2+r_{ozj}^2}\{(r_{oxj}^2\varepsilon_x+r_{oxj}r_{oyj}\varepsilon_y+r_{oxj}r_{ozj}\varepsilon_z)\hat{i}_x$$
$$+(r_{oxj}r_{oyj}\varepsilon_x+r_{oyj}^2\varepsilon_y+r_{oyj}r_{ozj}\varepsilon_z)\hat{i}_y$$
$$+(r_{oxj}r_{ozj}\varepsilon_x+r_{oyj}r_{ozj}\varepsilon_y+r_{ozj}^2\varepsilon_z)\hat{i}_z\} \qquad (6\text{-}6)$$

For the 1,2 isolator pair shown in figure 6-1 the following applies

$$r_{ox1}=r_o\cos\alpha$$

$$r_{oy1}=0$$

$$r_{oz1}=-r_o\sin\alpha \qquad (6\text{-}7)$$

$$r_{ox2}=-r_o\cos\alpha$$

$$r_{oy2}=0$$

$$r_{oz2}=-r_o\sin\alpha$$

The unstretched dimensions of isolator pair 3,4 written in IOG pedestal coordinates can be obtained in the following manner

$$\begin{bmatrix} r_{ox3} \\ r_{oy3} \\ r_{oz3} \end{bmatrix} = \begin{bmatrix} \cos 120° & \sin 120° & 0 \\ -\sin 120° & \cos 120° & 0 \\ 0 & 0 & 1 \end{bmatrix} \begin{bmatrix} r_{ox1} \\ r_{oy1} \\ r_{oz1} \end{bmatrix} \qquad (6\text{-}8)$$

$$\begin{bmatrix} r_{ox4} \\ r_{oy4} \\ r_{oz4} \end{bmatrix} = \begin{bmatrix} \cos 120° & +\sin 120° & 0 \\ -\sin 120° & \cos 120° & 0 \\ 0 & 0 & 1 \end{bmatrix} \begin{bmatrix} r_{ox2} \\ r_{oy2} \\ r_{oz2} \end{bmatrix}$$

Similarly the unstretched dimensions of isolator pair 5,6 in IOG pedestal coordinates can be written as

$$\begin{bmatrix} r_{ox5} \\ r_{oy5} \\ r_{oz5} \end{bmatrix} = \begin{bmatrix} \cos 120° & -\sin 120° & 0 \\ \sin 120° & \cos 120° & 0 \\ 0 & 0 & 1 \end{bmatrix} \begin{bmatrix} r_{ox2} \\ r_{oy2} \\ r_{oz2} \end{bmatrix} \qquad (6\text{-}9)$$

$$\begin{bmatrix} r_{ox6} \\ r_{oy6} \\ r_{oz6} \end{bmatrix} = \begin{bmatrix} \cos 120° & -\sin 120° & 0 \\ \sin 120° & \cos 120° & 0 \\ 0 & 0 & 1 \end{bmatrix} \begin{bmatrix} r_{ox1} \\ r_{oy1} \\ r_{oz1} \end{bmatrix}$$

Substituting the appropriate dimensions for the unstretched spring length given for the various isolator pairs into equation (6-6) results in

$$F_{s1,2}=2K[(\cos^2\alpha)\varepsilon_x\hat{i}_x+(\sin^2\alpha)\varepsilon_z\hat{i}_z] \tag{6-10}$$

$$F_{s3,4} = K\{[\tfrac{1}{2}\cos^2\alpha\varepsilon_x+\tfrac{\sqrt{3}}{2}\cos^2\alpha\varepsilon_y]\hat{i}_x+[\tfrac{\sqrt{3}}{2}\cos^2\alpha\varepsilon_x+\tfrac{3}{2}\cos^2\alpha\varepsilon_y]\hat{i}_y+[2\sin^2\alpha\varepsilon_z]\hat{i}_z\} \tag{6-11}$$

$$F_{s5,6} = K\{[\tfrac{1}{2}\cos^2\alpha\varepsilon_x-\tfrac{\sqrt{3}}{2}\cos 2\alpha\varepsilon_y]\hat{i}_x+[-\tfrac{\sqrt{3}}{2}\cos^2\alpha\varepsilon_x+\tfrac{3}{2}\cos^2\alpha\varepsilon_y]\hat{i}_y+[2\sin^2\alpha\varepsilon_z]\hat{i}_z\} \tag{6-12}$$

The total linear compliance force is given by

$$F_s = F_{s1,2}+F_{s3,4}+F_{x5,6}$$

$$F_s = K\{[3\cos^2\alpha]\varepsilon_x\hat{i}_x+[3\cos^2\alpha]\varepsilon_y\hat{i}_y+[6\sin^2\alpha]\varepsilon_z\hat{i}_z\} \tag{6-13}$$

Hence the linear spring constants using the same notation as defined in section 2.0,

$$\begin{aligned} 4K_x &= 4K_y = K_{x,y} = 3K\cos^2\alpha \\ 4K_z &= 6K\sin^2\alpha \end{aligned} \tag{6-14}$$

Similarly, since the damping forces are applied in the same direction as the spring compliance force the following applies

$$\begin{aligned} 4D_x &= 4D_y = D_{x,y} = 3D\cos^2\alpha \\ 4D_z &= 6D\sin^2\alpha \end{aligned} \tag{6-15}$$

where

D = Damping coefficient along the axial spring direction $(\frac{\text{n-sec}}{\text{m}})$

The torque applied by the suspension to the IOG pedestal due to pedestal rotation is given by

$$T_{sj} = R_j \times F_{sj} \tag{6-16}$$

and

$$\varepsilon = \theta \times R_j \tag{6-17}$$

Assuming R_j has only an x and y component and substituting equation (6-17) into equation (6-6) and then substituting the results in equation (6-16) results in

$$T_{sj} = \frac{K}{r_{oxj}^2+r_{oyj}^2+r_{ozj}^2}\{r_{ozj}^2 R_{yj}\theta_x - r_{ozj}^2 R_{xy} R_{yj}\theta_y + (r_{oyj} r_{ozj} R_{xj} R_{yj} - r_{oxj} r_{ozj} R_{yj}^2)\theta_z]\hat{i}_x$$

$$+[-r_{ozj}^2 R_{xj} R_{yj}\theta_x + r_{ozj}^2 R_{xj}^2\theta_y + (r_{oxj} r_{ozj} R_{xj} R_{yj} - r_{oyj} r_{ozj} R_{xj}^2)\theta_z]\hat{i}_y$$

$$+[r_{oyj} r_{ozj} R_{xj} R_{yj} - r_{oxj} r_{ozj} R_{yj}^2)\theta_x + (r_{oxj} r_{ozj} R_{xj} R_{yj} - r_{oyj} r_{ozj} R_{xj}^2)\theta_y$$

$$+(r_{oyj} R_{xj} - r_{oxj} R_{yj})^2\theta_z]\hat{i}_z\} \qquad (6\text{-}18)$$

For the case under consideration

$$R_{1,2} = -R\hat{i}_y$$

$$R_{3,4} = -\frac{\sqrt{3}}{2} R\hat{i}_x + \frac{1}{2} R\hat{i}_y \qquad (6\text{-}19)$$

$$R_{5,6} = \frac{\sqrt{3}}{2} R\hat{i}_x + \frac{1}{2} R\hat{i}_y$$

Substituting equations (6-7), (6-10), (6-11), and (6-19) into equation (6-18) gives

$$T_{s1,2} = 2R^2K\{(\sin^2\alpha)\theta_x\hat{i}_x + (\cos^2\alpha)\theta_z\hat{i}_z\} \qquad (6\text{-}20)$$

$$T_{s3,4} = R^2K\{[\frac{1}{2}\sin^2\alpha\theta_x + \frac{\sqrt{3}}{2}\sin^2\alpha\theta_y]\hat{i}_x + [\frac{3}{2}\sin^2\alpha\theta_y + \frac{\sqrt{3}}{2}\sin^2\alpha\theta_x]\hat{i}_y + [2\cos^2\alpha\theta_z]\hat{i}_z\} \qquad (6\text{-}21)$$

$$T_{s5,6} = R^2K\{[\frac{1}{2}\sin^2\alpha\theta_x - \frac{\sqrt{3}}{2}\sin^2\alpha\theta_y]\hat{i}_x + [\frac{3}{2}\sin^2\alpha\theta_y - \frac{\sqrt{3}}{2}\sin^2\alpha\theta_x]\hat{i}_y + [2\cos^2\alpha\theta_z]i_z\} \qquad (6\text{-}22)$$

The total torque applied to the IOG pedestal is given by

$$T_s = T_{s1,2} + T_{s3,4} + T_{x5,6} \qquad (6\text{-}23)$$

$$T_s = KR^2\{[3\sin^2\alpha]\theta_x\hat{i}_x+[3\sin^2\alpha]\theta_y\hat{i}_y+[6\cos^2\alpha]\theta_z\hat{i}_z\} \quad (24)$$

Hence the rotational stiffness coefficients of the suspension are given by

$$k_x = k_y = 3KR^2\sin^2\alpha$$

$$k_z = 6KR^2\cos^2\alpha \quad (25)$$

Similarly the rotational damping coefficients of the suspension are given by

$$d_x = d_y = 3DR^2\sin^2\alpha$$

$$d_z = 6DR^2\cos^2\alpha \quad (26)$$

The parameters presently being proposed by Donier Systems for the suspension analyzed are listed below:

$K = 800 \frac{n}{m}$

$D = 240 \frac{n\text{-}m\text{-}sec}{rad}$

$\alpha = 24.1$ deg

$R = 0.25$ m

Substituting these parameters in equations (14), (15), (25) and (26) results in the following

$K_x = K_y = 2000 \frac{n}{m}$

$K_z = 800 \frac{n}{m}$

$D_x = D_y = 600 \frac{n\text{-}sec}{m}$

$$D_z = 240 \frac{\text{n-sec}}{\text{m}}$$

$$k_x = k_y = 25 \frac{\text{n-m}}{\text{rad}}$$

$$k_z = 250 \frac{\text{n-m}}{\text{rad}}$$

$$d_x = d_y = 7.5 \frac{\text{n-m-sec}}{\text{rad}}$$

$$d_z = 75 \frac{\text{n-m-sec}}{\text{rad}}$$

6.2 Inherent Relationships Between Suspension Parameters for the Coincident Gimbal System

Examination of equations (6-14), (6-15), (6-20) and (6-26) indicate that there are only four independent parameters that can be used to set all of the suspension characteristics. Since there are twelve parameters (i.e., linear stiffness and damping along three axes, rotational stiffness and damping about three axes) to be set for the suspension it is clear that these cannot be set independently with only four parameters. In addition, the linear stiffness along the three axes cannot be set independently since the stiffness along the x and y axes must always be equal with the stiffness along z set to some desired value by adjustment of the angle "α". The linear damping along the x, y, and z axes can only be controlled by varying the damping coefficient "D". Examination of equation (6-15) indicates that the damping coefficient along the x and y axes are always equal but can be set to a desired level. However, the damping coefficient along the z axis is now determined and cannot be controlled.

Assuming that the damping coefficient "D" is set so that a particular damping ratio "ζ" is obtained about the x and y axes, this can be written as

$$\zeta_{x,y} = \frac{1}{2} \frac{D_{x,y}}{\sqrt{K_{x,y} m}} \tag{6-27}$$

The damping ratio along the z axis is given by

$$\zeta_z = \frac{1}{2} \frac{D_z}{\sqrt{K_z m}} \tag{6-28}$$

However

$$D_z = 2\tan^2\alpha D_{x,y} \tag{6-29}$$

$$K_z = 2\tan^2\alpha K_{x,y}$$

Substituting equation (6-29) into equation (6-28) results in

$$\zeta_z = \sqrt{2}\tan\alpha\zeta_2 \tag{6-30}$$

Examination of equation (6-30) indicates that the linear damping ratio along the z-axis will equal that of the x and y axes for α = 35.26 deg. For values of "x" below this value the damping along the z-axis decreases while it increases for α above 35.26 deg. If the α angle is set at 15 deg. or below, appreciable reduction in linear damping along the z-axis results which can result in deteriorated system response characteristics.

The rotational stiffness of the mount about the x and y axes can be set by varying the distance "R" as indicated in equation (6-25). However, the rotational stiffness about the "z" axis is determined and cannot be controlled. In addition, the rotational damping coefficients about the x, y, and z axes are now determined and cannot be separately controlled.

It will be shown (section 7) that the critical suspension parameters that govern IOG pointing performance are the rotational stiffness about the x and y axes and the translational stiffness along the z axis. Hence, one might conclude that increasing the linear stiffness along the x and y axes would result in a reduction of the radius of the base of the Coincident Gimbal pedestal since it seems reasonable that the longitudinal stiffness K of the isolators would increase. However, if equations (6-14) are divided by each other the following results

$$\tan\alpha = \left(\frac{K_z}{2K_{x,y}}\right)^{1/2} \tag{6-31}$$

Equation (6-31) implies the geometrical relationship shown in figure 6-2.

The value of K from equation (6-14) and the geometrical relationships shown in figure 6-2 can be written as

$$K = \frac{K_{x,y}}{3\cos^2\alpha} = \frac{K_{x,y}}{3\left[\frac{2K_{x,y}}{K_z+2K_{x,y}}\right]} = \frac{2K_{x,y}+K_z}{6} \tag{6-32}$$

Substituting equation (6-32) and the geometrical relationships into equation (6-25) yields:

$$k_x = k_y = k_{x,y} = 3\left[\frac{2K_{x,y}+K_z}{6}\right]\left[\frac{K_z}{2K_{x,y}+K_z}\right]R^2 = \left(\frac{K_z}{2}\right)R^2 \qquad (6\text{-}33)$$

therefore

$$R = \left(\frac{2k_{x,y}}{K_z}\right) \qquad (6\text{-}34)$$

Equation (6-34) indicates that the radius of the base of the Coincident Gimbal pedestal is completely determined by the rotational stiffness about the x and y axes and the linear stiffness along the z axis. Therefore, varying the linear stiffness along the x and y axes will not affect the radius of the pedestal base and cannot be used to affect a size reduction.

6.3 Comparison of Coincident Gimbal Suspension System with Square Based Suspension System - A comparison can be made as to the required area of the pedestal base for the Coincident Gimbal Suspension System and the corresponding square base suspension. Assuming that the rotational stiffness about the x and y axes and the translational stiffness along the z axis are equivalent for both systems, the side of the square base suspension system can be written as

$$2\alpha_{120} = 2\left(\frac{k_{x,y}}{K_z}\right)^{1/2} \qquad (6\text{-}35)$$

where

$2\alpha_{120}$ = length of one side of the square base

The area required by the square base suspension is then given by

$$A_{S.B.} = \frac{4k_{x,y}}{K_z} \qquad (6\text{-}36)$$

The area of the corresponding Coincident Gimbal pedestal base using equation (6-34) is given by

$$A_{C.G.} = \pi\left(\frac{2k_{x,y}}{k_z}\right)$$

or the ratio of the area of the Coincident Gimbal Base to the square base is

$$\frac{A_{C.G.}}{A_{S.B.}} = \frac{\pi}{2} = 1.571 \qquad (6\text{-}37)$$

Hence, the area of the Coincident Gimbal pedestal base is almost 60 percent greater than the required area for the square base suspension system.

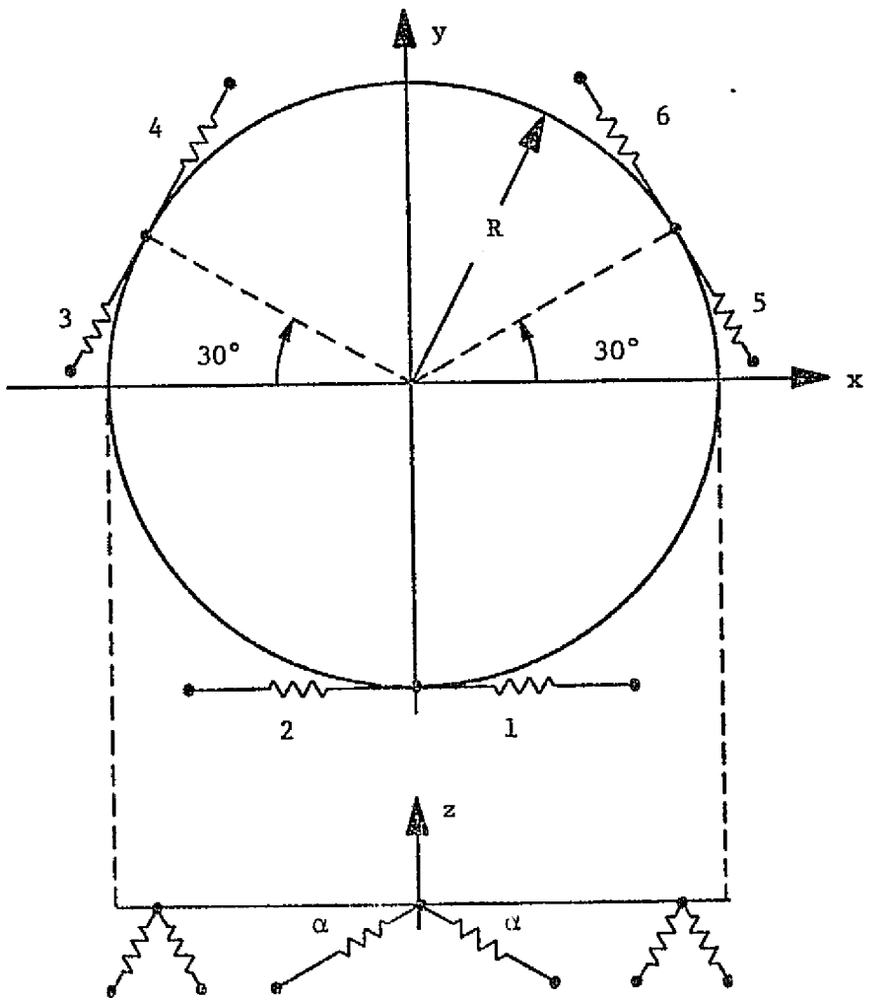

Figure 6-1. Skewed Spring Suspension System

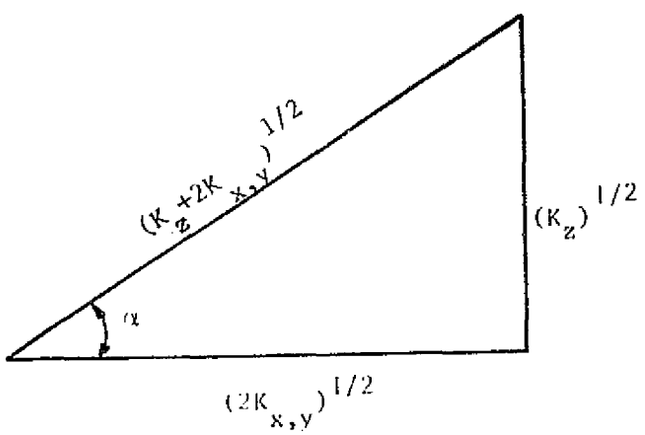

Figure 6-2. Geometrical Relationship Between Suspension Parameters

7. COINCIDENT GIMBAL SYSTEM PERFORMANCE

In the sections that follow, the Coincident Gimbal system performance is described for the nominal suspension parameters specified by Dornier Systems. Both stellar pointing and earth tracking performance are discussed for the given suspension system. Based on the results obtained, the suspension parameters are modified in order to improve the performance of the Coincident Gimbal System in both stellar pointing and earth tracking. Representative system performance characteristics are shown for the modified suspension system and a recommendation is made as to the suspension parameters that should be implemented for the Coincident Gimbal System.

7.1 Coincident Gimbal Pointing Performance - In order to obtain the Coincident Gimbal geometrical system configuration the following parameters must be modified from the values shown in table 2-1 as outlined below:

$$m_2 = 138.45 \text{ Kg}$$

$$J_{2x} = 12.695 \text{ Kg-m}^2$$

$$J_{2y} = 16.313 \text{ Kg-m}^2$$

$$J_{2z} = 5.417 \text{ Kg-m}^2$$

$$R_{E20} = .1017\ \hat{i}_x - .0029\ \hat{i}_y - .5251\ \hat{i}_z \text{ m}$$

$$R_{120} = -4.822\ \hat{i}_x + 0.0029\ \hat{i}_y - 1.429\ \hat{i}_z \text{ m}$$

$$r_1 = 0.1017\ \hat{i}_x - 0.0029\ \hat{i}_y + .275\ \hat{i}_z \text{ m}$$

System time responses were taken for the suspension parameters furnished by Dornier which entail changing the baseline parameters in the following manner.

$$4D_x = 4D_y = 600 \frac{\text{n-sec}}{\text{m}}$$

$$4D_z = 240 \frac{\text{n-sec}}{\text{m}}$$

$$4K_x = 4K_y = 2000 \text{ n/m}$$

$$4K_z = 800 \text{ n/m}$$

$d_x = d_y = 7.5$ n-m-sec

$d_z = 75$ n-m-sec

$k_x = k_y = 25 \frac{\text{n-m}}{\text{sec}}$

$k_z = 250 \frac{\text{n-m}}{\text{rad}}$

For a telescope look angle of sixty degrees and a crew motion disturbance applied along the z axis the peak pointing error incurred about the telescope y axis was 4.34×10^{-6} rad (.895 arc-second). This value of pointing error from one source is too large if an arc-second of pointing stability is to be realized when considering all of the other contributing system error sources (e.g., sensor and actuator noise, gimbal nonlinearities, sampling and quantization, etc.). Hence, it is clear that the y axis pointing error must be reduced. Since it is not advisable to increase the pointing control loop bandwidth beyond 2 Hz from system noise and structural flexibility considerations the only way to reduce this error is to reduce the suspension linear stiffness in the z direction to at least the baseline set of parameters which would yield similar pointing performance as that obtained for the IOG as outlined in section 4.

Figures 7-1 through 7-21 show system pointing performance for a telescope look angle of zero degrees with the crew motion disturbance shown in figure 4-1 applied simultaneously along the x, y and z axes of the shuttle orbiter for the Coincident Gimbal System parameters specified by Dornier Systems. Figures 7-22 through 7-42 and figures 7-43 through 7-63 show Coincident Gimbal pointing performance for telescope look angles of 40 and 60 degrees respectively with all other parameters being the same as above. The legend used in these figures are explained in table 4-1.

7.2 Coincident Gimbal Earth Tracking Performance - Using the earth tracking command profiles described in section 4.2, the performance of the Coincident Gimbal System as defined by Dornier Systems was determined. The result of this determination are shown in figures 7-64 through 7-84. A definition of the nomenclature used in these plots are given in table 4-1. Examination of figure 7-66 indicates that the peak tracking error incurred was 0.262×10^{-5} rad (.540 arc-second) while an examination of figures 7-72, 7-77 and 7-79 indicate that the pedestal y rotation was 0.311 rad (17.8 deg) with the x and y translation of the pedestal C.M. equal to 0.164 m (6.46 in) and .034 m (1.34 in) respectively. These values correspond to an isolator elongation of 4.169×10^{-2} m (1.641 in)

which is too large and could not be accommodated within the framework of a reasonable design. This situation becomes worse as altitude of the orbit is reduced from 438 KM for which the above values apply. Hence it is clear that if the IPS is to have a reasonable earth tracking capability the suspension parameters proposed by Dornier should be modified by stiffening the suspension rotationally and translationally as much as possible while still meeting stellar pointing requirements. This approach will be fully discussed in section 7.4.

7.3 Coincident Gimbal Raster Scanning Performance - Examination of experiments proposed to be integrated with the IPS indicate that many have raster scan requirements. In order to examine, in a preliminary fashion, the raster scan capability of the Coincident Gimbal System the raster scan performance of a particular experiment was determined. The experiment chosen for this evaluation was the X-UV (soft x-ray) Spectroheliograph. A schematic diagram of this telescope with its associated mass characteristics is shown in figure 7-85.

The raster scan field that was considered was 90 x 90 arc-second with a scan time per line of 1.12 arc-second which yields a scan rate of 3.897×10^{-4} rad/sec (80.36 arc-second/second). The desired accuracy was that the tracking error should be within $\pm$ 1.7 arc-second for ninety percent of the time it takes to scan a line (i.e., 1.12 second). The technique used to accomplish the raster scan profile was to use simultaneous rate and position commands to the Coincident Gimbal pointing control system. The rate and position command profiles employed are depicted in figure 7-86.

Two computer runs were made for the X-UV Spectroheliograph using the above profiles. The first was to raster scan the telescope about the y axis only. The second was to raster scan the telescope about an axis in the x,y plane making inclined 45 degrees with respect to the x and y coordinate axes. For both cases the telescope was positioned so as to allow a symmetrical scan about zero look angle, and the pointing control loop bandwidth was set at 2 Hz.

The results of these studies indicate that the system did not meet the accuracy specification of 1.7 arc-second for ninety percent of the line scan time for both cases investigated. The tracking errors remained above 1.7 arc-second for approximately 0.82 second of the 1.12 second that it takes to scan one line with a peak tracking error of approximately 9 arc-seconds. However, the peak control torque required was 2.89 n-m which

is well within the torque capability of the Coincident Gimbal torque motor capability. These results indicate that raster scanning to the accuracy described above cannot be met by the "simple" scan profiles employed. It is anticipated, however, that if a torque command used in conjunction with consistant rate and position command profiles were employed, system raster scanning performance would be greatly improved and the accuracies desired would probably be achieved. It is recommended that future effort should be expended to implement this raster scan command technique and determine the accuracies that can be achieved.

7.4 Pointing Performance with Modified Suspension Characteristics - It has been shown in sections 7.1 and 7.2 that "large" pointing errors (i.e., 0.895 arc-second) result in the presence of crew motion disturbances while excessive pedestal rotations and translations with accompanying "large" (i.e., 1.7 in) isolator elongations occur during earth tracking translations for the isolator parameters defined by Dornier Systems. Hence, it is evident that the suspension parameters should be modified in order to give the IPS a reasonable slewing capability while still meeting stellar pointing performance requirements. It has been demonstrated that increasing the rotational stiffness of the suspension system about the x and y axes reduces the pedestal rotations and translation from those incurred using the nominal suspension parameters for the IOG system. Hence, it would similarly be desirable to increase the rotational stiffness of the coincident gimbal suspension over those specified by Dornier which are approximately the same as those of nominal IOG in order to minimize pedestal rotations and translations incurred during slewing. However, the maximum radius that the coincident gimbal base can have from mounting considerations is 0.9 meters. Since from stellar pointing considerations it would be advisable to reduce the translational stiffness along the z axis to 500 n/m in order to reduce the pointing error incurred due to crew motion disturbances, the maximum rotational stiffness that could be realized about the x and y axes is 202.5 n-m/rad (see section 6.2).

The other suspension parameter that can be varied is the translational stiffness along the x and y axes keeping the translational stiffness along the z axis equal to 500 n/m and the rotational stiffness about the x and y axes equal to 202.5 n-m/rad. The effect of this parameterization on peak pointing error for a telescope look angle of 60 degrees is outlined in figures 7-87 and 7-88. It should be noted that in the parameterization of the linear suspension stiffness along the x and y axes the linear suspension damping ratio was maintained at 0.1 along these axes when considering all of the mass above the suspension point (i.e., m_2+m_3).

Examination of these figures indicates that the y axis pointing error decreases from 0.866 arc-second to 0.555 arc-second when the linear suspension stiffness is increased from 500 n/m to 10,000 n/m along the x and y axes for a crew motion disturbance applied along the z axis. Examination of figure 7-25 indicates that the peak pointing error incurred about the x axis is independent of the linear stiffness along the x and y axes further demonstrating that the suspension system does not act primarily as a classical isolator for these errors as described in section 4.1. It should also be noted that most of the pointing improvement is realized when the suspension linear stiffness along the x and y axes is increased to between 2000 and 4000 n/m. Hence, in order to minimize the changes to the suspension parameters specified by Dornier while still realizing most of the advantages that can be achieved within the constraints of the coincident gimbal system the recommended suspension parameters are listed in table 7-1.

The suspension parameter values given in table 7-1 result in the following Coincident Gimbal suspension system isolator design characteristics.

$K = 750$ n/m

$D = 178.2$ n-sec/m

$\alpha = 19.47$ deg

$R = 0.9$ m

System time responses for the recommended suspension parameters with crew motion disturbances applied along the x, y and z shuttle orbiter axes simultaneously are given in figures 7-89 through 7-109, 7-110 through 7-130, and 7-131 through 7-151 for telescope look angles of zero, 40, and 60 degrees respectively. The nomenclature used in these plots is explained in table 4-1. Examination of the plots for the angular rotation and the translation of the CM of the pedestal indicate that they do not seem to be returning to zero. This is in fact the case since the crew motion disturbance, which is mmomentum conservative, will still cause the shuttle to rotate through some small angle from its initial starting point. This will then cause the pedestal to rotate through the same angle once the transients die down. Since the translation "ε_{12}" of the pedestal C.M. is measured with respect to R_{120} which is an inertial vector it will also approach a nonzero value once transients die down due to shuttle orbiter rotation.

Table 7-1. Recommended Suspension Parameters

$4K_x = 4K_y = 2000$ n/m
$4K_z = 500$ n/m
$4D_x = 4D_y = 475.2 \frac{\text{n-sec}}{\text{m}}$
$4D_z = 118.8 \frac{\text{n-sec}}{\text{m}}$
$k_x = k_y = 202.5 \frac{\text{n-m}}{\text{rad}}$
$k_z = 3.242 \times 10^3 \frac{\text{n-m}}{\text{rad}}$
$d_x = d_y = 48.11$ n-m-sec
$d_z = 769.8$ n-m-sec

7.5 Coincident Gimbal Earth Tracking Performance with Recommended Suspension Parameters - Using the earth tracking command profiles described in section 4.2 the performance of Coincident Gimbal system with the recommended suspension parameters was determined. These results are shown in figures 7-152 through 7-172. A definition of the nomenclature used in these figures is given in table 4-1. Examination of figures 7-90 indicates that the peak tracking error incurred was 0.352×10^{-5} rad (.726 arc-second) which is withint the desired ± 1 arc-second tracking accuracy but is approximately 34 percent worse than that realized for the suspension parameter specified by Dornier. However, the peak pedestal rotation was 0.0273 rad (1.564 deg) and the peak pedestal C.M. translations were 15.6 mm (.61 in) and 2.42 mm (.095 in) along the x and z axes respectively. These values are more than an order of magnitude smaller than those incurred for the suspension parameters defined by Dornier. These values will result in isolator elongations of approximately 8.5 mm (.0335 in) which can easily be accommodated by the Coincident Gimbal suspension system design. Hence, it has been demonstrated that the recommended suspension parameters not only meet the stellar pointing stability requirements of $\pm$ 1 arc-second in the presence of crew motion disturbances, but also greatly reduces the pedestal rotations and translations and hence isolator elongations incurred during earth tracking making these values consistent with a reasonable suspension design.

Additionally, a comparison between system response for the recommended Dornier suspension parameters (figures 7-65 through 7-85) and that obtained for the recommended suspension parameters indicate that the system responses are considerably different in functional form. The difference in response is due to the stiffening of the suspension system for the recommended parameters which results in the more oscillatory response characteristics for this system. However, the increased oscillatory nature of the response has no detrimental effect on overall system performance.

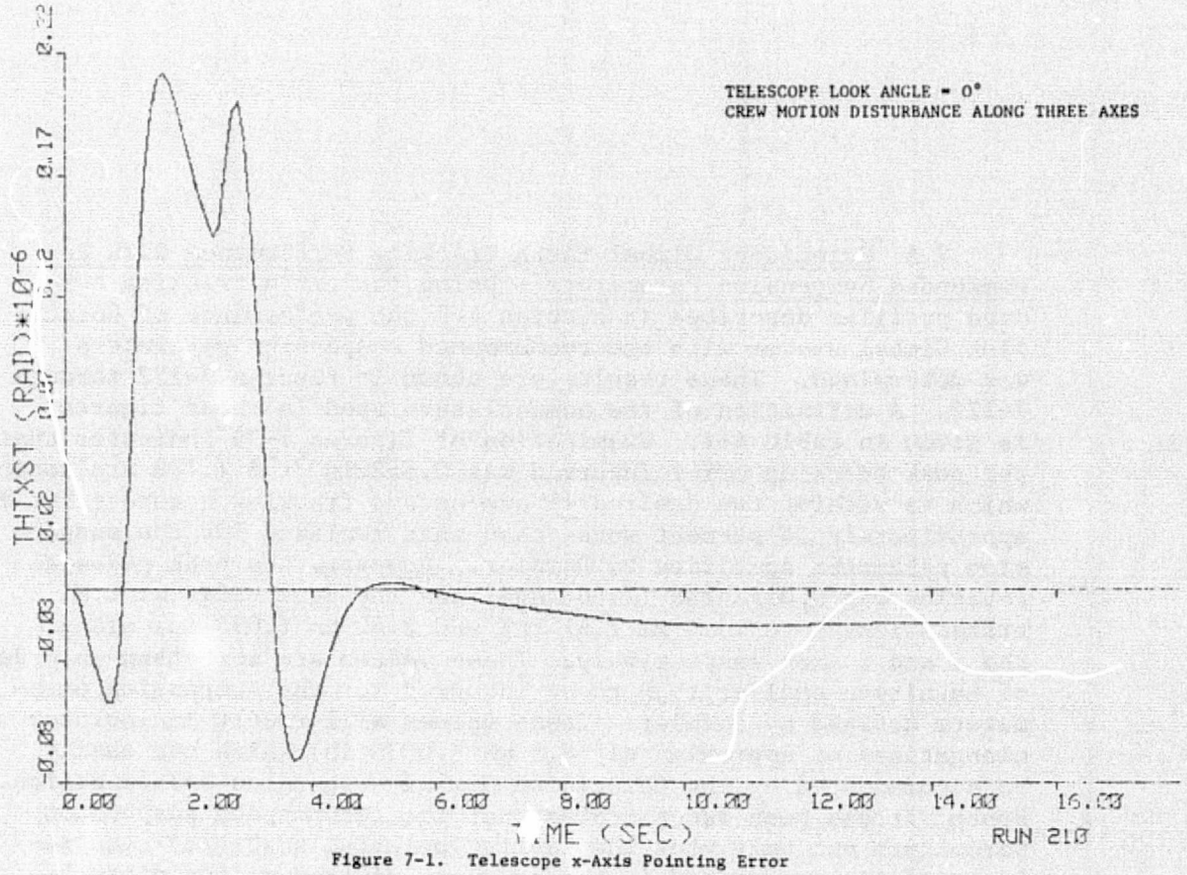

Figure 7-1. Telescope x-Axis Pointing Error

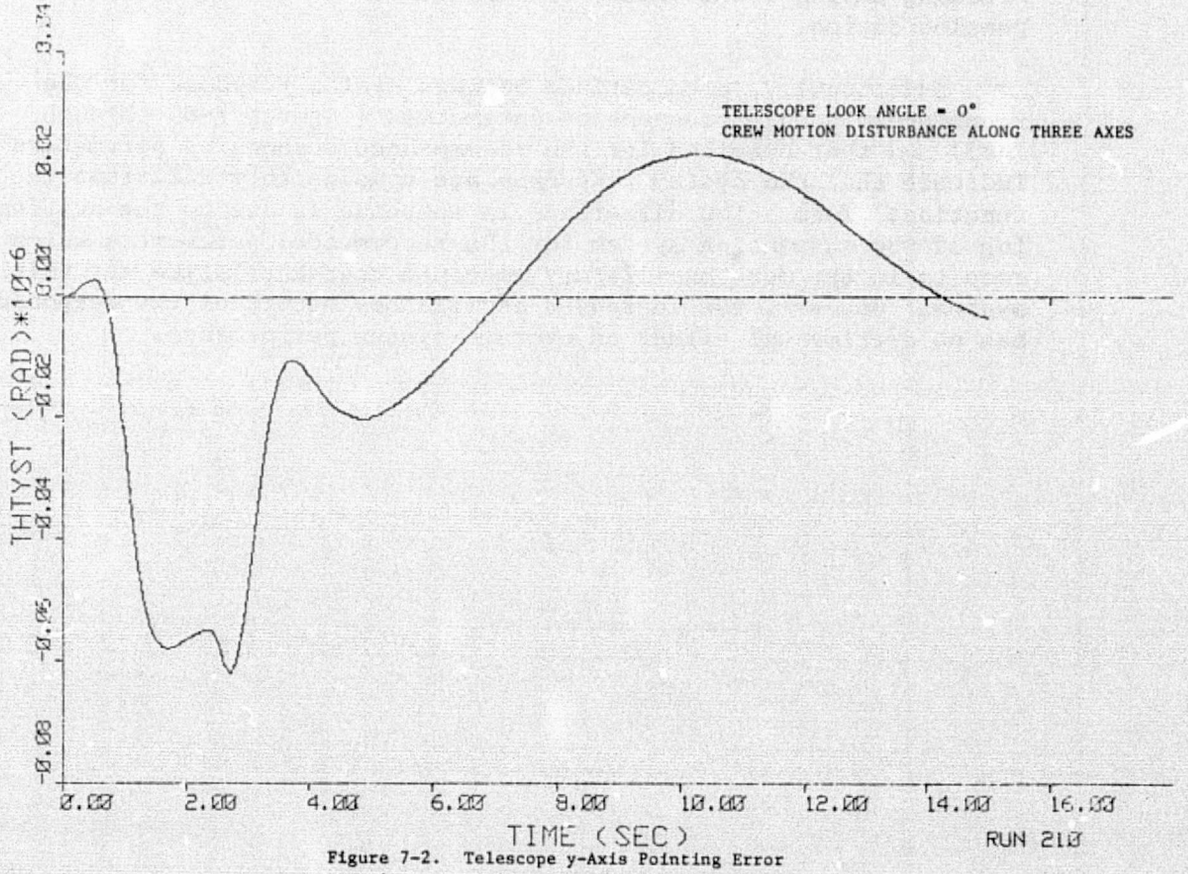

Figure 7-2. Telescope y-Axis Pointing Error

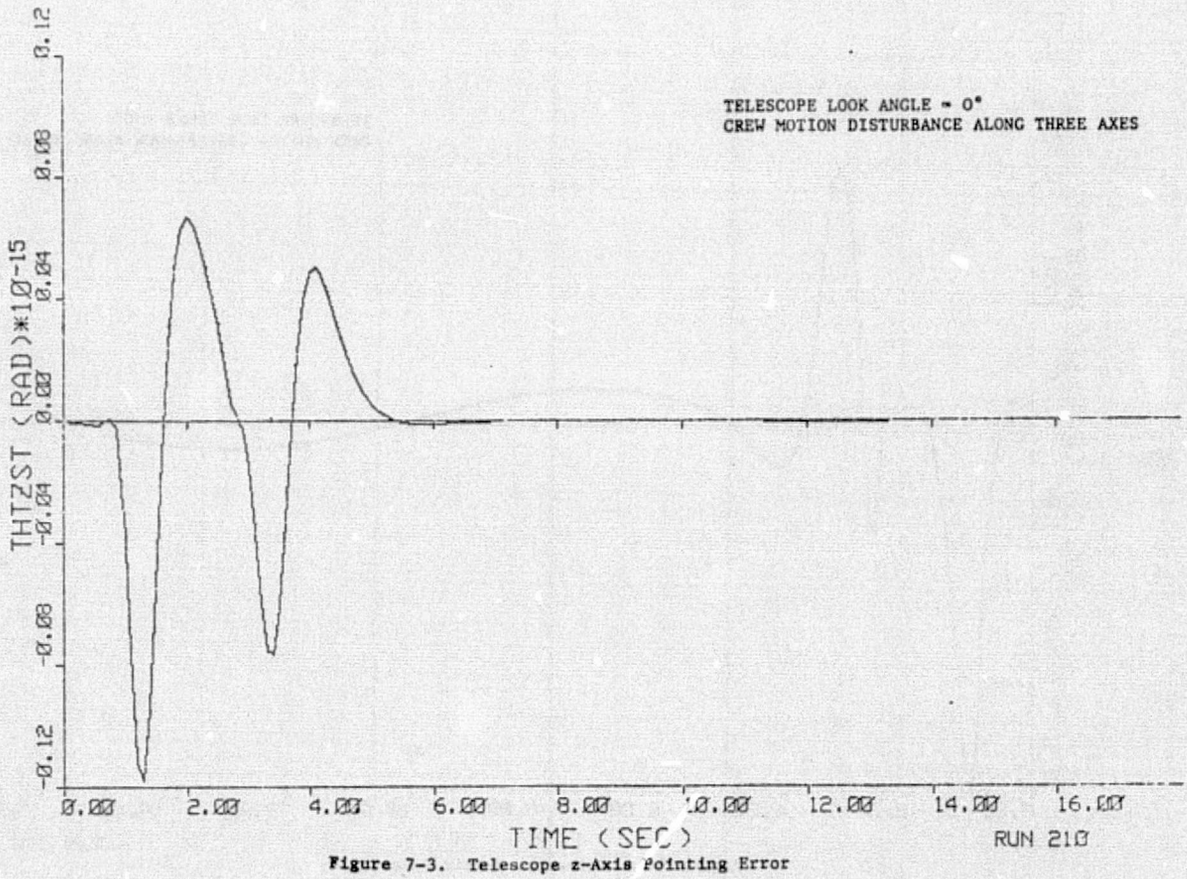

Figure 7-3. Telescope z-Axis Pointing Error

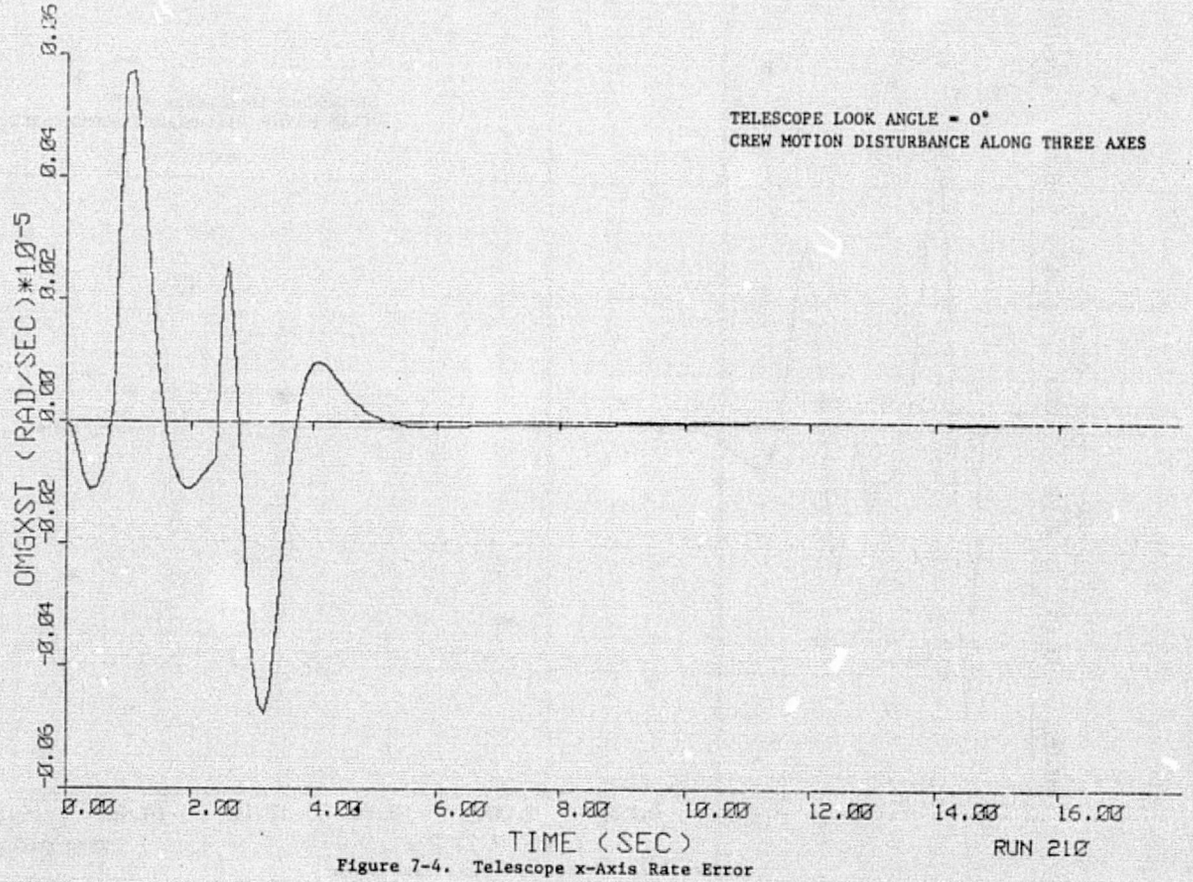

Figure 7-4. Telescope x-Axis Rate Error

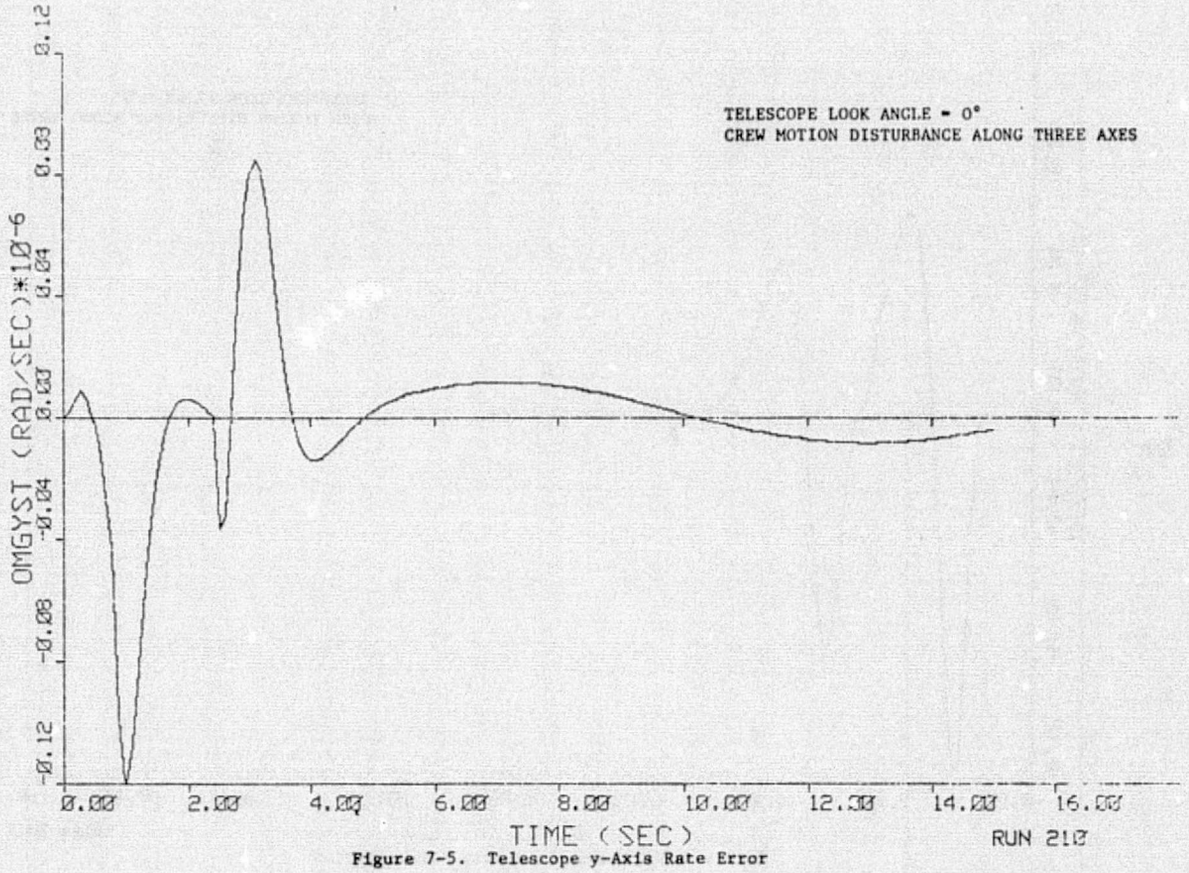

Figure 7-5. Telescope y-Axis Rate Error

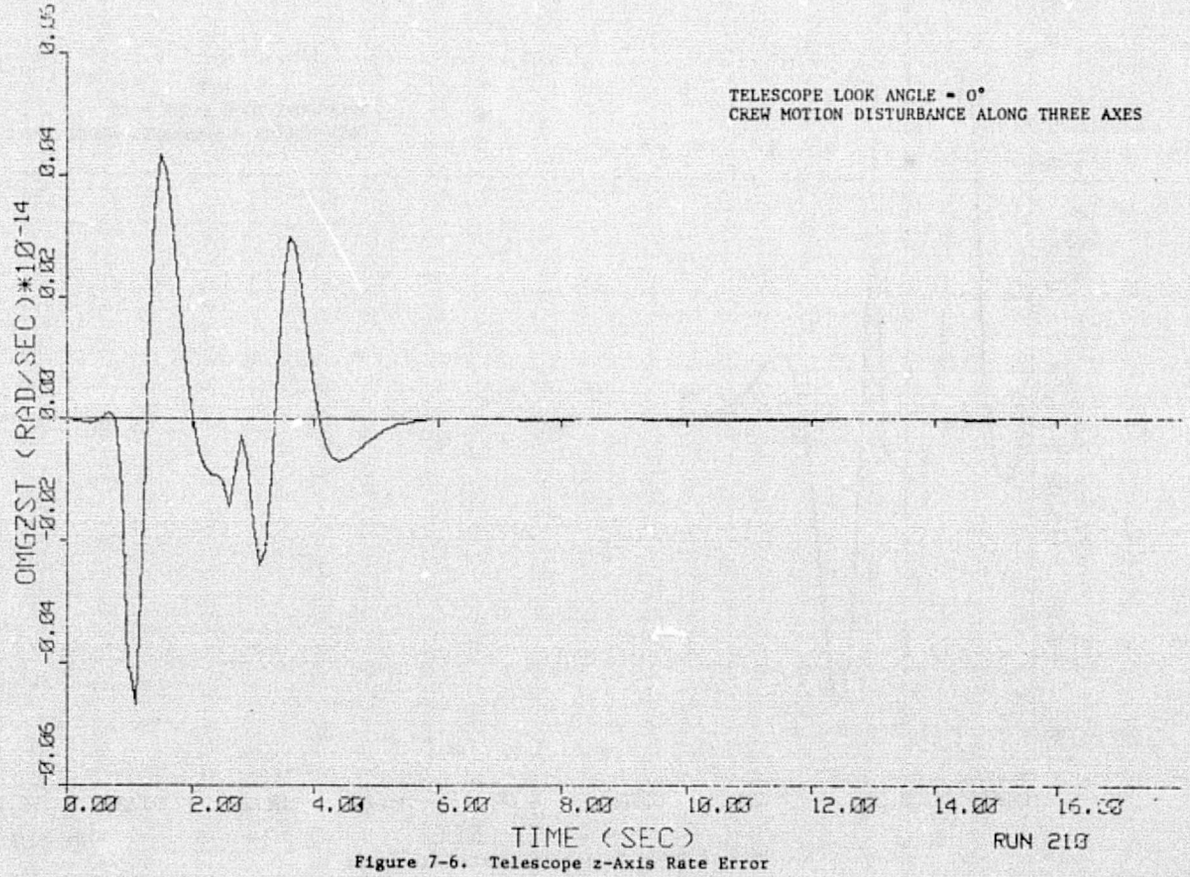

Figure 7-6. Telescope z-Axis Rate Error

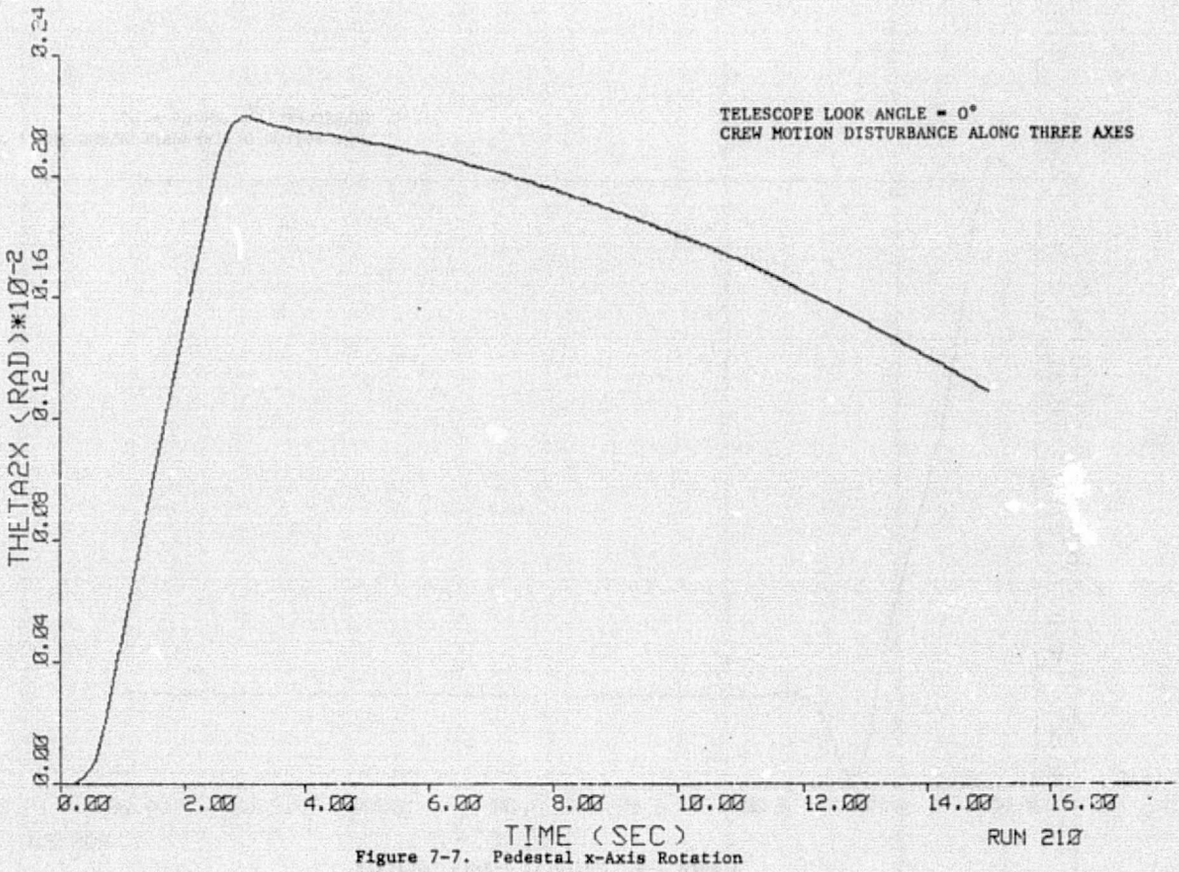

Figure 7-7. Pedestal x-Axis Rotation

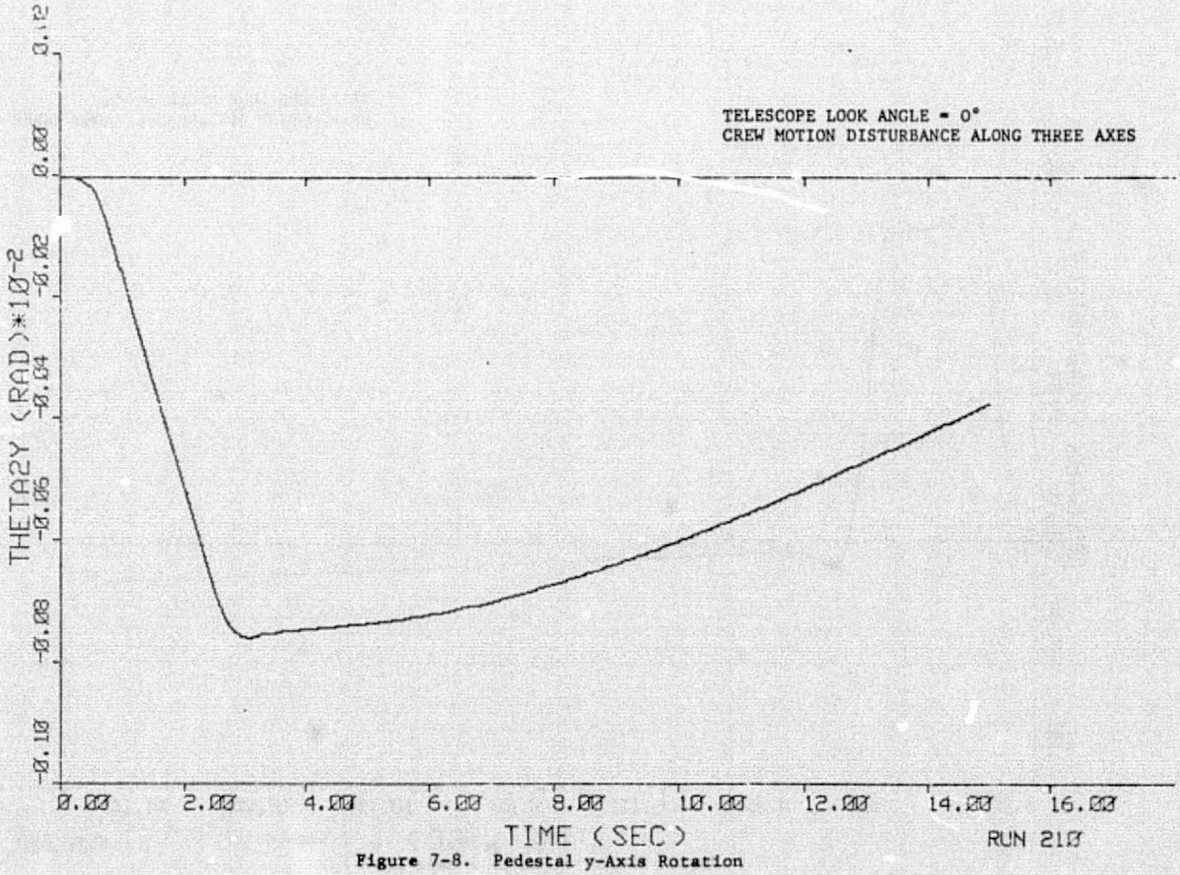

Figure 7-8. Pedestal y-Axis Rotation

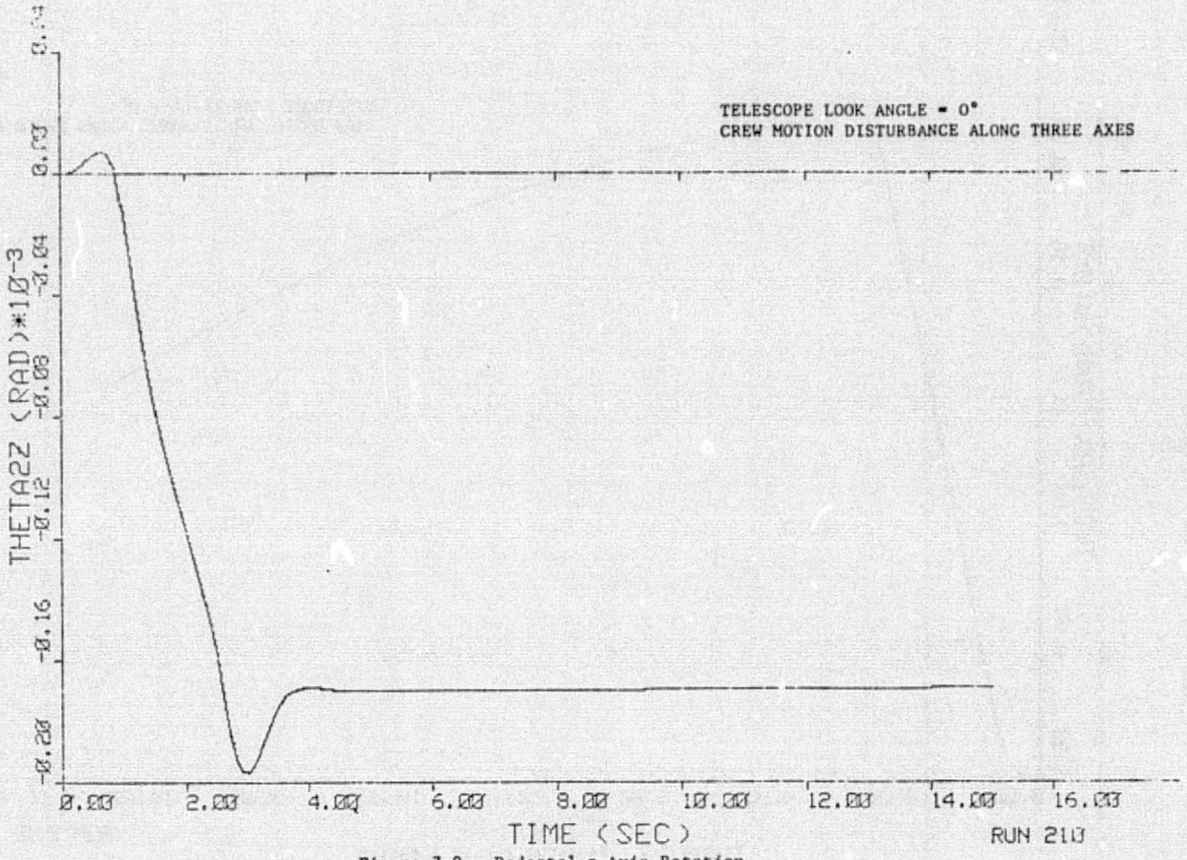

Figure 7-9. Pedestal z-Axis Rotation

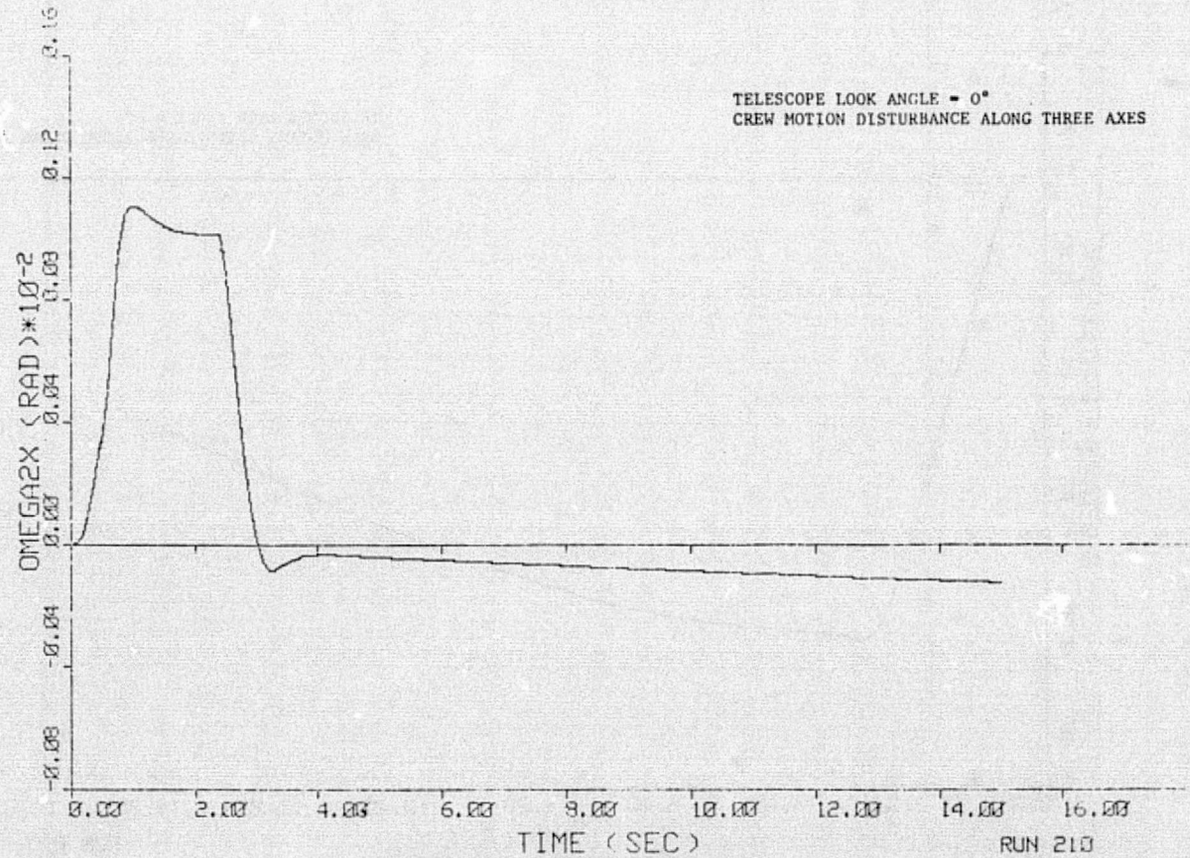

Figure 7-10. Pedestal x-Axis Rate

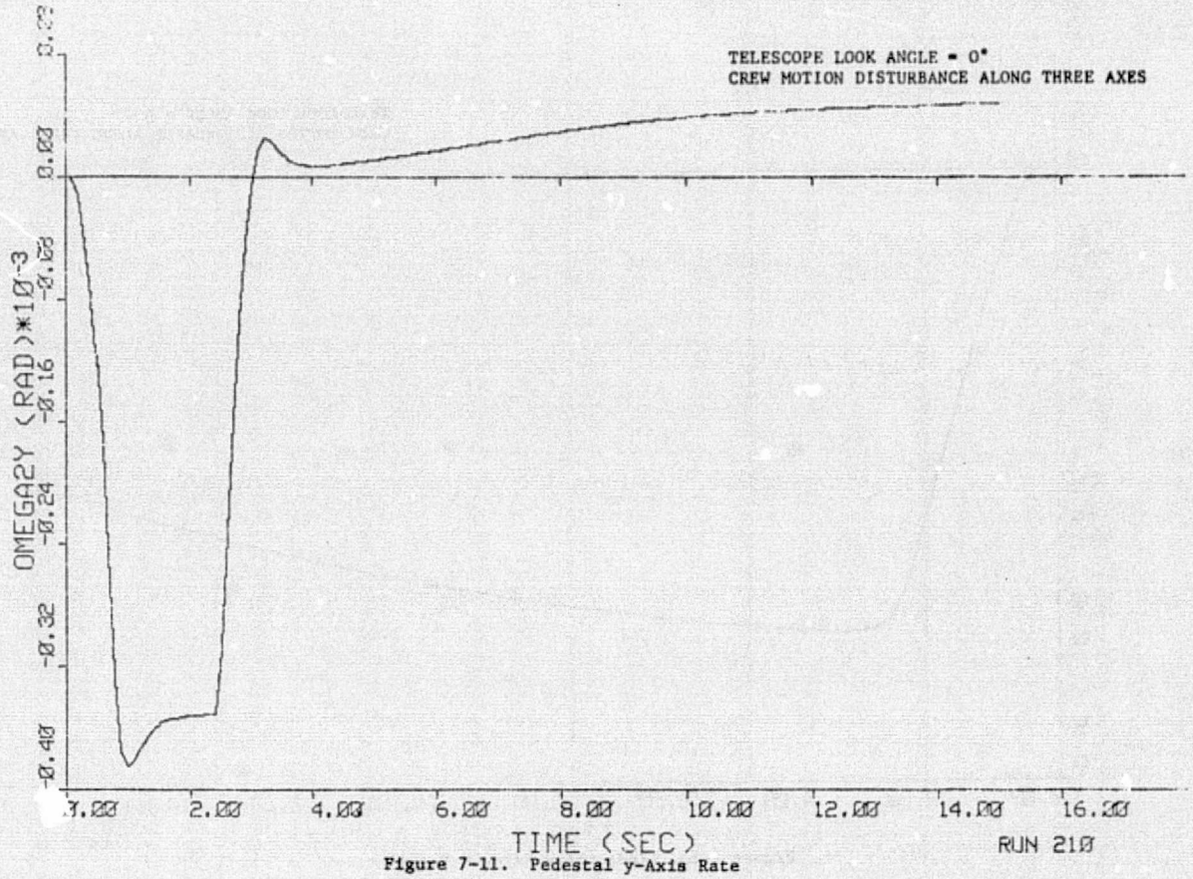

Figure 7-11. Pedestal y-Axis Rate

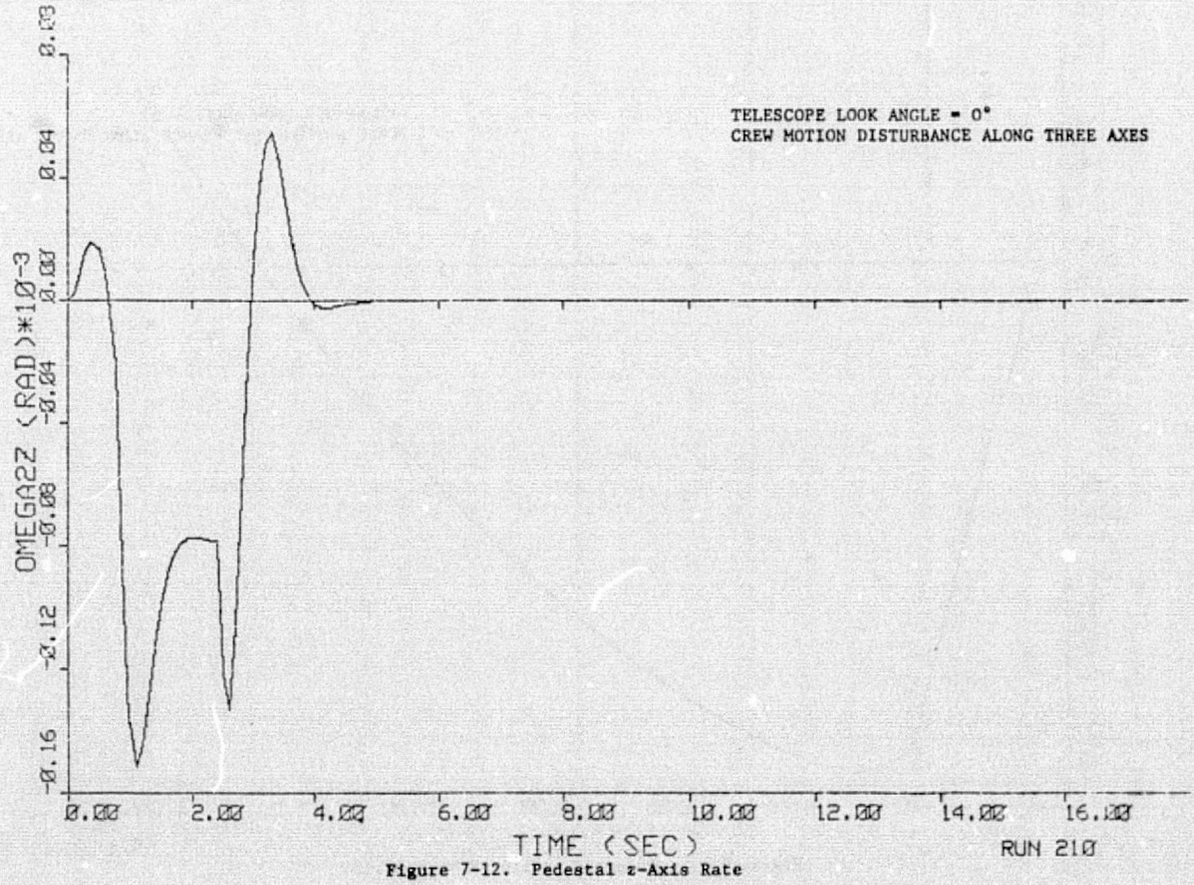

Figure 7-12. Pedestal z-Axis Rate

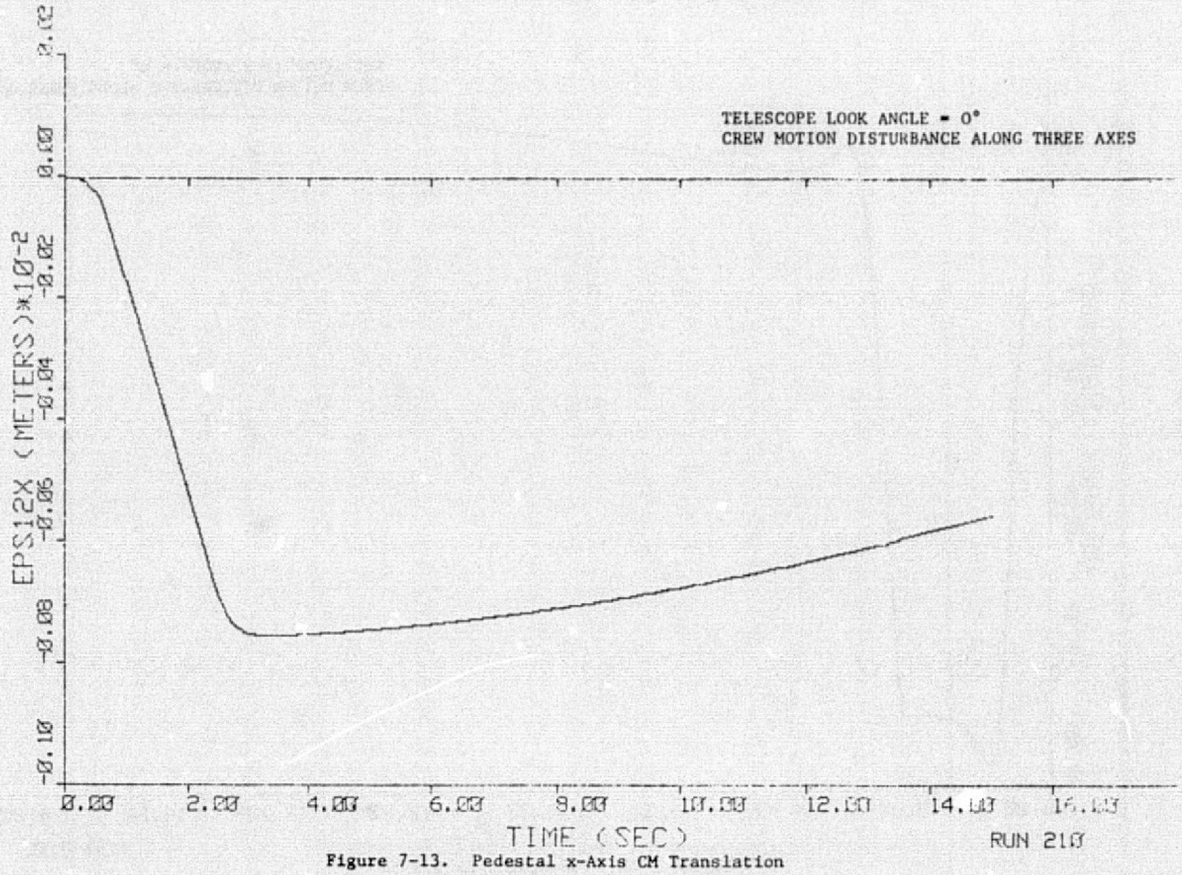

Figure 7-13. Pedestal x-Axis CM Translation

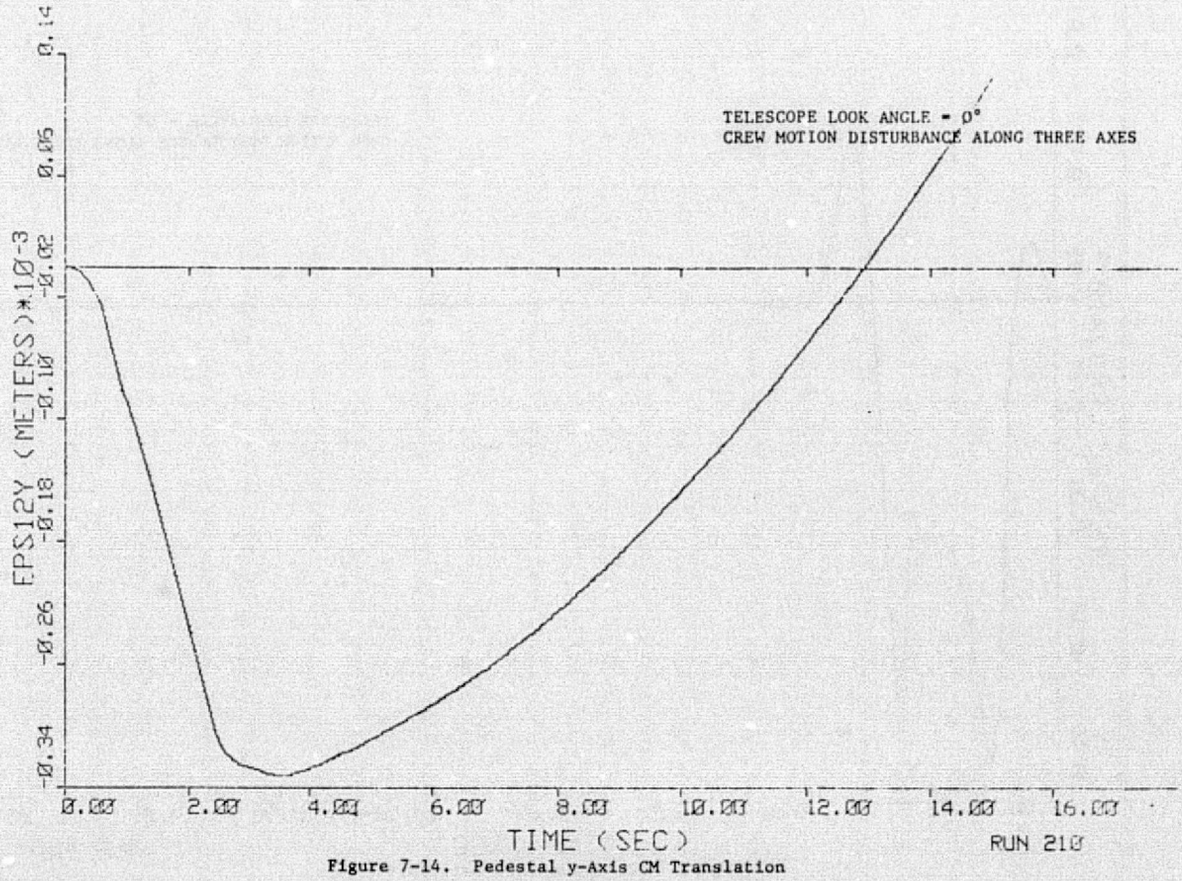

Figure 7-14. Pedestal y-Axis CM Translation

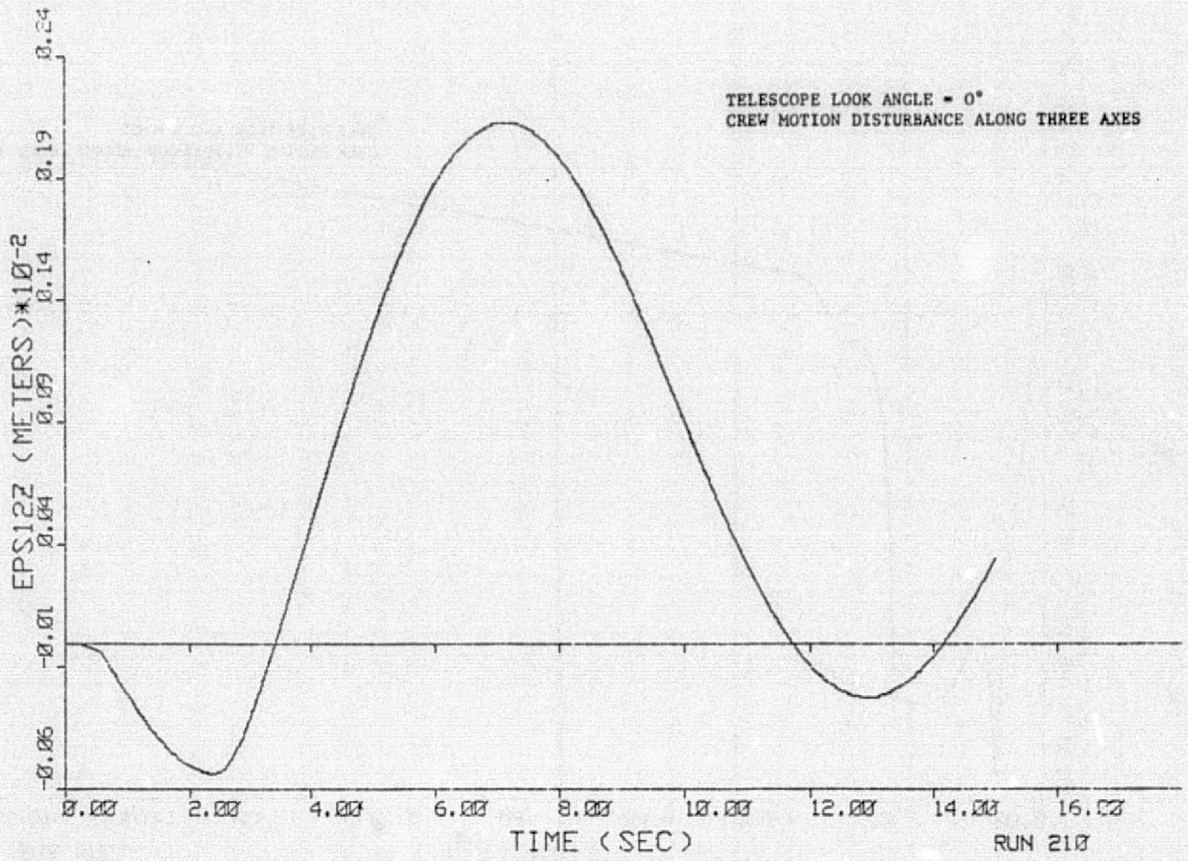

Figure 7-15. Pedestal z-Axis CM Translation

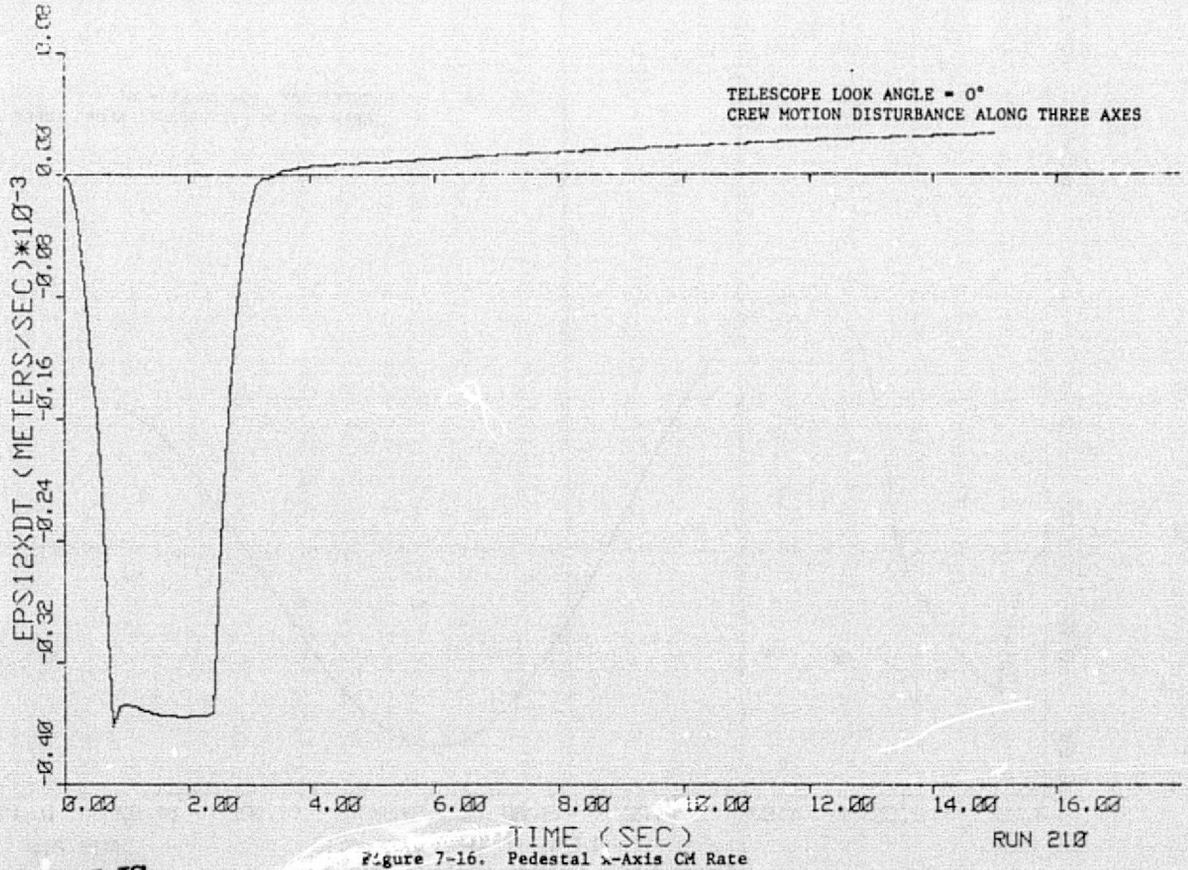

Figure 7-16. Pedestal x-Axis CM Rate

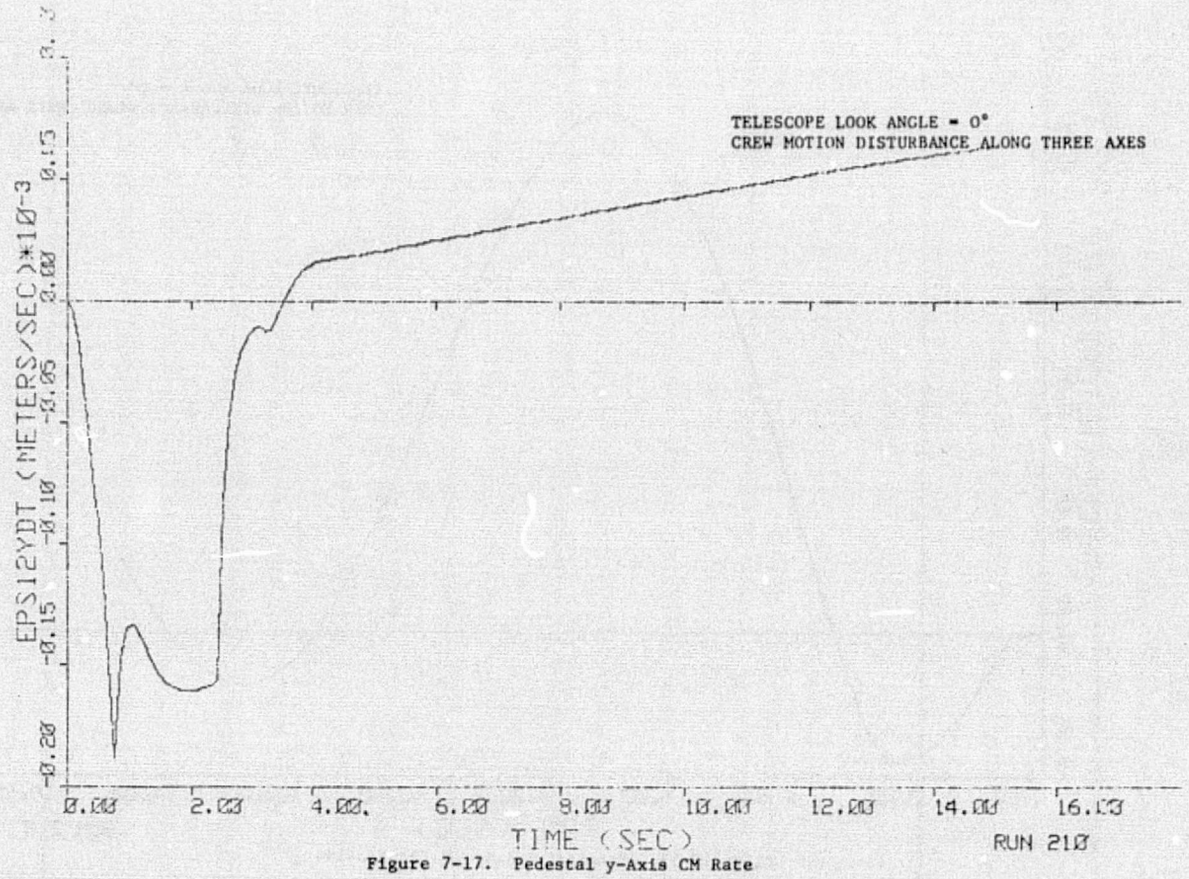

Figure 7-17. Pedestal y-Axis CM Rate

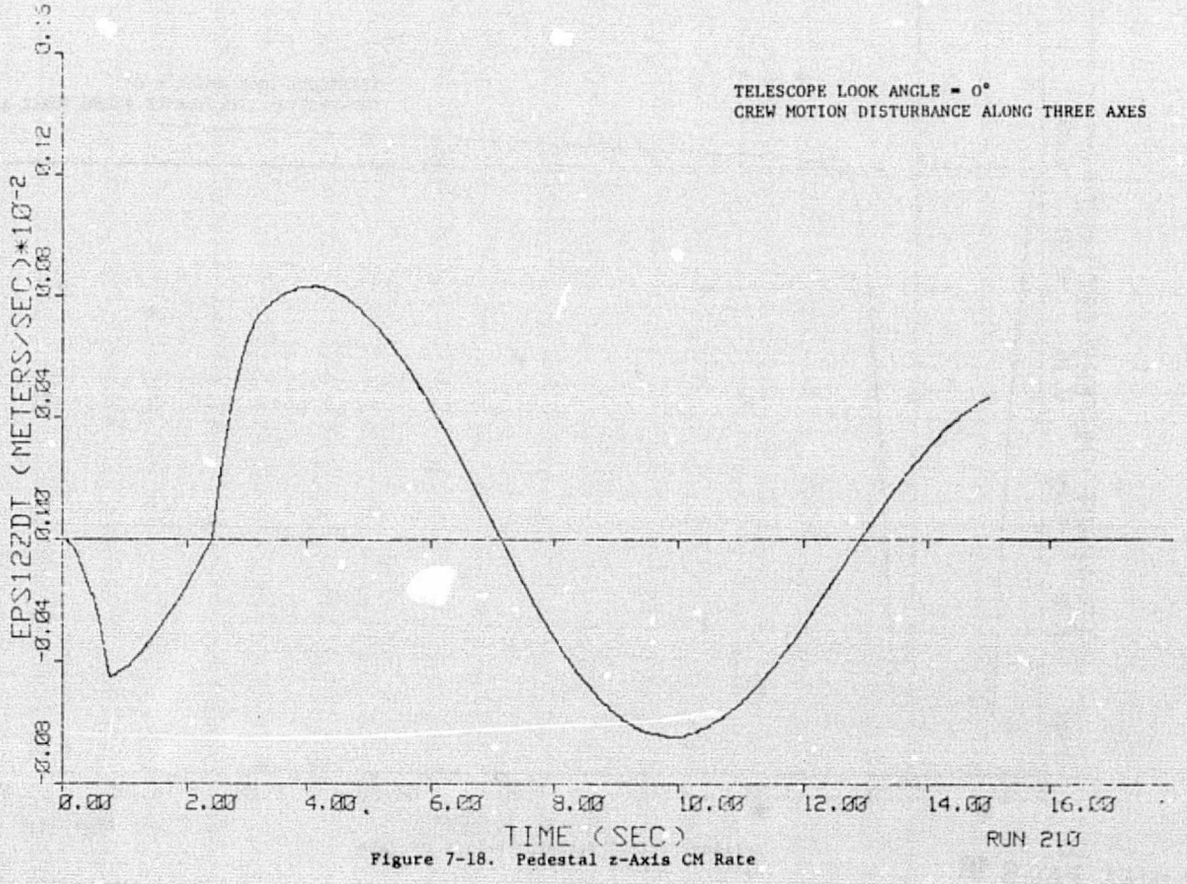

Figure 7-18. Pedestal z-Axis CM Rate

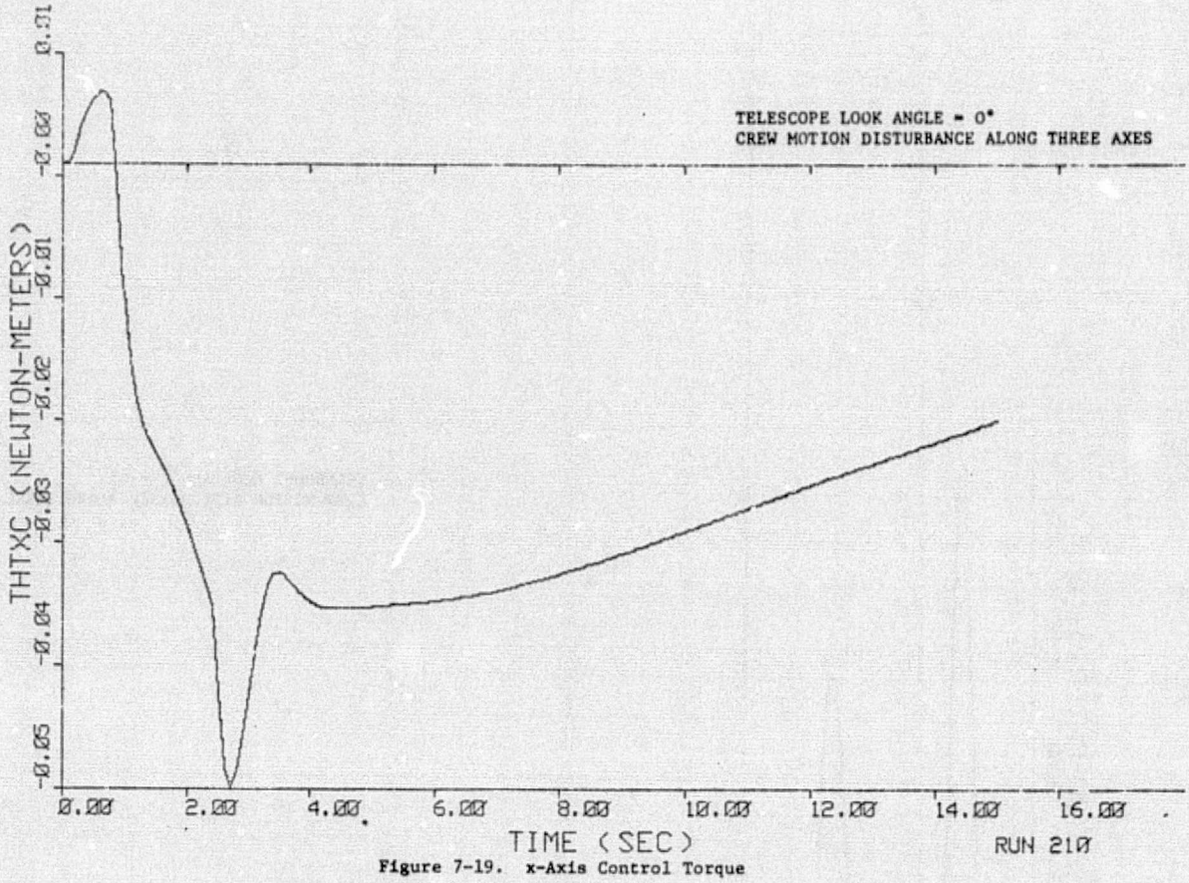

Figure 7-19. x-Axis Control Torque

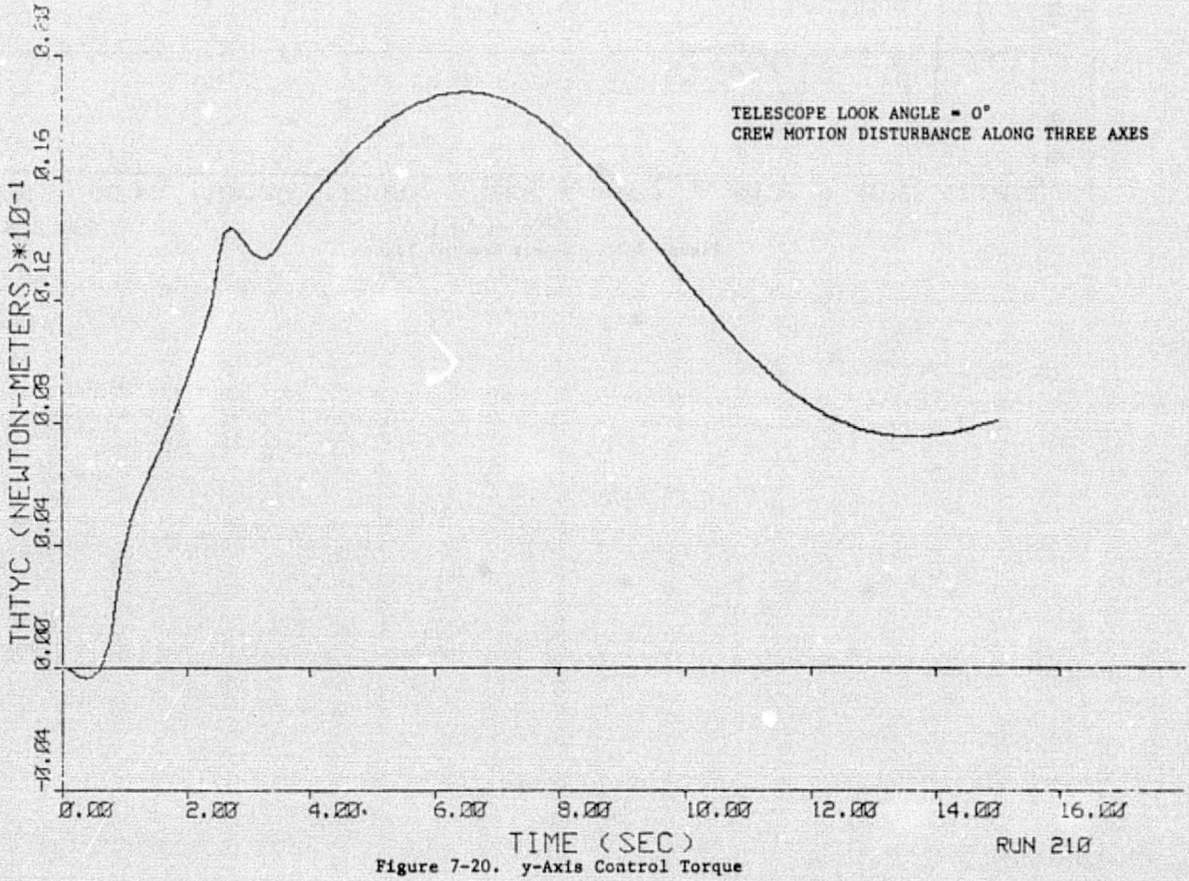

Figure 7-20. y-Axis Control Torque

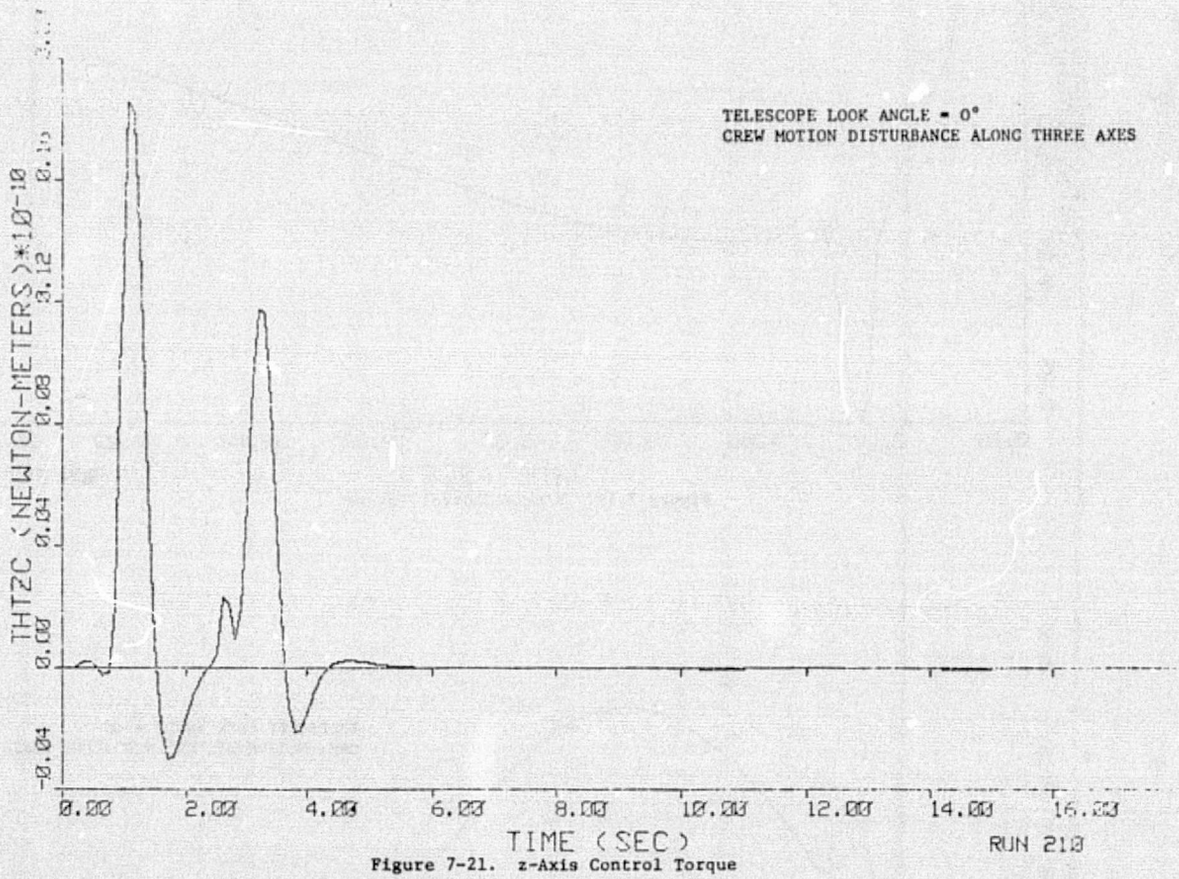

Figure 7-21. z-Axis Control Torque

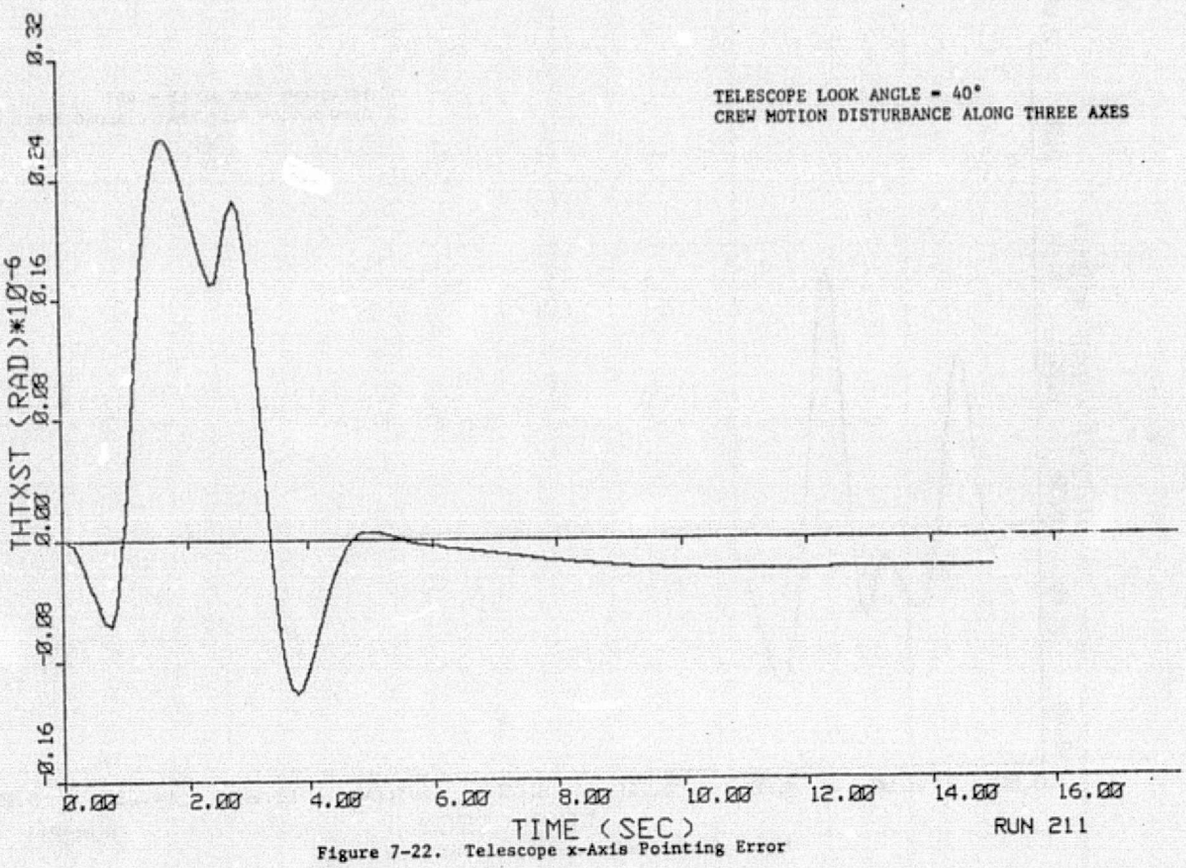

Figure 7-22. Telescope x-Axis Pointing Error

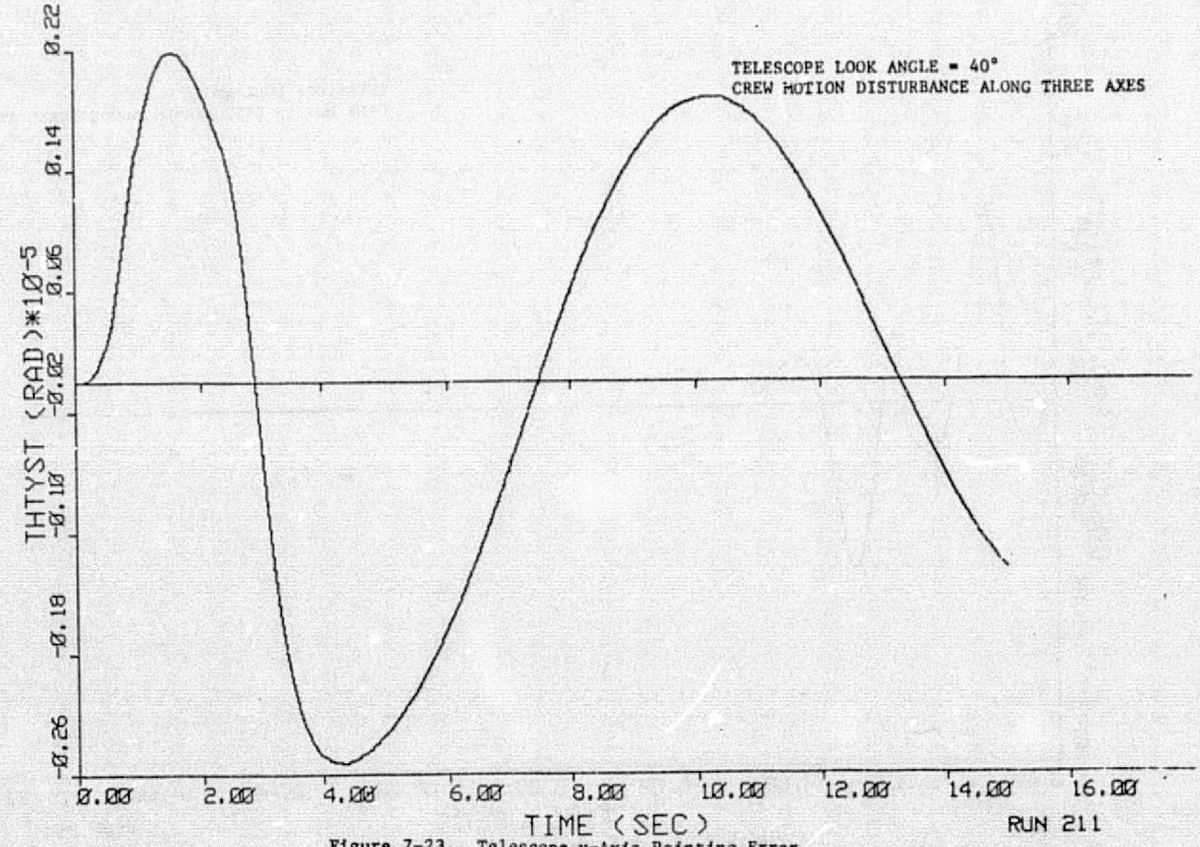

Figure 7-23. Telescope y-Axis Pointing Error

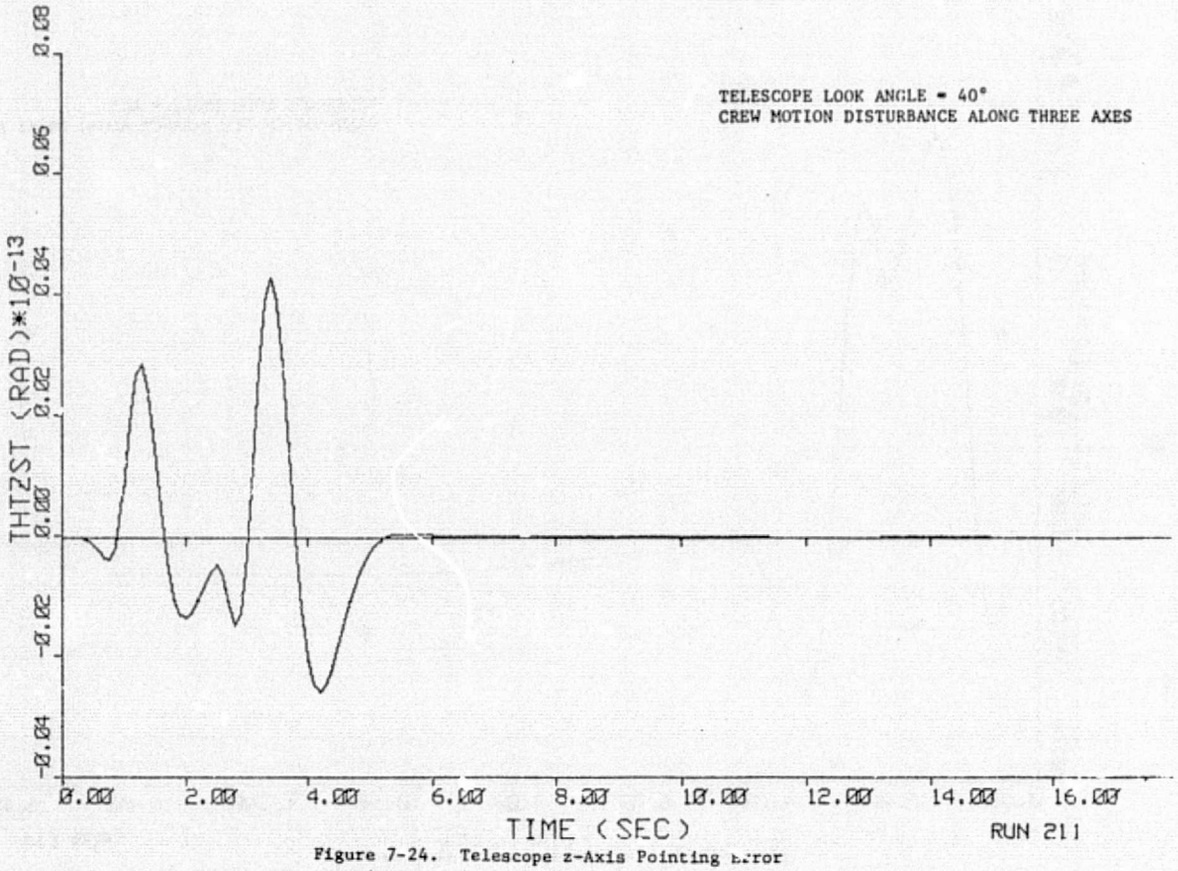

Figure 7-24. Telescope z-Axis Pointing Error

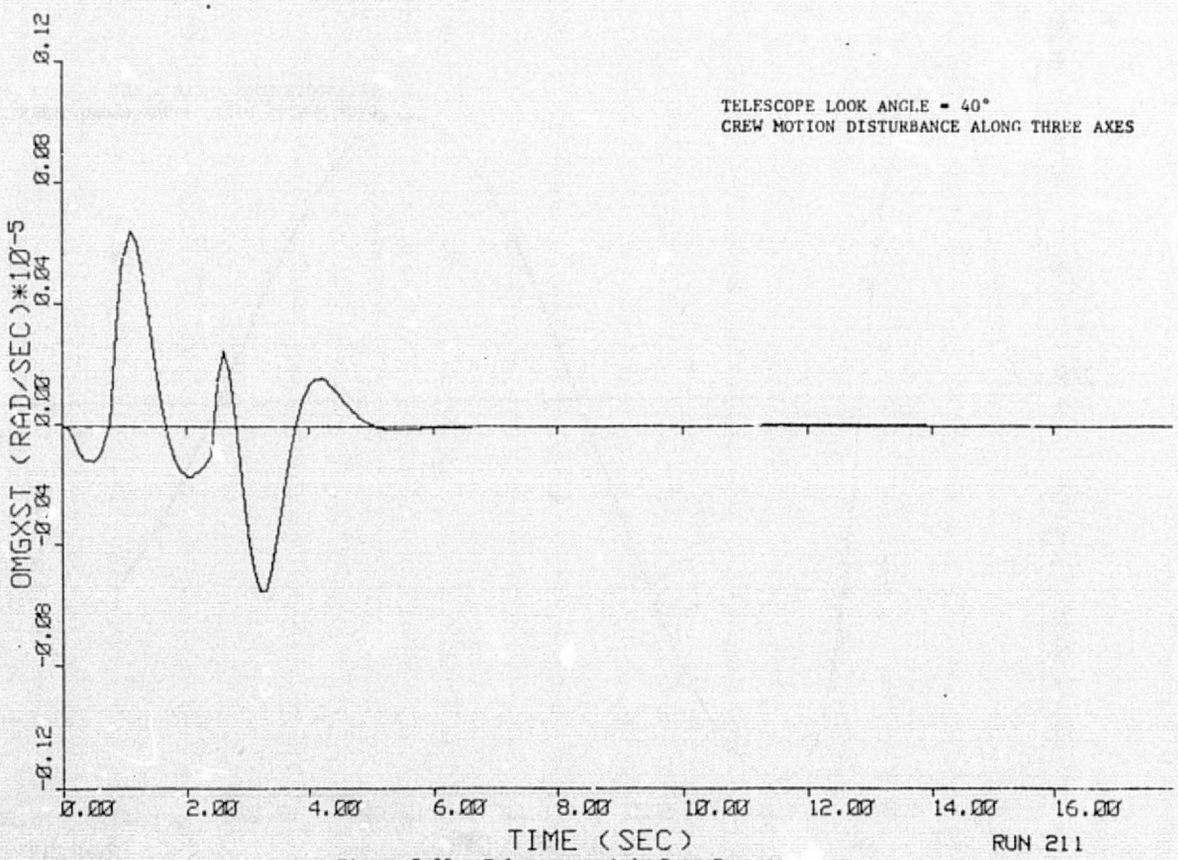

Figure 7-25. Telescope x-Axis Rate Error

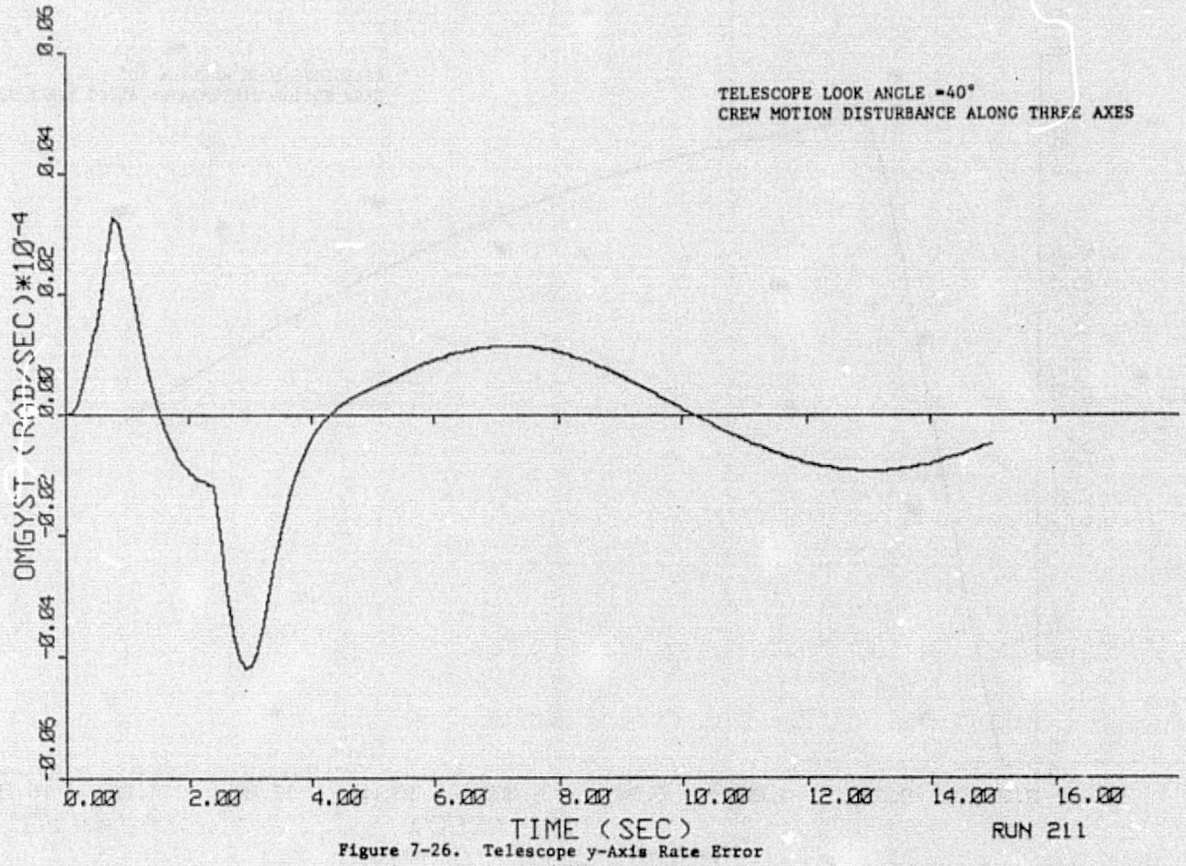

Figure 7-26. Telescope y-Axis Rate Error

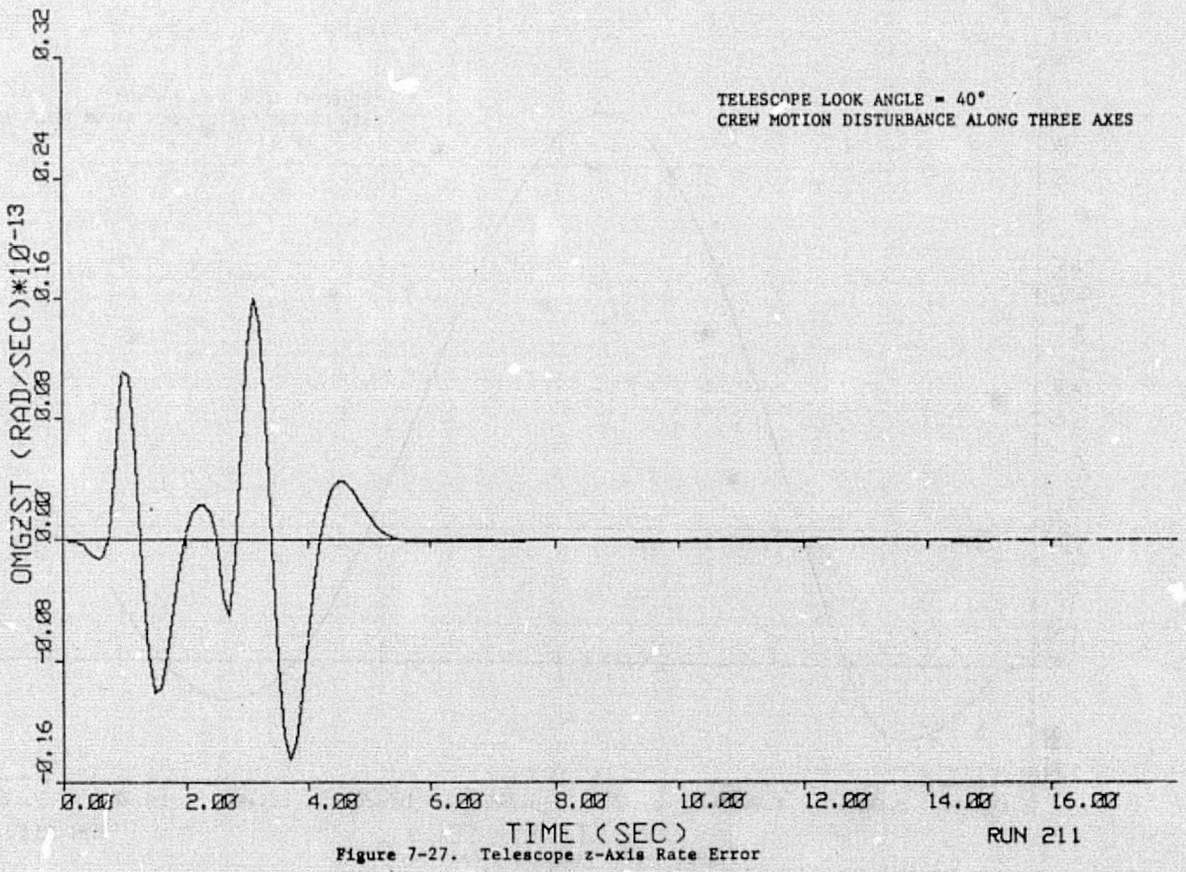

Figure 7-27. Telescope z-Axis Rate Error

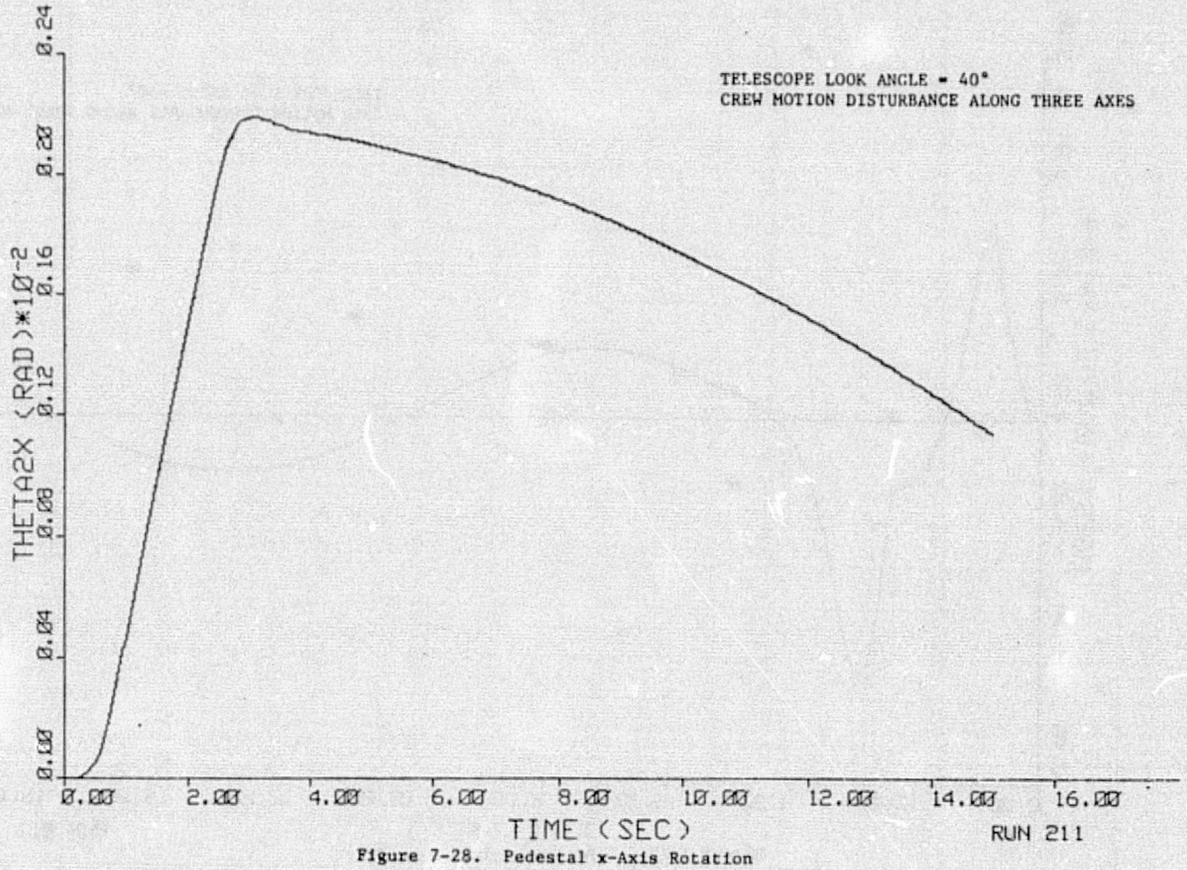

Figure 7-28. Pedestal x-Axis Rotation

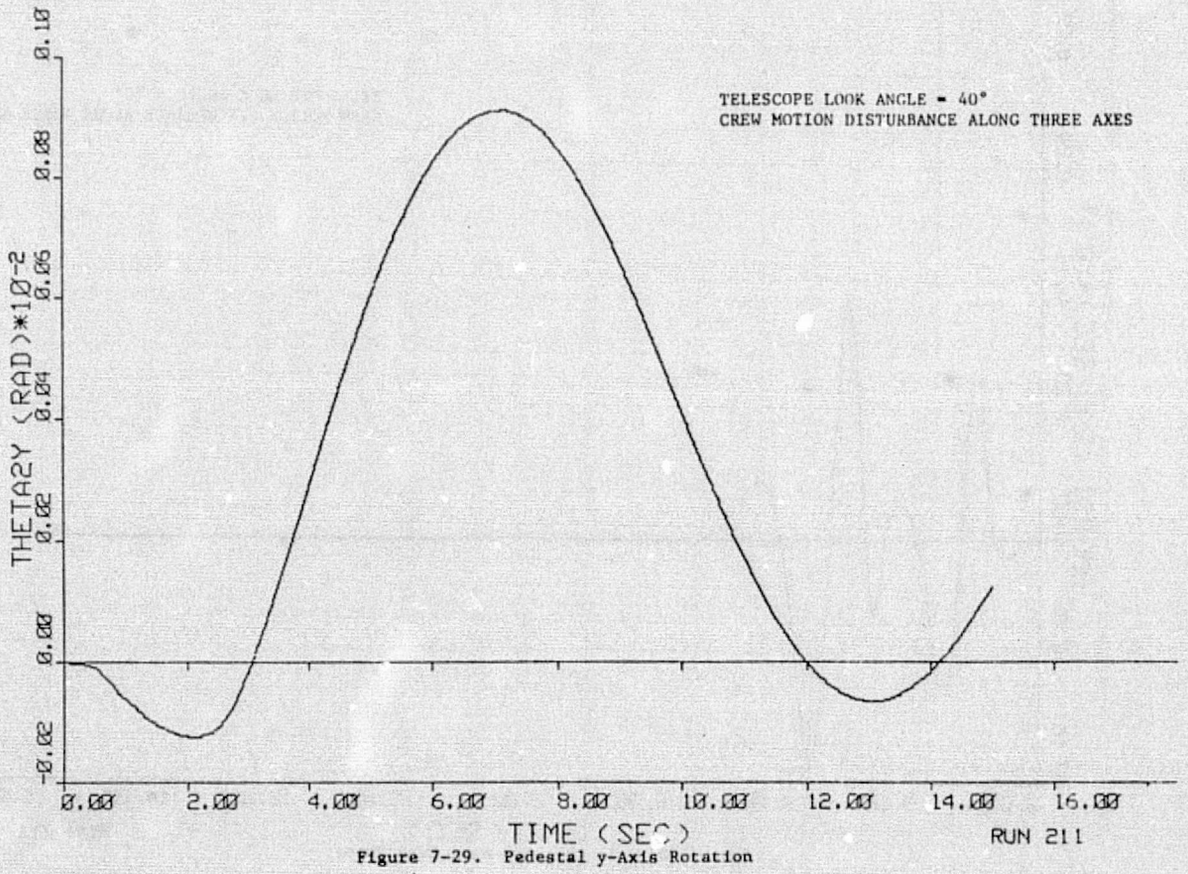

Figure 7-29. Pedestal y-Axis Rotation

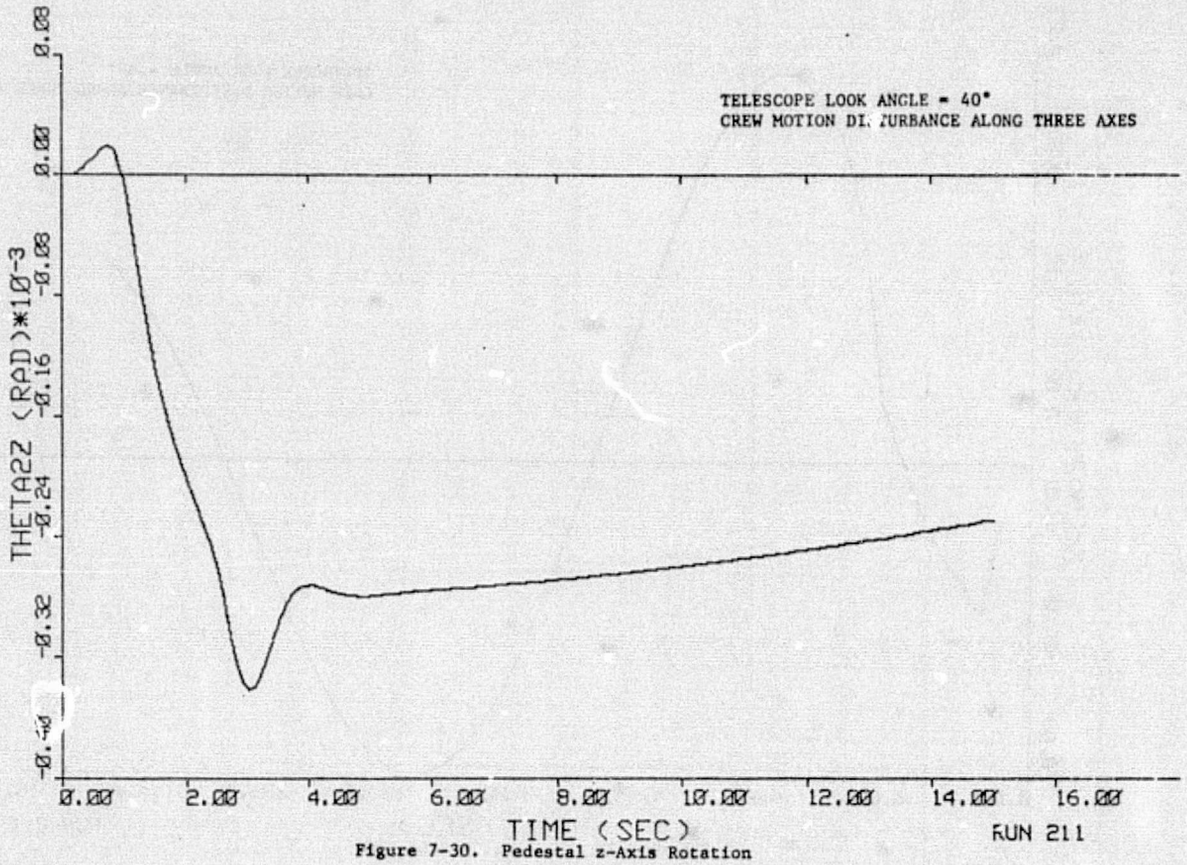

Figure 7-30. Pedestal z-Axis Rotation

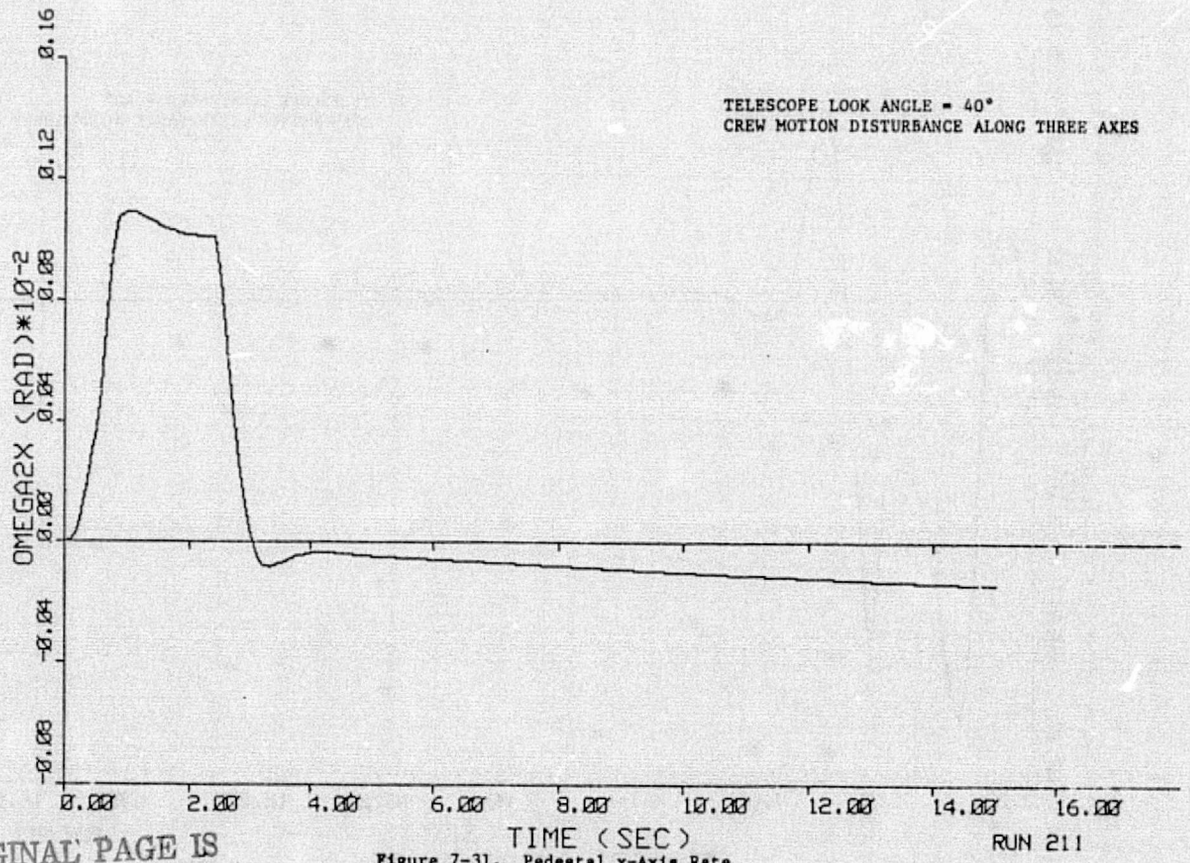

Figure 7-31. Pedestal x-Axis Rate

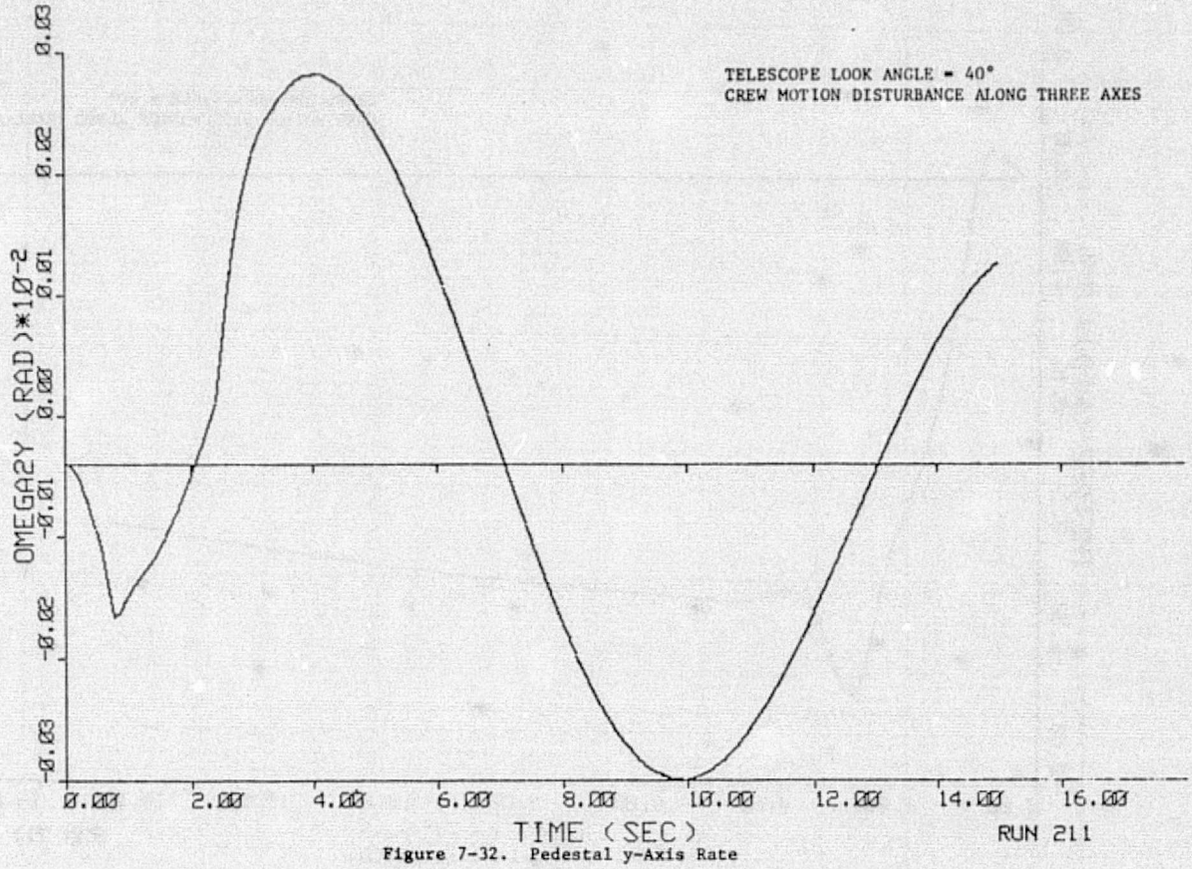

Figure 7-32. Pedestal y-Axis Rate

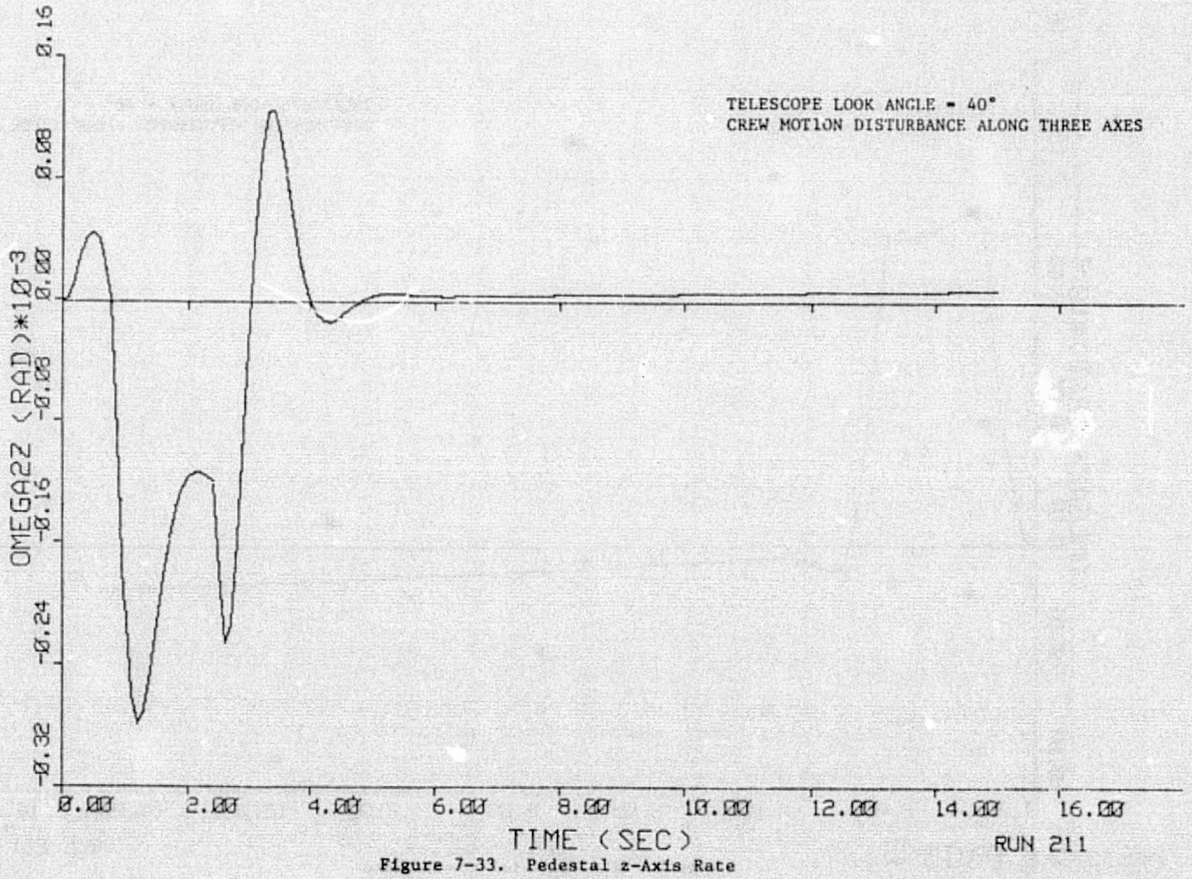

Figure 7-33. Pedestal z-Axis Rate

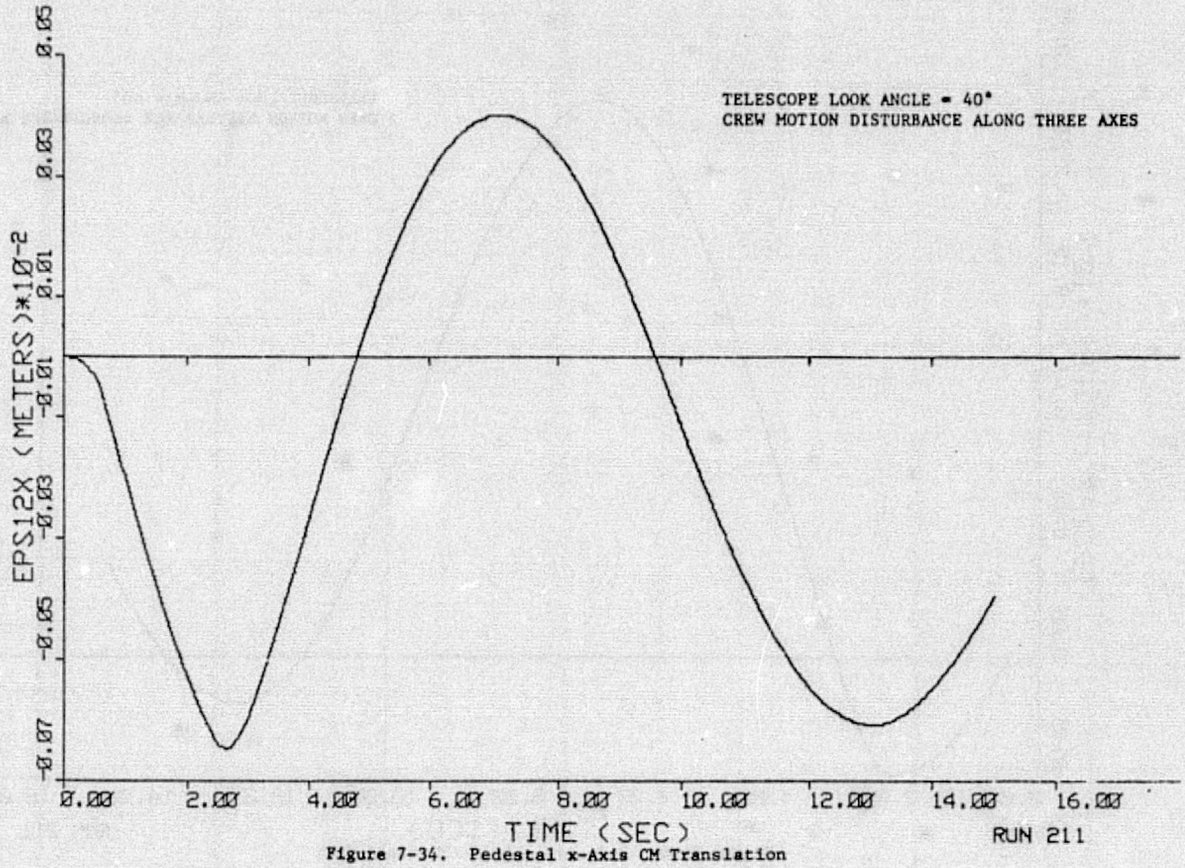

Figure 7-34. Pedestal x-Axis CM Translation

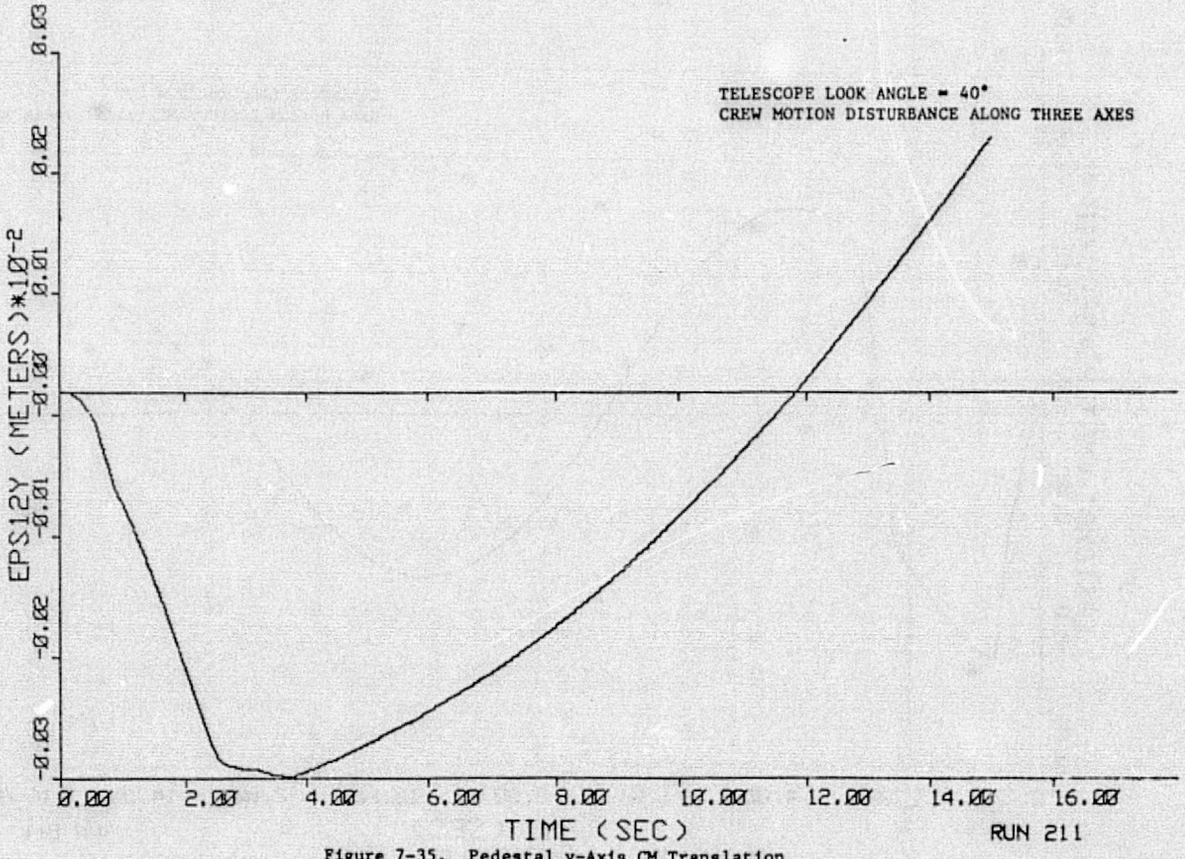

Figure 7-35. Pedestal y-Axis CM Translation

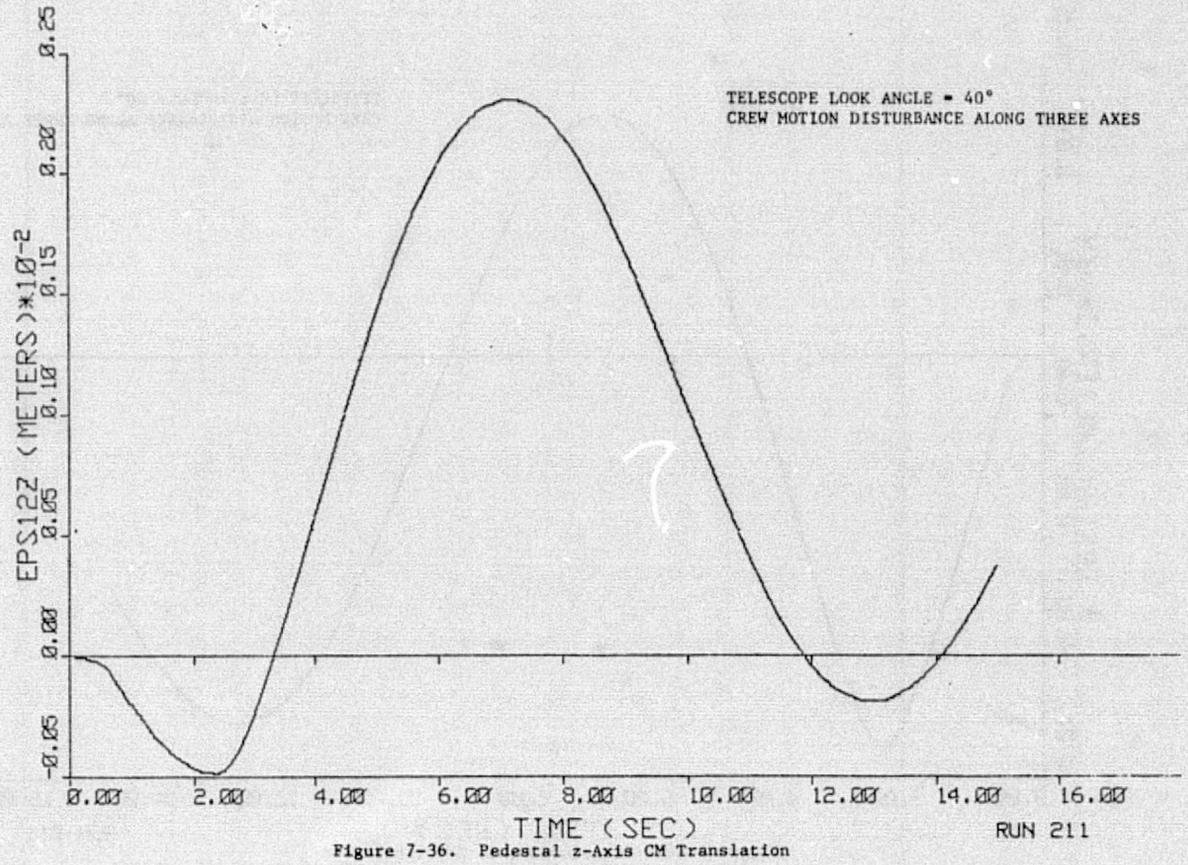

Figure 7-36. Pedestal z-Axis CM Translation

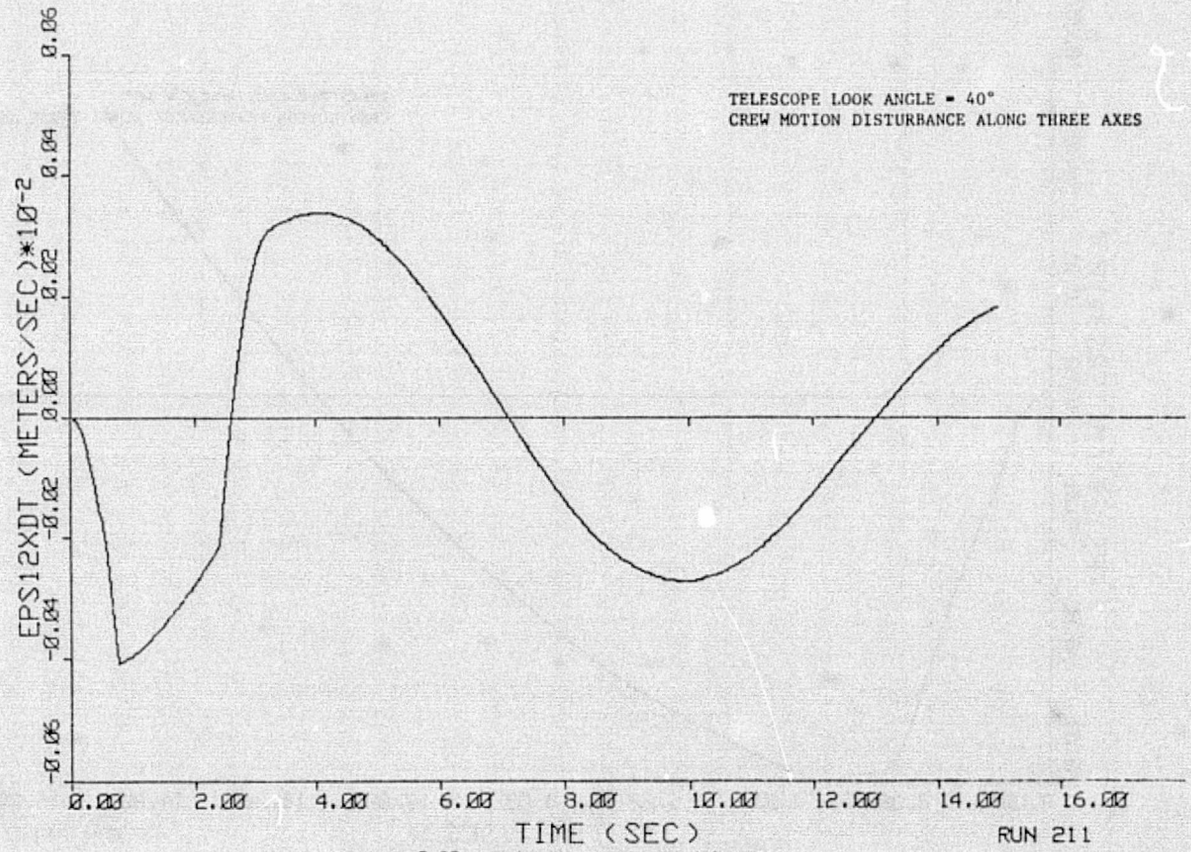

Figure 7-37. Pedestal x-Axis CM Velocity

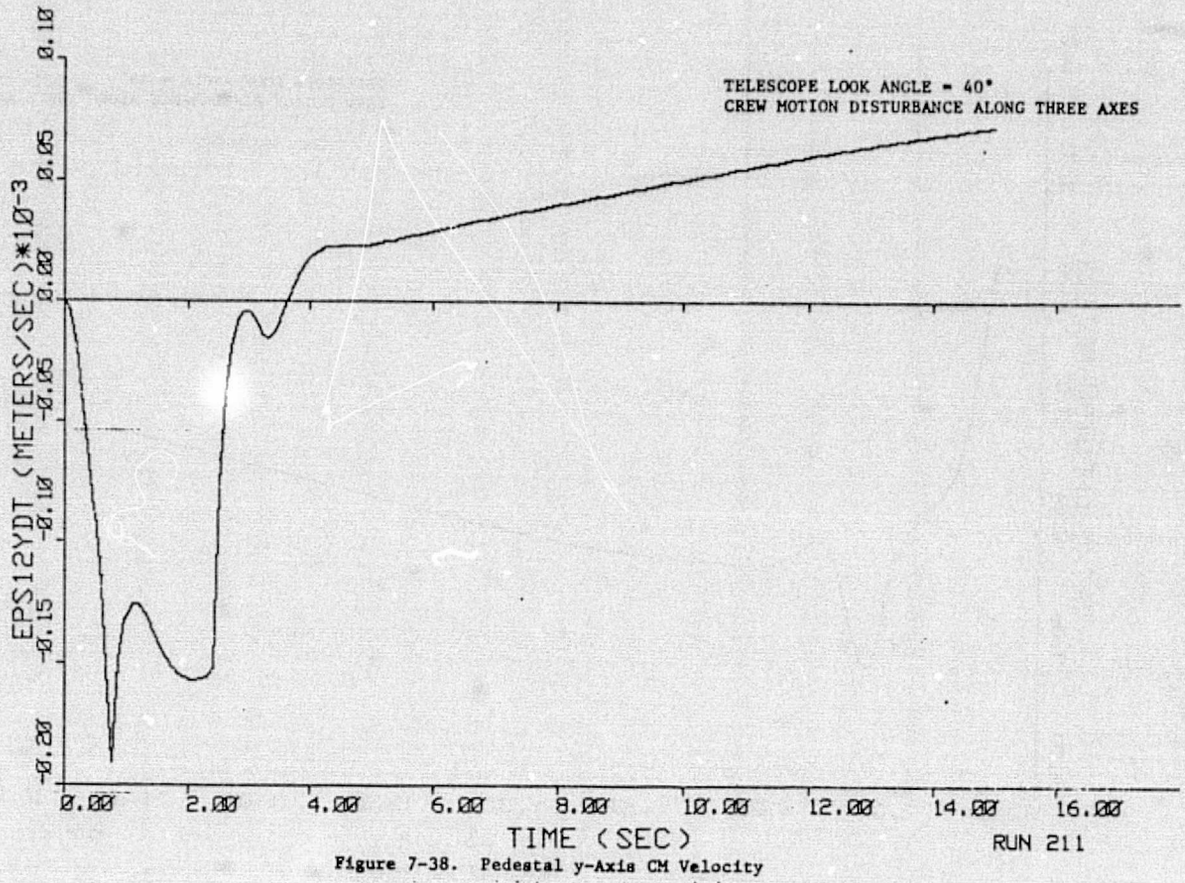

Figure 7-38. Pedestal y-Axis CM Velocity

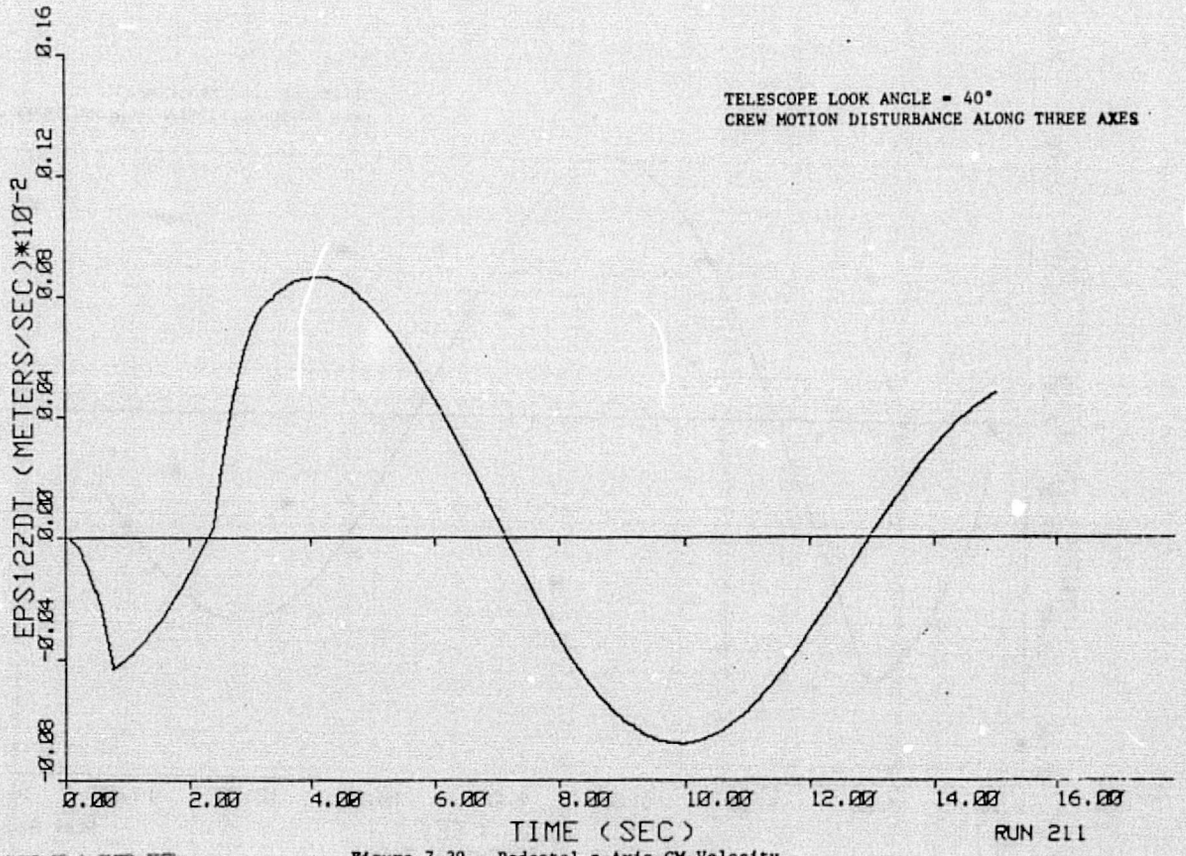

Figure 7-39. Pedestal z-Axis CM Velocity

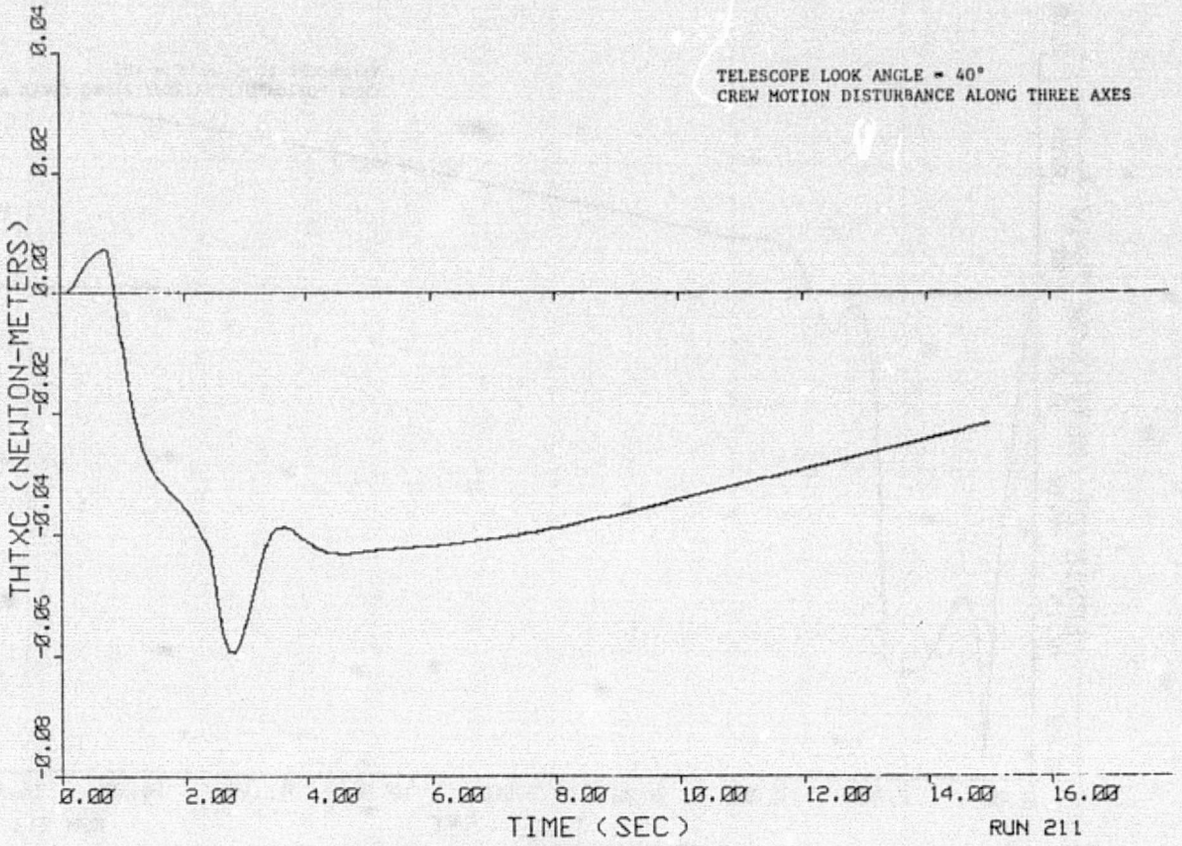

Figure 7-40. x-Axis Control Torque

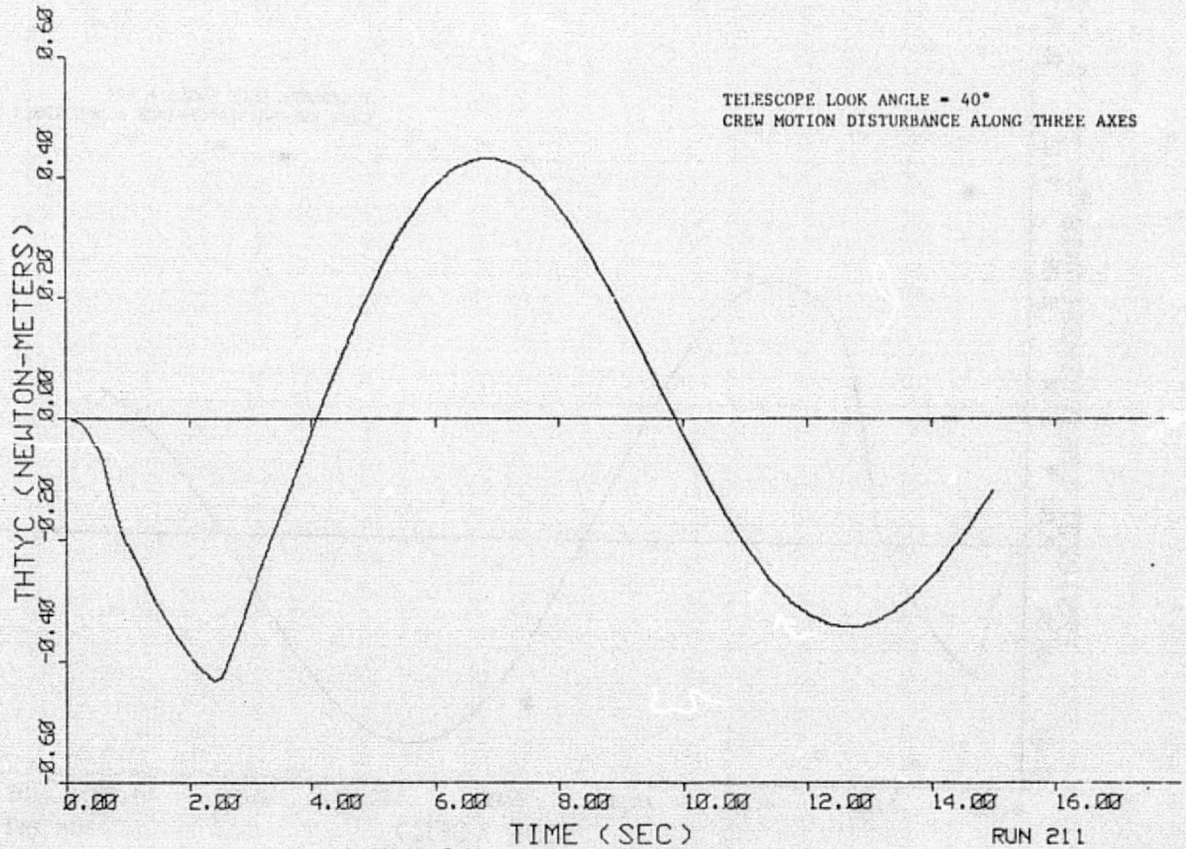

Figure 7-41. y-Axis Control Torque

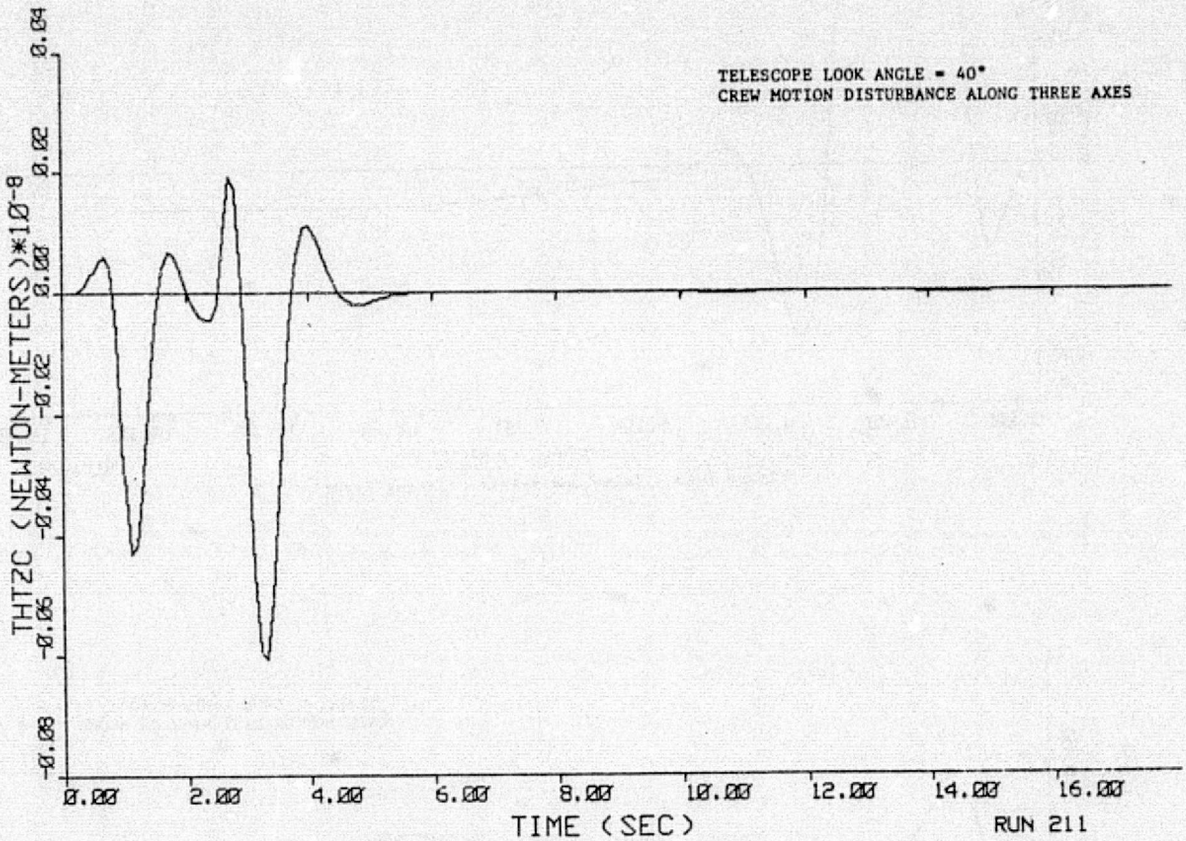

Figure 7-42. z-Axis Control Torque

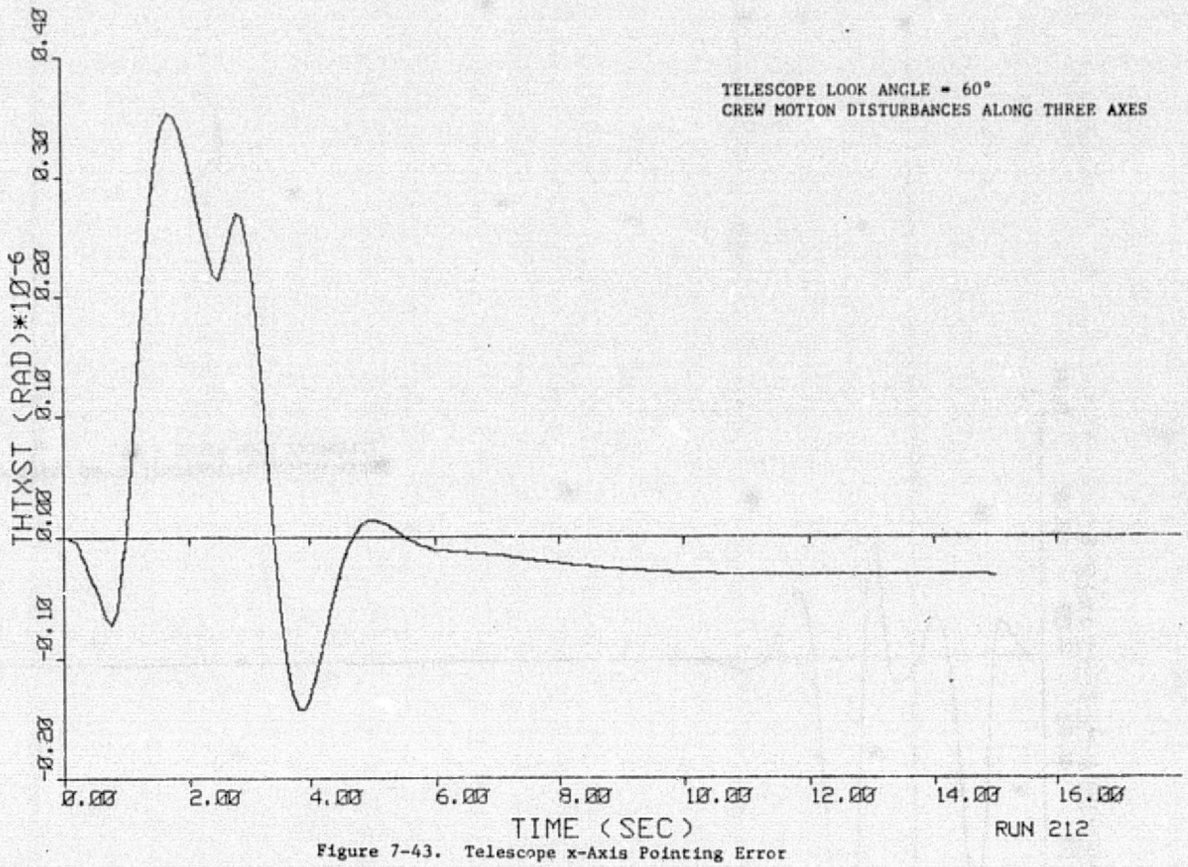

Figure 7-43. Telescope x-Axis Pointing Error

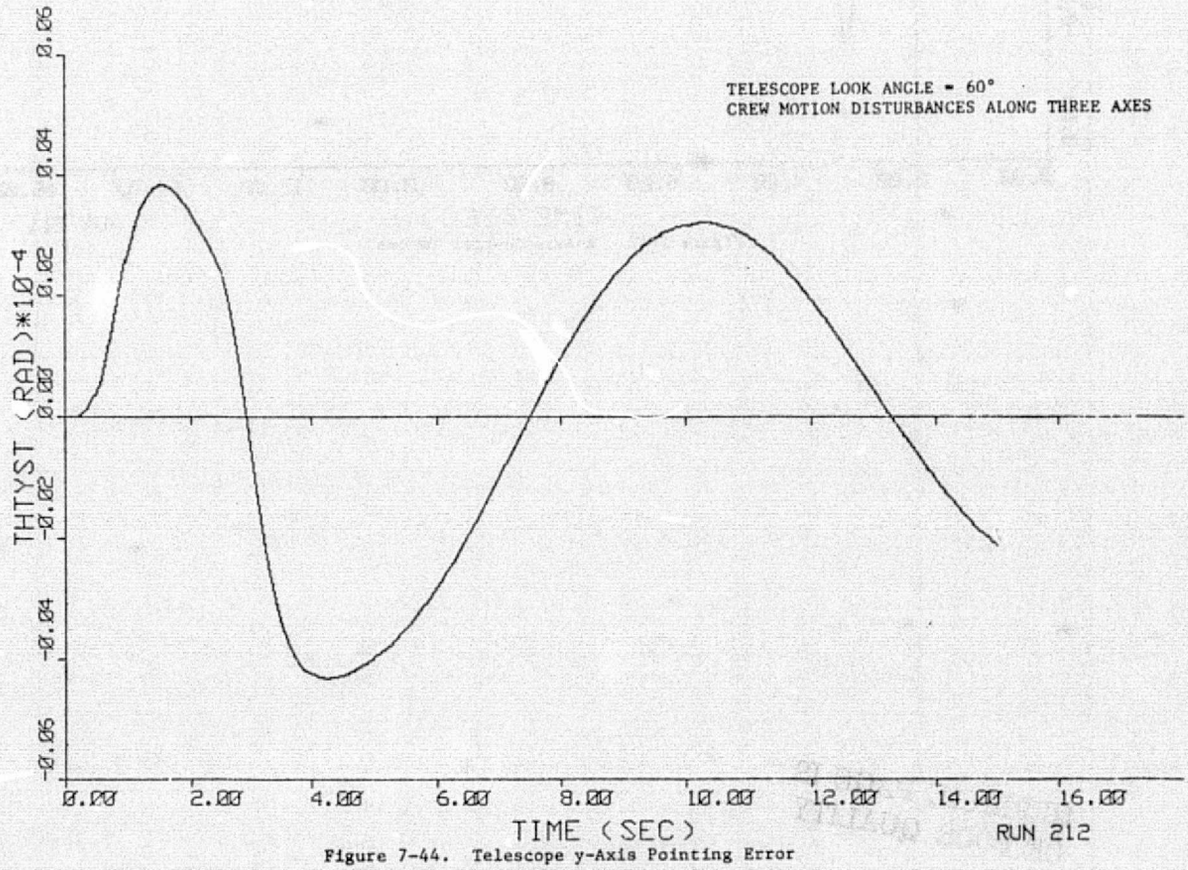

Figure 7-44. Telescope y-Axis Pointing Error

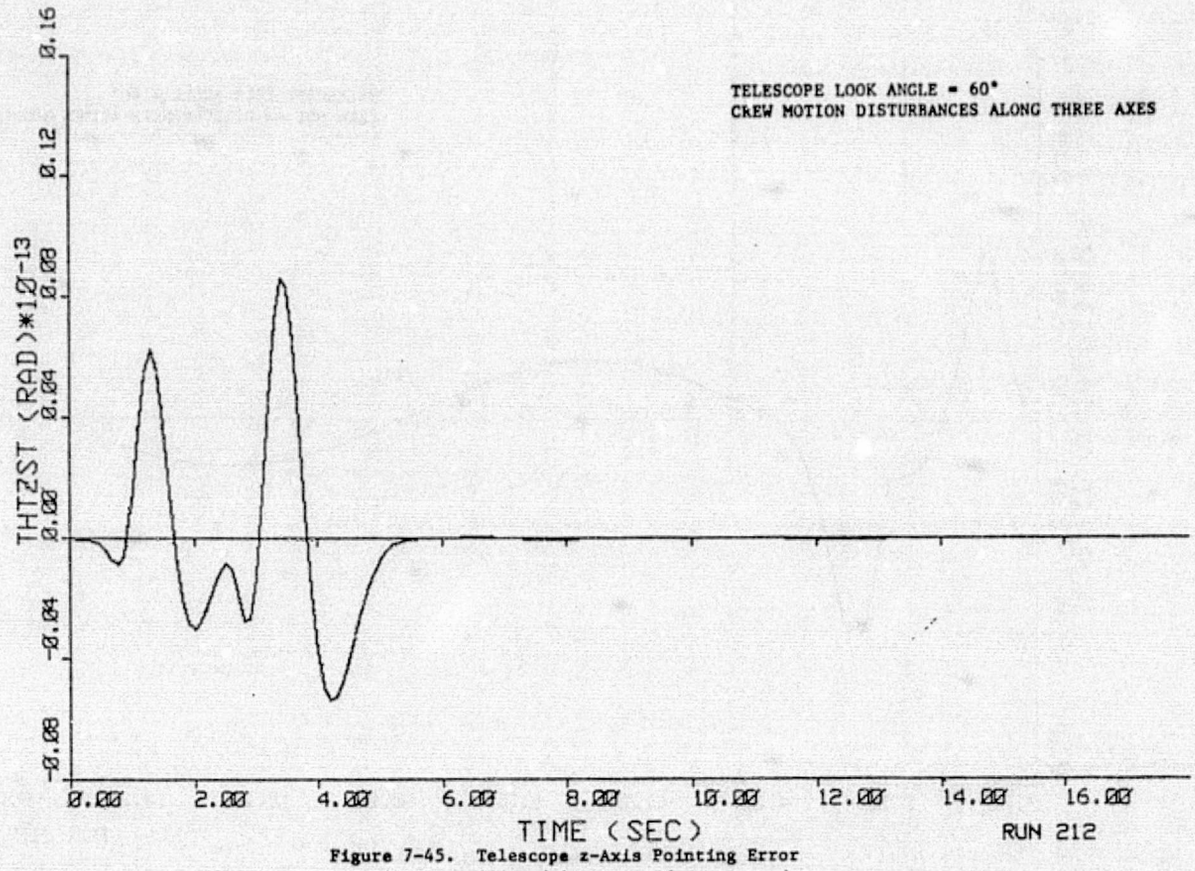

Figure 7-45. Telescope z-Axis Pointing Error

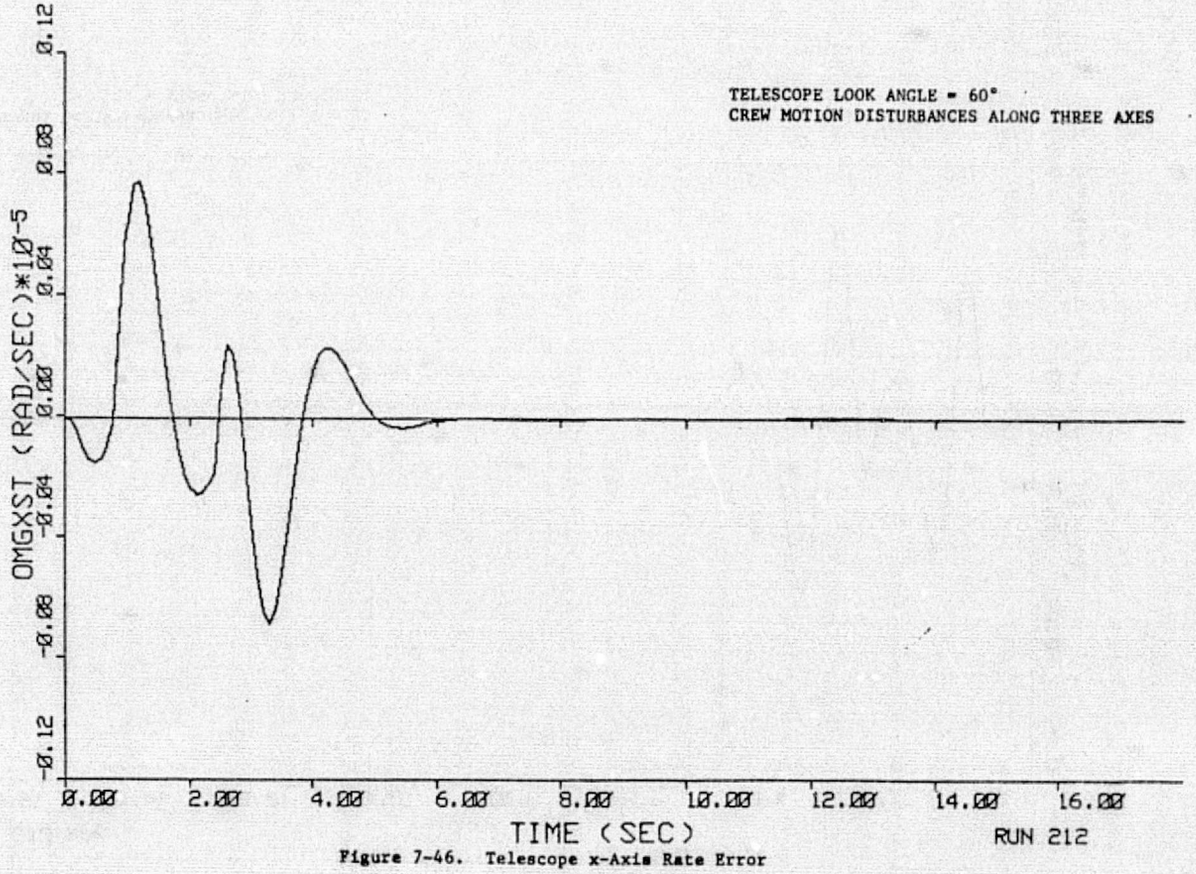

Figure 7-46. Telescope x-Axis Rate Error

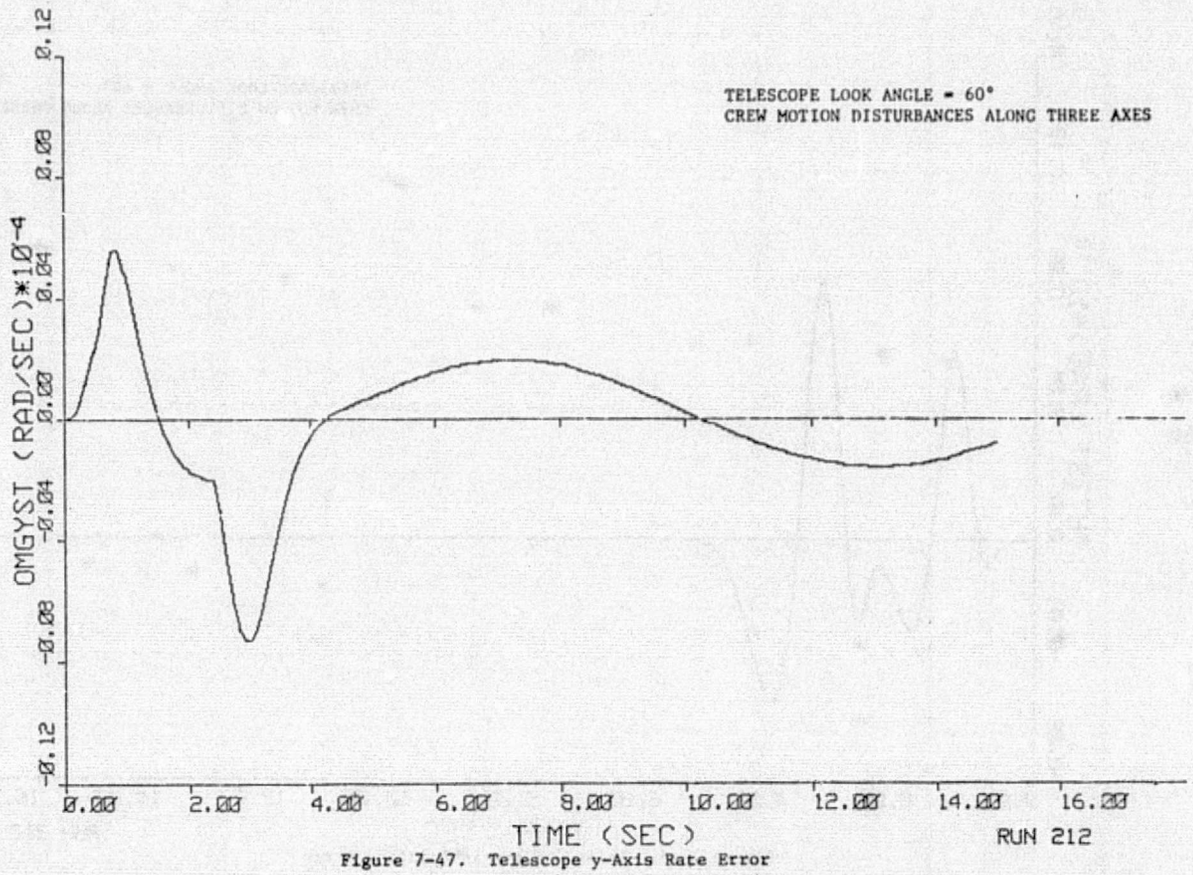

Figure 7-47. Telescope y-Axis Rate Error

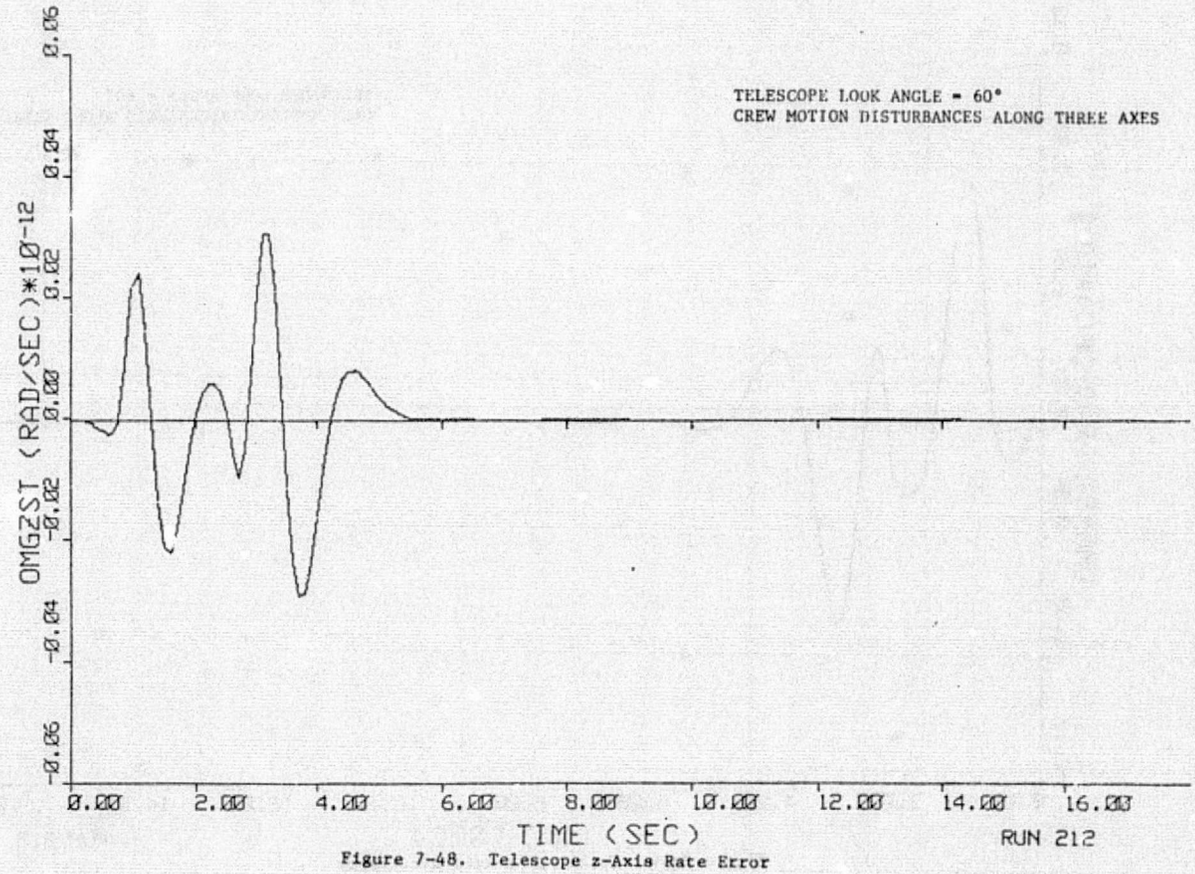

Figure 7-48. Telescope z-Axis Rate Error

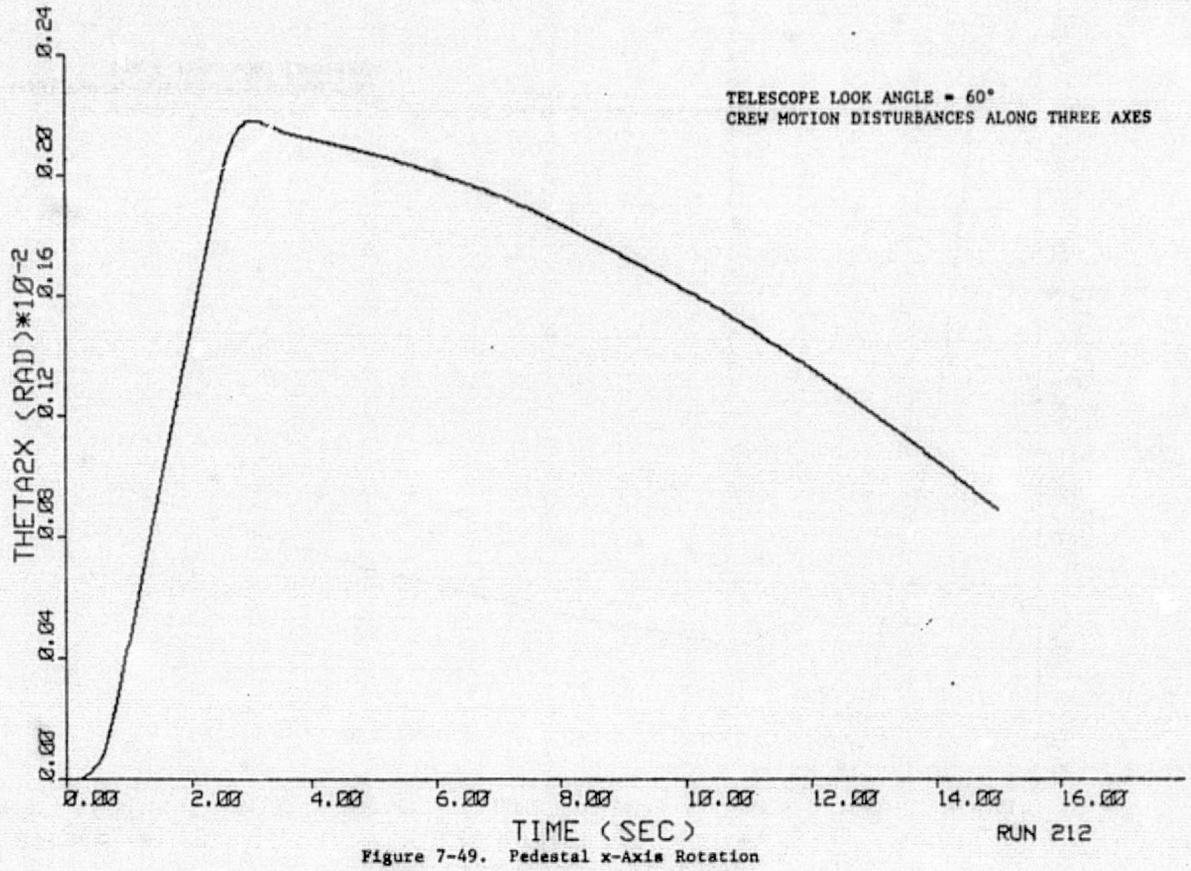

Figure 7-49. Pedestal x-Axis Rotation

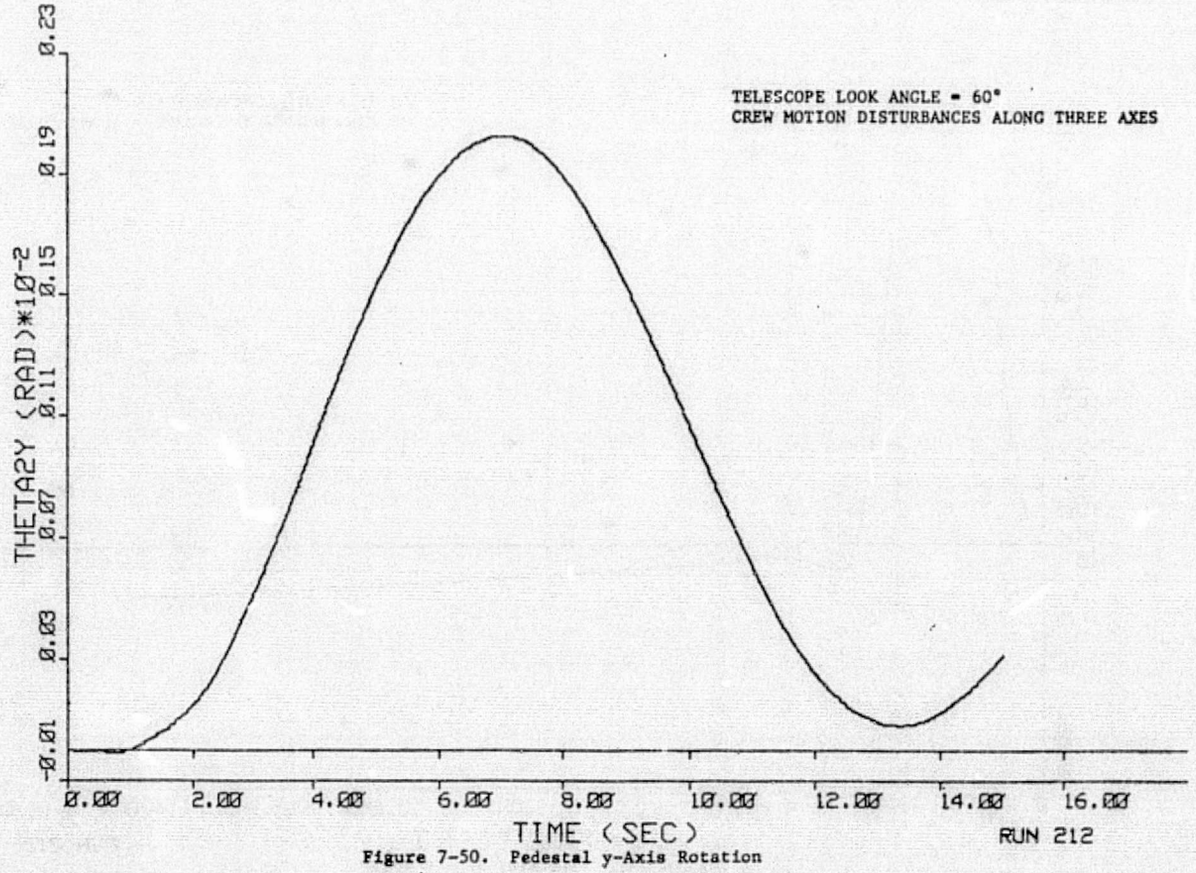

Figure 7-50. Pedestal y-Axis Rotation

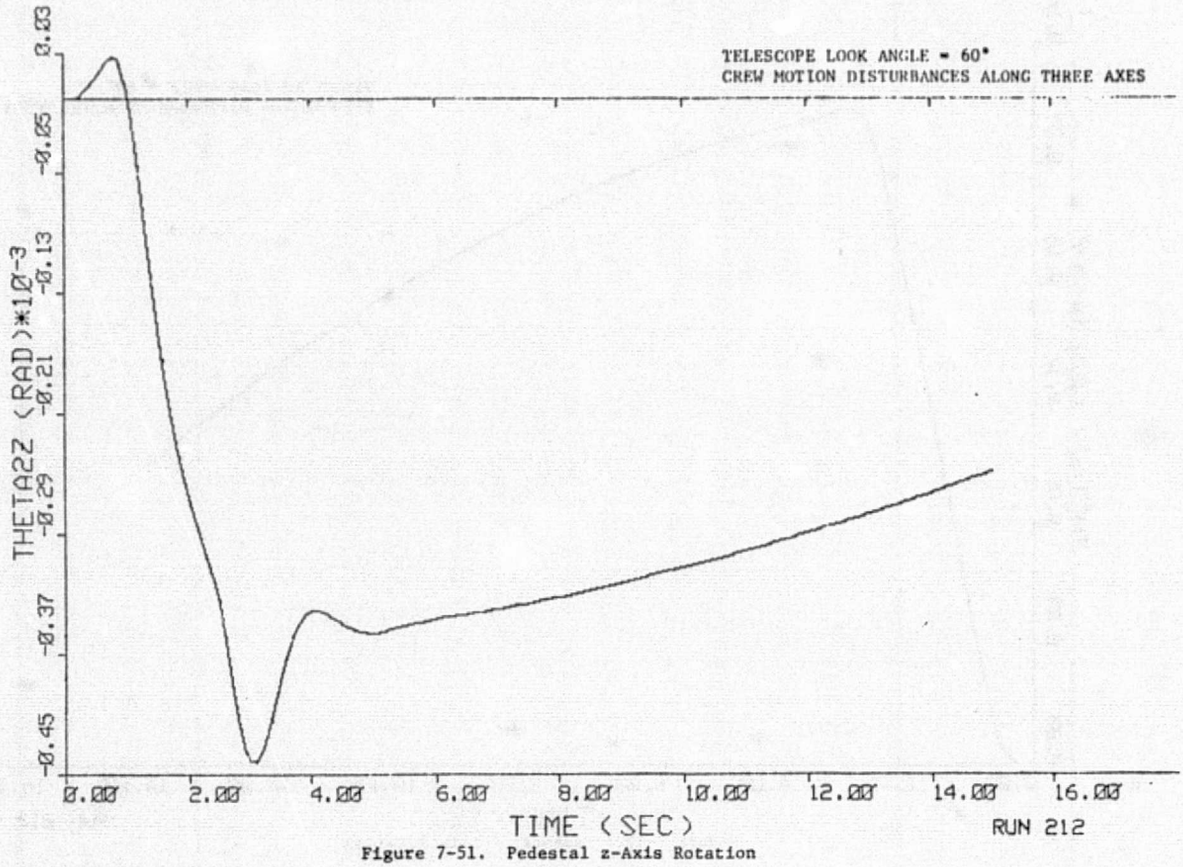

Figure 7-51. Pedestal z-Axis Rotation

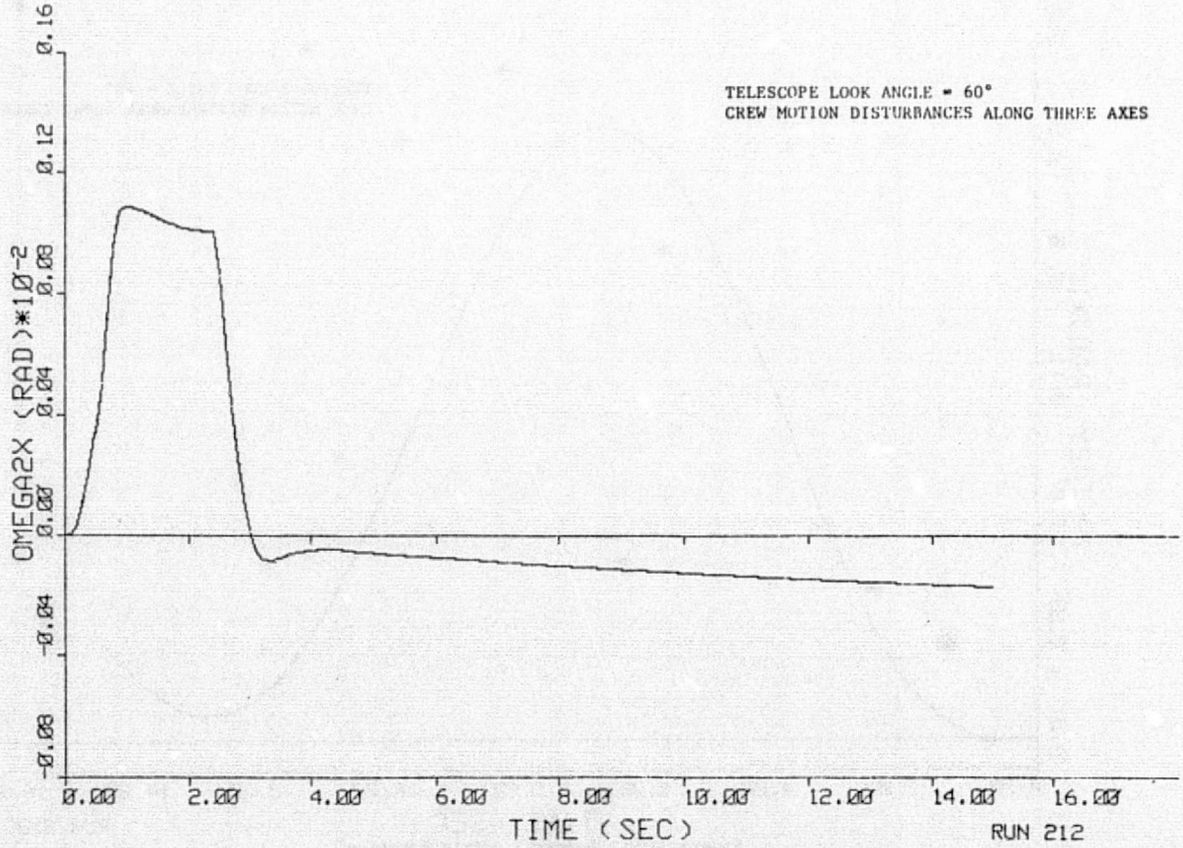

Figure 7-52. Pedestal x-Axis Rate

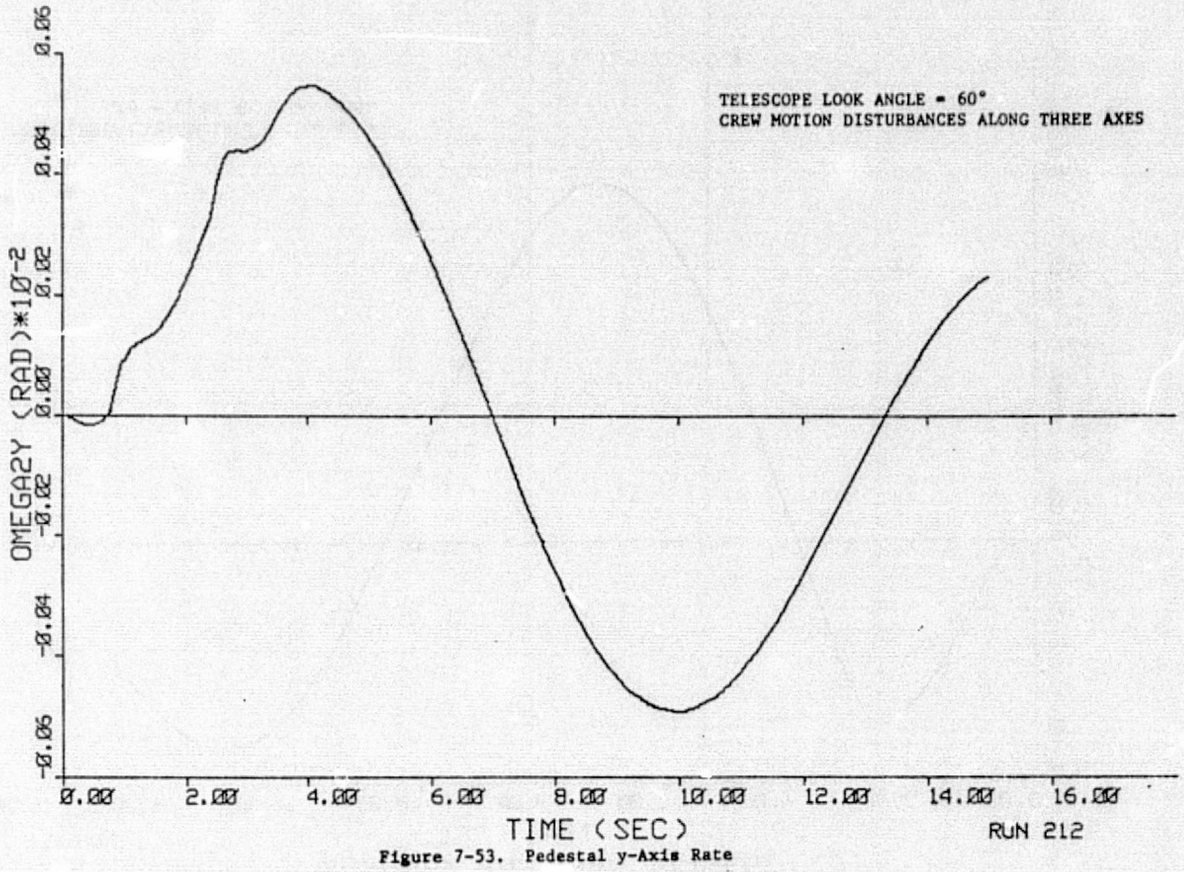

Figure 7-53. Pedestal y-Axis Rate

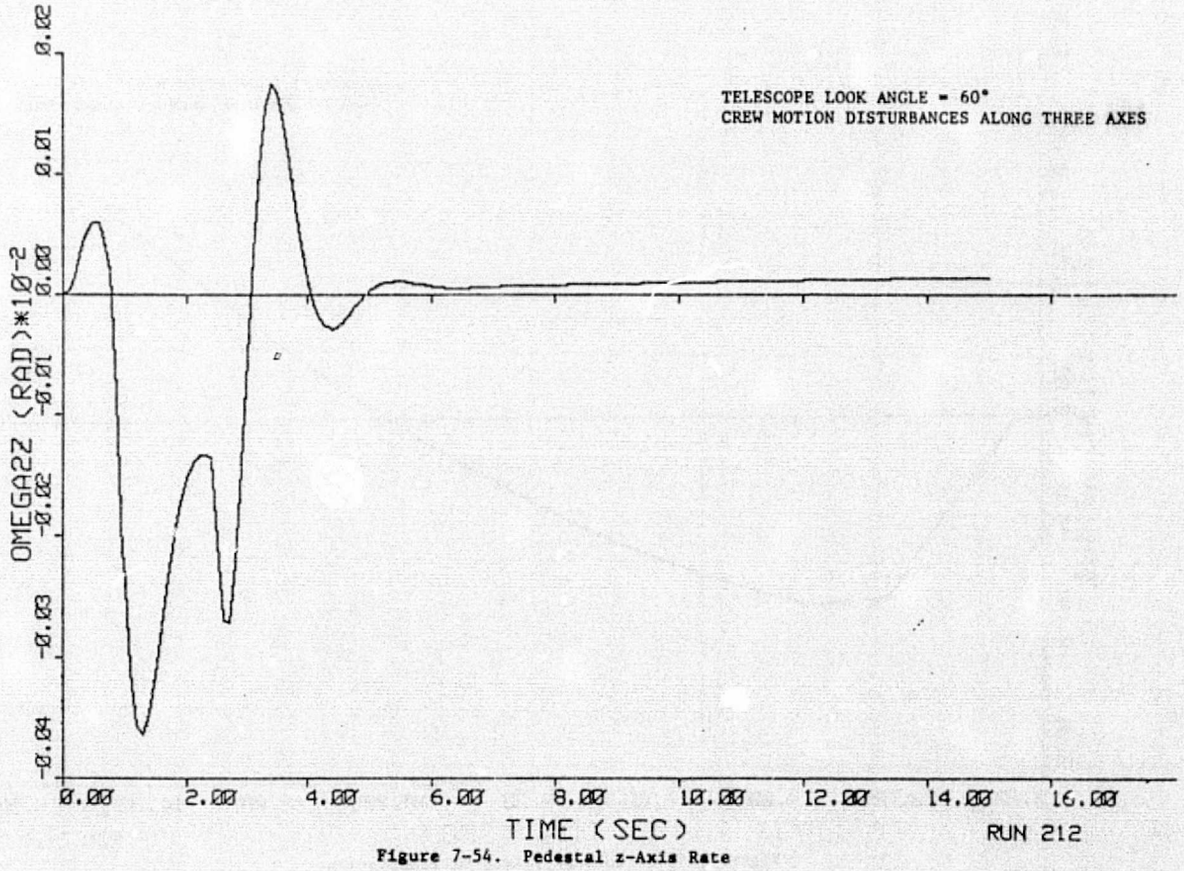

Figure 7-54. Pedestal z-Axis Rate

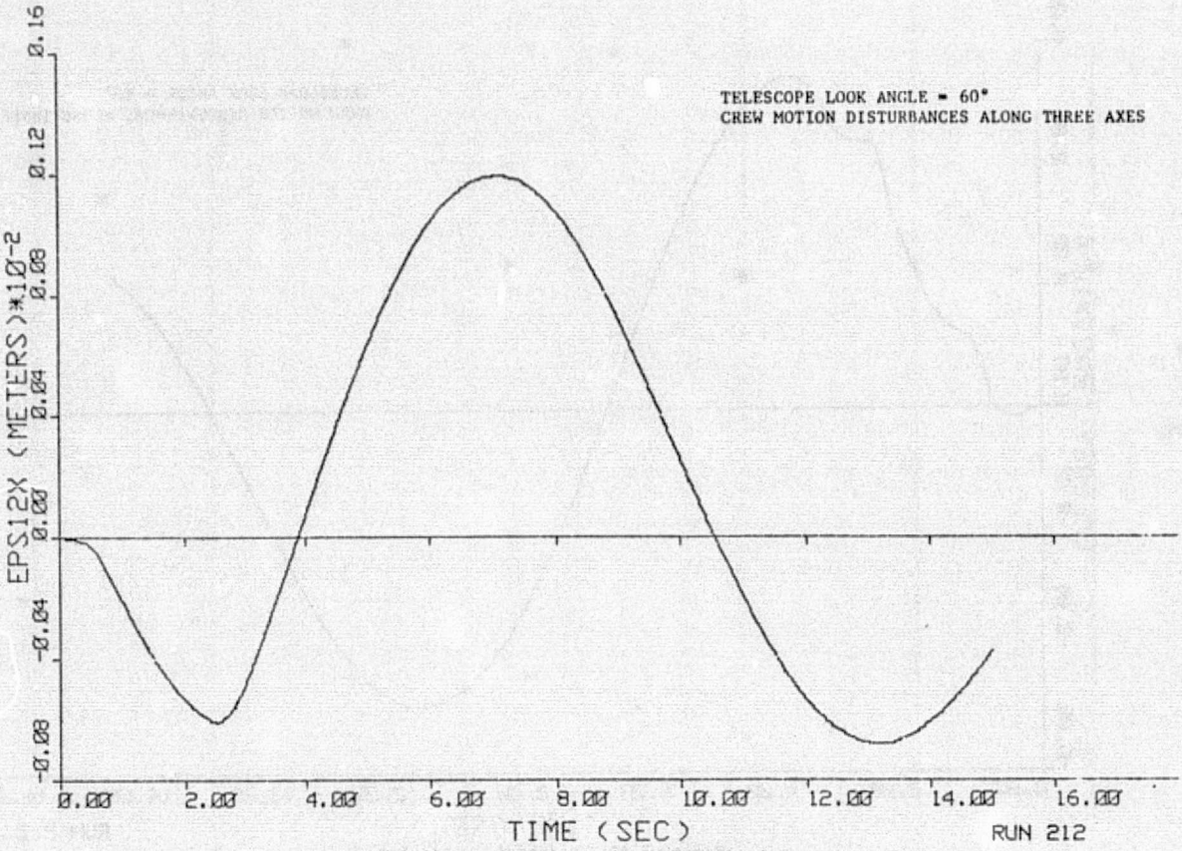

Figure 7-55. Pedestal x-Axis CM Translation

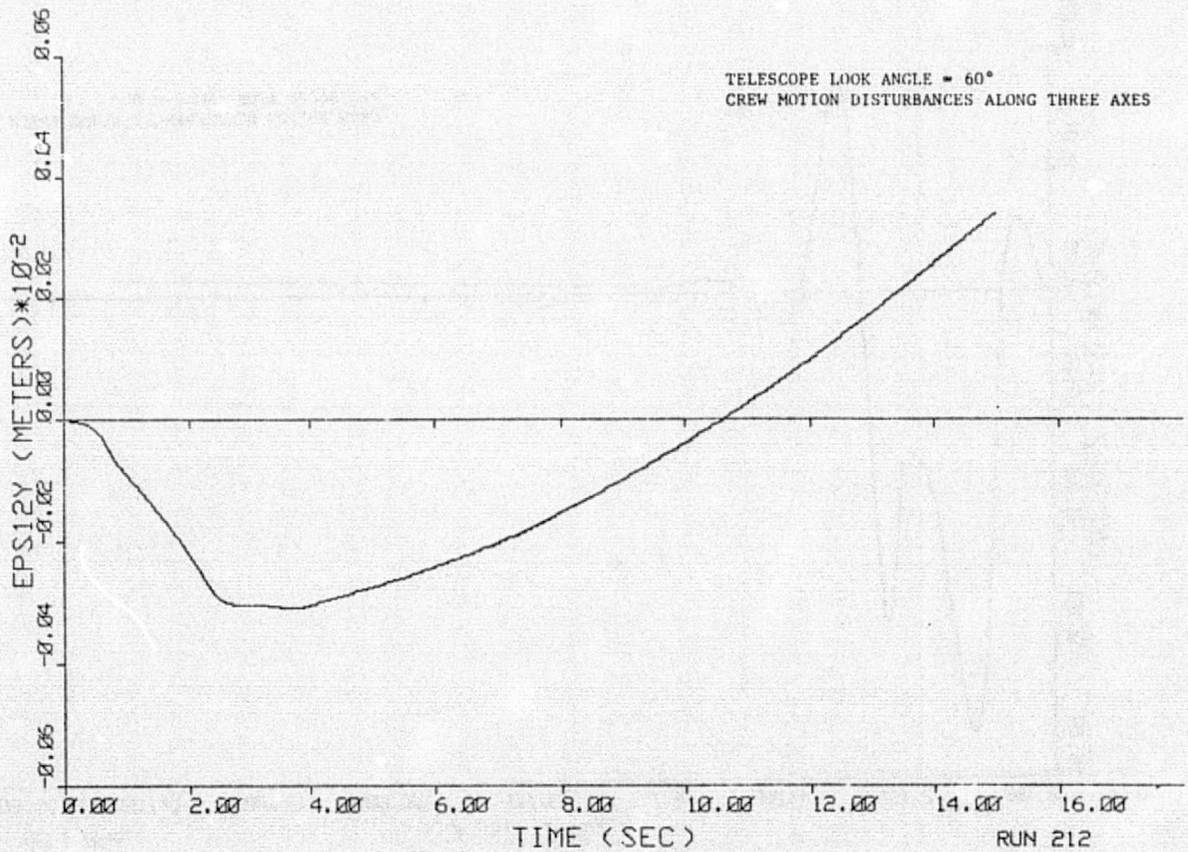

Figure 7-56. Pedestal y-Axis CM Translation

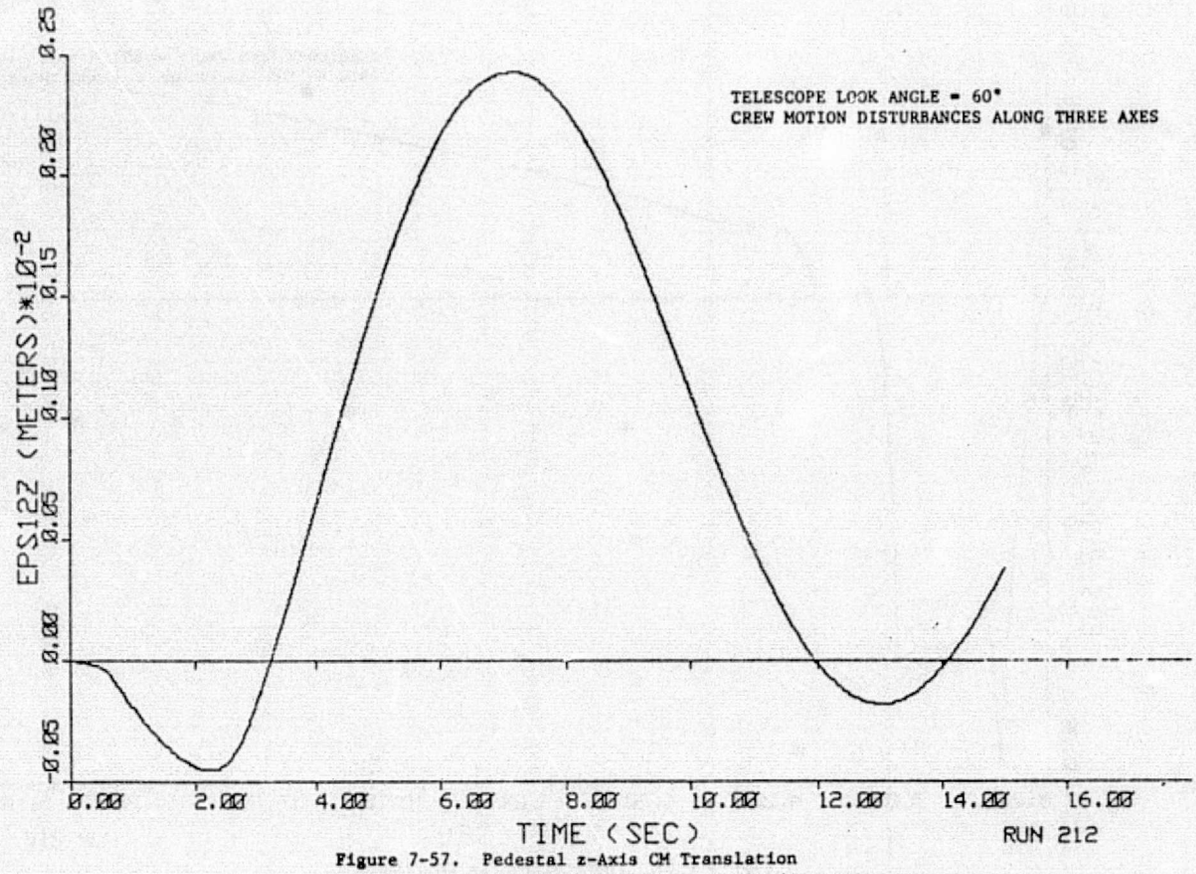

Figure 7-57. Pedestal z-Axis CM Translation

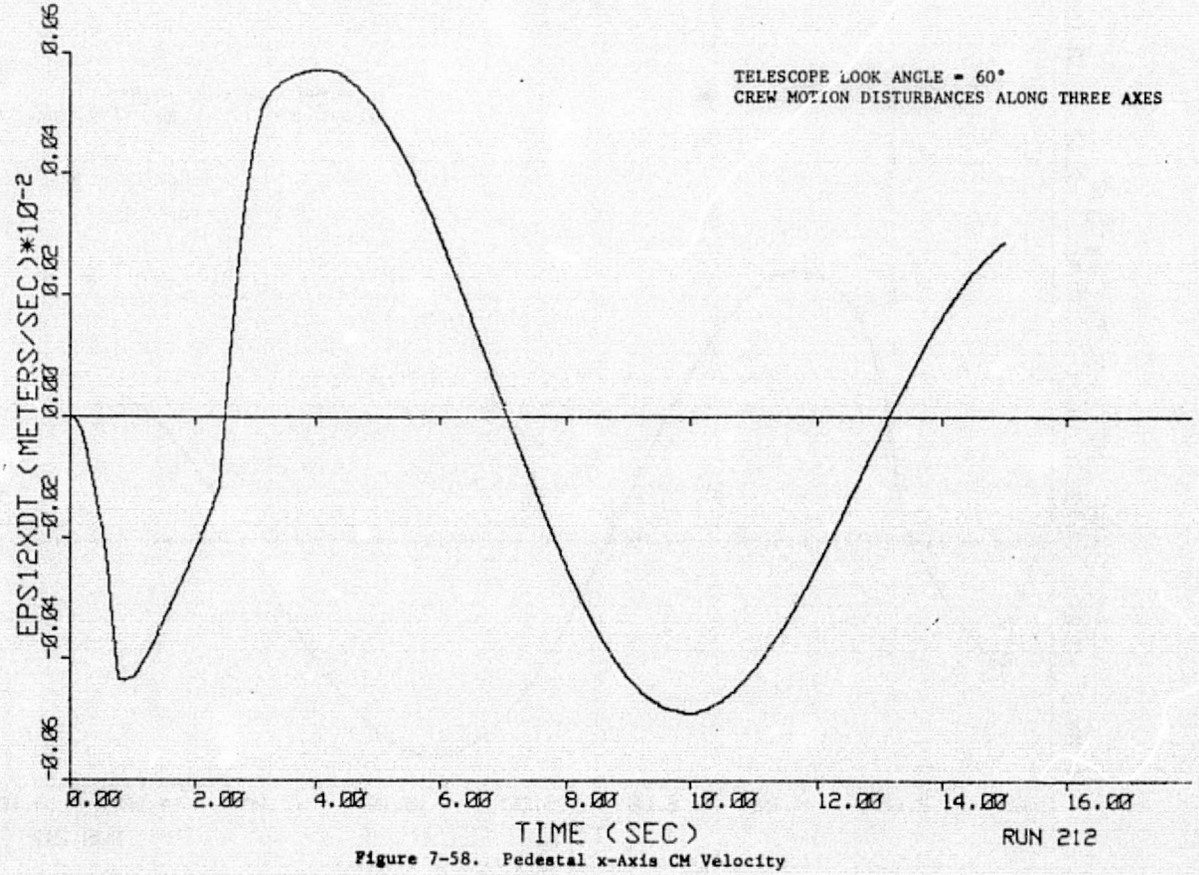

Figure 7-58. Pedestal x-Axis CM Velocity

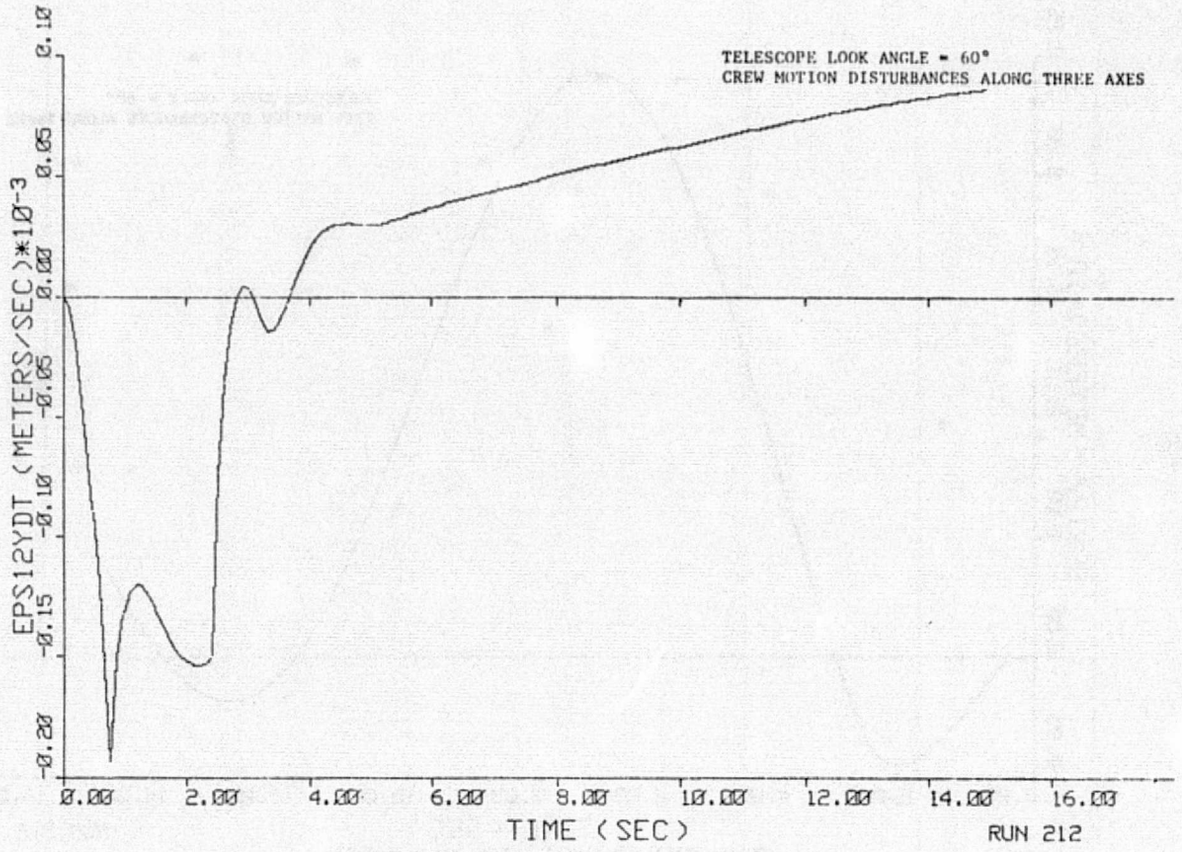

Figure 7-59. Pedestal y-Axis CM Velocity

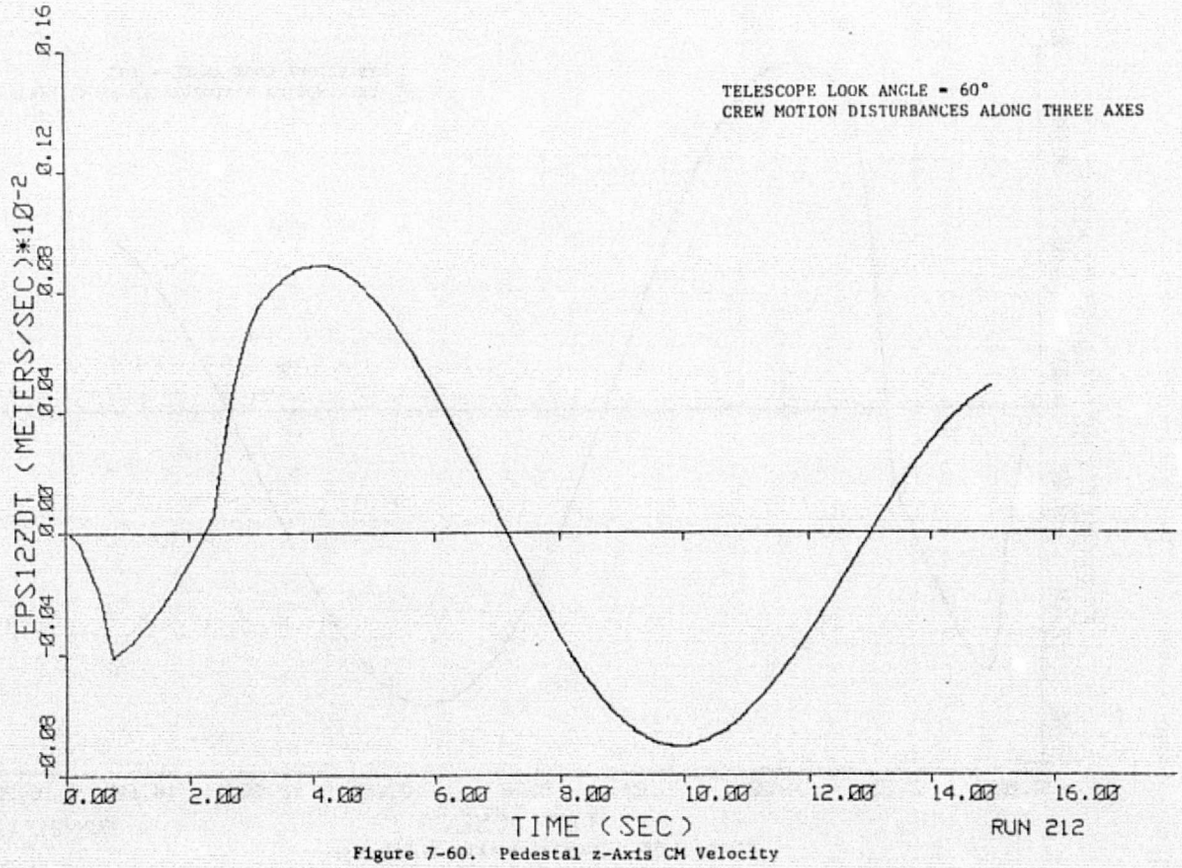

Figure 7-60. Pedestal z-Axis CM Velocity

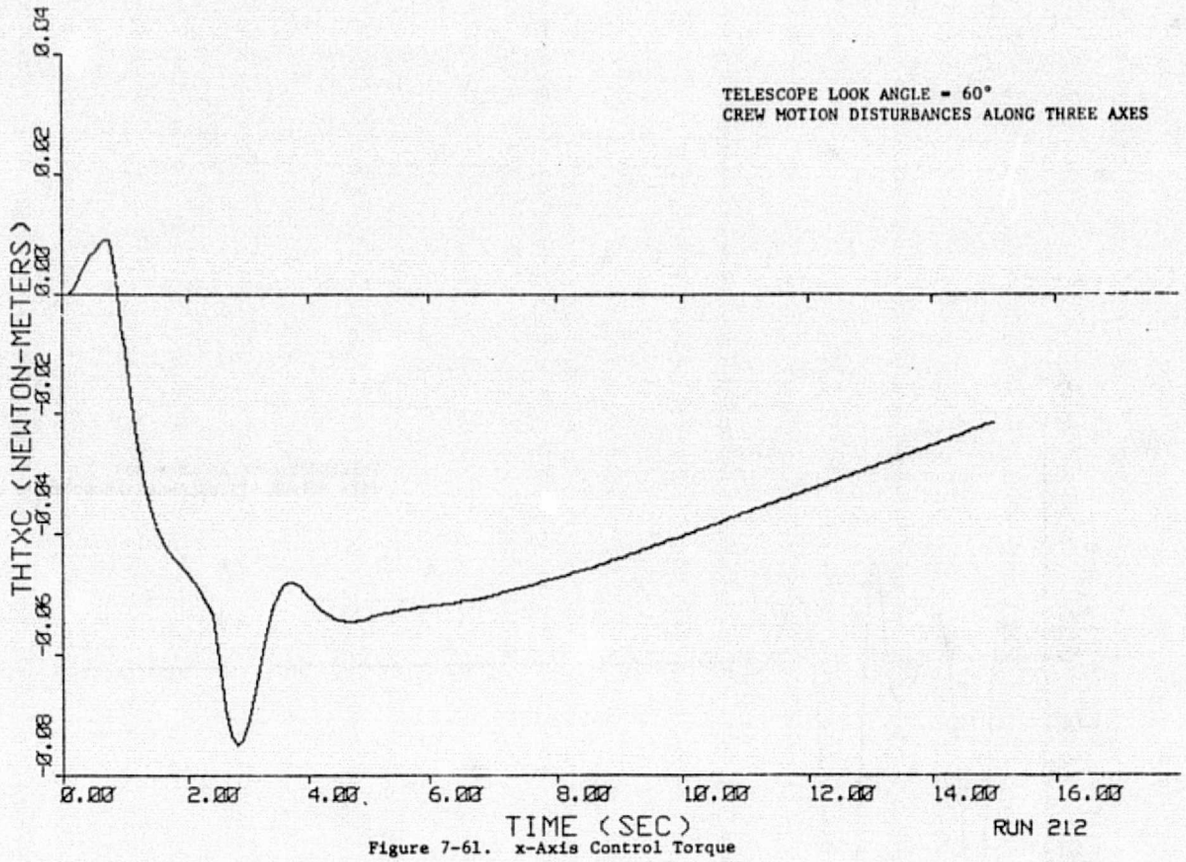

Figure 7-61. x-Axis Control Torque

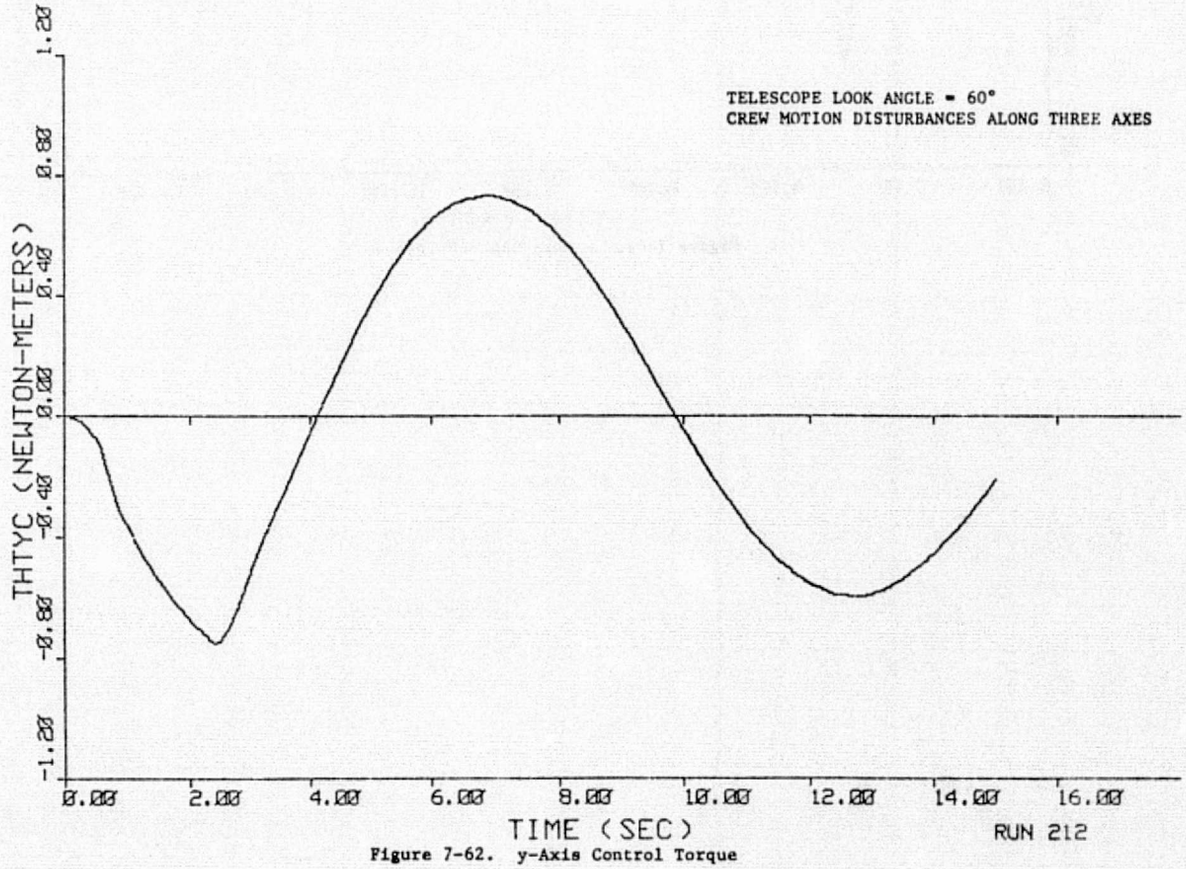

Figure 7-62. y-Axis Control Torque

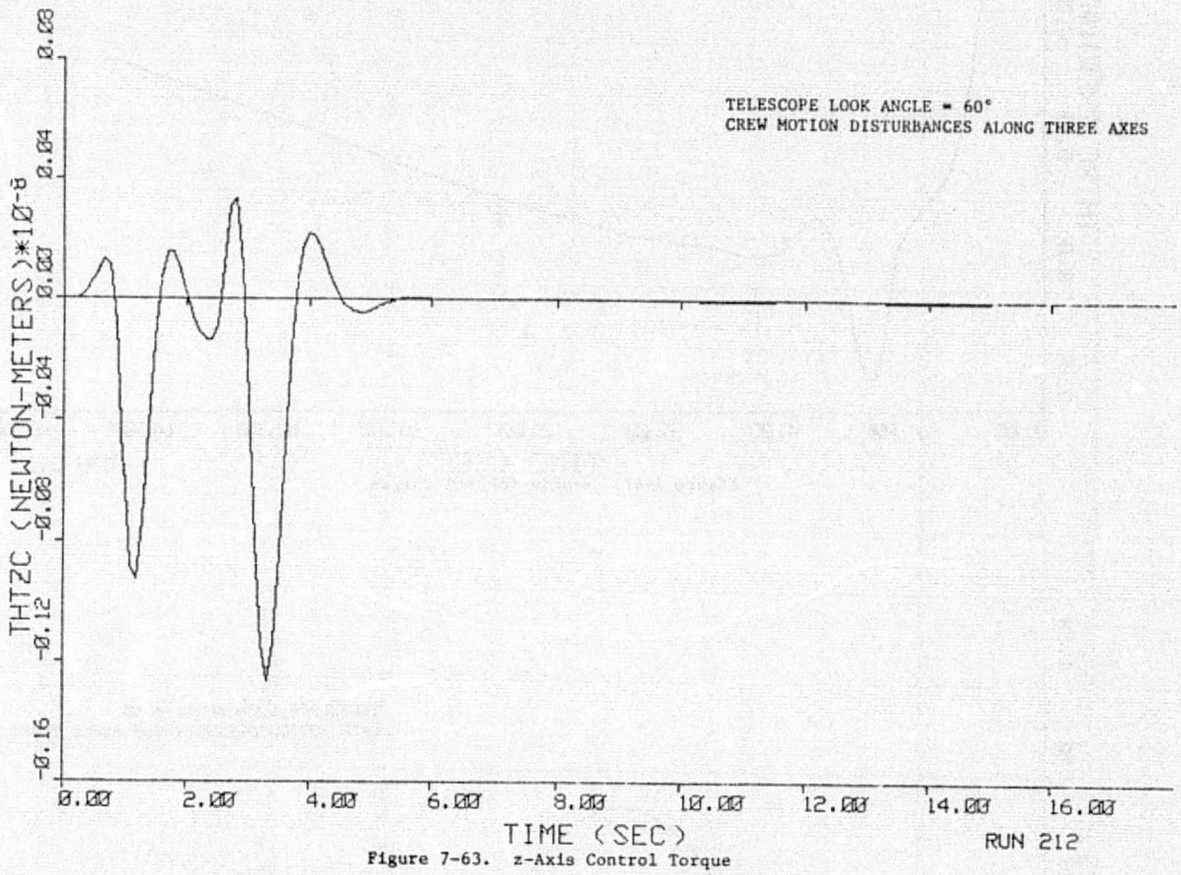

Figure 7-63. z-Axis Control Torque

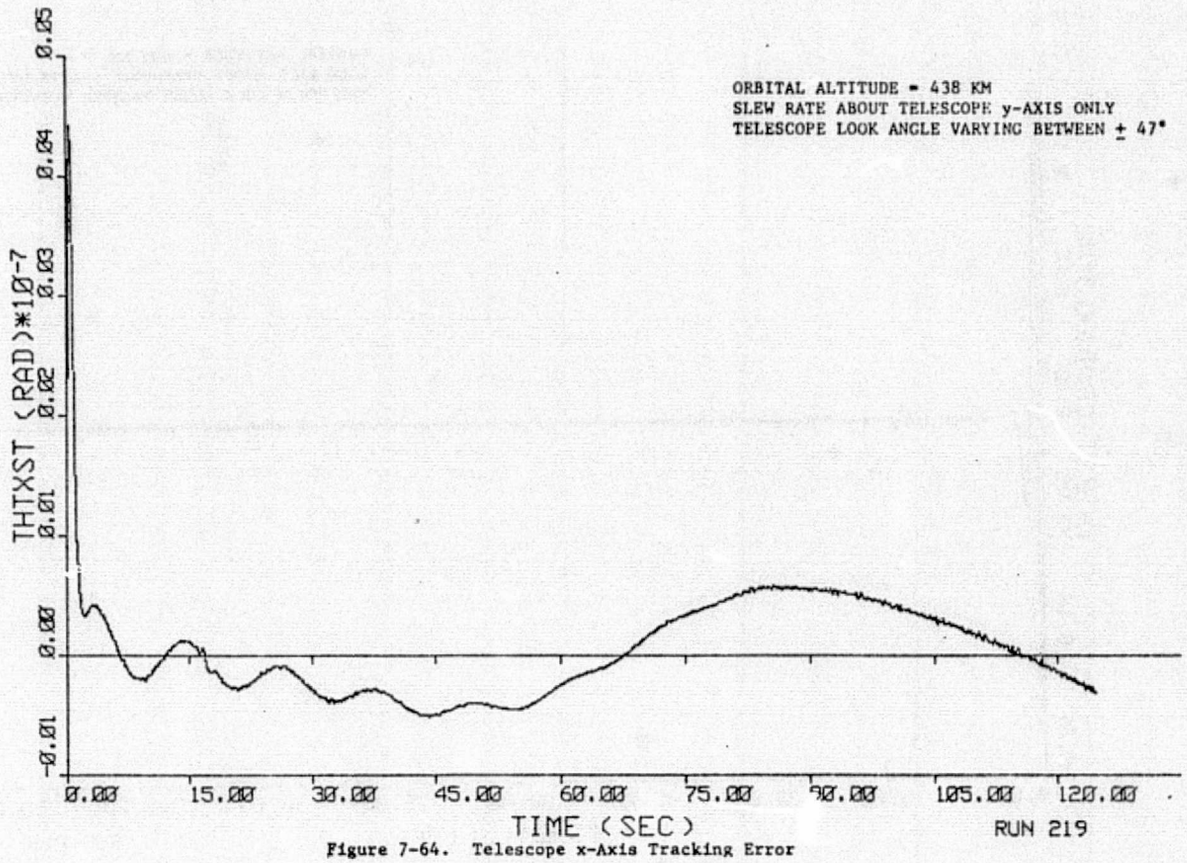

Figure 7-64. Telescope x-Axis Tracking Error

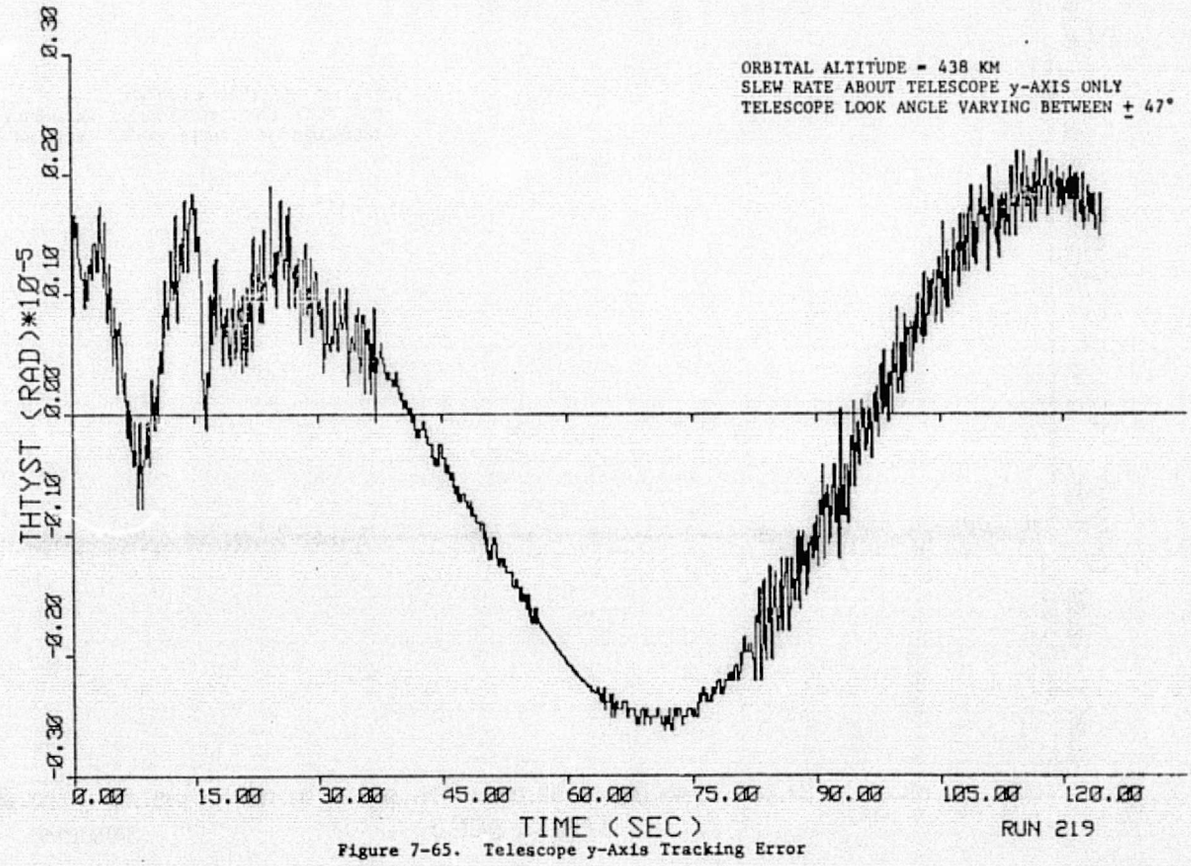

Figure 7-65. Telescope y-Axis Tracking Error

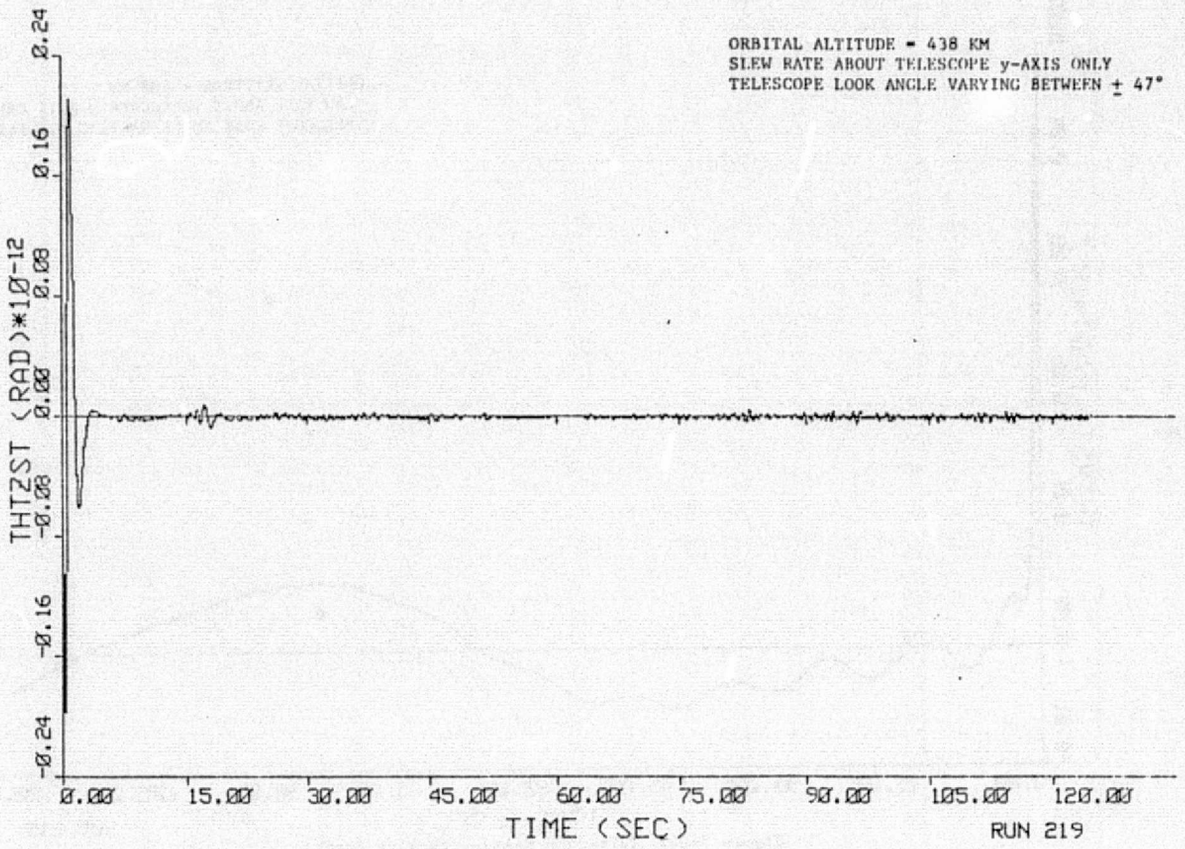

Figure 7-66. Telescope z-Axis Tracking Error

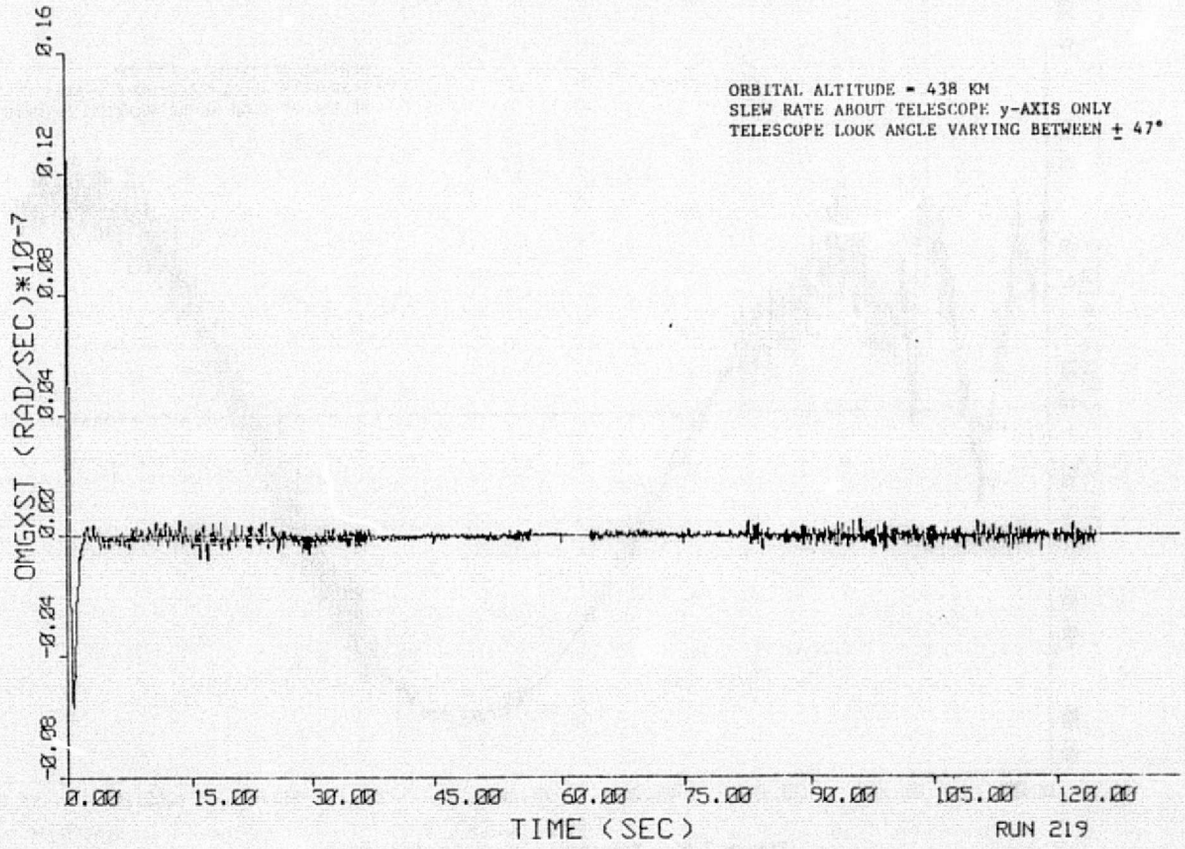

Figure 7-67. Telescope x-Axis Tracking Rate Error

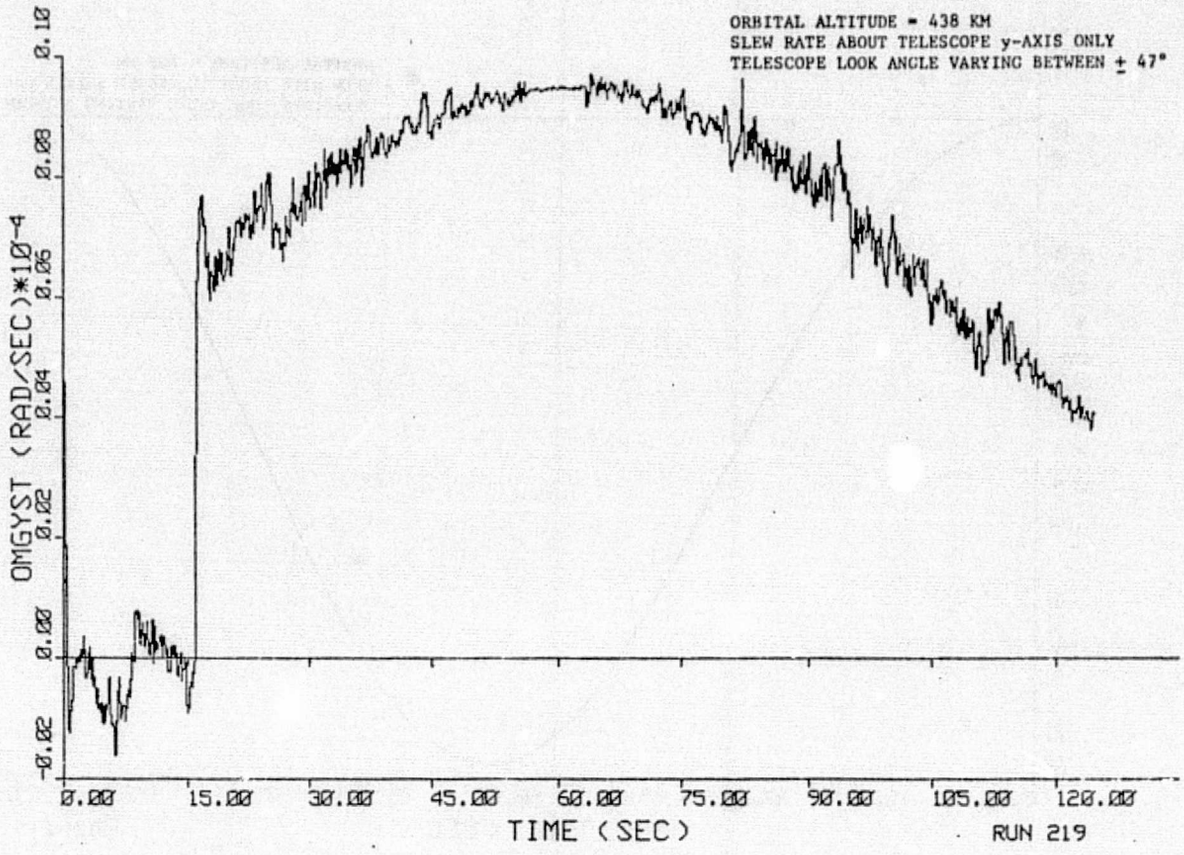

Figure 7-68. Telescope y-Axis Tracking Rate Error

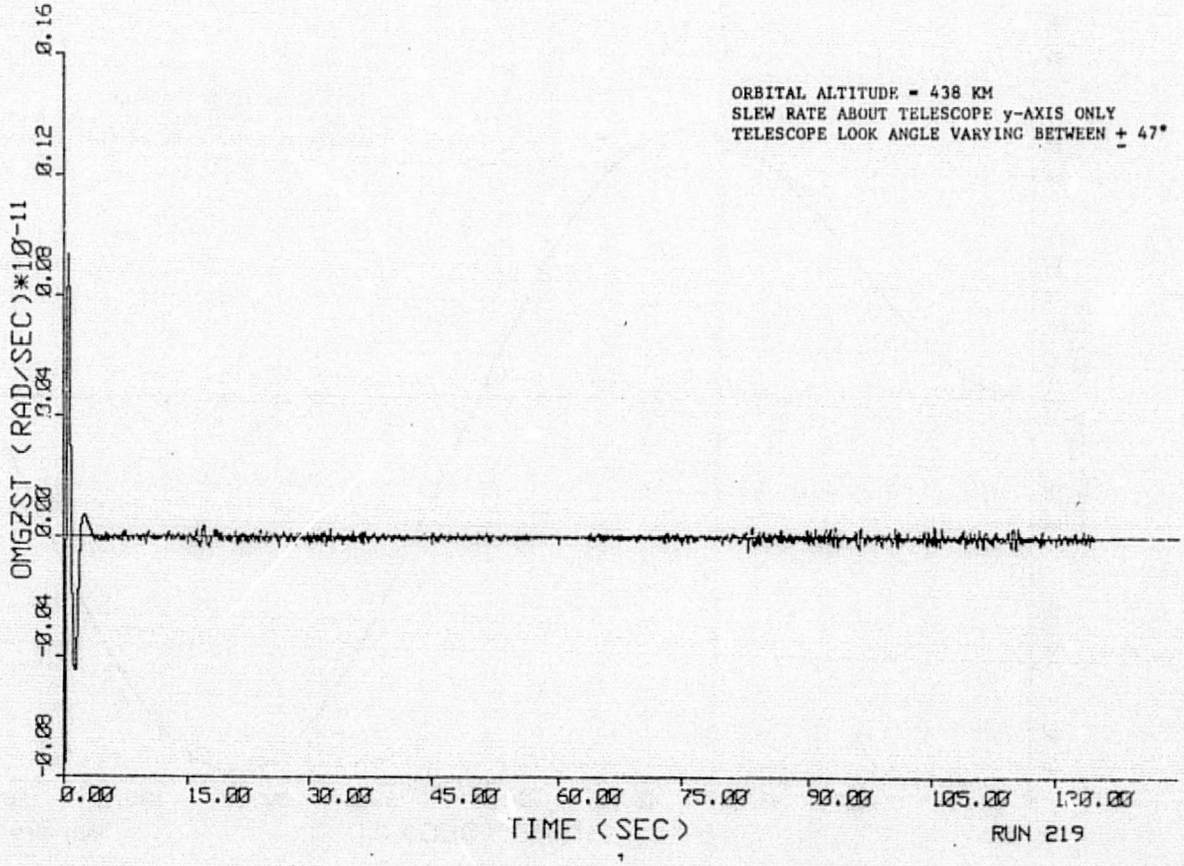

Figure 7-69. Telescope z-Axis Tracking Rate Error

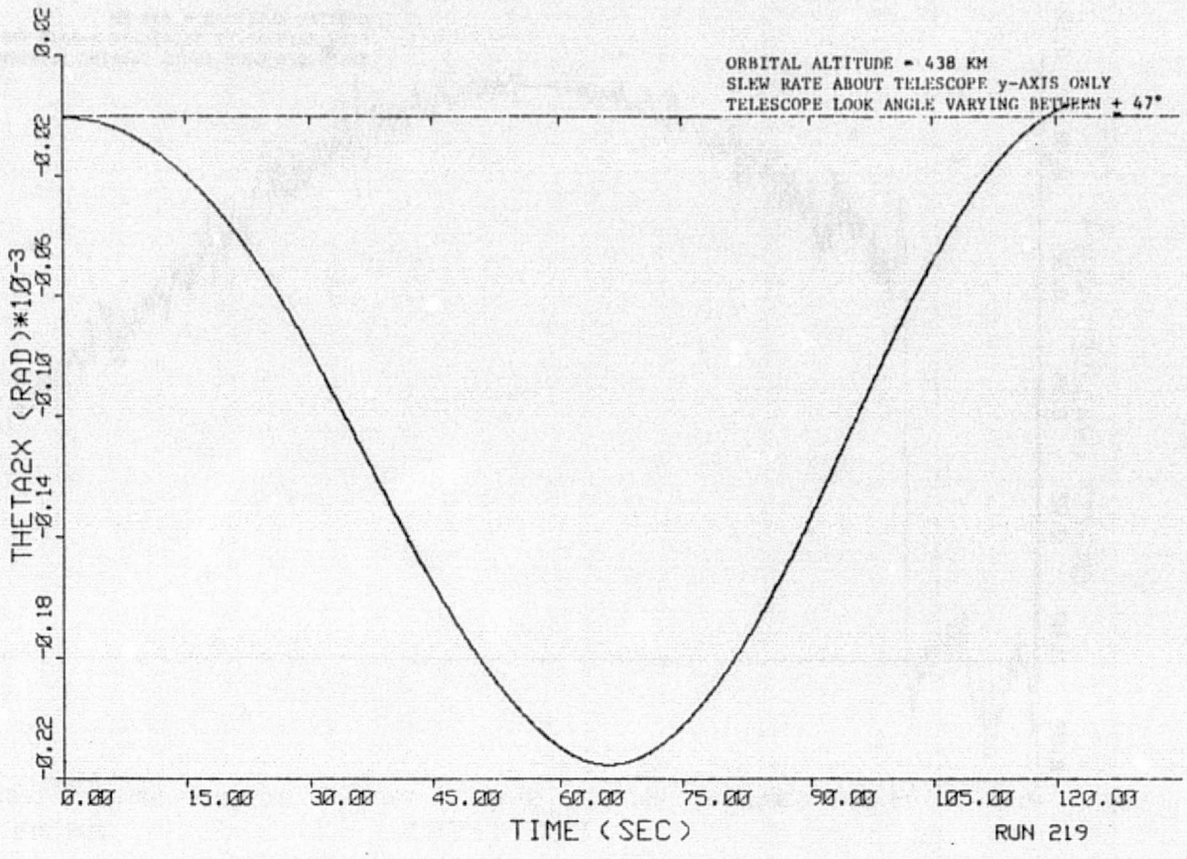

Figure 7-70. Pedestal x-Axis Rotation

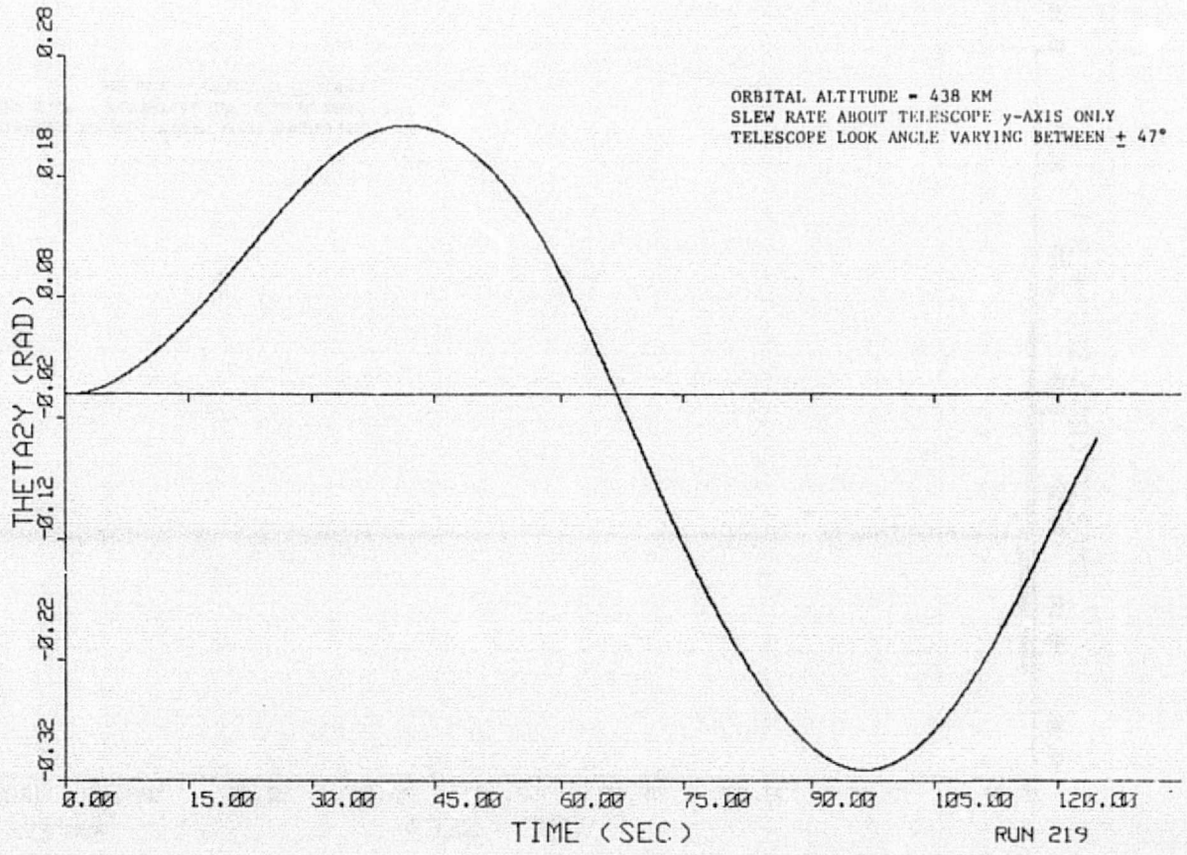

Figure 7-71. Pedestal y-Axis Rotation

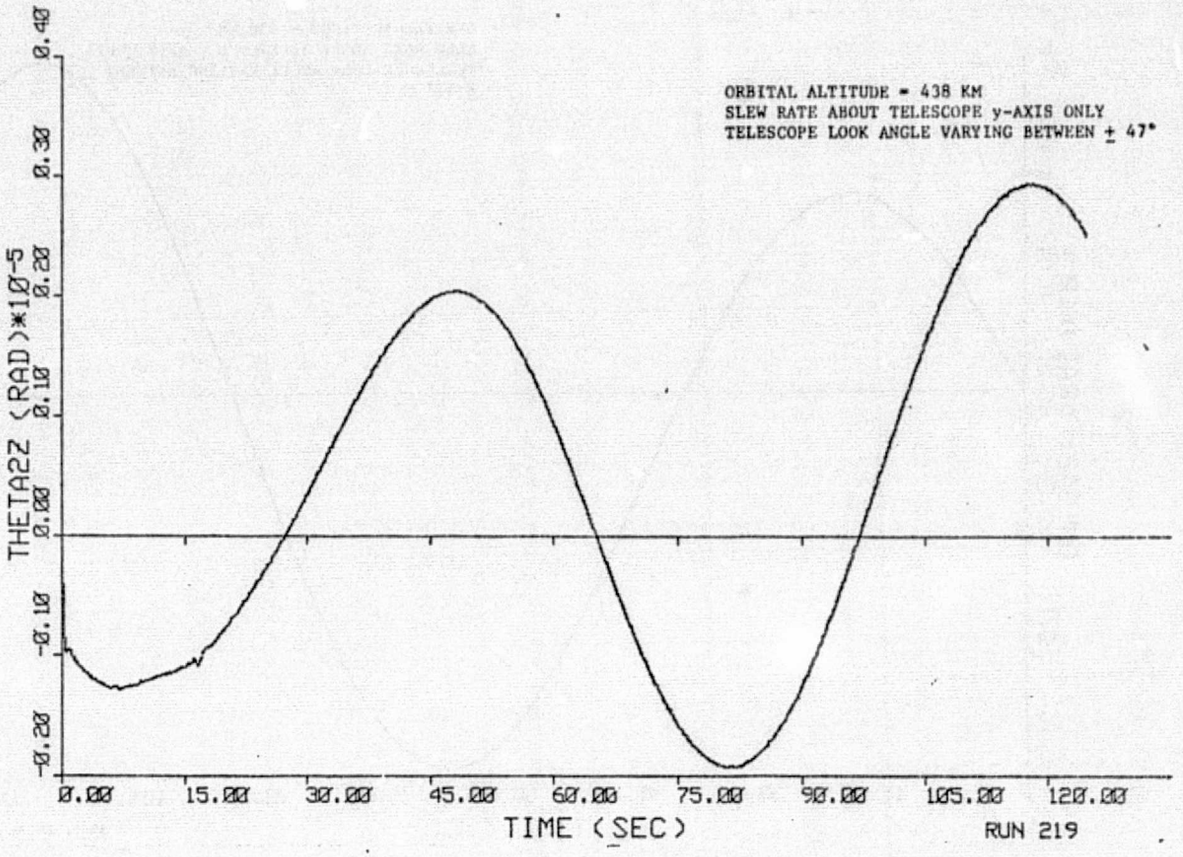

Figure 7-72. Pedestal z-Axis Rotation

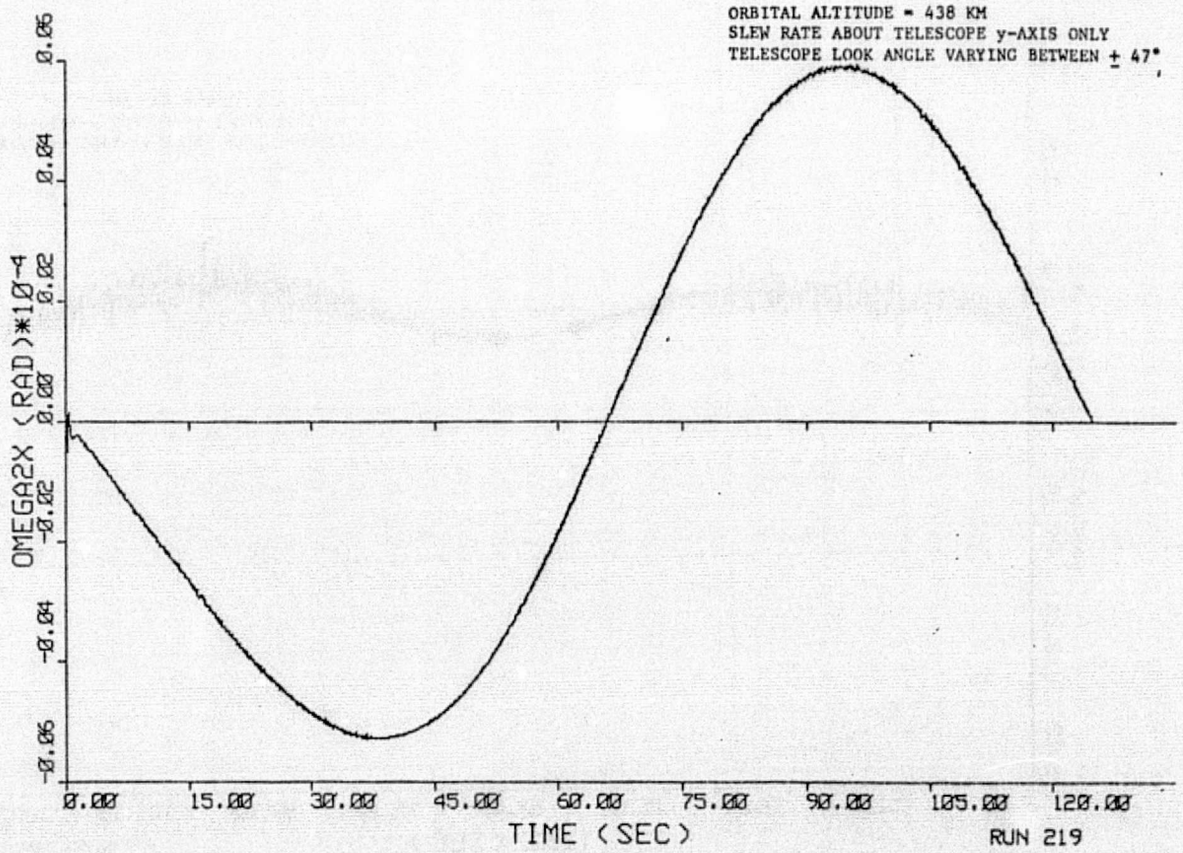

Figure 7-73. Pedestal x-Axis Rate

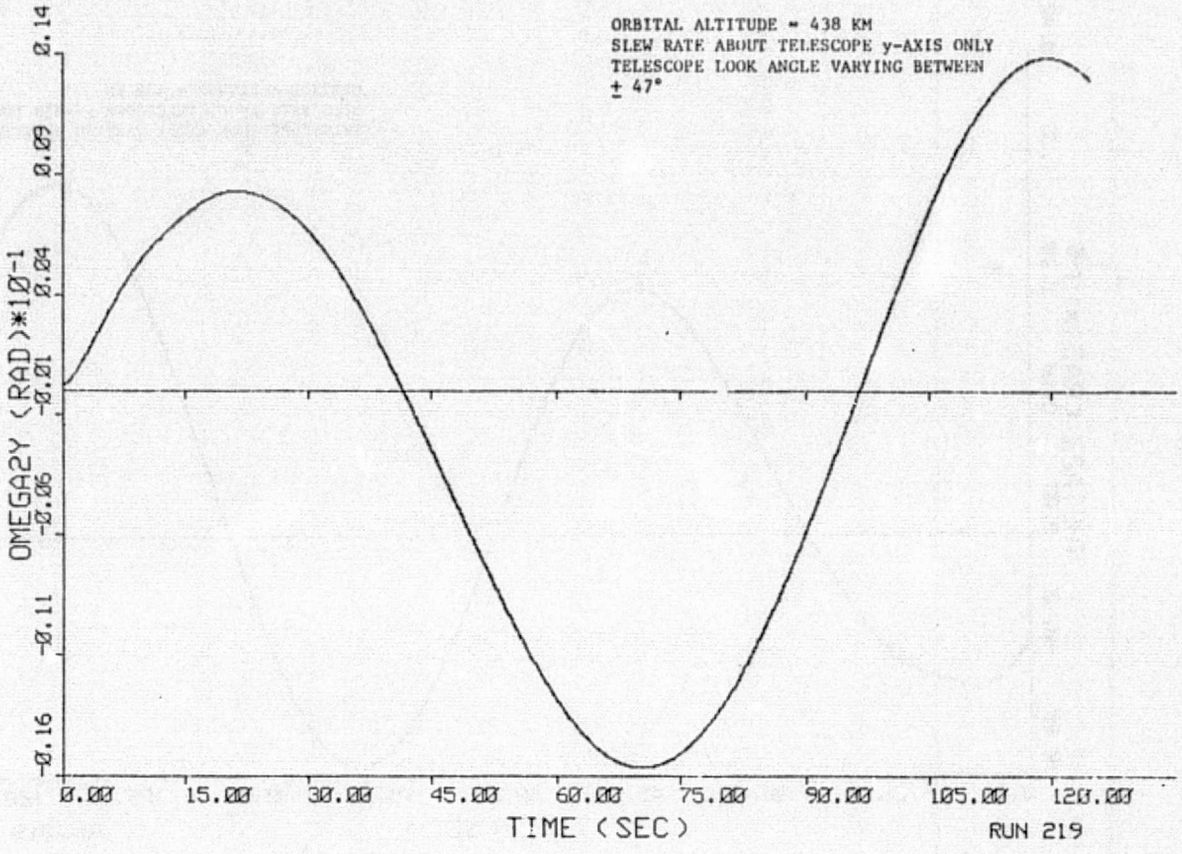

Figure 7-74. Pedestal y-Axis Rate

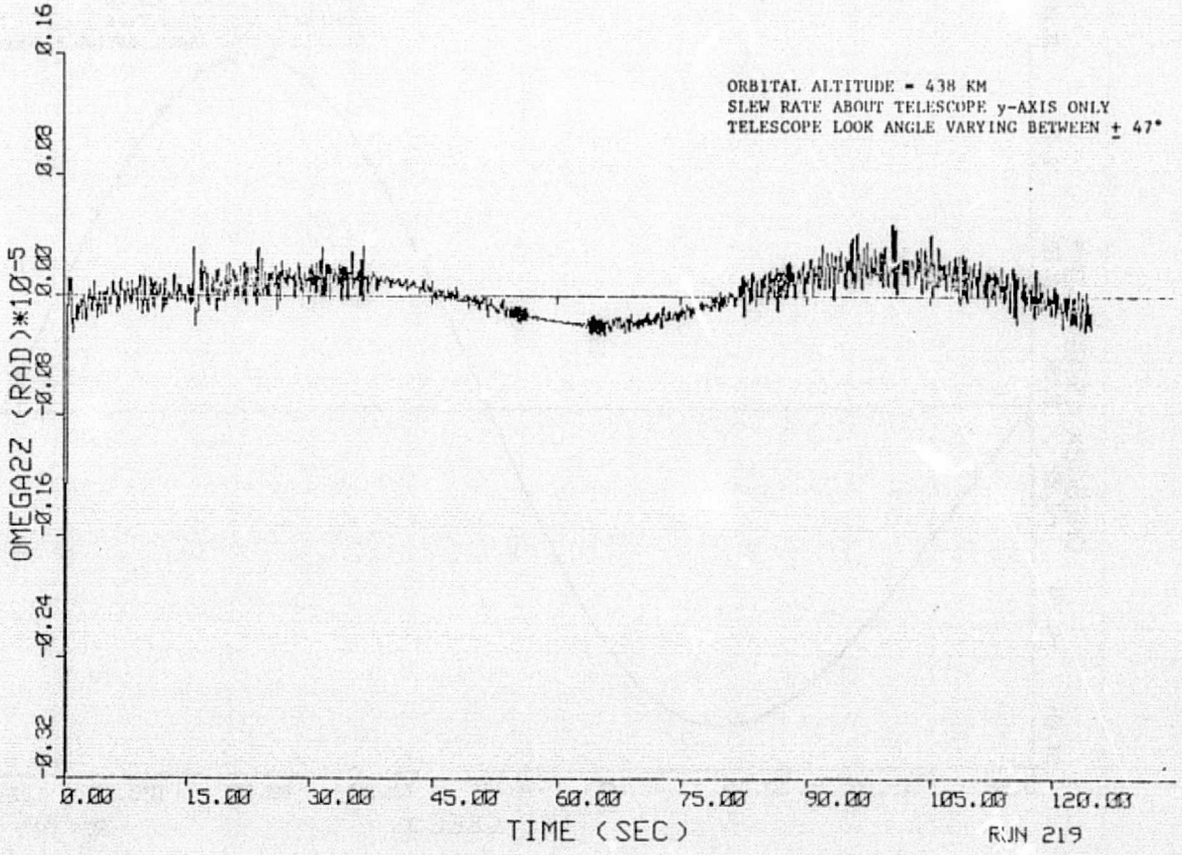

Figure 7-75. Pedestal z-Axis Rate

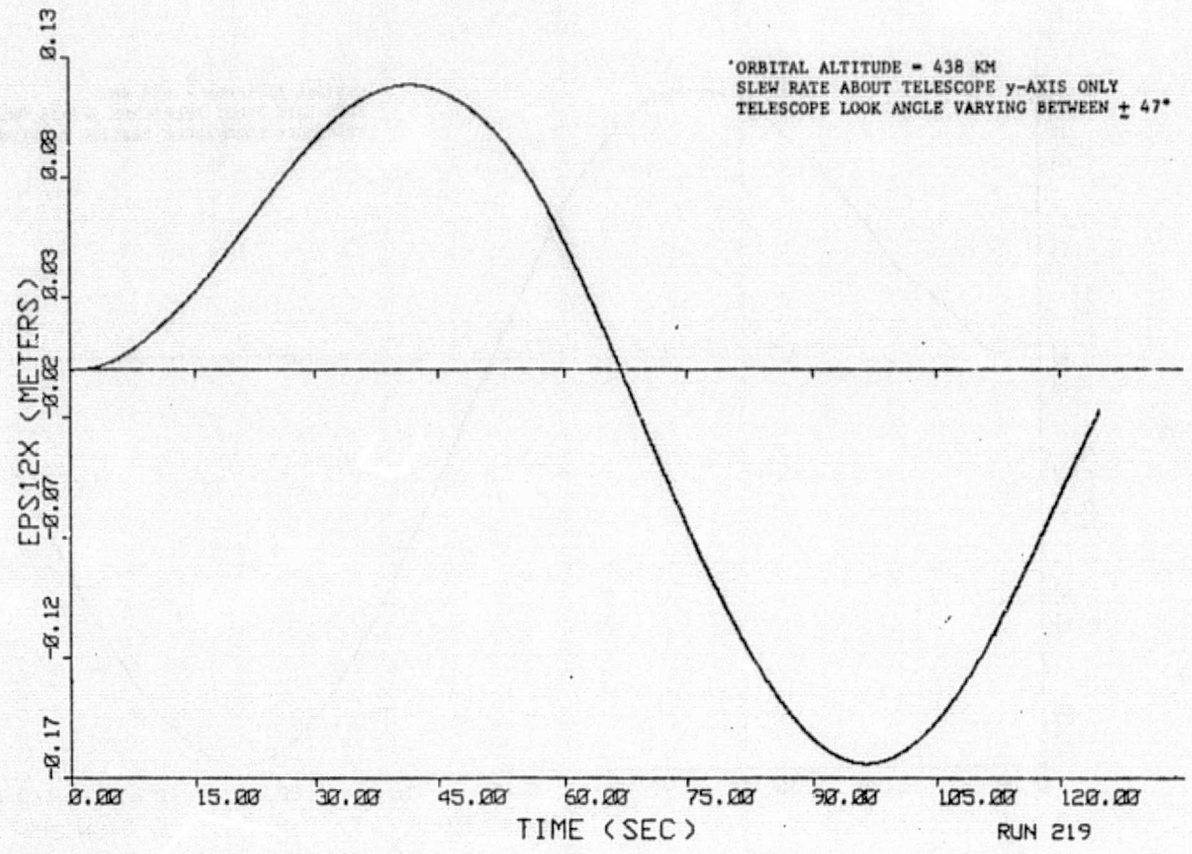

Figure 7-76. Pedestal x-Axis CM Translation

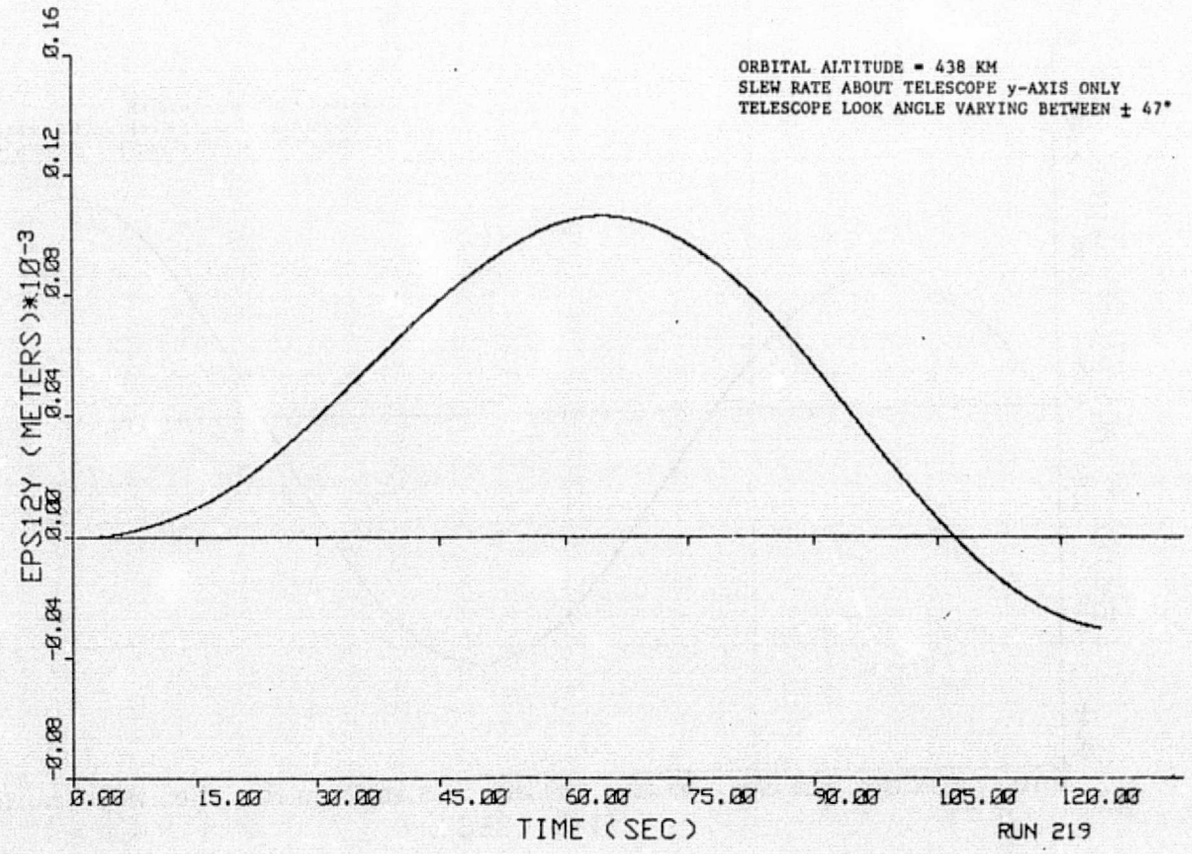

Figure 7-77. Pedestal y-Axis CM Translation

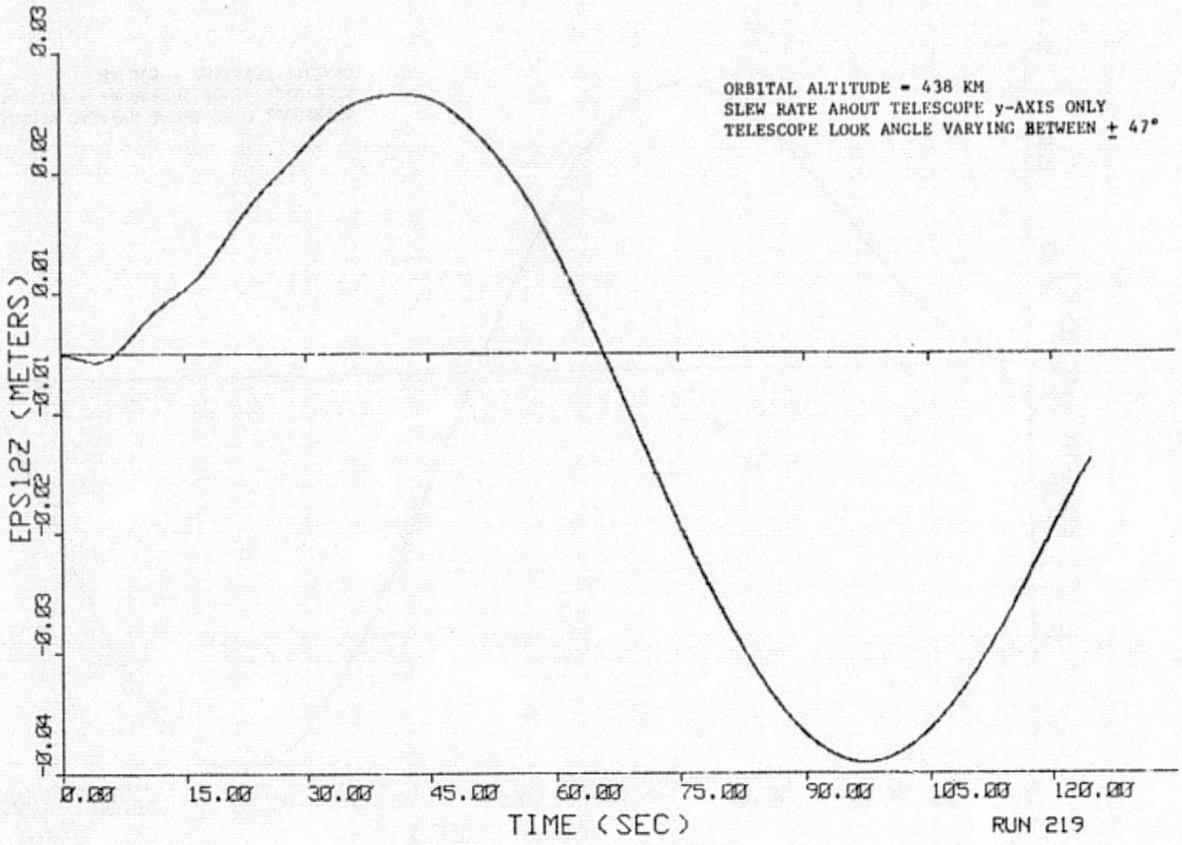

Figure 7-78. Pedestal z-Axis CM Translation

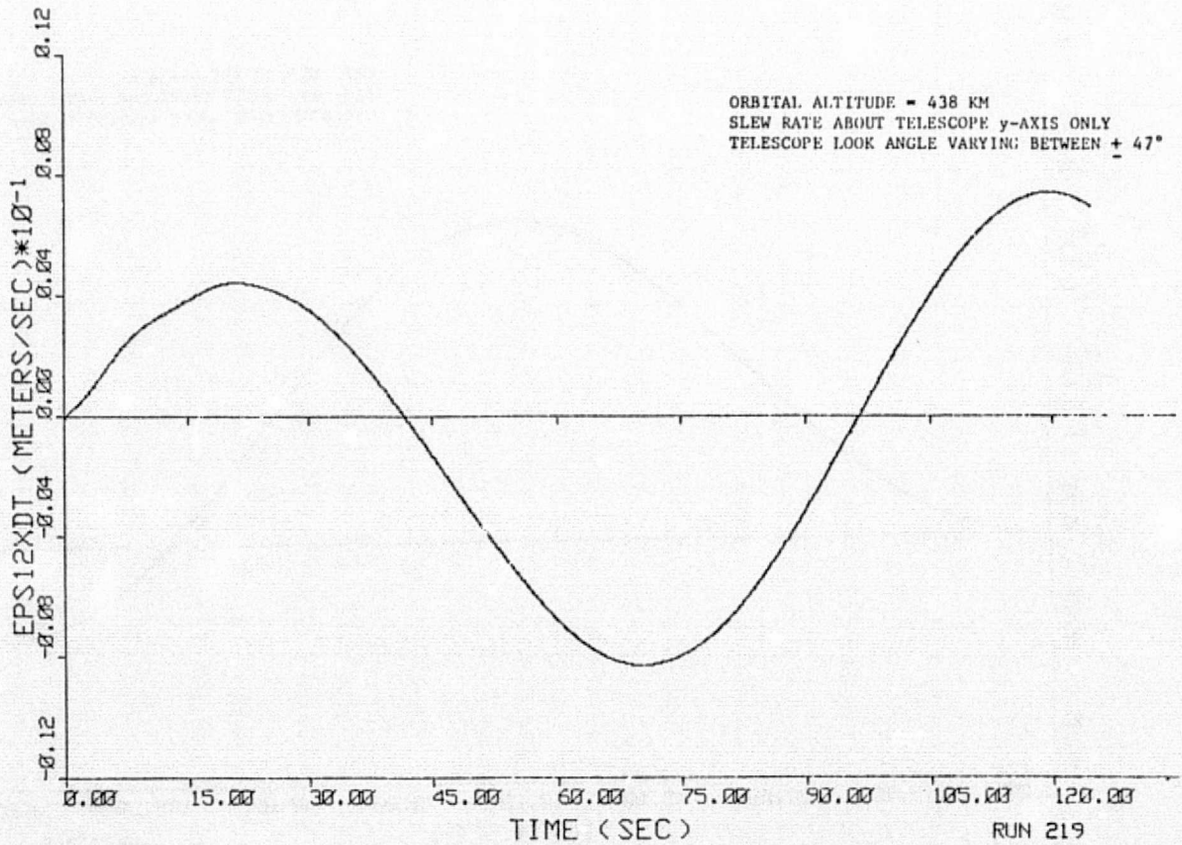

Figure 7-79. Pedestal x-Axis CM Velocity

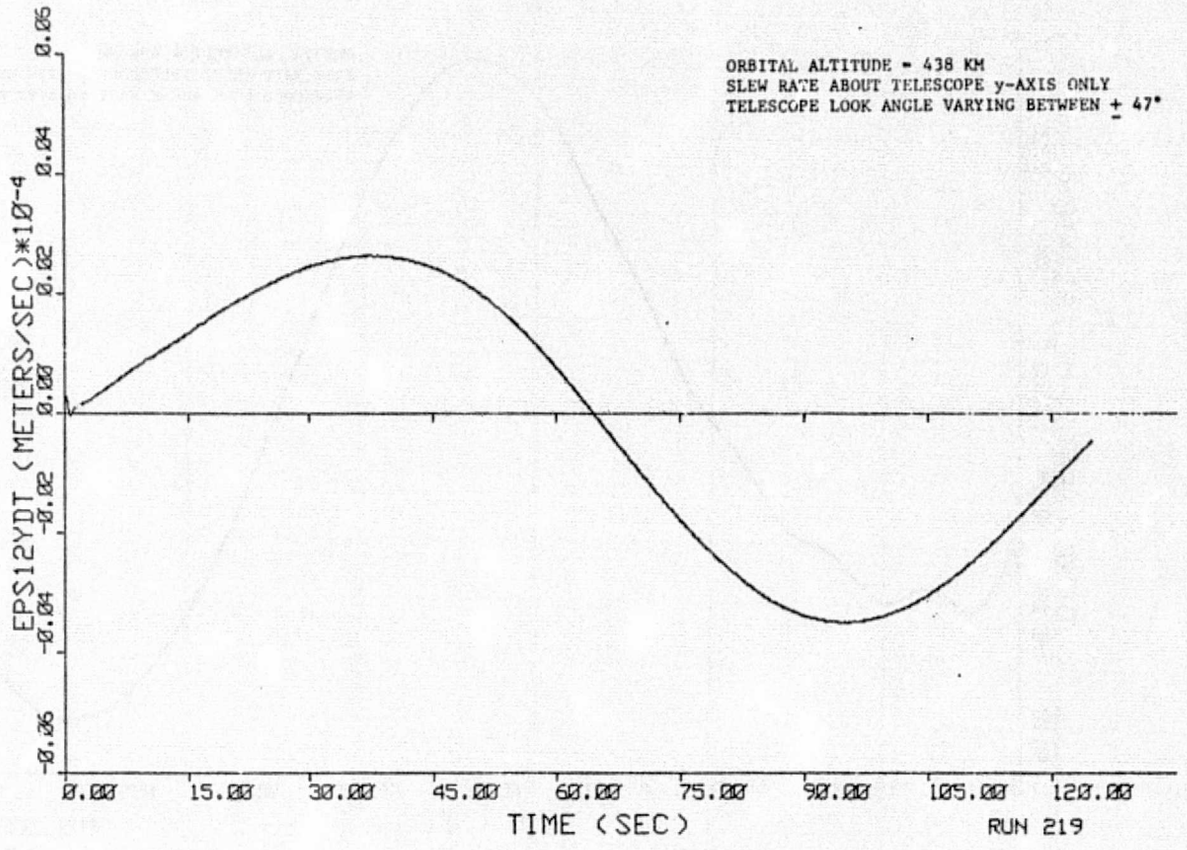

Figure 7-80. Pedestal y-Axis CM Velocity

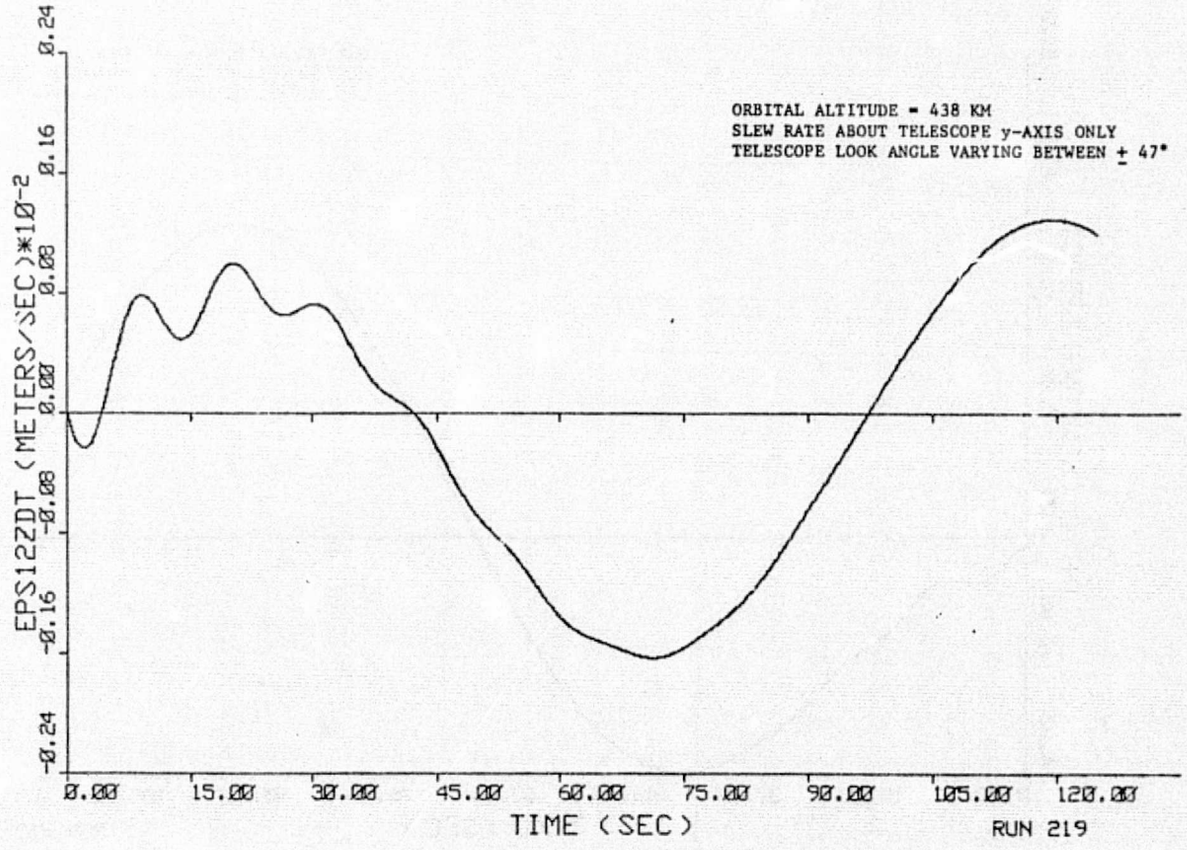

Figure 7-81. Pedestal z-Axis CM Velocity

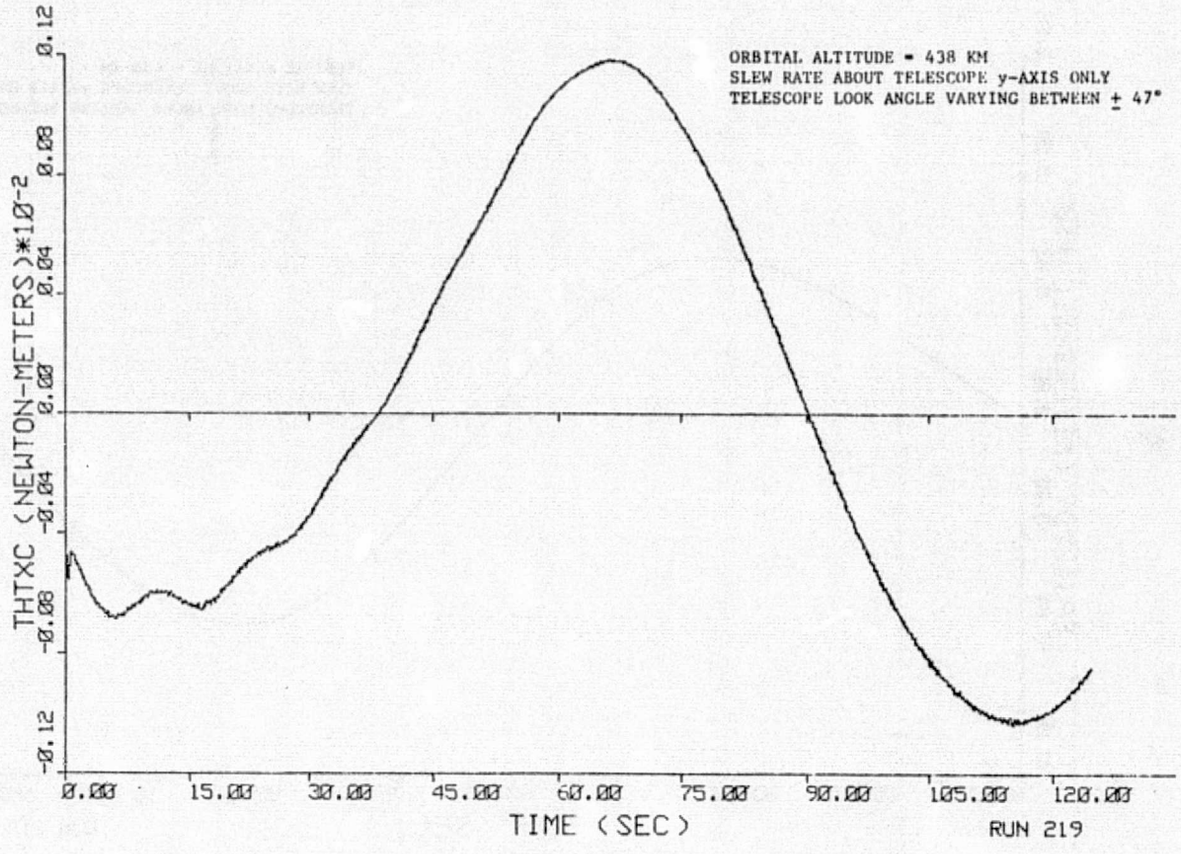

Figure 7-82. x-Axis Control Torque

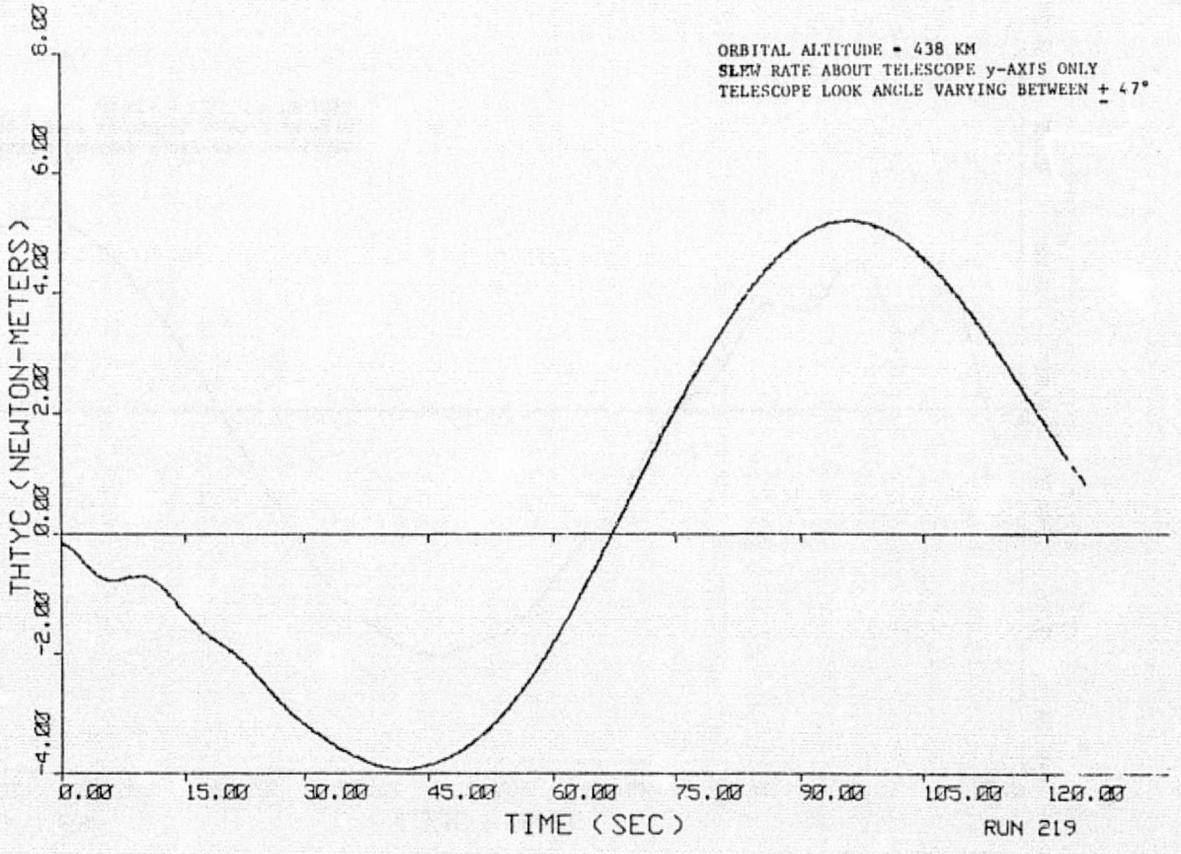

Figure 7-83. y-Axis Control Torque

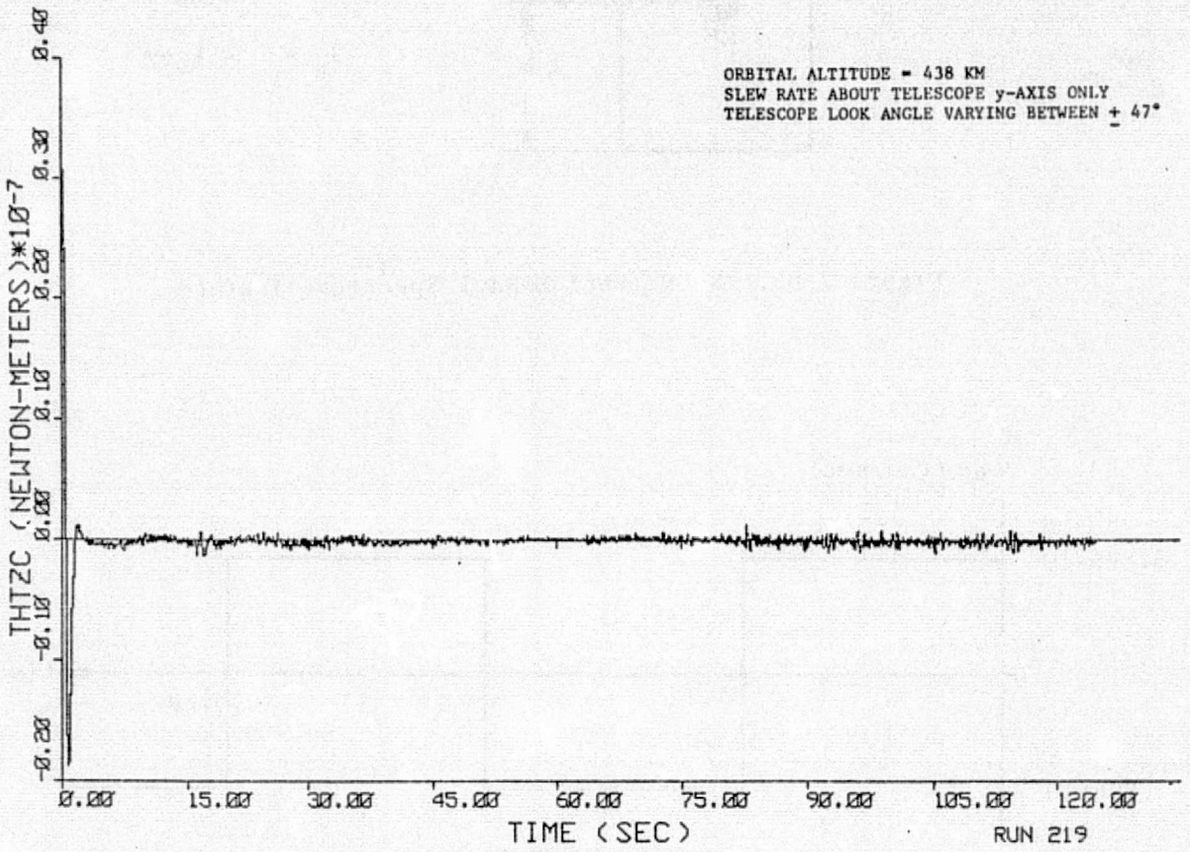

Figure 7-84. z-Axis Control Torque

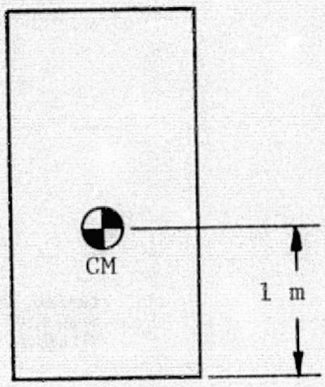

$m = 250$ kg

$J_x = 87$ kg-m^2

$J_y = 84$ kg-m^2

$J_z = 4$ kg-m^2

Figure 7-85. X-UV (Soft X-Ray) Spectroheliograph

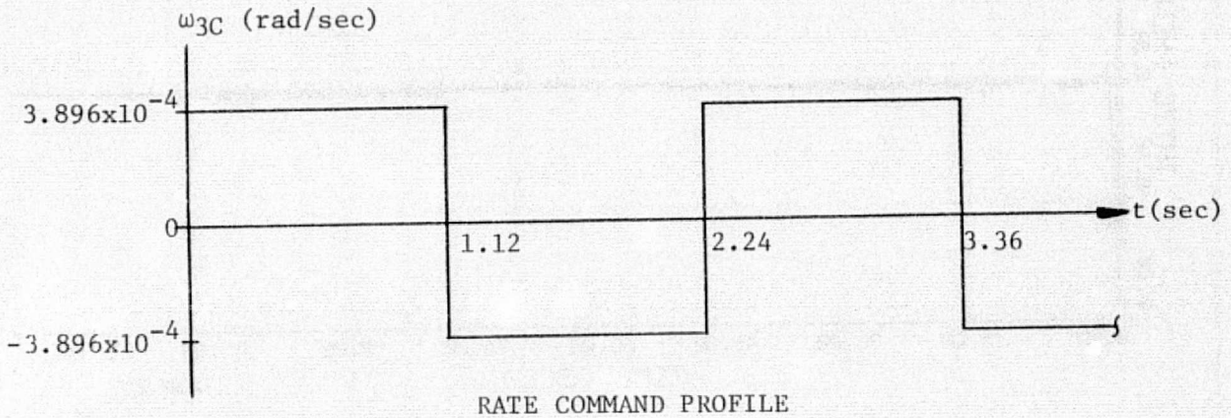

RATE COMMAND PROFILE

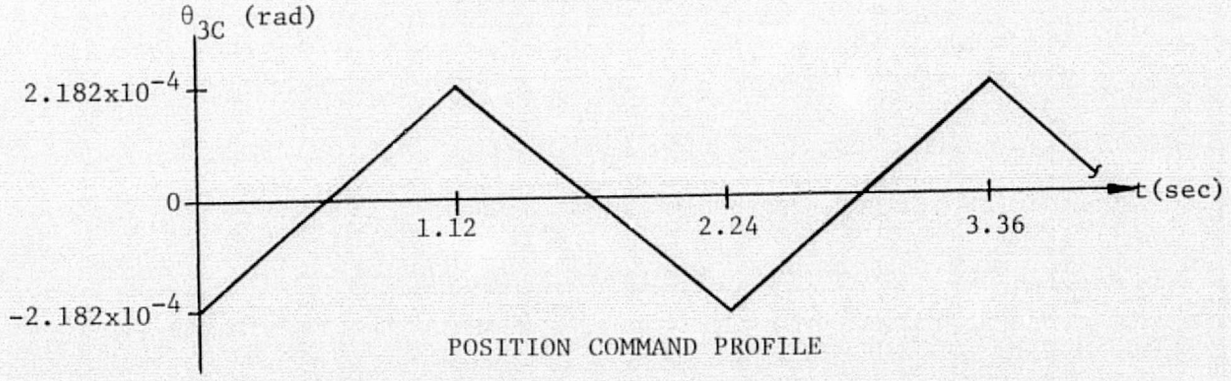

POSITION COMMAND PROFILE

Figure 7-86. Raster Scan Command Profiles

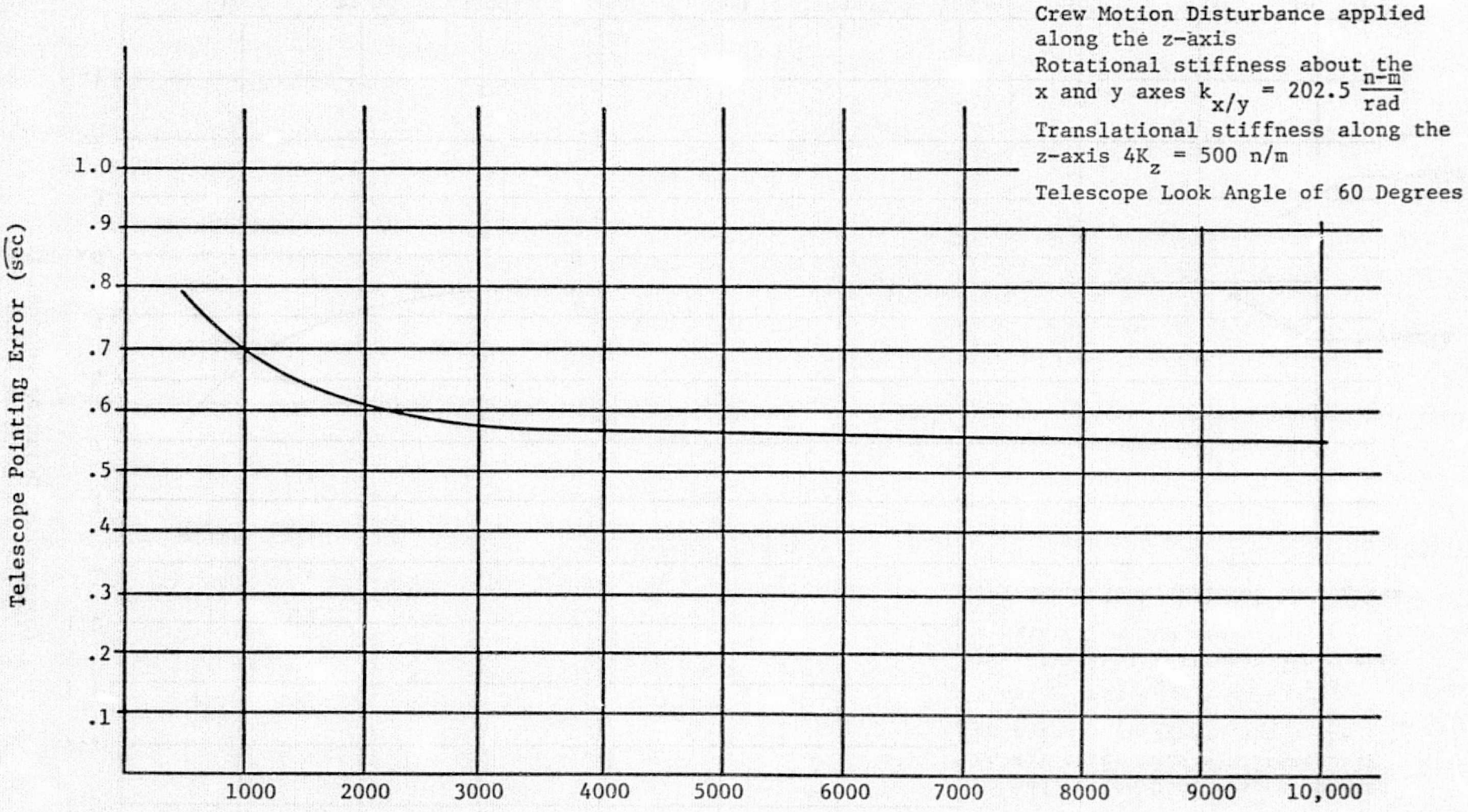

Figure 7-87. Telescope y-Axis Peak Pointing Error vs x and y Linear Suspension Stiffness

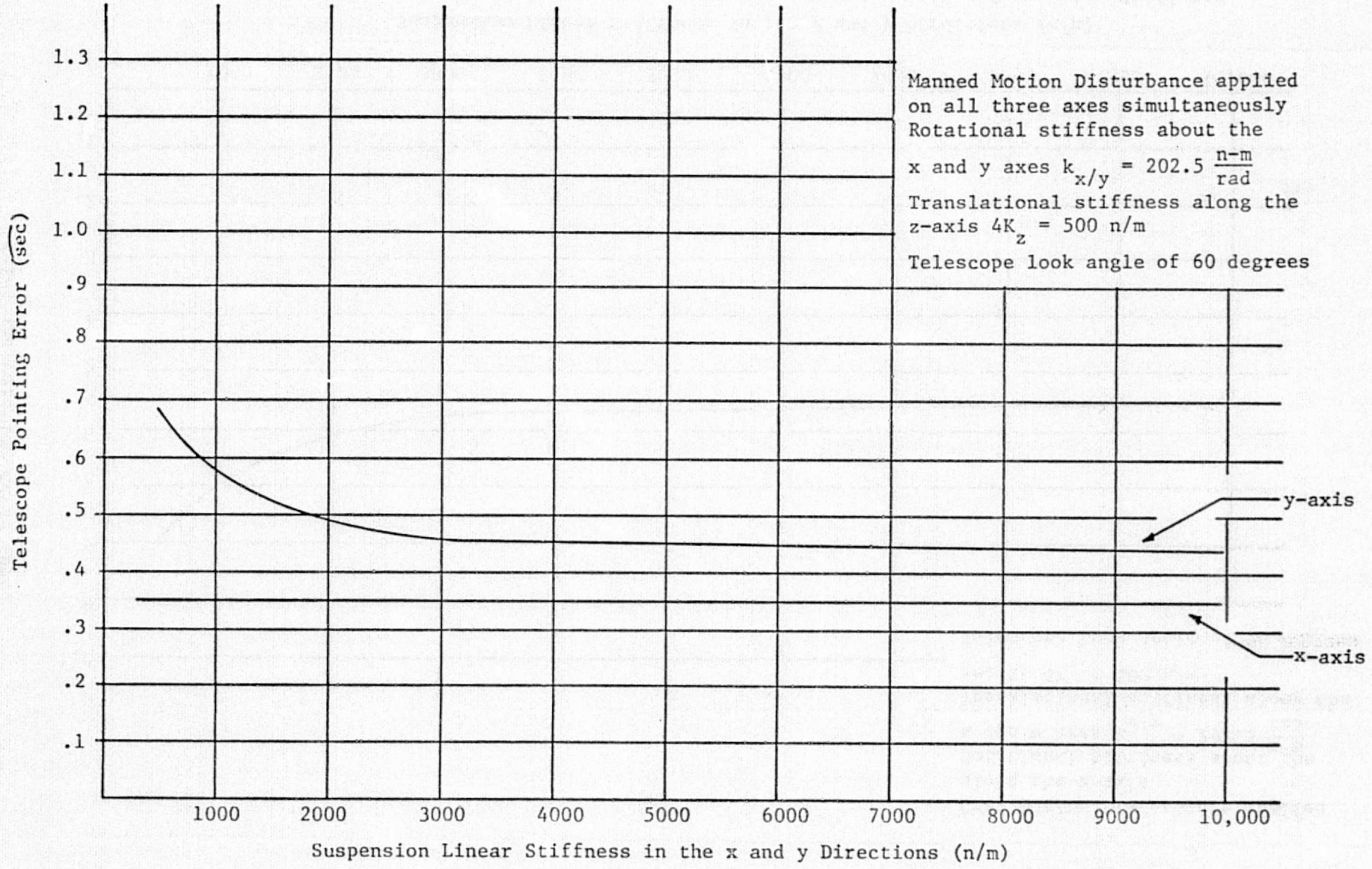

Figure 7-88. Telescope Peak Pointing Error vs Linear Suspension Stiffness

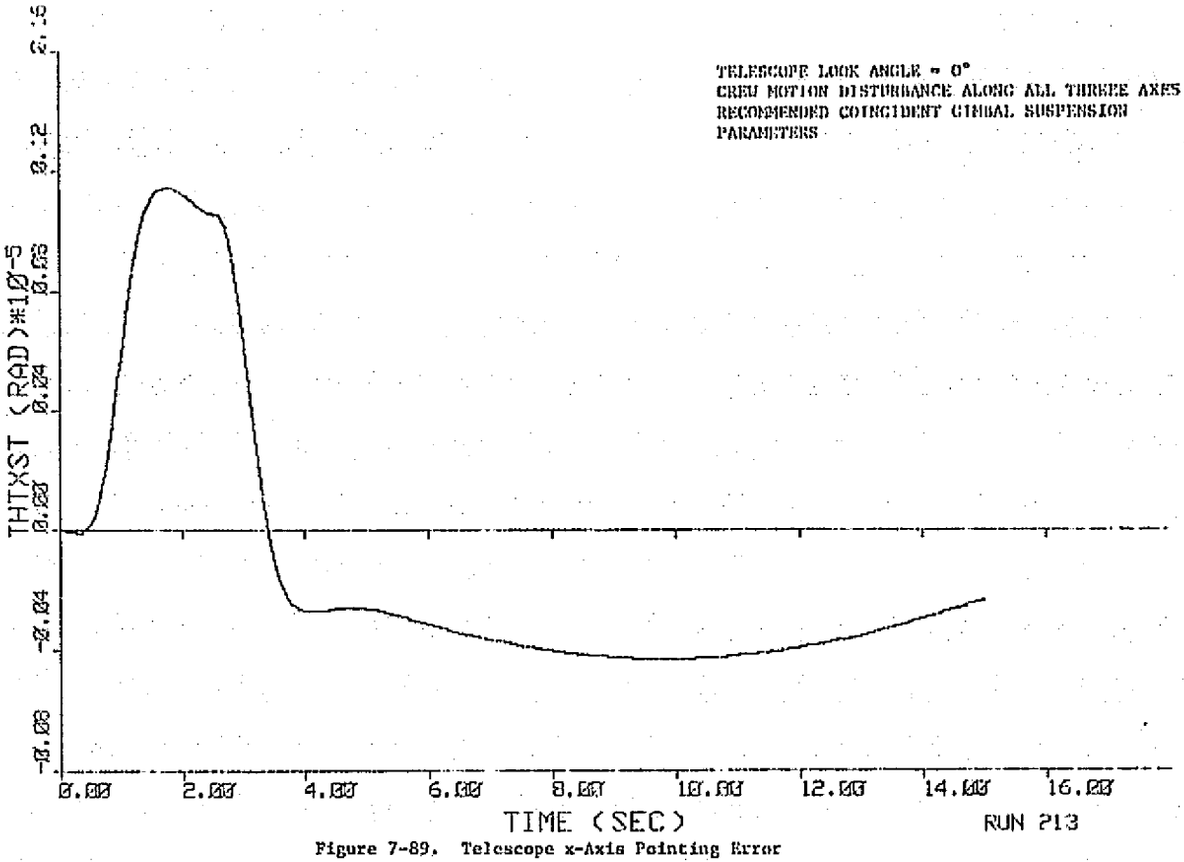

Figure 7-89. Telescope x-Axis Pointing Error

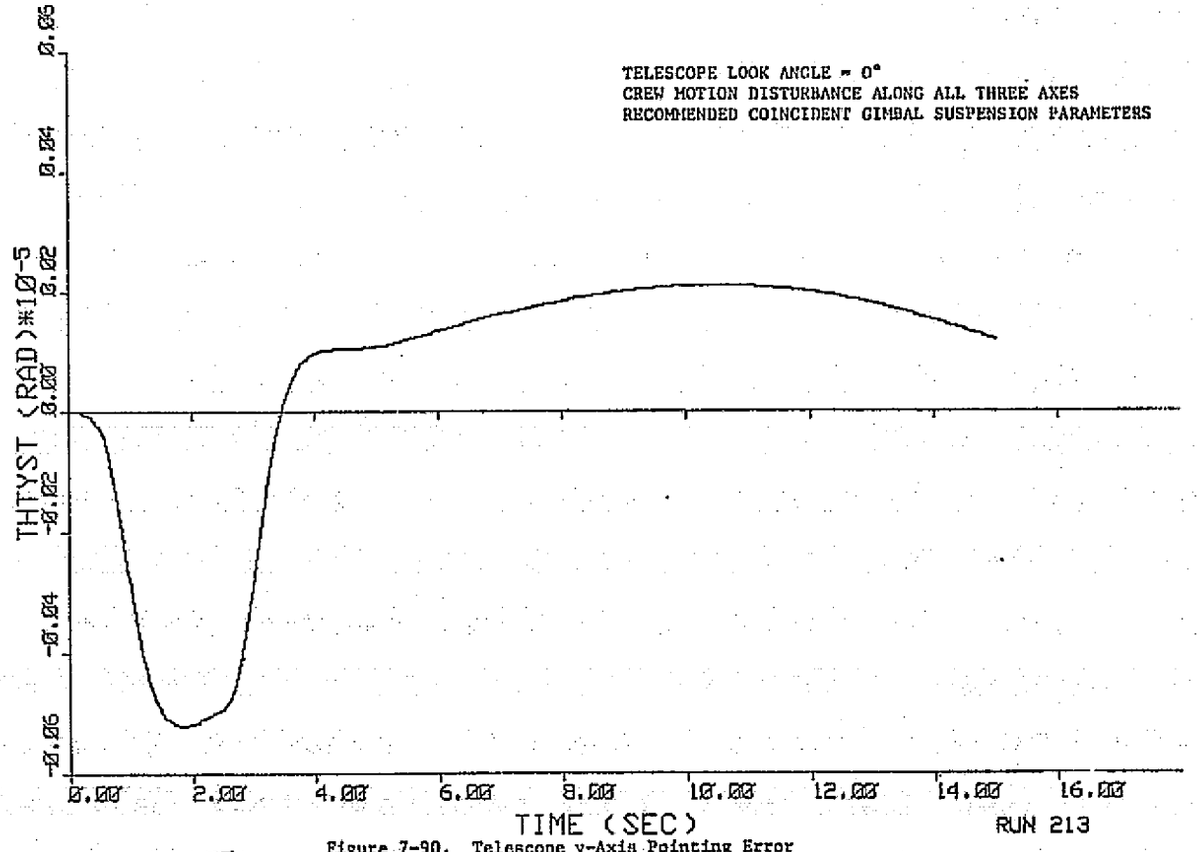

Figure 7-90. Telescope y-Axis Pointing Error

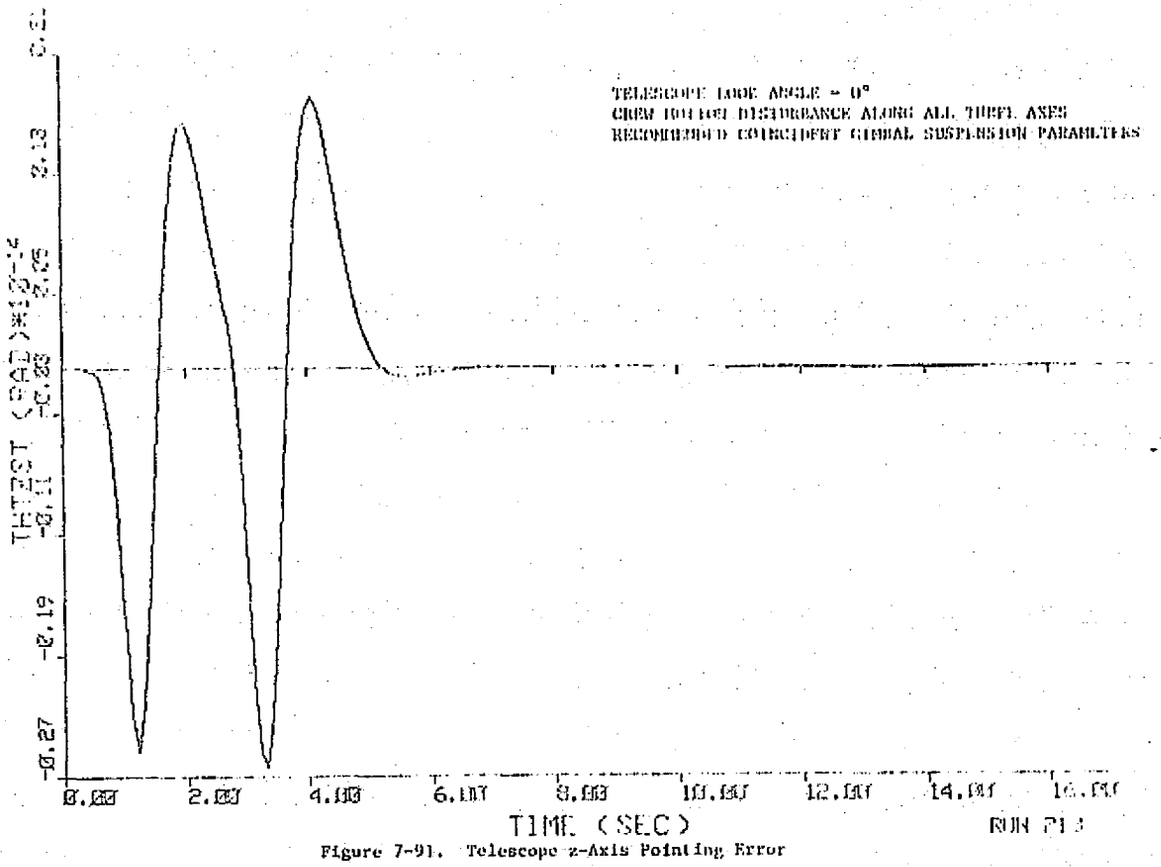

Figure 7-91. Telescope z-Axis Pointing Error

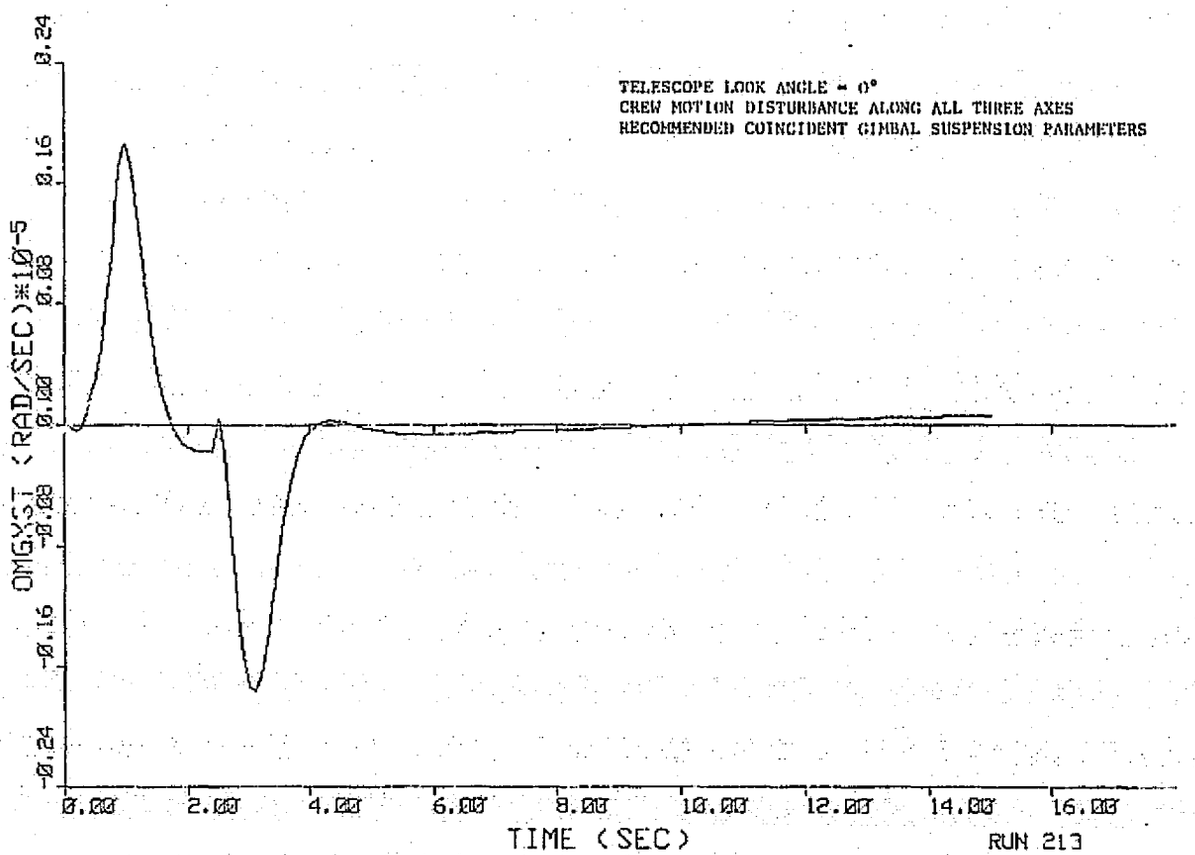

Figure 7-92. Telescope x-Axis Rate Error

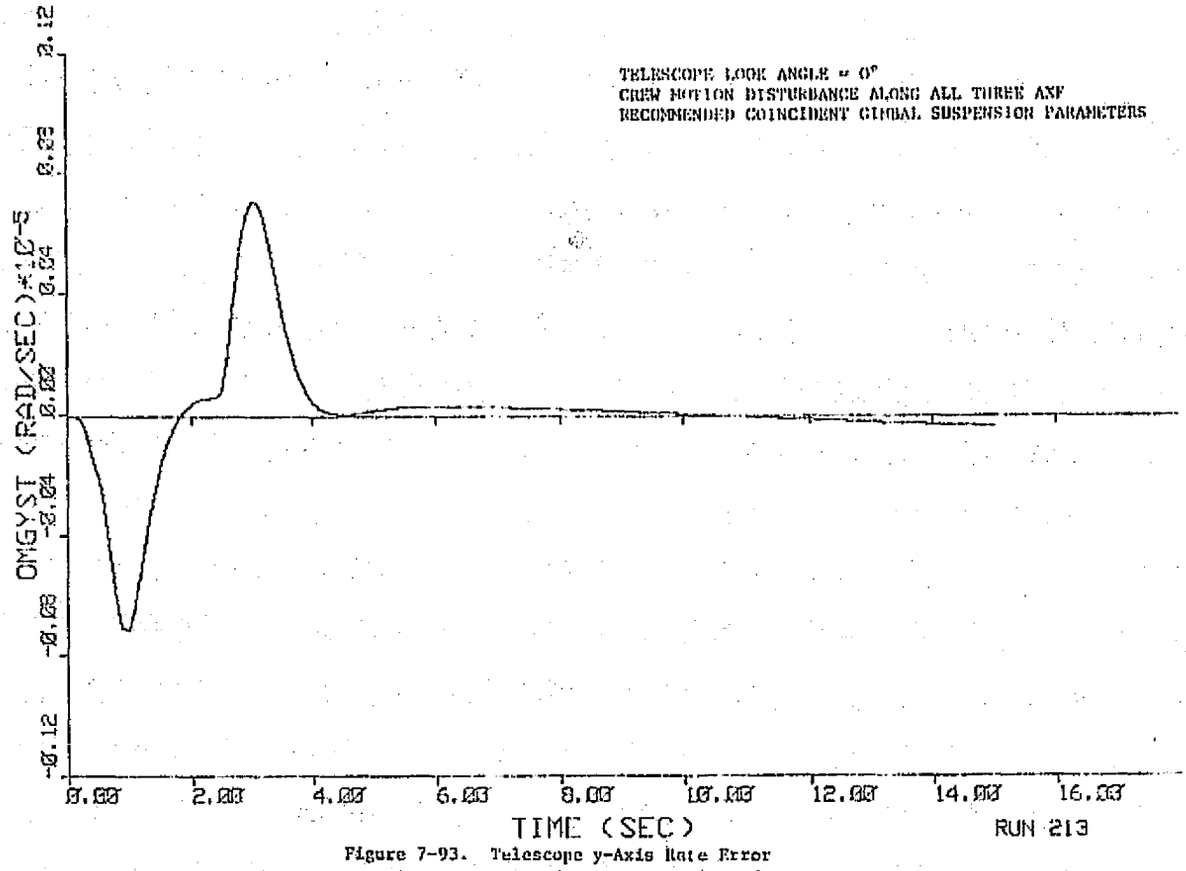

Figure 7-93. Telescope y-Axis Rate Error

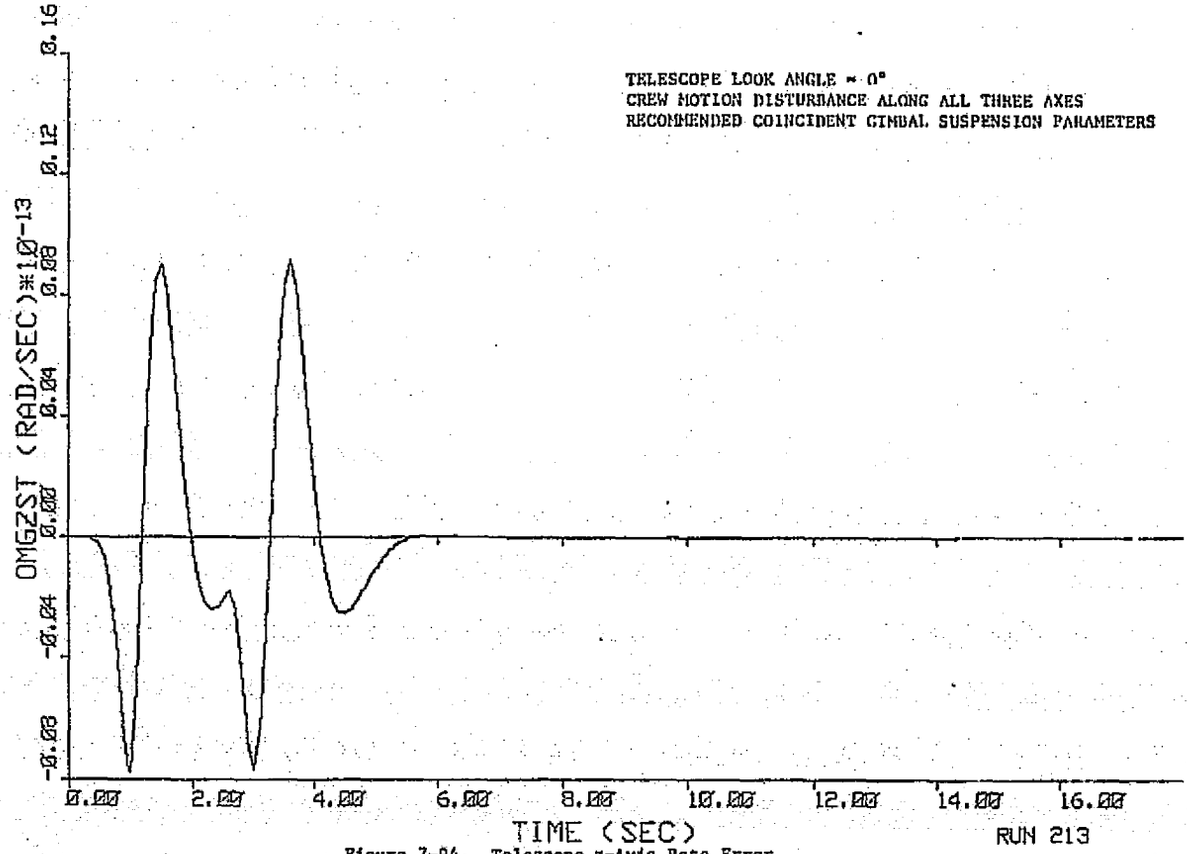

Figure 7-94. Telescope z-Axis Rate Error

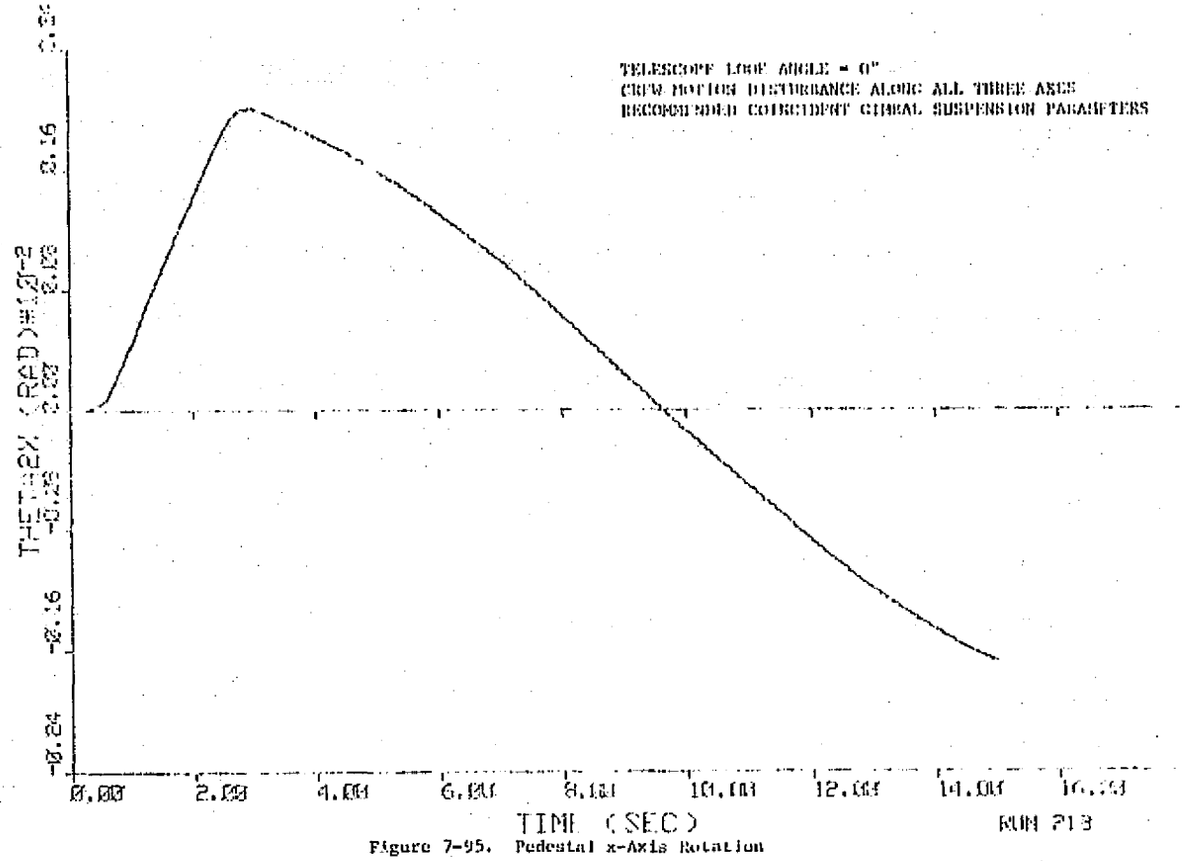

Figure 7-95. Pedestal x-Axis Rotation

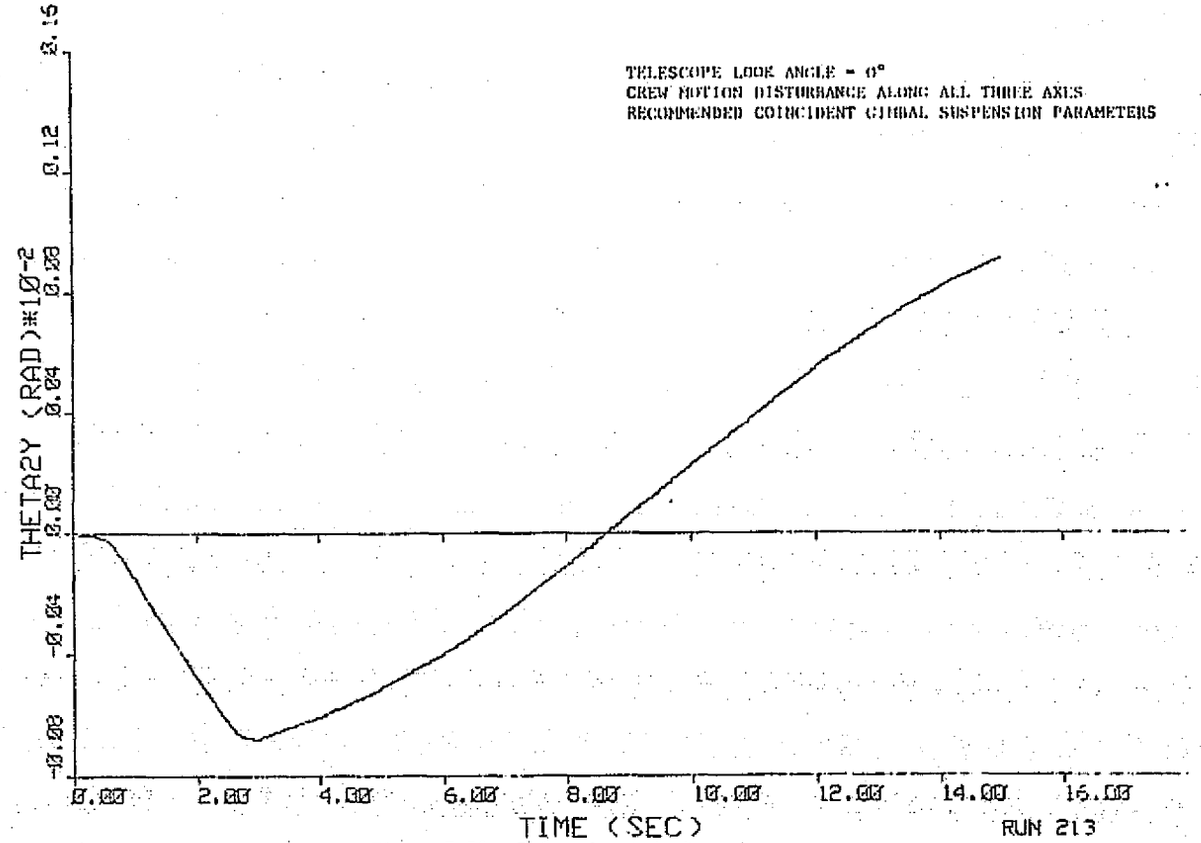

Figure 7-96. Pedestal y-Axis Rotation

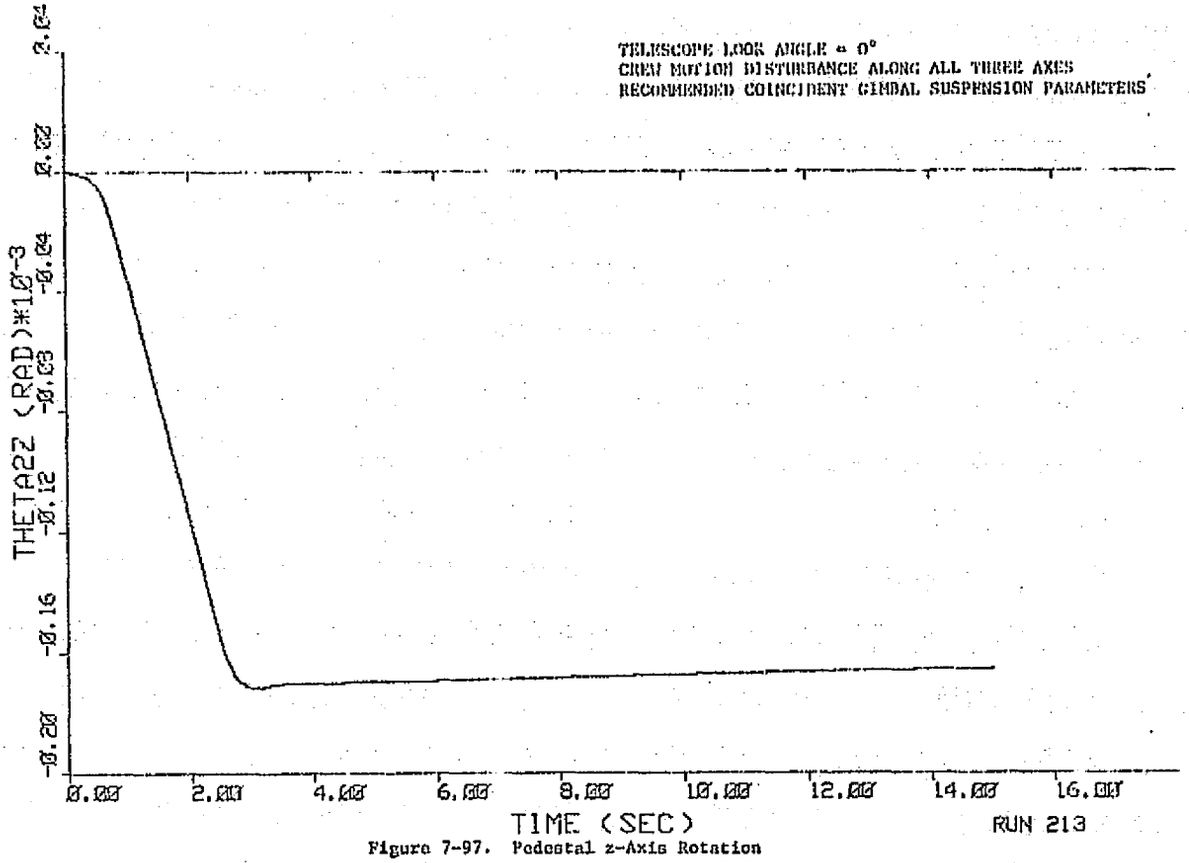

Figure 7-97. Pedestal z-Axis Rotation

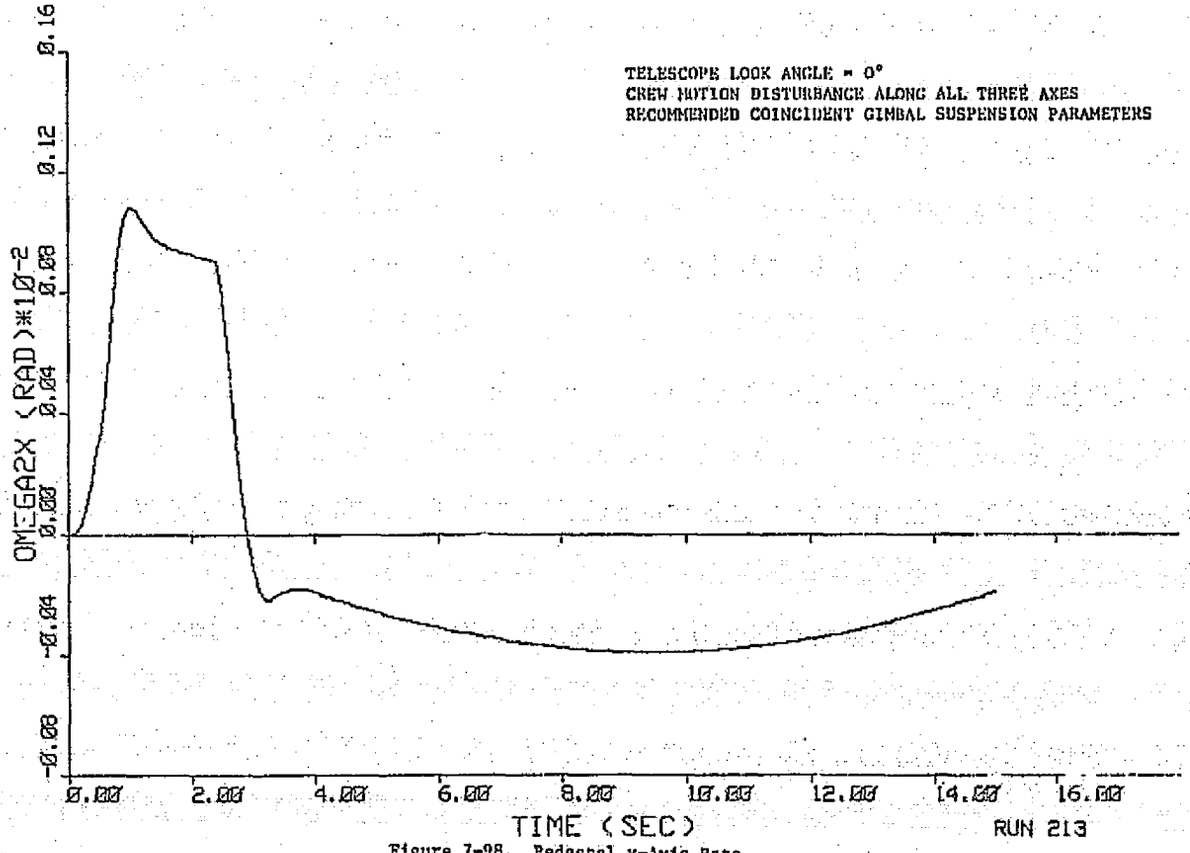

Figure 7-98. Pedestal x-Axis Rate

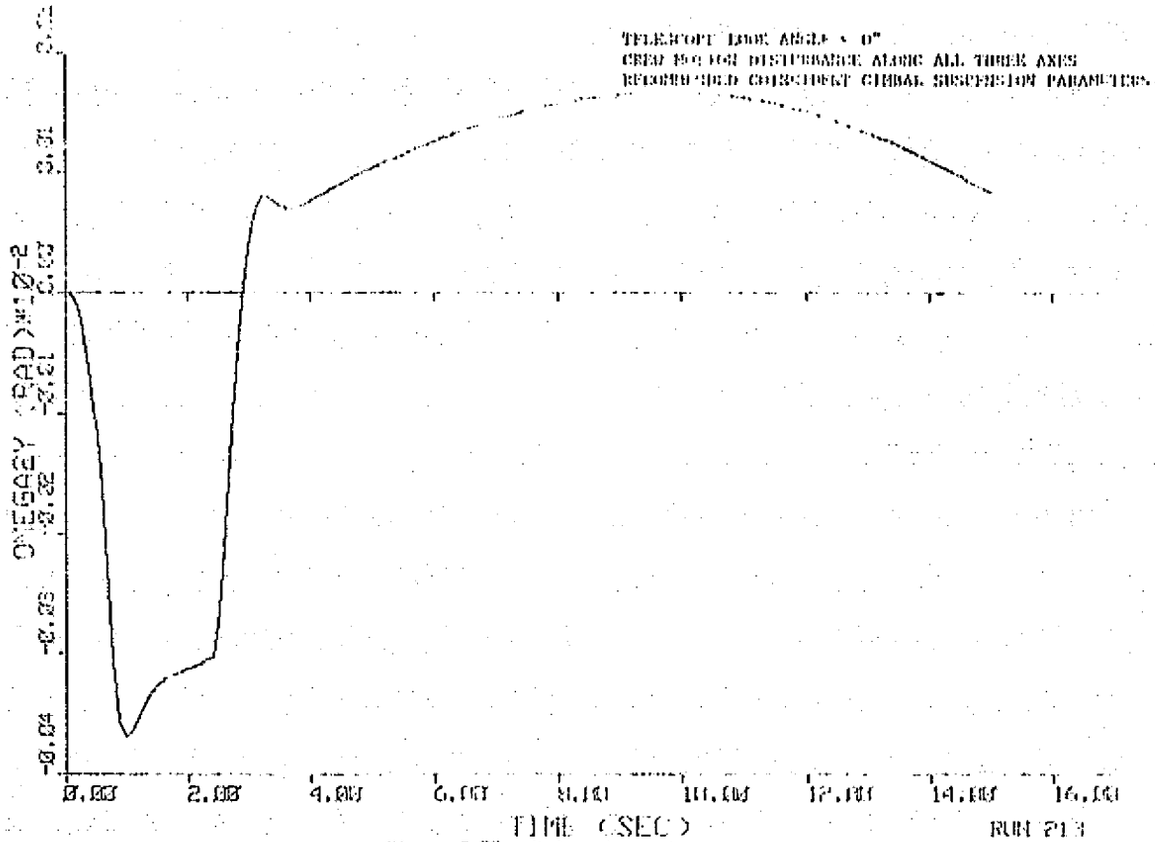

Figure 7-99. Pedestal y-Axis Rate

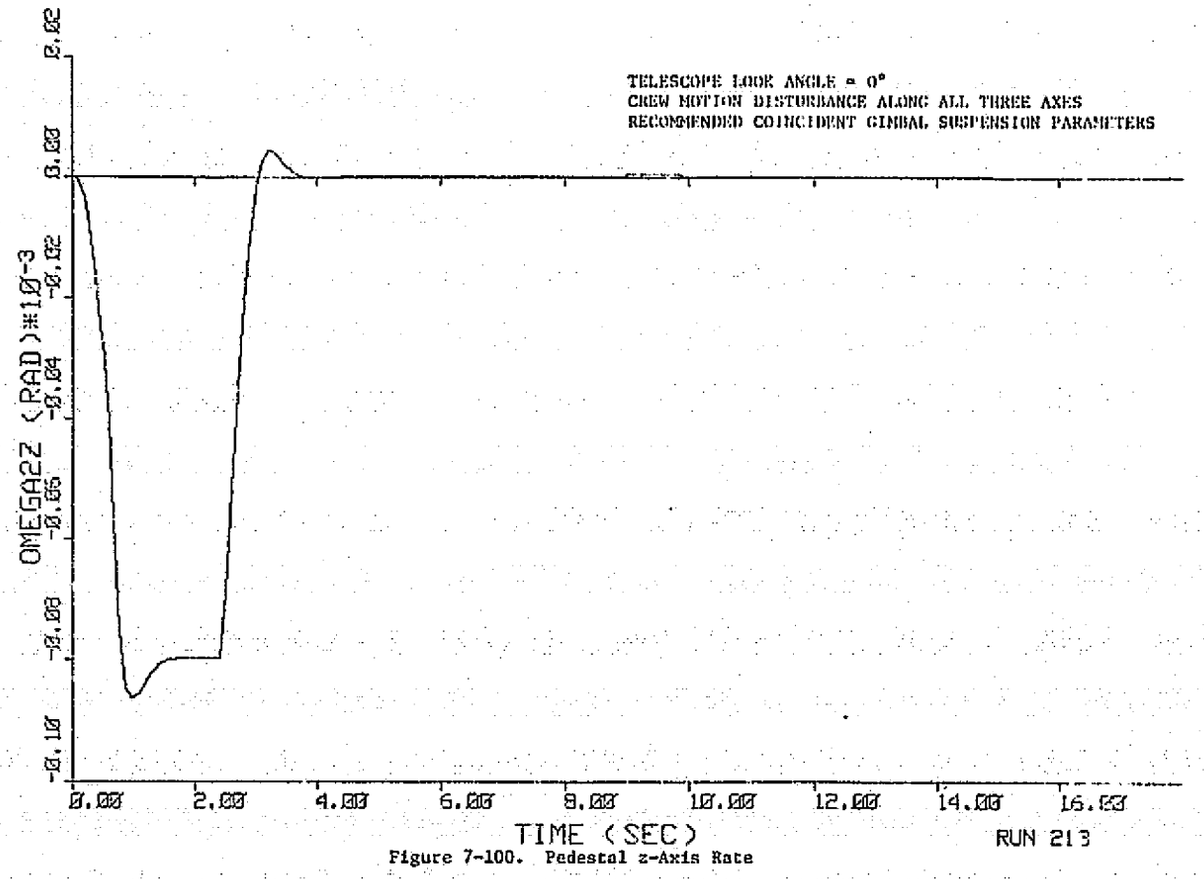

Figure 7-100. Pedestal z-Axis Rate

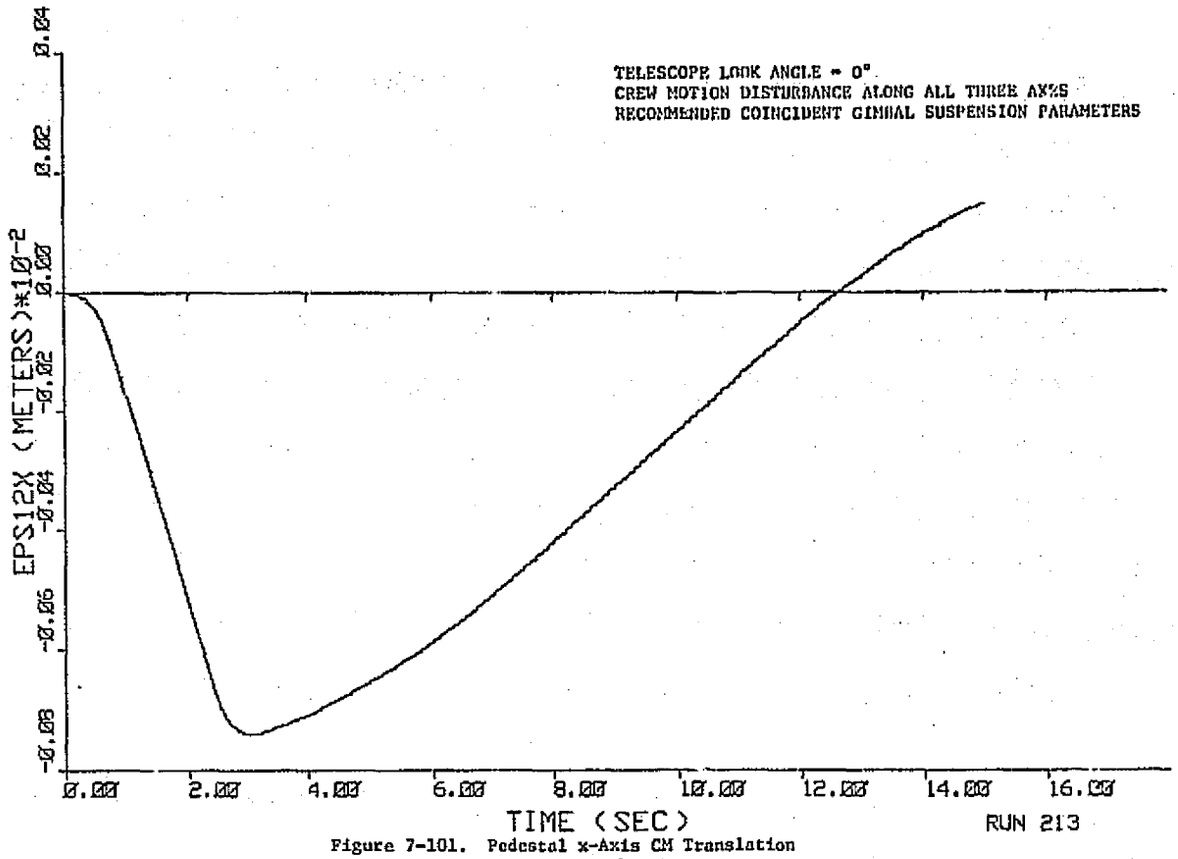

Figure 7-101. Pedestal x-Axis CM Translation

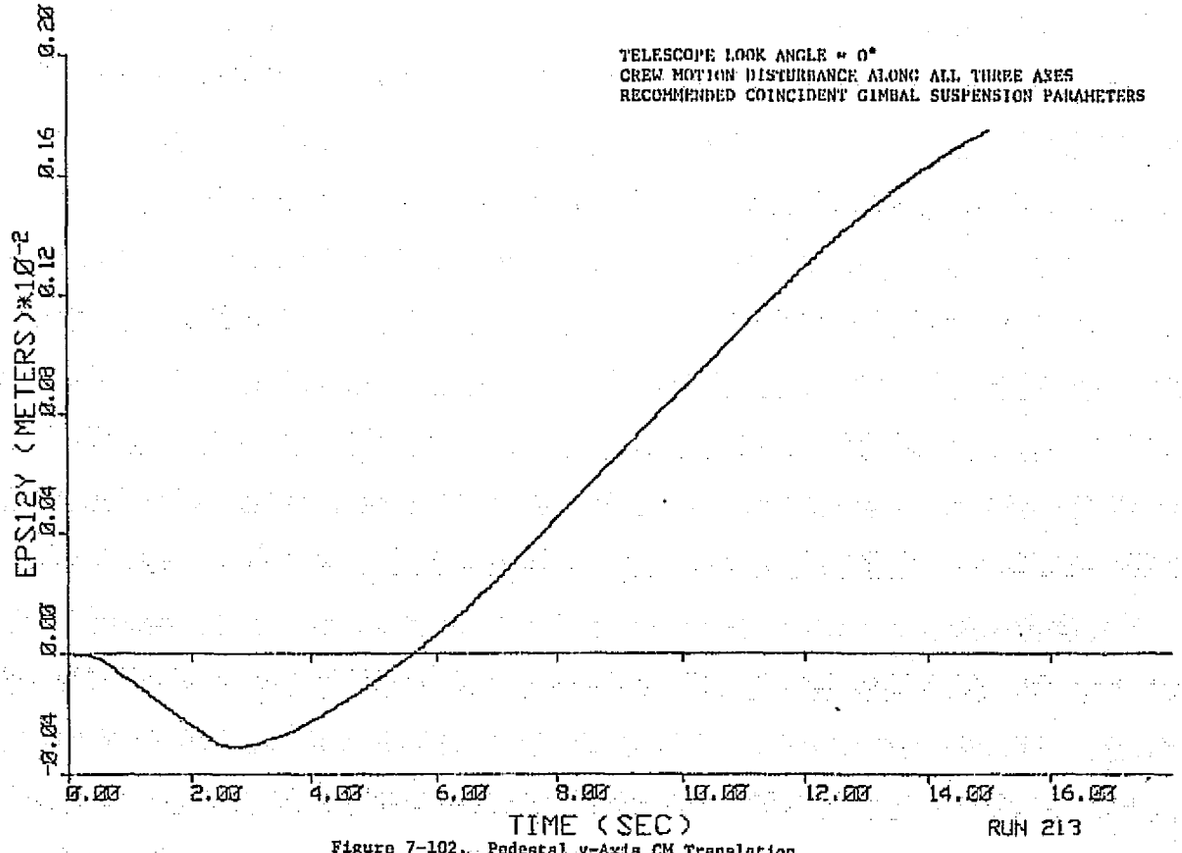

Figure 7-102. Pedestal y-Axis CM Translation

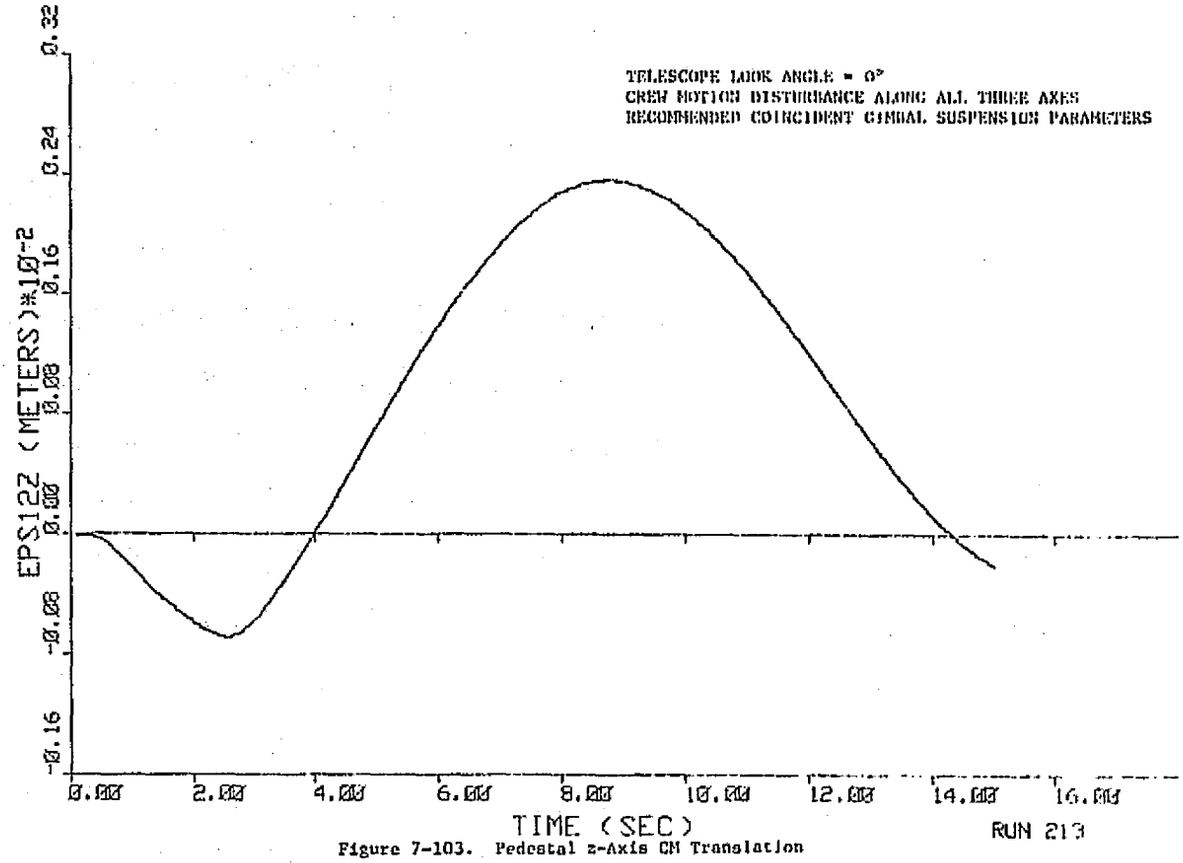

Figure 7-103. Pedestal z-Axis CM Translation

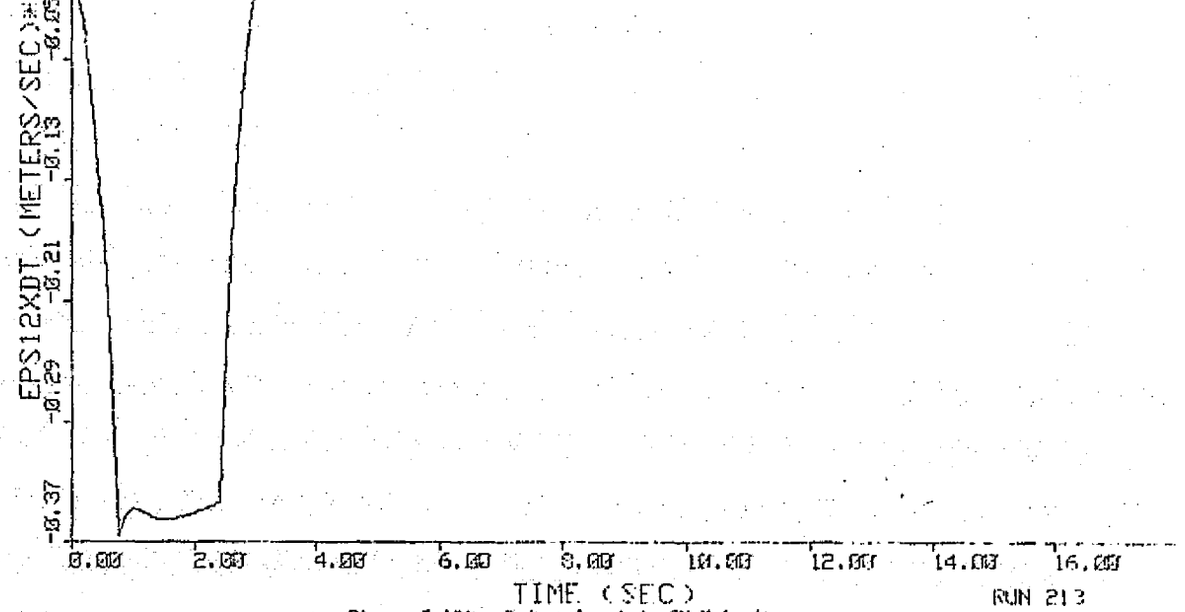

Figure 7-104. Pedestal x-Axis CM Velocity

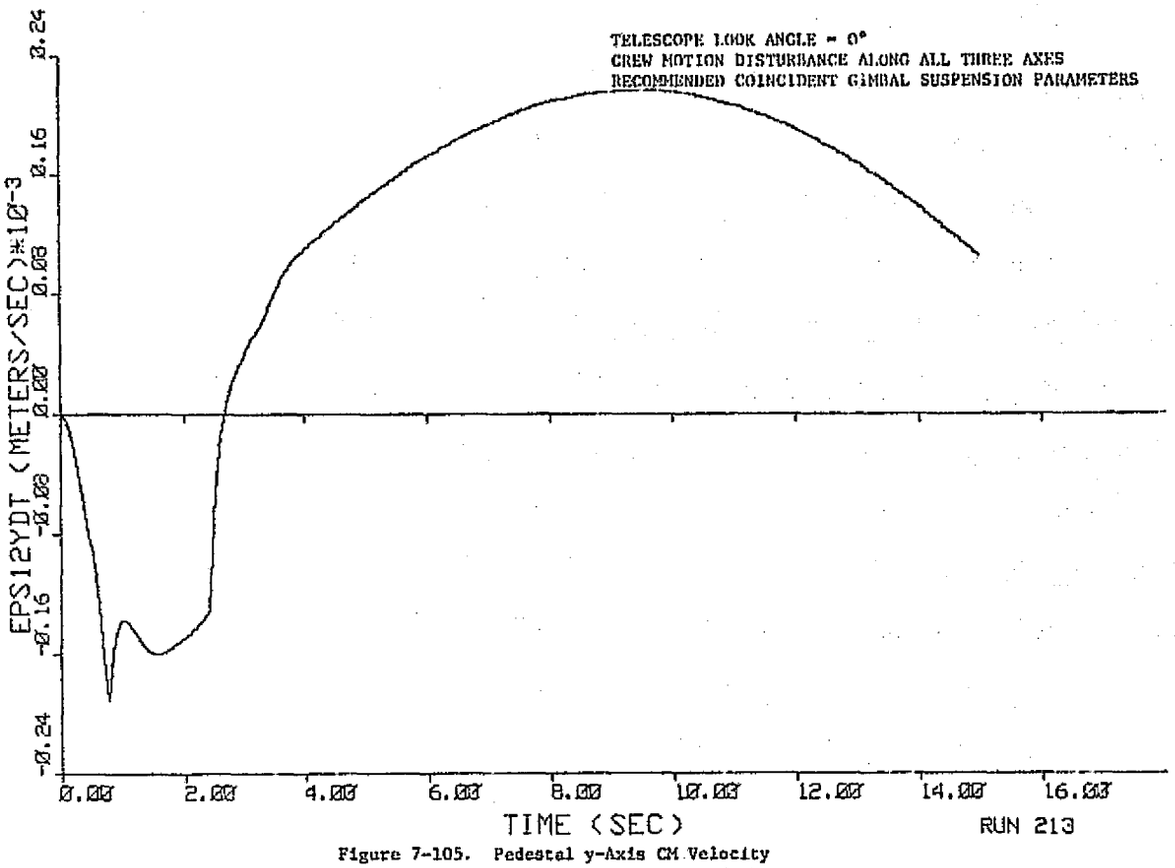

Figure 7-105. Pedestal y-Axis CM Velocity

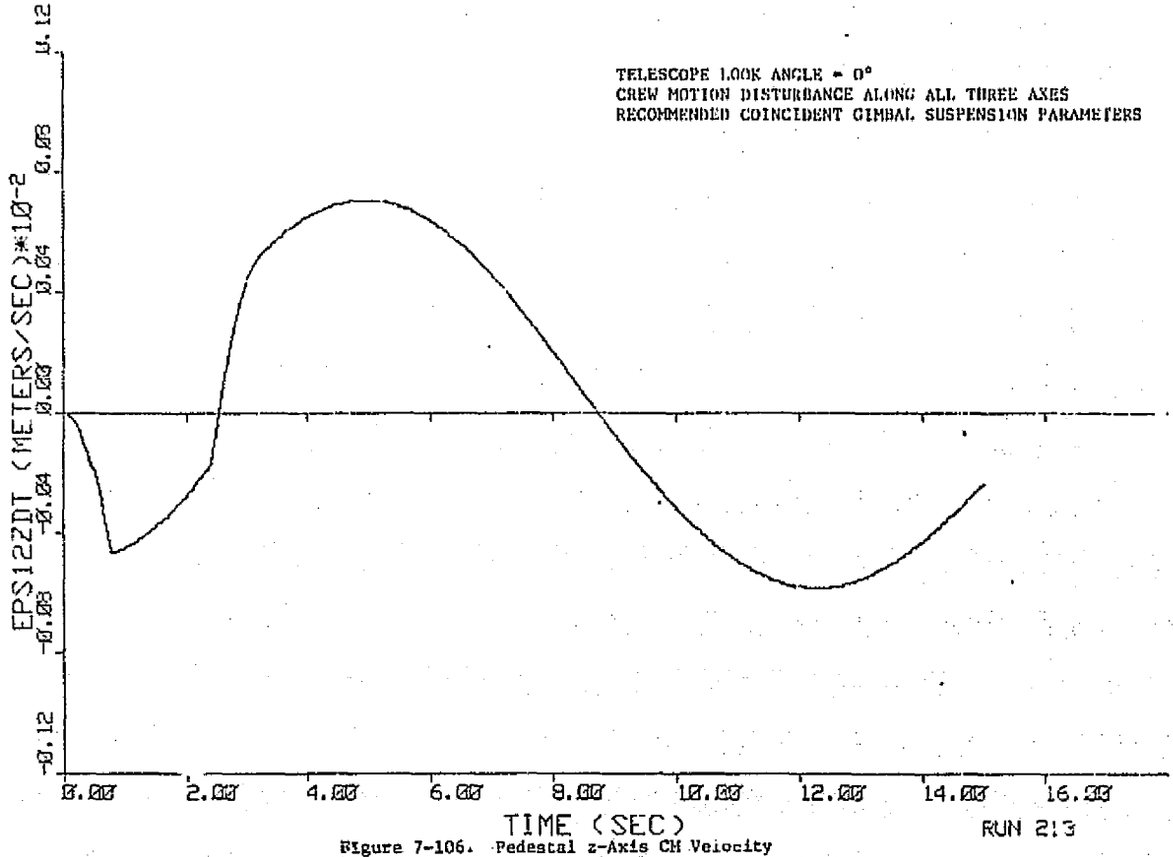

Figure 7-106. Pedestal z-Axis CM Velocity

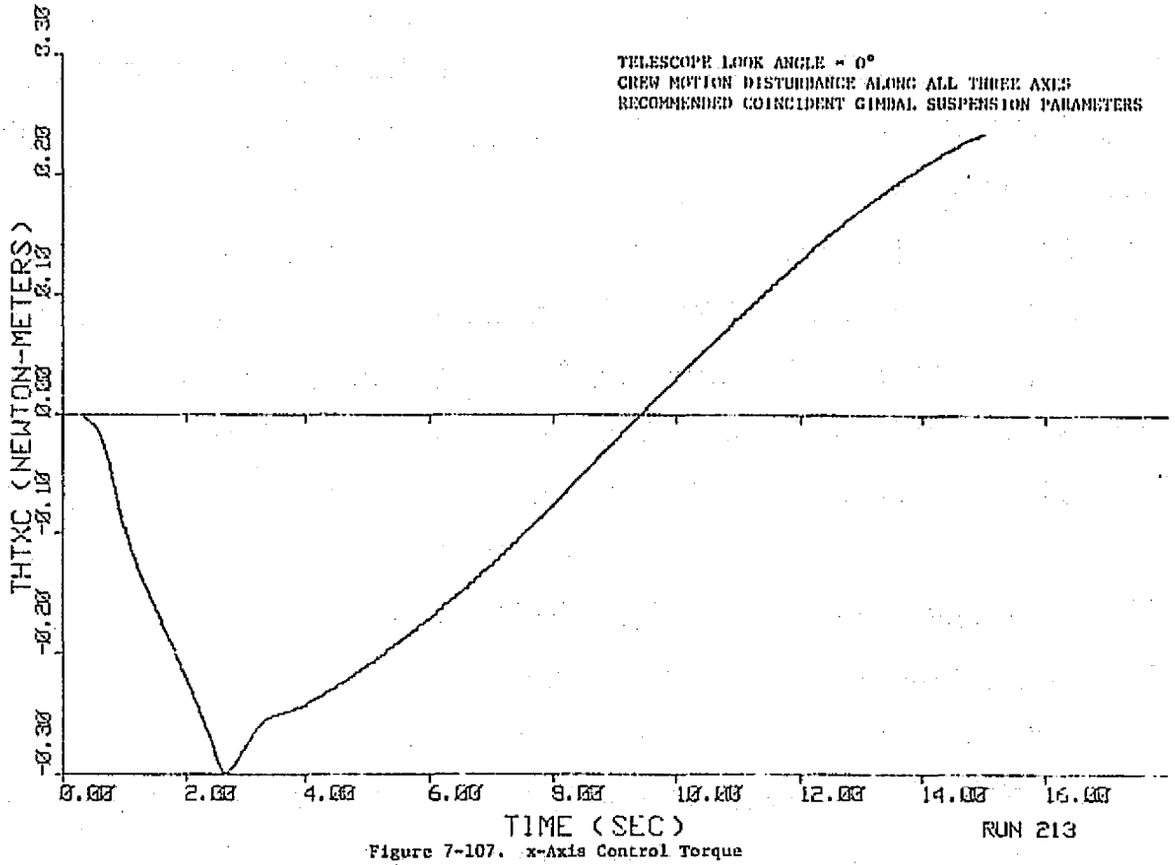

Figure 7-107. x-Axis Control Torque

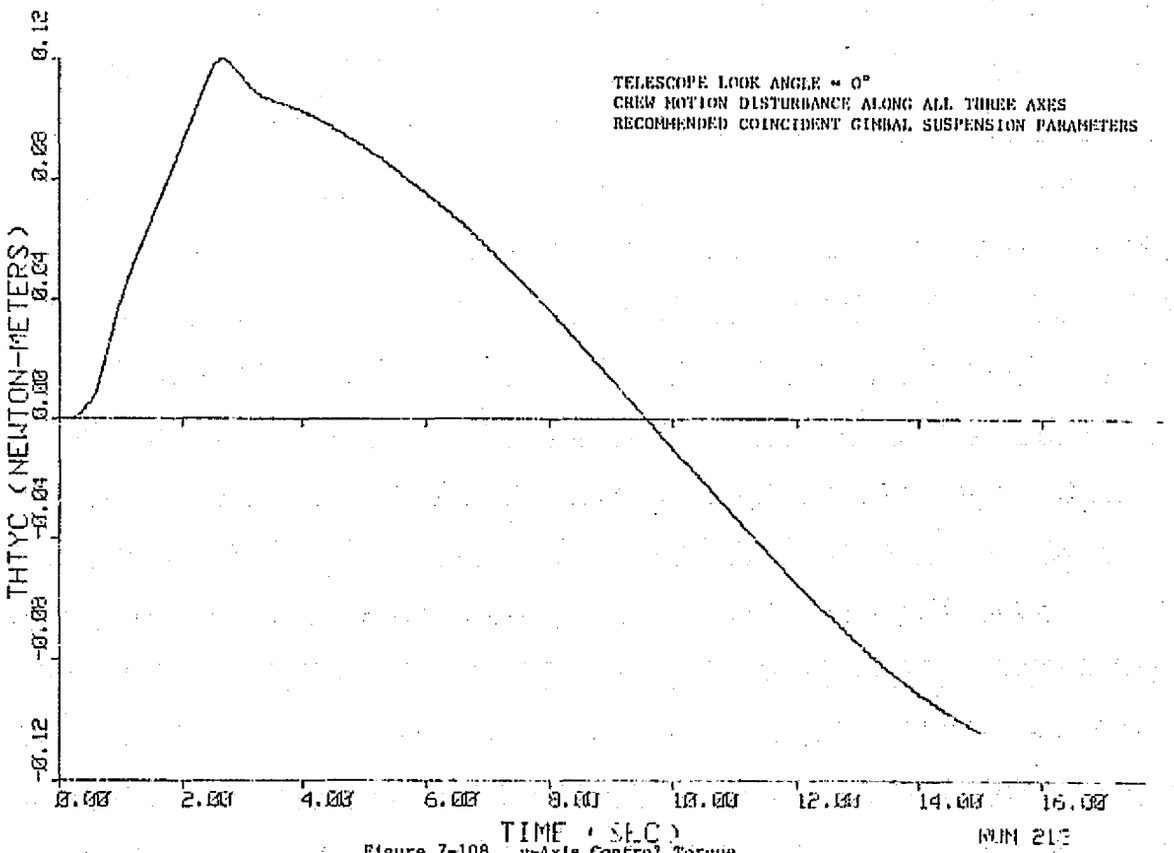

Figure 7-108. y-Axis Control Torque

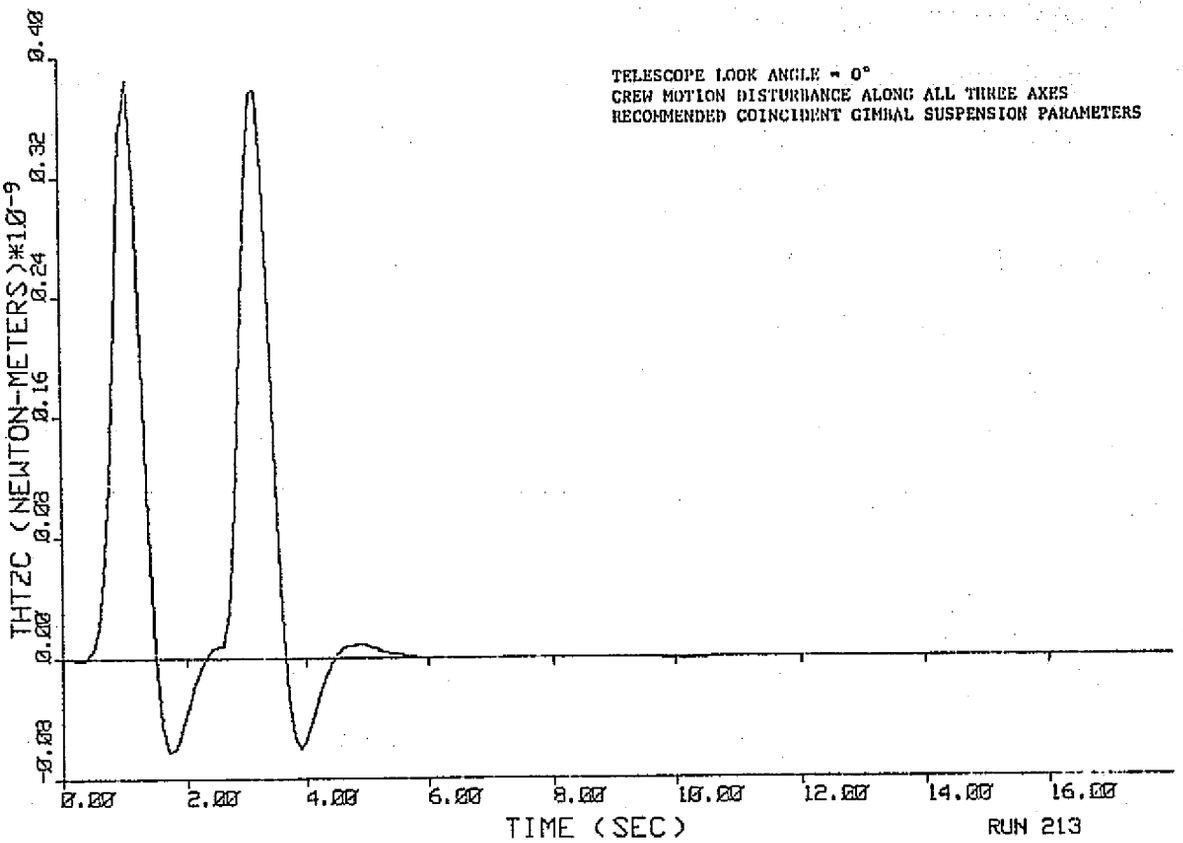

Figure 7-109. z-Axis Control Torque

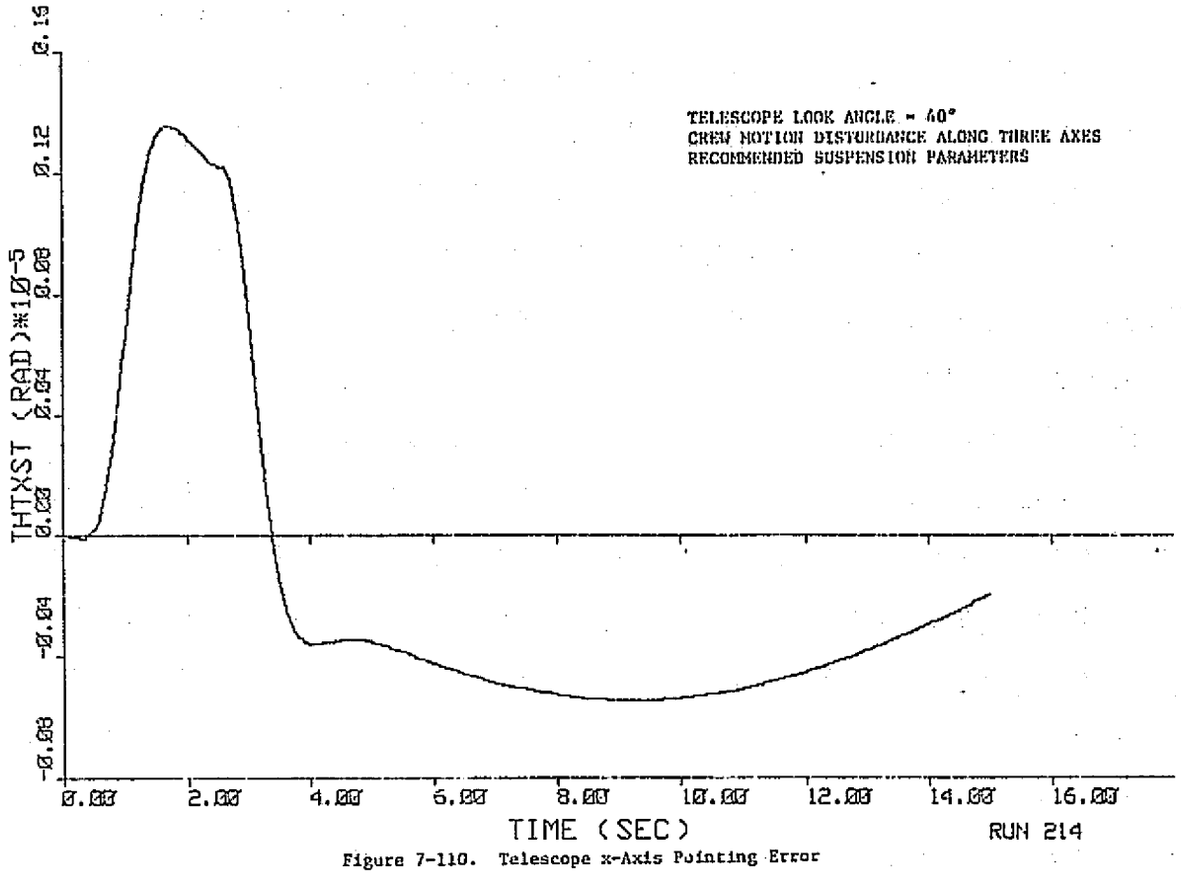

Figure 7-110. Telescope x-Axis Pointing Error

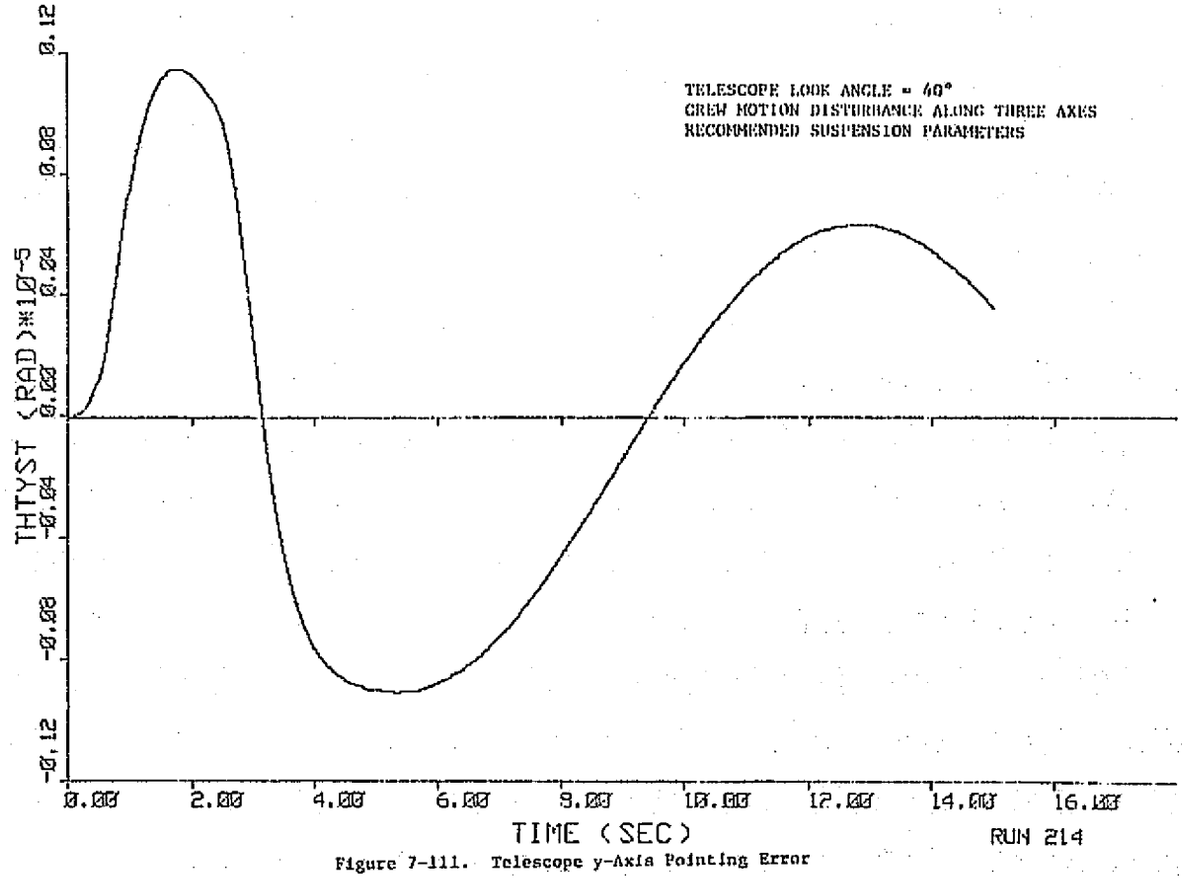

Figure 7-111. Telescope y-Axis Pointing Error

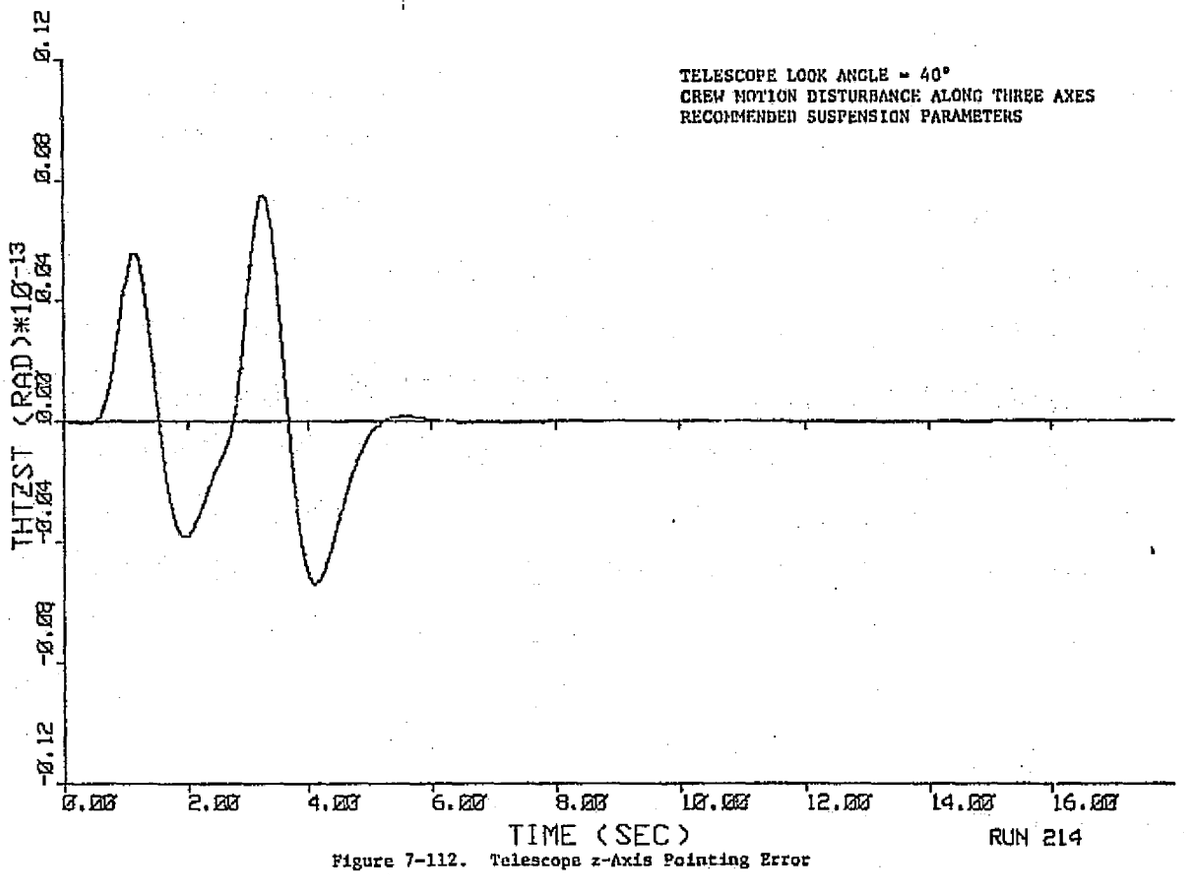

Figure 7-112. Telescope z-Axis Pointing Error

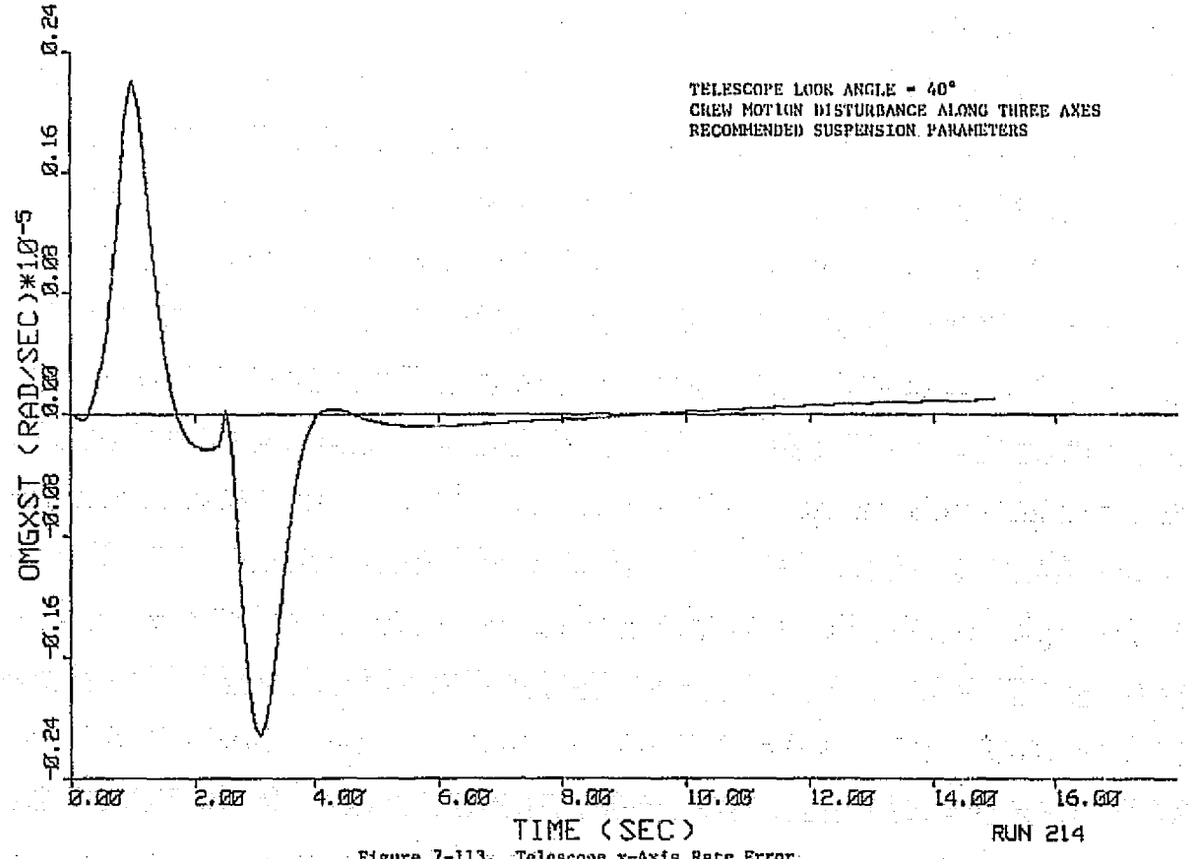

Figure 7-113. Telescope x-Axis Rate Error

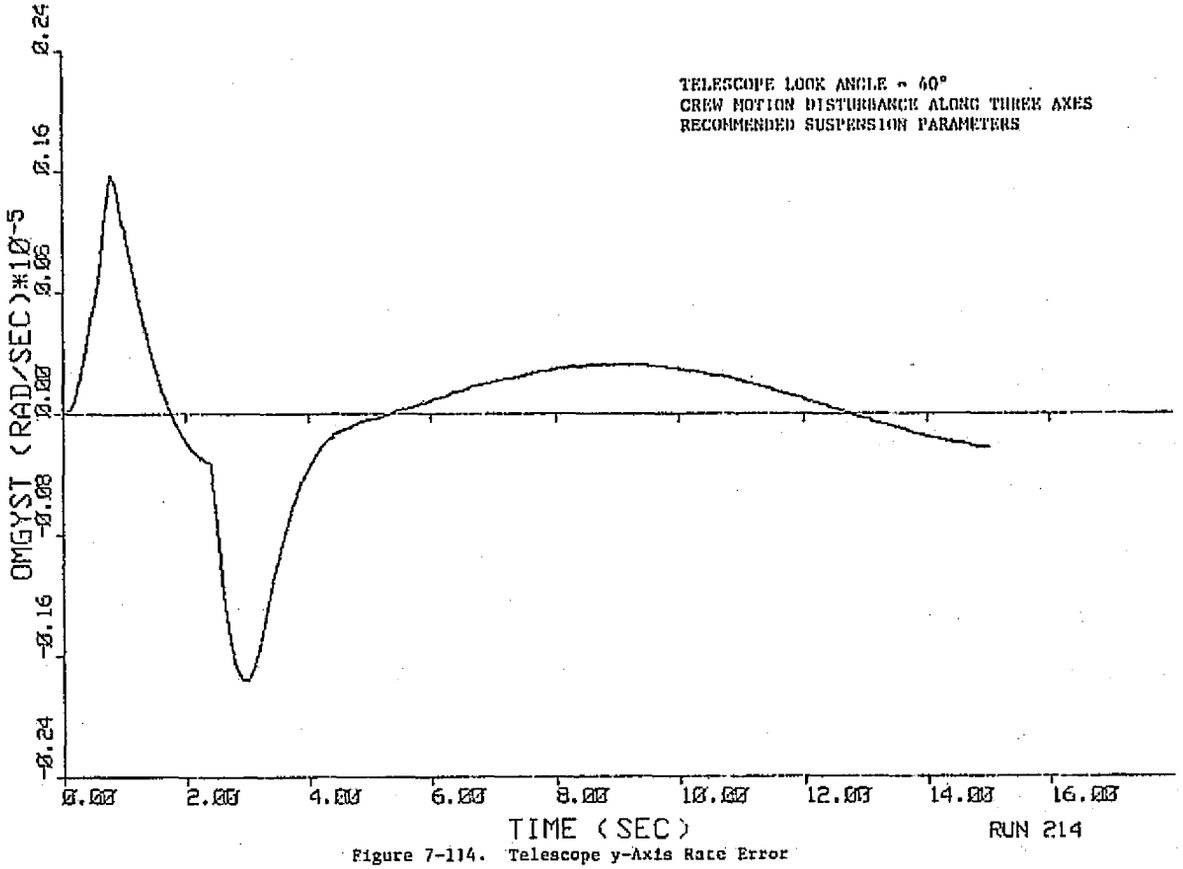

Figure 7-114. Telescope y-Axis Rate Error

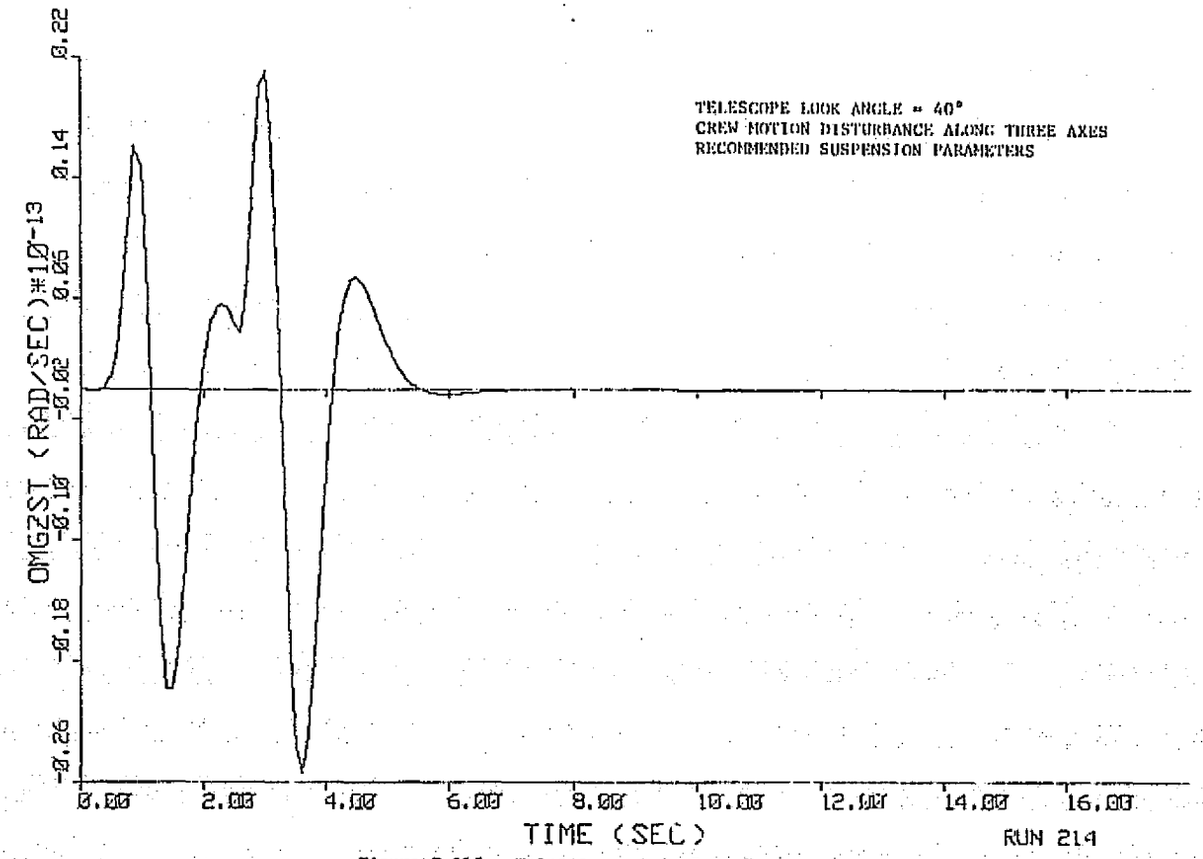

Figure 7-115. Telescope z-Axis Rate Error

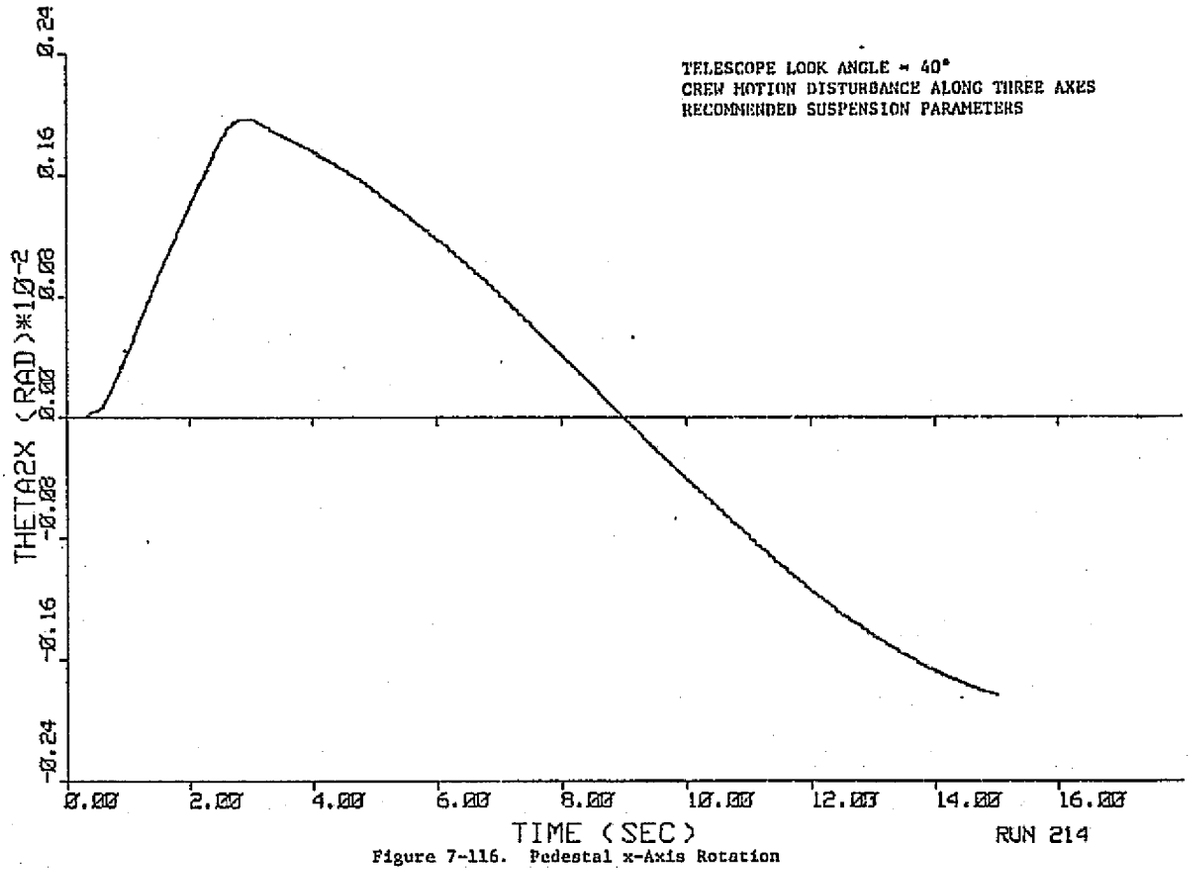

Figure 7-116. Pedestal x-Axis Rotation

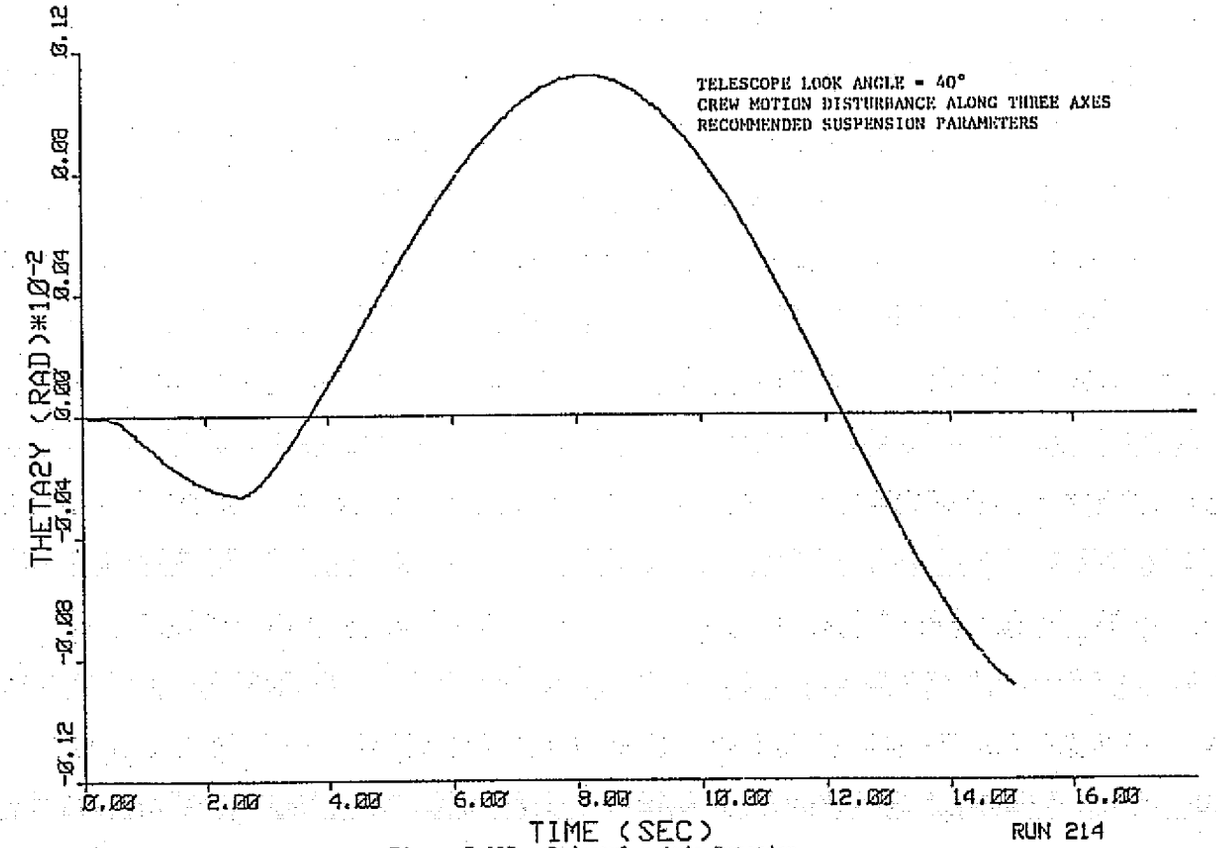

Figure 7-117. Pedestal y-Axis Rotation

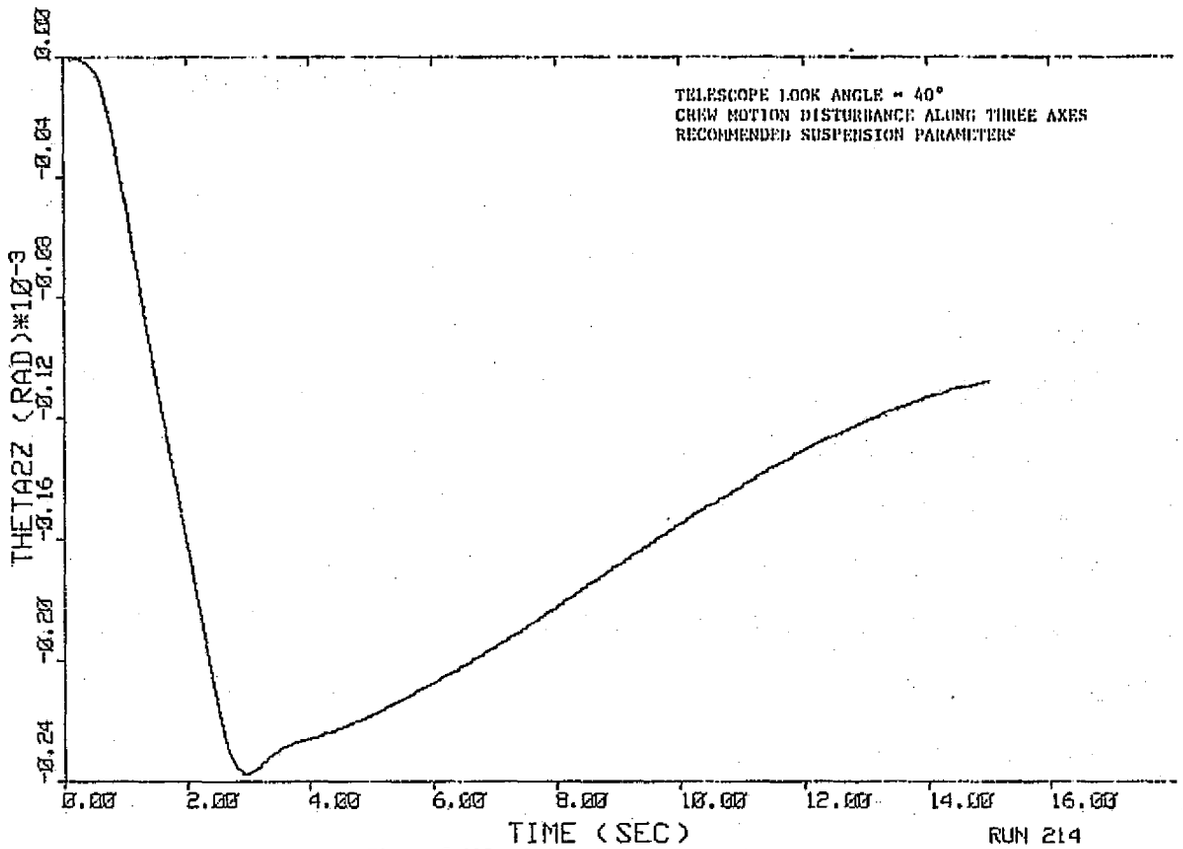

Figure 7-118. Pedestal z-Axis Rotation

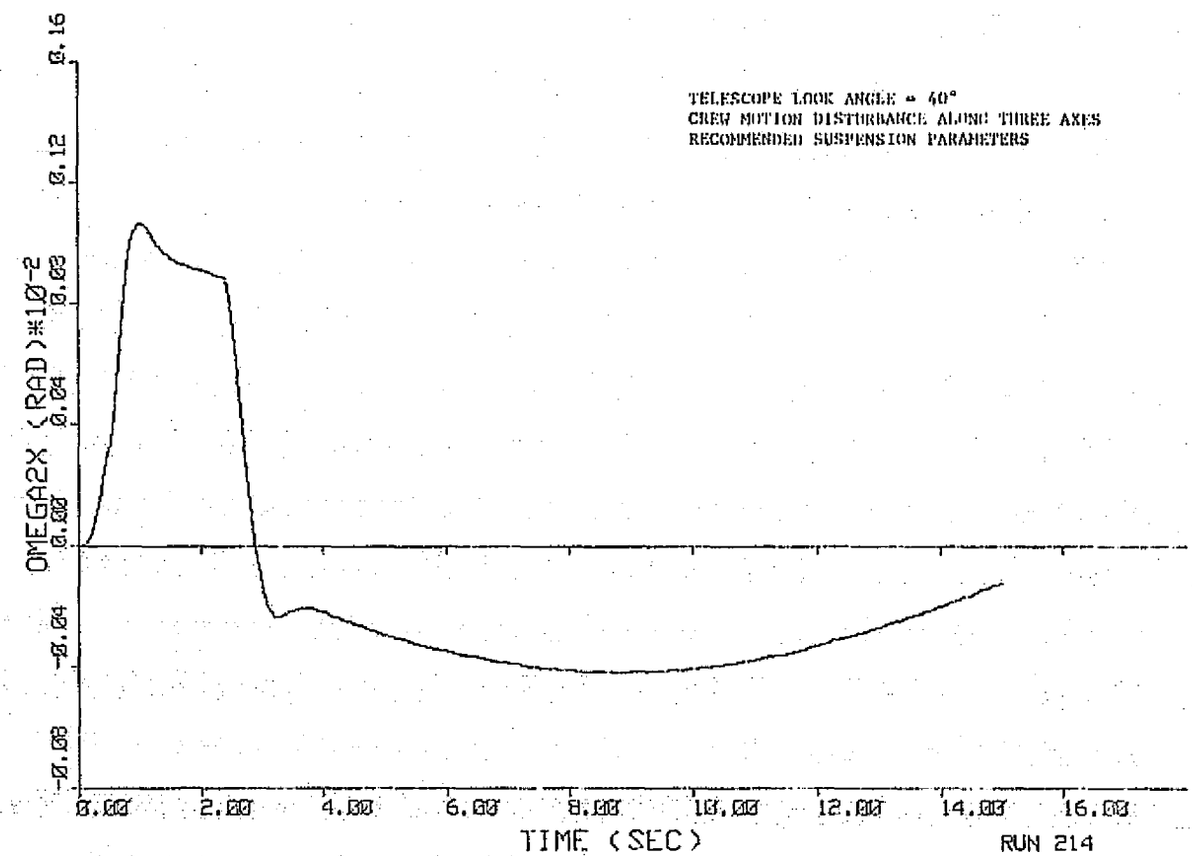

Figure 7-119. Pedestal x-Axis Rate

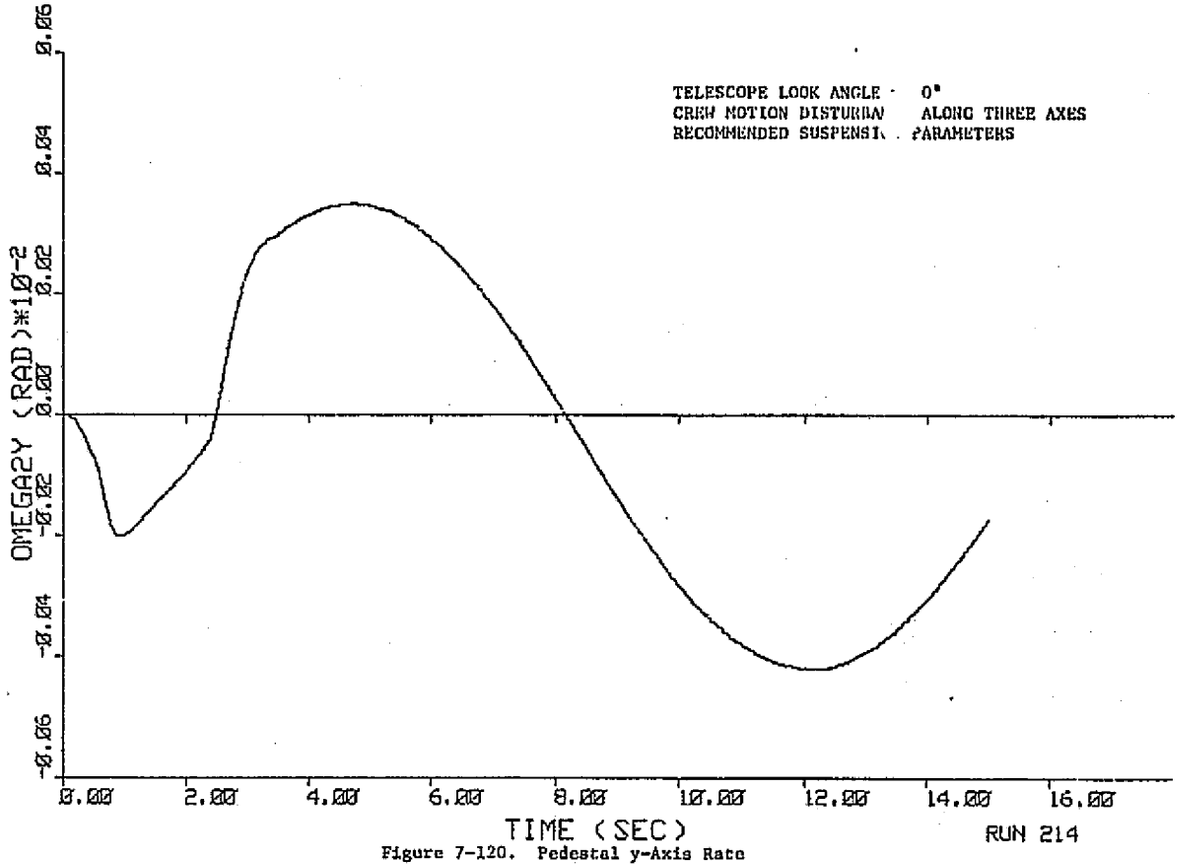

Figure 7-120. Pedestal y-Axis Rate

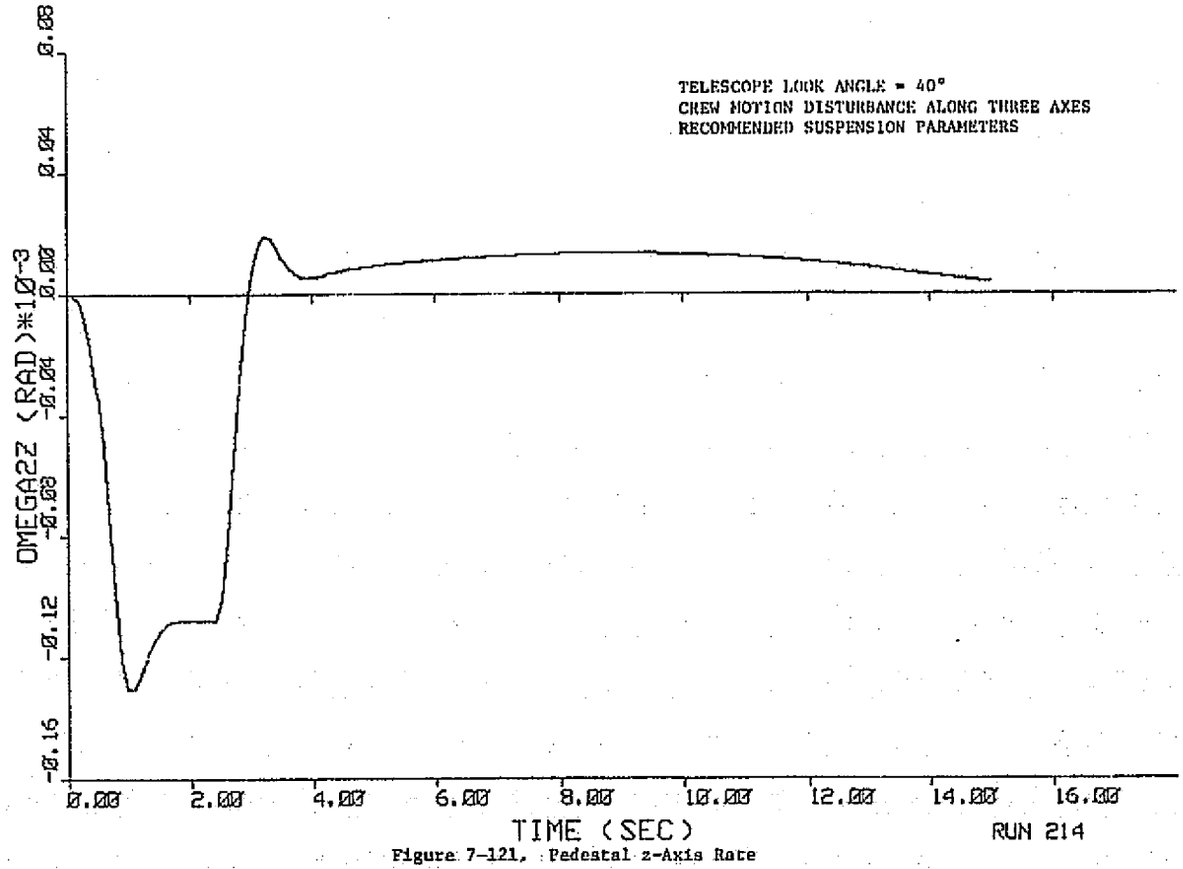

Figure 7-121. Pedestal z-Axis Rate

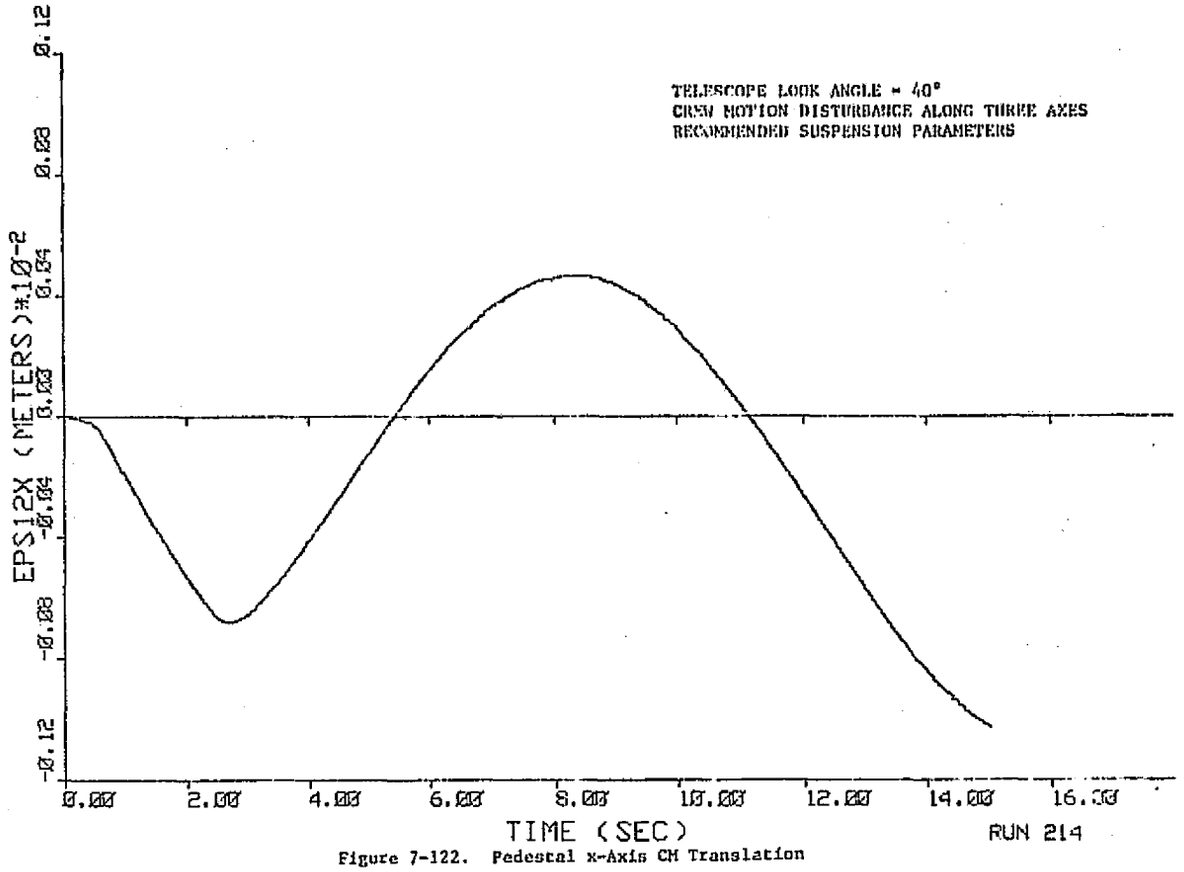

Figure 7-122. Pedestal x-Axis CM Translation

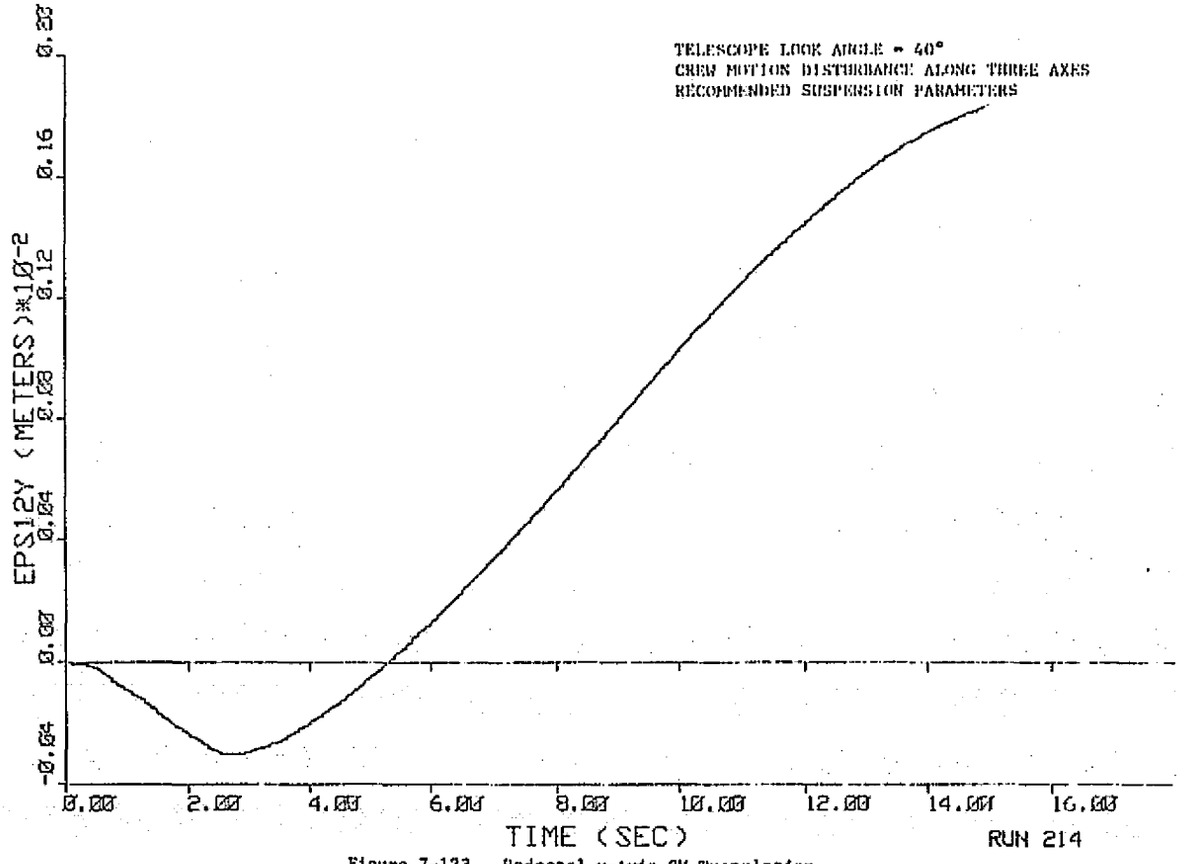

Figure 7-123. Pedestal y-Axis CM Translation

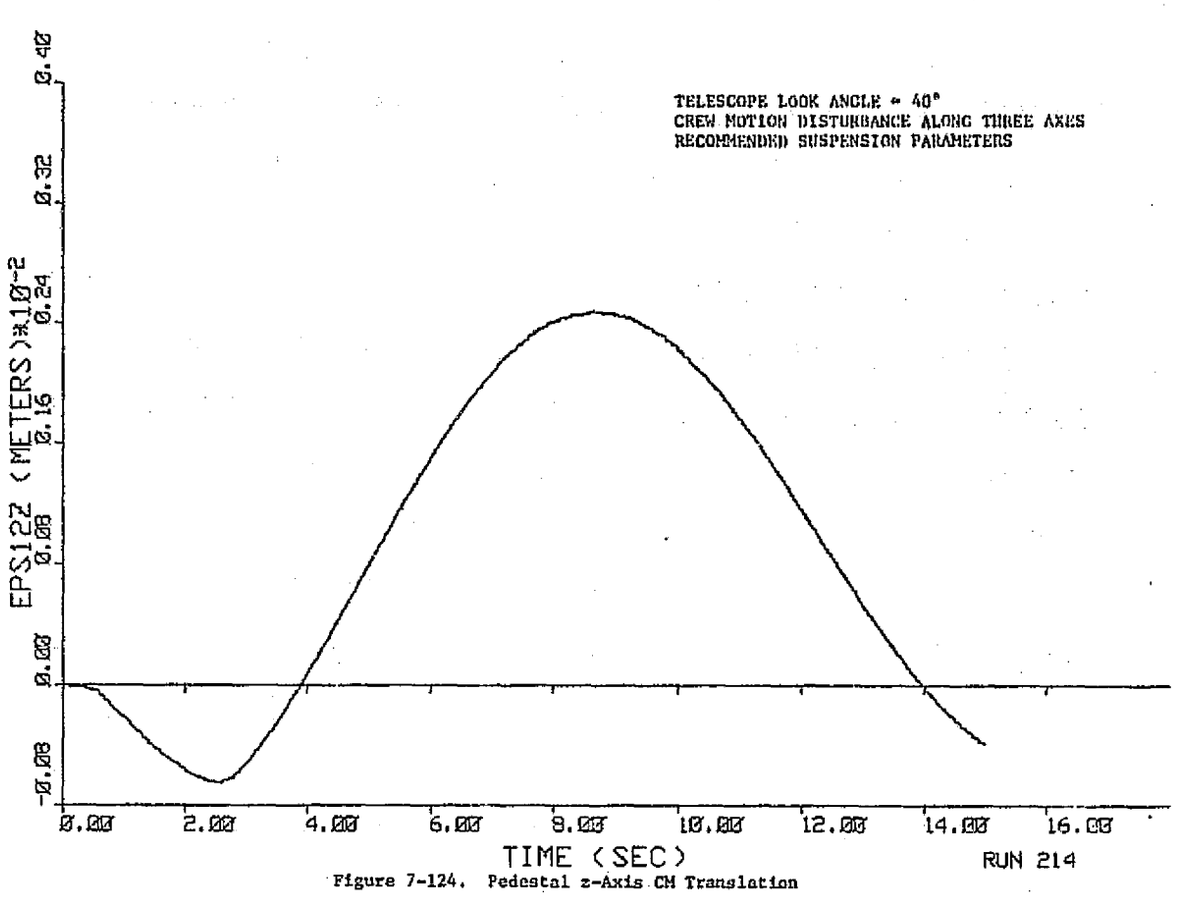

Figure 7-124. Pedestal z-Axis CM Translation

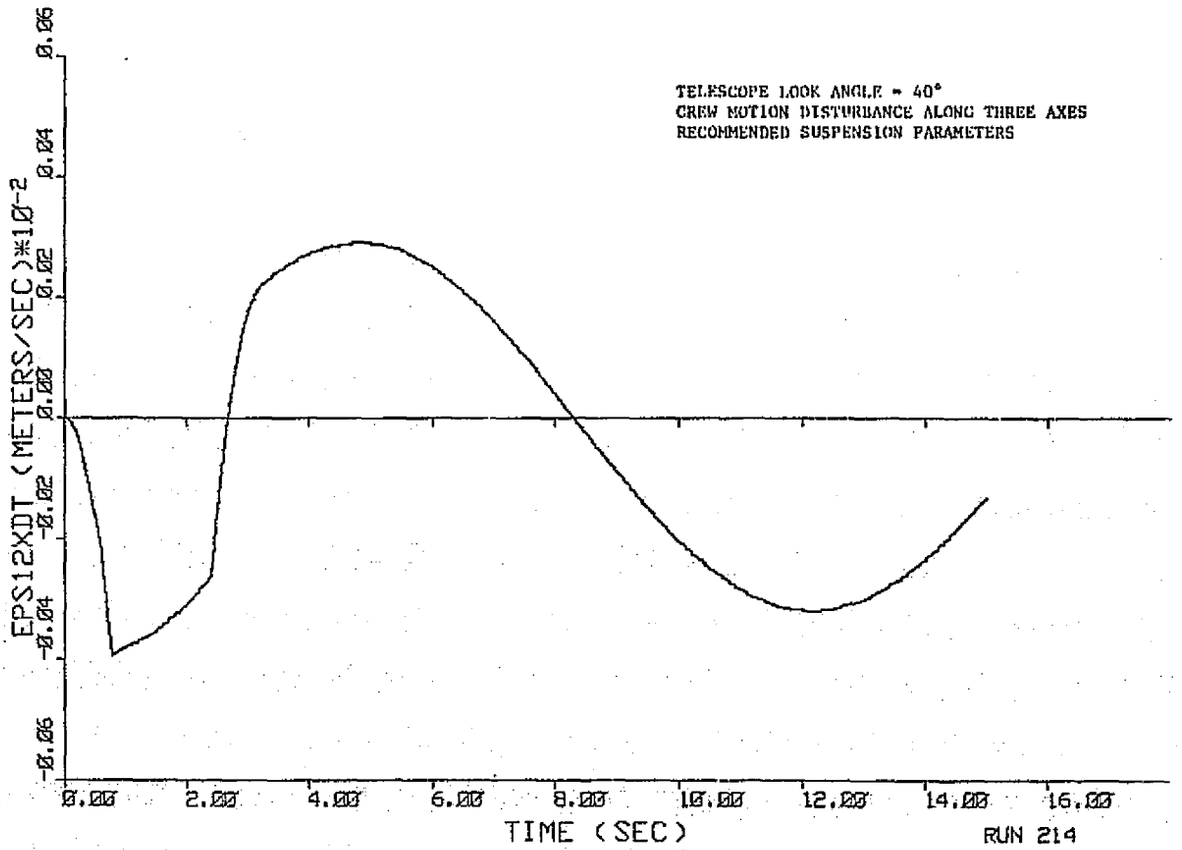

Figure 7-125. Pedestal x-Axis CM Velocity

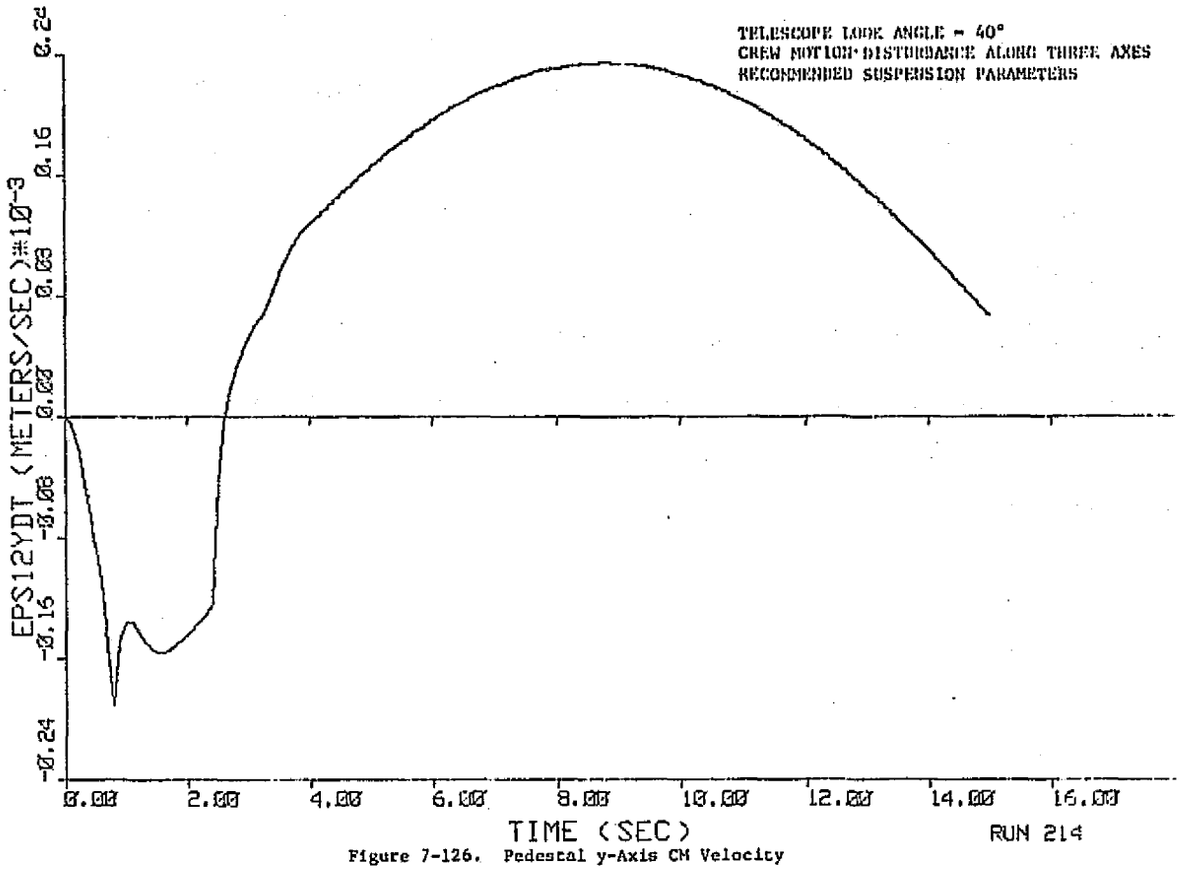

Figure 7-126. Pedestal y-Axis CM Velocity

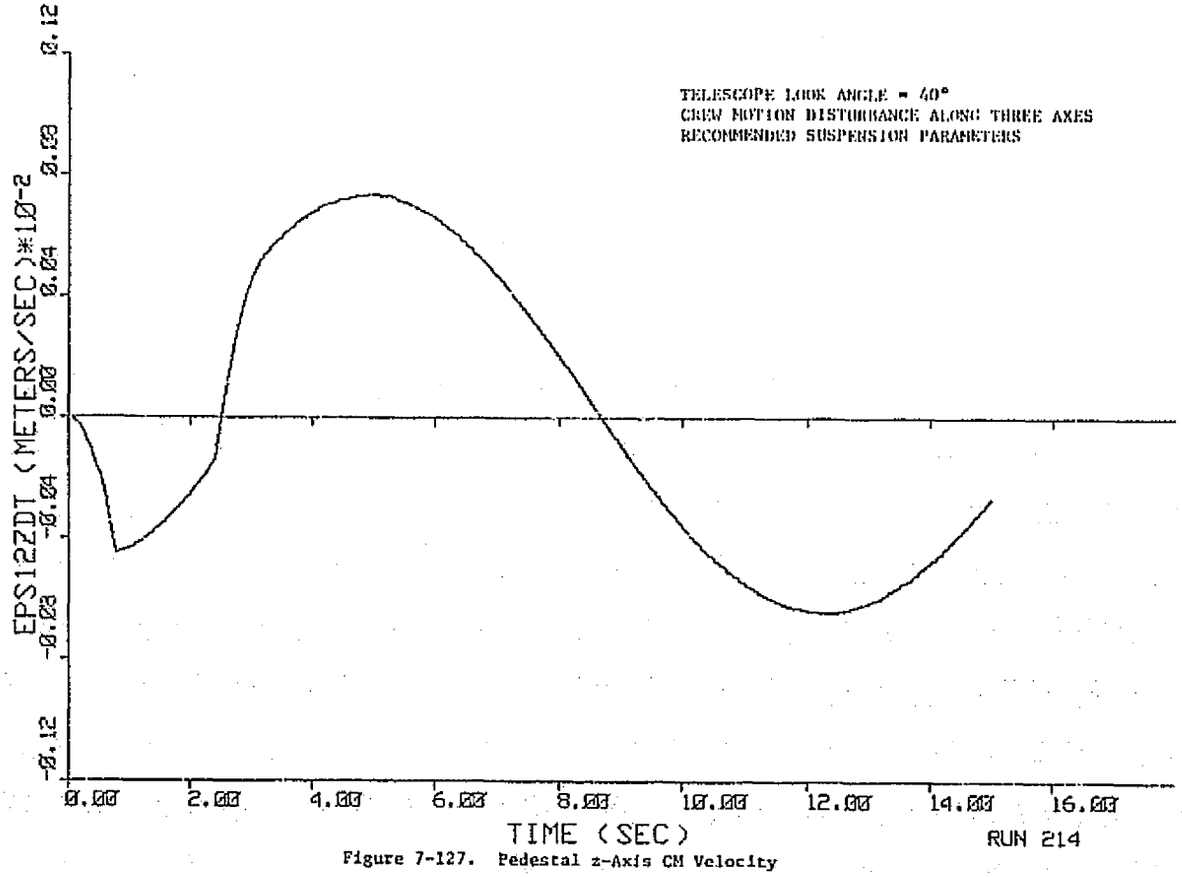

Figure 7-127. Pedestal z-Axis CM Velocity

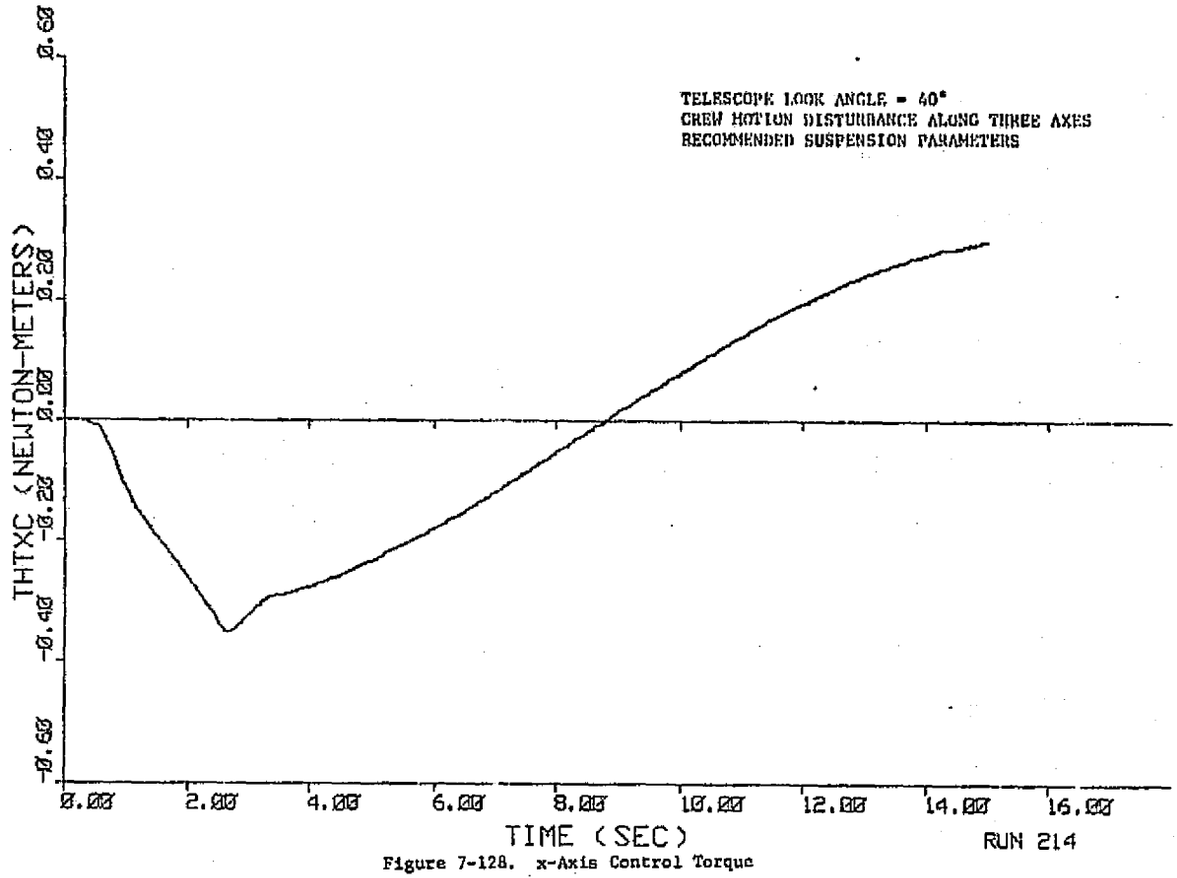

Figure 7-128. x-Axis Control Torque

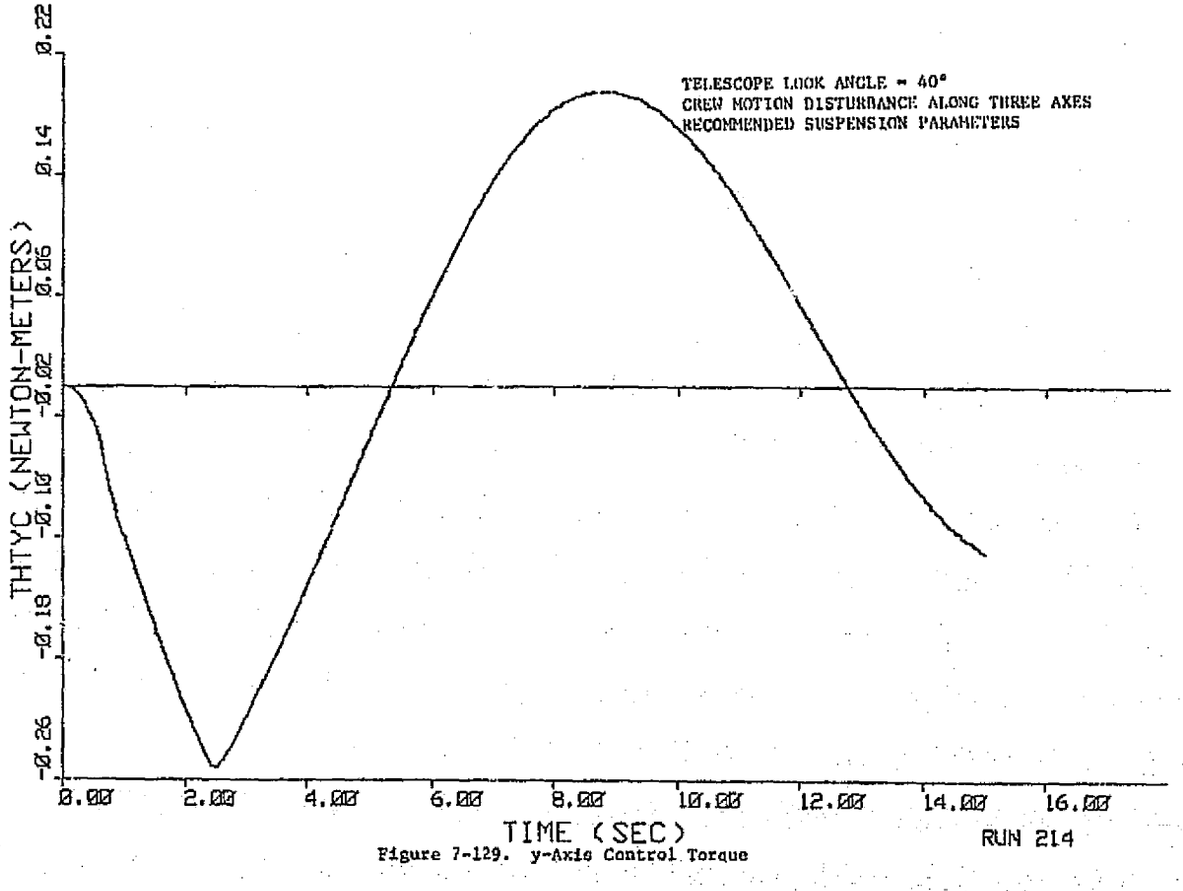

Figure 7-129. y-Axis Control Torque

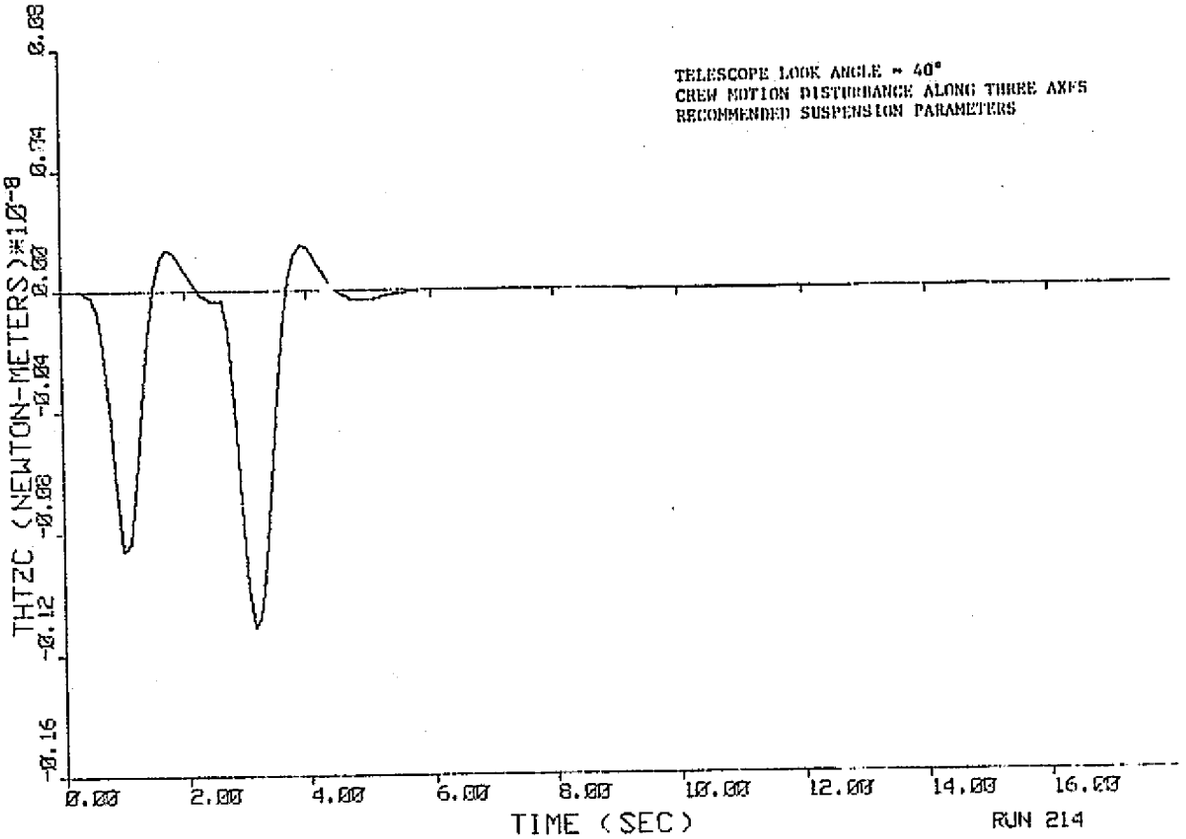

Figure 7-130. z-Axis Control Torque

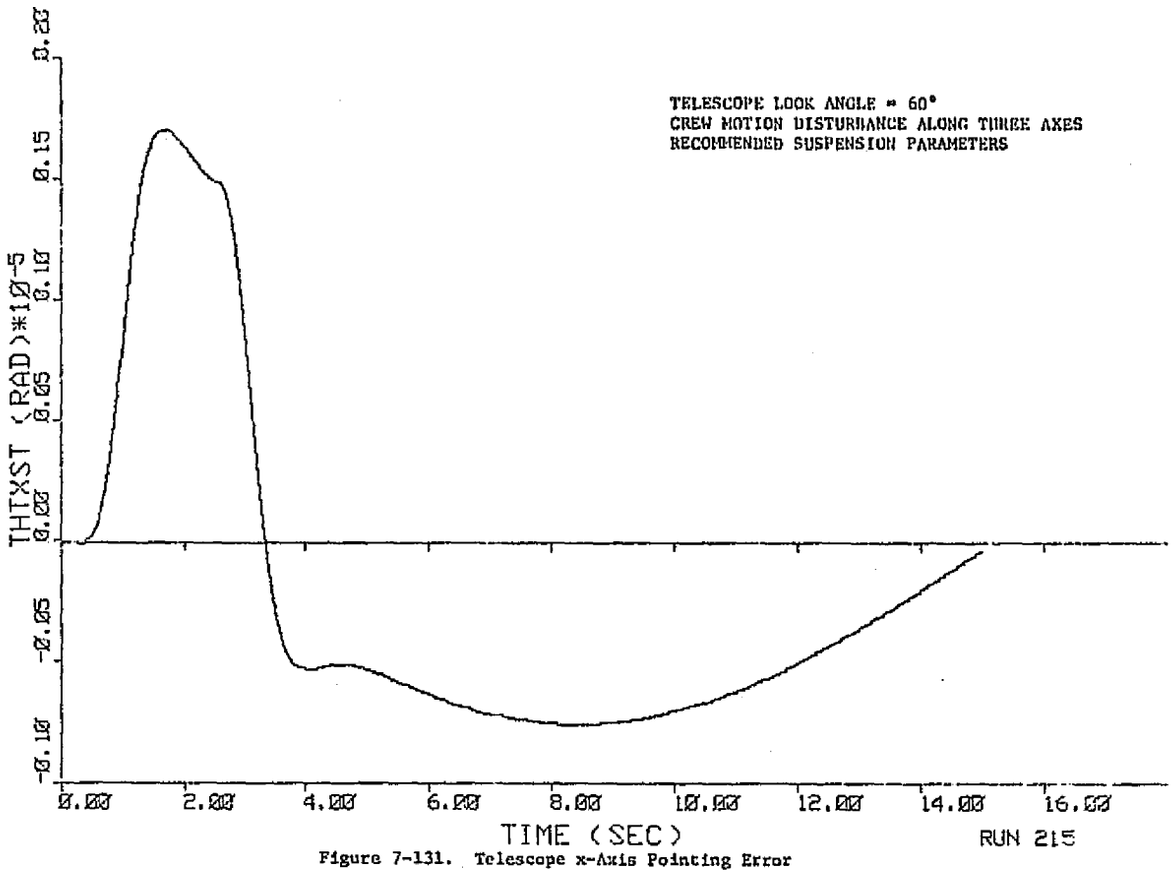

Figure 7-131. Telescope x-Axis Pointing Error

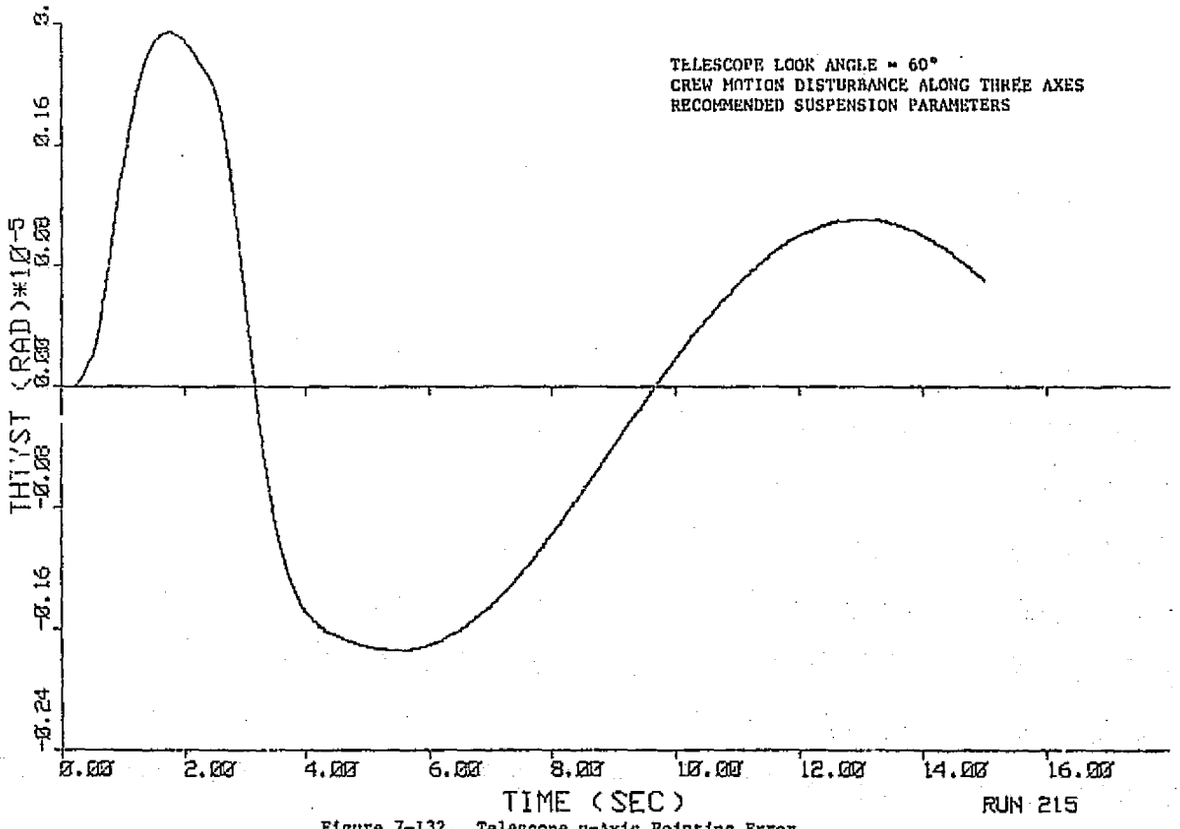

Figure 7-132. Telescope y-Axis Pointing Error

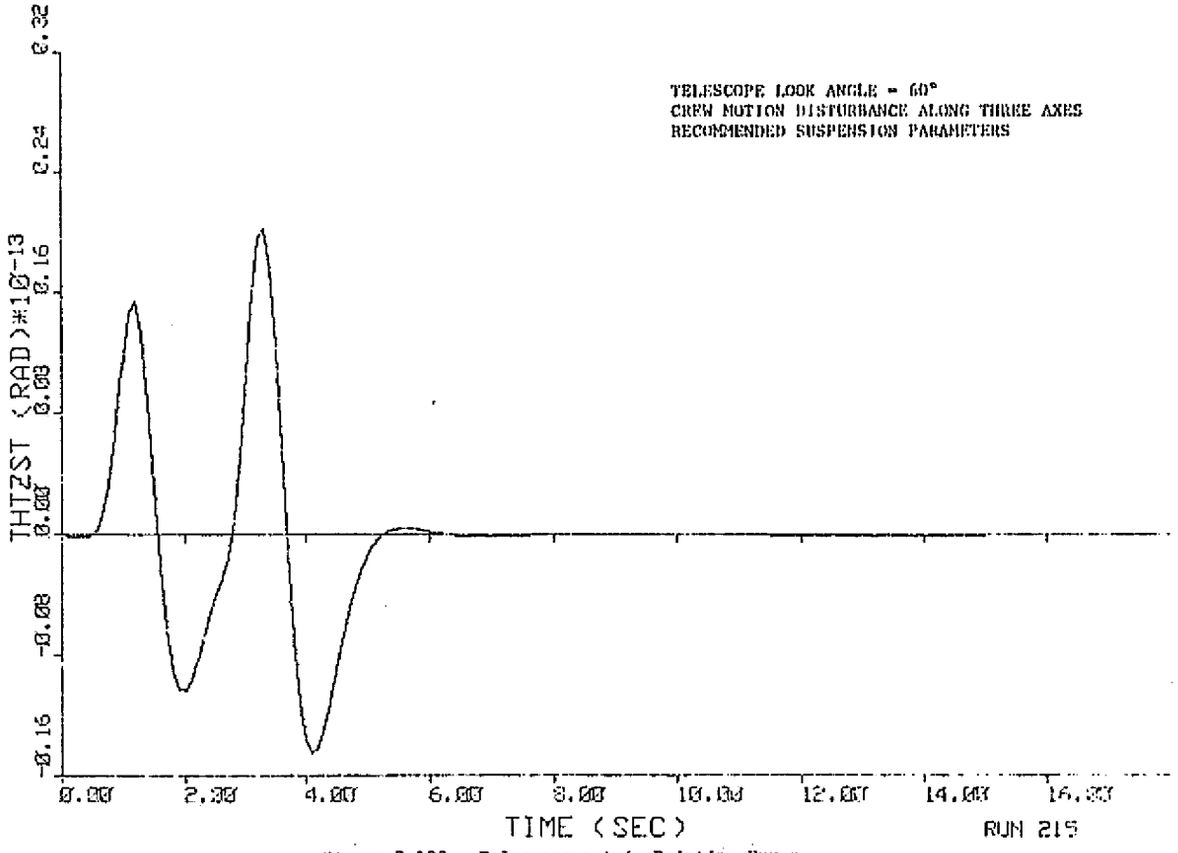

Figure 7-133. Telescope z-Axis Pointing Error

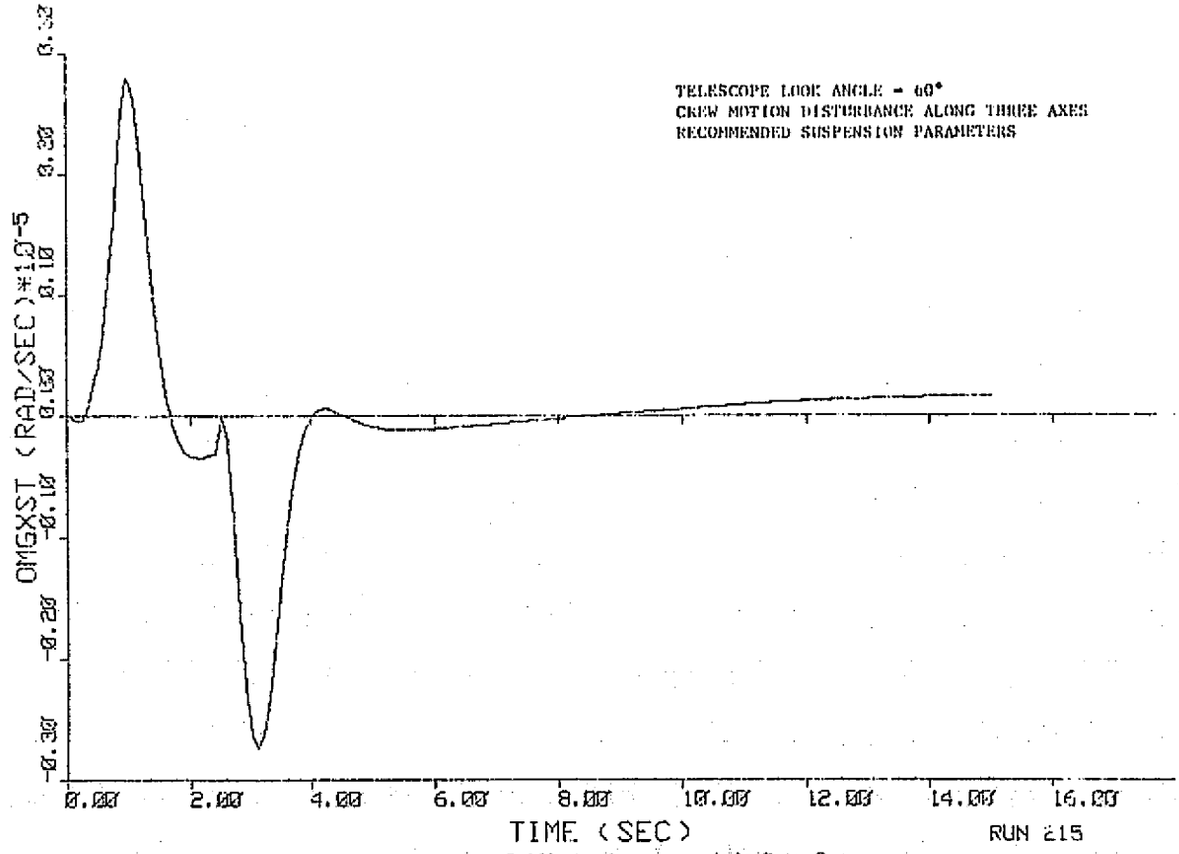

Figure 7-134. Telescope x-Axis Rate Error

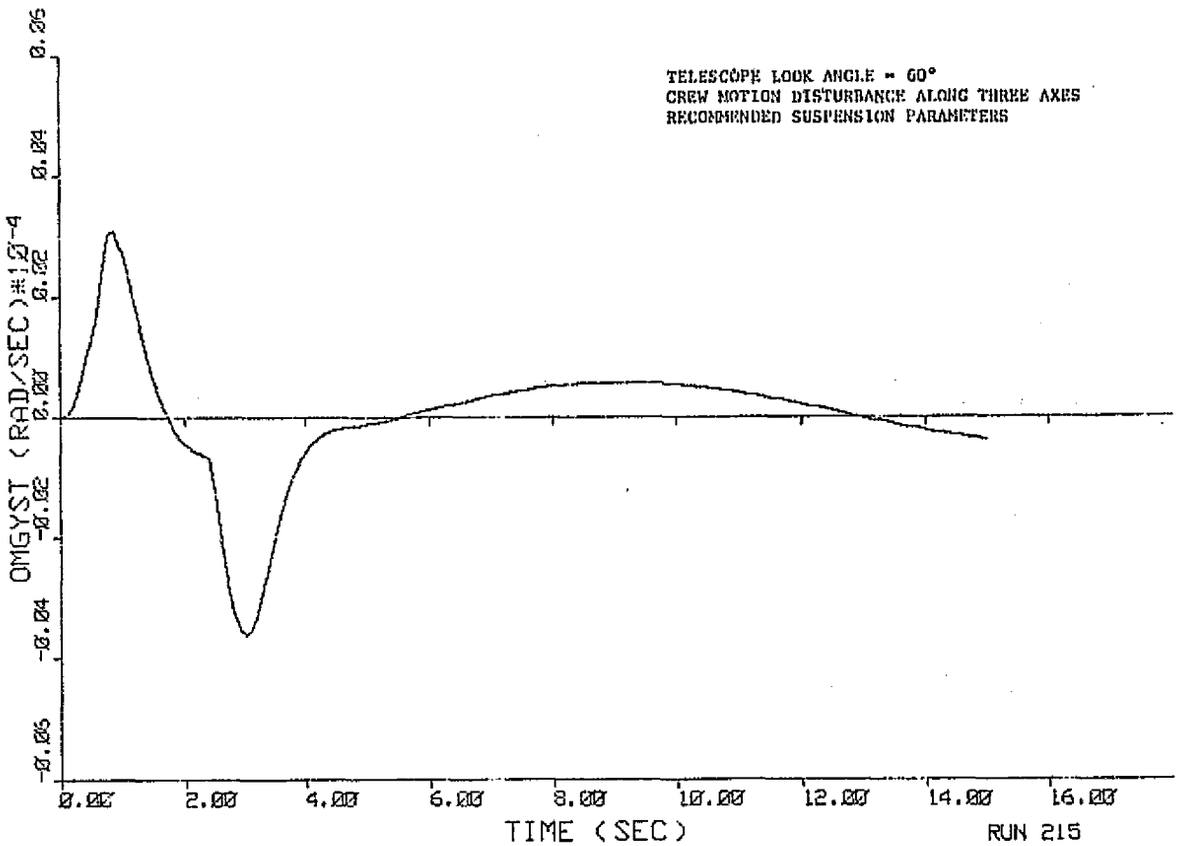

Figure 7-135. Telescope y-Axis Rate Error

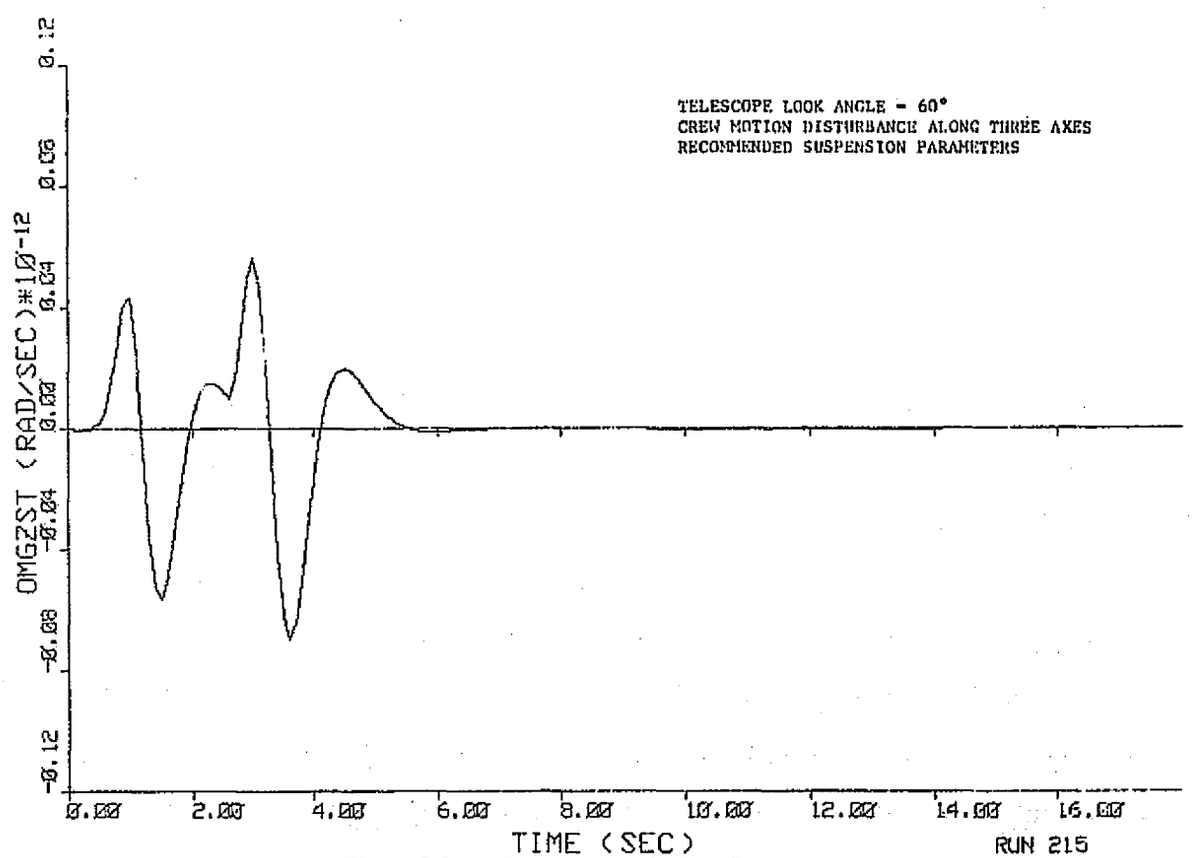

Figure 7-136. Telescope z-Axis Rate Error

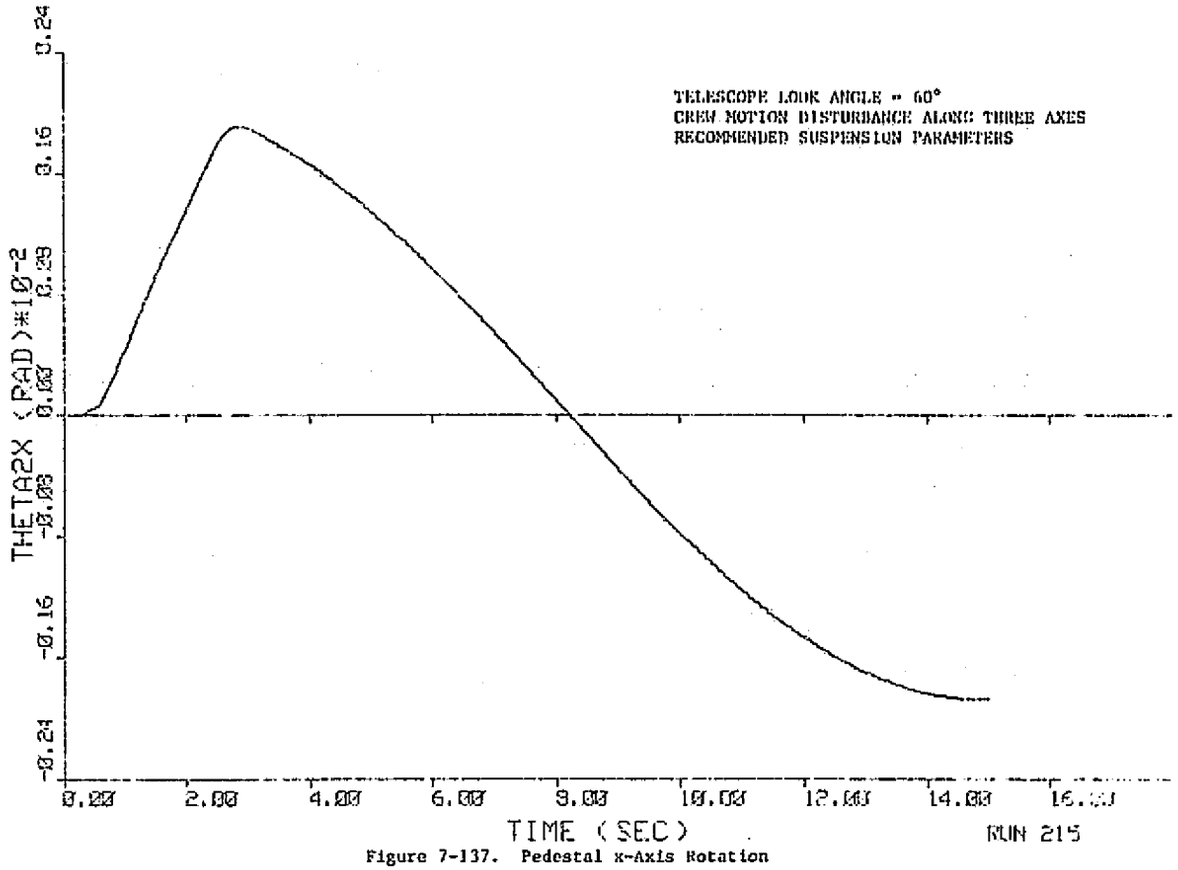

Figure 7-137. Pedestal x-Axis Rotation

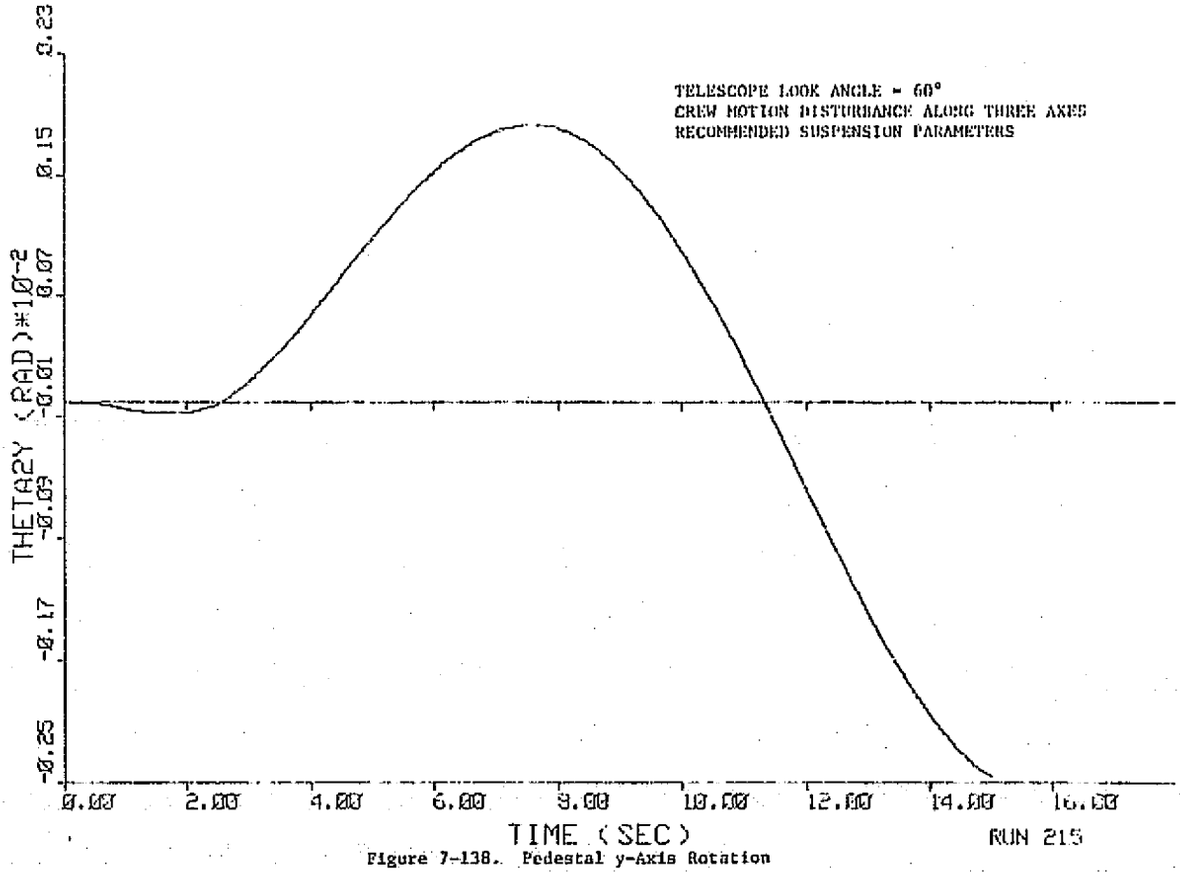

Figure 7-138. Pedestal y-Axis Rotation

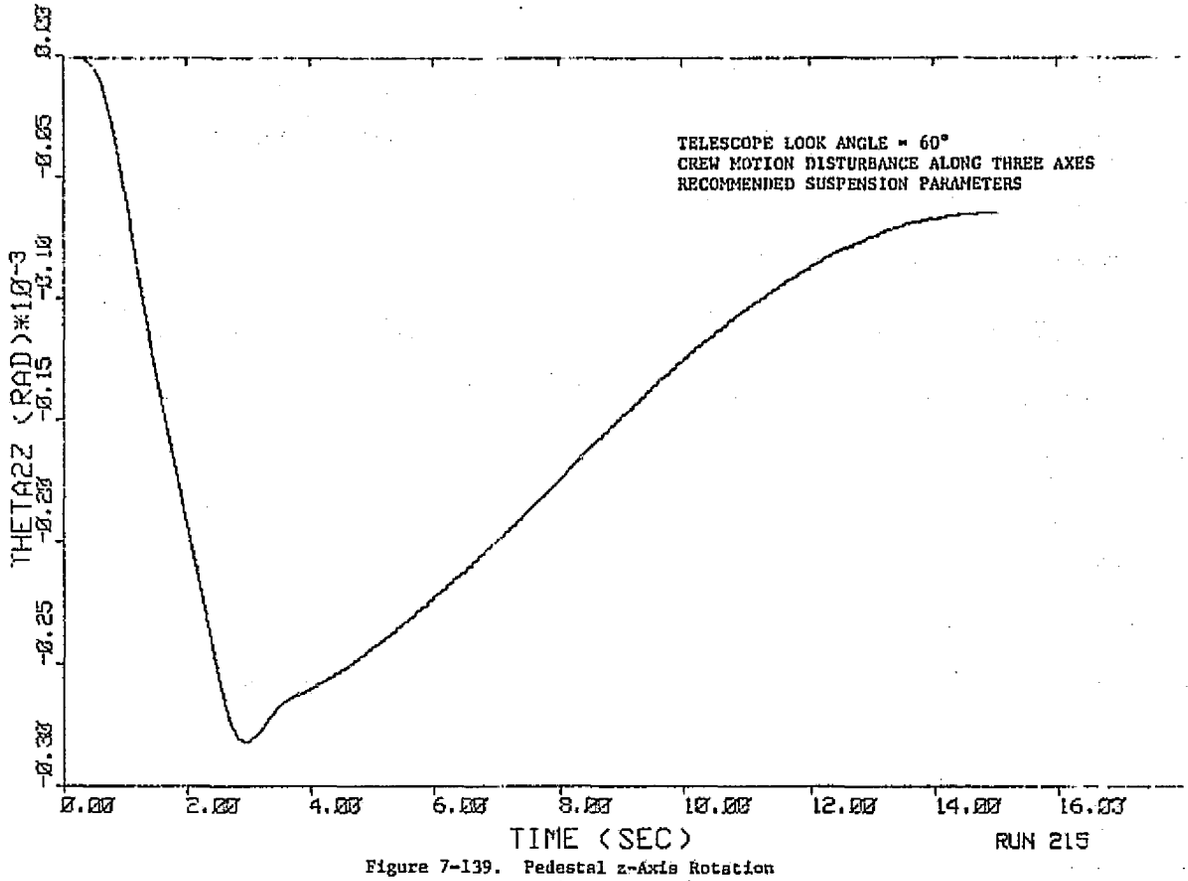

Figure 7-139. Pedestal z-Axis Rotation

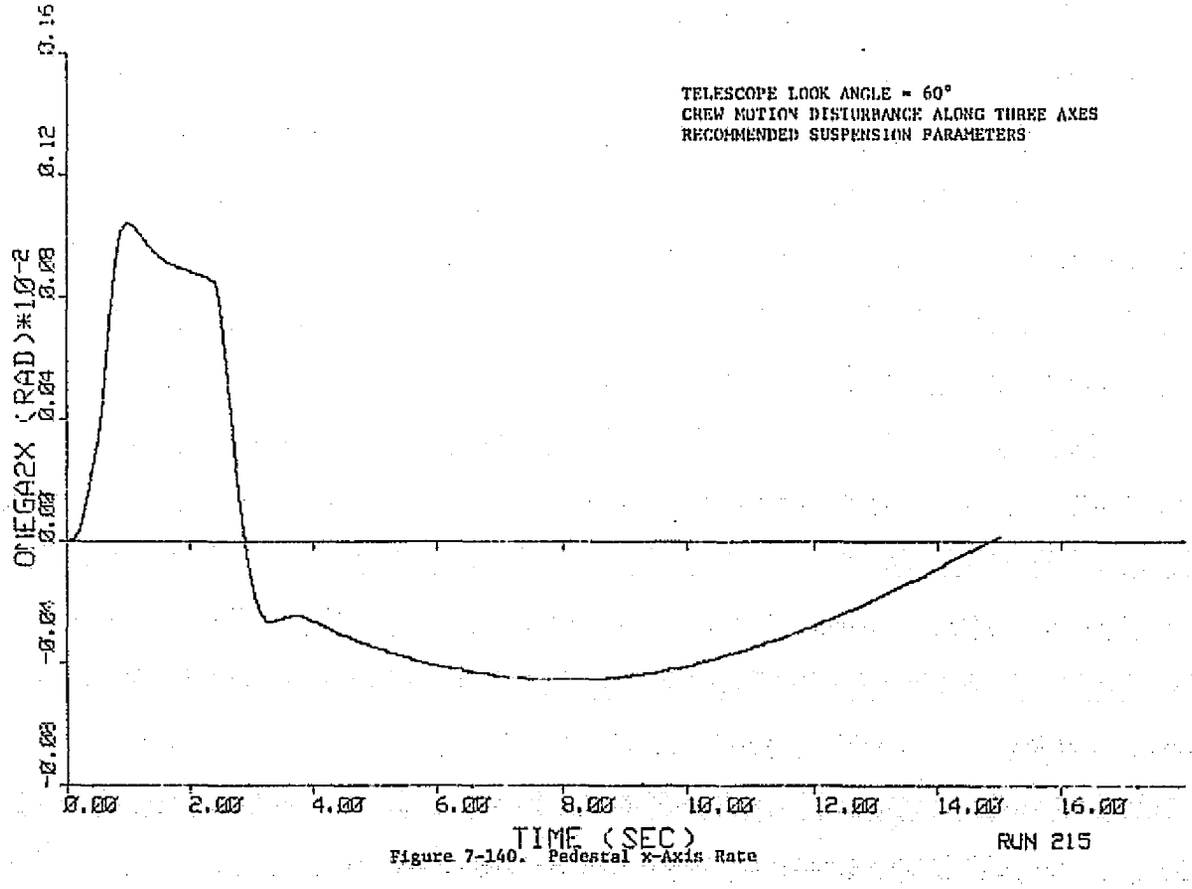

Figure 7-140. Pedestal x-Axis Rate

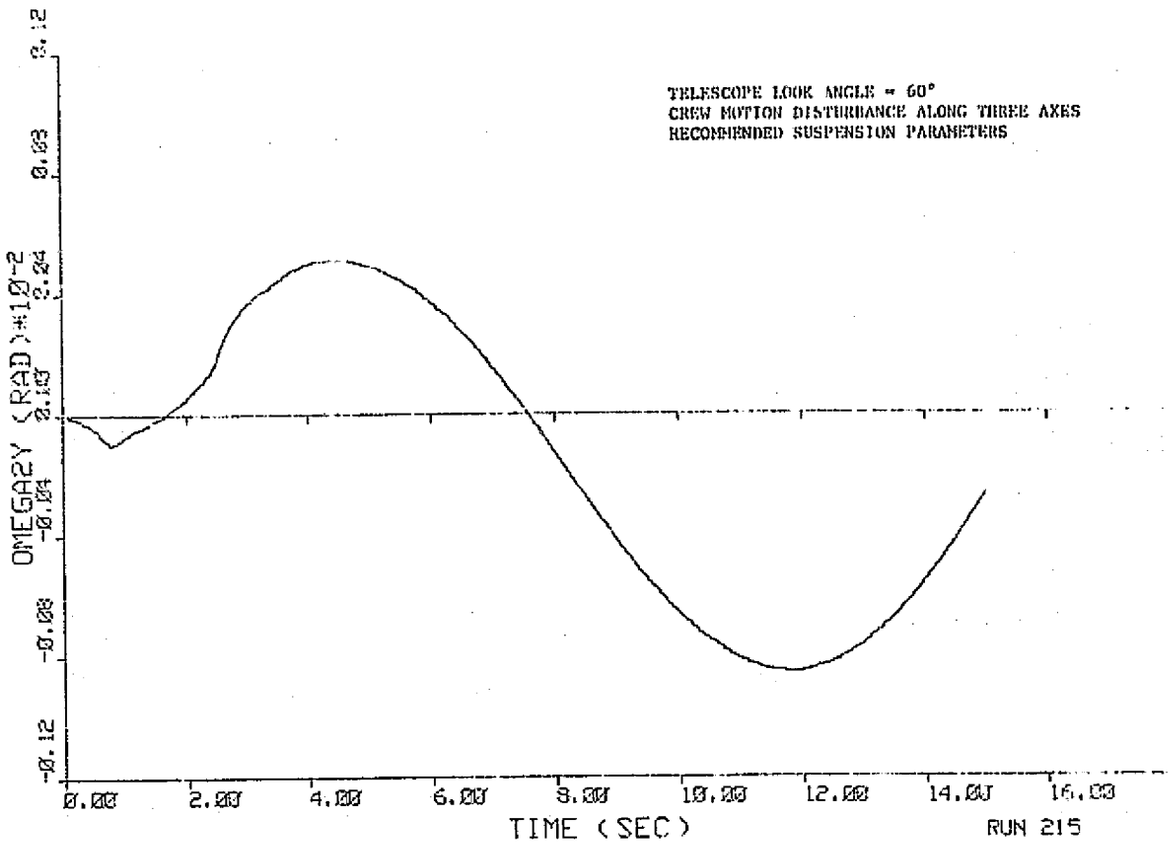

Figure 7-141. Pedestal y-Axis Rate

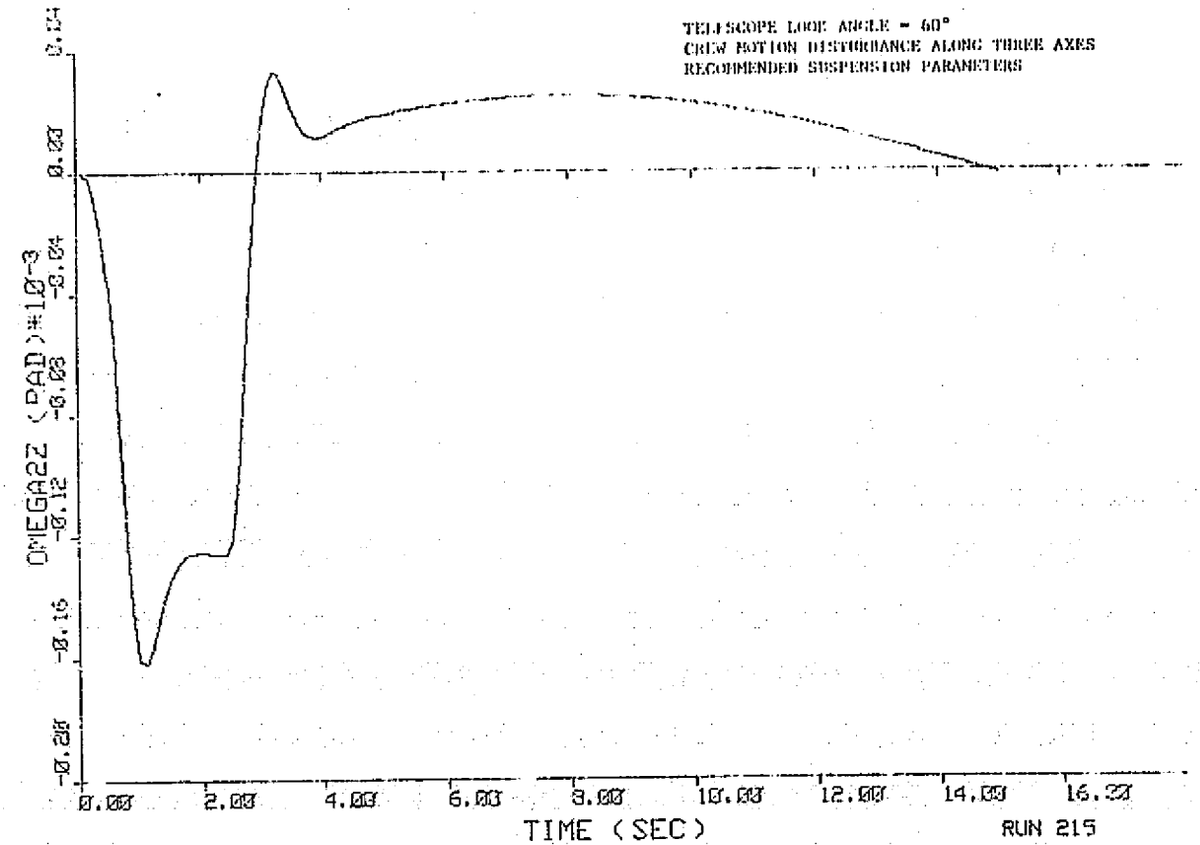

Figure 7-142. Pedestal z-Axis Rate

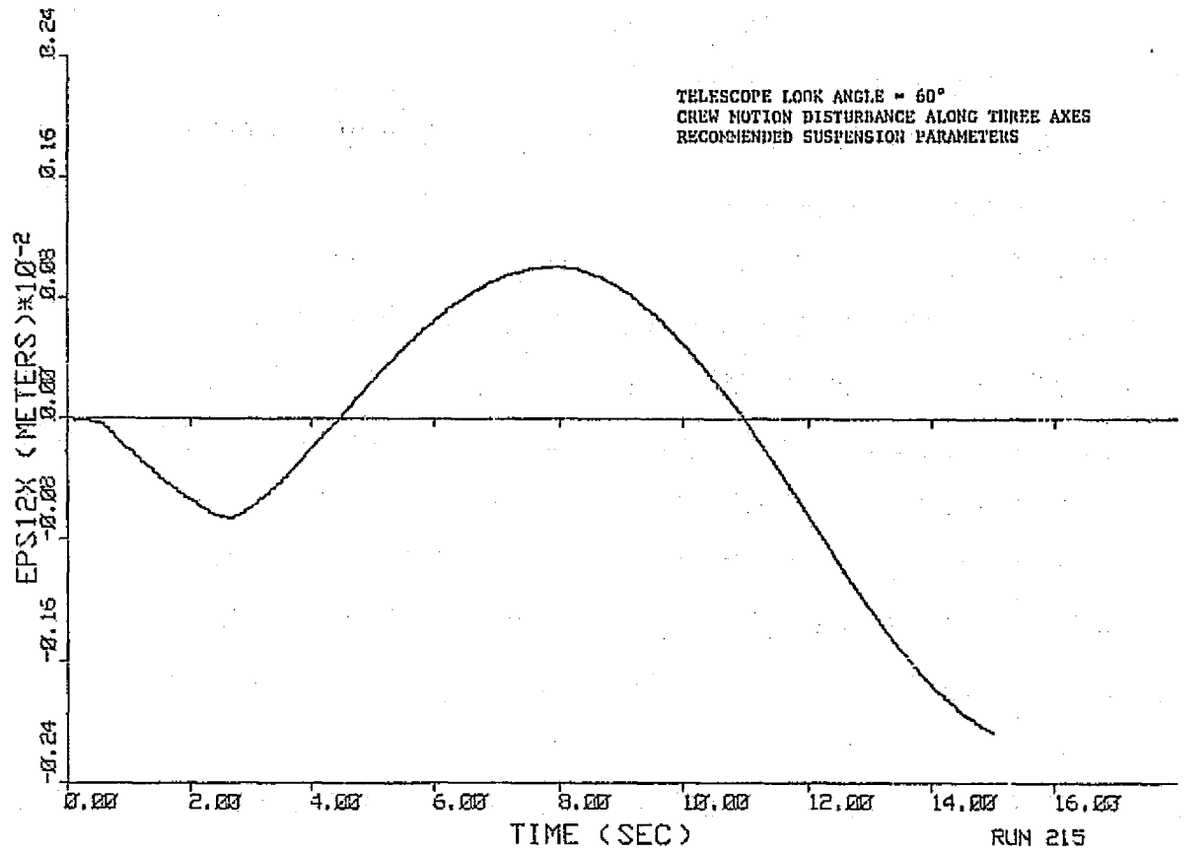

Figure 7-143. Pedestal x-Axis CM Translation

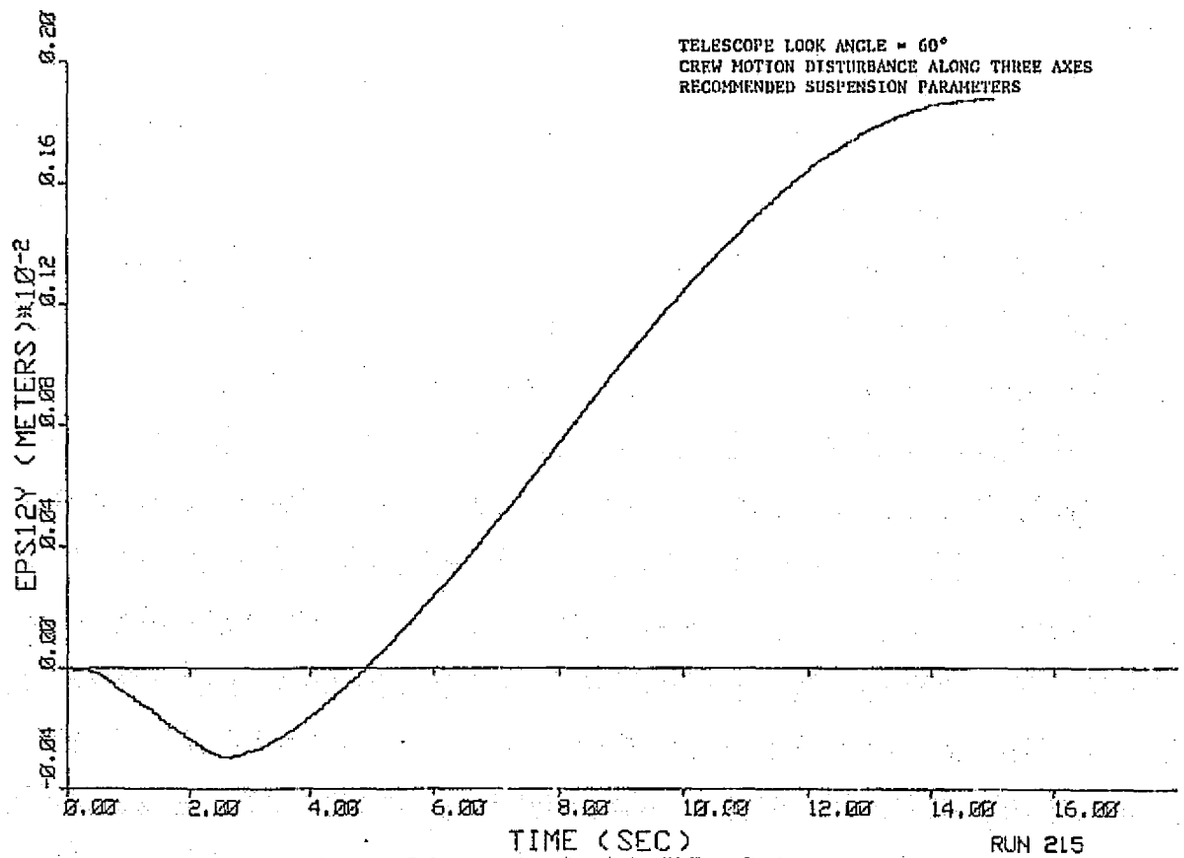

Figure 7-144. Pedestal y-Axis CM Translation

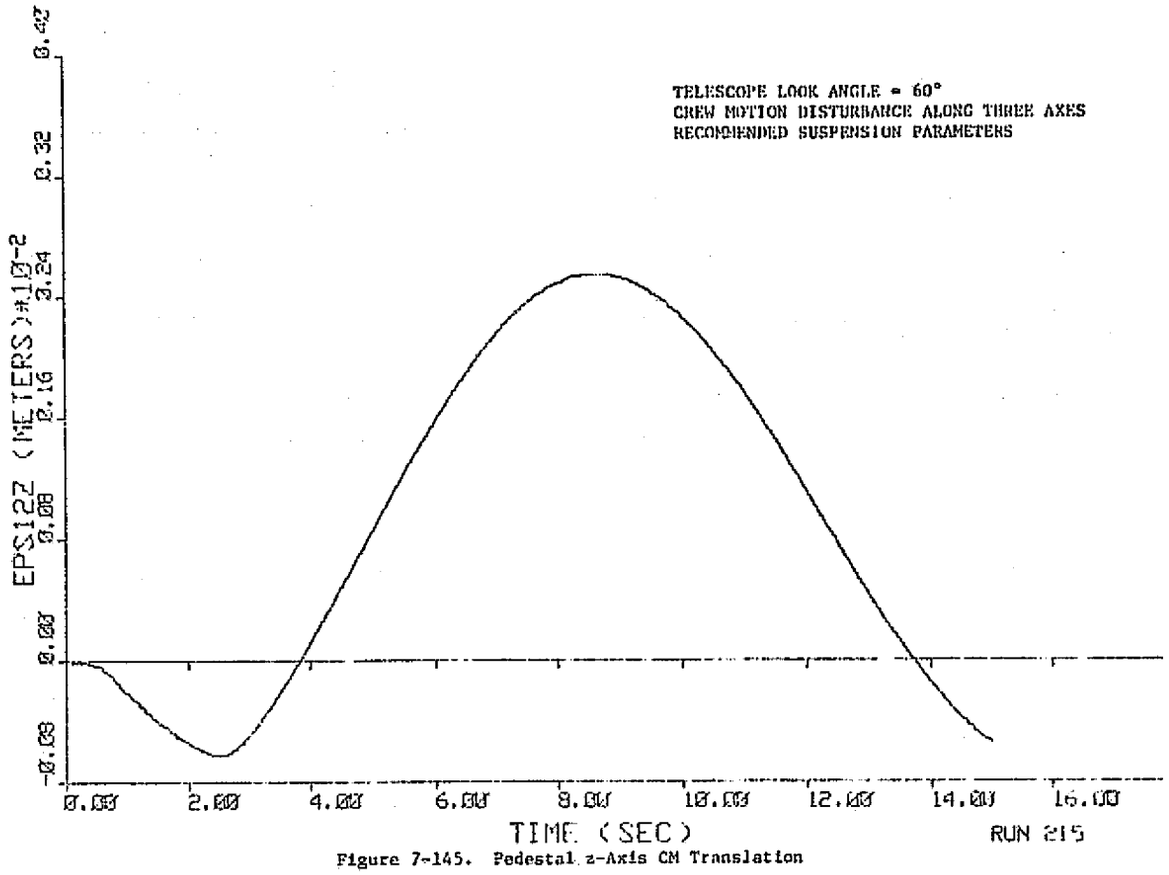

Figure 7-145. Pedestal z-Axis CM Translation

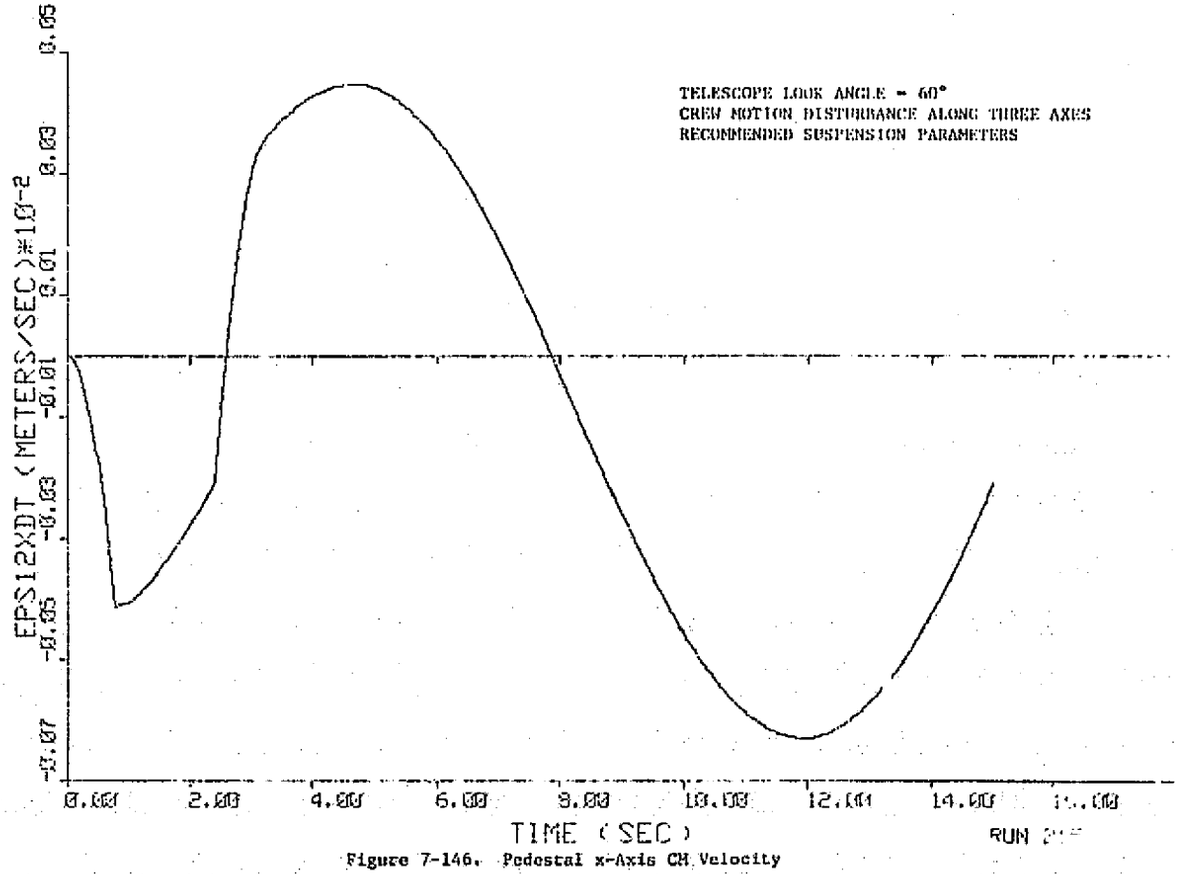

Figure 7-146. Pedestal x-Axis CM Velocity

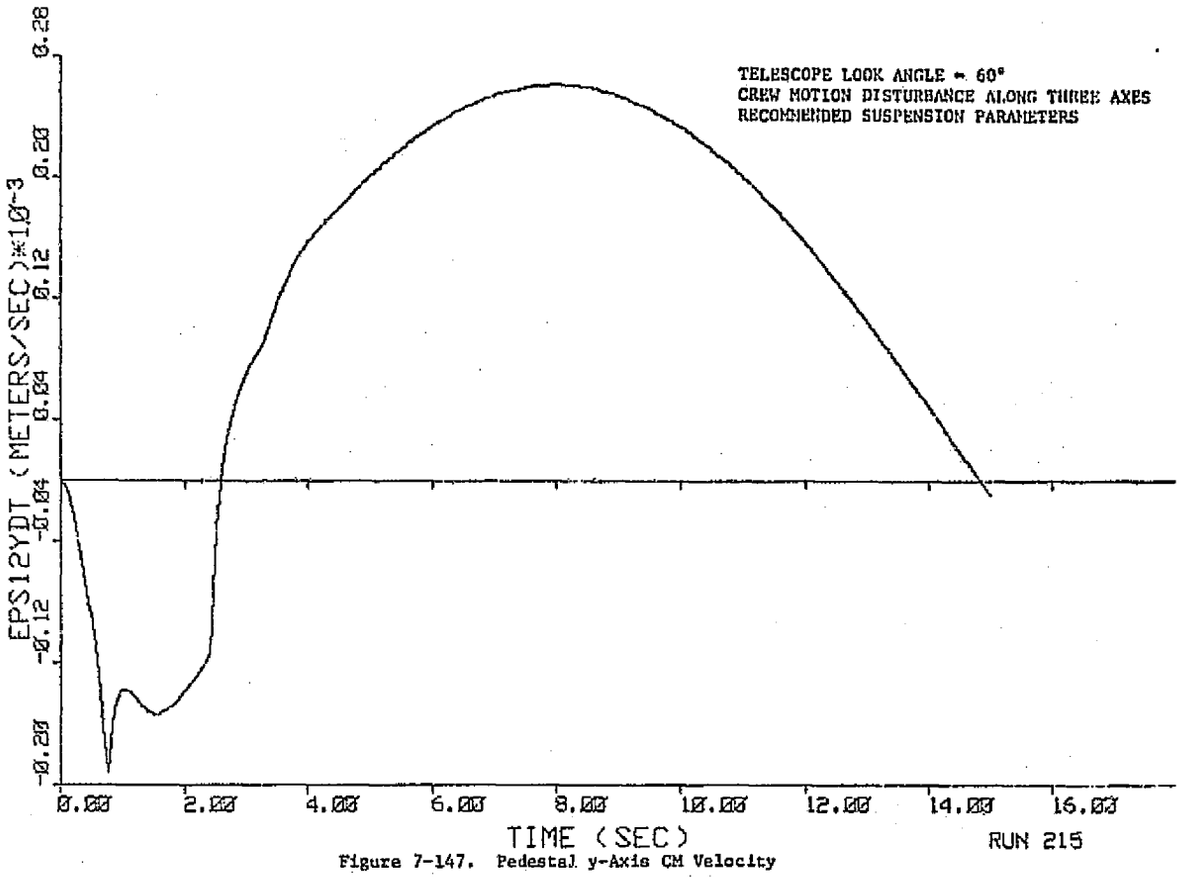

Figure 7-147. Pedestal y-Axis CM Velocity

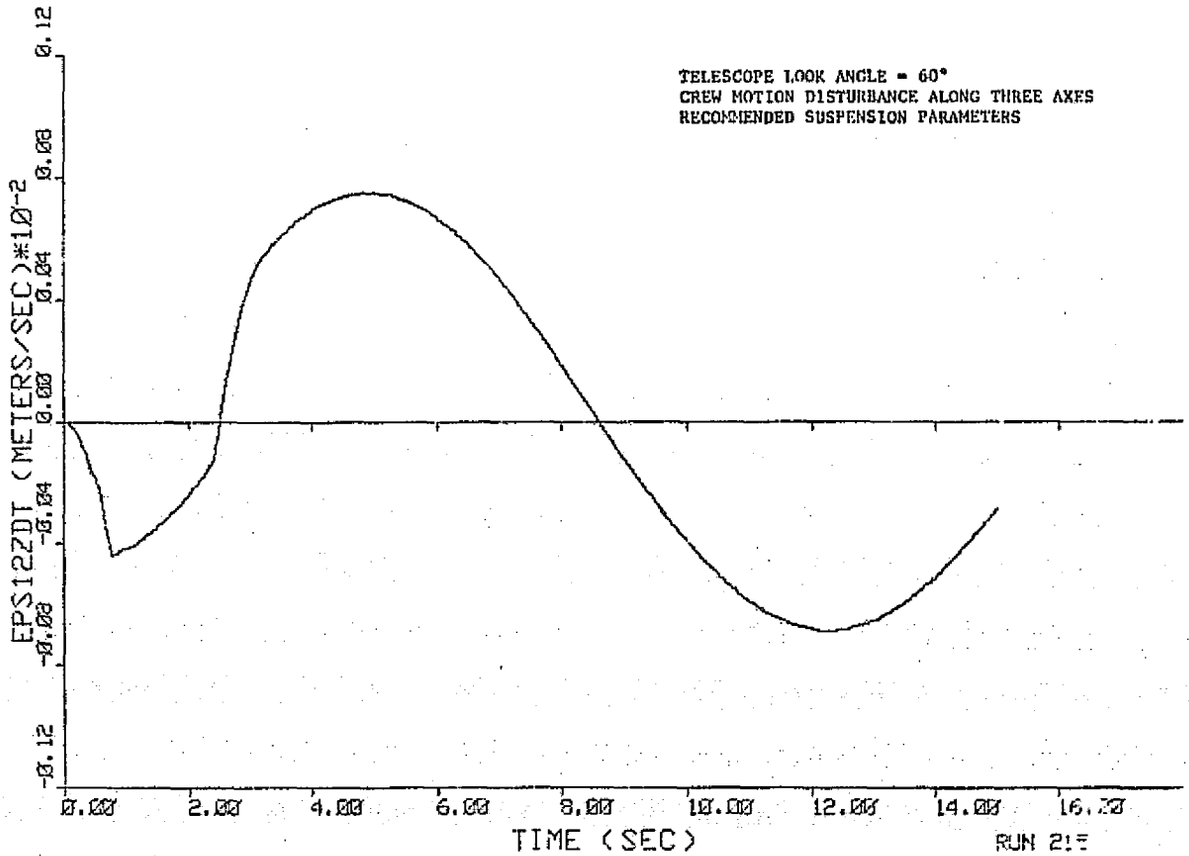

Figure 7-148. Pedestal z-Axis CM Velocity

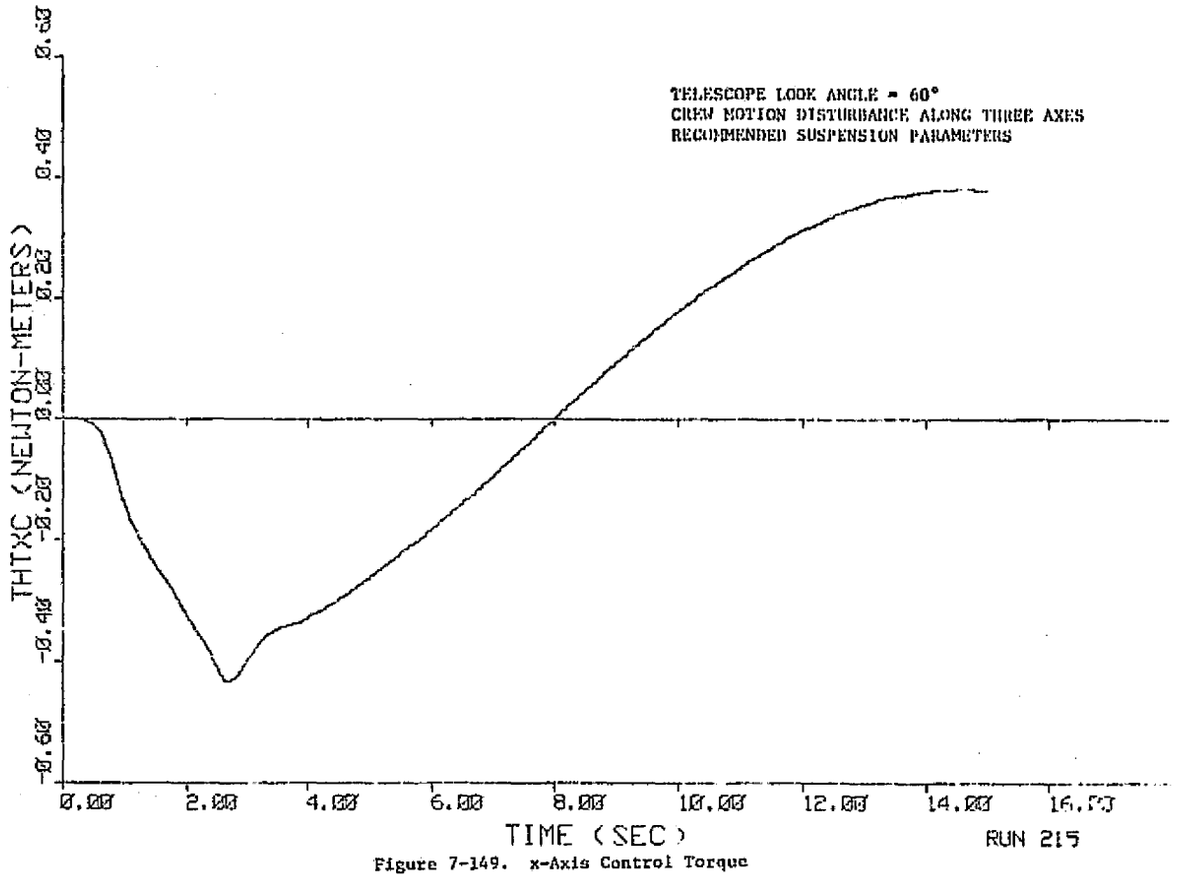

Figure 7-149. x-Axis Control Torque

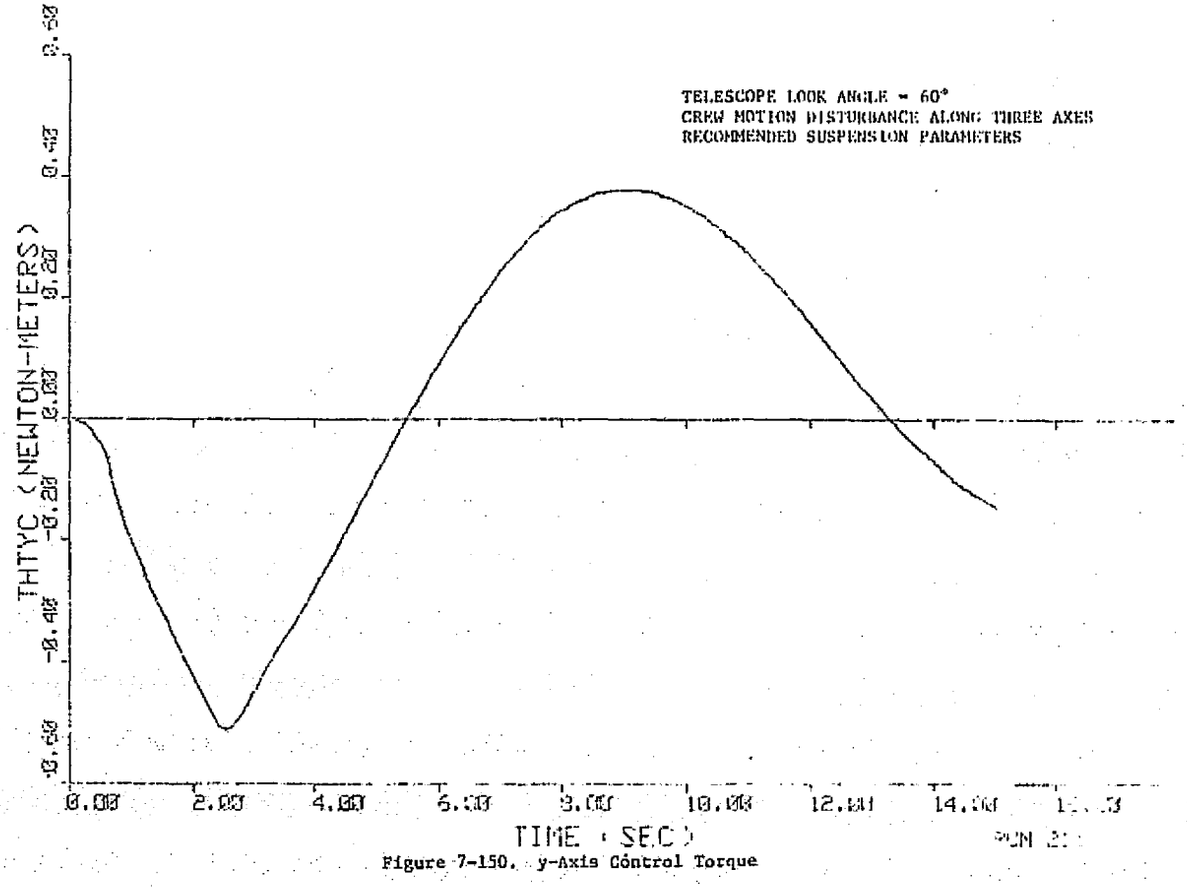

Figure 7-150. y-Axis Control Torque

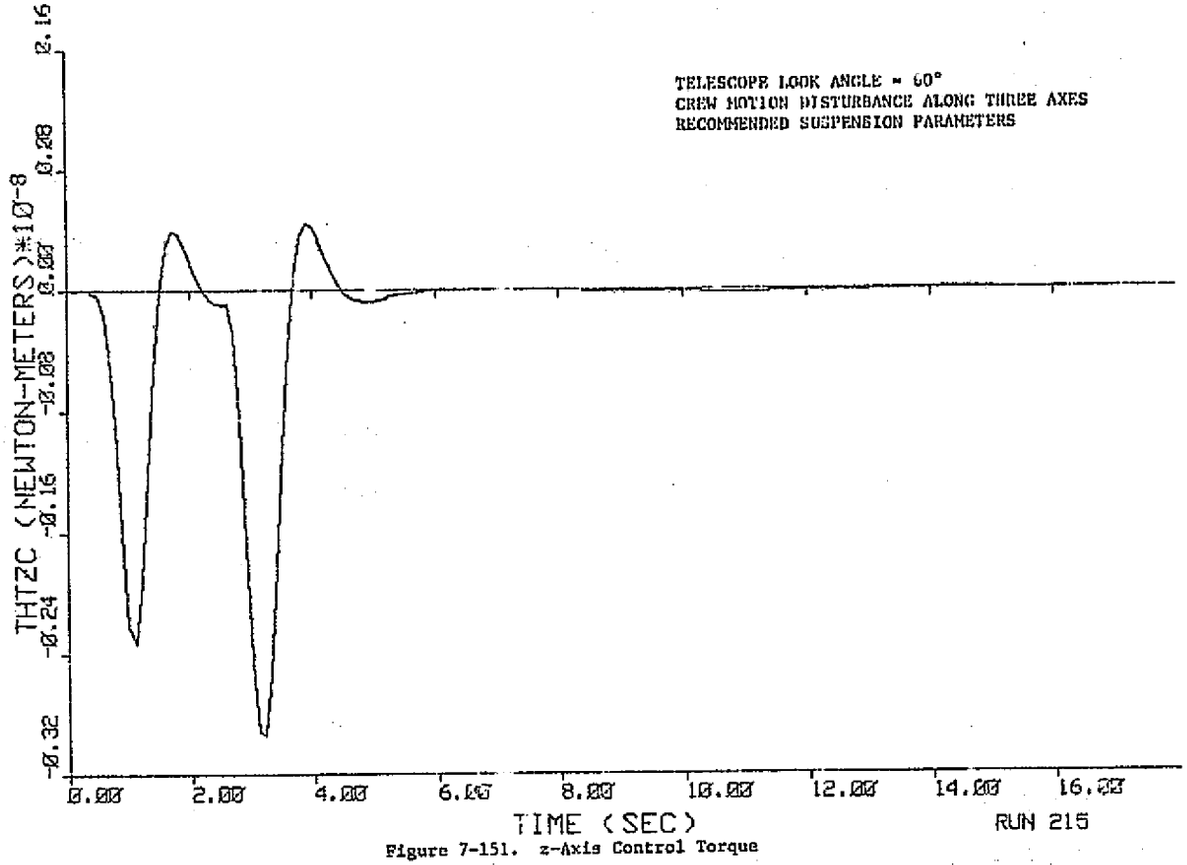

Figure 7-151. z-Axis Control Torque

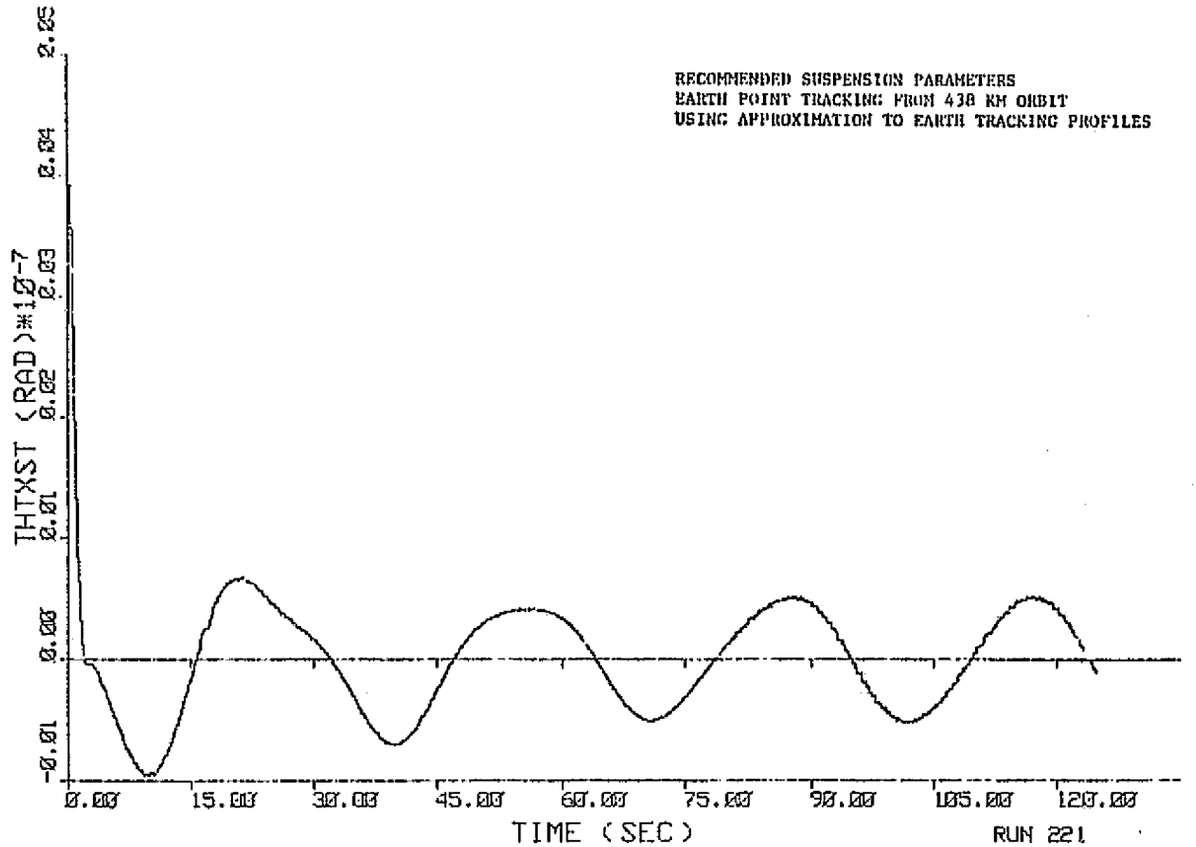

Figure 7-152. Telescope x-Axis Tracking Error

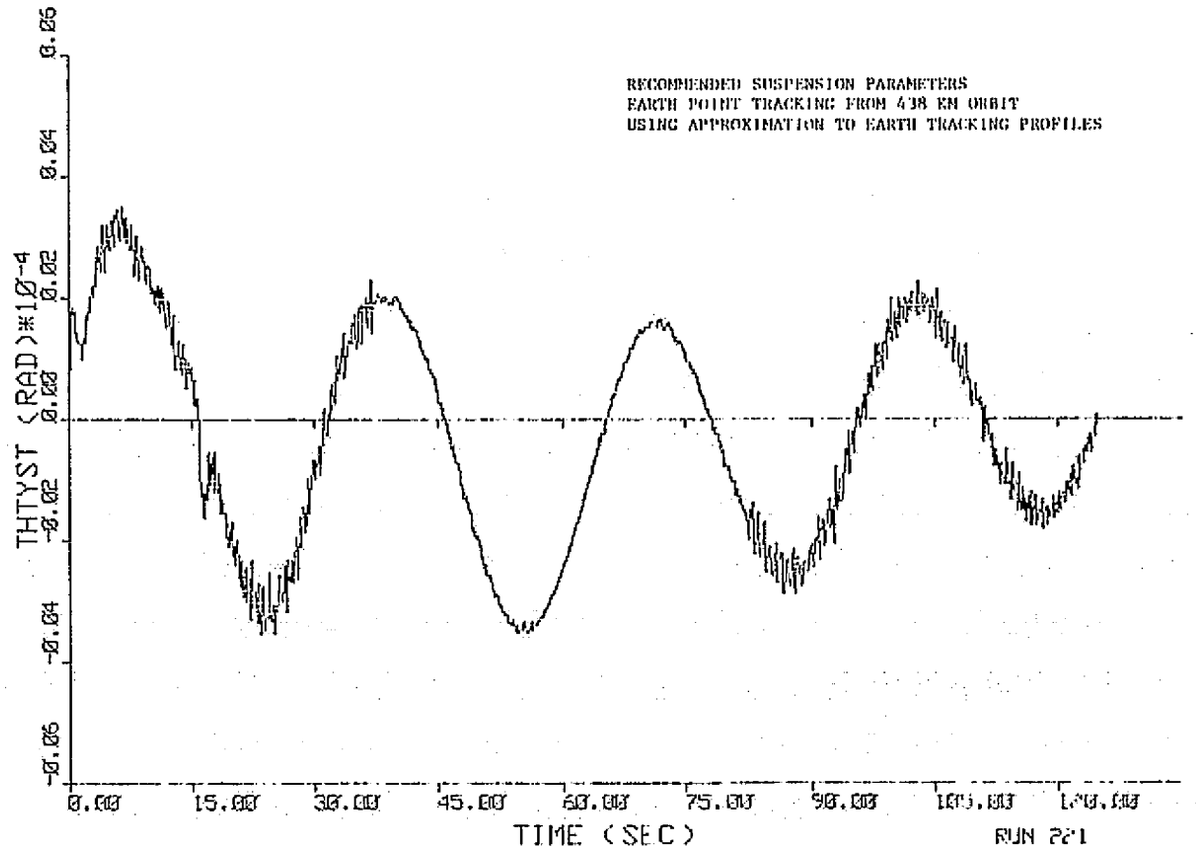

Figure 7-153. Telescope y-Axis Tracking Error

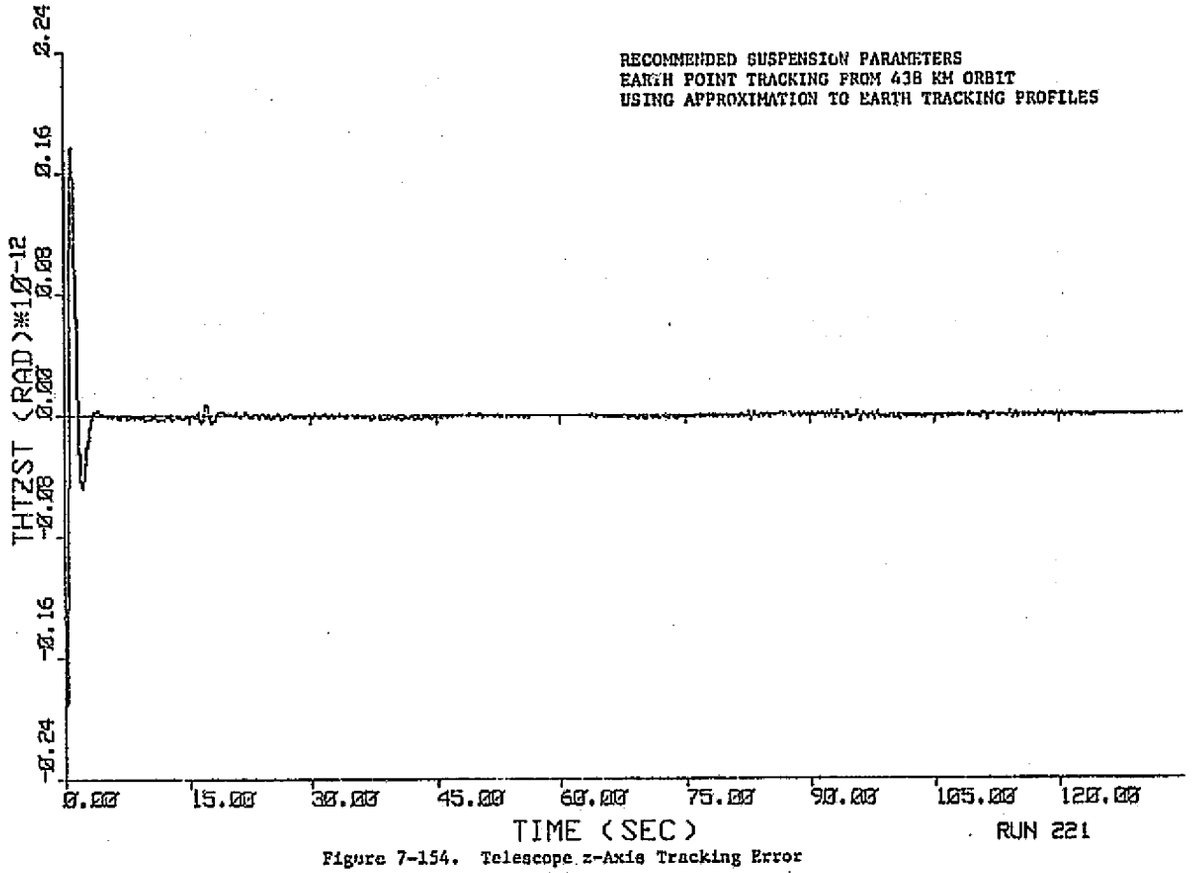

Figure 7-154. Telescope z-Axis Tracking Error

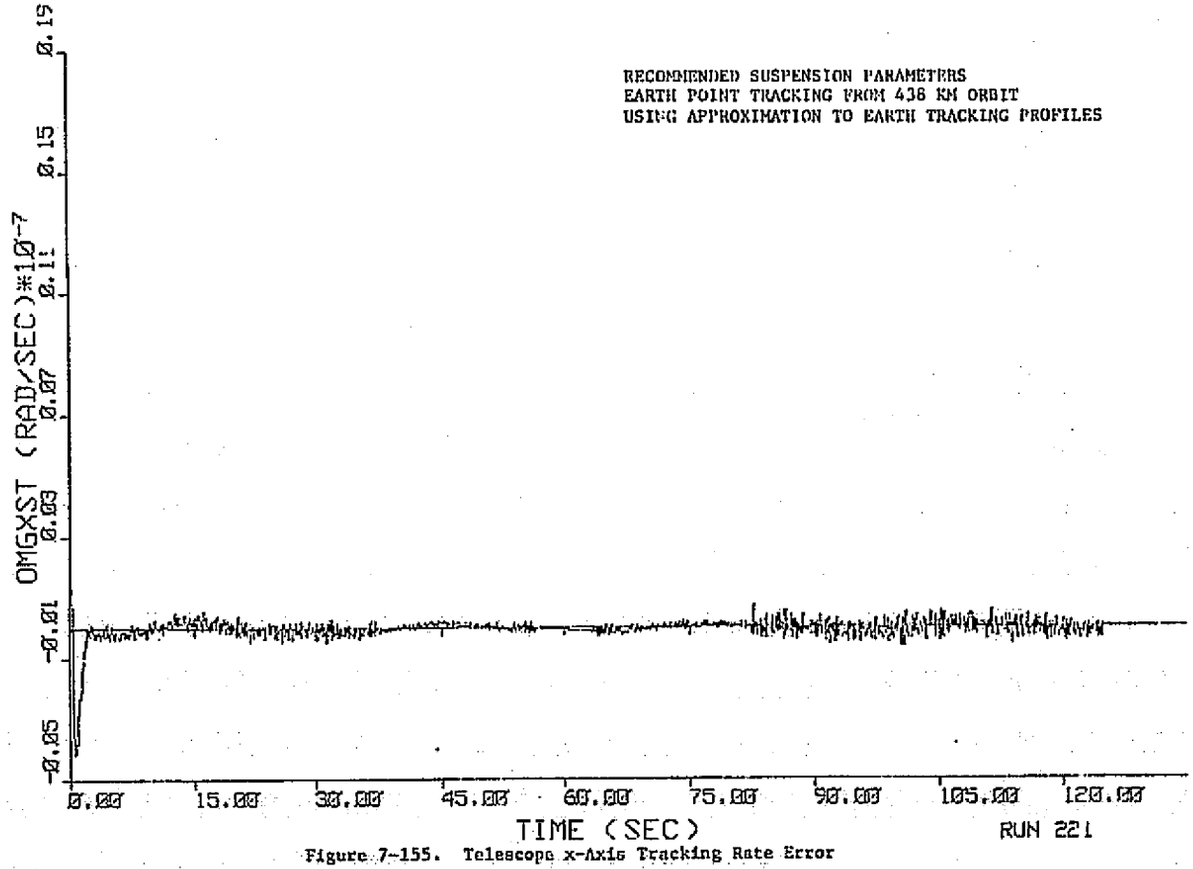

Figure 7-155. Telescope x-Axis Tracking Rate Error

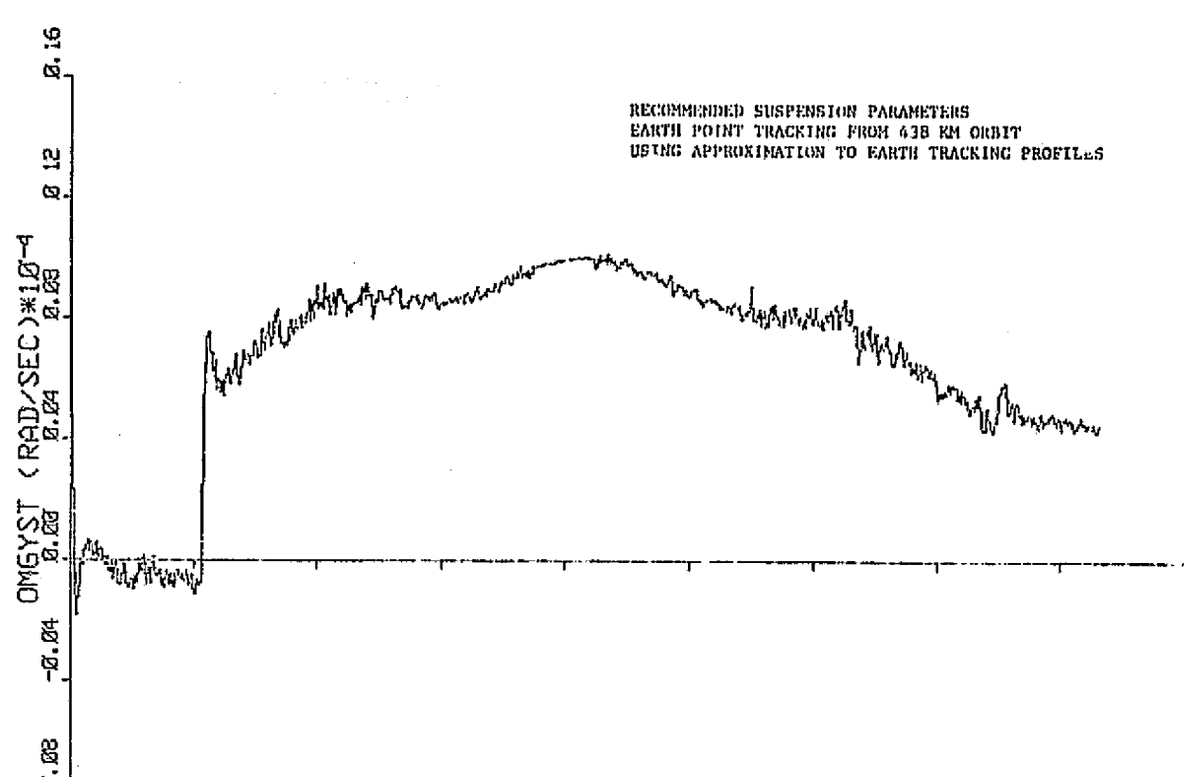

Figure 7-156. Telescope y-Axis Tracking Rate Error

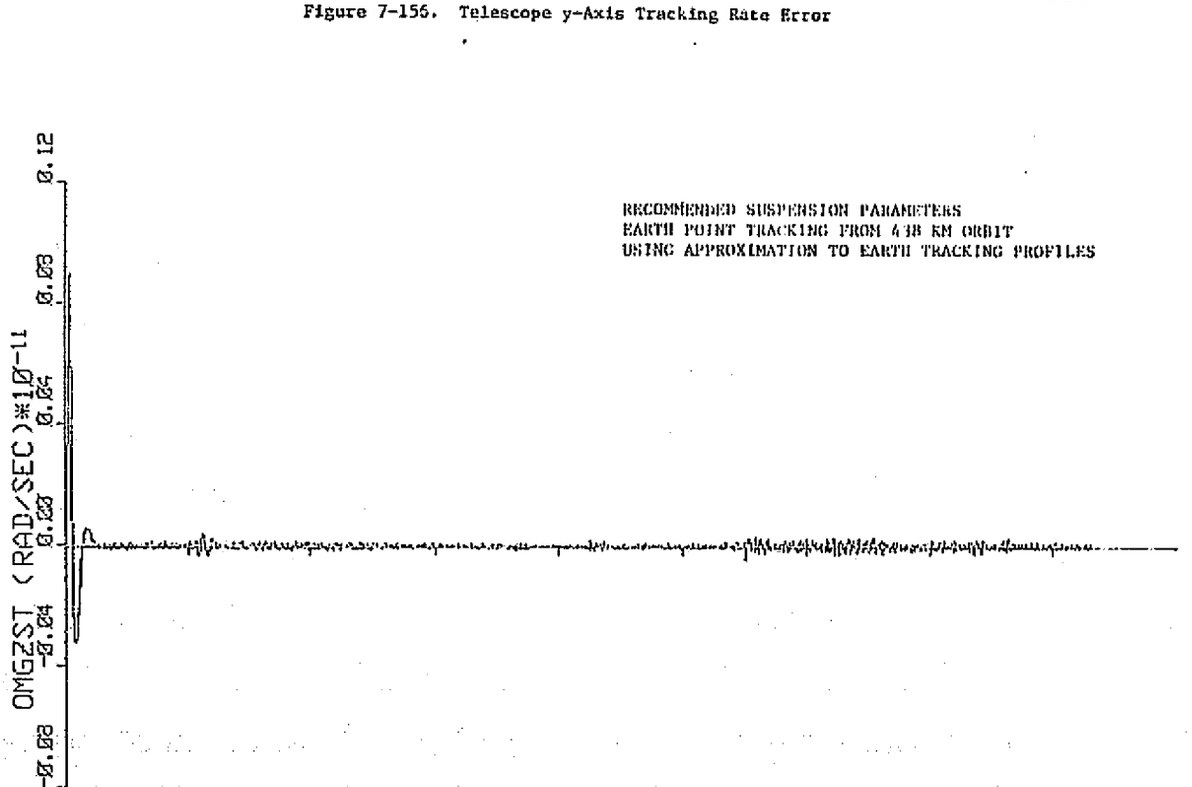

Figure 7-157. Telescope z-Axis Tracking Rate Error

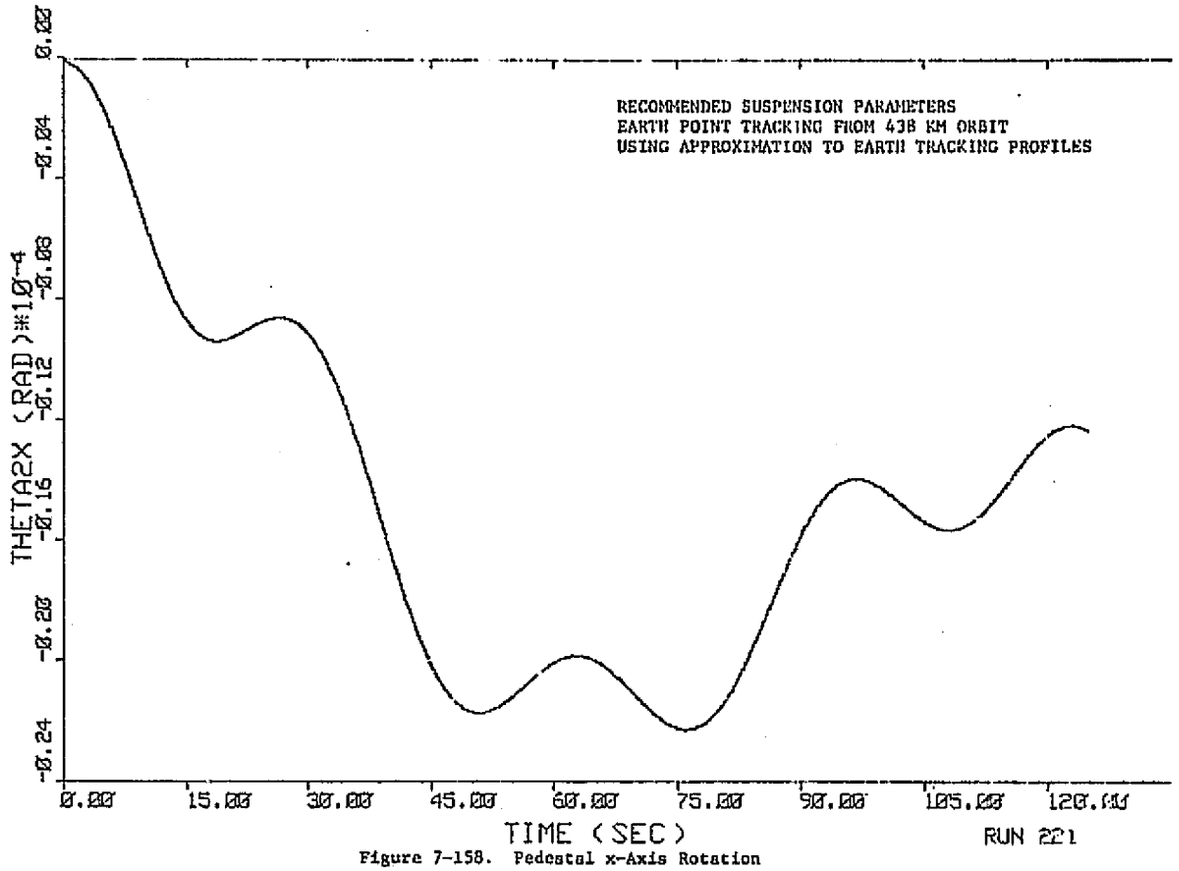

Figure 7-158. Pedestal x-Axis Rotation

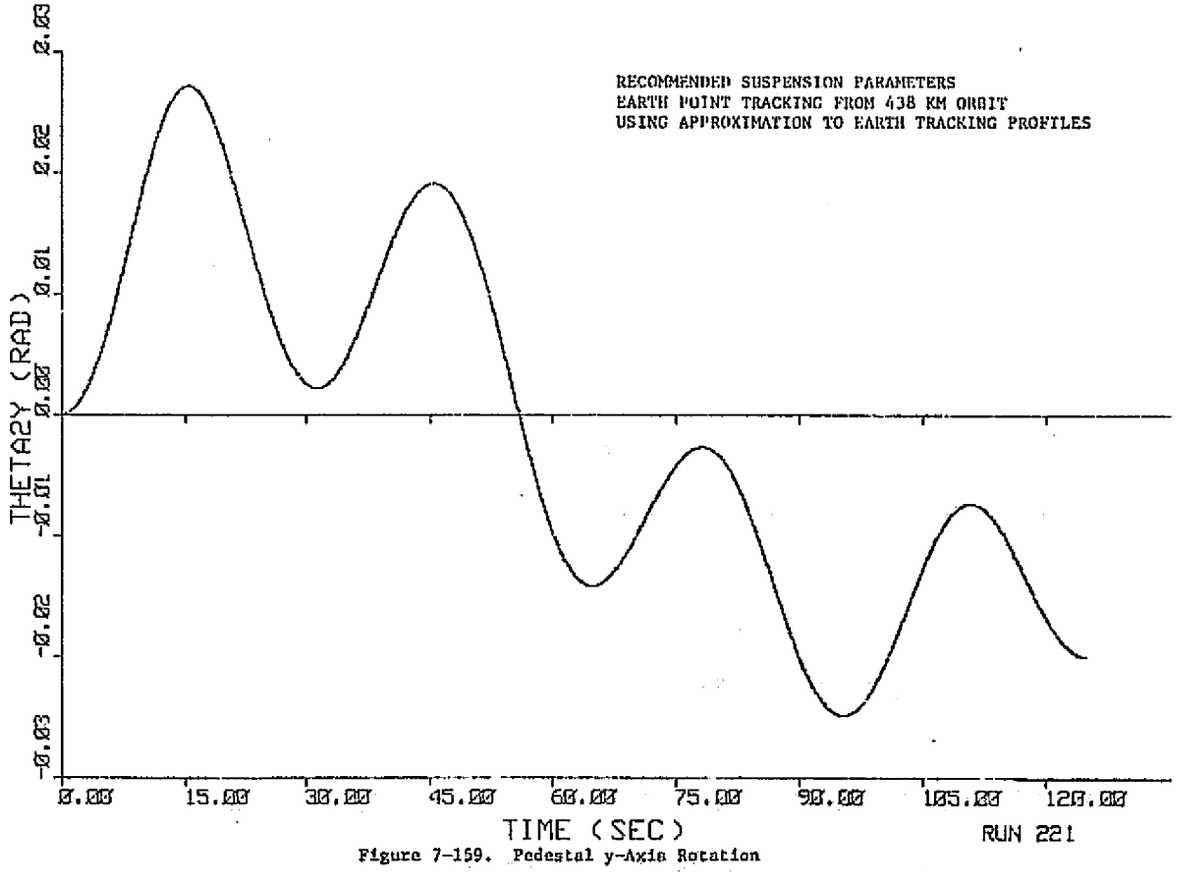

Figure 7-159. Pedestal y-Axis Rotation

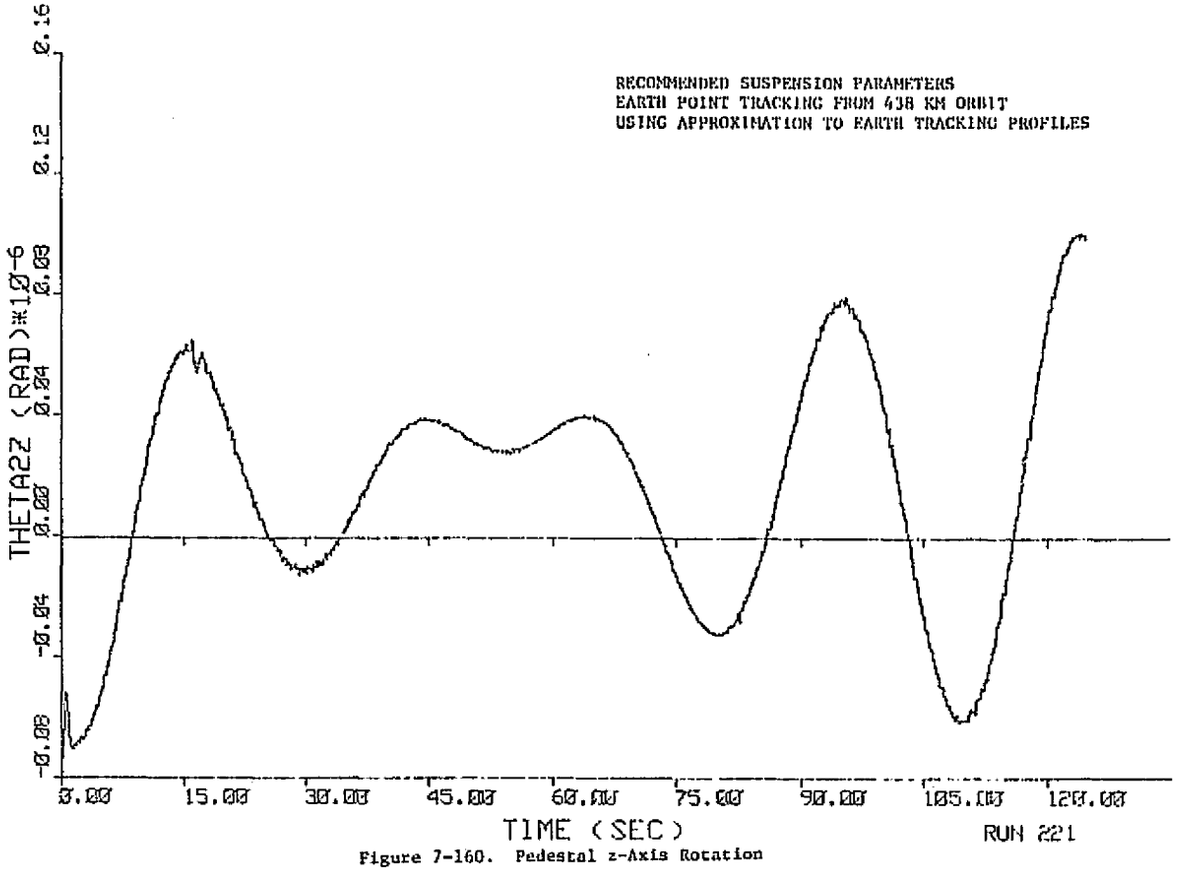

Figure 7-160. Pedestal z-Axis Rotation

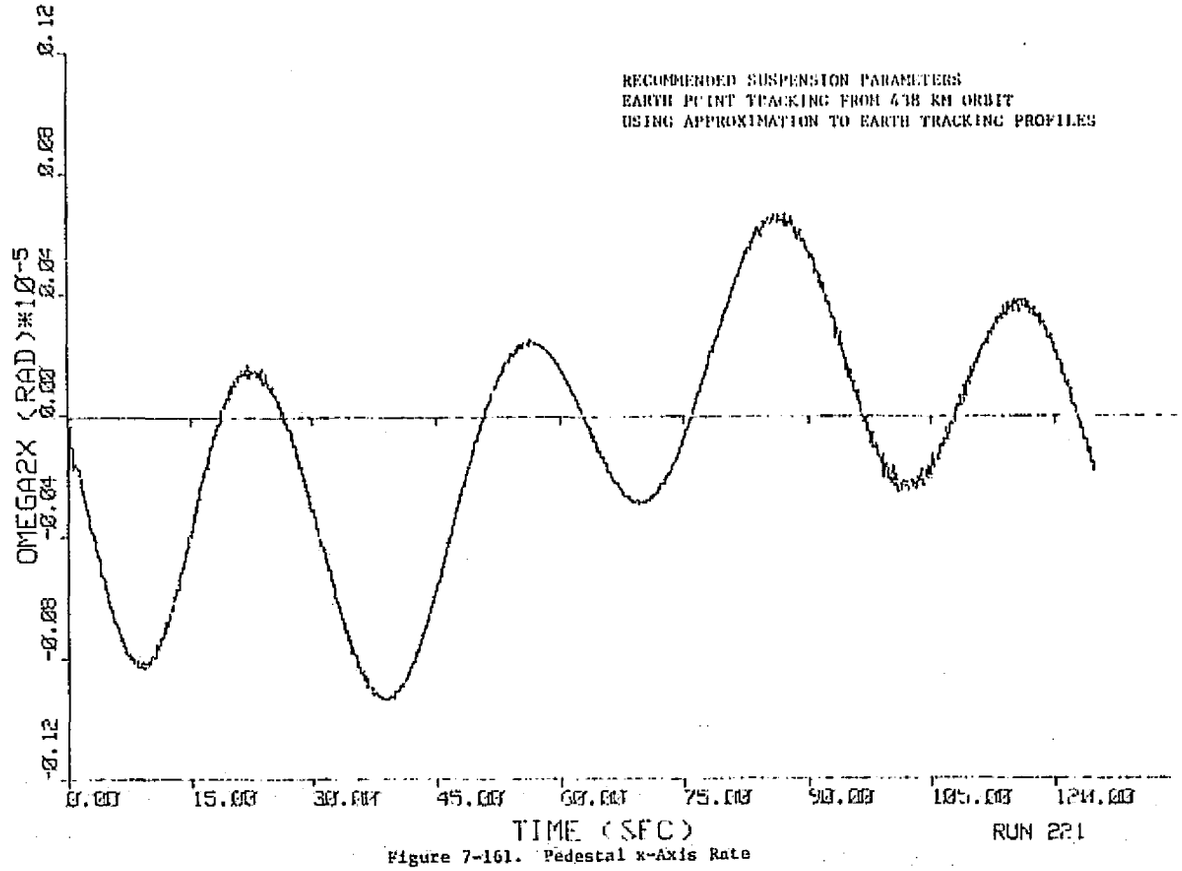

Figure 7-161. Pedestal x-Axis Rate

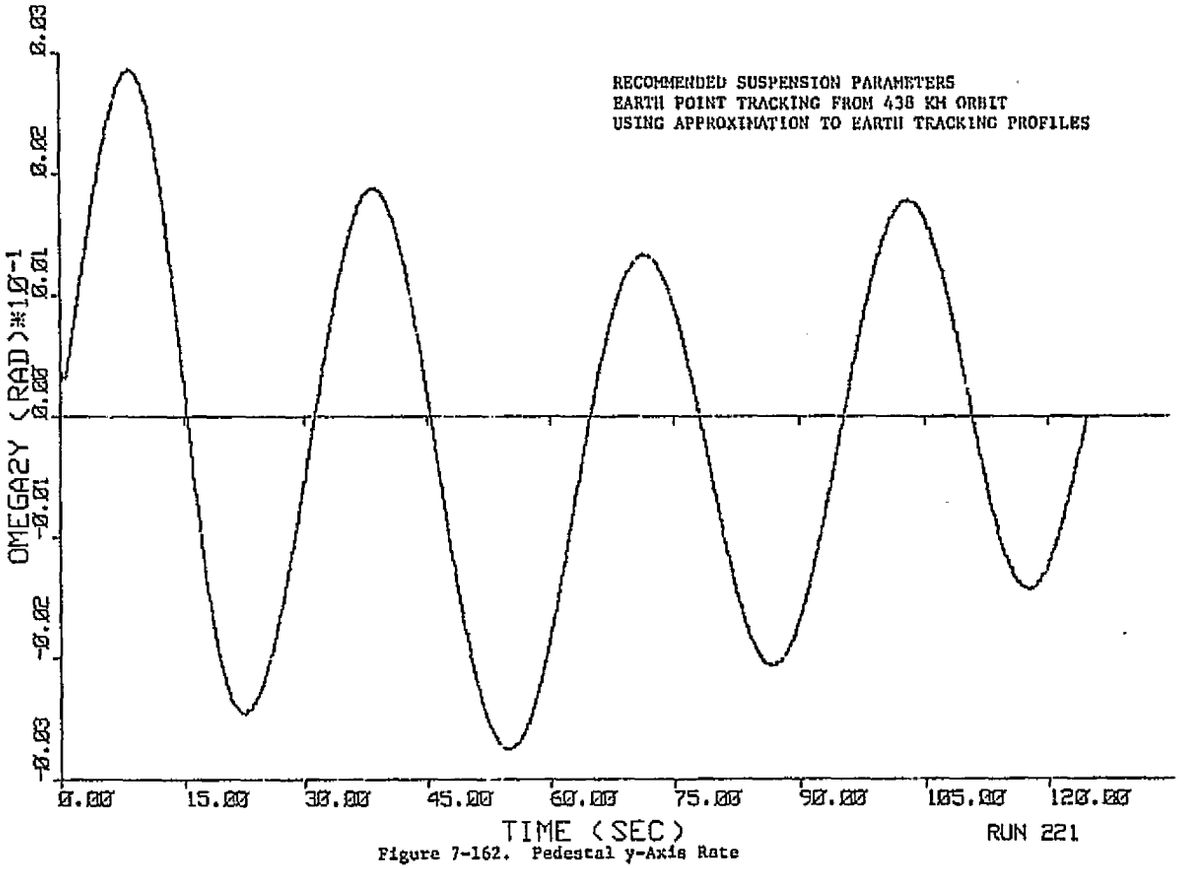

Figure 7-162. Pedestal y-Axis Rate

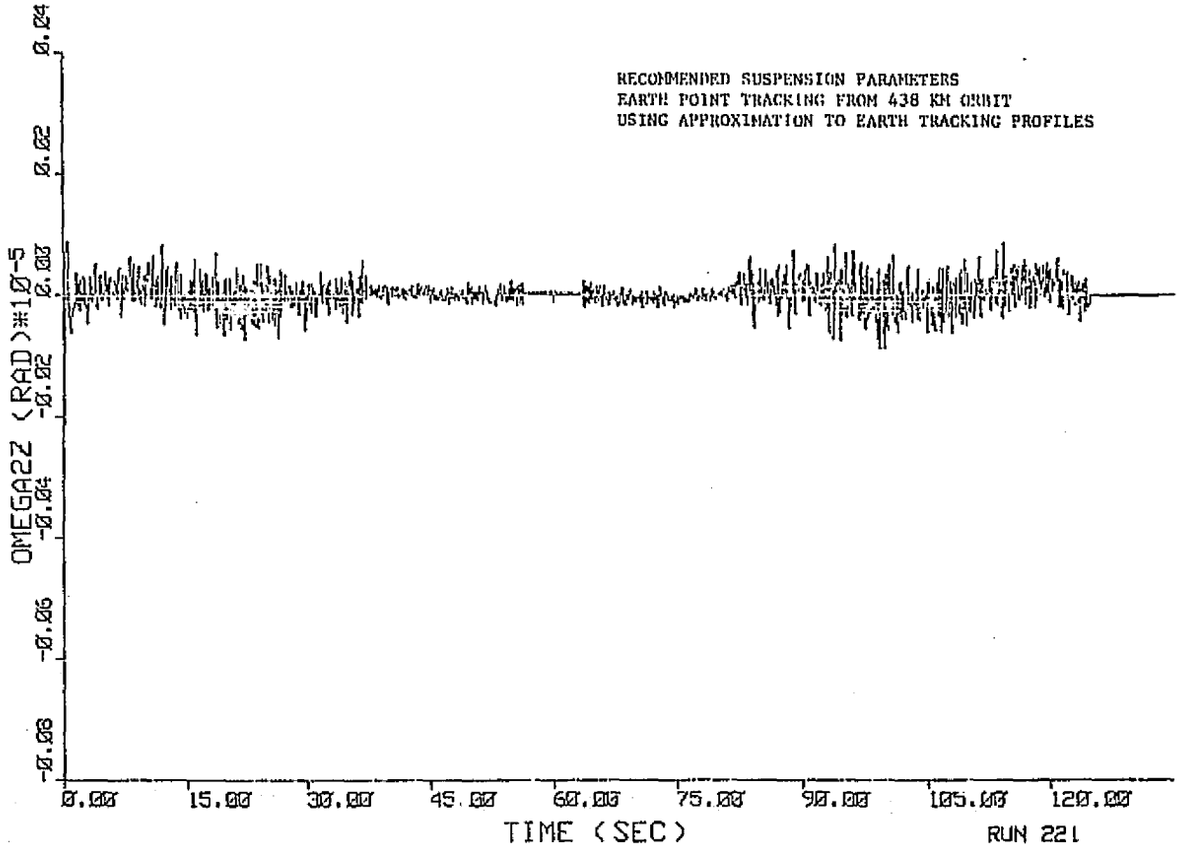

Figure 7-163. Pedestal z-Axis Rate

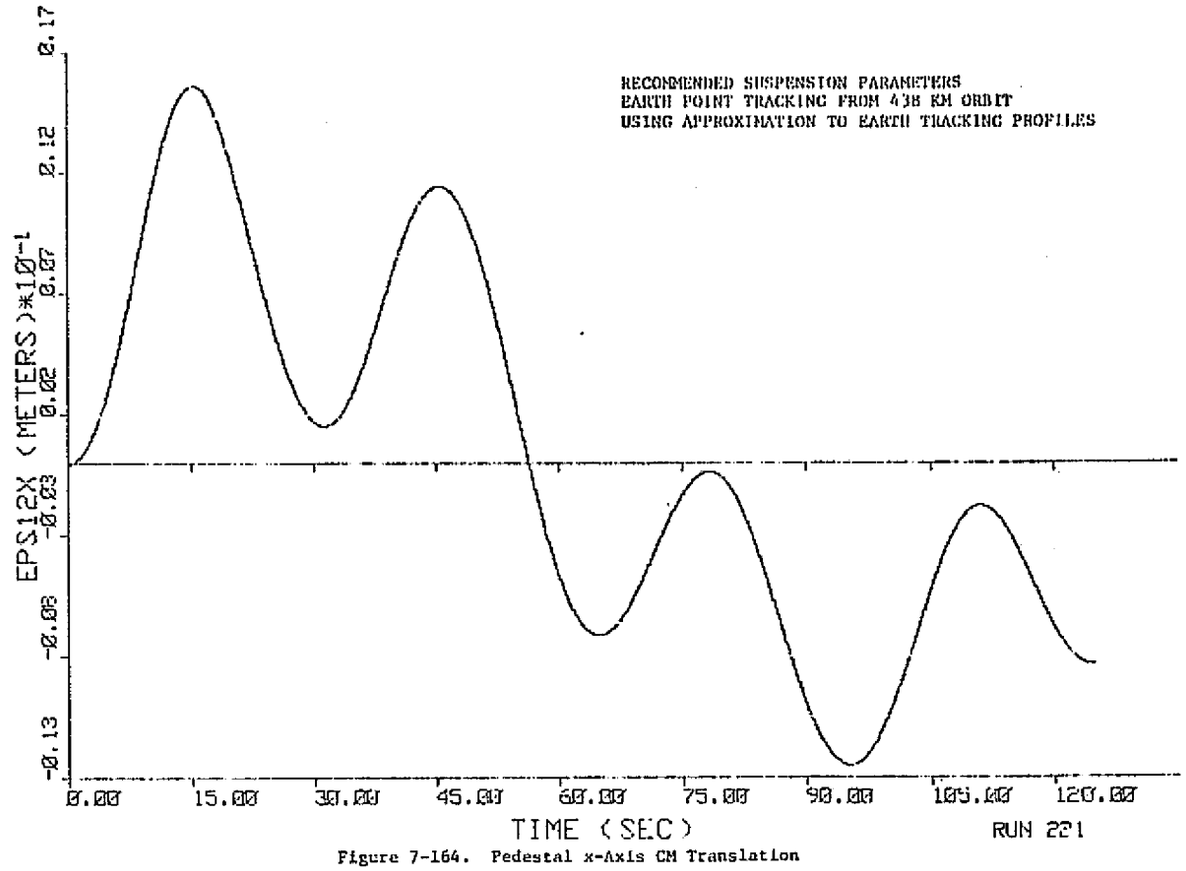

Figure 7-164. Pedestal x-Axis CM Translation

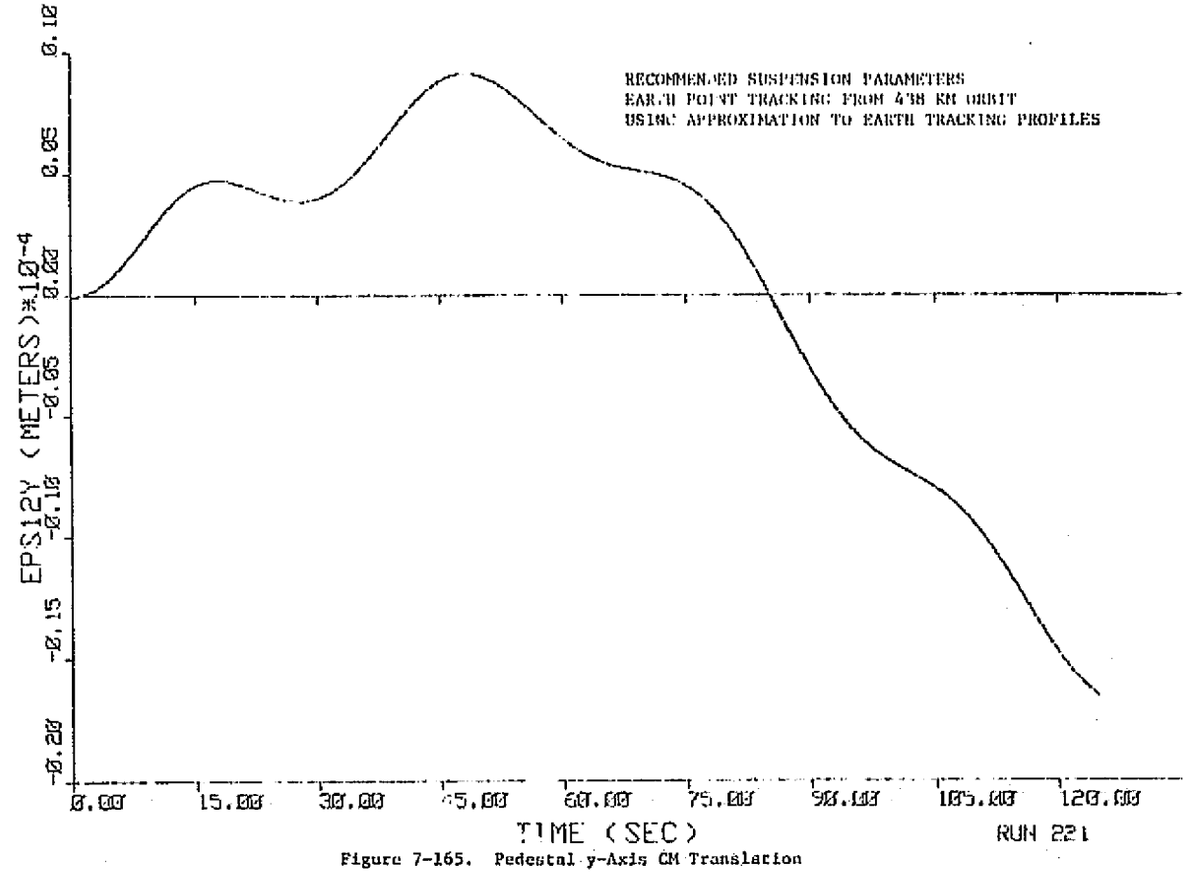

Figure 7-165. Pedestal y-Axis CM Translation

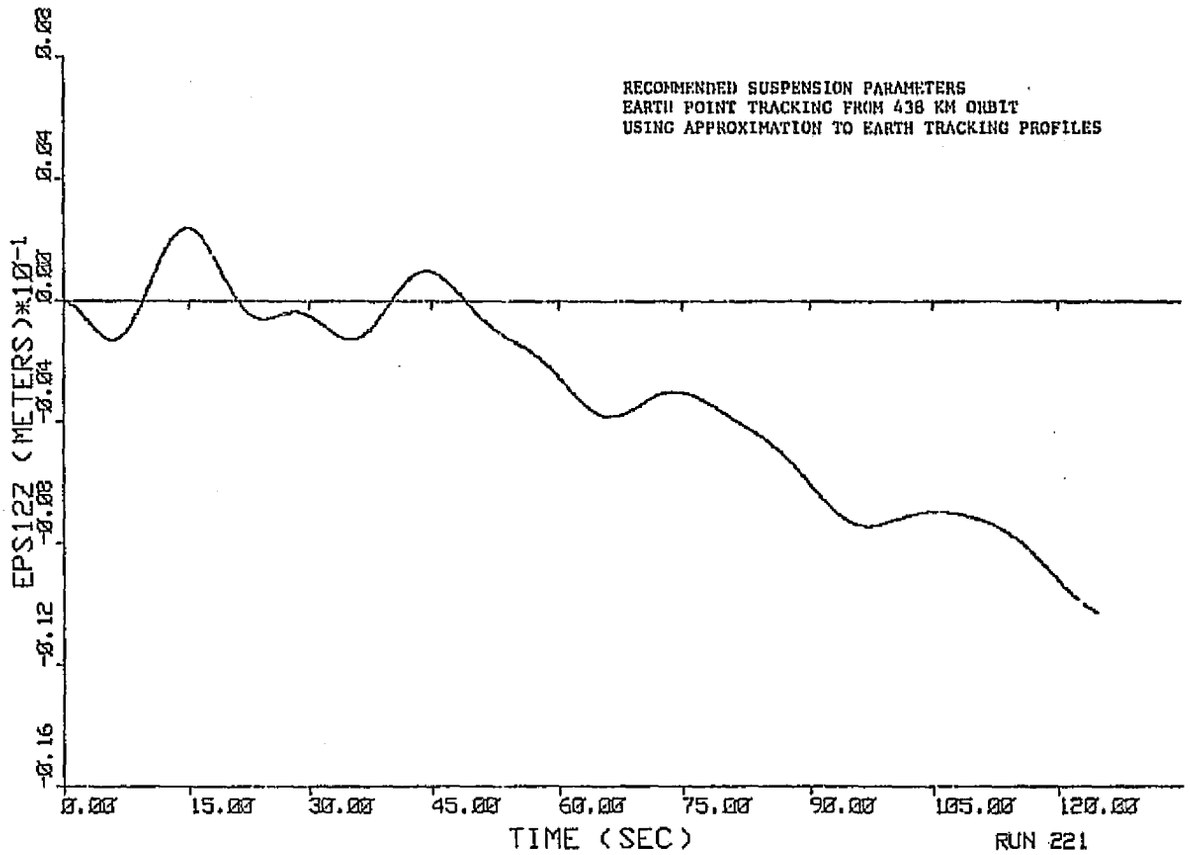

Figure 7-166. Pedestal z-Axis CM Translation

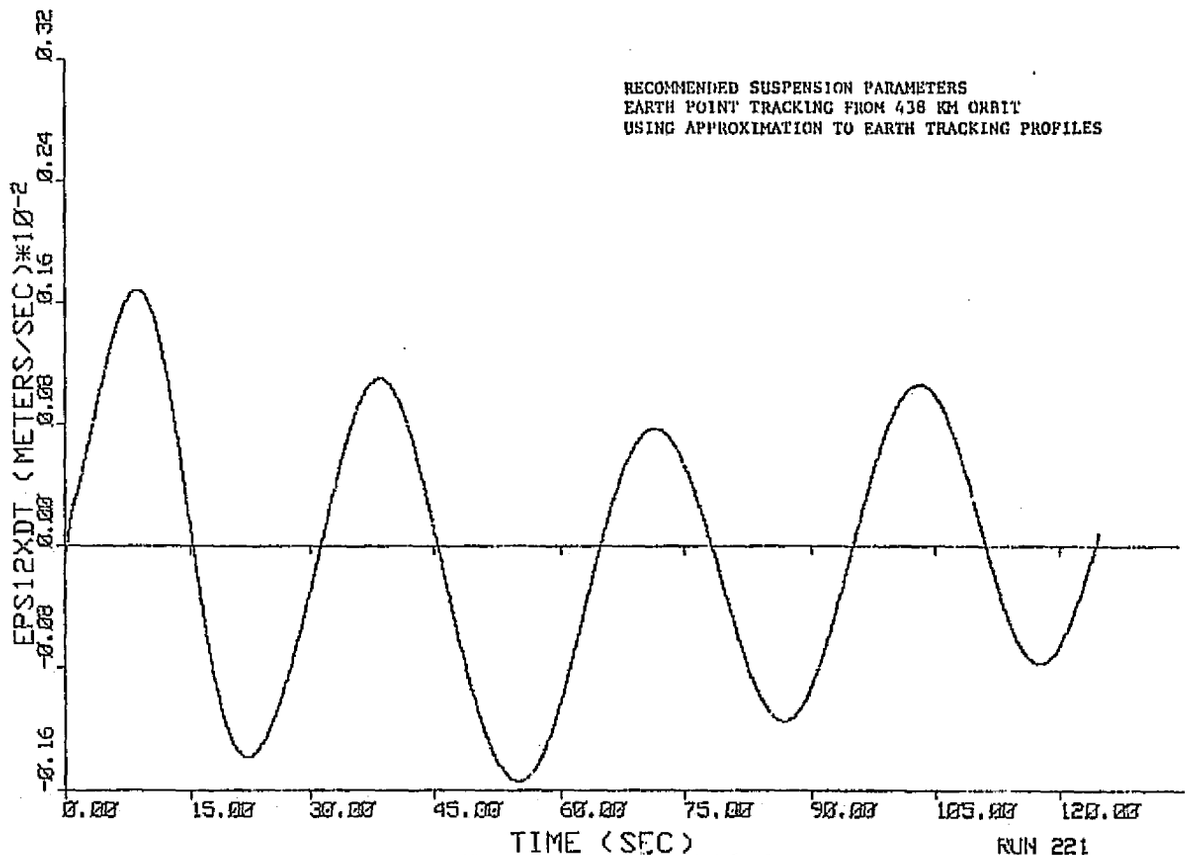

Figure 7-167. Pedestal x-Axis CM Velocity

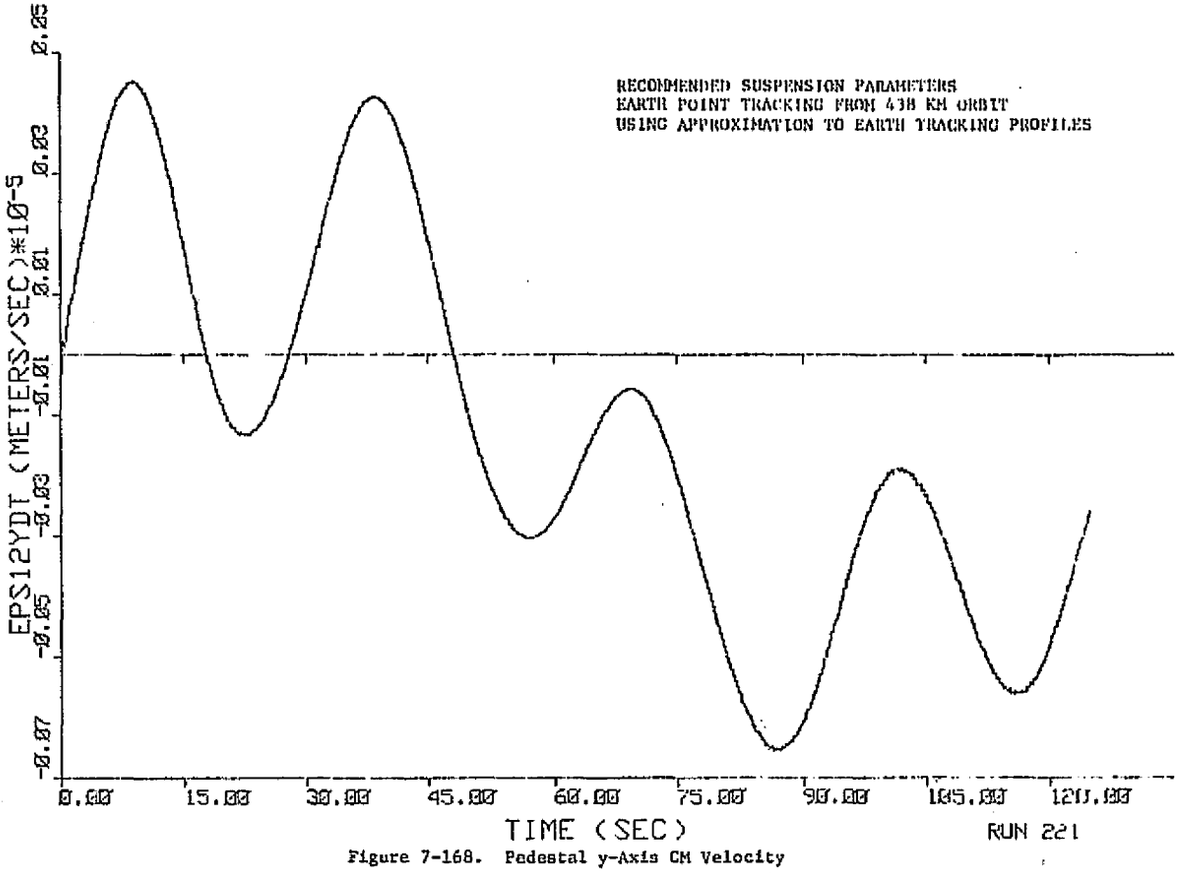

Figure 7-168. Pedestal y-Axis CM Velocity

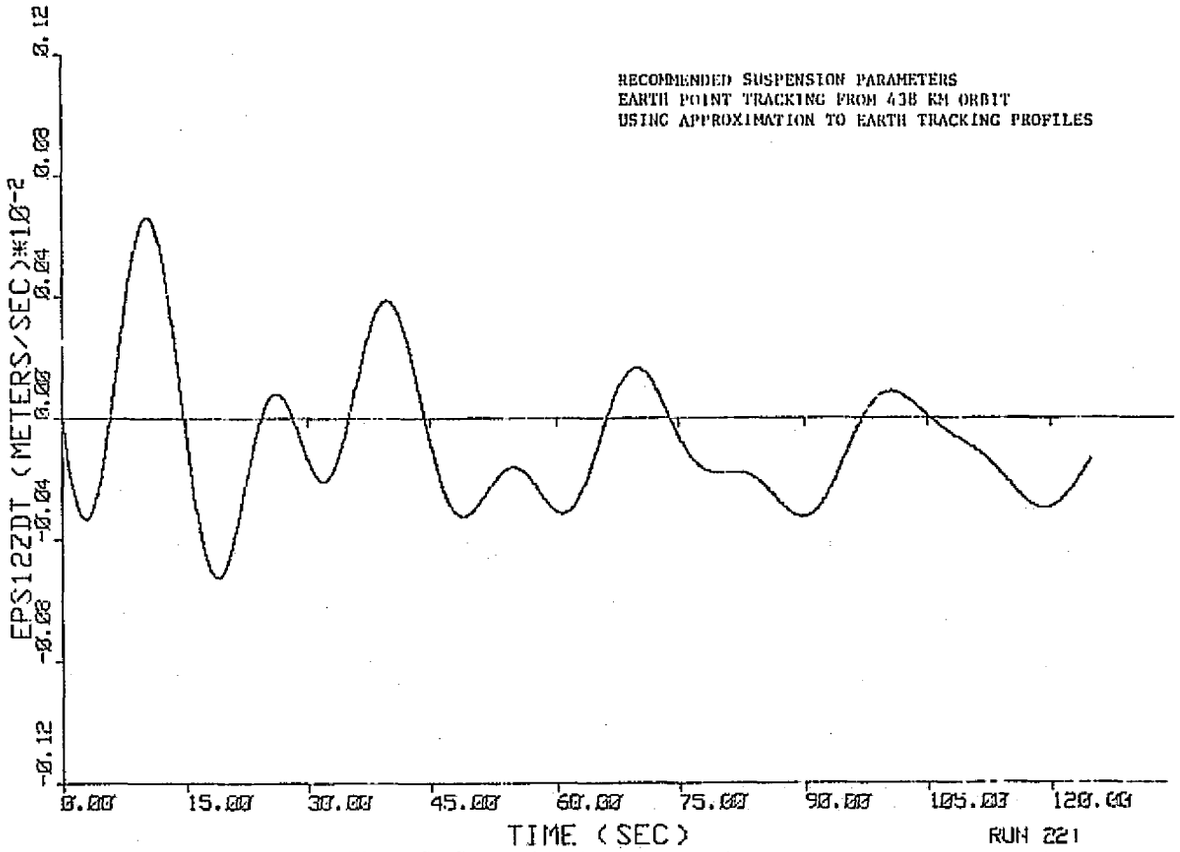

Figure 7-169. Pedestal z-Axis CM Velocity

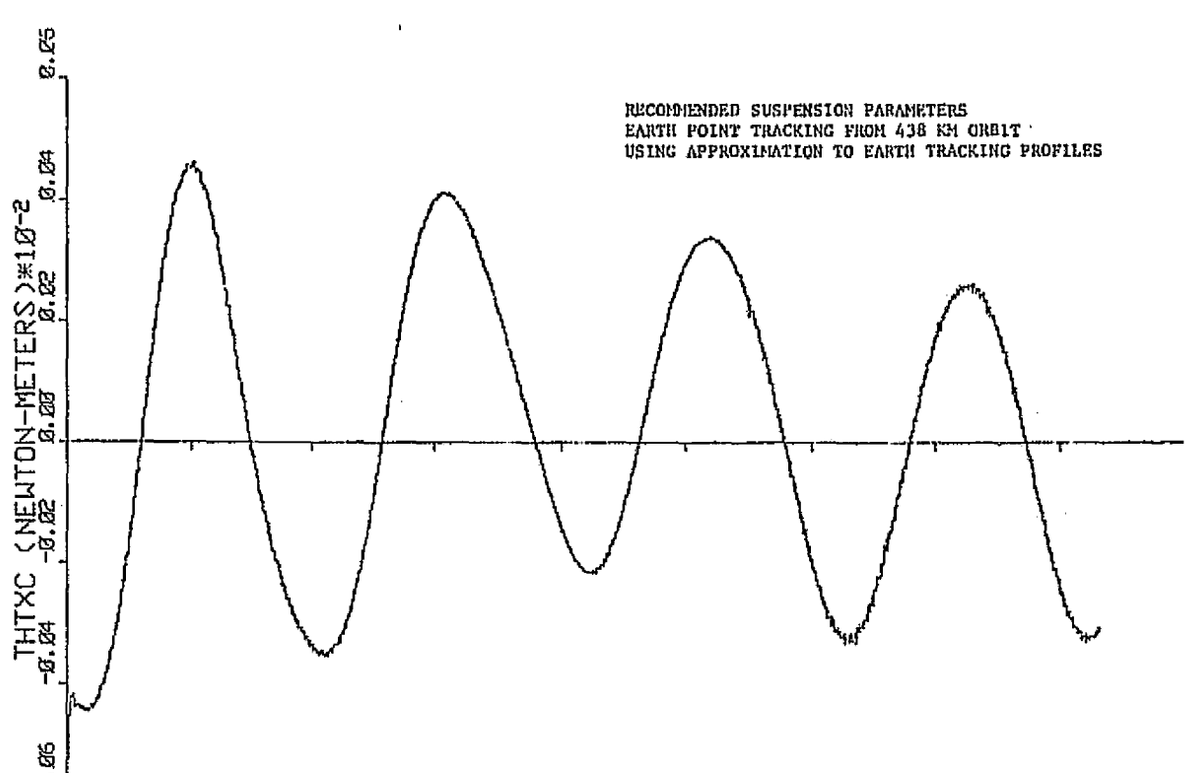

Figure 7-170. x-Axis Control Torque

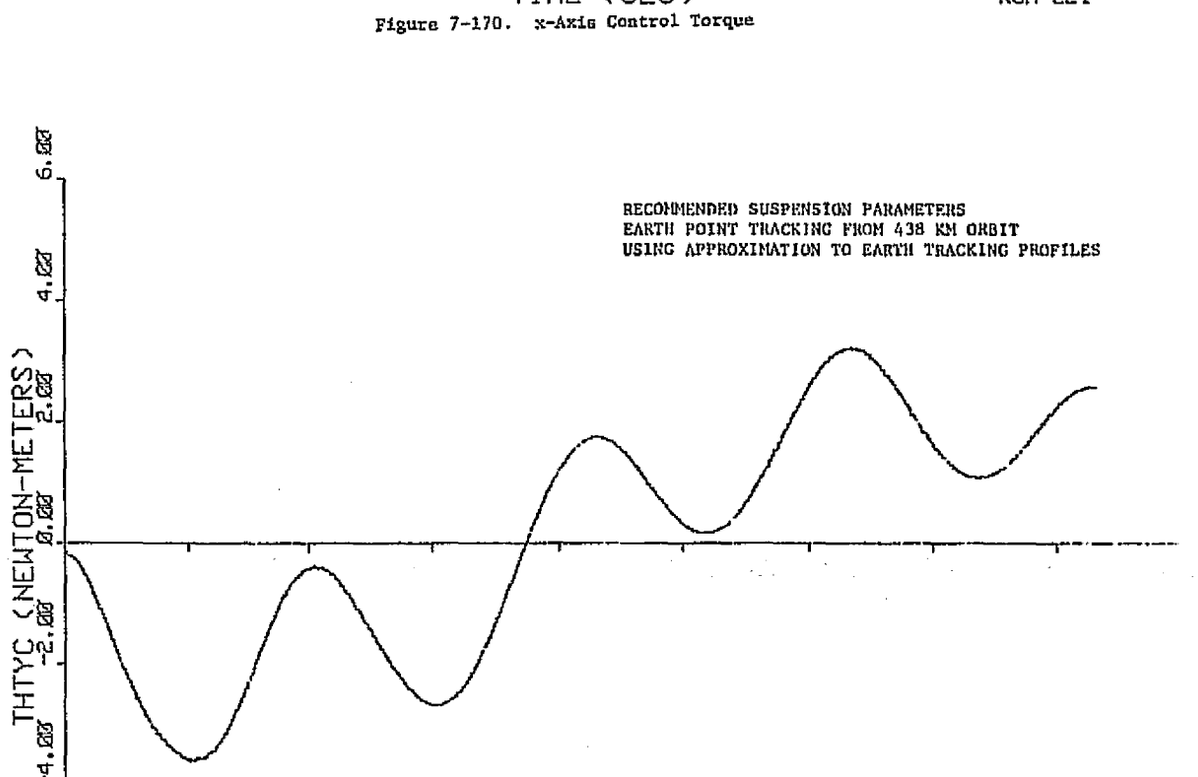

Figure 7-171. y-Axis Control Torque

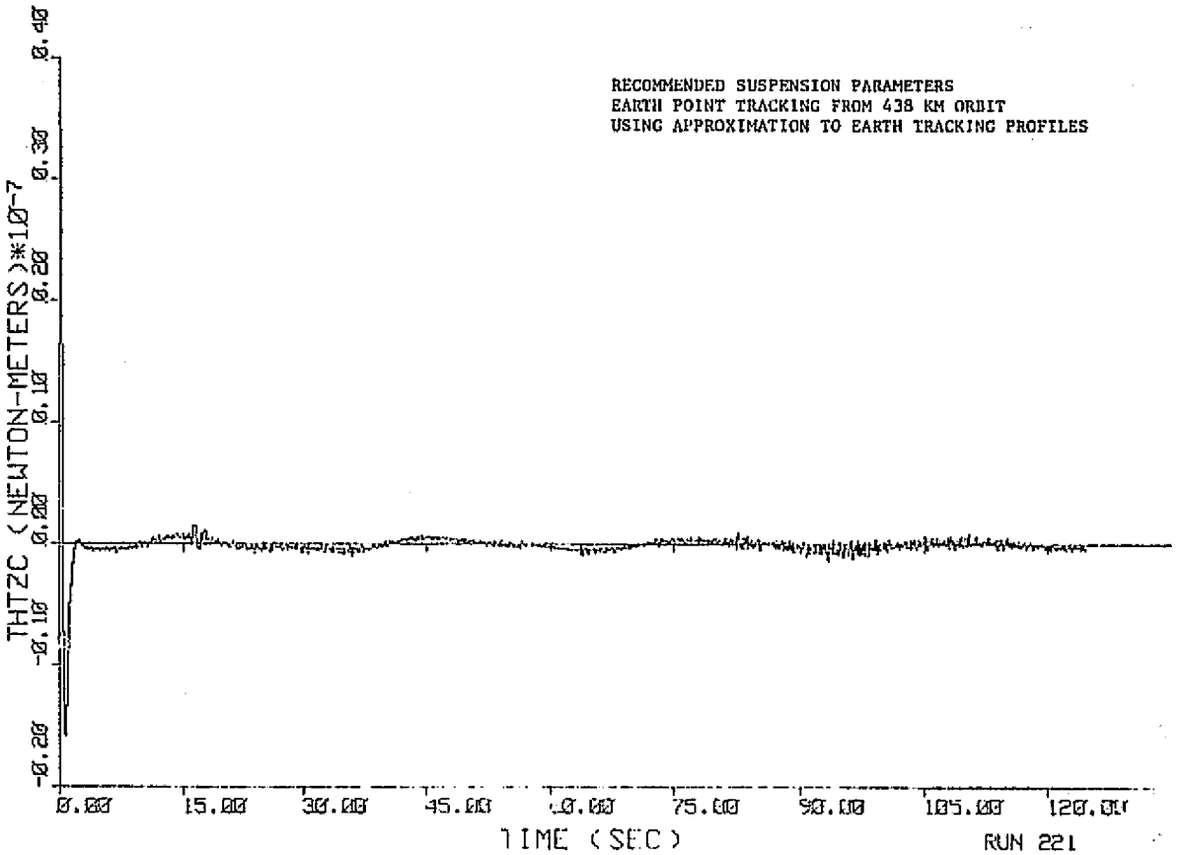

Figure 7-172. z-Axis Control Torque

8. ANALYSIS OF EARTH TRACKING PROFILES

In this section the profiles that are required to perform earth point tracking from earth orbit will be derived. In this derivation a circular orbit and spherical earth are assumed and the effects of earth rotation is neglected. The maximum acceleration points for the earth tracking profile will be determined as a function of the various orbital parameters and an approximate formula will be derived which gives peak acceleration as a function of orbital altitude. In addition, the peak rate of change of acceleration will be determined as a function of orbital parameters from which an approximate relation will be derived which gives peak rate of change of acceleration as a function of orbital altitude. These approximate relationships will be used to explain the behavior of the Coincident Gimbal System earth tracking performance characteristics, given in section 9.0.

8.1 Derivation of Earth Tracking Profiles - Figure 8-1 is a schematic diagram of a vehicle in a circular earth orbit.

The coordinate frame shown in figure 8-1 is inertial with the y axis along the orbit normal and the x and z axes in the orbital plane. Since the effects of earth rotation are being neglected in what follows, it can be assumed that the inertial coordinate frame is attached to the earth with its origin located at the earth's center. Using the vector quantities shown in figure 8-1 a unit vector along the line of sight from the vehicle to some arbitrary point on earth can be written as

$$\frac{R}{|R|} = \hat{i}_{L.S.} = \frac{R_L - R_o}{|R_L - R_o|} \qquad (8\text{-}1)$$

where

$\hat{i}_{L.S.}$ = Unit vector along the line of sight from the vehicle to an arbitrary point on the earth's surface.

R_L = Vector from center of earth to point on earth's surface

R_o = Vector from center of earth to vehicle.

Assuming a constant orbital rate ω_o about the positive y axis R_o can be expressed as

$$\begin{bmatrix} R_{ox} \\ R_{oy} \\ R_{oz} \end{bmatrix} = \begin{bmatrix} \cos\theta & 0 & -\sin\theta \\ 0 & 1 & 0 \\ \sin\theta & 0 & \cos\theta \end{bmatrix} \begin{bmatrix} R_e + h \\ 0 \\ 0 \end{bmatrix} \tag{8-2}$$

and

$$\theta = \omega_o t \tag{8-3}$$

where

R_{ox}; R_{oy}; R_{oz} = x, y and z components of R_o expressed geocentric coordinates

R_e = Radius of the earth

h = Orbital altitude

ω_o = Orbital Rate

Expressing R_L as

$$R_L = X_L \hat{i}_x + Y_L \hat{i}_y + Z_L \hat{i}_z \tag{8-4}$$

and substituting equations (8-2) and (8-4) into (8-1) gives

$$\hat{i}_{L.S.} = \frac{[X_L - (R_e+h)\cos\theta]\hat{i}_x + Y_L \hat{i}_y + [Z_L + (R_e+h)\sin\theta]\hat{i}_z}{\{[X_L - (R_e+h)\cos\theta]^2 + Y_L^2 + [Z_L + (R_e+h)\sin\theta]^2\}^{1/2}} \tag{8-5}$$

Letting

$$A = X_L - (R_e+h)\cos\theta \tag{8-6}$$

$$B = Z_L + (R_e+h)\sin\theta \tag{8-7}$$

The inertial rate of change of the unit vector along the line of sight can be written as

$$\frac{d\hat{\imath}_{L.S.}}{dt} = \frac{\left[(\dot{A}B - A\dot{B})B + Y_L^2\dot{A}\right]\hat{\imath}_x - Y_L(\dot{A}A + \dot{B}B)\hat{\imath}_y + \left[Y_L^2\dot{B} + (A\dot{B} - \dot{A}B)A\right]\hat{\imath}_z}{(A^2 + Y_L^2 + B^2)^{3/2}} \tag{8-8}$$

The inertial rate of change of the unit vector along the line of sight from the vehicle to a point on the earth can also be written as

$$\frac{d\hat{\imath}_{L.S.}}{dt} = \omega \times \hat{\imath}_{L.S.} = \begin{bmatrix} \hat{\imath}_x & \hat{\imath}_y & \hat{\imath}_z \\ \omega_x & \omega_y & \omega_z \\ i_{L.S.x} & i_{L.S.y} & i_{L.S.z} \end{bmatrix} \tag{8-9}$$

where

ω = An inertial rate written in geocentric coordinates.

Expanding equation (8-9) gives

$$\frac{d\hat{\imath}_{L.S.}}{dt} = (\omega_y i_{LSz} - \omega_z i_{LSy})\hat{\imath}_x + (\omega_z i_{LSx} - \omega_x i_{LSz})\hat{\imath}_y + (\omega_x i_{LSy} - \omega_y i_{LSx})\hat{\imath}_z \tag{8-10}$$

Comparing terms in equation (8-10) with those in equation (8-8) yields the following for the inertial rates required for earth point tracking written in geocentric coordinates

$$\omega_x = \frac{Y_L\dot{B}}{A^2 + Y_L^2 + B^2} \tag{8-11}$$

$$\omega_y = \frac{(\dot{A}B - A\dot{B})}{A^2 + Y_L^2 + B^2} \tag{8-12}$$

$$\omega_z = \frac{-Y_L\dot{A}}{A^2 + Y_L^2 + B^2} \tag{8-13}$$

and

$$\dot{A} = \omega_o (R_e + h) \sin\theta \tag{8-14}$$

$$\dot{B} = \omega_o (R_e + h) \cos\theta \tag{8-15}$$

It should be noted that if the body rates required to perform earth tracking would be desired for an arbitrary telescope orientation the rates given in equations (8-11) through (8-13) would have to be transferred to telescope coordinates and the transformation would need to be continually updated via a strapdown equation formulation.

Assuming the point on earth to be tracked is contained in the orbital plane (which would yield maximum tracking rates and accelerations) and assuming that the earth point is along the x axis of the geocentric coordinate frame shown in figure 8-1 gives the following relationships

$$X_L = R_e \tag{8-16}$$

$$Y_L = Z_L = 0 \tag{8-17}$$

Substituting equations (8-6), (8-7), (8-14), (8-15), (8-16) and (8-17) into equations (8-11) through (8-13) yields

$$\omega_x = \omega_z = 0 \tag{8-18}$$

$$\omega_y = \frac{[(R_e+h)^2 - R_e(R_e+h)\cos\theta]\,\omega_o}{(R_e+h)^2 + R_e^2 - 2R_e(R_e+h)\cos\theta} \tag{8-19}$$

The line of sight angle about the y axis can be obtained by integration of equation (8-19) or by derivation with the aid of figure 8-2.

Referring to figure 8-2, the following relationship applies between the variables

$$\frac{R_e + h}{\sin(180-\varphi)} = \frac{R_e}{\sin[180-(180-\varphi+\theta)]} \tag{8-20}$$

or

$$\frac{R_e + h}{\sin \varphi} = \frac{R_e}{\sin (\varphi - \theta)} \qquad (8\text{-}21)$$

where

ϕ = Line of sight angle and is equal to the direct integral of ω_y

Solving equation (8-21) for ϕ yields

$$\varphi = \tan^{-1}\left[\frac{(R_e + h)\sin\theta}{(R_e + h)\cos\theta - R_e}\right] \qquad (8\text{-}22)$$

Equations (8-19) and (8-22) are the functional form of the angular rate and position command profiles (i.e., ω_{3c} and θ_{3c}) that are employed to command the telescope attitude control system to accomplish earth tracking. These profiles must be modified by the appropriate constants to reflect the desired telescope slew axis (i.e., they get multiplied by the components of a unit vector along the desired slew axis) which enables telescope slewing about any axis or alternatively allows the telescope to be in any orientation with respect to the orbit normal.

The angular acceleration required to earth point track is obtained by differentiating equation (8-19) with the following result

$$\dot{\omega}_y = -\left\{\frac{R_e h (R_e + h)(2R_e + h)\sin\theta}{\left[R_e^2 + (R_e + h)^2 - 2R_e(R_e + h)\cos\theta\right]^2}\right\}\omega_o^2 \qquad (8\text{-}23)$$

To obtain the points at which peak acceleration occurs, equation (8-23) is differentiated with respect to time and the results set equal to zero which gives the following

$$\ddot{\omega}_y = -\omega_o^3 R_e h (R_e + h)(2R_e + h)\left\{\frac{\left[R_e^2 + (R_e + h)^2\right]\cos\theta - 2R_e(R_e + h)\left[\cos^2\theta + 2\sin^2\theta\right]}{\left[R_e^2 + (R_e + h)^2 - 2R_e(R_e + h)\cos\theta\right]^3}\right\} \qquad (8\text{-}24)$$

Setting equation (8-24) equal to zero results in the following

$$2R_e(R_e+h)\cos^2\theta + \left[R_e^2 + (R_e+h)^2\right]\cos\theta - 4R_e(R_e+h) = 0 \qquad (8\text{-}25)$$

Solving equation (8-25) for cosθ gives the following consistent solution for the peak acceleration points.

$$\cos\theta = \frac{-\left[R_e^2 + (R_e+h)^2\right] + \left\{\left[R_e^2 + (R_e+h)^2\right]^2 + 32R_e^2(R_e+h)^2\right\}^{1/2}}{4R_e(R_e+h)} \qquad (8\text{-}26)$$

Notice that two solutions exist for θ, one positive, the other negative which will yield two equal and opposite peak acceleration points equally positioned about the point where the vehicle is directly overhead (i.e., θ = 0).

The equations given above for the tracking command angular position, rates, accelerations and rate of change of acceleration involve the orbital rate ω_o which in itself is a function of orbital altitude. The relationship between ω_o and orbital altitude can be obtained in the following manner.

For an orbital vehicle in a circular orbit assuming a spherical earth, the following relationship applies

$$\frac{G m_e m_v}{(R_e+h)^2} = m_v(R_e+h)\omega_o^2 \qquad (8\text{-}27)$$

where

G = Gravitational Constant

m_e = Mass of the earth

m_v = Mass of the vehicle

Solving equation (8-27) for the orbital rate gives

$$\omega_o^2 = \frac{G m_e}{(R_e+h)^3} \qquad (8\text{-}28)$$

However, for a vehicle on the surface of the earth the following applies

$$\frac{G m_e m_v}{R_e^2} = m_v g \tag{8-29}$$

where

g = Gravitational acceleration on earth's surface

hence

$$G m_e = g R_e^2 \tag{8-30}$$

Substituting equation (8-30) into equation (8-28) yields

$$\omega_o^2 = \frac{g R_e^2}{(R_e+h)^3} \tag{8-31}$$

Combining equation (8-31) with those describing the angular command position, rate, acceleration, and rate of change of acceleration profiles give these in terms of the orbital altitude and time only with all other terms being constants.

For ease in initializing the computer simulation for the Coincident Gimbal to perform earth tracking it is desirable to have orbital angle "θ" as a function of telescope look angle "ϕ". This is accomplished by solving equation (8-22) for "θ" as a function of ϕ which results in

$$\sin\theta = \frac{-2R_e(R_e+h)\tan\varphi + \left\{4R_e^2(R_e+h)^2\tan^2\varphi + 4(R_e+h)^2\left[(R_e+h)^2 - R_e^2\right]\tan^2\varphi\left(1+\tan^2\varphi\right)\right\}^{1/2}}{2(R_e+h)^2\left(1+\tan^2\varphi\right)} \tag{8-32}$$

8.2 Comparison Between Actual Earth Tracking Profiles and the Hyperbolic Approximations - Approximate earth tracking profiles were employed in the evaluation of earth tracking performance of the IOG and the Coincident Gimbal system for the suspension parameters specified by Dornier as described in sections 4.2 and 7.2 respectively. In order to show that the results obtained using these profiles are valid, a comparison between the actual proviles derived is section 8.1 and the hyperbolic approximations described in section 4.2 will be performed in what follows.

C.4

In order to perform this comparison the orbital altitude for which the approximations are valid must be determined. In order to accomplish this a relationship that relates peak tracking rate to altitude must be determined. This can be done by noting that peak angular tracking rate occurs for $\theta = 0$. Hence from equation (8-19) the following applies

$$\omega_y|_{max} = \frac{R_e + h}{h}\omega_o \tag{8-33}$$

Substituting equation (8-31) into equation (8-33) and rearranging terms yields the following relationship

$$h^3 + R_e h - \frac{g R_e^2}{\omega_y|_{max}^2} = 0 \tag{8-34}$$

Solving equation (8-34) for the peak tracking rate of 1.748×10^{-2} rad/sec when the approximate hyperbolic earth tracking profiles are employed yields an altitude of 438 KM.

It is now necessary to determine the peak angular acceleration and the look angles for which they occur for the approximate profiles. In order to facilitate this determination the profiles given in section 4.2 are written in functional form.

$$\varphi(t) = K \tanh(K_1 - \alpha t) \tag{8-35}$$

$$\omega(t) = -K\alpha \operatorname{sech}^2(K_1 - \alpha t) \tag{8-36}$$

Differentiating equation (8-36) twice yields the following

$$\dot{\omega}(t) = -2K\alpha^2 \operatorname{sech}^2(K_1 - \alpha t)\tanh(K_1 - \alpha t) \tag{8-37}$$

$$\ddot{\omega}(t) = 2K\alpha^3 \operatorname{sech}^4(K_1 - \alpha t) - 4K\alpha^3 \tanh^2(K_1 - \alpha t)\operatorname{sech}^2(K_1 - \alpha t) \tag{8-38}$$

In order to determine the peak acceleration point equation (8-38) is set to zero which results in the following

$$\operatorname{sech}^2 \chi - 2\tanh^2 \chi = 0 \tag{8-39}$$

where

$$\chi = K_1 - \alpha t \tag{8-40}$$

Substituting the exponential form for the hyperbolic functions in equation (8-39) yields the following

$$e^{2x} - \sqrt{2}\, e^{x} - 1 = 0 \qquad (8-41)$$

Solving equation (8-40) for e^{x} gives

$$e^{x} = (\sqrt{2} + \sqrt{6})/2 = 1.932 \qquad (8-42)$$

or

$$x = 0.6585 \qquad (8-43)$$

Using the values for K_1 and α defined in section 4.2 gives

$$\frac{372 - t}{65} = 0.6585 \qquad (8-44)$$

or the time at which peak acceleration occurs is

$$t = 329.2 \text{ sec} \qquad (8-45)$$

Putting equation (8-37) in exponential form and substituting equation (8-42) yields

$$\dot{\omega}(x)\Big|_{max} = -8K\alpha^2\left[\frac{e^{x} - e^{-x}}{(e^{x} - e^{-x})^3}\right] = -8K\alpha^2\left[\frac{1.932 - \frac{1}{1.932}}{(1.932 + \frac{1}{1.932})^3}\right] = -0.7698\,K\alpha^2 \qquad (8-46)$$

Using the values defined in section 4.2 for K and α gives the following peak acceleration

$$\ddot{\omega}\Big|_{max} = 2.07 \times 10^{-4} \text{ rad/sec}^2 \qquad (8-47)$$

The telescope look angle for which this occurs can be determined by substituting the appropriate values into equation (8-35) which yields

$$\varphi = 0.6559 \text{ rad} = 37.58 \text{ deg} \qquad (8-48)$$

The peak acceleration and the telescope look angle at which this peak occurs for the actual earth tracking profiles are 1.856×10^{-4} rad/sec^2 and 31.1 degree respectively. These values compare favorably with those obtained using the approximate profiles thus validating the results obtained using the approximations.

8.3 Approximate Relationship Between Peak Angular Acceleration and Orbital Altitude - Using the relationships given in equations (8-23) and (8-26) the peak angular acceleration as a function of orbital altitude can be computed. A series of these computations are given in table 8-1.

The values shown in table 8-1 are plotted in figure 8-3. Examination of this figure indicates that the peak acceleration can be written as

$$\dot{\omega}|_{peak} = K_a h^b \tag{8-49}$$

where b is the slope of the line shown in figure 8-3 which is -2.099. Using a least square fit to estimate the constant K_a yields the following

$$\dot{\omega}|_{peak} = 23.6\, h^{-2.099} \tag{8-50}$$

where h is in miles

Equation (8-50) can also be written as

$$\dot{\omega}|_{peak} = 64.06\, h^{-2.099} \tag{8-51}$$

where h is in Km. These expressions can certainly be used with good precision (error less than 3 percent) over the range of their derivation and apply quite well to altitudes of 1000 miles, yielding results that are within 15 percent of the actual values.

8.4 Approximate Relationships Between Peak Rate of Change of Acceleration and Orbital Altitude - Examination of equation (8-24) indicates that peak rate of change of angular acceleration occurs when θ equals zero. Setting θ equal to zero and substituting equation (8-28) yields

$$\ddot{\omega}_{y}|_{peak} = -\left[\frac{gR_e^2}{(R_e+h)^3}\right]^{3/2}\left[\frac{R_e(R_e+h)(2R_e+h)}{h^3}\right] \tag{8-52}$$

Table 8-1. Peak Angular Acceleration as a Function of Orbital Altitude

ORBITAL ALTITUDE		PEAK ANGULAR ACCELERATION RAD/SEC^2
MILES	KILOMETERS	
100	160.9	1.494×10^{-3}
150	241.4	6.478×10^{-4}
200	321.9	3.557×10^{-4}
250	402.3	2.224×10^{-4}
300	482.8	1.508×10^{-4}
350	563.3	1.082×10^{-4}
400	643.7	3.102×10^{-4}
450	724.2	6.258×10^{-5}
500	804.7	4.957×10^{-5}

Using the above expression the peak rate of change of acceleration is given in table 8-2.

A plot of the values given in table 8-2 is shown in figure 8-4. Examination of this indicates that the peak rate of change of acceleration can be written in the same form indicated in section 8.3 for the peak acceleration. Following the same procedure as outlined above, the peak rate of change of acceleration can be written as

$$\dddot{\rho}\Big|_{peak} = \frac{1.832 \times 10^{9}}{h^{3.134}} \qquad (8-52)$$

where h is in Km

The approximate expressions derived in sections 8.3 and 8.4 will be used in the explanation of the earth tracking performance of the Coincident Gimbal system.

Table 8-2. Peak Rate of Change of Acceleration

ORBITAL ALTITUDE KM	PEAK RATE OF CHANGE OF ACCELERATION RAD/SEC^3
160	2.245×10^{-4}
240	6.415×10^{-5}
320	2.611×10^{-5}
400	1.29×10^{-5}
480	7.209×10^{-6}

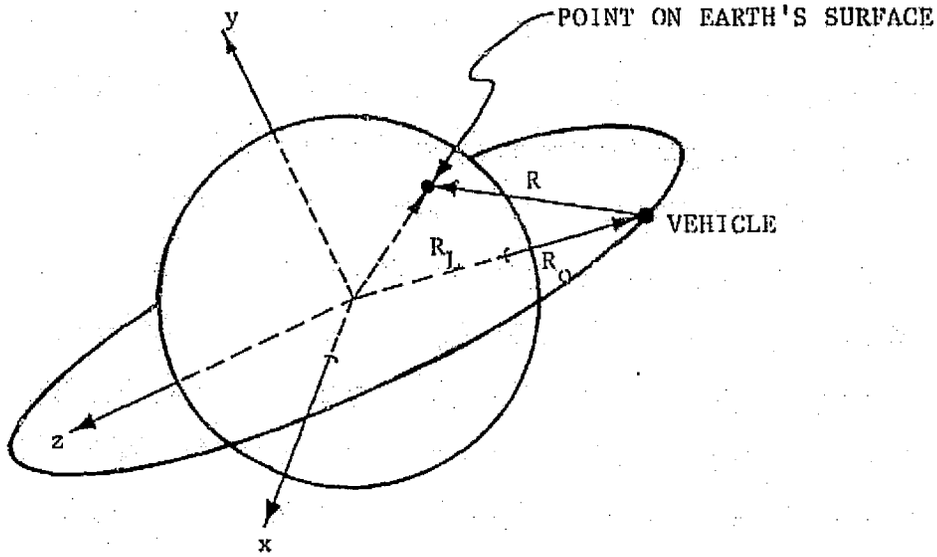

Figure 8-1. Schematic of Vehicle in Earth Orbit

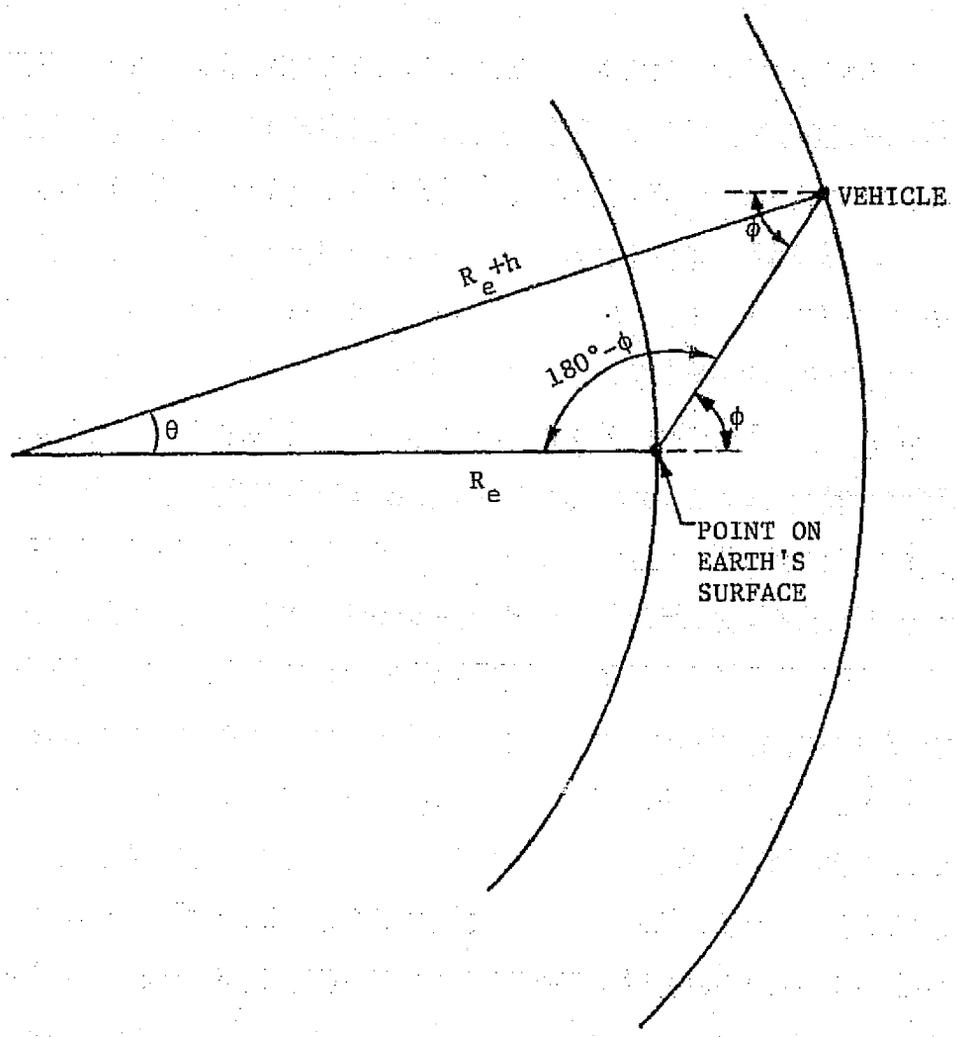

Figure 8-2. Planar Schematic of Vehicle in Earth Orbit

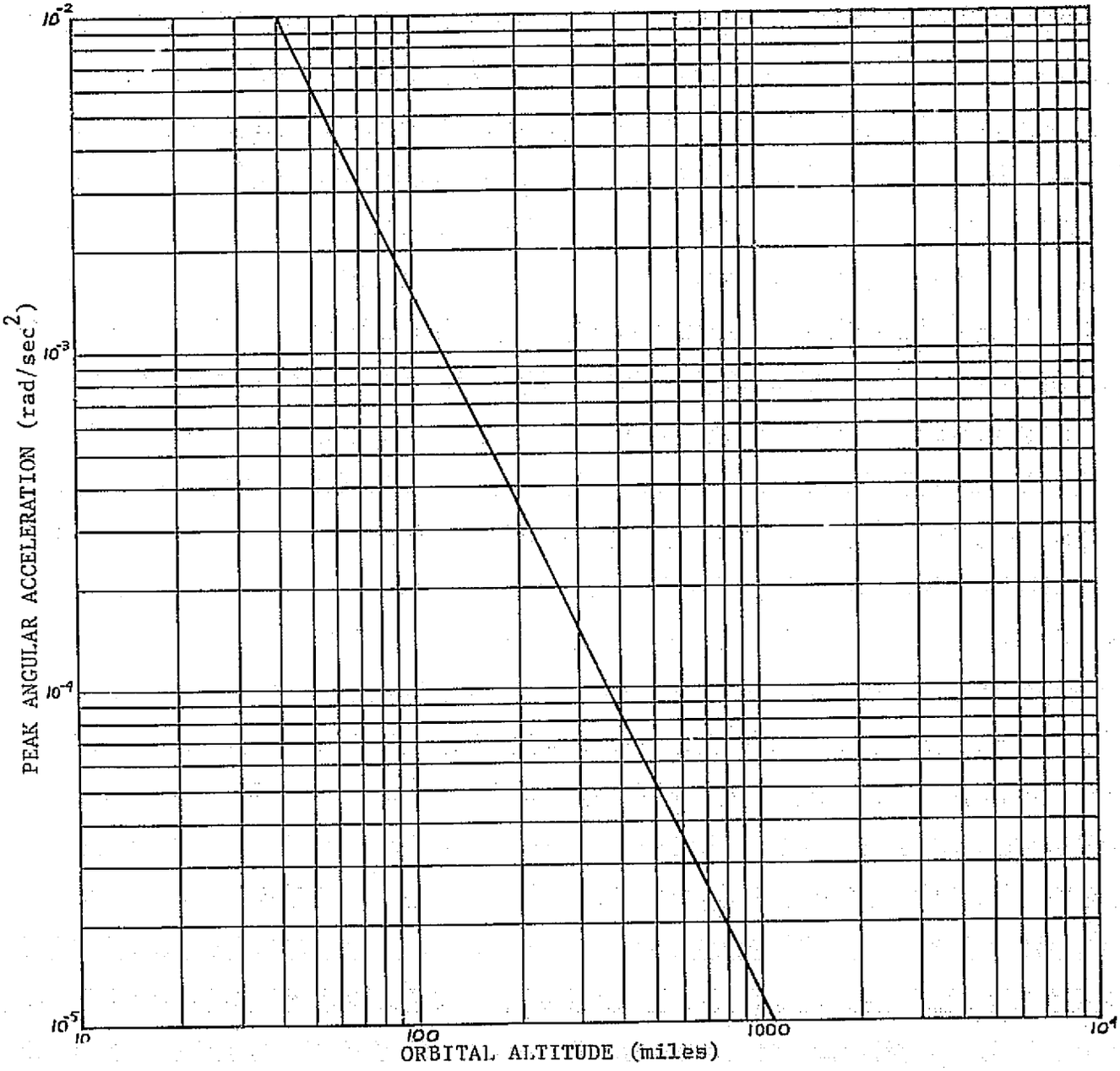

Figure 8-3. Peak Angular Acceleration vs. Orbital Altitude

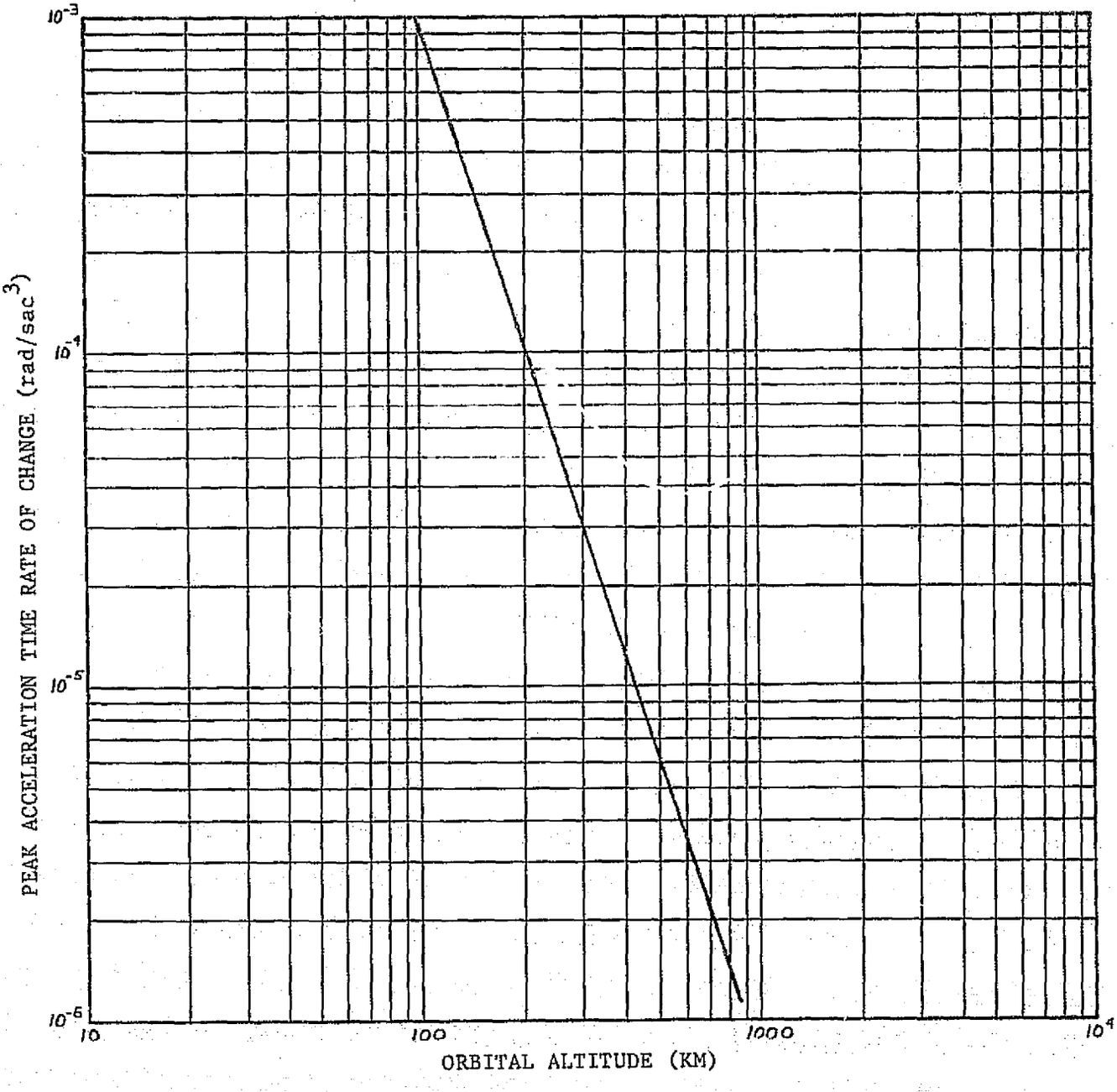

Figure 8-4. Peak Rate of Change of Acceleration vs. Orbital Altitude

9. COINCIDENT GIMBAL SYSTEM EARTH POINT TRACKING PERFORMANCE

In this section the earth tracking performance of the Coincident Gimbal system is described. The torque required to perform earth point tracking is estimated analytically and compared to the values obtained from the time simulation. An explanation of the large difference between the estimated and actual torques required is presented and verified via subsequent computer simulation. The payload mass and inertia that can be accommodated by the IPS in the earth point tracking mode as a function of orbital altitude is then established under the constraint the gimbal torque required will not exceed 80 percent of the torque capability of the gimbal torquers, or 16 n-m. The tracking accuracy, pedestal rotations and translations with the accompanying isolator elongations, is also specified. All of the earth point tracking studies described in this section were performed for the recommended suspension parameters given in table 7-1.

9.1 Estimated Torque Required to Perform Earth Point Tracking - In order to determine the telescope mass and inertia that could be accommodated by the IPS in the earth point tracking mode under any gimbal torque constraint, the torque required to perform earth point tracking should be estimated analytically in order to give a reasonable starting point in this determination.

This can be done by using the approximate relationship for peak angular acceleration shown in equation (8-50) for the particular orbital altitude of interest. An examination of orbital altitude requirements of experiments presently anticipated for integration with the IPS show that they vary between 160 and 480 Km. Choosing the 160 Km altitude, the approximate peak angular acceleration that will be encountered by the experiment is given by

$$\dot{\omega}\Big|_{peak} = \frac{64.06}{(160)^{2.099}} = 1.514 \times 10^{-3} \text{ rad/sec}^2 \qquad (9\text{-}1)$$

The peak torque required to perform earth point tracking should be between the torques required to achieve the peak angular acceleration in equation (9-1) when the telescope rotates about its center of mass to when it rotates about the hinge point. Using the mass properties for the nominal telescope given in table 2-1 the telescope inertia about its CM assuming that the earth tracking profiles will be applied about the y axis only is

$$J_{3y} = 2.648\text{x}10^{3}\ \text{Kg-m}^2 \tag{9-2}$$

The y axis moment of inertia of the telescope about the gimbal hinge point is given by

$$J'_{3y} = 2.648\text{x}10^{3} + (2.683\text{x}10^{3})(1.689)^2 = 1.03\text{x}10^{4}\ \text{Kg-m}^2 \tag{9-3}$$

Hence, the torque required to perform earth point tracking from a 160 Km orbit should be between the minimum and maximum values listed below

$$T_{min} = (2.648\text{x}10^{3})(1.514\text{x}10^{-3}) = 4.009\ \text{n-m} \tag{9-4}$$

$$T_{max} = (1.03\text{x}10^{4})(1.514\text{x}10^{-3}) = 15.59\ \text{n-m} \tag{9-5}$$

IPS earth point tracking performance for the nominal telescope from a 160 Km orbit is shown in figures 9-1 through 9-21. Examination of y axis control torque shown in figure (9-20) indicates that the peak gimbal torque required for this earth tracking maneuver was 47 n-m, a factor of three larger than the peak required torque estimated above.

A possible explanation of this phenomenon is that the integrator in the control torque formulation is charging to too large a value hence causing the large overshoot in y axis control torque. An examination of figure 9-20 does not seem to bear this out since an overcharged integrator should show up as a torque spike on the time scale of figure 9-20 since the pointing control loop bandwidth is two Hz and the integrator would discharge rapidly. However, in order to substantiate that the integrator in the y axis control torque formulation is not causing the observed large y axis control torques, IPS time response was determined for the same conditions as above only with the integral gain in the y axis controller set to zero. Figures 9-22 through 9-42 summarize these results. Comparison of these results with those obtained above (i.e., figures 9-1 through 9-21) indicate that the only differences in response were in the y axis tracking position and rate errors (figures 9-23 and 9-26 respectively) which, as expected, was appreciably larger than those incurred when the y axis integrator gain was at its nominal value. All other system parameters including the y axis control torque, exhibited virtually identical responses as those obtained when the y axis integrator gain was at its nominal value, thus substantiating that the integrator in the y axis controller was not the reason for the large y axis control torque.

Another possible explanation for the above phenomenon is that the IPS pedestal is applying hinge forces to the telescope due to its dynamic behavior which, in turn, cause disturbance moments that must be counteracted by the telescope control system. In order to determine the validity of this contention, the telescope hinge point and pedestal CM were made coincident with the IPS suspension center of elasticity and the computer run for landmark tracking from 160 Km orbit was repeated. These revisions should minimize the dynamic hinge forces applied to the telescope by the pedestal since the rotation about the suspension center of elasticity is also consistent with rotation about the pedestal CM and telescope hinge point, thus greatly reducing hinge point linear accelerations and the accompanying telescope disturbances.

The IPS time response for these conditions are shown in figures 9-43 through 9-51. Examination of these results indicate that the torque required to earth point track was 15.9 n-m (see figure 9-51) which is in line with the analytical projections. The y axis control torque peak of 23.8 n-m that occurs at 3.7 seconds into the run is primarily due to a transient condition in the initialization of the run since not all states are set at their proper values corresponding to when the earth point tracking profiles are picked up. Therefore, the second peak which occurs at 28.5 seconds into the run is indicative of the torque required to earth point track. These results indeed verify the above contention that the pedestal dynamic motions are resulting in hinge forces which give rise to telescope disturbance torques which must be overcome by the control system. Hence, from the earth point tracking viewpoint, it is desirable that the telescope hinge point and pedestal CM be as close to the suspension center of elasticity as possible, within the constraints of practical design considerations.

However, previous studies (i.e., "Evaluation of Alternate Telescope Pointing Schemes" NASA Contract No. NAS8-30889) indicate that making the telescope hinge point and the pedestal CM coincident with the center of elasticity of the IPS suspension has a detrimental effect on pointing performance for disturbances applied in the x,y plane. Figure 9-52 is a reproduction of figure 3-4 from Volume I of the final report titled, "Evaluation of Alternate Telescope Pointing Schemes," issued May 1975. Examination of the curve for which $r_1 = R_{E40} = R_{340} = 0$, which makes the pedestal CM and telescope hinge point coincident with the suspension center of elasticity, indicates, that if the linear suspension stiffness exceeds approximately 400 n/m $\pm$ 1 arc-second pointing stability will be exceeded in the presence of crew motion

disturbances for a zero degree telescope look angle. The reason for this phenomenon is that the telescope hinge point does not translate under the influence of the applied disturbance and the control torques applied to tne pedestal by the pointing control loop, which reduces the translation acceleration disturbance coupling into the telescope. In fact, with the recommended linear suspension stiffness of 2000 n/m to reduce pedestal translation and rotation incurred during landmark tracking and improve stellar pointing performance, the resultant pointing error for zero telescope look angle for a crew motion disturbance along the orbiter y axis obtained from figure 1 is approximately 5.3 arc-second. If pointing stability requirements are to be achieved, the suspension linear stiffness in the x and y directions would have to be reduced by an order of magnitude (i.e., 200 n/m). Although this reduction in linear stiffness in the x,y direction would tend to increase the pedestal translations incurred during earth point tracking, making the gimbal hinge point, pedestal CM, and suspension center of elasticity to coincide reduces the pedestal translations and rotations incurred. Hence, a trade should be conducted which determines the pedestal translations, rotations, and isolator elongations for different separations between gimbal hinge point, pedestal CM, and suspension center of elasticity once the suspension parameters have been set to yield satisfactory stellar pointing performance for each particular set of geometrical parameters being considered. This type of study would indicate if there is a geometrical configuration coupled with a set of suspension parameters that would yield better overall (i.e., stellar pointing and earth point tracking) IPS performance than those realized with the specified geometry and recommended suspension parameters.

9.2 Payload Mass Characteristics That Can Be Accommodated By the IPS In the Earth Point Tracking Mode for Various Orbital Altitudes - In the section that follows, the payload mass characteristics that could be accommodated by the Coincident Gimbal system in the earth point tracking mode is described. In this determination the nominal payload mass and inertia values given in table 2-1 were varied about all three axes by the same ratio while keeping the distance from the hinge point to the telescope CM (i.e., r_2) constant. In addition, the control gains were adjusted in each case to maintain a pointing control loop bandwidth of two Hz. The gimbal torque was constrained not to exceed 80 percent of its full torque capability of 20 n-m which set the maximum allowable gimbal torque at 16 n-m, during the determination of the payload mass and inertia characteristics that could be accommodated by the IPS during earth point tracking.

For the conditions enumerated above the telescope mass and inertia characteristics that could be accommodated by the IPS during earth point tracking as a function of orbital altitude and the peak tracking error incurred are given in table 9-1.

The values given in table 9-1 are plotted in figure 9-53. Examination of this figure indicates that the inertia that can be accommodated by the IPS during earth point tracking without exceeding a required gimbal torque of 16 n-m can be written in the form

$$J = K_j h^b \tag{9-6}$$

where b is the slope of the line shown in figure 9-53. Measuring this slope gives a value of

$$b = 2.157 \tag{9-7}$$

This value is within 2.7 percent of the negative slope of 2.099 shown in equation (8-50) which gives the approximate relationship between the peak acceleration and orbital altitude. Hence it is seen that the telescope inertia that could be accommodated by the IPS is a function of the peak angular acceleration required to earth point track. Or another way of looking at this result is by realizing that the peak torque required is proportional to the telescope inertia times the peak acceleration or

$$T_{peak} = K_T J \dot{\omega}\Big|_{peak} \tag{9-8}$$

Substituting equation (8-50) into equation (9-8) gives

$$T_{peak} = \frac{23.6 K_T J}{h^{2.099}} \tag{9-9}$$

Solving equation (9-9) for the inertia keeping the peak torque constant at 16 n-m gives the following

$$J = K_j h^{2.099} \tag{9-10}$$

which is within 2.7 percent of the results obtained above and defined by equations (9-6) and (9-7).

Table 9-1. Telescope Tracking Error Mass and Inertia Characteristics That Can Be Accommodated by the IPS During Earth Point Tracking

ORBITAL ALTITUDE (Km)	TELESCOPE MASS (Kg)	TELESCOPE INERTIA $Kg-m^2$	TELESCOPE Y AXIS PEAK TRACKING ERROR (rad)	TELESCOPE Y AXIS PEAK TRACKING ERROR (ARC-SECOND)
160	1.309×10^3	1.292×10^3	9.93×10^{-5}	20.47
240	2.937×10^3	2.898×10^3	2.55×10^{-5}	5.258
320	5.698×10^3	5.622×10^3	1.11×10^{-5}	2.289
400	8.987×10^3	8.867×10^3	5.76×10^{-6}	1.188
480	1.422×10^4	1.402×10^4	3.31×10^{-6}	0.683

9.3 Peak Tracking Error Incurred During Earth Point Tracking - Figure 9-54 is a plot of the values given in table 9-1 for telescope tracking error vs orbital altitude incurred during earth point tracking. Examination of figure 9-54 indicates that the tracking error can be expressed in the same functional exponential form as the telescope inertia discussed in section 9.2. The exponent which is equal to the slope of the line in figure 9-54 is measured to be 3.092. This value compares favorably with the 3.136 exponent in the expression for the rate of change of acceleration given in equation (8-52) being within 1.4 percent of it. Hence, it is seen that the telescope tracking error incurred depends on the rate of change of angular acceleration which is directly proportional to the rate of change of torque rather than the peak torque required to perform earth point tracking. This is not surprising since there is integral control and the effectiveness of the integral control in reducing telescope tracking error depends on how fast the torque requirements change. This implies that if the pointing control loop bandwidth were kept constant, regardless of telescope inertia variations, then the peak tracking error incurred would similarly remain constant. This would be exactly true if it weren't for the effect of the disturbance torque applied to the telescope due to pedestal dynamics which is appreciable as described in section 9.1. Table 9-2 lists the telescope tracking error incurred for a 160 Km orbit as a function of mass and inertia variations for the recommended suspension parameters and a 2 Hz pointing control loop bandwidth. Examination of table 9-2 indicates that telescope tracking error indeed does not follow the variation in telescope mass and inertia. The tracking error incurred for the nominal telescope mass and inertia (i.e., 2.683×10^3 Kg, 2.648×10^3 Kg-m^2) and for one-fifth those values (i.e., 536.6 Kg; 529.6 Kg-m^2) are essentially the same. This essentially substantiates the contention that the telescope tracking error incurred is essentially independent of telescope mass and inertia or required torque for a given orbital altitude as long as the pointing control loop bandwidth is kept constant. The relatively large pointing error incurred at one-half nominal telescope mass and inertia is considered to be due to a peculiar interaction with the pedestal dynamics.

9.4 Pedestal Rotations, Translations and Isolator Elongations Incurred During Earth Point Tracking - Table 9-2 gives the pedestal peak y axis rotations and x axis CM translations incurred during earth point tracking for the cases discussed above.

Table 9-2. Peak Pedestal Rotations and CM Translations Incurred During Earth Point Tracking

ORBITAL ALTITUDE (KM)	PEDESTAL PEAK Y AXIS ROTATION (rad)	PEDESTAL PEAK Y AXIS ROTATION (deg)	PEDESTAL PEAK X AXIS CM TRANSLATION (mm)	PEDESTAL PEAK X AXIS CM TRANSLATION (in)
160	0.1141	6.54	65.76	2.589
240	0.1138	6.52	65.94	2.596
320	0.1116	6.394	65.89	2.594
400	0.1099	6.297	66.45	2.616
480	0.1095	6.274	67.76	2.668

Examination of table 9-2 indicates that the pedestal rotations and corresponding CM translations are essentially constant for the cases investigated. Since the peak torque required in each case was kept constant at 16 n-m, this implies that the pedestal translations and rotations depend to first order on the peak torque required to earth point track, and does not depend on the rate of change of the required torque (i.e., its frequency characteristics). This is the case since the rate of change of torque required to earth point track is still well below the bandwidth of the pointing control loop and isolator dynamics so that the angular rotations and CM translations of pedestal reach the same peak values although the points in time which these values occur change as the orbital altitude changes.

The isolator elongations associated with the pedestal rotations and translations given in table 9-2 is approximately 33 mm (1.29 in) which is still too large to be accommodated by the Coincident Gimbal suspension system design. Hence the telescope inertia that could be accommodated during earth point tracking is limited by allowable isolator elongations rather than the gimbal torque limitation, and a determination should be made of the telescope inertias that could be accommodated at various altitudes while yielding acceptable isolator elongations.

9.5 Techniques for Improving Telescope Tracking Accuracy During Earth Point Tracking - It has been shown in section 9.3 that the incurred telescope tracking error is primarily dependent on orbital altitude and essentially independent of telescope inertia as long as the loop bandwidth remains constant. Referring to figure 9-54 it is seen that a 1 arc-second peak tracking error during earth point tracking can only be maintained if the orbital altitude is greater than 420 Km for a 2 Hz pointing control loop bandwidth using angular rate and position commands. Since many earth pointing experiments are slated to fly at lower altitudes a method for improving tracking accuracy is desirable. One possible way of improving earth point tracking accuracy is to add a torque command to the angular rate and position commands already being implemented. One possibility that comes to mind is to add a torque command whose functional form will be the same as the orbital acceleration profile given in equation (8-23). However, as pointed out in section 9.1, the constant that would multiply the orbital acceleration profile would have to be greater than the telescope inertia about the hinge point. A method of determining the constant that would multiply the acceleration profile would be to set that constant times the peak acceleration at the time the peak torque occurs equal to the peak torque that is required to

perform earth tracking for a particular telescope at a particular altitude. It is clear that if this technique is to work then the control torque required to earth point track cannot deviate from the command torque which is functionally the same as the acceleration profile to any "large" extent. It should be noted that not only is the magnitude of the difference important but the rate at which the torque divergence takes place is of critical importance since that determines the degree of effectivity of the integral control. In order to determine just what the deviations in the actual required control torque are from the command torque which is characterized as described above, a 160 Km orbit with telescope and inertia mass characteristics that were one-half the nominal values described in table 2-1 and the recommended suspension parameters was chosen as a test case. Figures 9-55 through 9-75 show system response for this case.

Using equation (8-23) the torque command profile can be written as

$$T_c = -J_E \omega_o^2 \left\{ \frac{R_e h (R_e + h)(2R_e + h) \sin[\omega_o t - \theta_o]}{[R_e^2 + (R_e + h)^2 - 2R_e(R_e + h)\cos(\omega_o t - \theta_o)]^2} \right\} \qquad (9\text{-}11)$$

where

θ_o = Orbital angle with respect to local vertical where earth point tracking commences.

J_E = Constant that multiplies the angular acceleration profile

For the 160 Km example cited the following numerical values for the terms in equation 9-11 apply

$\omega_o = 1.195 \times 10^{-3}$ rad/sec

$\theta_o = 2.036 \times 10^{-2}$ rad/sec

$R_e = 6378$ Km

$h = 160$ Km

The point in time at which the peak control torque of -16.4 n-m occurs is at 25.508 seconds into the run. However, the peak acceleration that occurs in the neighborhood of this time actually occurs at 29 seconds into the run. Hence, if the constant J_E

is determined by requiring that the command torque and the actual required torque match at the point in time that the peak control torque occurs, the command torque would still be increasing until 29 seconds is reached. Performing the actual computations the angular acceleration at 25.08 seconds, the point at which the peak control torque of -16.4 n-m occurs, is equal to 1.397×10^{-3} rad/sec. The peak angular acceleration which occurs at 29 seconds is equal to 1.512×10^{-3}. Hence if equation (9-11) were used as the command torque profile the torque that would be commanded at 29 seconds would be equal to

$$T_c\Big|_{29sec} = 16.4\left(\frac{1.512 \times 10^{-3}}{1.397 \times 10^{-3}}\right) = 17.75 \text{ n-m} \qquad (9\text{-}12)$$

The control torque is actually required at 29 seconds is -12.8 n-m or a difference of 4.95 n-m. This torque difference that must be made up by the control system is appreciable but perhaps even more importantly this torque difference occurs over four seconds of time. This makes the rate of divergence between the actual required torque and the command torque profile given by equation (9-11) appreciable which means that the integral control will not be very effective. The same behavior between peak acceleration and peak control torque is exhibited at the other altitudes investigated. Thus, although it is anticipated that using a torque command profile as described by equation (9-11) would reduce the telescope tracking error than those that are presently incurred without it, it is doubtful that a tracking accuracy of $\pm$ 1 arc-second could be achieved. If such accuracies are desirable then the torque command profile would have to be more complicated than that shown in equation (9-11). It is therefore recommended that system performance with the command profile shown in equation (9-11) and the form of the torque profiles that would be required to yield $\pm$ 1 arc-second tracking errors should be the subject of future study.

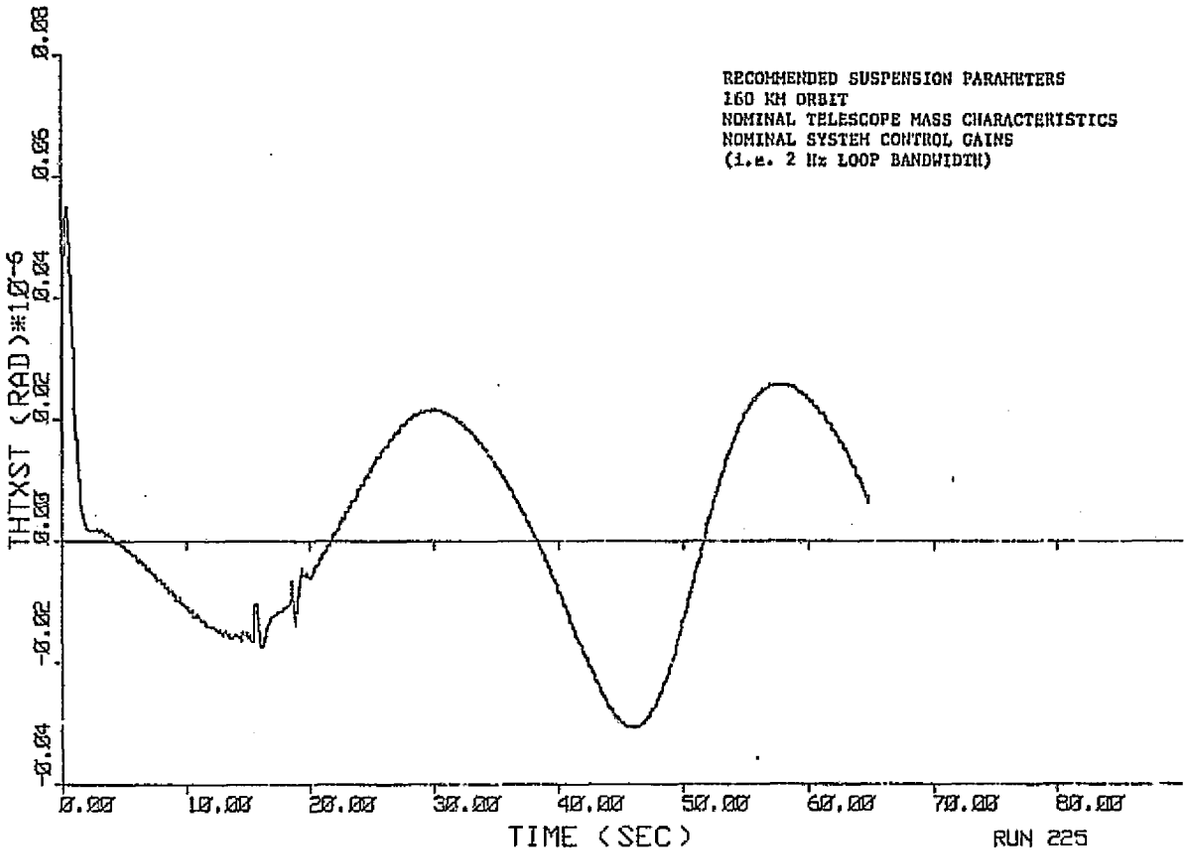

Figure 9-1. Telescope x-Axis Tracking Error

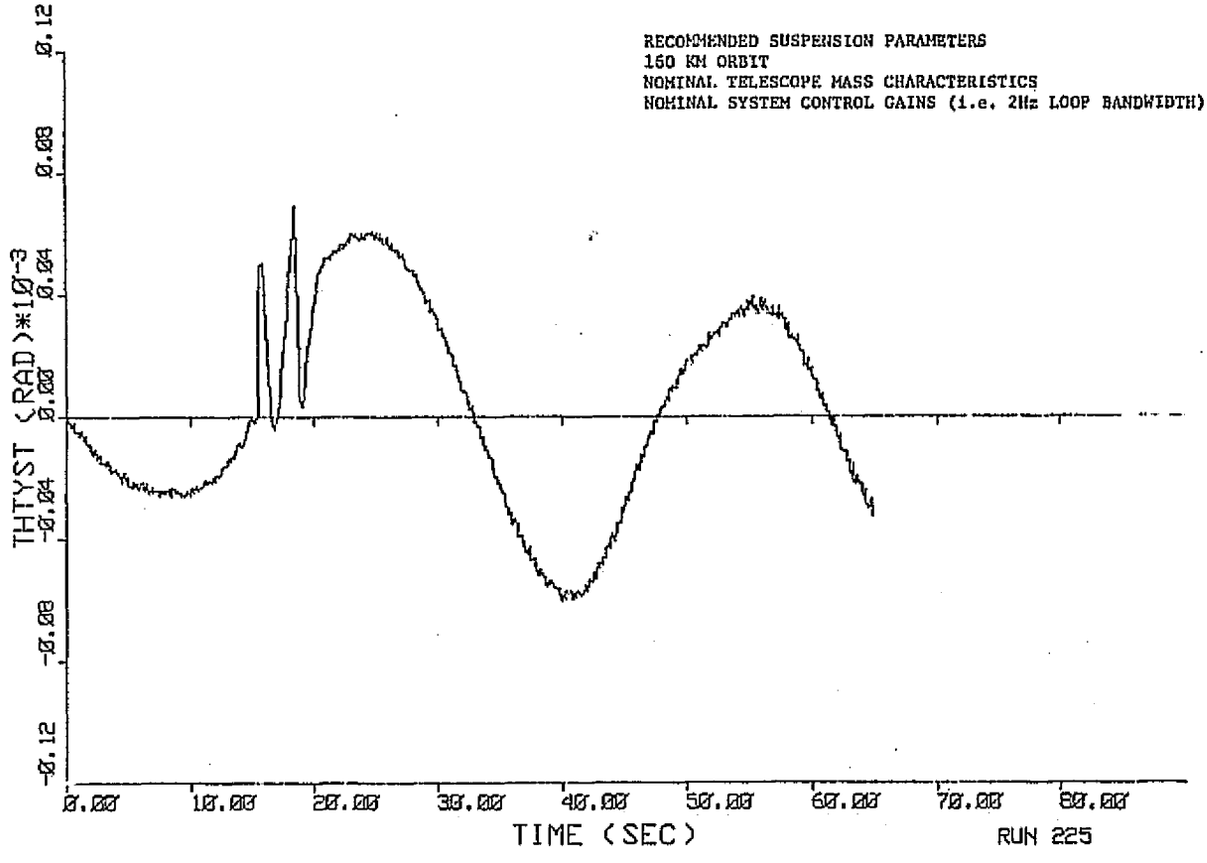

Figure 9-2. Telescope y-Axis Tracking Error

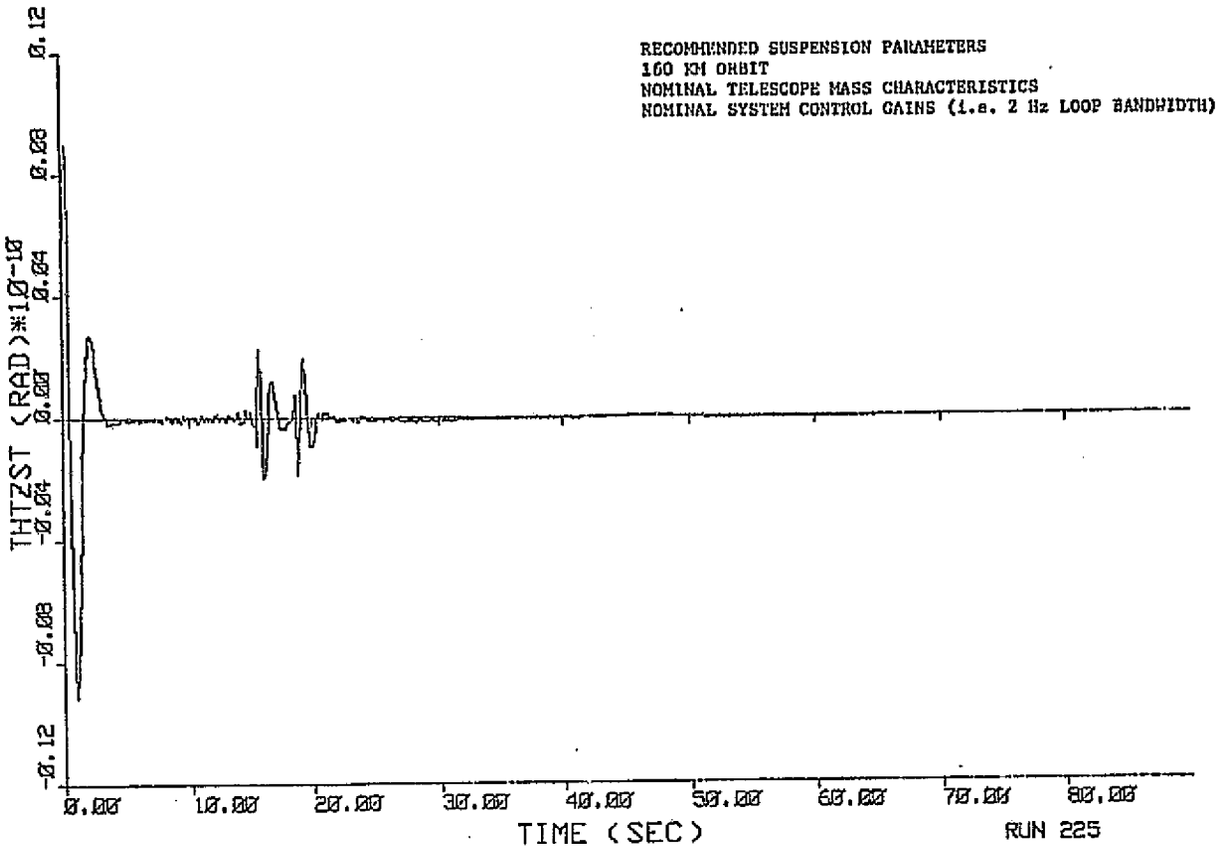

Figure 9-3. Telescope z-Axis Tracking Error

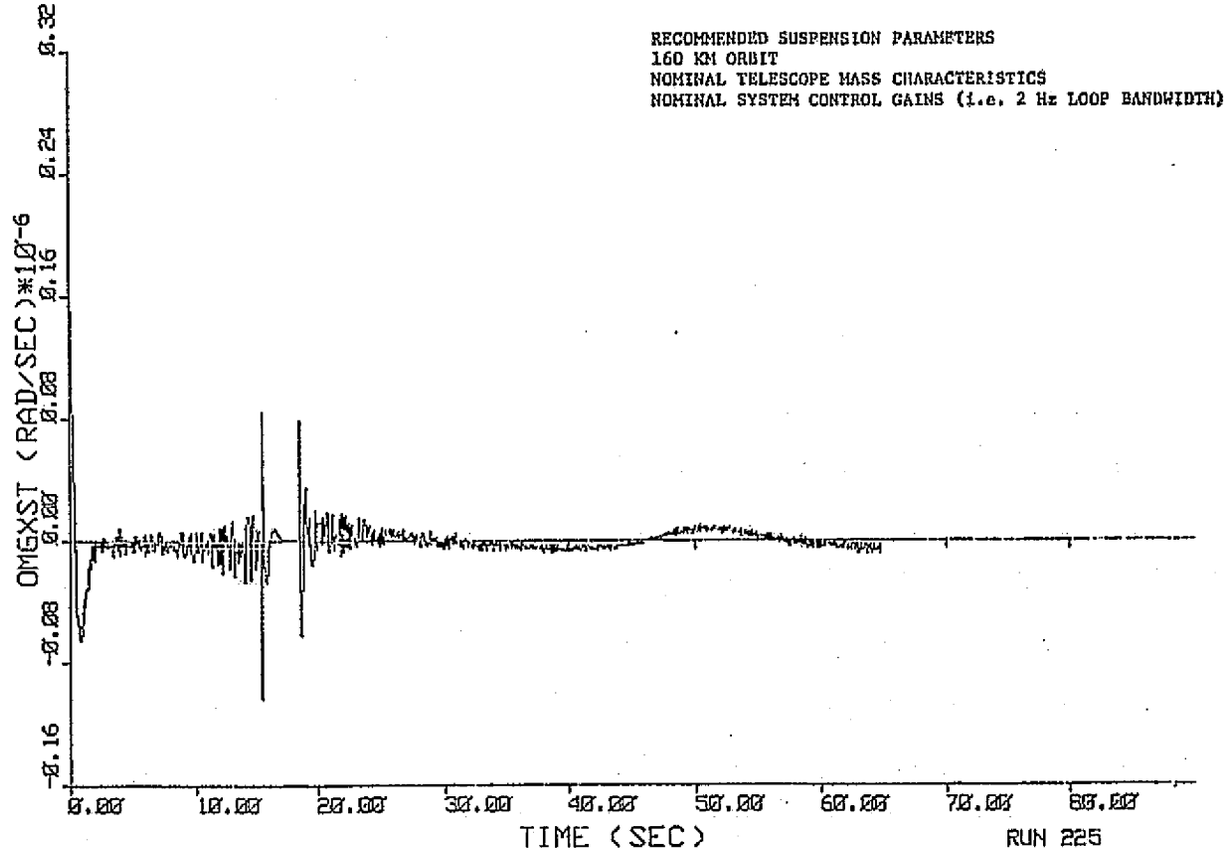

Figure 9-4. Telescope x-Axis Tracking Rate Error

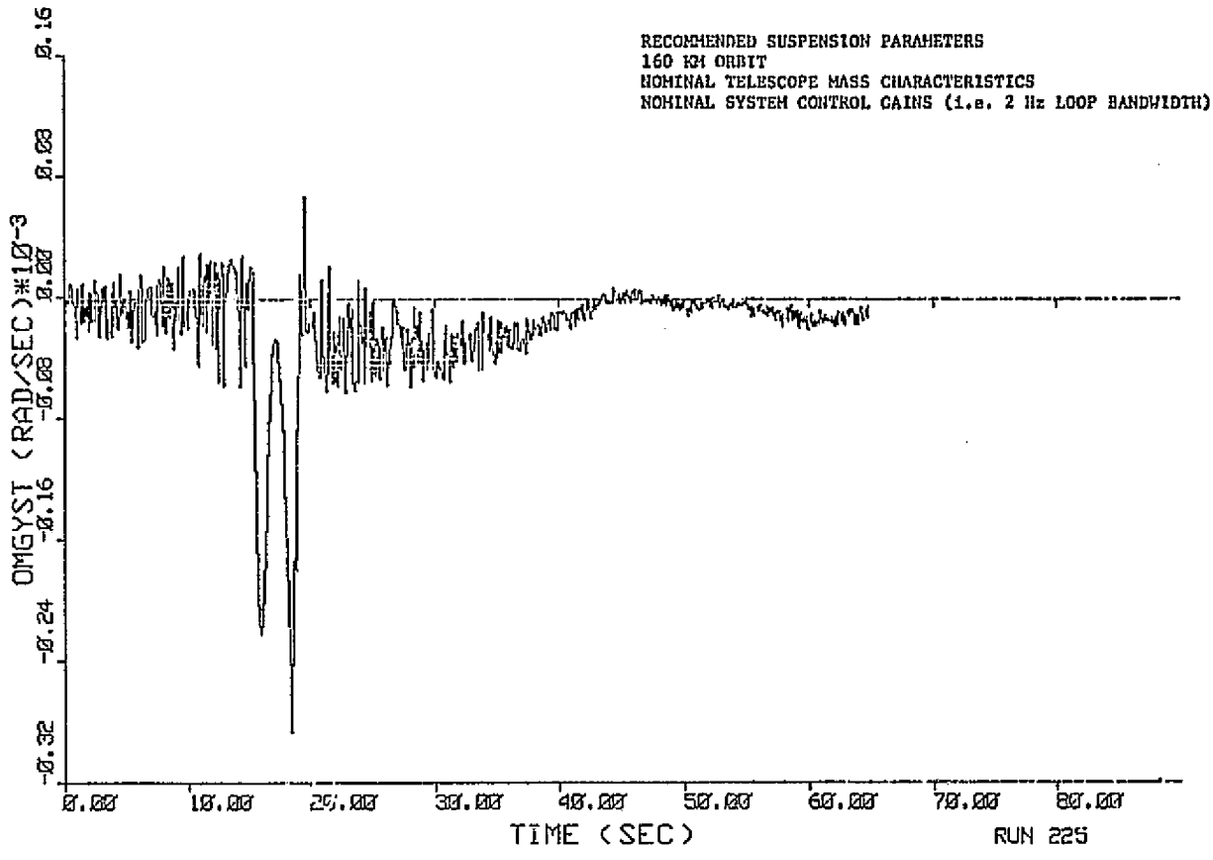

Figure 9-5. Telescope y-Axis Tracking Rate Error

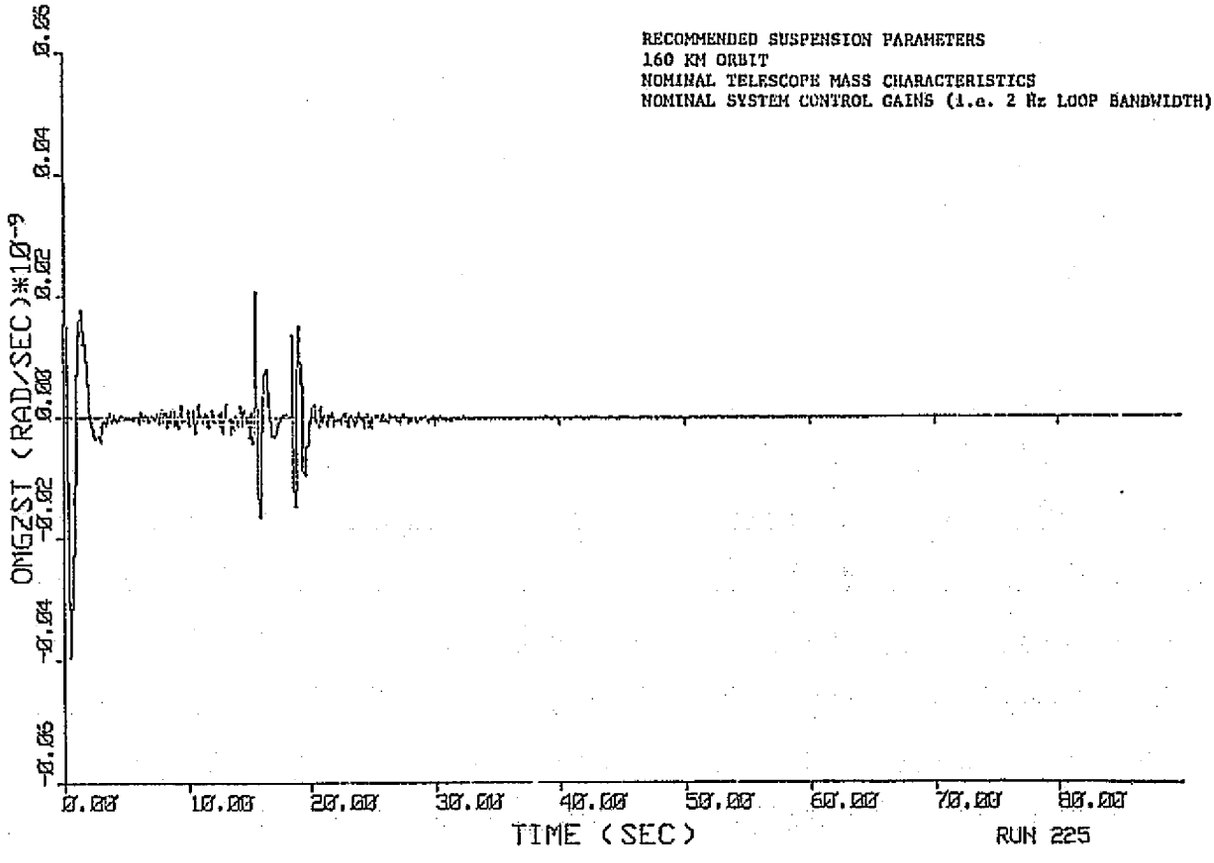

Figure 9-6. Telescope z-Axis Tracking Rate Error

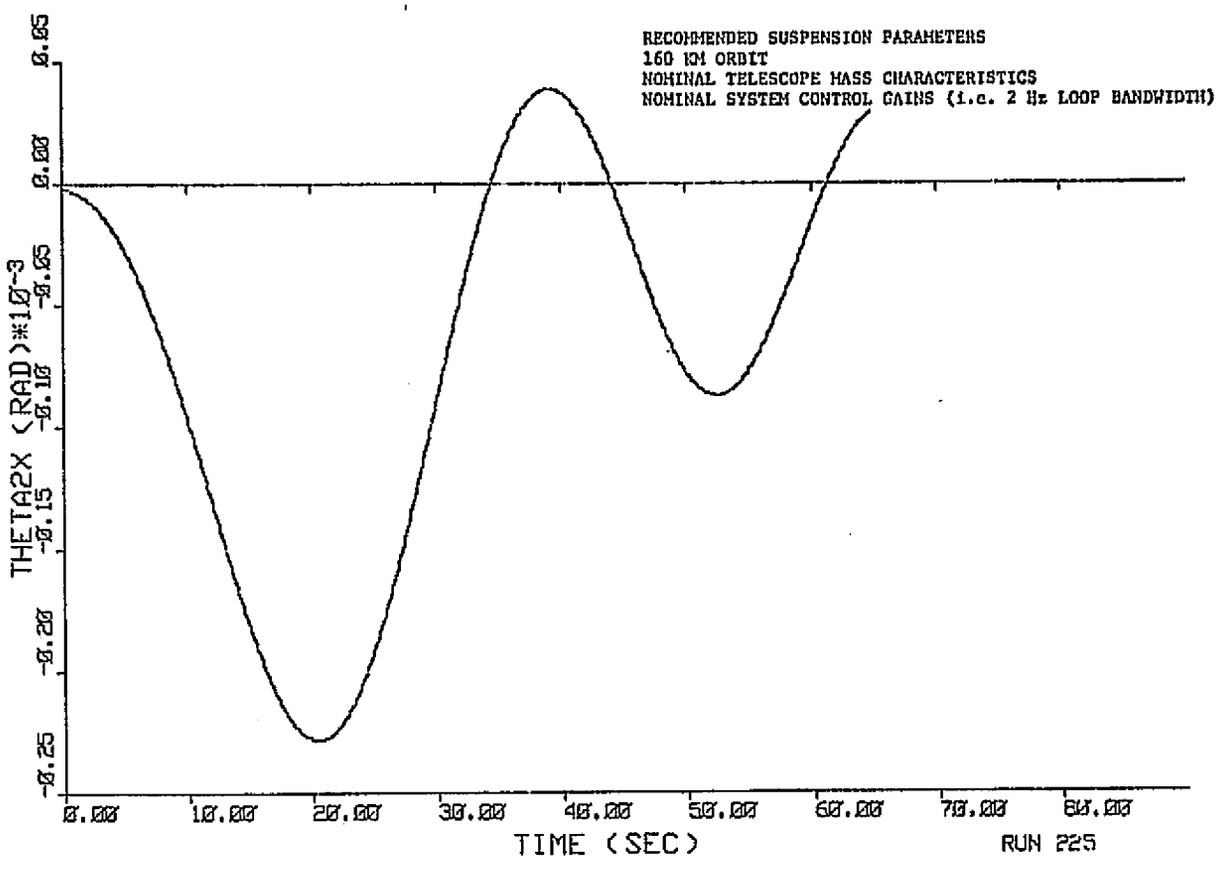

Figure 9-7. Pedestal x-Axis Rotation

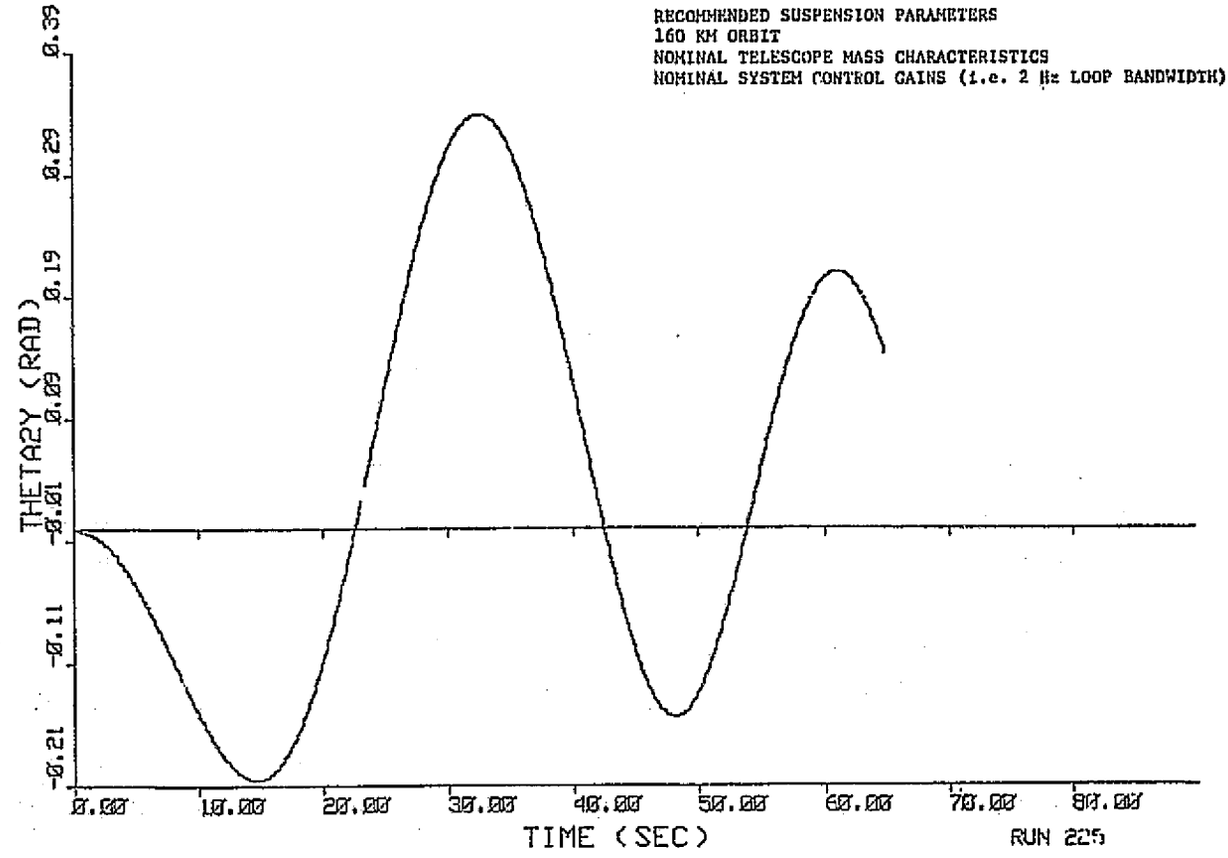

Figure 9-8. Pedestal y-Axis Rotation

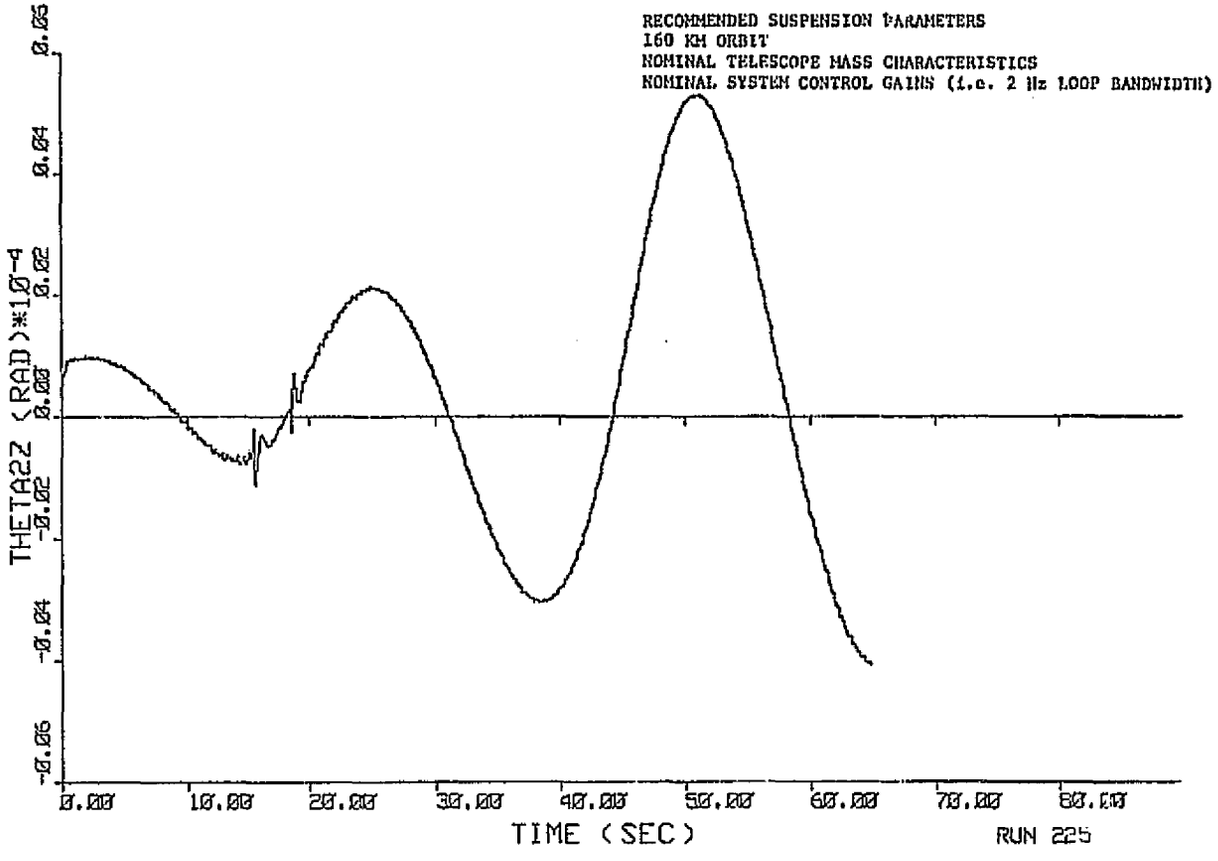

Figure 9-9. Pedestal z-Axis Rotation

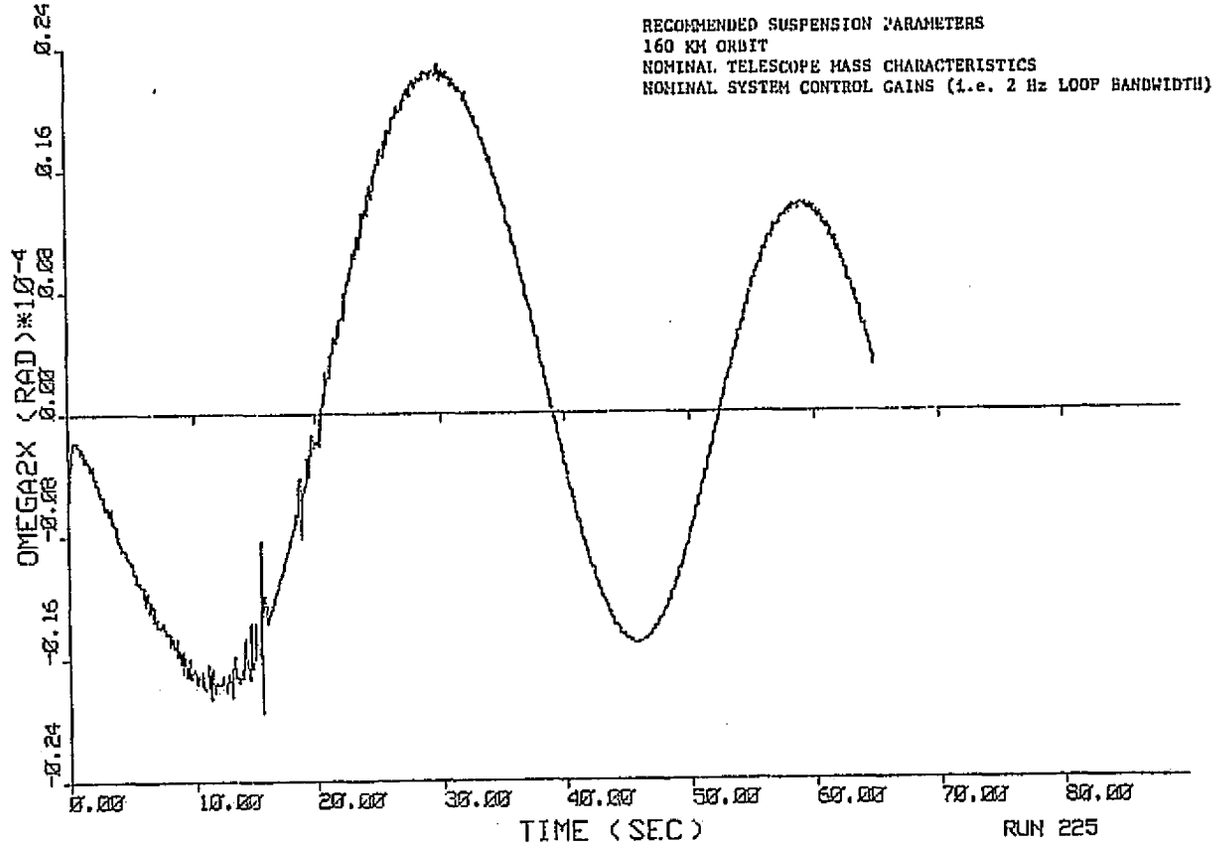

Figure 9-10. Pedestal z-Axis Rate

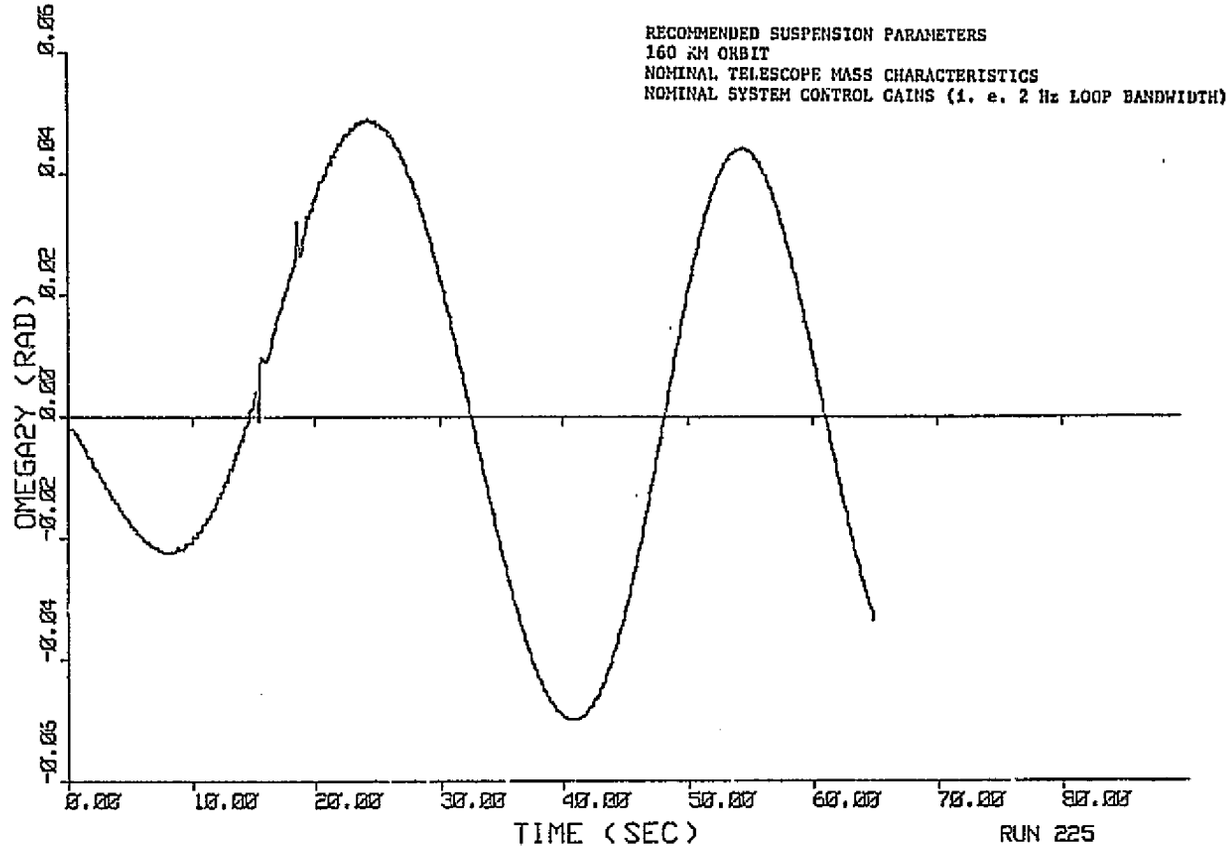

Figure 9-11. Pedestal y-Axis Rate

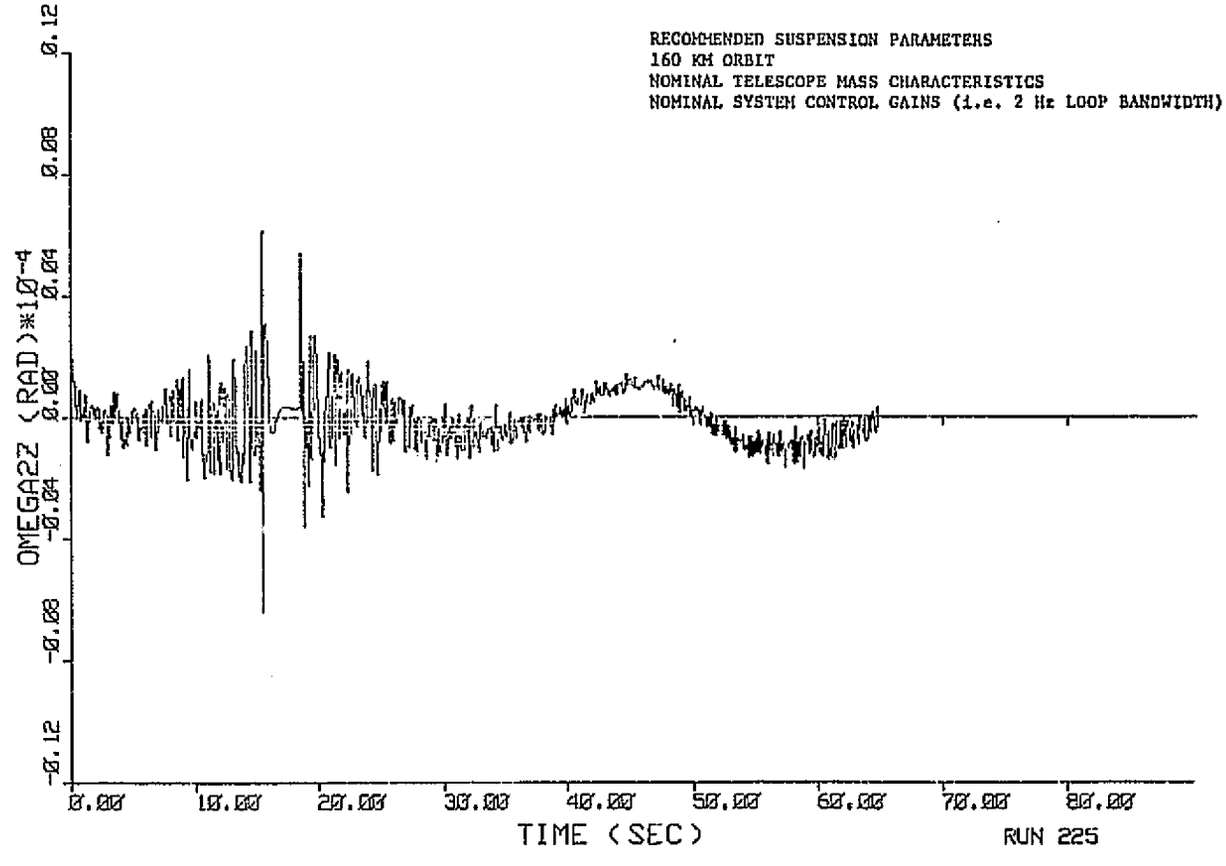

Figure 9-12. Pedestal z-Axis Rate

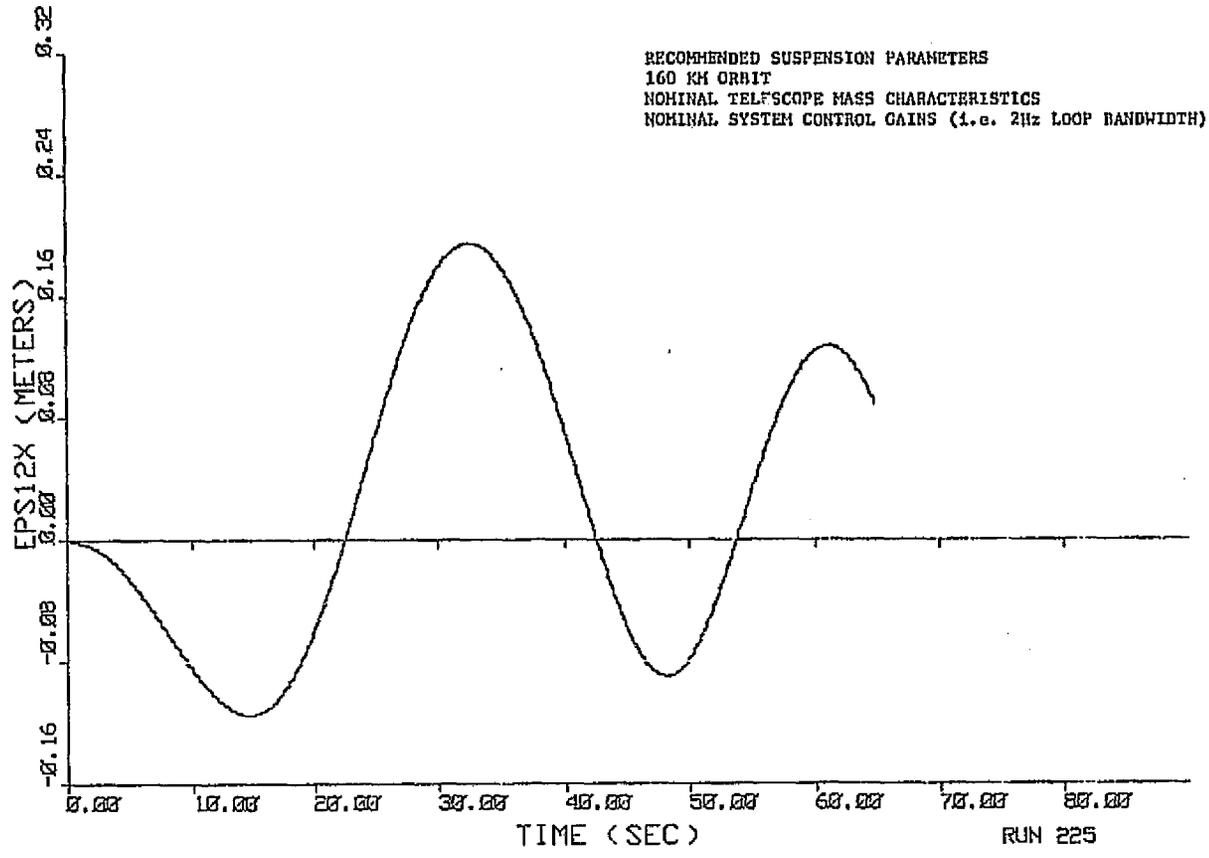

Figure 9-13. Pedestal x-Axis CM Translation

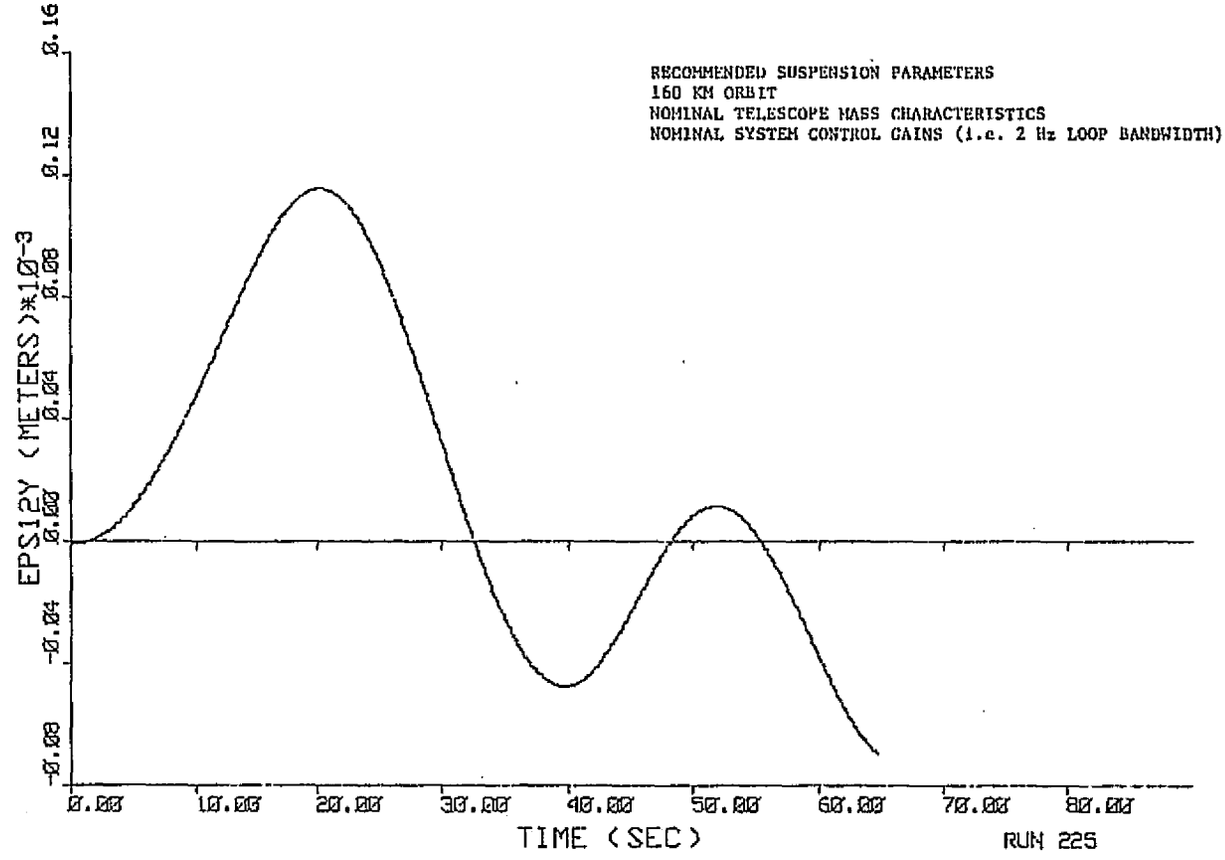

Figure 9-14. Pedestal y-Axis CM Translation

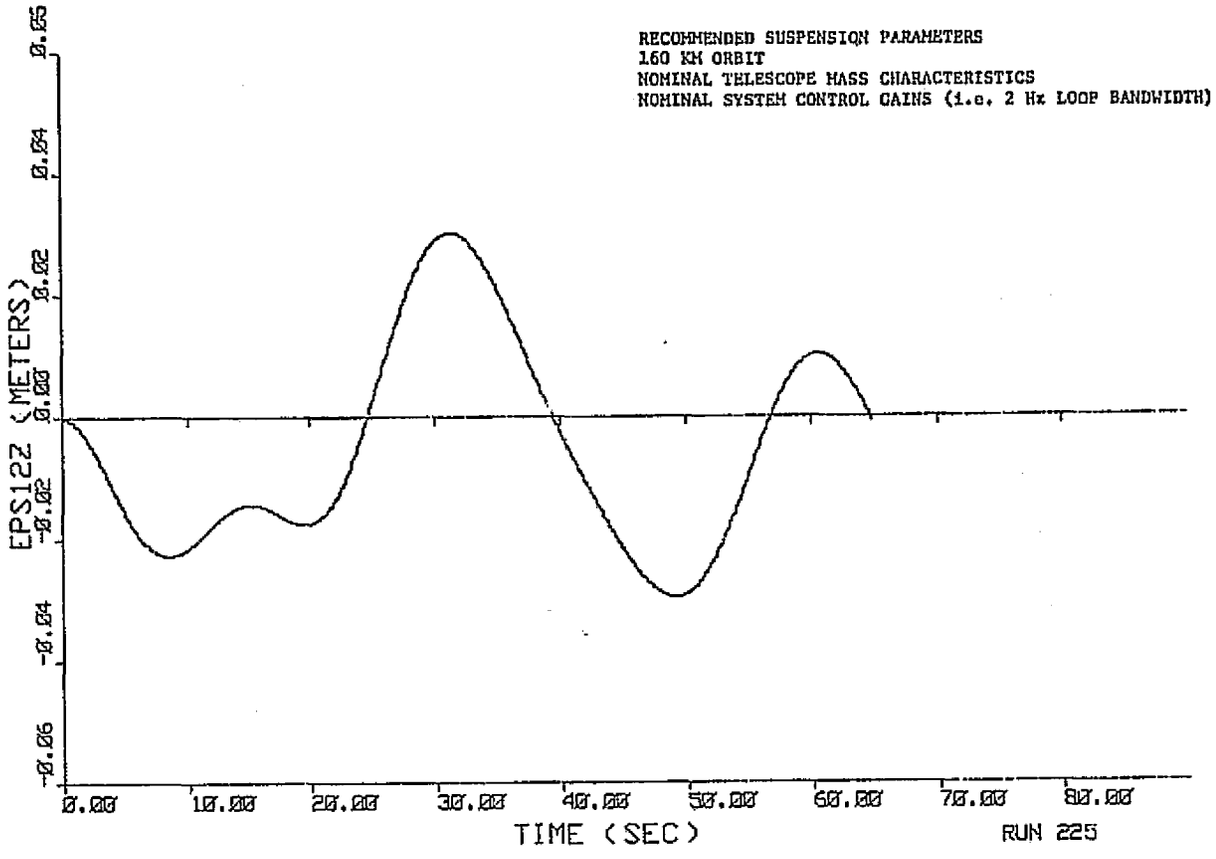

Figure 9-15. Pedestal z-Axis CM Translation

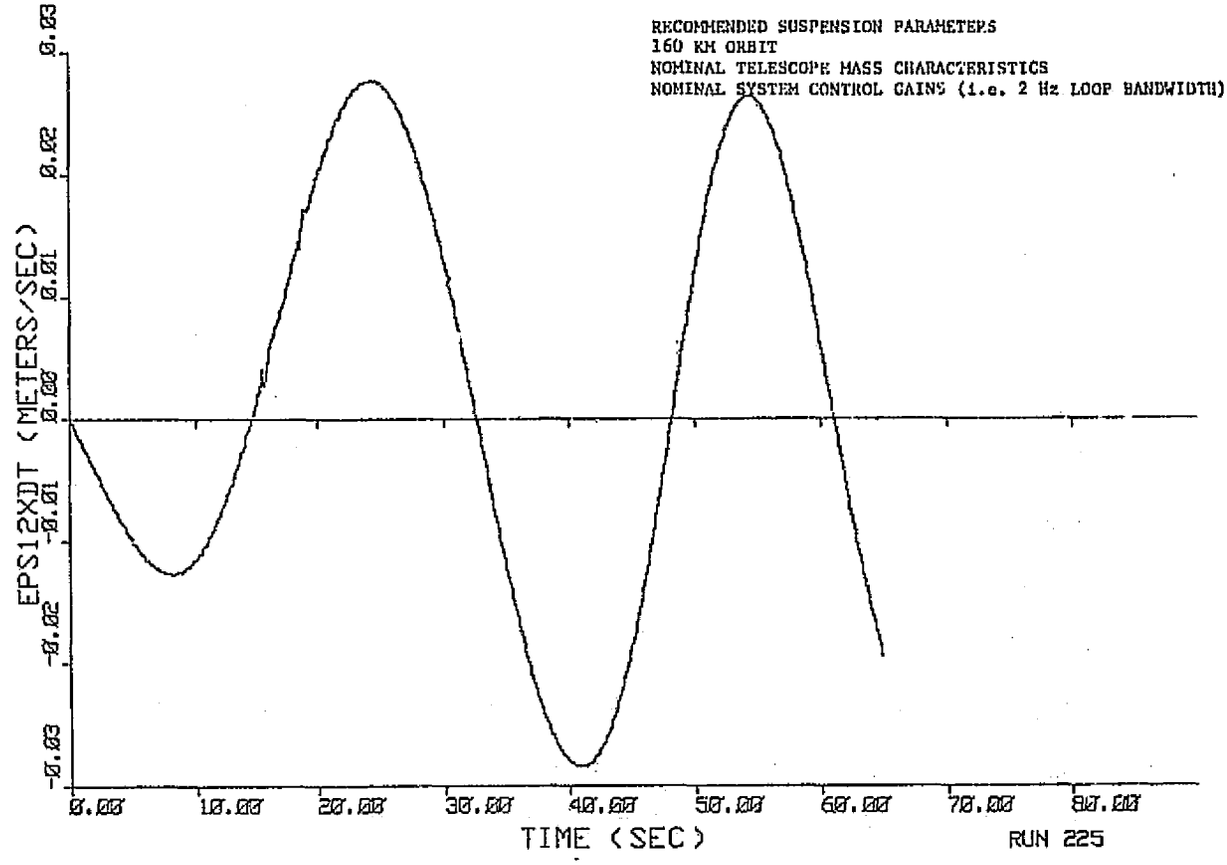

Figure 9-16. Pedestal x-Axis CM Velocity

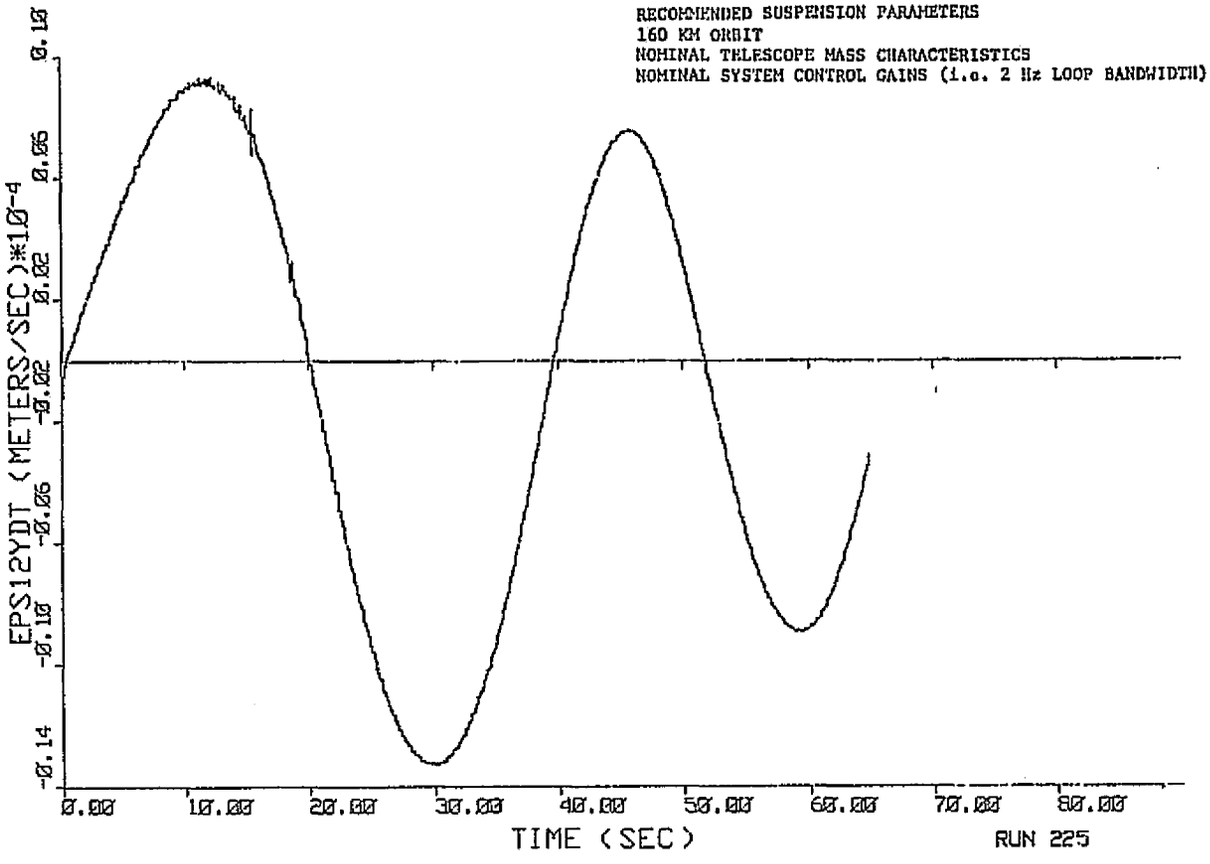

Figure 9-17. Pedestal y-Axis CM Velocity

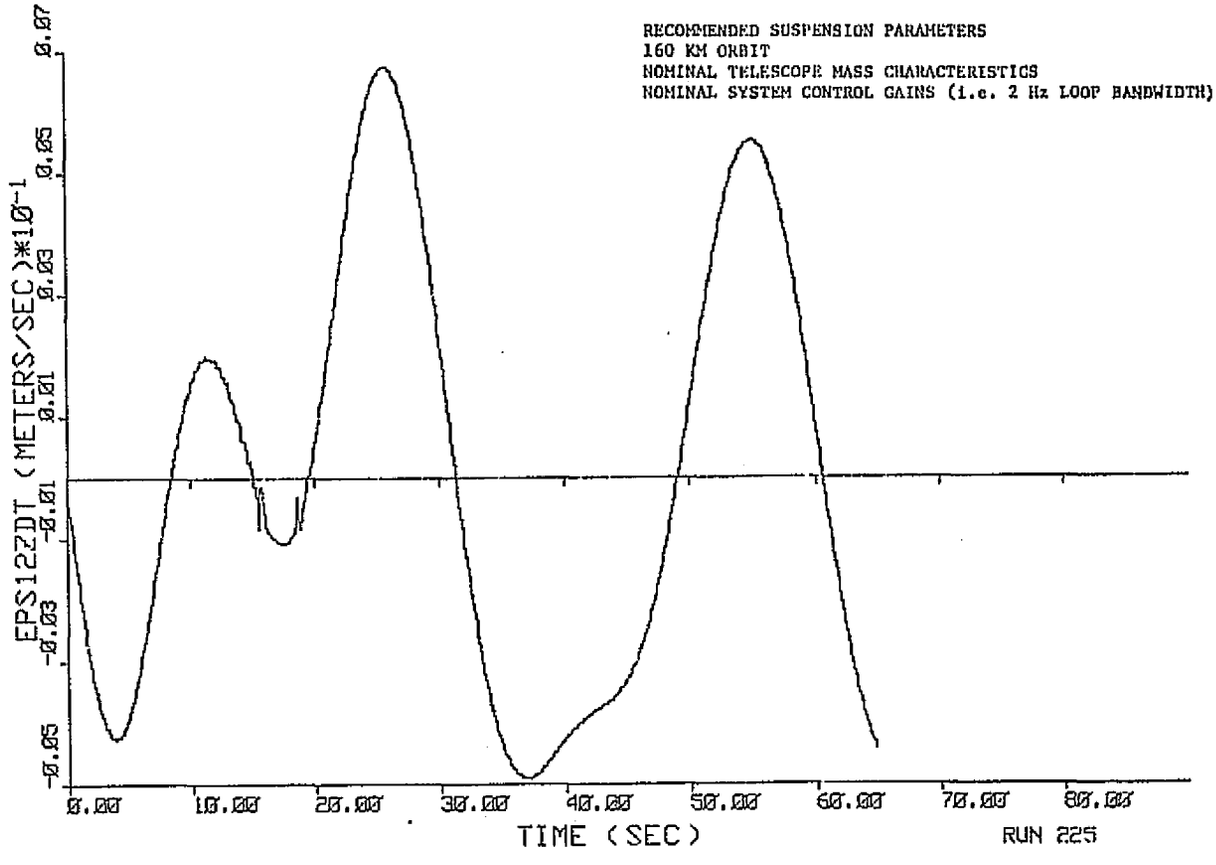

Figure 9-18. Pedestal z-Axis CM Velocity

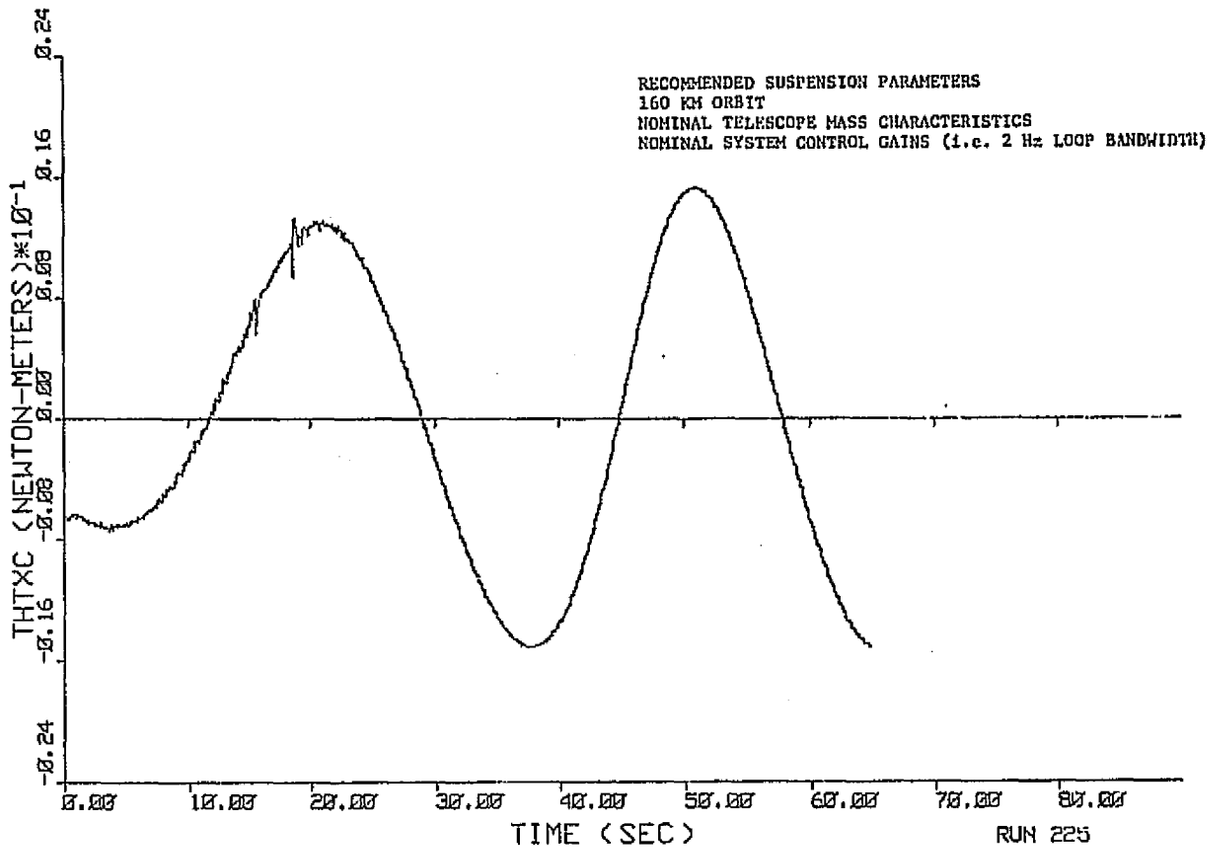

Figure 9-19. x-Axis Control Torque

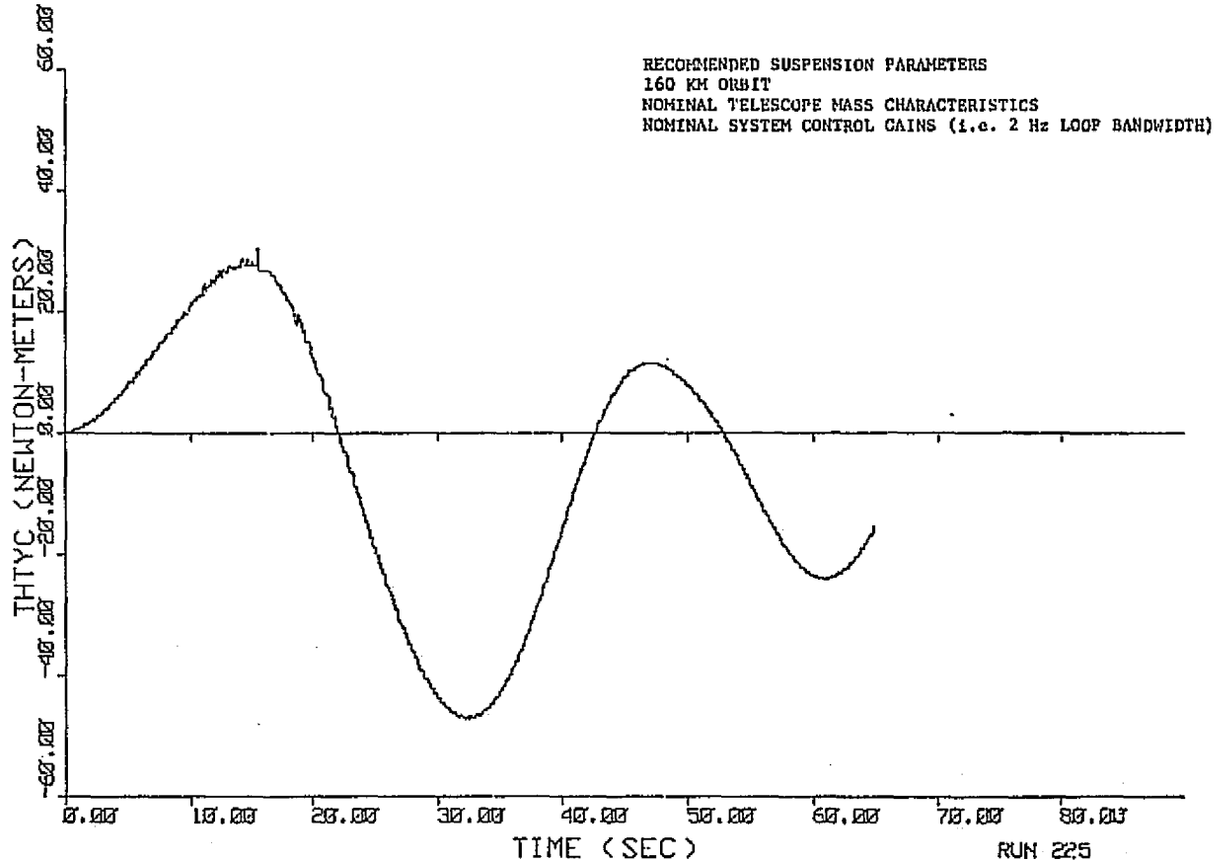

Figure 9-20. y-Axis Control Torque

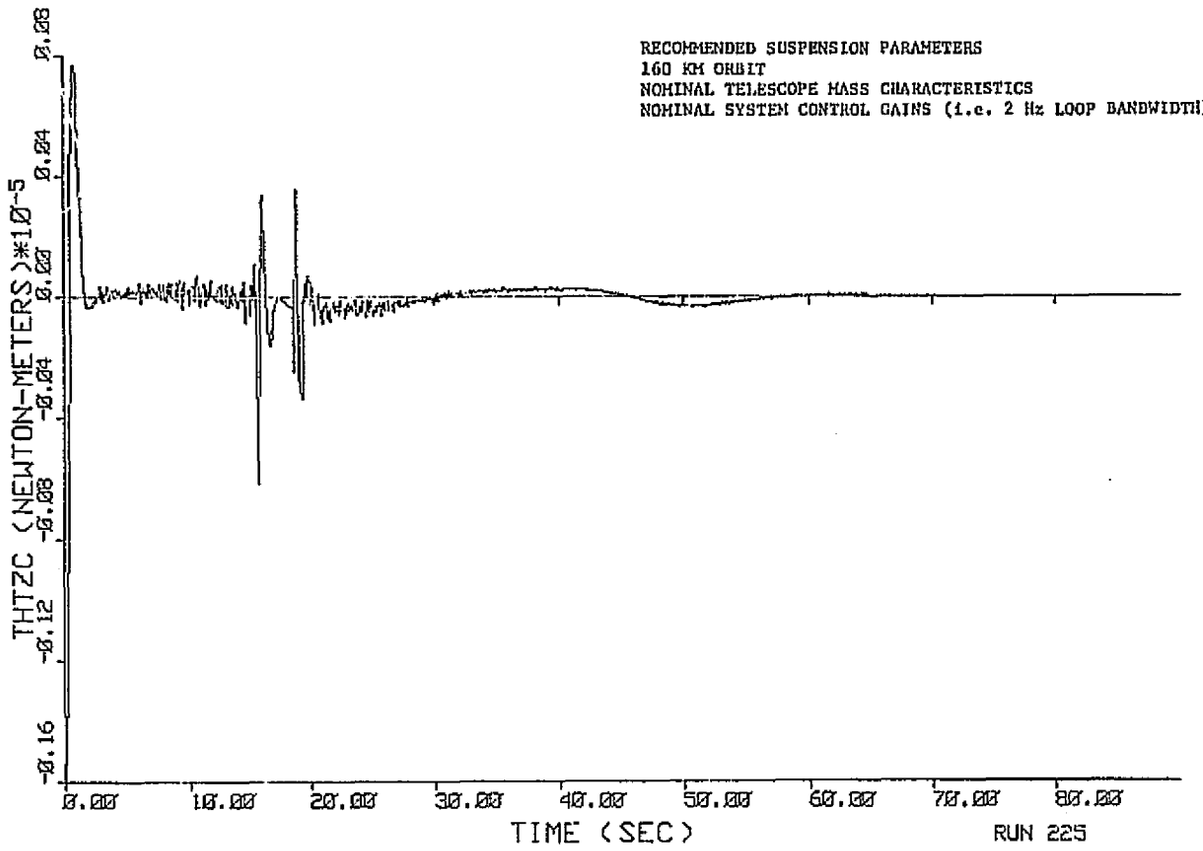

Figure 9-21. z-Axis Control Torque

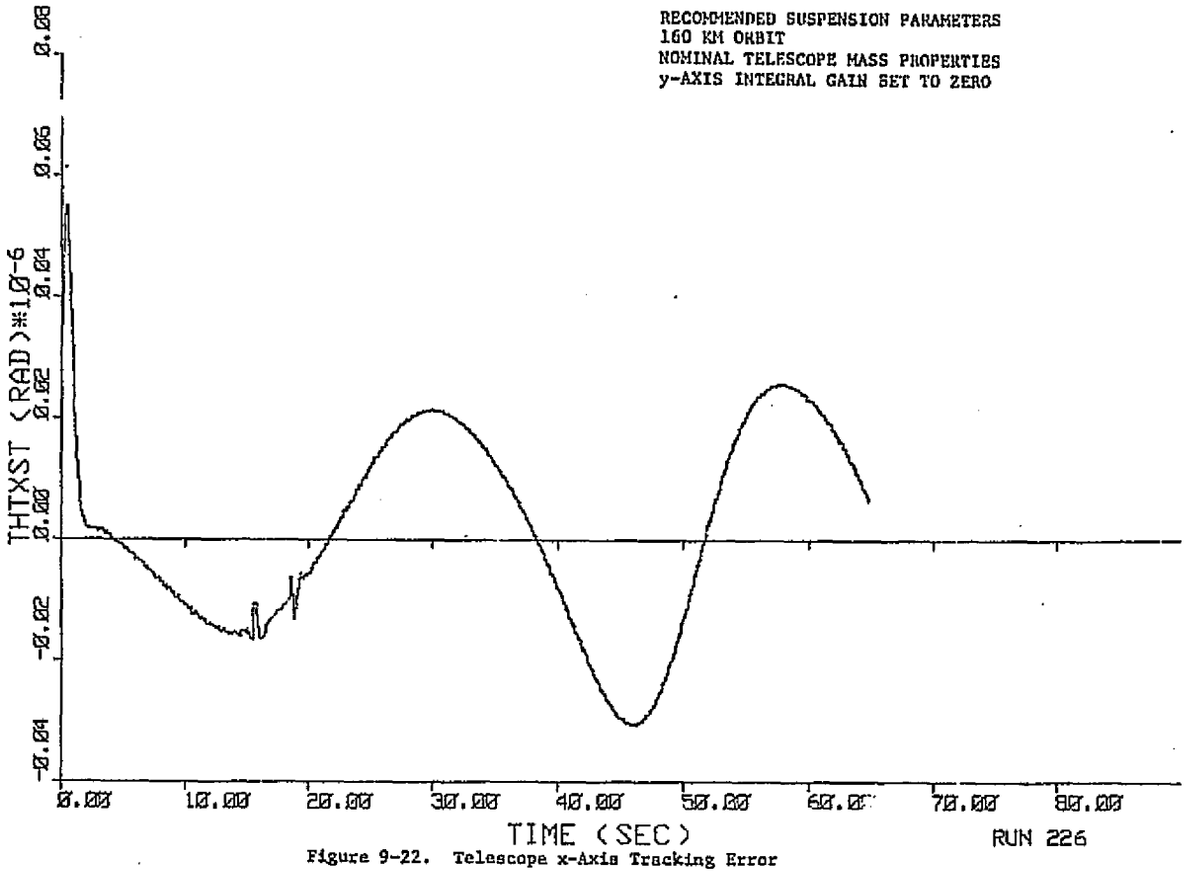

Figure 9-22. Telescope x-Axis Tracking Error

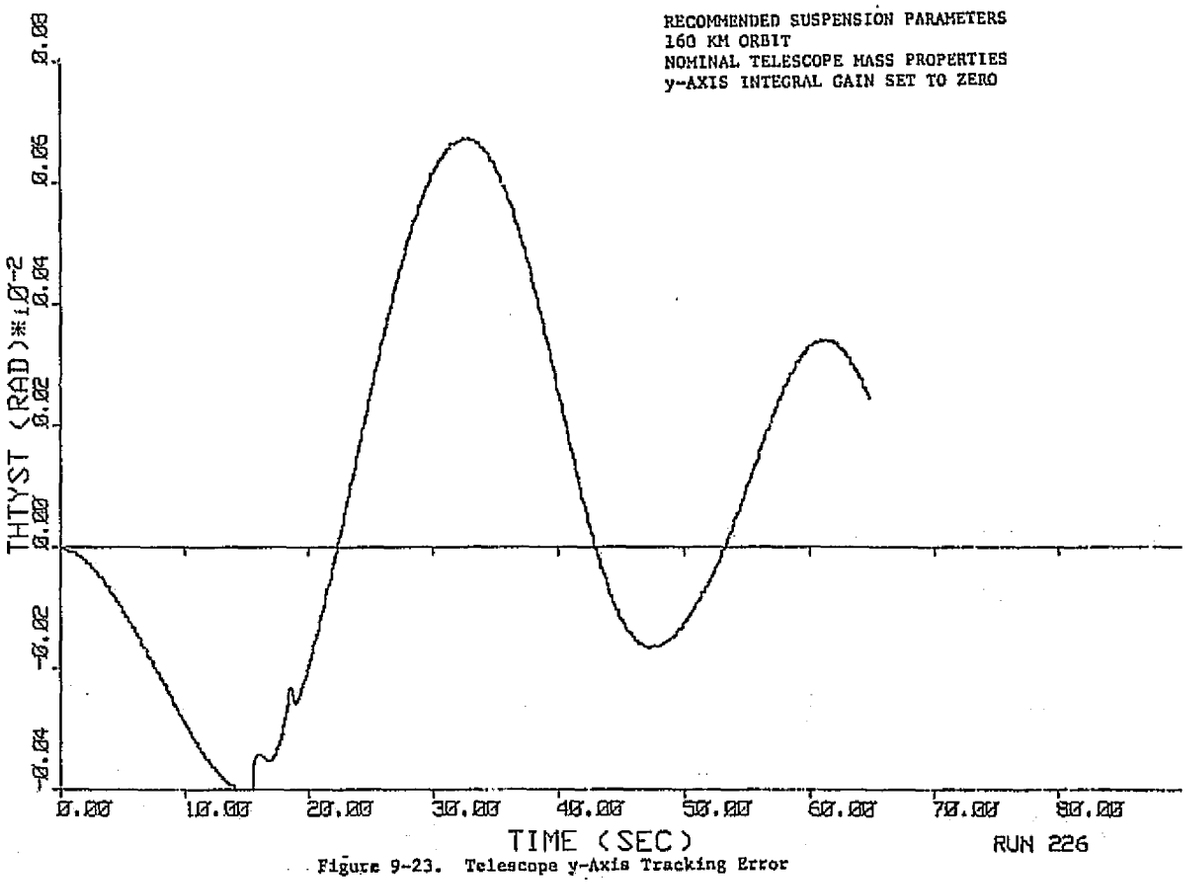

Figure 9-23. Telescope y-Axis Tracking Error

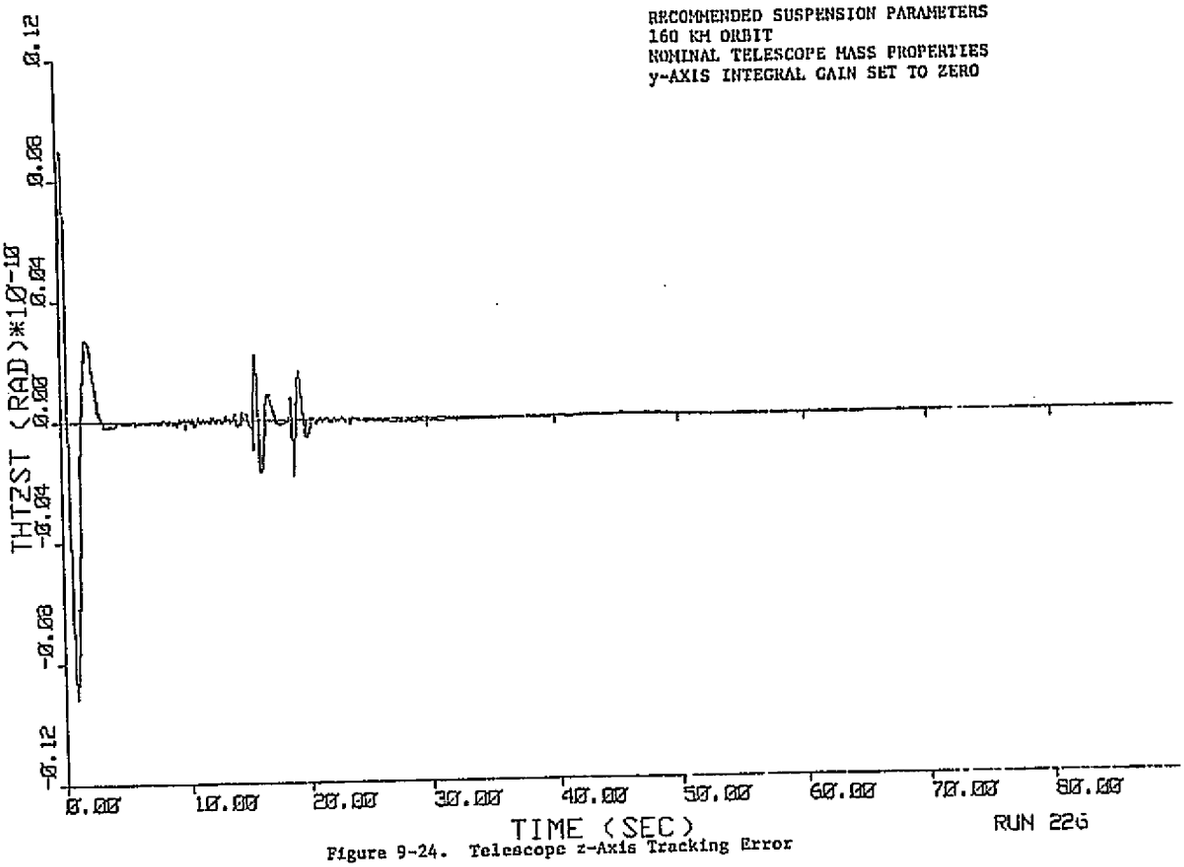

Figure 9-24. Telescope z-Axis Tracking Error

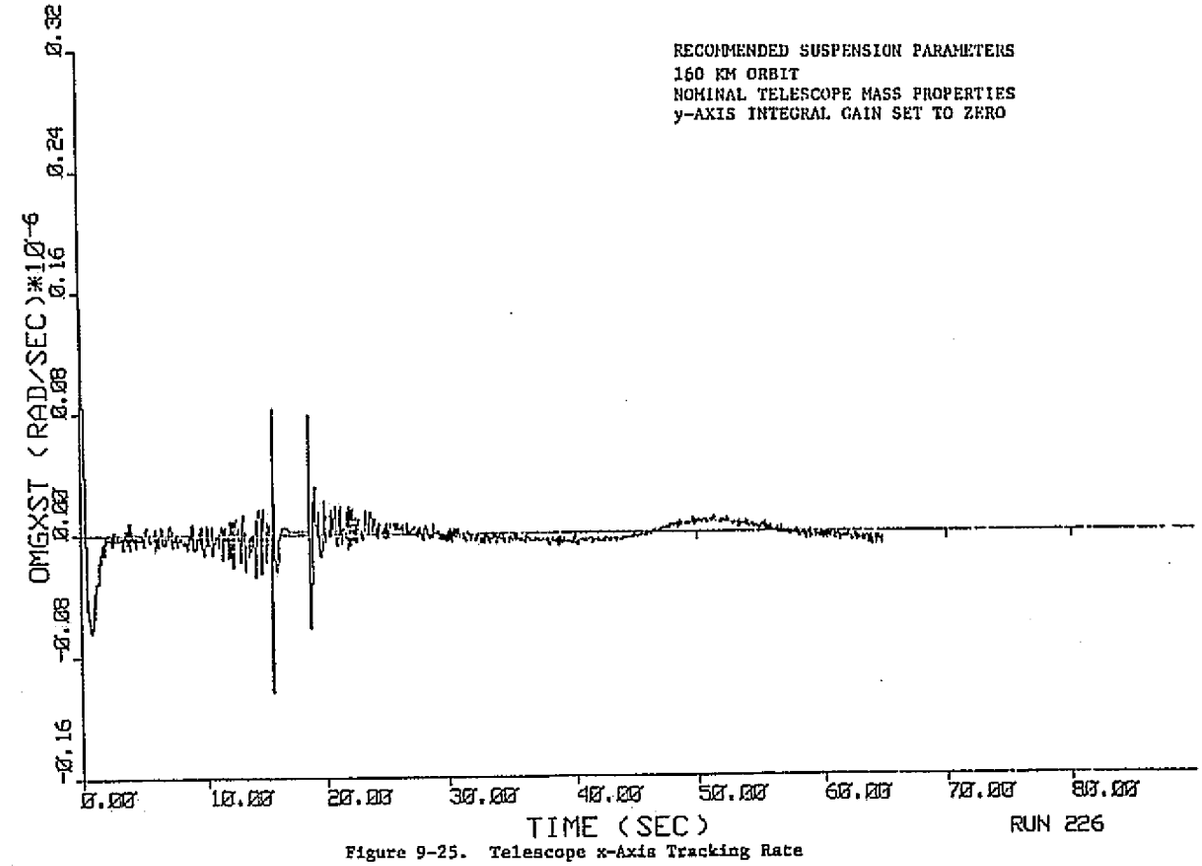

Figure 9-25. Telescope x-Axis Tracking Rate

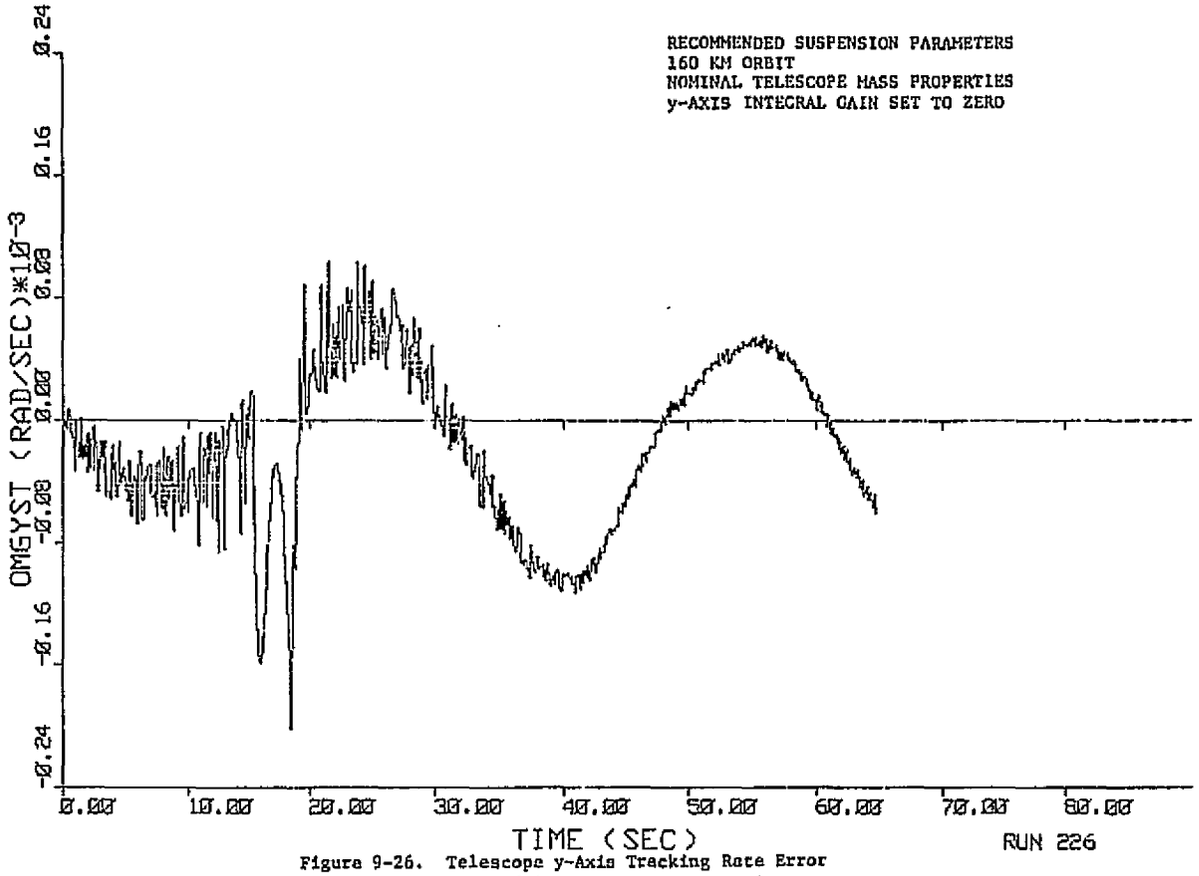

Figure 9-26. Telescope y-Axis Tracking Rate Error

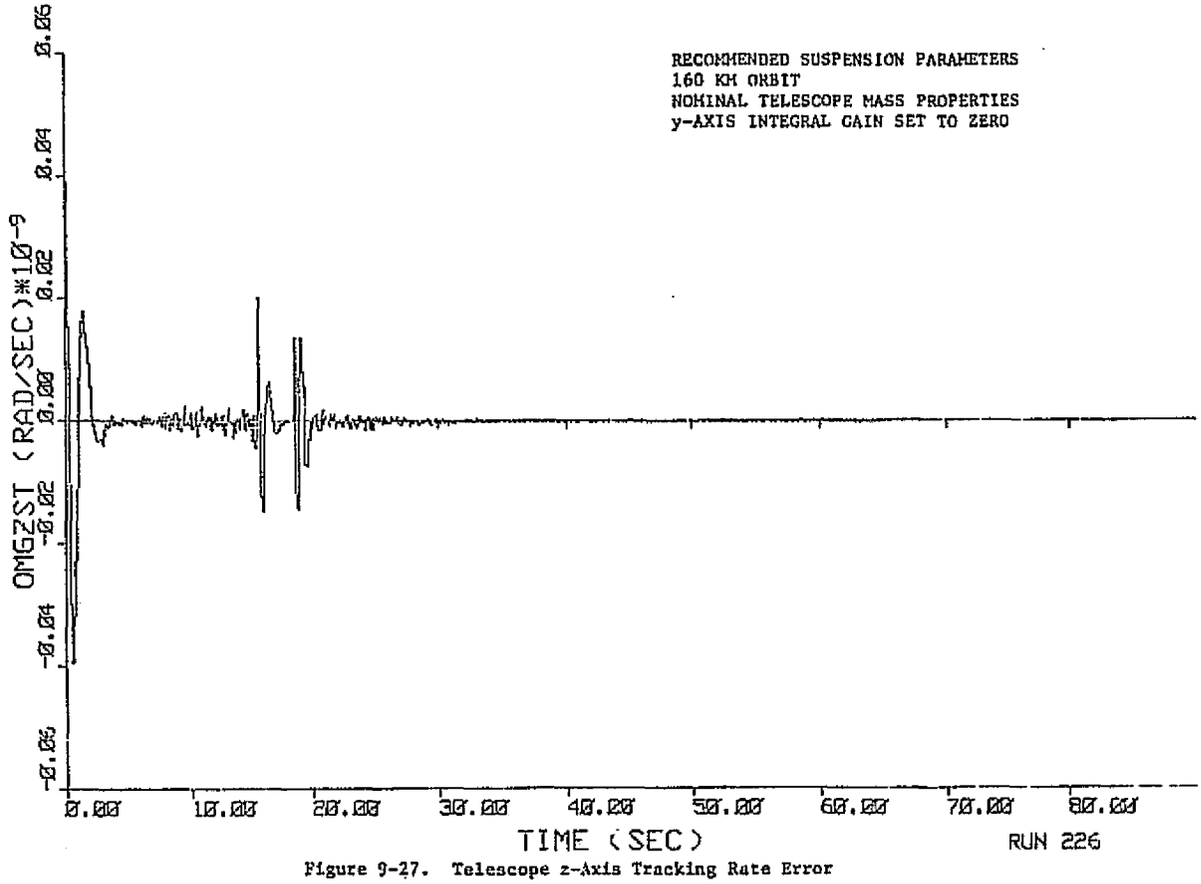

Figure 9-27. Telescope z-Axis Tracking Rate Error

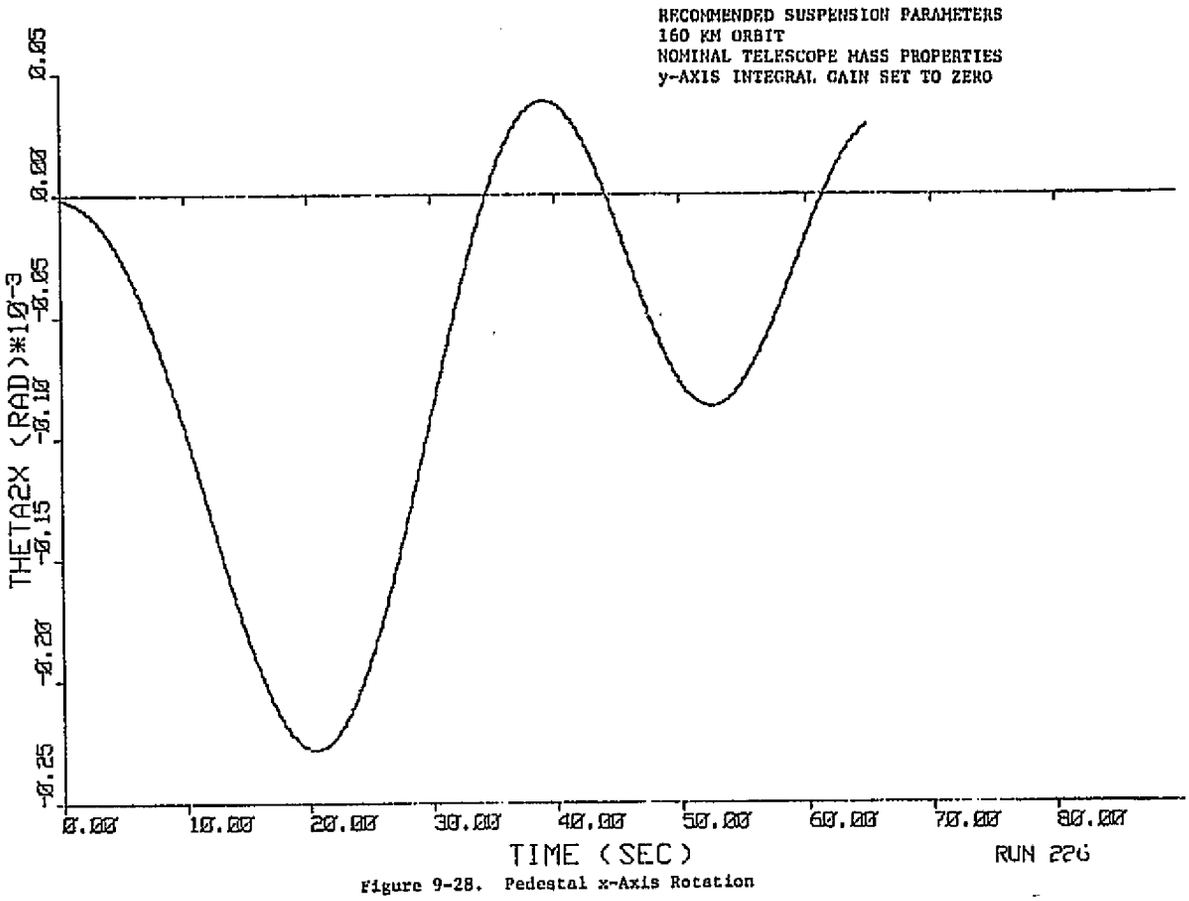

Figure 9-28. Pedestal x-Axis Rotation

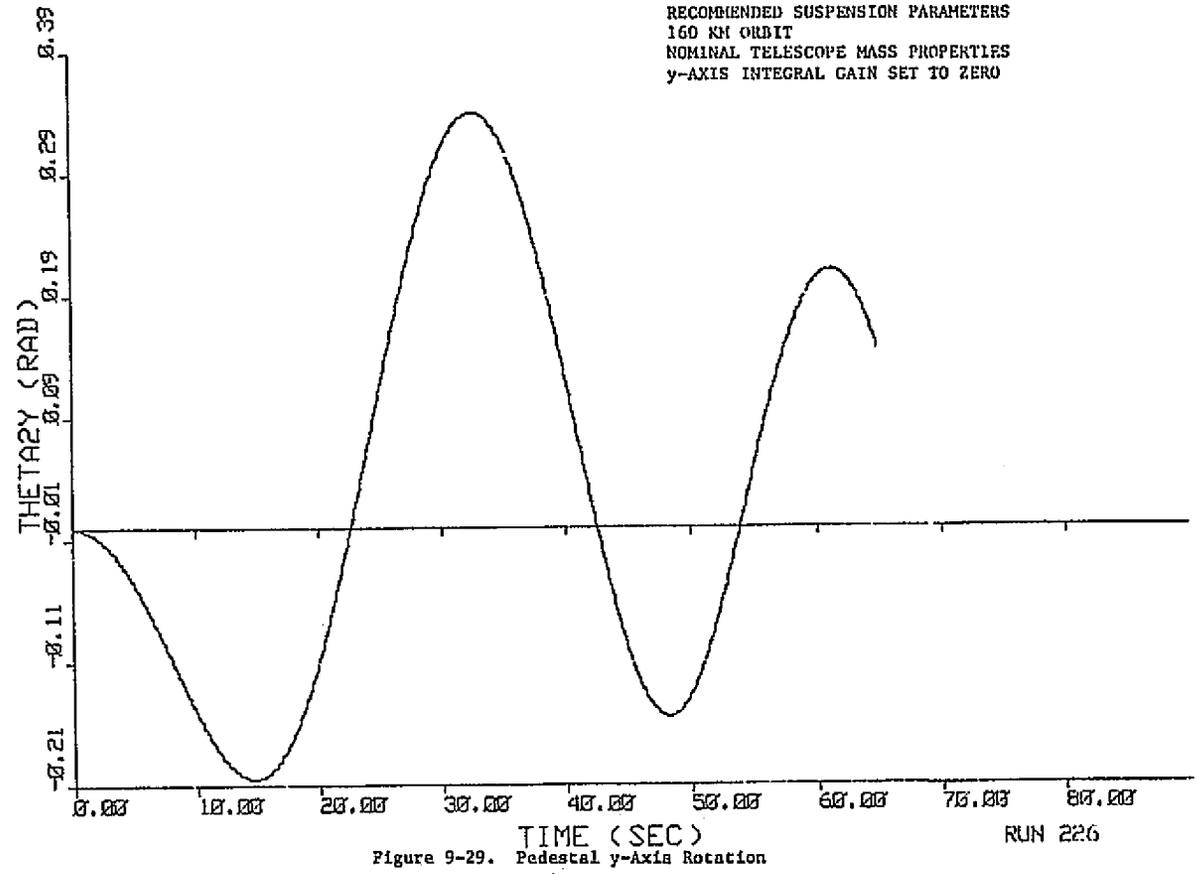

Figure 9-29. Pedestal y-Axis Rotation

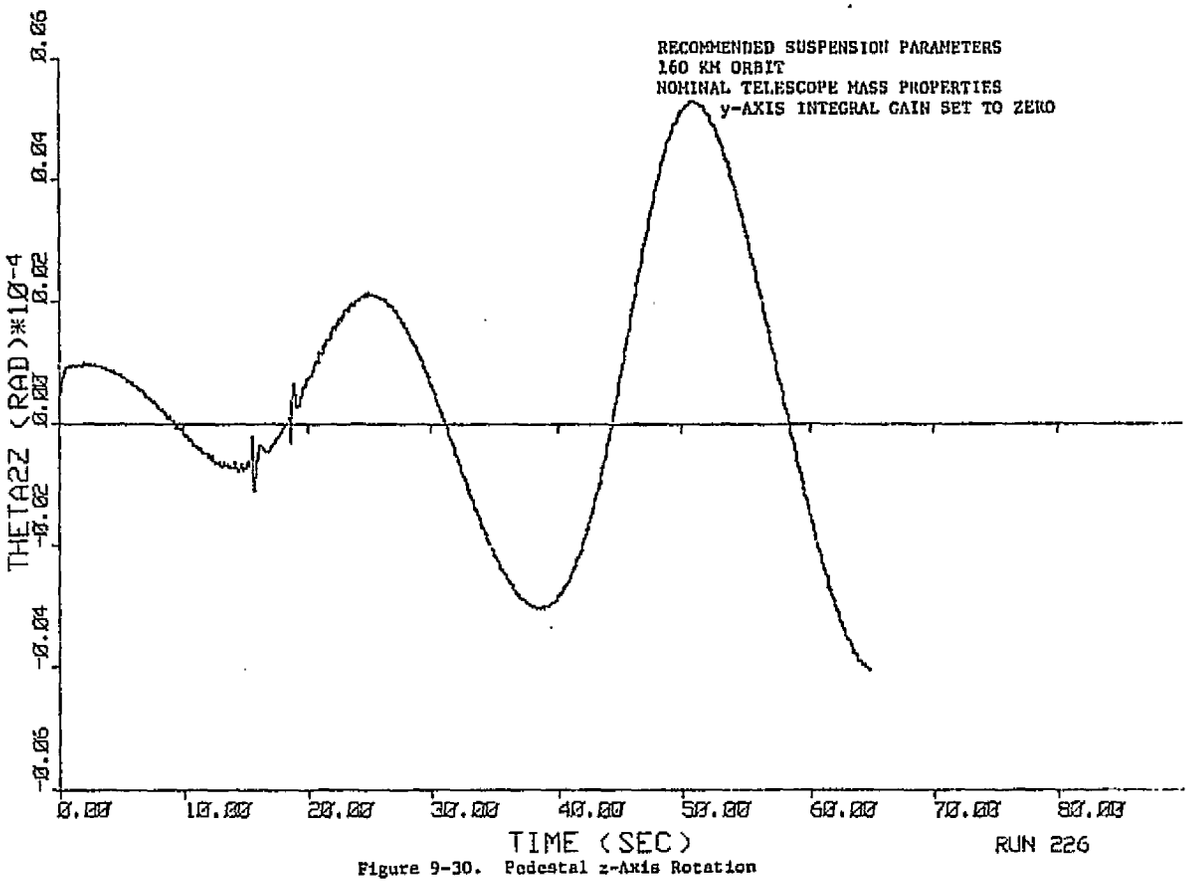

Figure 9-30. Pedestal z-Axis Rotation

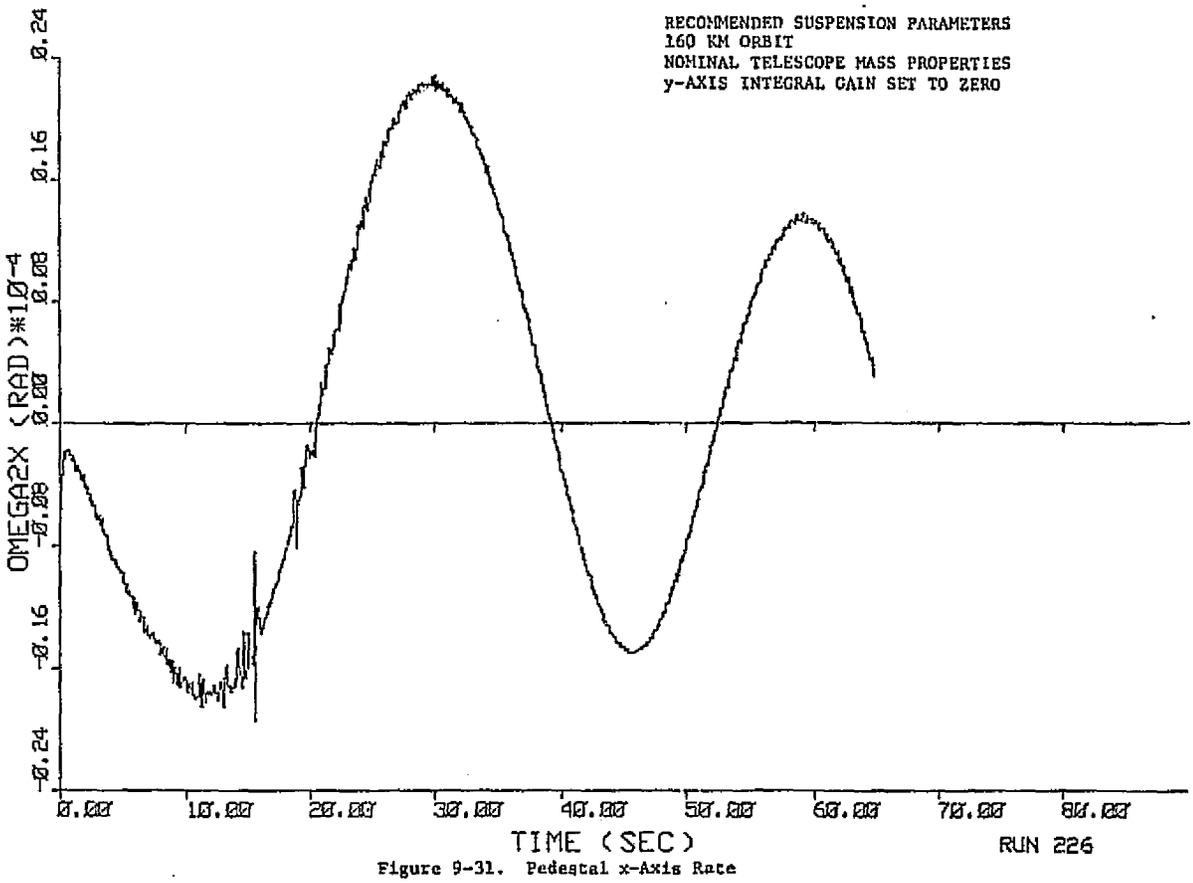

Figure 9-31. Pedestal x-Axis Rate

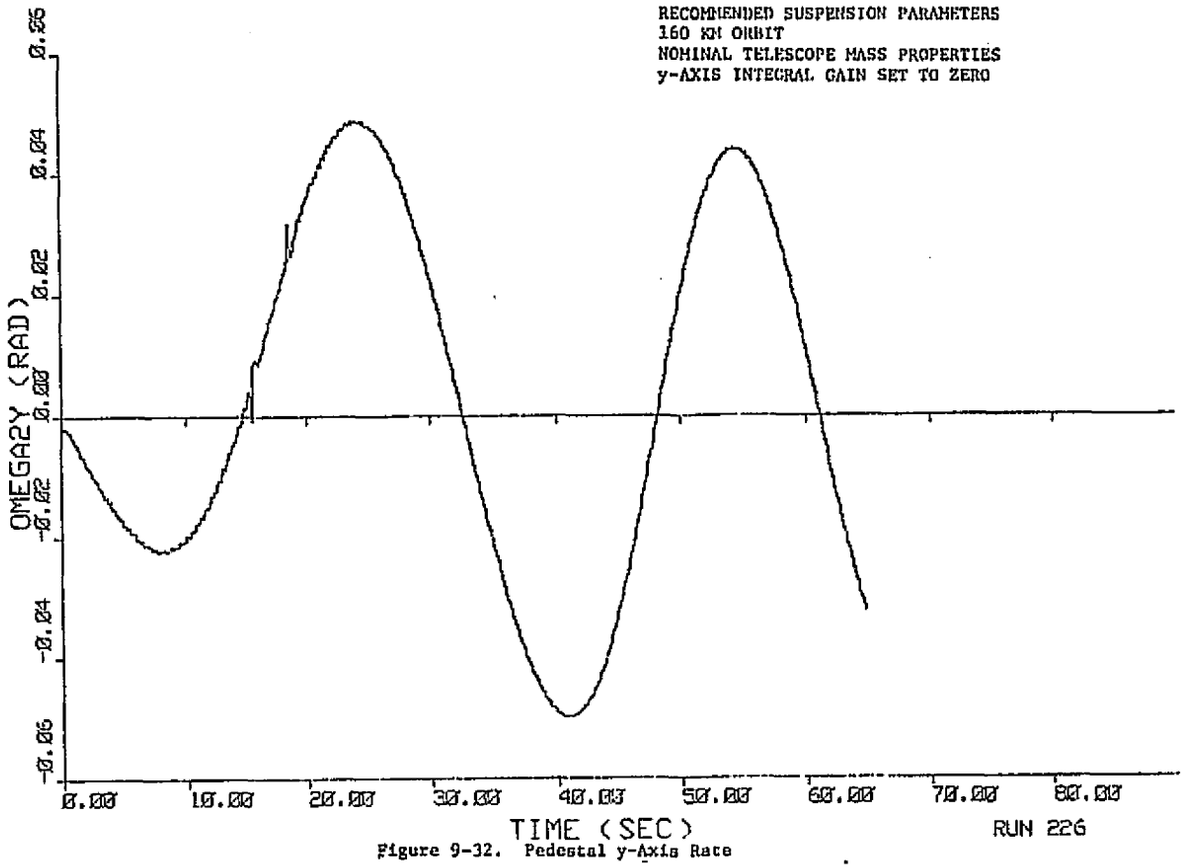

Figure 9-32. Pedestal y-Axis Rate

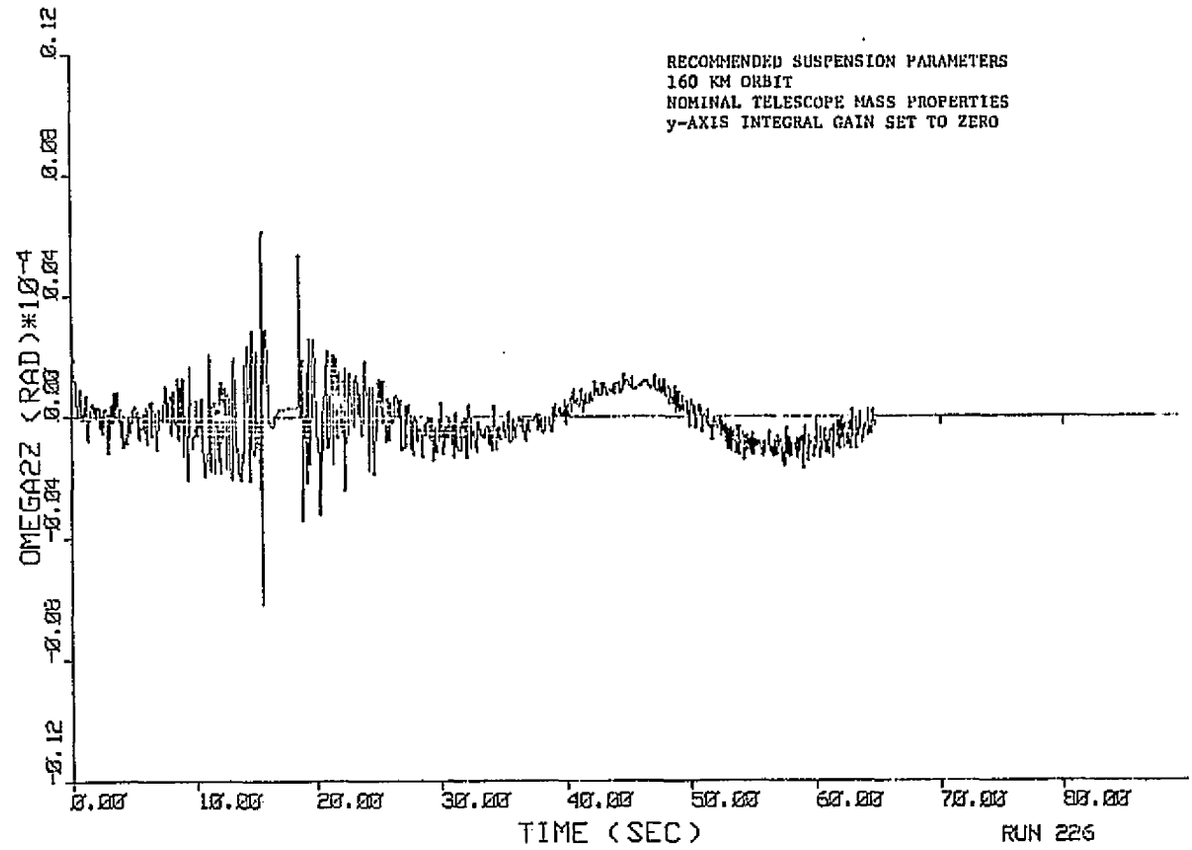

Figure 9-33. Pedestal z-Axis Rate

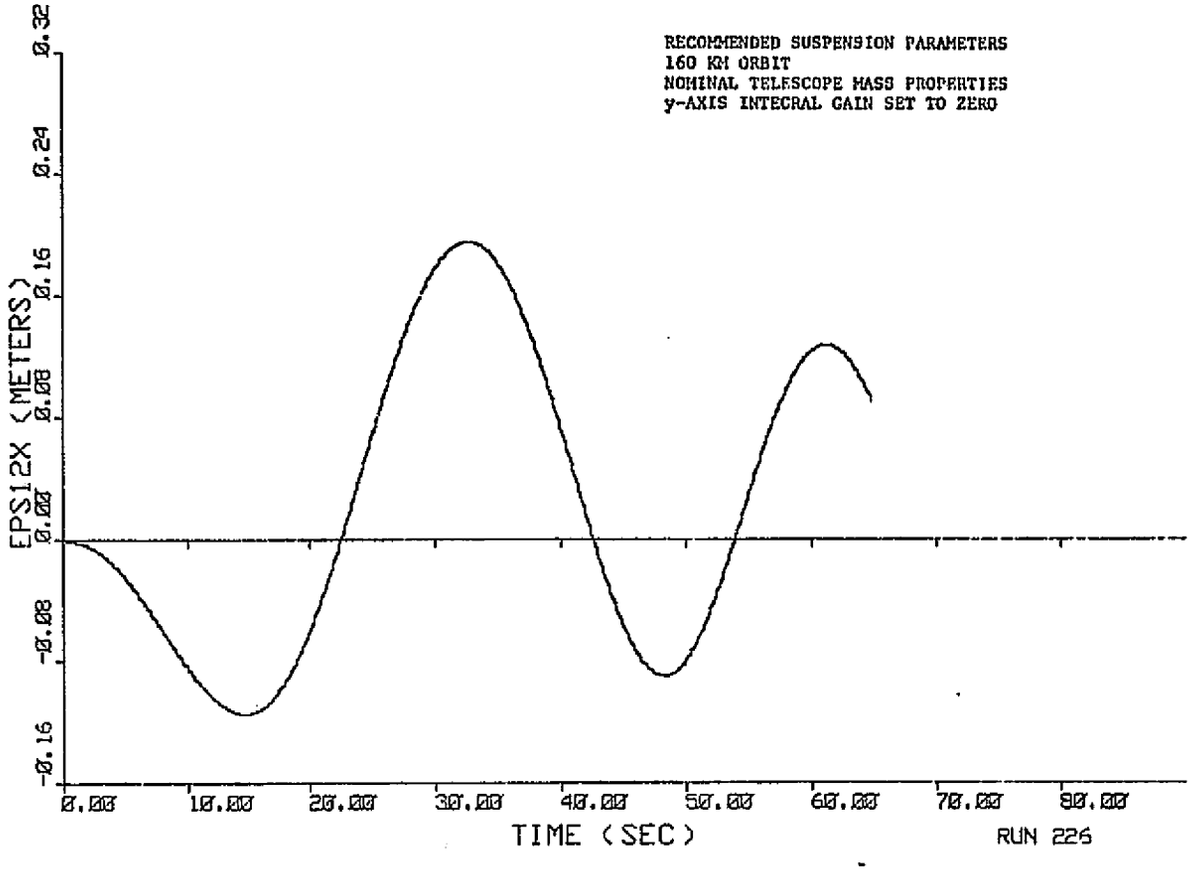

Figure 9-34. Pedestal x-Axis CM Translation

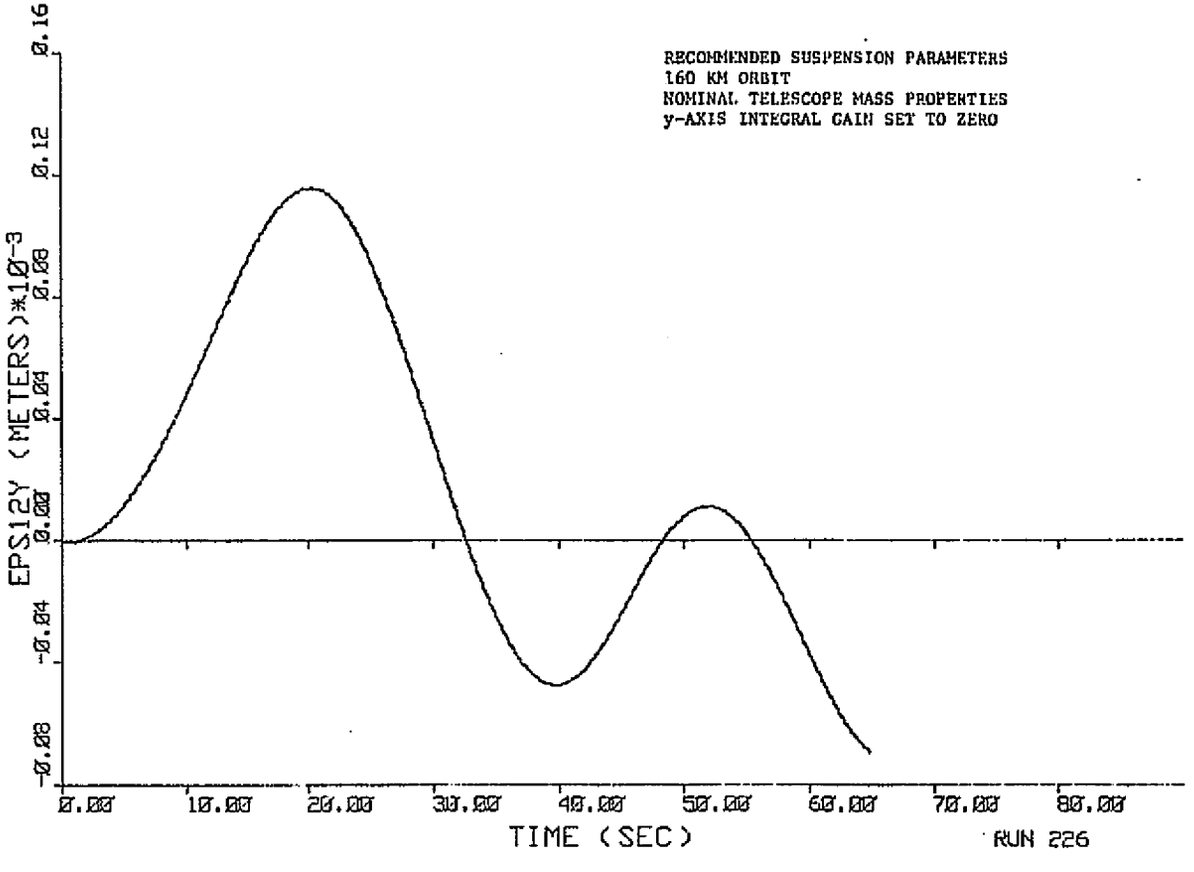

Figure 9-35. Pedestal y-Axis CM Translation

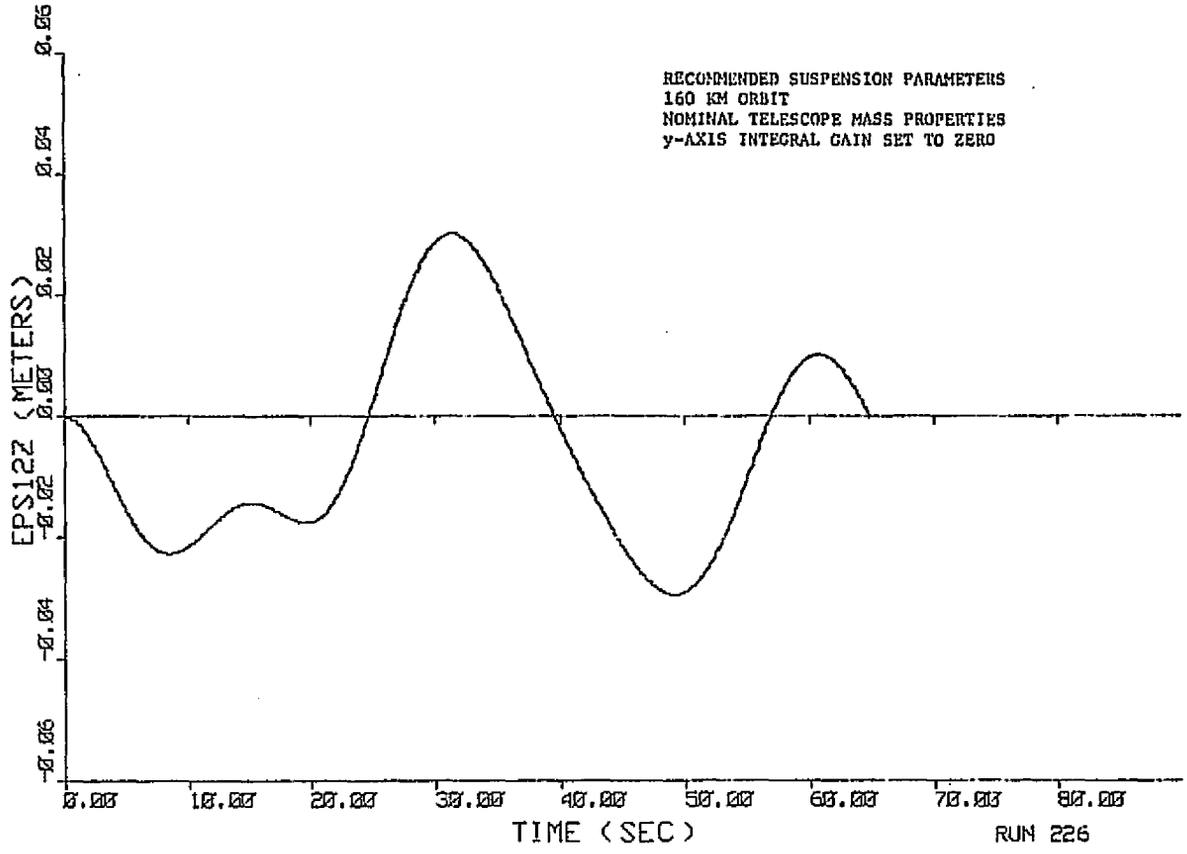

Figure 9-36. Pedestal z-Axis CM Translation

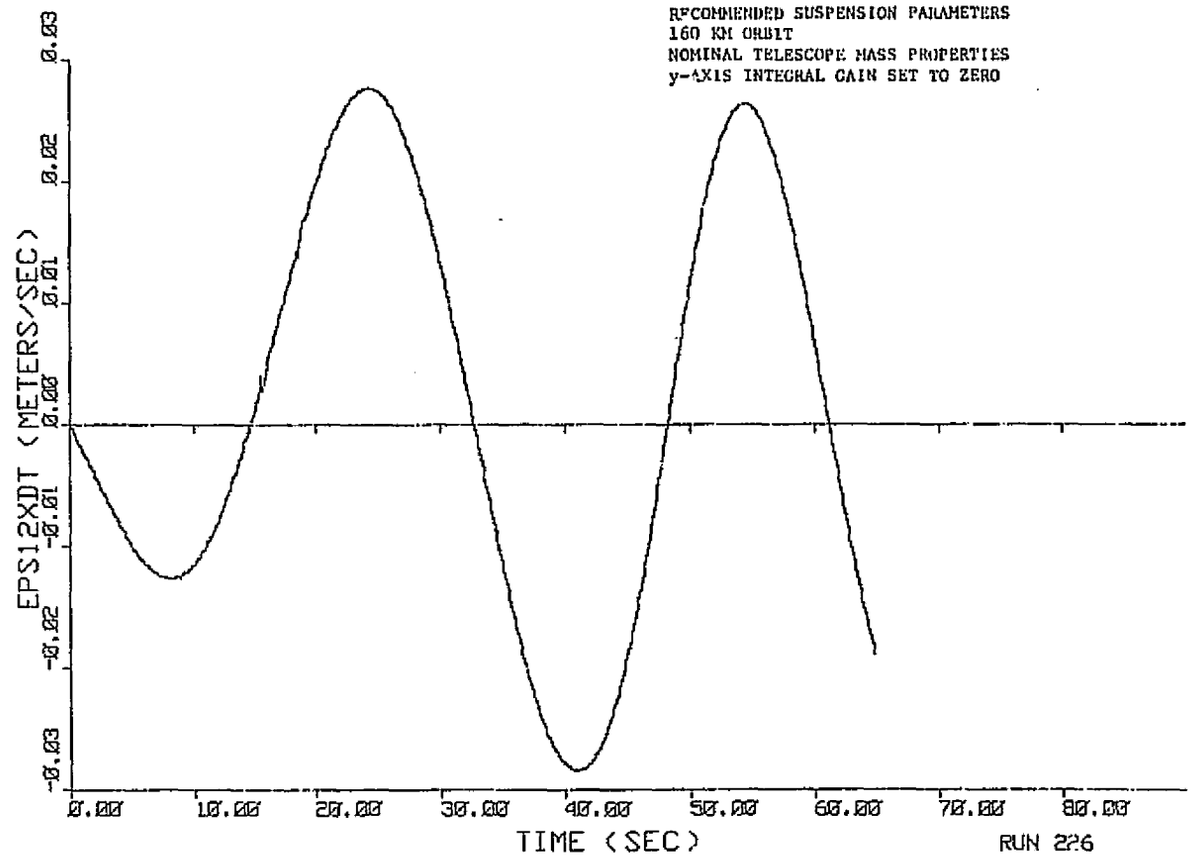

Figure 9-37. Pedestal x-Axis CM Velocity

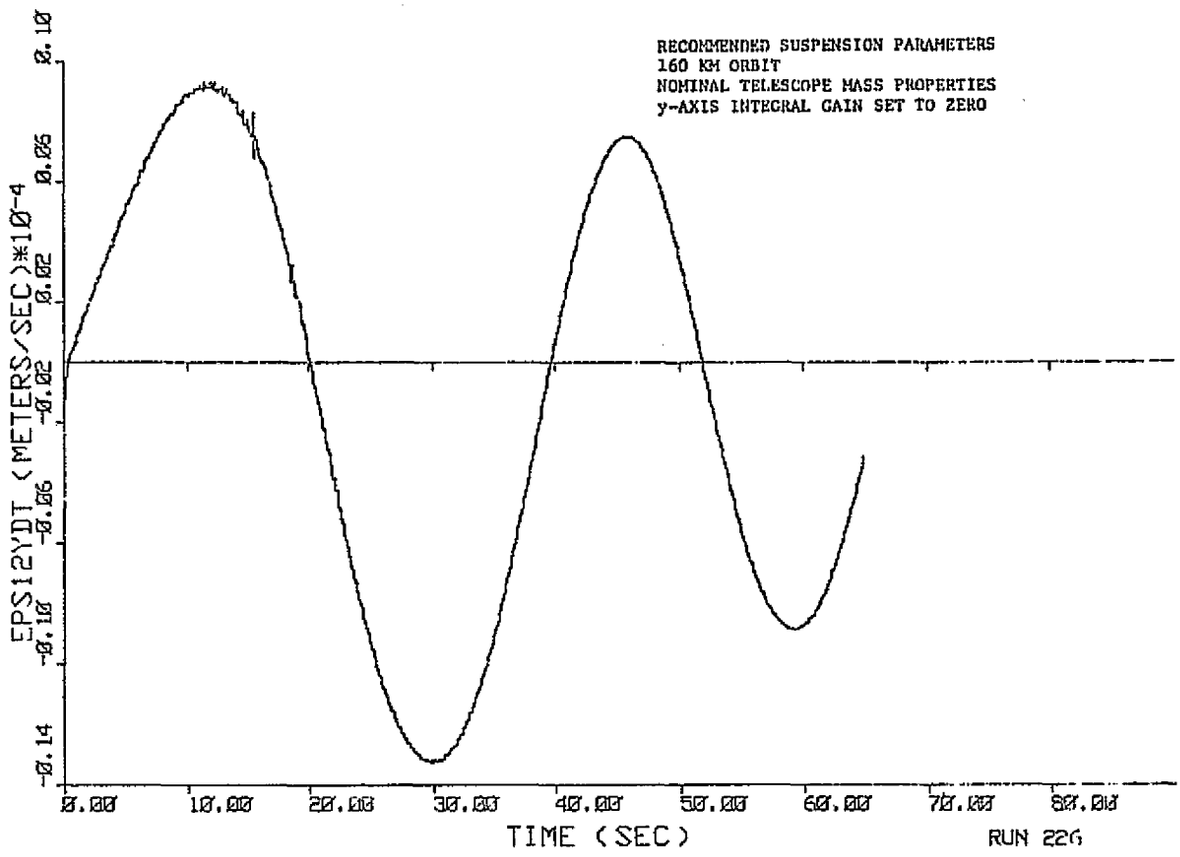

Figure 9-38. Pedestal y-Axis CM Velocity

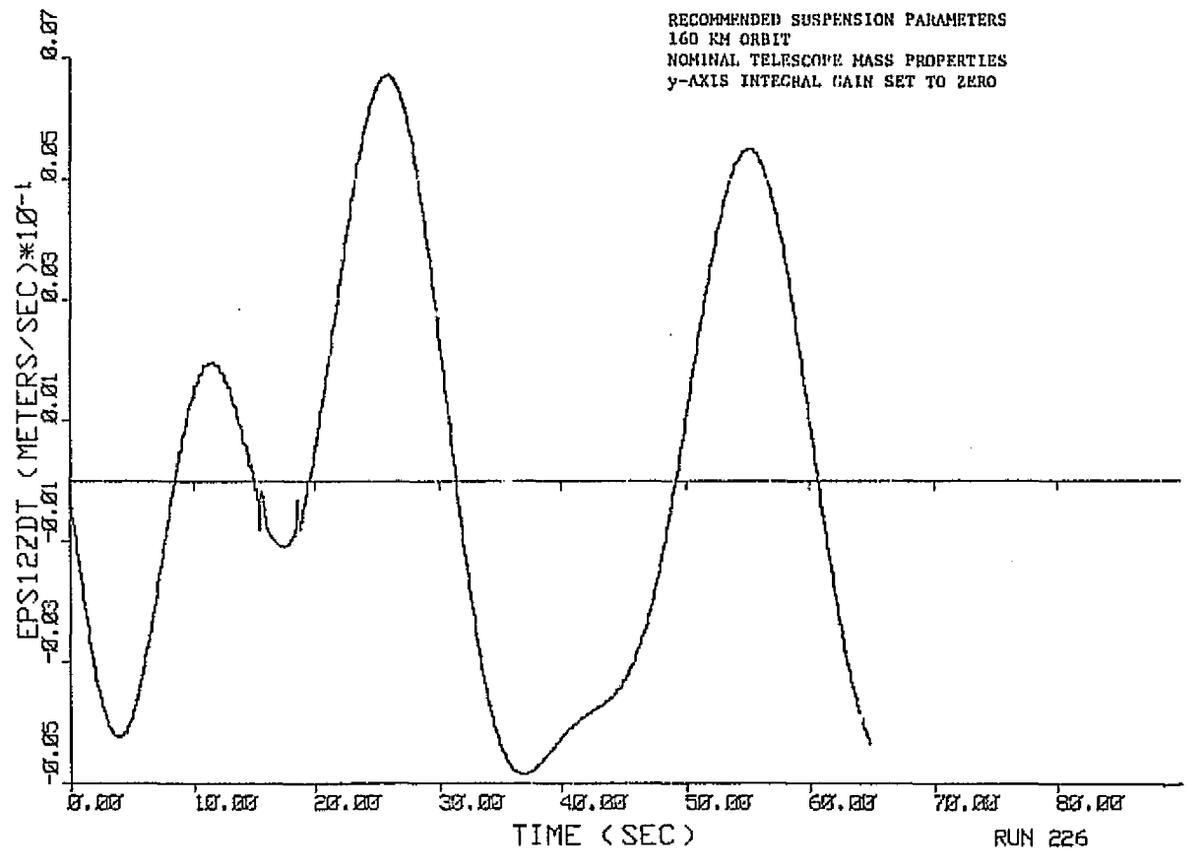

Figure 9-39. Pedestal z-Axis CM Velocity

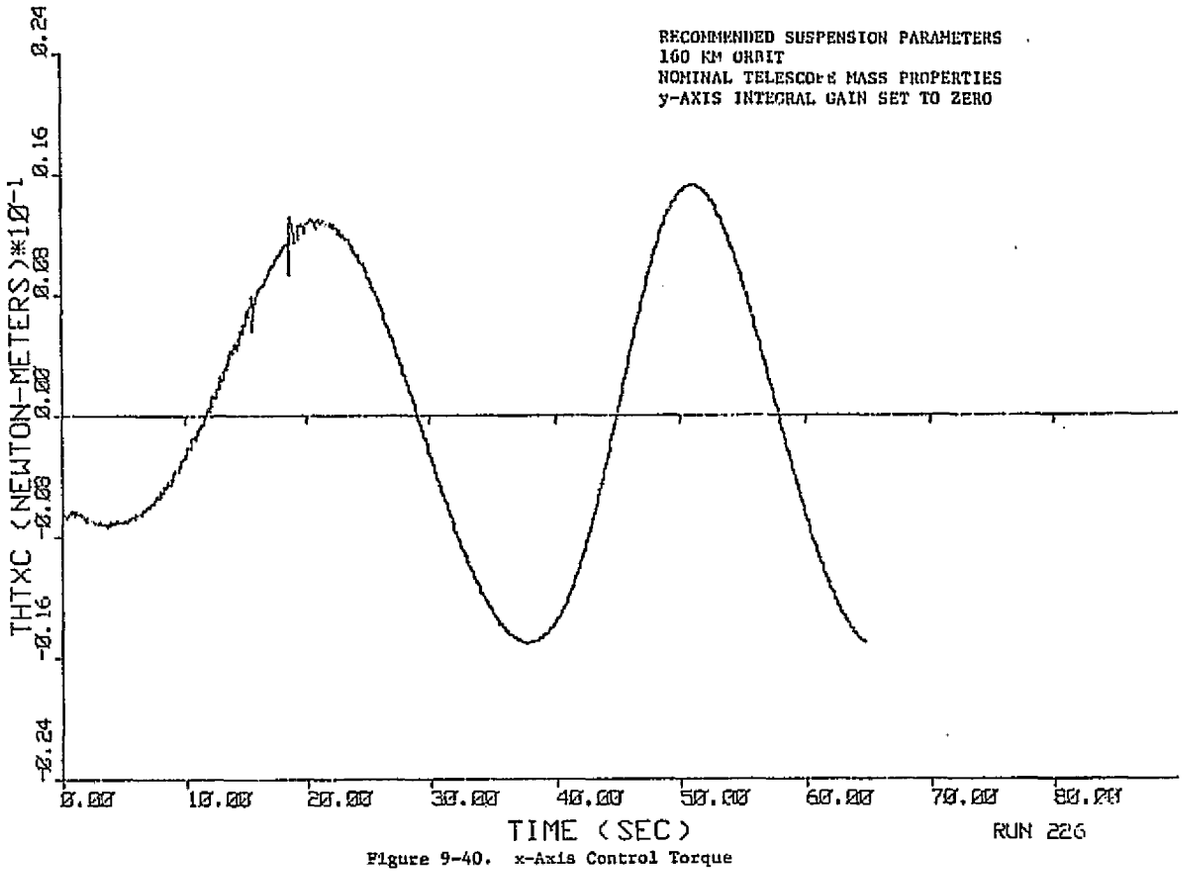

Figure 9-40. x-Axis Control Torque

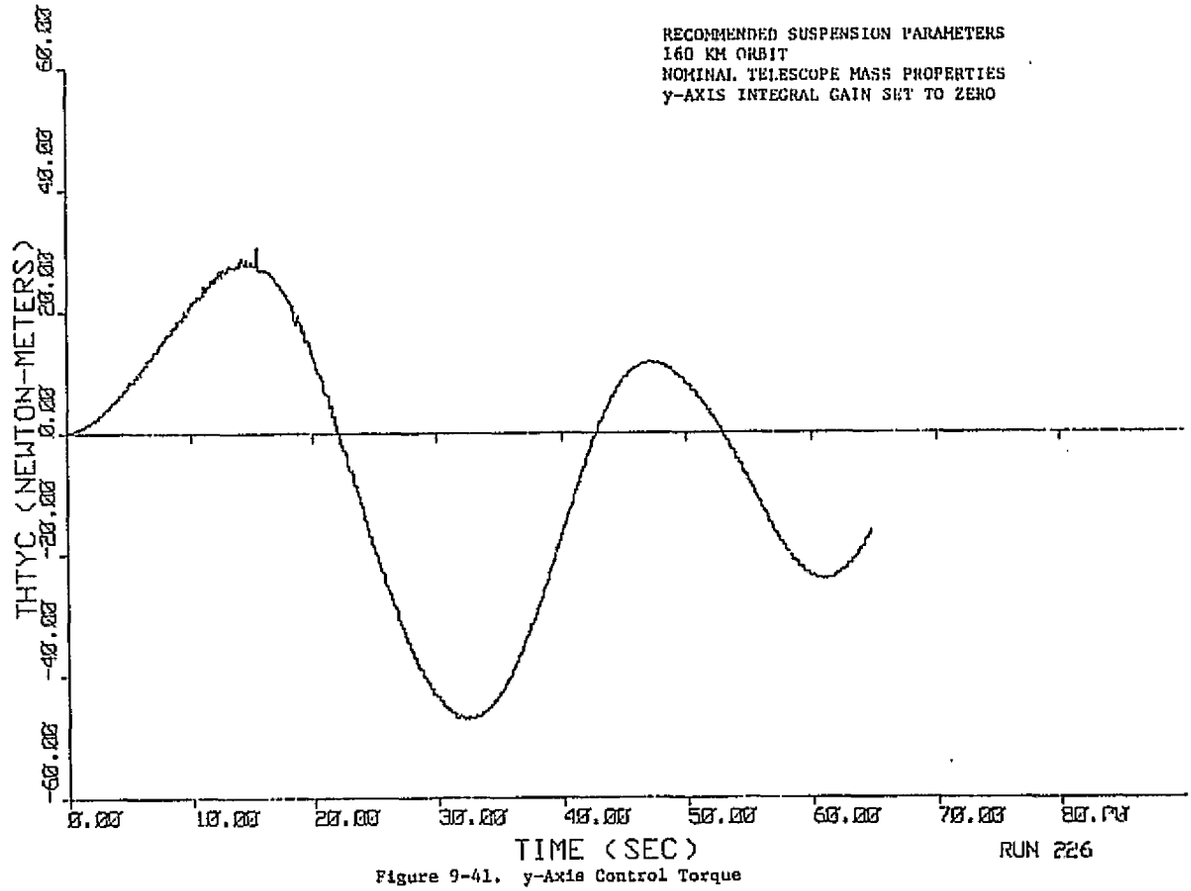

Figure 9-41. y-Axis Control Torque

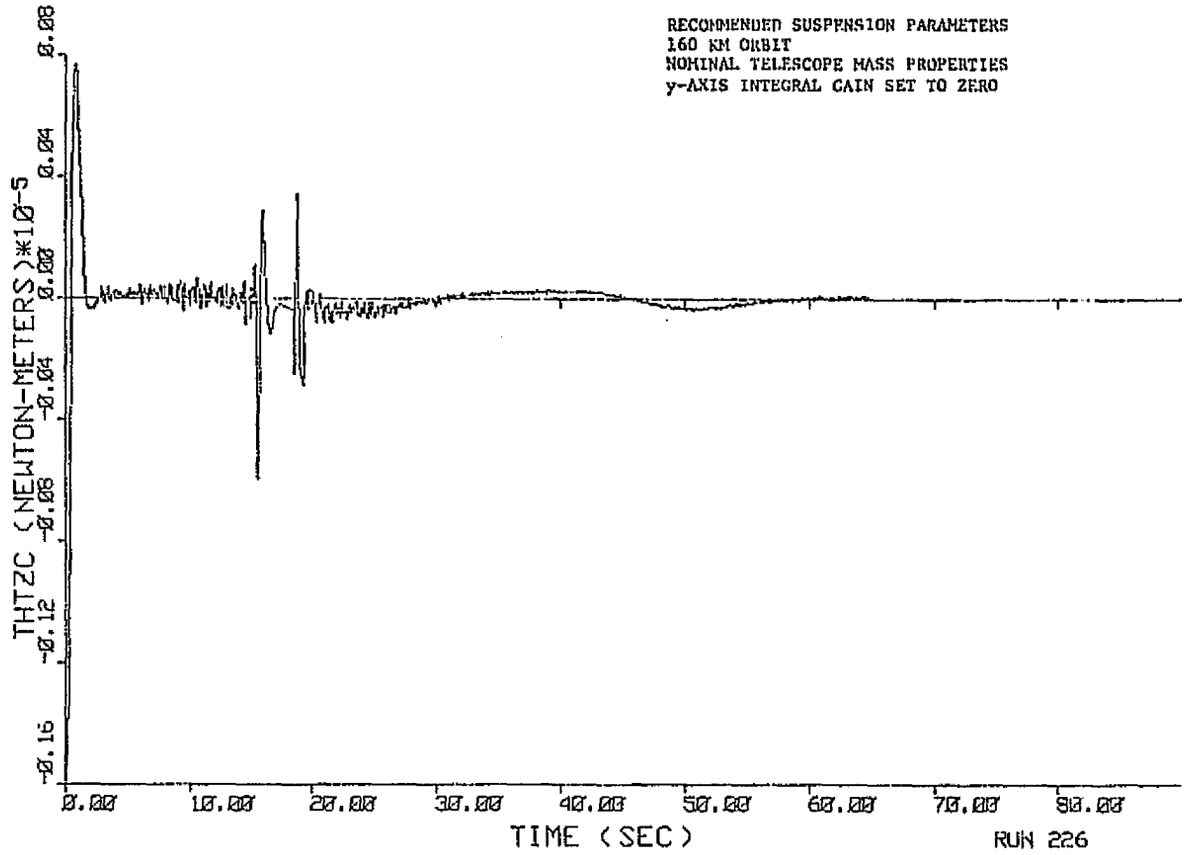

Figure 9-42. z-Axis Control Torque

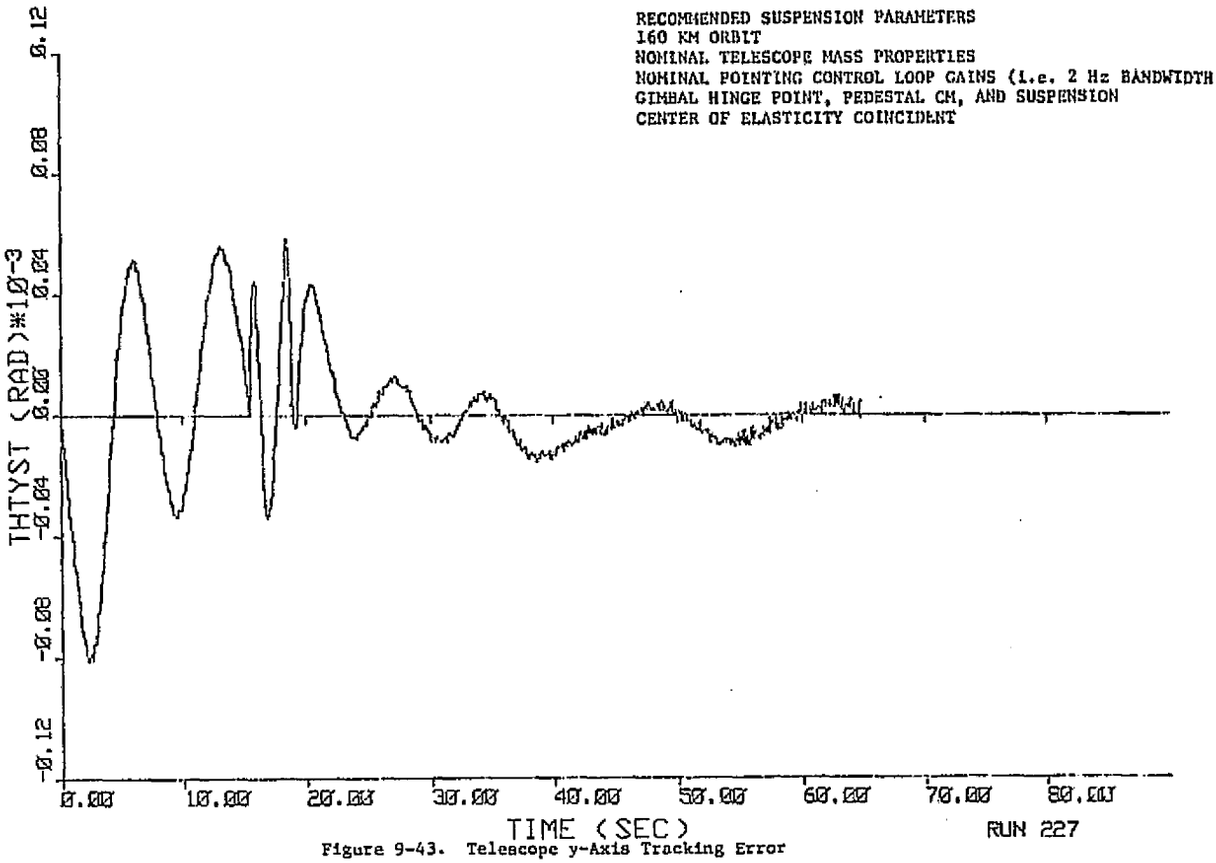

Figure 9-43. Telescope y-Axis Tracking Error

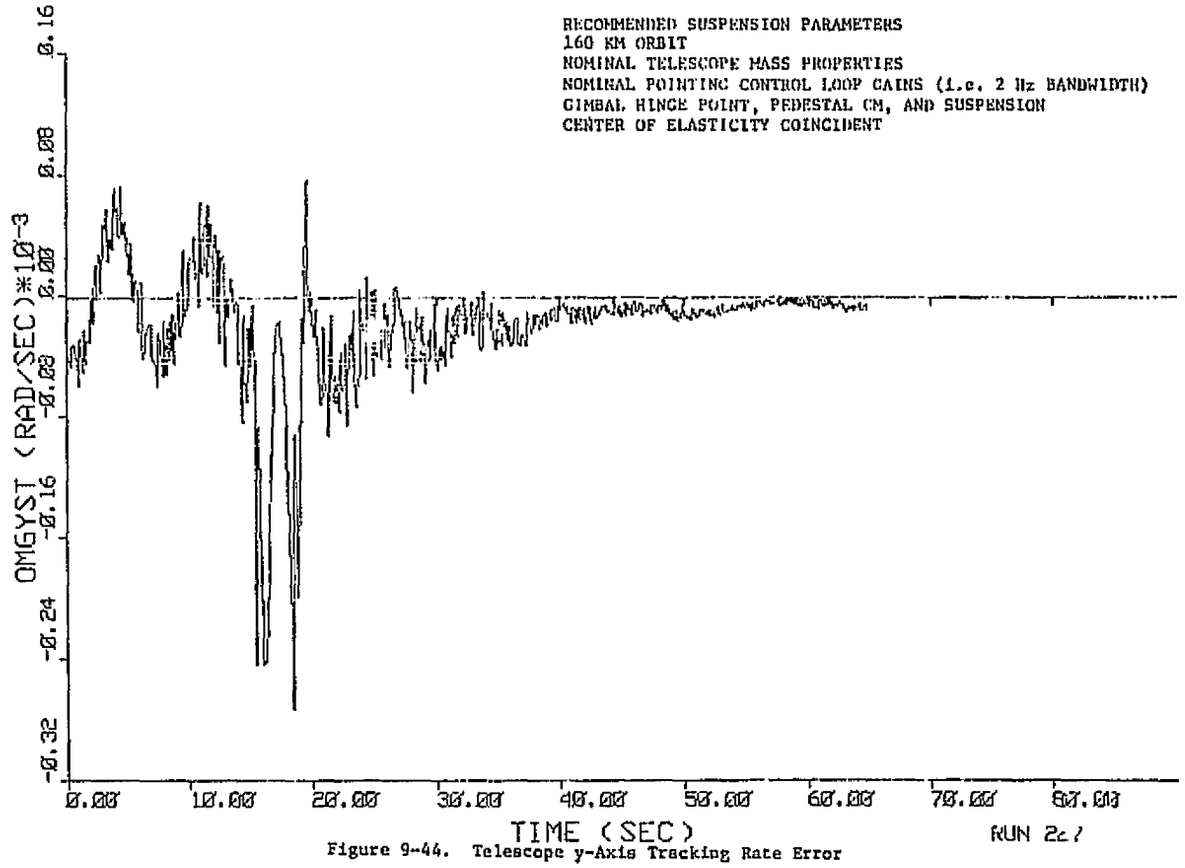

Figure 9-44. Telescope y-Axis Tracking Rate Error

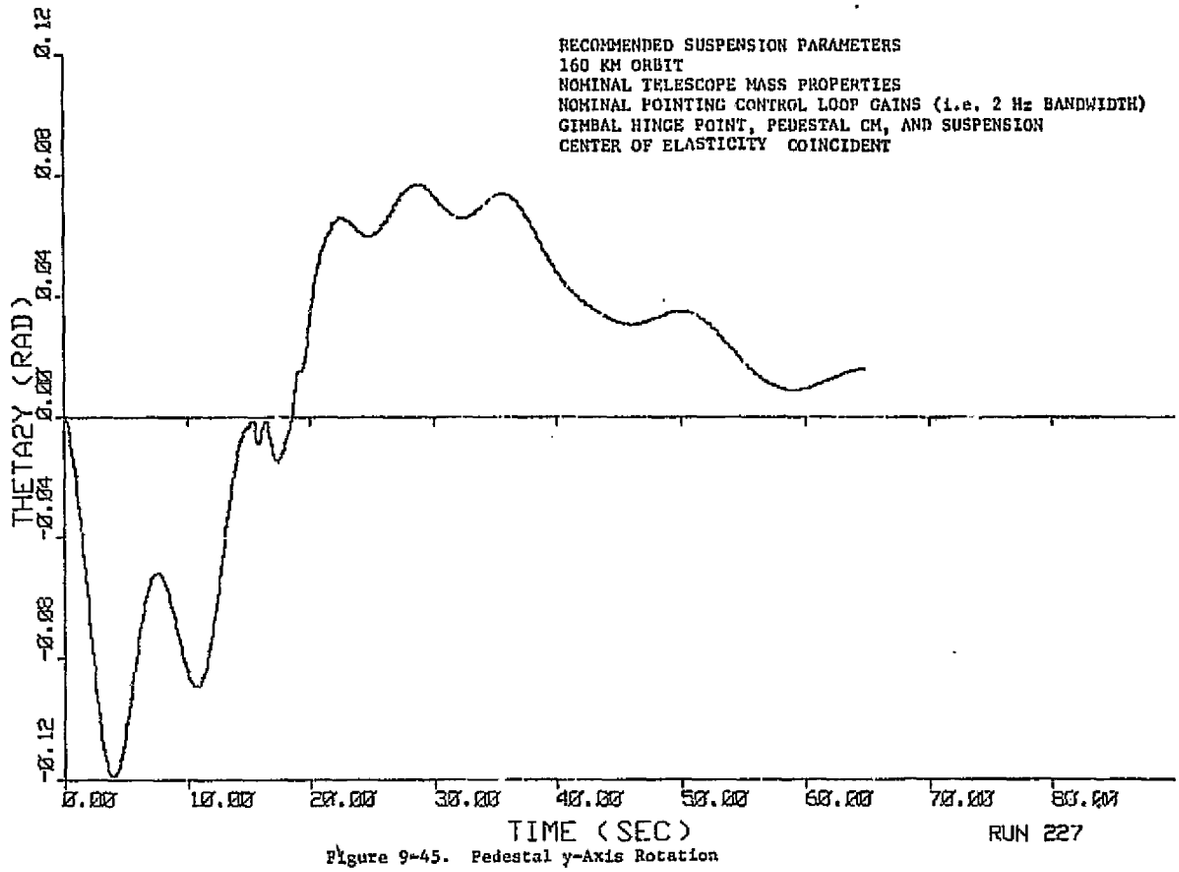

Figure 9-45. Pedestal y-Axis Rotation

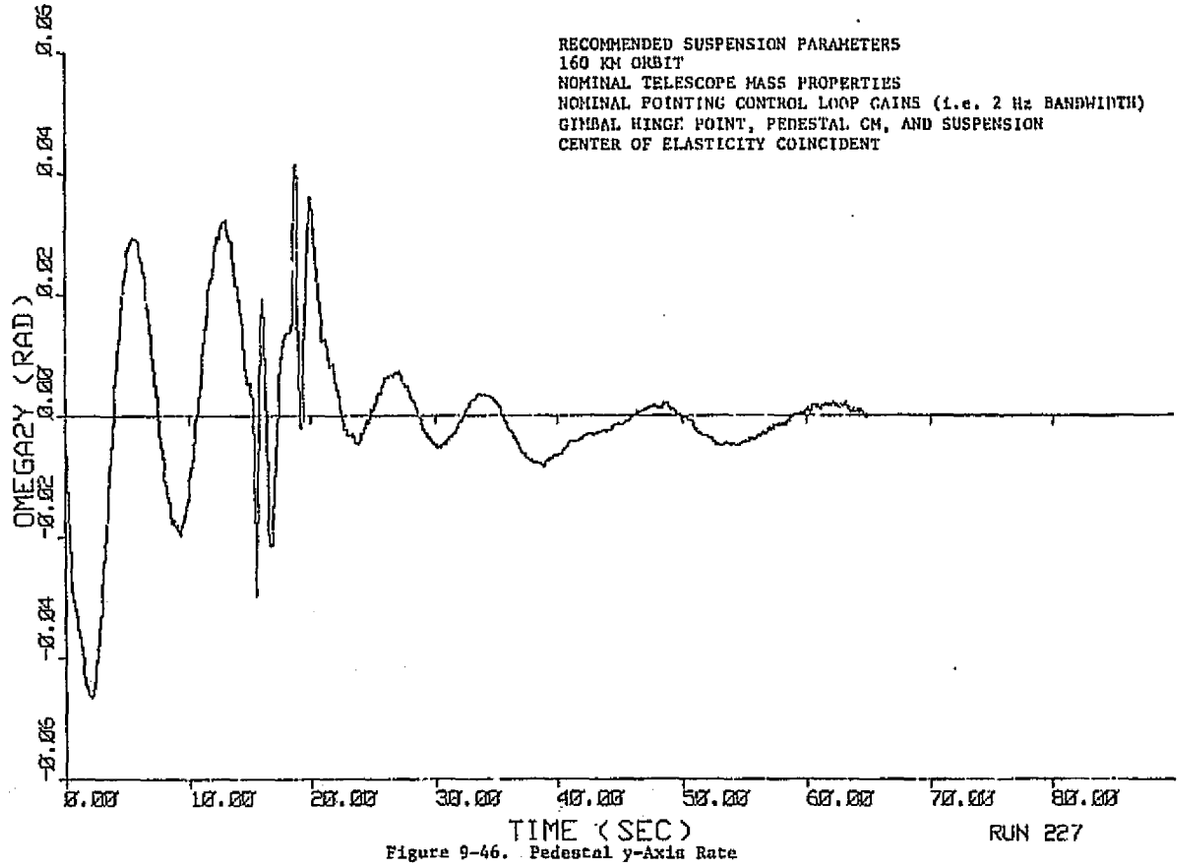

Figure 9-46. Pedestal y-Axis Rate

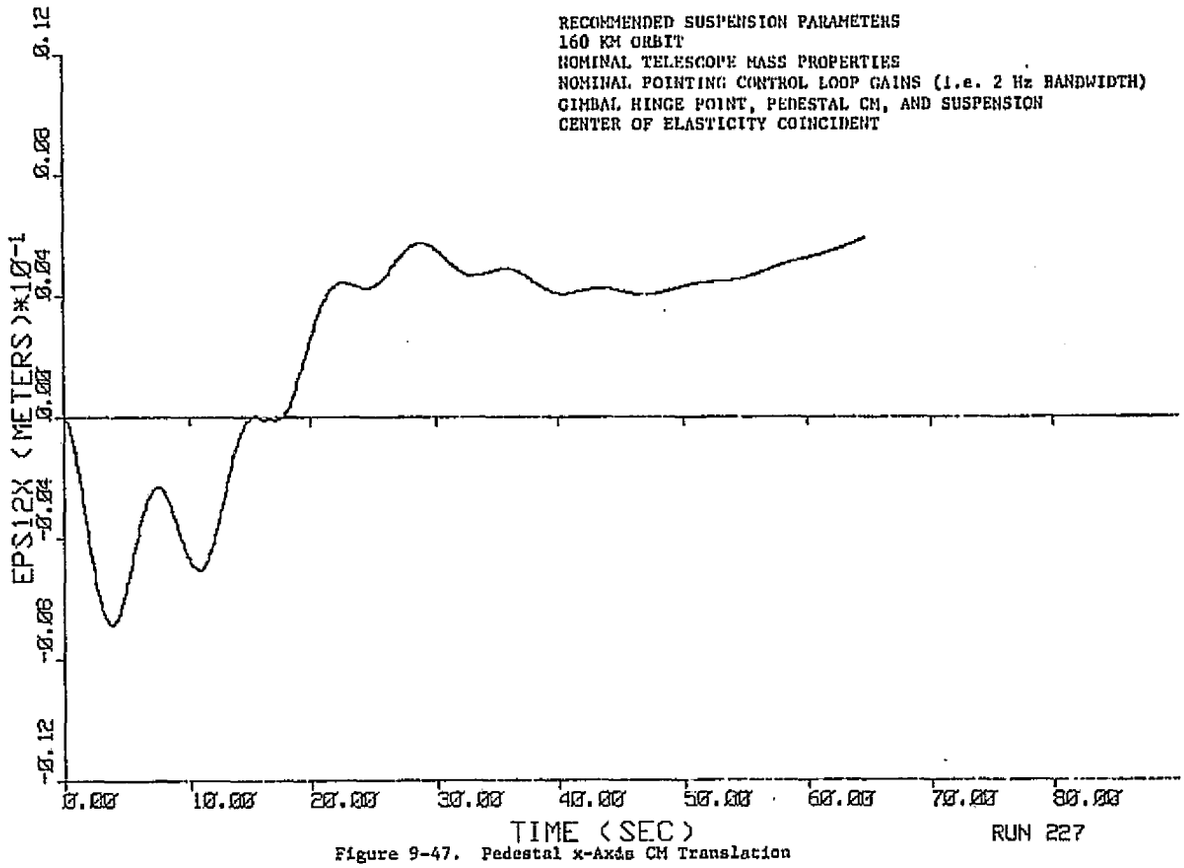

Figure 9-47. Pedestal x-Axis CM Translation

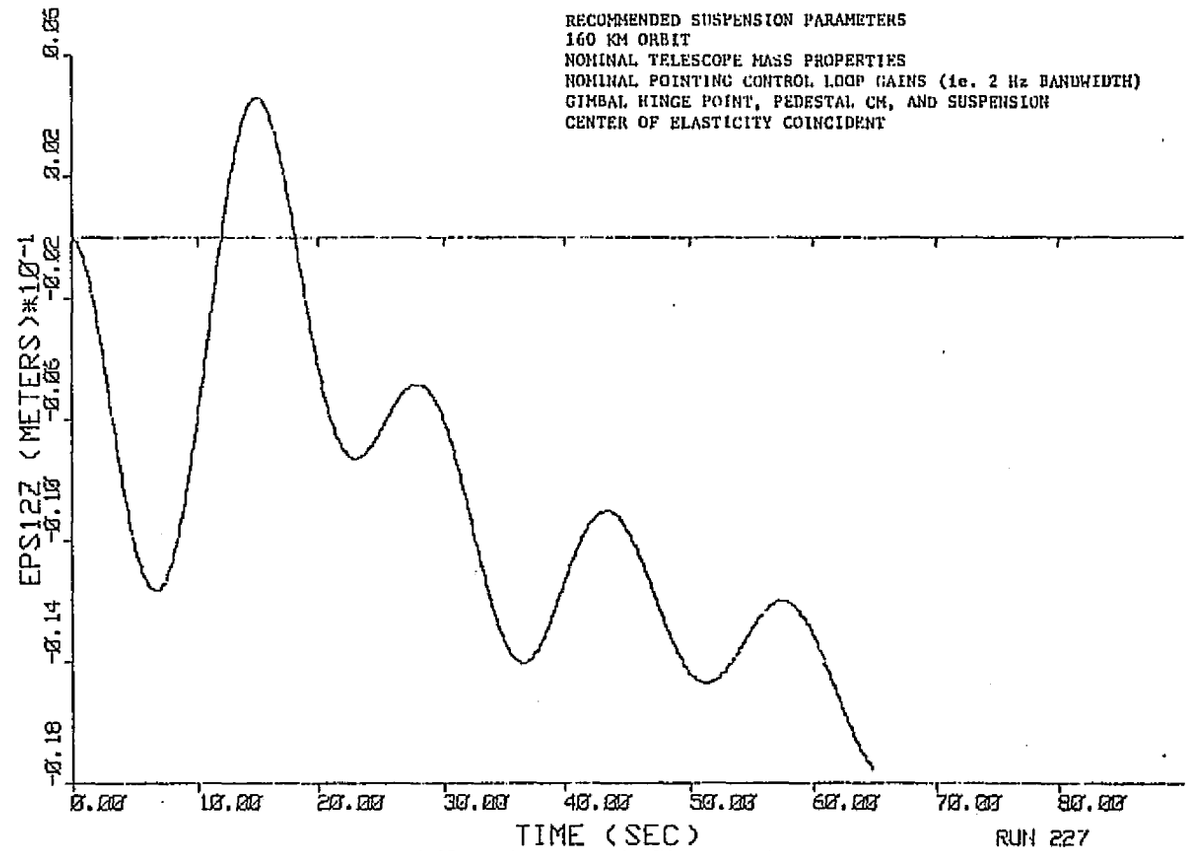

Figure 9-48. Pedestal z-Axis CM Translation

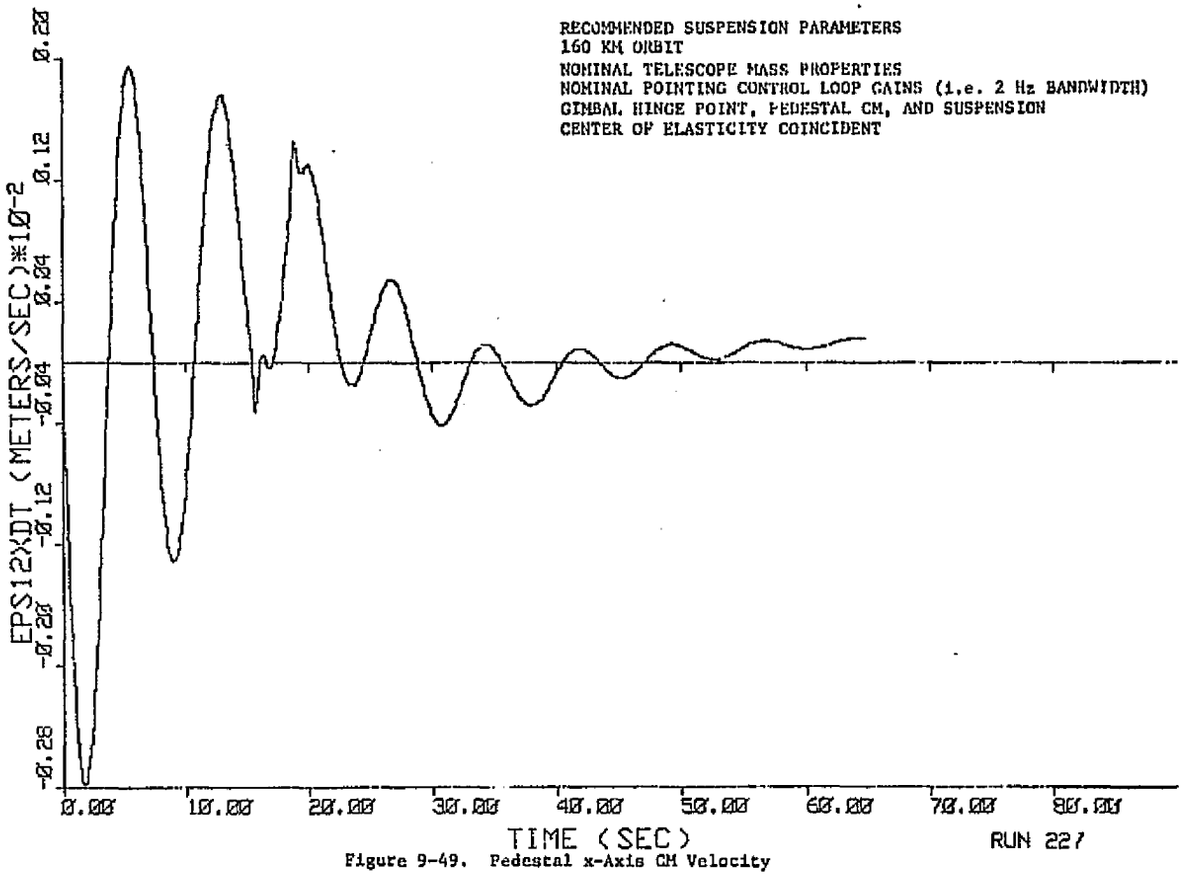

Figure 9-49. Pedestal x-Axis CM Velocity

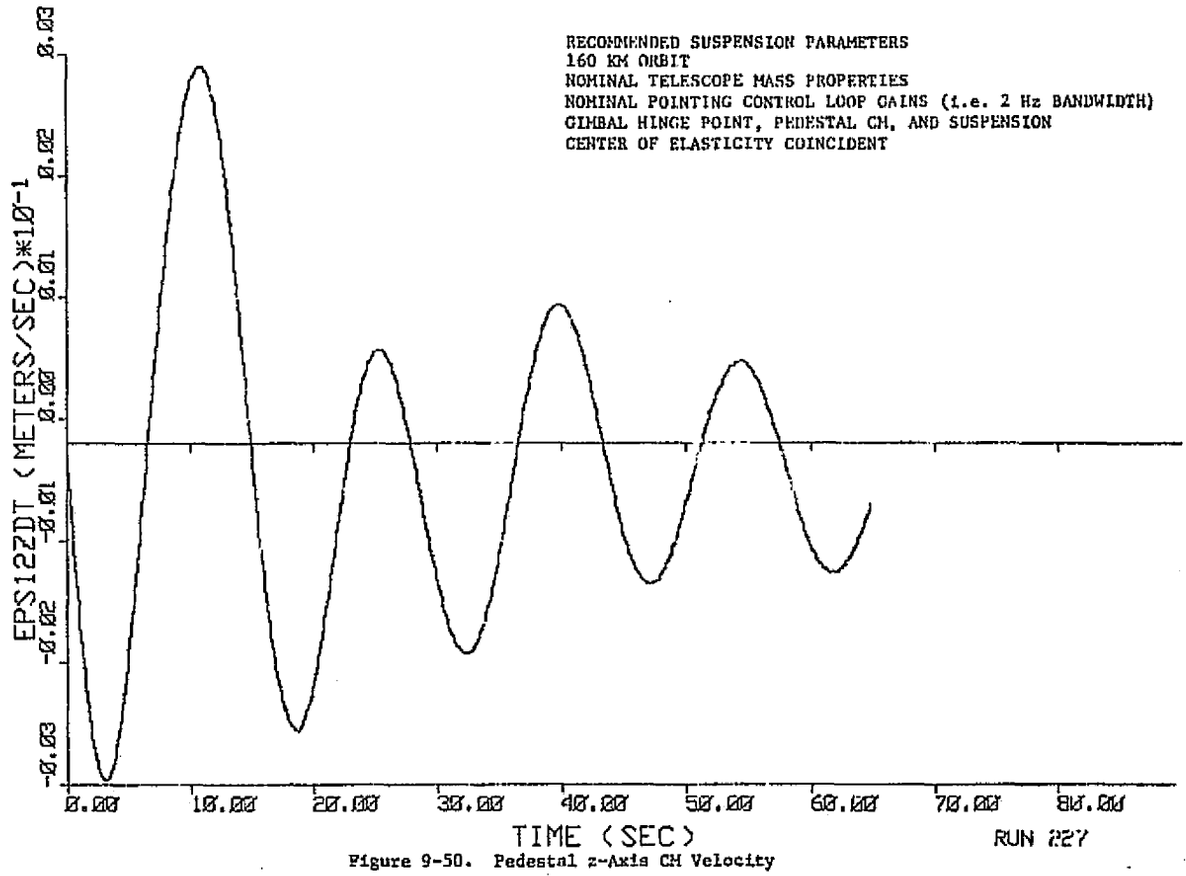

Figure 9-50. Pedestal z-Axis CM Velocity

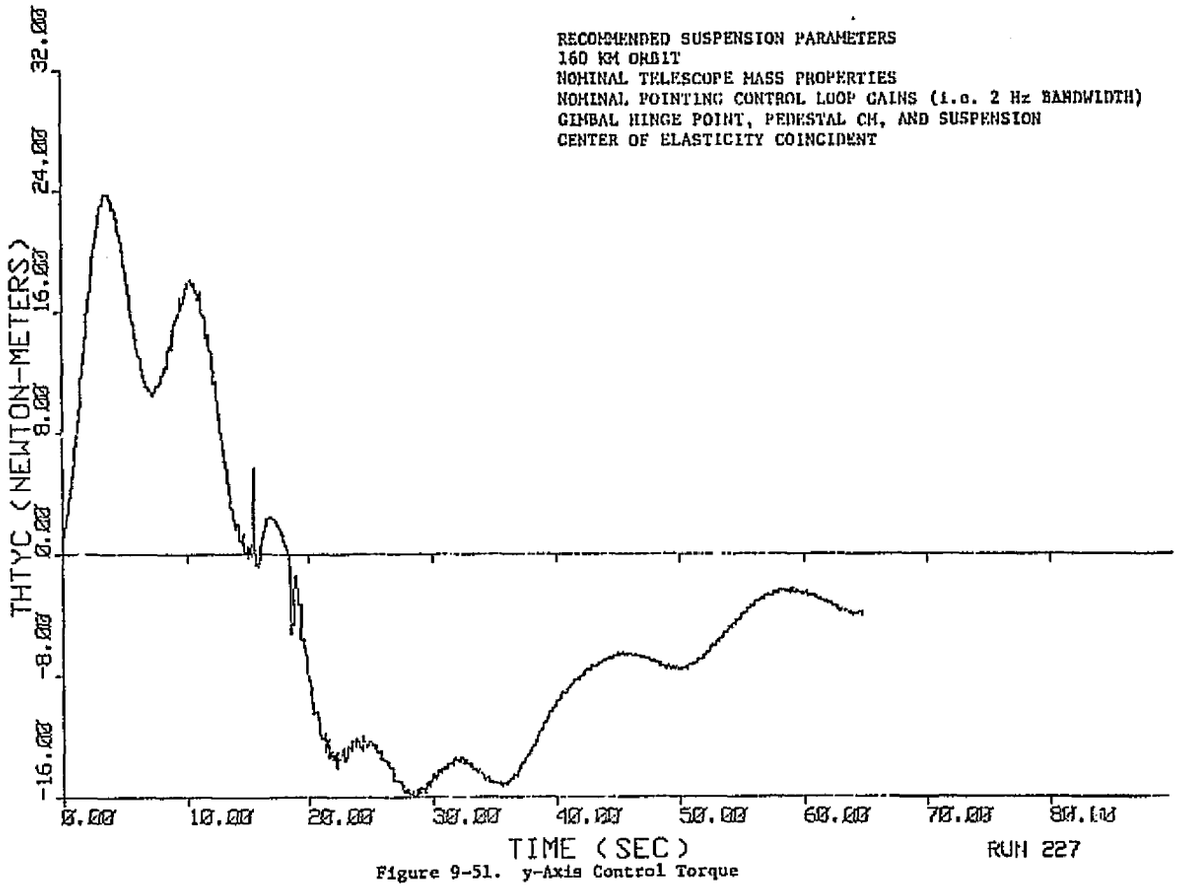

Figure 9-51. y-Axis Control Torque

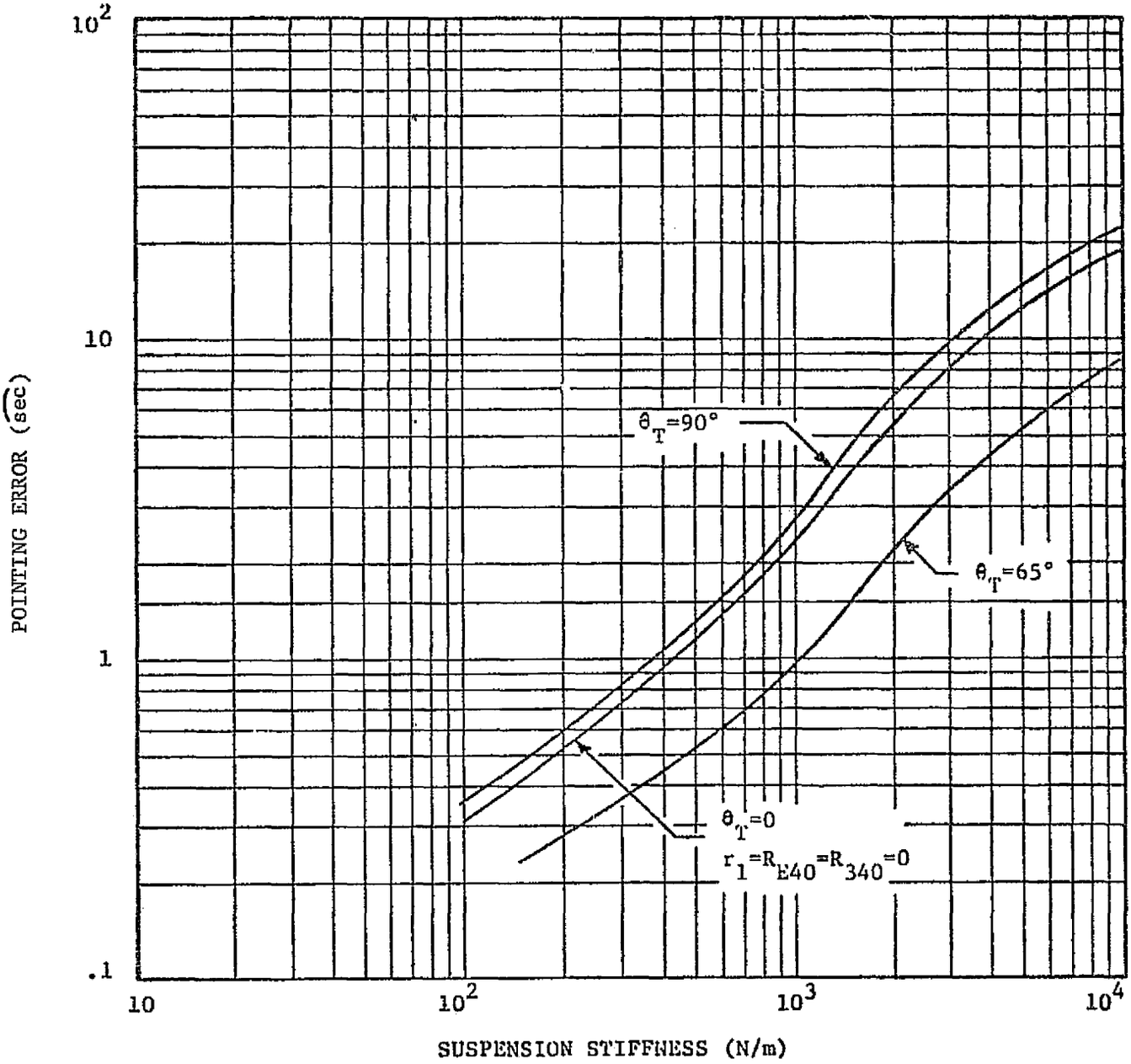

Figure 9-52. Telescope Pointing Error vs Suspension Stiffness For 2 Hz Pointing Control Loop Bandwidth

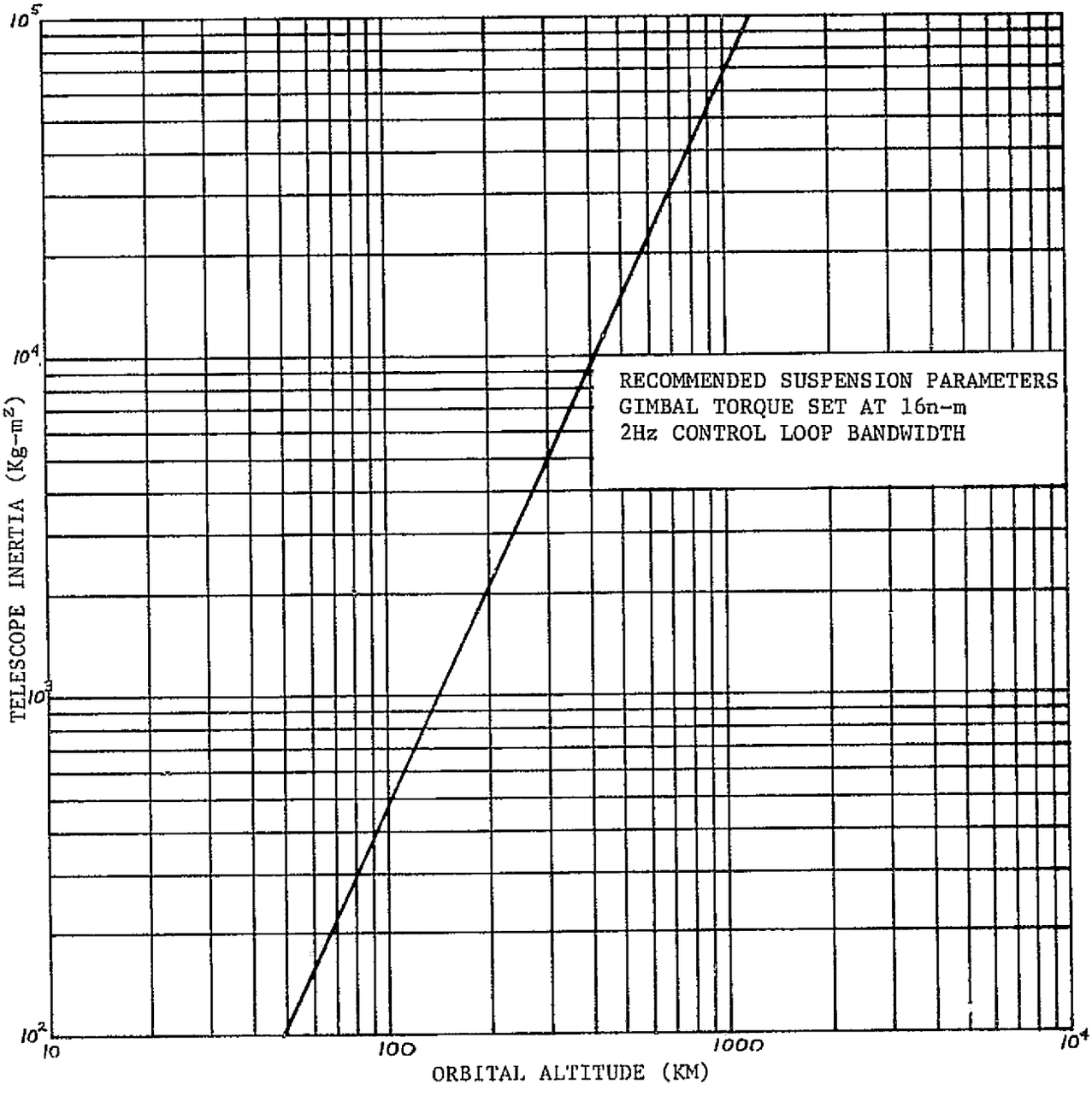

Figure 9-53. Telescope Inertia vs. Orbital Altitude

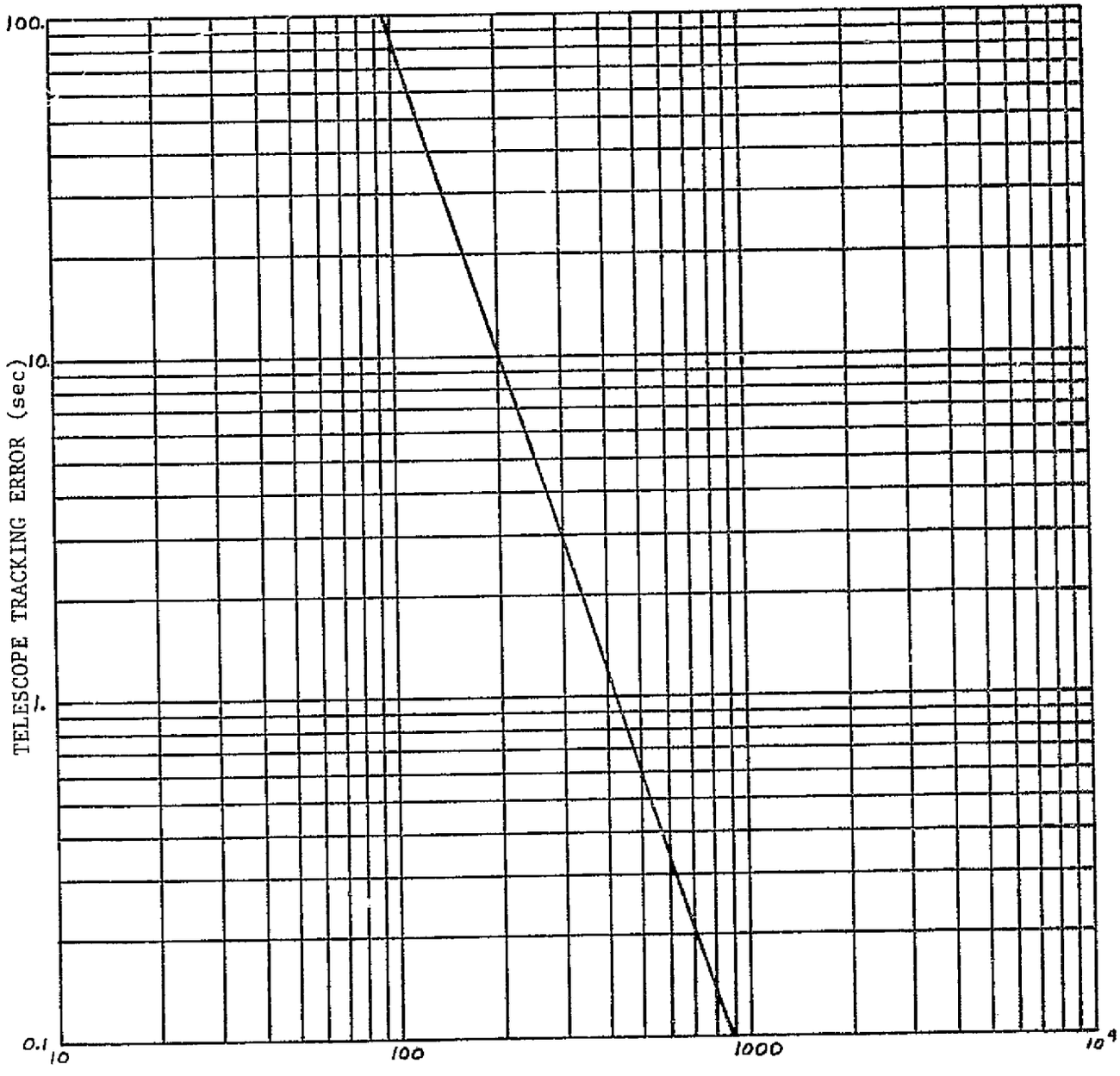

Figure 9-54. Orbital Altitude (KM)

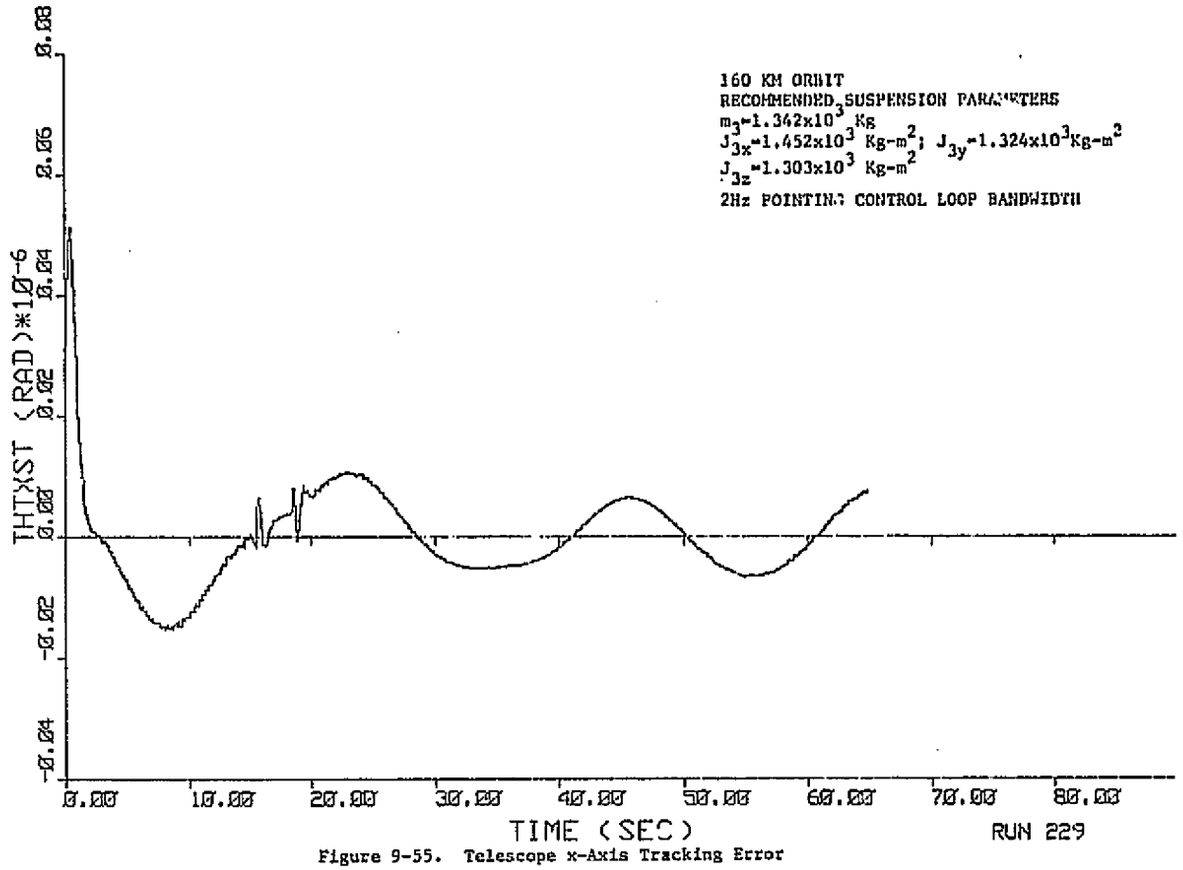

Figure 9-55. Telescope x-Axis Tracking Error

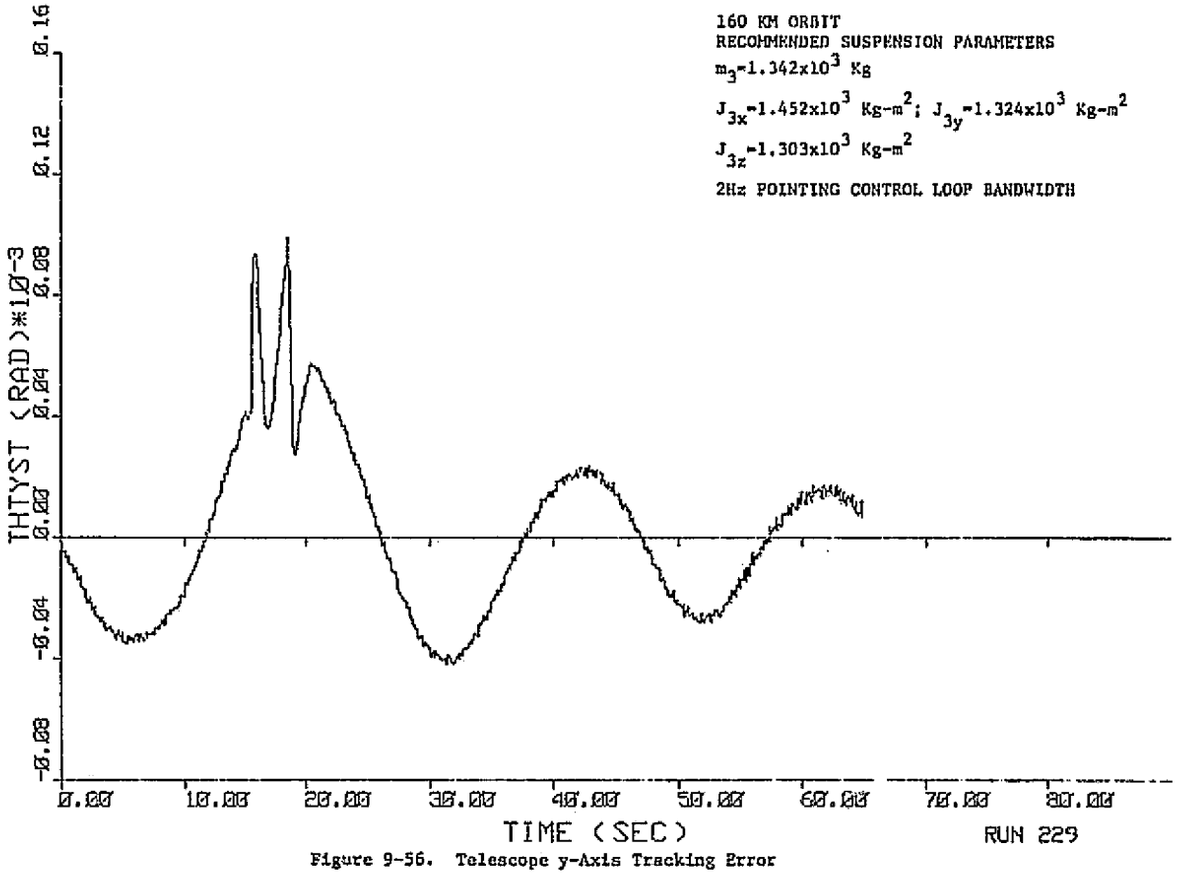

Figure 9-56. Telescope y-Axis Tracking Error

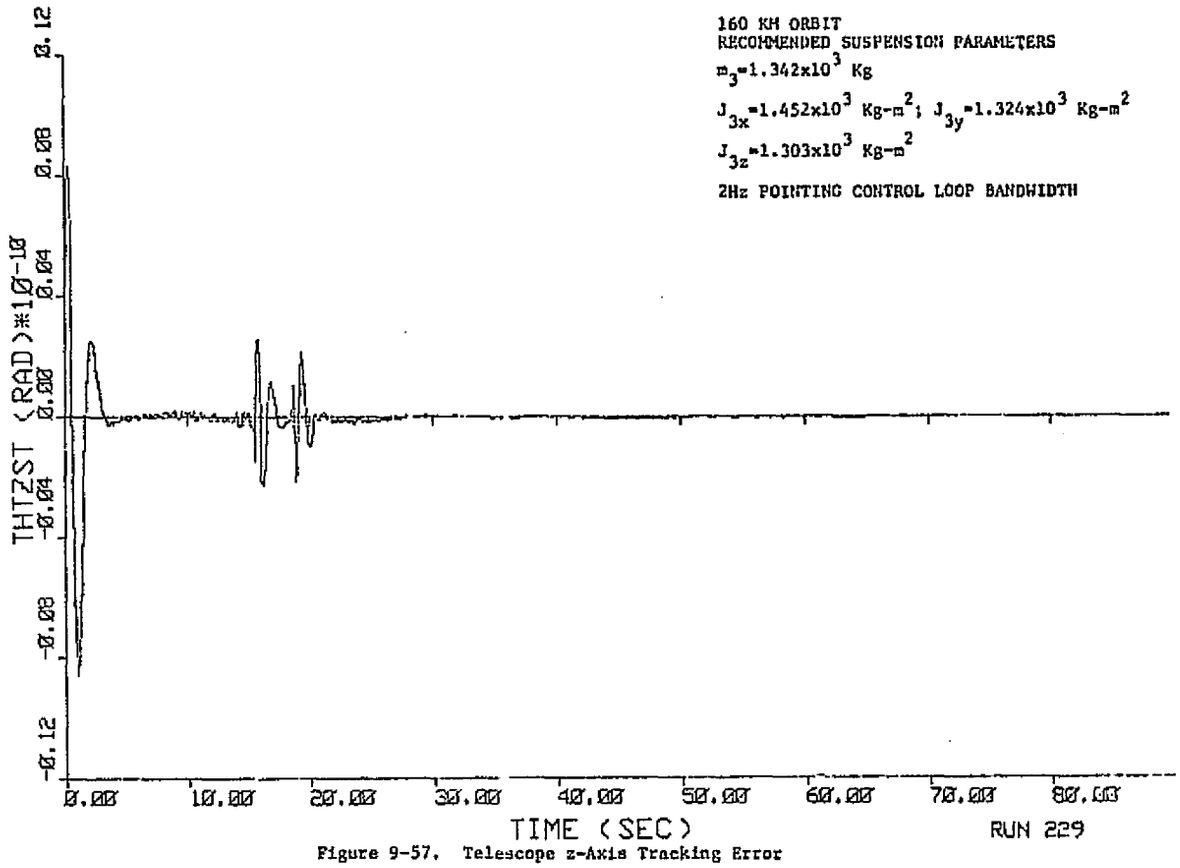

Figure 9-57. Telescope z-Axis Tracking Error

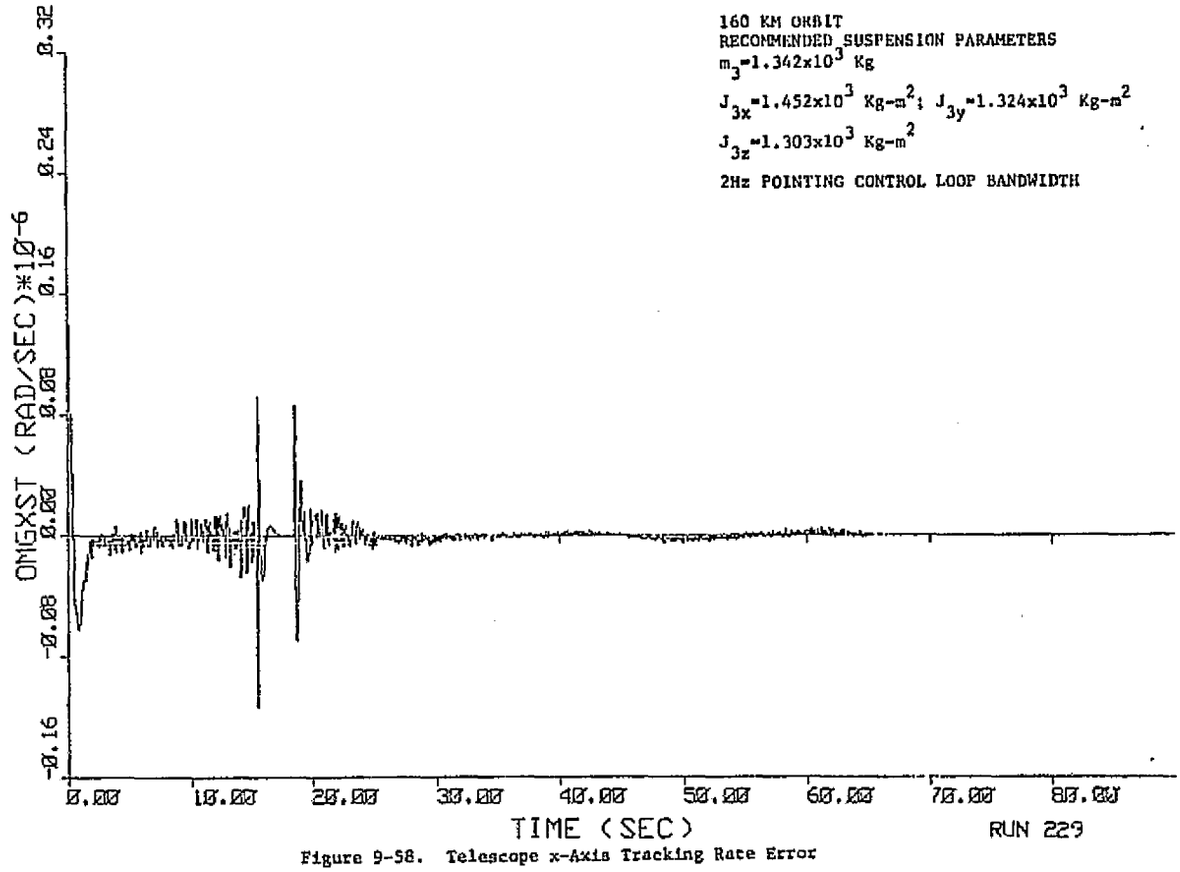

Figure 9-58. Telescope x-Axis Tracking Rate Error

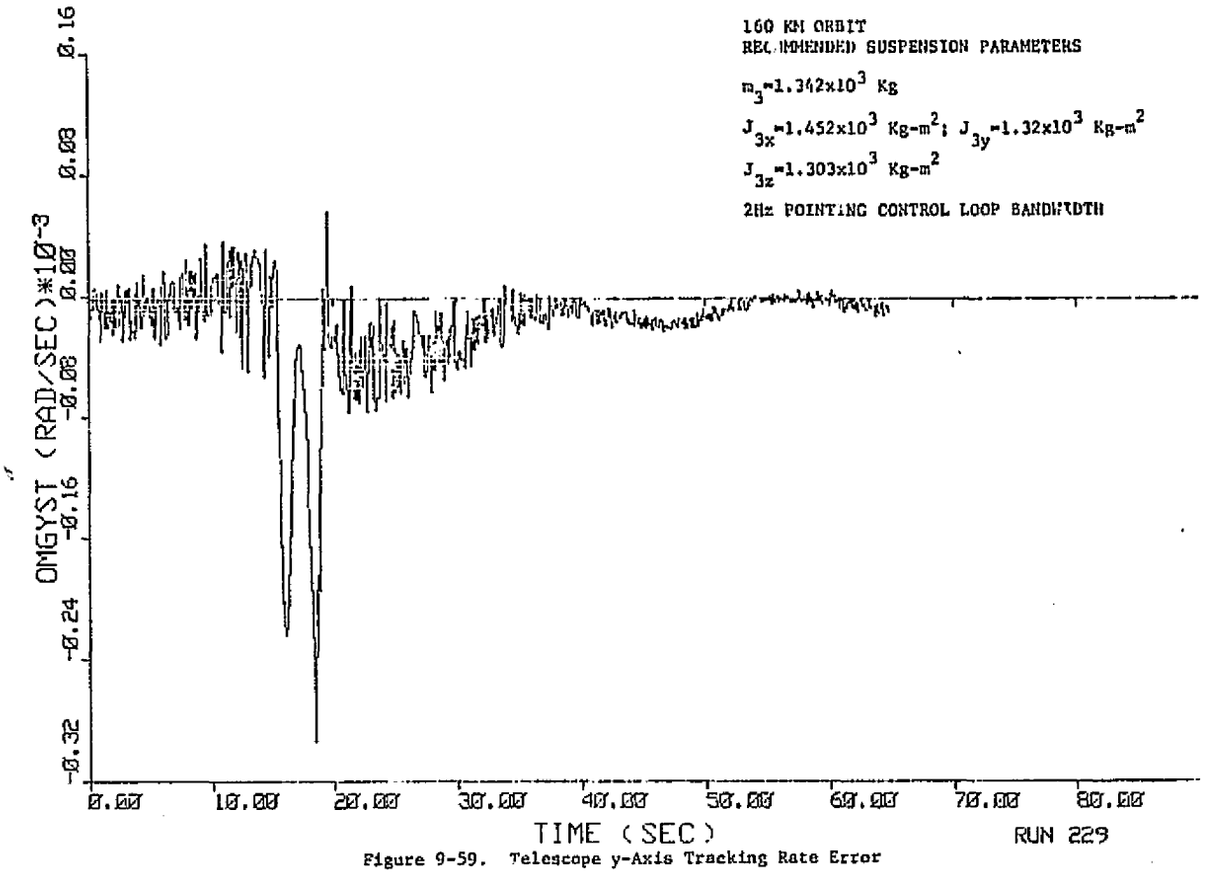

Figure 9-59. Telescope y-Axis Tracking Rate Error

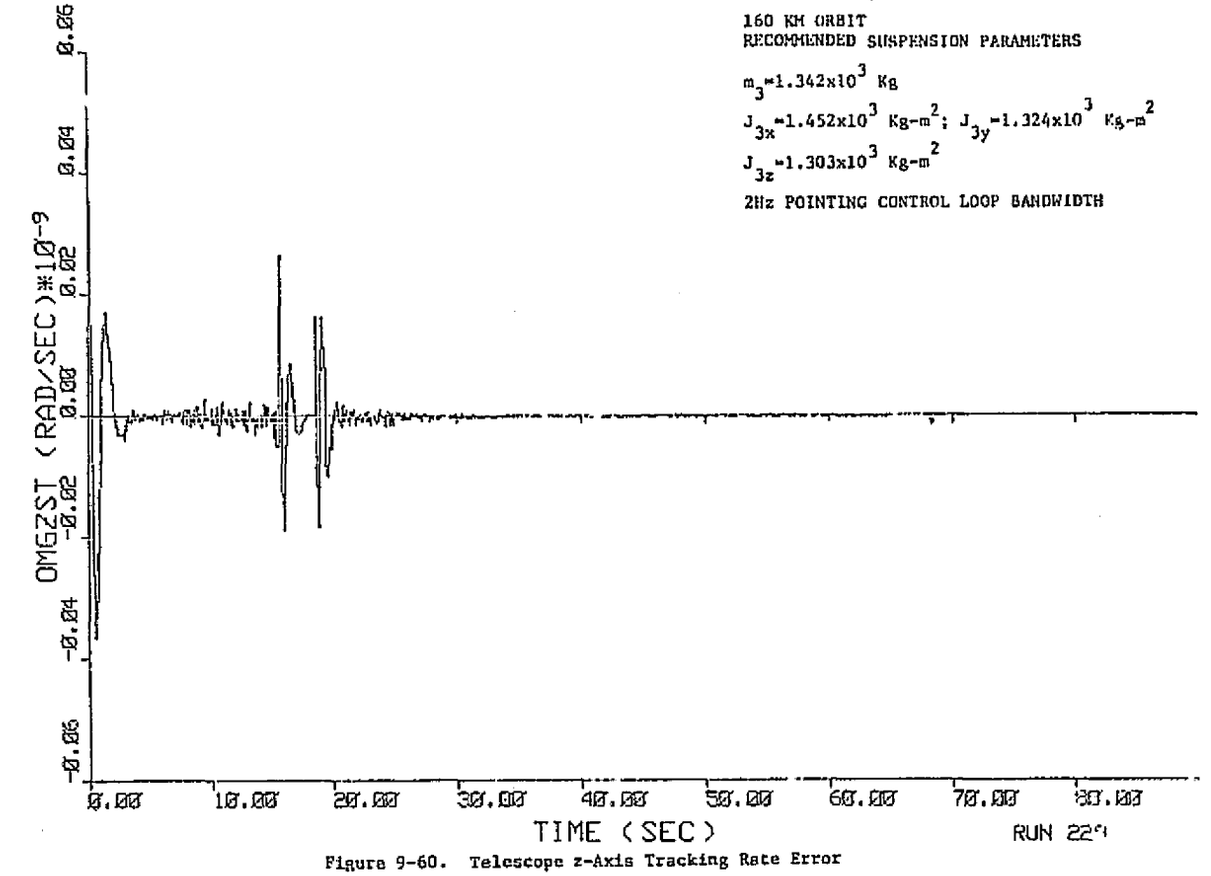

Figure 9-60. Telescope z-Axis Tracking Rate Error

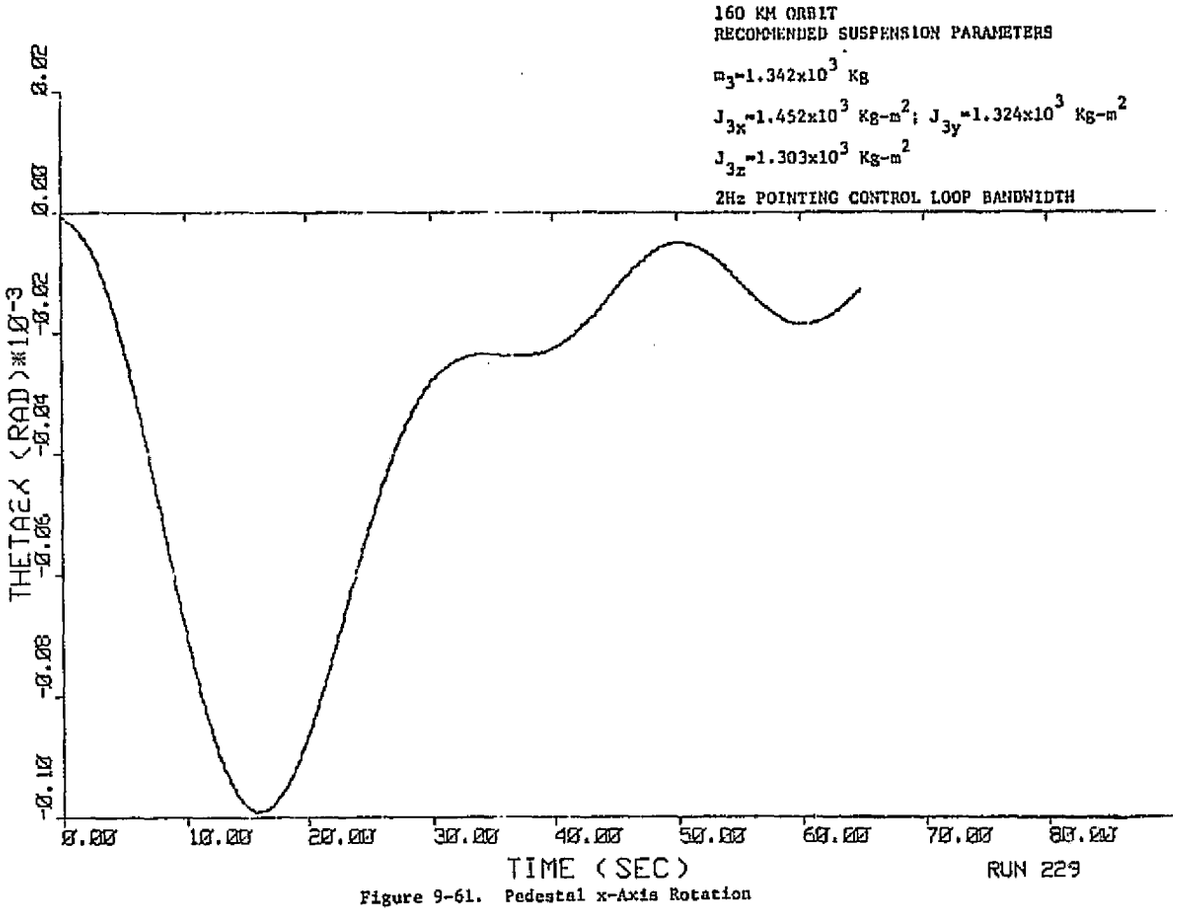

Figure 9-61. Pedestal x-Axis Rotation

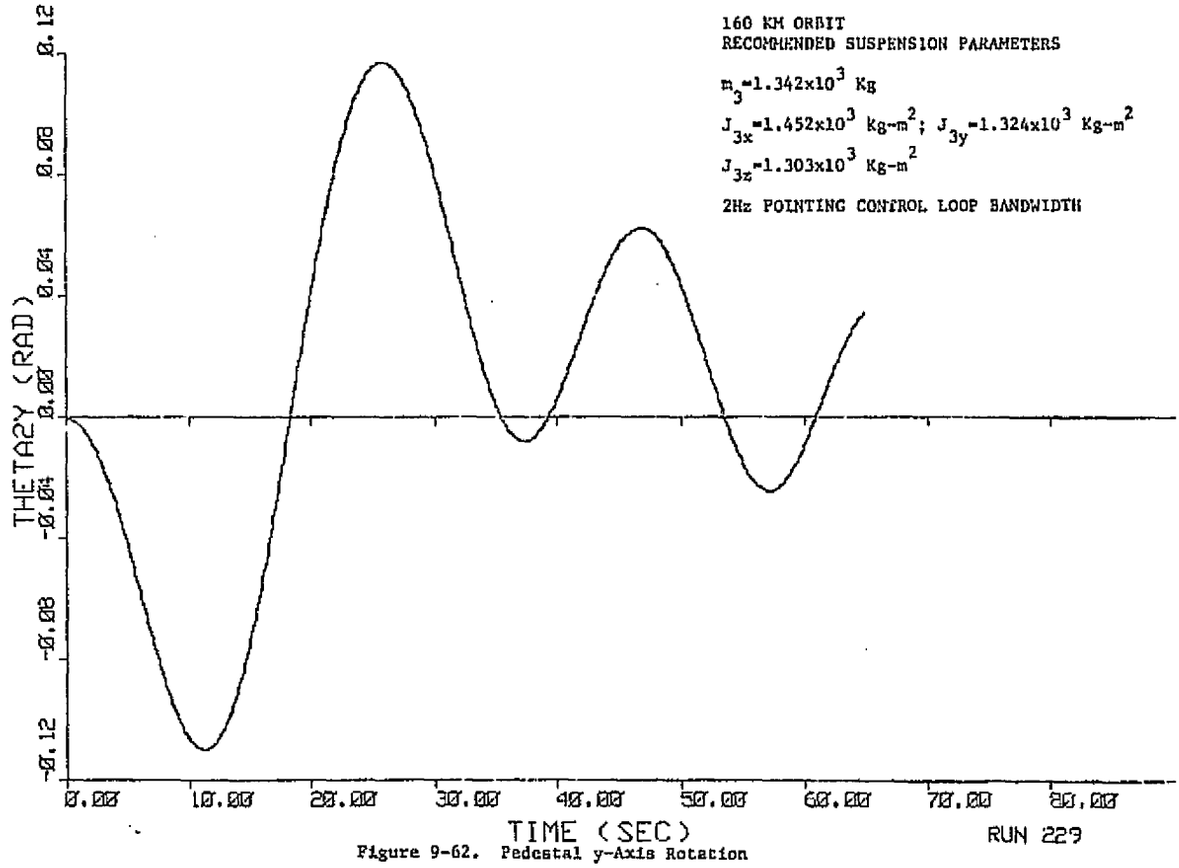

Figure 9-62. Pedestal y-Axis Rotation

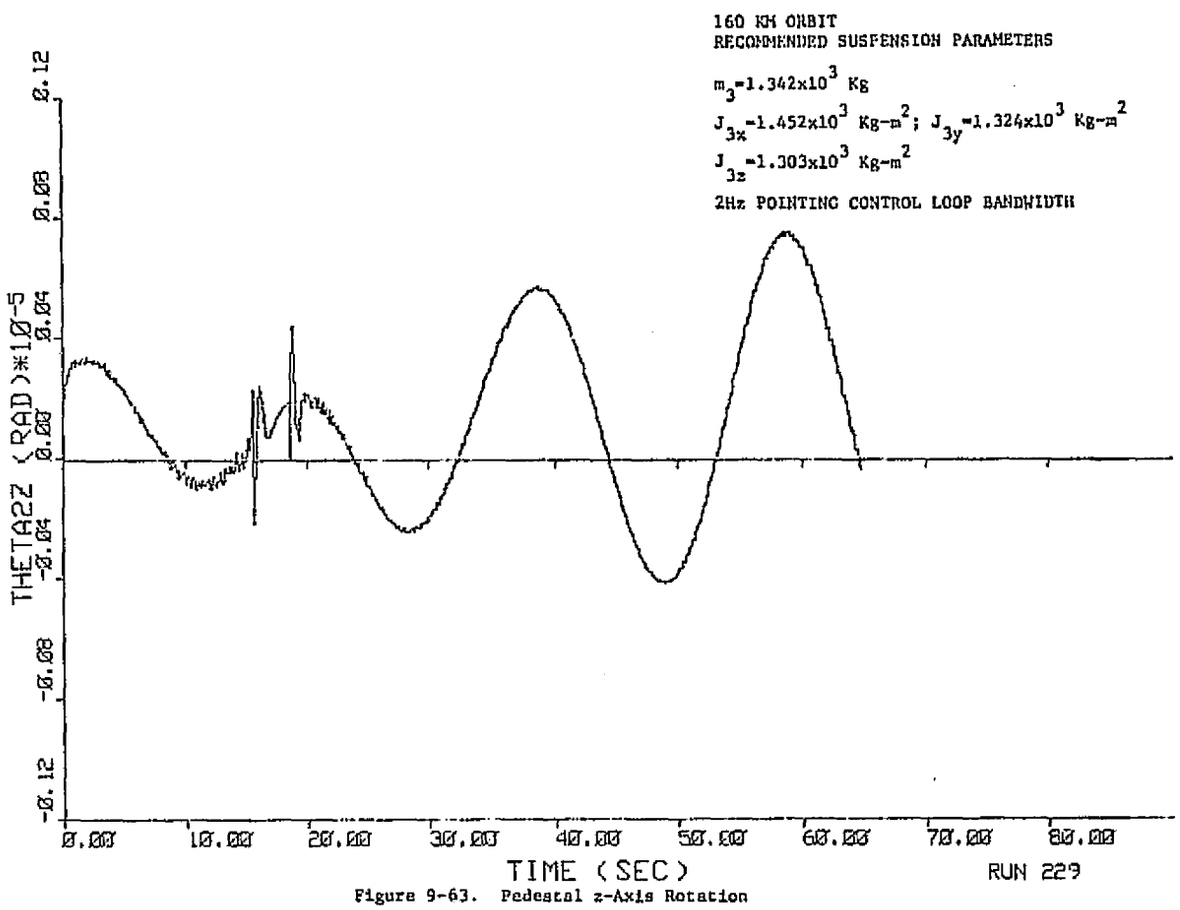

Figure 9-63. Pedestal z-Axis Rotation

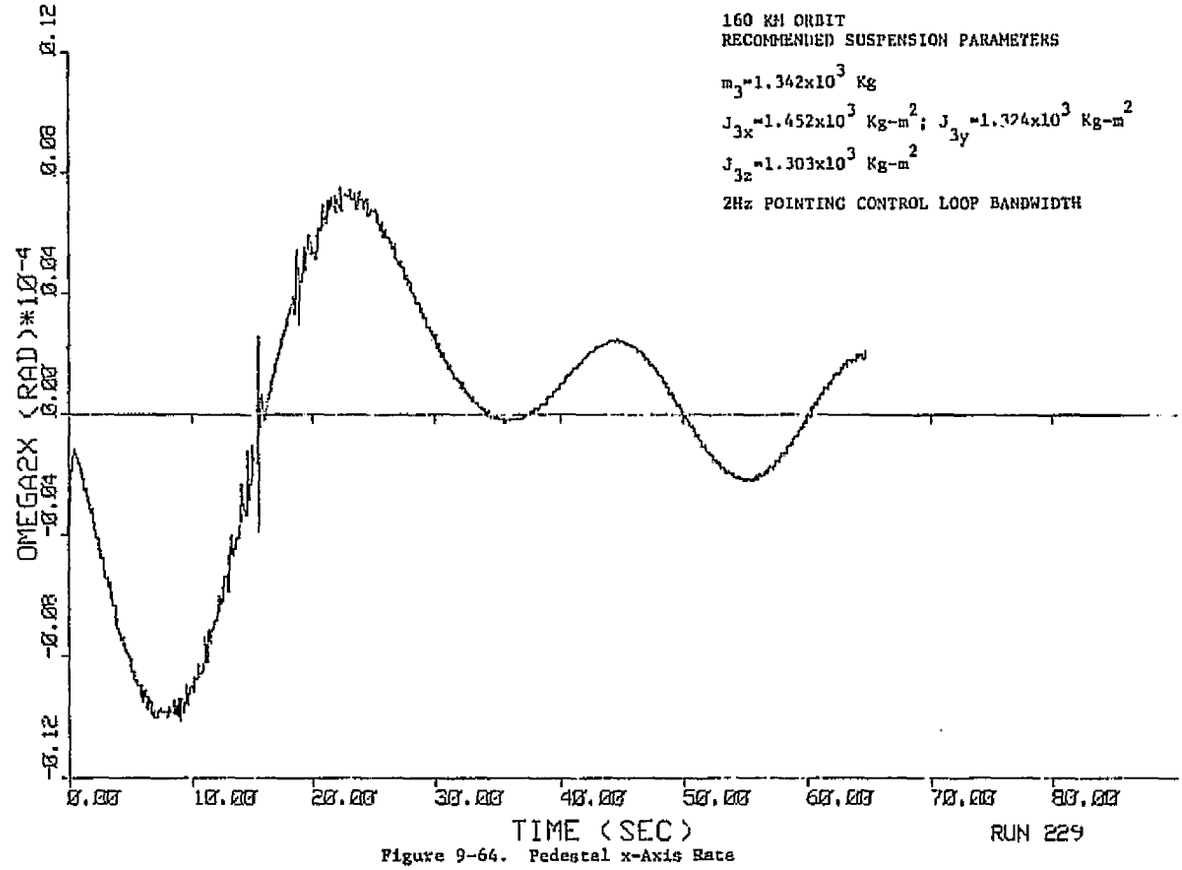

Figure 9-64. Pedestal x-Axis Rate

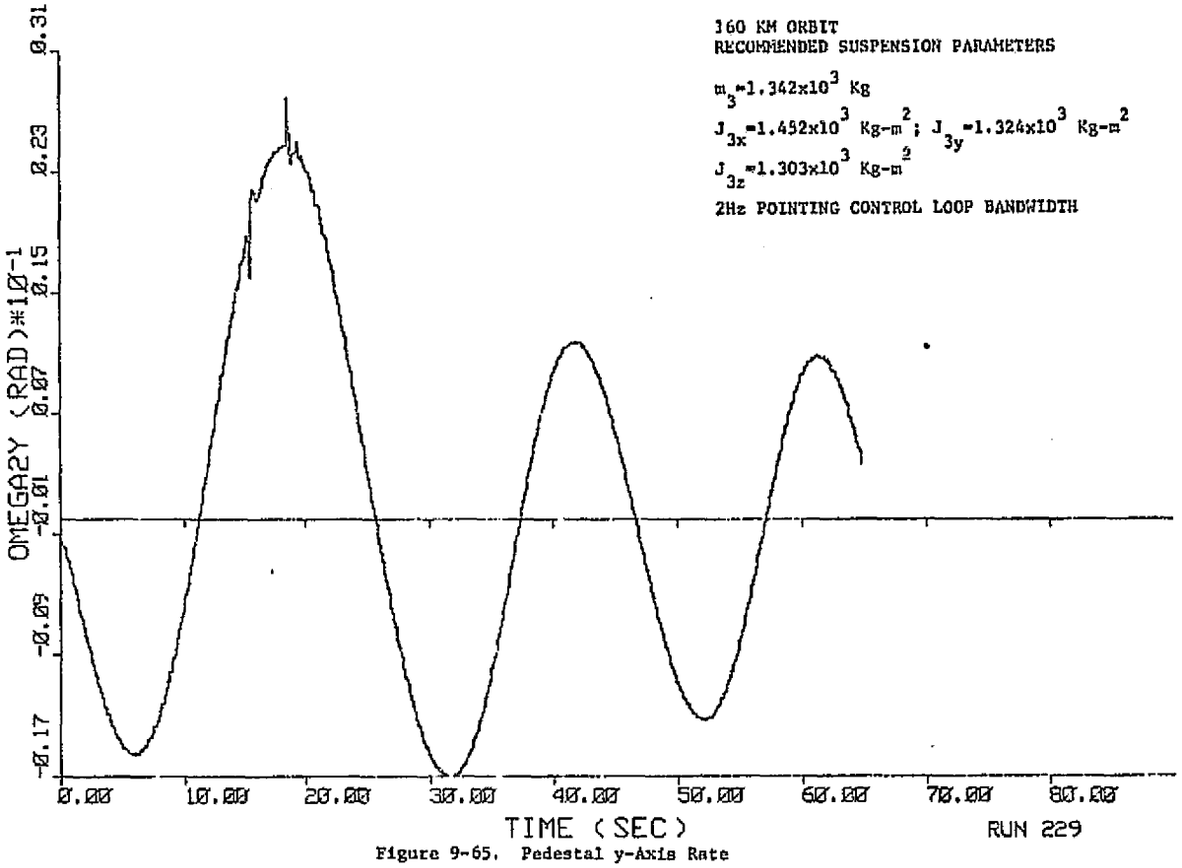

Figure 9-65. Pedestal y-Axis Rate

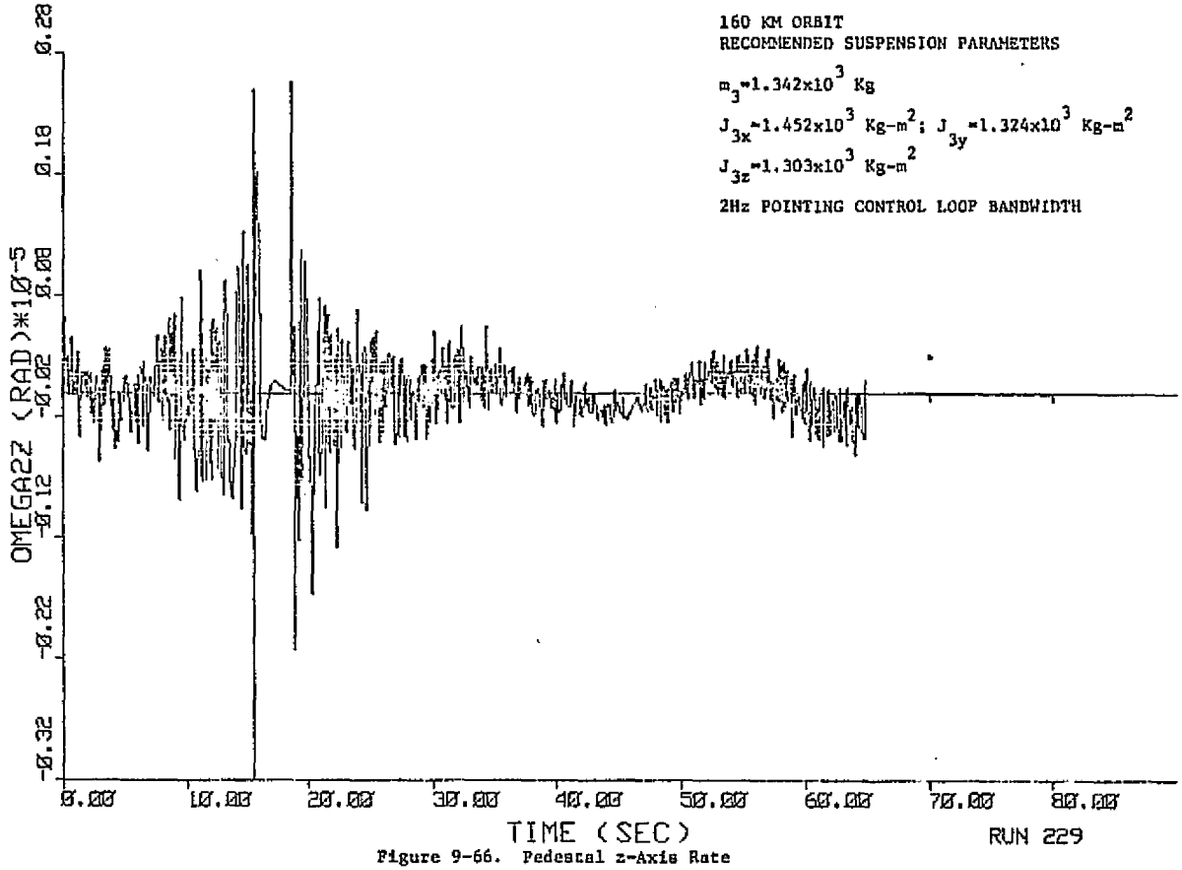

Figure 9-66. Pedestal z-Axis Rate

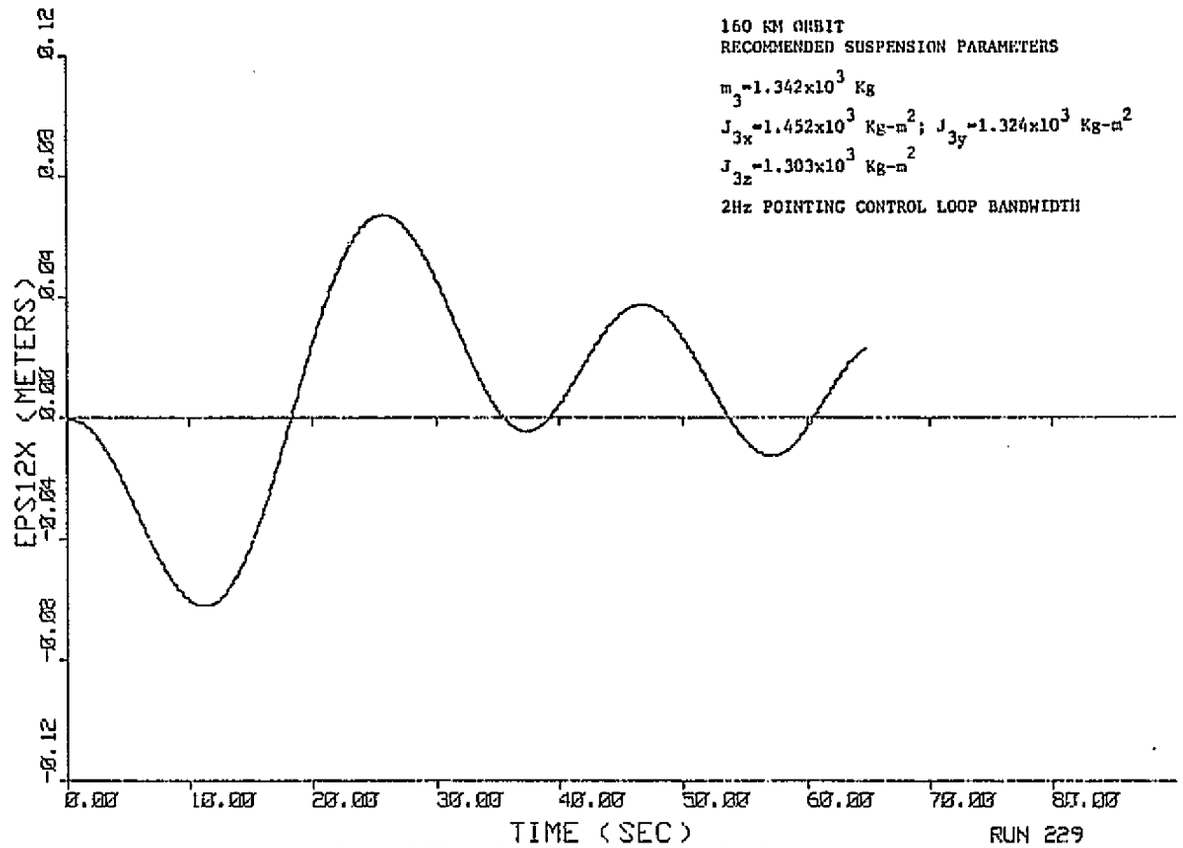

Figure 9-67. Pedestal x-Axis CM Translation

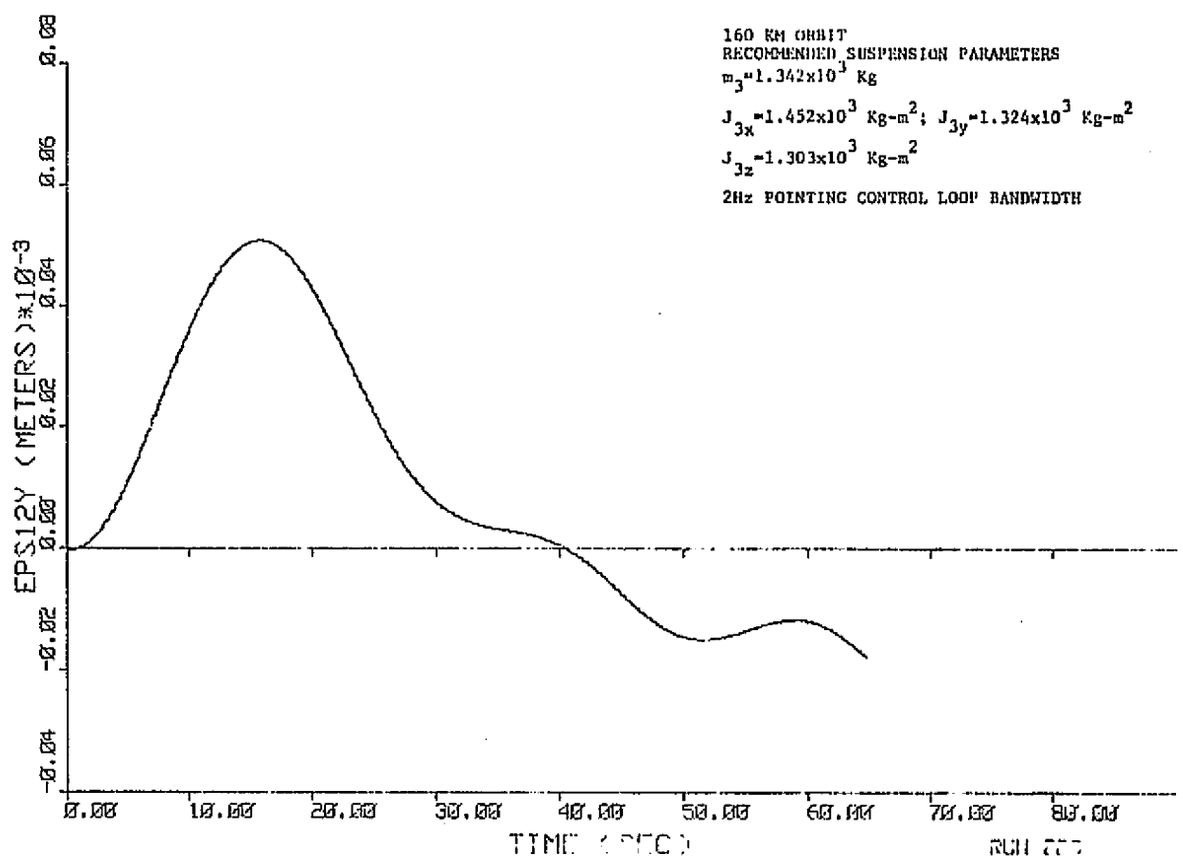

Figure 9-68. Pedestal y-Axis CM Translation

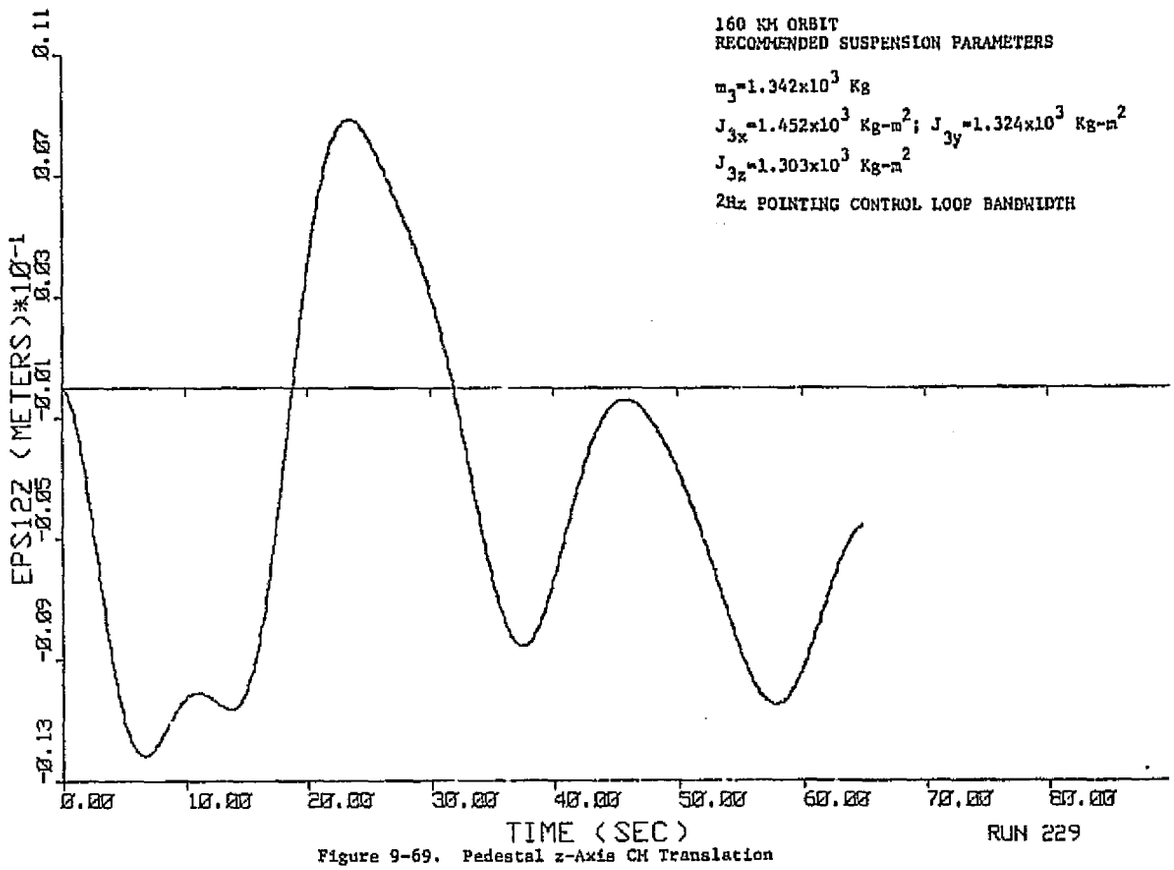

Figure 9-69. Pedestal z-Axis CM Translation

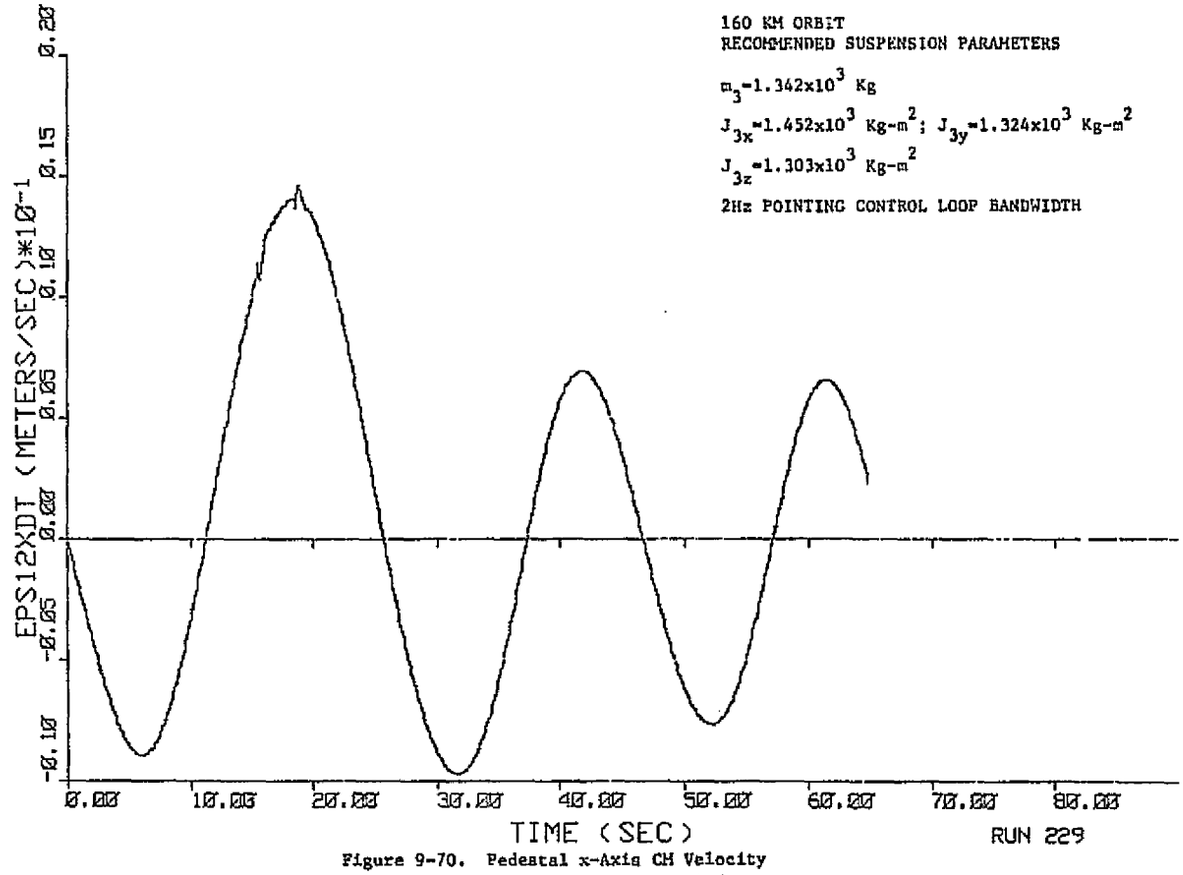

Figure 9-70. Pedestal x-Axis CM Velocity

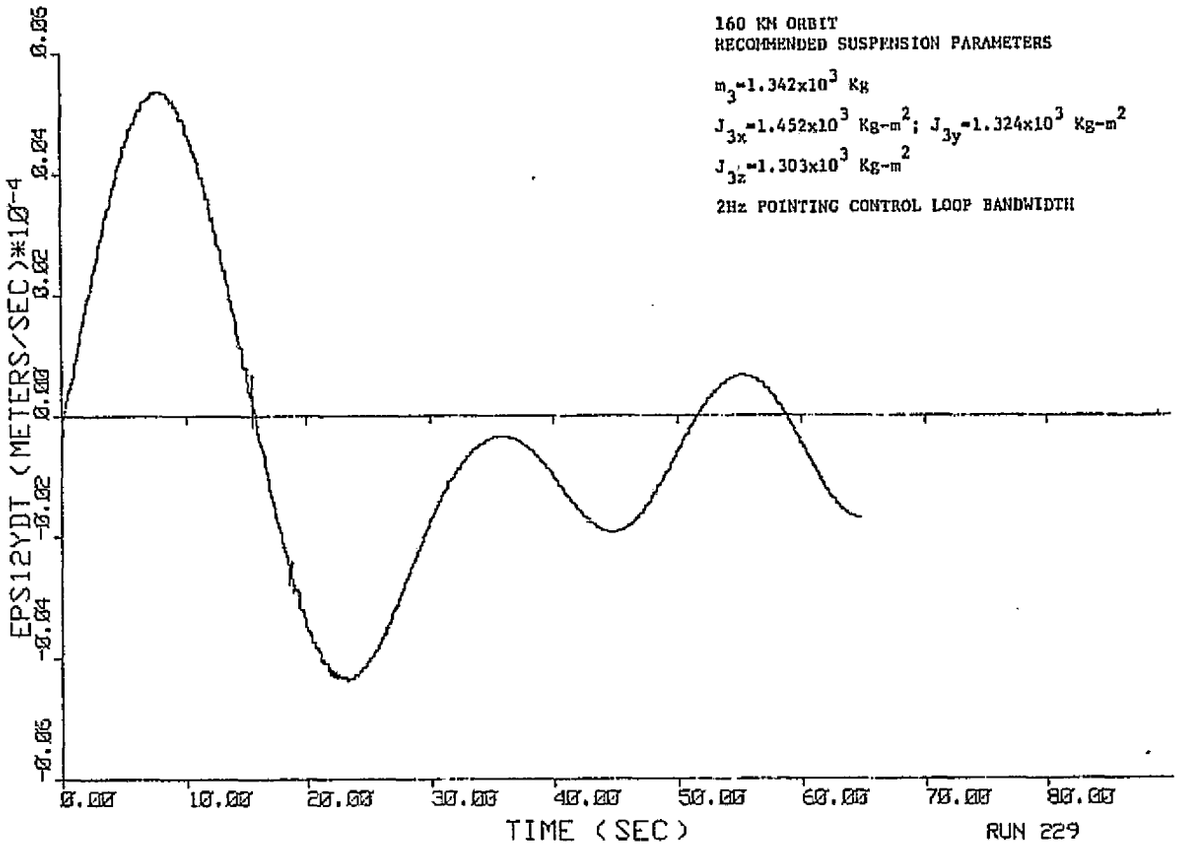

Figure 9-71. Pedestal y-Axis CM Velocity

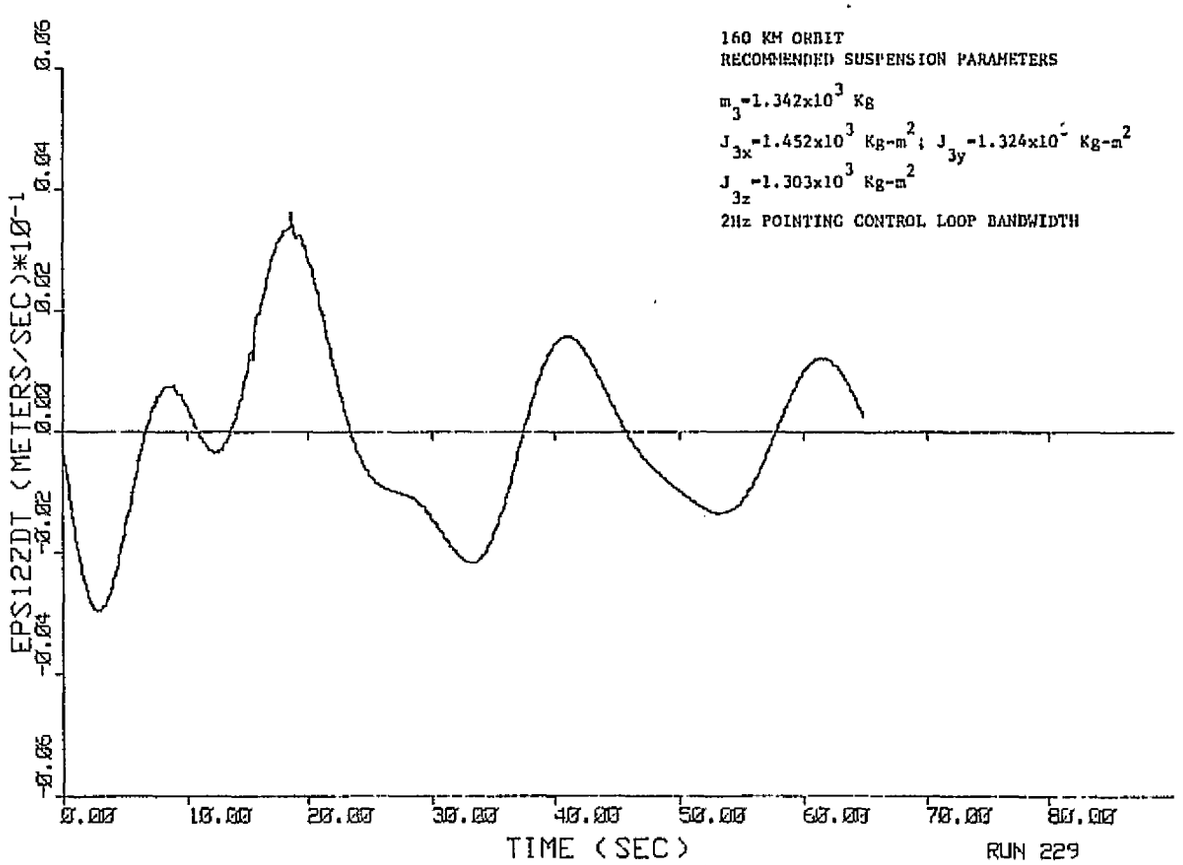

Figure 9-72. Pedestal z-Axis CM Velocity

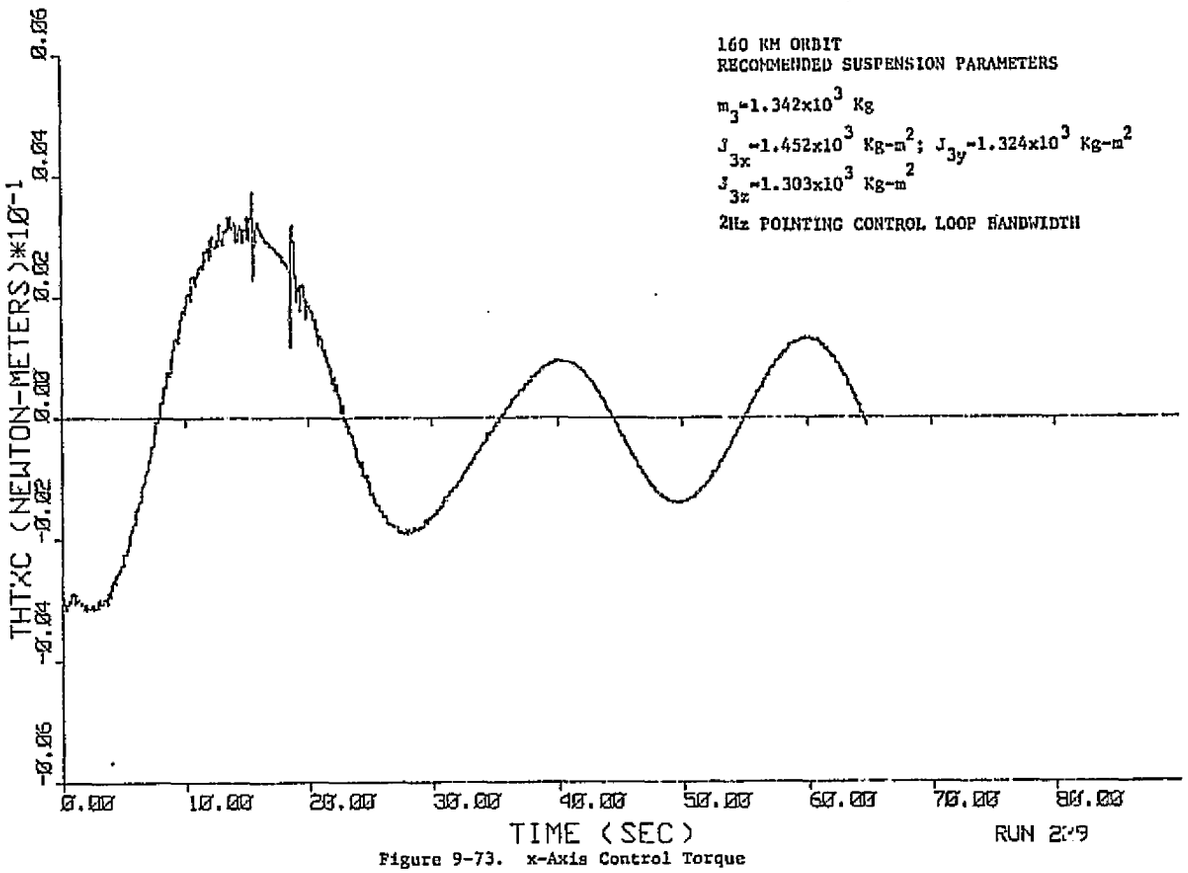

Figure 9-73. x-Axis Control Torque

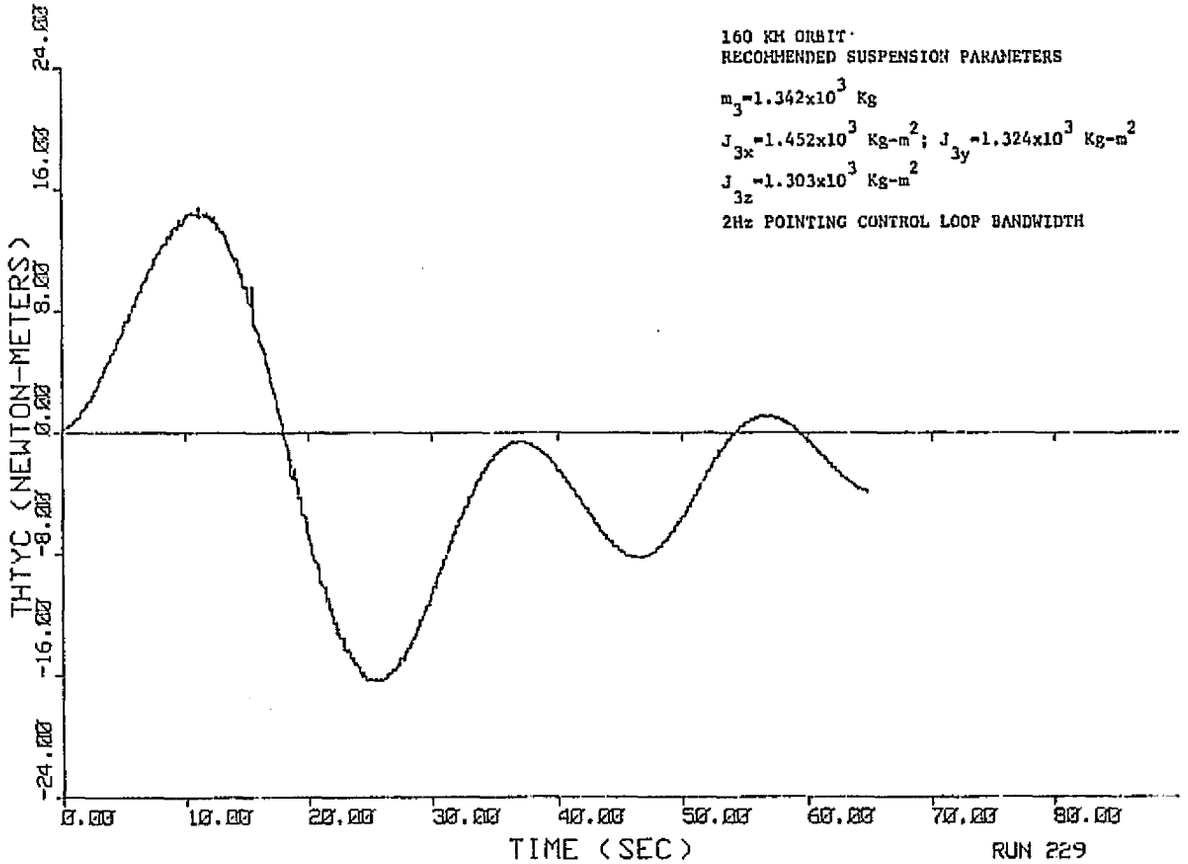

Figure 9-74. y-Axis Control Torque

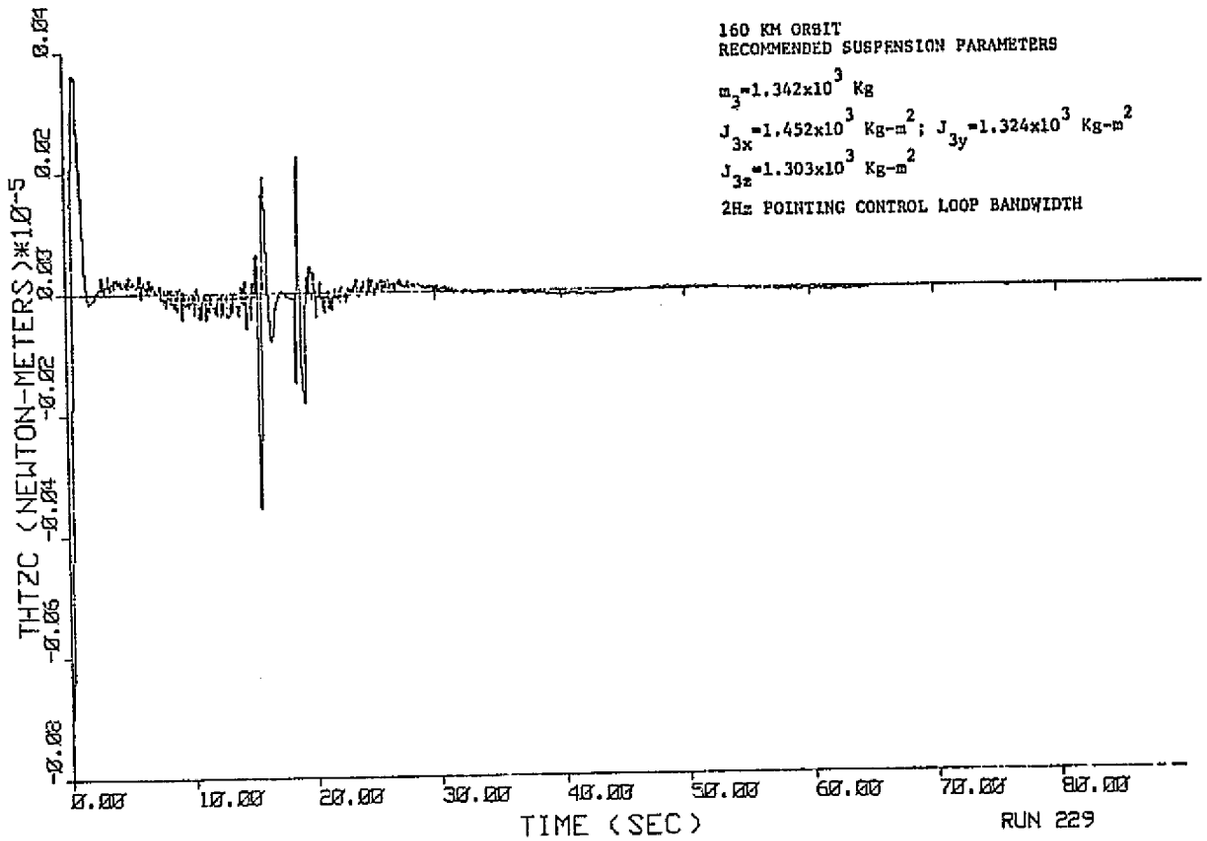

Figure 9-75. z-Axis Control Torque

10. INSTRUMENT POINTING SYSTEM (IPS) NOISE ANALYSIS

This section will develop, via analytical techniques, an insight into the pointing errors as a function of control loop bandwidth for the IPS resulting from sensor and actuator (i.e., gimbal torquers) noise. Various alternate sensing implementations are considered in these evaluations and include the following:

a. Separate Rate Plus Position Sensors

b. Derived Rate

c. Rate Gyro Control

The torque range used by sensor noise for the sensor implementations considered is also derived. These calculations will be used to determine the allowable sensor noise from the viewpoint of both pointing accuracy and the utilization of torquer range. In addition, optimal control loop bandwidths which result in minimum pointing error in the attitude estimate will be determined as a function of gyro and position sensor noise levels. In this evaluation both white and colored noise for the gyros will be considered.

10.1 Separate Rate Plus Position Sensor Implementation

10.1.1 Pointing Error Due to Position Sensor Noise - A simplified single axis linear representation of the telescope control loop using the inside-out gimbal configuration is shown in figure 10-1 where

K_P = position gain (n-m/rad)

K_R = rate gain (n-m/rad/sec)

J = telescope inertia ($Kg\text{-}m^2$)

N = sensor noise input

T_c = control torque (n-m)

The transfer function between sensor noise input N and angular output is given by

$$H(s) = \frac{K_P}{J} \frac{1}{s^2 + \frac{K_R}{J}s + \frac{K_P}{J}} \qquad (10\text{-}1)$$

which can be written as

$$H(s) = \frac{\omega_n^2}{s^2+2\zeta\omega_n s+\omega_n^2} \qquad (10\text{-}2)$$

where

$$\frac{K_P}{J} = \omega_n^2$$

$$\frac{K_R}{J} = 2\zeta\omega_n$$

Equation (10-2) can be rewritten as

$$H(s) = \frac{\omega_n^2}{(s+\zeta\omega_n+j\omega_d)(s+\zeta\omega_n-j\omega_d)} \qquad (10\text{-}3)$$

where

$$\omega_d = \omega_n\sqrt{1-\zeta^2}$$

$$H(j\omega) = \frac{\omega_n^2}{[\zeta\omega_n+j(\omega+\omega_d)][\zeta\omega_n+j(\omega-\omega_d)]} \qquad (10\text{-}4)$$

$$|H(j\omega)|^2 = \frac{\omega_n^4}{[\zeta^2\omega_n^2+(\omega+\omega_d)^2][\zeta^2\omega_n^2+(\omega-\omega_d)^2]} \qquad (10\text{-}5)$$

Expanding equation (10-5) results in

$$|H(j\omega)|^2 = \frac{\omega_n^4}{[\omega^2+2\omega\omega_d+(\omega_d^2+\zeta^2\omega_n^2)][\omega^2-2\omega\omega_d+(\omega_d^2+\zeta^2\omega_n^2)]} \qquad (10\text{-}6)$$

Factoring equation (10-6) gives

$$|H(j\omega)|^2 = \frac{\omega_n^4}{(\omega+\omega_d+j\zeta\omega_n)(\omega+\omega_d-j\zeta\omega_n)(\omega-\omega_d+j\zeta\omega_n)(\omega-\omega_d-j\zeta\omega_n)} \qquad (10\text{-}7)$$

It can be shown that the mean squared vehicle pointing error is given by

$$\lim_{T\to\infty} \frac{1}{2T} \int_{-T}^{T} \theta_o^2(t)dt = \overline{\theta_o^2(t)} = \int_{-\infty}^{+\infty} |H(j\omega)|^2 \Phi_{ii}(\omega)d\omega \qquad (10\text{-}8)$$

where

$\Phi_{ii}(\omega)$ = input noise power spectral density

$\theta_o(t)$ = vehicle angular error

Assuming a flat power spectral density (i.e., white noise) and substituting equation (10-7) into equation (10-8) gives

$$\overline{\theta_o^2(t)} = K_{p.s.} \int_{-\omega}^{+\omega} \frac{\omega_n^4}{(\omega+\omega_d+j\zeta\omega_n)(\omega+\omega_d-j\zeta\omega_n)(\omega-\omega_d+j\zeta\omega_n)(\omega-\omega_d-j\zeta\omega_n)} d\omega \qquad (10\text{-}9)$$

where $K_{p.s.}$ is the amplitude of the flat power density spectrum. The integral shown in equation (10-9) can be evaluated via contour integration using the contour shown in figure 10-2.

$$\overline{\theta_o^2(t)} = K_{p.s.}\omega_n^4 2\pi j \left[\frac{1}{(-\omega_d+j\zeta\omega_n+\omega_d+j\zeta\omega_n)(-\omega_d+j\zeta\omega_n-\omega_d+j\zeta\omega_n)(-\omega_d+j\zeta\omega_n-\omega_d-j\zeta\omega_n)} \right.$$

$$\left. + \frac{1}{(\omega_d+j\zeta\omega_n+\omega_d+j\zeta\omega_n)(\omega_d+j\zeta\omega_n+\omega_d-j\zeta\omega_n)(\omega_d+j\zeta\omega_n-\omega_d+j\zeta\omega_n)} \right] \qquad (10\text{-}10)$$

Equation (10-10) can be written as

$$\overline{\theta_o^2(t)} = \omega_n^4 K_{p.s.} 2\pi j \left[\frac{1}{j8\zeta\omega_n\omega_d(\omega_d-j\zeta\omega_n)} + \frac{1}{j8\zeta\omega_n\omega_d(\omega_d+j\zeta\omega_n)} \right] \qquad (10\text{-}11)$$

which can be written as

$$\overline{\theta_o^2(t)} = \frac{2\pi\omega_n^4 K_{p.s.}}{8\zeta\omega_n\omega_d} \frac{2\omega_d}{\omega_d^2+\zeta^2\omega_n^2} \qquad (10\text{-}12)$$

or

$$\overline{\theta_o^2(t)} = \frac{\pi\omega_n}{2\zeta} K_{p.s.} = \frac{\pi^2 f_n}{\zeta} K_{p.s.} \qquad (10\text{-}13)$$

The rms pointing error is given by

$$\theta_o(t)\big|_{rms}=\pi\sqrt{\frac{K_{p.s.}}{\zeta}\,f_n}^{1/2} \qquad (10\text{-}14)$$

Assuming that 20 percent of the total pointing error will be budgeted for position noise the amplitude of the allowable position noise power spectral density is given by

$$K_{p.s.}=\frac{6.741\times10^{-14}}{f_n}\,\frac{\text{rad}^2}{\frac{\text{rad}}{\text{sec}}}=\frac{4.235\times10^{-13}}{f_n}\,\frac{\text{rad}^2}{\frac{\text{rad}}{\text{sec}}} \qquad (10\text{-}15)$$

where a damping ratio of $\frac{\sqrt{2}}{2}$ was assumed.

10.1.2 Angular Error Due to Rate Gyro Noise Assuming Separate Rate and Position Sensors - Using the block diagram shown in figure 10-3, the transfer function between position error and noise input is given by

$$\frac{\theta_o}{N}=H(s)=-\frac{K_R}{J}\left[\frac{1}{s^2+\frac{K_R}{J}s+\frac{K_p}{J}}\right]=-2\zeta\omega_n\left[\frac{1}{s^2+2\zeta\omega_n s+\omega_n^2}\right] \qquad (10\text{-}16)$$

Using the same techniques as outlined in section 10.1.1

$$|H(j\omega)|^2=4\zeta^2\omega_n^2\left[\frac{1}{[\zeta^2\omega_n^2+(\omega+\omega_d)^2][\zeta^2\omega_n^2+(\omega-\omega_d)^2]}\right] \qquad (10\text{-}17)$$

$$\overline{\theta_o^2(t)}=2\pi jK_{R.G.}\,4\zeta^2\omega_n^2\left[\frac{2\omega_d}{8\zeta\omega_n\omega_d(\omega_d^2+\zeta^2\omega_n^2)}\right]=K_{R.G.}\,\frac{\pi\zeta}{2\omega_n}=K_{R.G.}\,\frac{\zeta}{4f_n}\ (\text{rad})^2 \qquad (10\text{-}18)$$

where

$K_{R.G.}$ = amplitude of flat rate gyro noise power spectral density $\dfrac{\left(\frac{\text{rad}}{\text{sec}}\right)^2}{\frac{\text{rad}}{\text{sec}}}$

Assuming that 20 percent of the allowable 1 sec rms pointing stability error were alloted to rate gyro noise the amplitude of the rate gyro power spectral density is given by

$$K_{R.G.}=5.323\times10^{-12}f_n\left(\frac{\text{rad}}{\text{sec}}\right)^2/\text{rad}\,|\,\text{sec} \qquad (10\text{-}19)$$

10.1.3 Angular Error Due to Torquer Noise - Using the block diagram shown in figure 10-4 the transfer function between angular error and torquer noise input is given by

$$\frac{\theta_o}{N_T} = -\frac{1}{Js^2+K_R s+K_P} = -\frac{1}{J}\frac{1}{s^2+\frac{K_R}{J}s+\frac{K_P}{J}} \tag{10-20}$$

$$|H(j\omega)|^2 = \left(\frac{1}{J^2}\right)\frac{1}{[\zeta^2\omega_n^2+(\omega+\omega_d)^2][\zeta^2\omega_n^2+(\omega-\omega_d)^2]} \tag{10-21}$$

Using the same techniques as outlined in section 10.1.1 the mean squared noise error is given by

$$\overline{\theta_o^2(t)} = \frac{K_{T.G.}}{2J^2\zeta\omega_n^3} = \frac{K_{T.G.}}{16\pi^2J^2\zeta f_n^3}\ (\text{rad})^2 \tag{10-22}$$

where

$K_{T.G.}$ = flat power spectral density amplitude of gimbal torquers $\frac{(n-m)^2}{\frac{rad}{sec}}$

Assuming that 20 percent of the allowable 1 sec pointing error is budgeted for this noise source the following results

$$K_{T.G.} = 1.051\times10^{-10}J^2f_n^3\ \frac{(n-m)^2}{\frac{rad}{sec}} \tag{10-23}$$

where a damping ratio of $\frac{\sqrt{2}}{2}$ was assumed for the control loop.

10.1.4 Torquer Range Used Due to Position Sensor Noise - Using the block diagram shown in figure 10-1 the transfer function between sensor noise input and the resulting torque noise is given by

$$H_T(s) = \frac{K_P Js^2}{Js^2+K_R s+K_P} \tag{10-24}$$

Equation (10-24) can be rewritten as

$$H_T(s) = \frac{(J\omega_n^2)s^2}{s^2+2\zeta\omega_n s+\omega_n^2} \qquad (10\text{-}25)$$

$$H_T(j\omega) = \frac{-J\omega_n^2\omega^2}{(\omega_n^2-\omega^2)+j2\zeta\omega_n\omega} \qquad (10\text{-}26)$$

$$|H_T(j\omega)|^2 = \frac{J^2\omega_n^4\omega^4}{(\omega_n^2-\omega^2)^2+4\zeta^2\omega_n^2\omega^2} \qquad (10\text{-}27)$$

Expanding equation (10-27) results in

$$|H_T(j\omega)|^2 = \frac{J^2\omega_n^4\omega^4}{\omega^4+(4\zeta^2\omega_n^2-2\omega_n^2)\omega^2+\omega_n^4} \qquad (10\text{-}28)$$

which can be written as

$$|H_T(j\omega)|^2 = J^2\omega_n^4\left[1-\frac{(4\zeta^2\omega_n^2-2\omega_n^2)\omega^2+\omega_n^4}{\omega^4+(4\zeta^2\omega_n^2-2\omega_n^2)\omega^2+\omega_n^4}\right] \qquad (10\text{-}29)$$

Using the results shown above (equations (10-3) through (10-7) equation (10-29) can be written as

$$|H_T(j\omega)|^2 = J^2\omega_n^4\left[1-\frac{(4\zeta^2\omega_n^2-2\omega_n^2)\omega^2+\omega_n^4}{(\omega+\omega_d+j\zeta\omega_n)(\omega+\omega_d-j\zeta\omega_n)(\omega-\omega_d+j\zeta\omega_n)(\omega-\omega_d-j\zeta\omega_n)}\right] \qquad (10\text{-}30)$$

The mean square torque noise is given by

$$\overline{T_o^2(t)} = \int_{-\infty}^{+\infty}\Phi_{ii}(\omega)|H_T(j\omega)|^2 d\omega =$$

$$J^2\omega_n^4 K\int_{-\infty}^{+\infty} d\omega - J^2\omega_n^4 K\int_{-\infty}^{+\infty}\frac{(4\zeta^2\omega_n^2-2\omega_n^2)\omega^2+\omega_n^4 d\ \omega}{(\omega+\omega_d+j\zeta\omega_n)(\omega+\omega_d-j\zeta\omega_n)(\omega-\omega_d+j\zeta\omega_n)(\omega-\omega_d-j\zeta\omega_n)} \qquad (10\text{-}31)$$

Examination of equation (10-31) indicates that if a completely flat power spectral density is assumed extending from $\pm\infty$ the first integral is unbounded as must be the case since at frequencies higher than the

servo loop bandwidth the torque transfer function approaches K_p or $J\omega_n^2$. Therefore a noise cutoff will be assumed which actually is the case since the sensors and actuators do have finite bandwidths which were neglected in this simplified analytical model. This noise cutoff will only be assumed in the evaluation of the first integral of equation (10-31). The second integral will be evaluated from $\pm\infty$ as indicated. The second integral in equation (10-31) can be evaluated by contour integration using the path shown in figure 10-2. Therefore

$$\overline{T_o^2(t)}=J^2\omega_n^4K_{p.s.}(2\omega_c)-J^2\omega_n^4K2\pi j$$

$$\left[\frac{(4\zeta^2\omega_n^2-2\omega_n^2)(-\omega_d+j\zeta\omega_n)^2+\omega_n^4}{(-\omega_d+j\zeta\omega_n+\omega_d+j\zeta\omega_n)(-\omega_d+j\zeta\omega_n-\omega_d+j\zeta\omega_n)(-\omega_d+j\zeta\omega_n-\omega_d-j\zeta\omega_n)}\right.$$

$$\left.+\frac{(4\zeta^2\omega_n^2-2\omega_n^2)(\omega_d+j\zeta\omega_n)^2+\omega_n^4}{(\omega_d+j\zeta\omega_n+\omega_d+j\zeta\omega_n)(\omega_d+j\zeta\omega_n+\omega_d-j\zeta\omega_n)(\omega_d+j\zeta\omega_n-\omega_d+j\zeta\omega_n)}\right] \quad (10\text{-}32)$$

where ω_c is the noise or sensor cutoff frequency. Simplifying equation (10-32) results in

$$\overline{T_o^2(t)}=J^2\omega_n^4K_{p.s.}(2\omega_c)\frac{-J^2\omega_n^5\pi K_{p.s.}}{2\zeta}(4\zeta^2-1) \quad (10\text{-}33)$$

Assuming that the sensor cutoff is five times the loop bandwidth ω_n then equation (10-33) can be written as

$$\overline{T_o^2(t)}=10J^2\omega_n^5K_{p.s.}\frac{-J^2\omega_n^5\pi K_{p.s.}}{2\zeta}(4\zeta^2-1) \quad (10\text{-}34)$$

Assuming a damping ratio of $\frac{\sqrt{2}}{2}$ equation (10-34) can be written as

$$T_o^2(t)=J^2\omega_n^5K_{p.s.}\left[10-\frac{\pi}{\sqrt{2}}\right]=7.78J^2\omega_n^5K_{p.s.} \quad (10\text{-}35)$$

Equation (10-35) can also be written as

$$\overline{T_o^2(t)}=7.617\text{x}10^4J^2f_n^5K_{p.s.} \quad (10\text{-}36)$$

Substituting equation (10-15) into equation (10-36) yields

$$\overline{T_o^2(t)} = 5.135 \times 10^{-9} J^2 f_n^4 \qquad (10\text{-}37)$$

$$T_o(t)\big|_{rms} = 7.166 \times 10^{-5} J f_n^2 \qquad (10\text{-}38)$$

The star sensor noise equivalent angle as a function of allowable torque noise can be obtained from equation (10-36) by assuming that the sensor has a bandpass that is five times greater than the corresponding vehicle loop bandwidth which can be expressed by the following relationship

$$\sigma_s^2 = \int_{-\infty}^{+\infty} \Phi_{ss}(\omega) \left| H_s(\omega) \right|^2 d\omega \approx \int_{-5\omega_n}^{5\omega_n} \Phi_{ss}(\omega) d\omega = (2\pi)(10) f_n K_{p.s.} \qquad (10\text{-}39)$$

where

σ_s = sensor noise equivalent angle

$\Phi_{ss}(\omega)$ = sensor noise power spectral density

$H_s(\omega)$ = sensor transfer function

Substituting equation (10-36) into equation (10-39), rearranging, simplifying, and taking the square root results in

$$\sigma_s = 2.872 \times 10^{-2} \frac{T_o(t)\big|_{rms}}{J f_n^2} \text{ rad} = 5.922 \times 10^{3} \frac{T_o(t)\big|_{rms}}{J f_n^2} \text{ sec} \qquad (10\text{-}40)$$

The position sensor noise equivalent angle can also be determined using equation (1' -15). This results in the following

$$\sigma'_s = \int_{-5\omega_n}^{5\omega_n} \frac{6.741 \times 10^{-14}}{f_n} d\omega \Bigg]^{1/2} = \left[20\pi (6.741 \times 10^{-14})\right]^{1/2} = 2.058 \times 10^{-6} \text{ rad} = .4244 \text{ sec} \qquad (10\text{-}41)$$

It should be noted that the position sensor noise equivalent angle was computed over a frequency range equal to five times the IPS pointing control loop bandwidth while using the value of power spectral density amplitude determined in equation (10-15). This was done in order to more realistically compare the impact resulting from pointing stability and torquer range utilization.

Equation (10-33) indicates that the sensor noise equivalent angle must be constant for any control loop bandwidth. It should be noted, however, that if the position sensor is used in an update mode the noise equivalent angle shown in equation (10-33) would only have to be met over the position update loop bandwidth. This can result in a large alleviation of the position sensor noise requirements as the position update loop bandwidth is decreased.

The value of loop bandwidth for which the position sensor noise equivalent angle is equal from both allowable torquer range utilization and pointing stability considerations is given by

$$f_n = 79\left(\frac{T_o(t)\big|_{rms}}{J}\right)^{1/2} \tag{10-42}$$

10.1.5 Torquer Range Used Due to Rate Gyro Noise Assuming Separate Rate and Position Sensors - Using the block diagram shown in figure 10-3 the transfer function between rate gyro noise input and torque output is given by

$$H(s) = \frac{T_o}{N} = \frac{K_R J s^2}{Js^2 + K_R s + K_P} = J\left(\frac{K_R}{J}\right)\frac{s^2}{s^2 + \frac{K_R}{J}s + \frac{K_P}{J}} = \frac{J(2\zeta\omega_n)s^2}{s^2 + 2\zeta\omega_n s + \omega_n^2} \tag{10-43}$$

$$|H(j\omega)|^2 = \frac{J^2 4\zeta^2\omega_n^2\omega^4}{[\zeta^2\omega_n^2 + (\omega+\omega_d)^2][\zeta^2\omega_n^2 + (\omega-\omega_d)^2]}$$

$$= J^2 4\zeta^2\omega_n^2\left[1 - \frac{4(\zeta^2\omega_n^2 - 2\omega_n^2)\omega^2 + \omega_n^4}{\omega^4 + 4(\zeta^2\omega_n^2 - 2\omega_n^2)\omega^2 + \omega_n^4}\right] \tag{10-44}$$

Using the same technique as outlined in section 10.1.4 the torque noise resulting from rate gyro noise is given by

$$\overline{T_o^2(t)} = 8J^2\zeta^2\omega_n^2\omega_c K_{R.G.} - 2\pi J^2\zeta\omega_n^3 K_{R.G.} \tag{10-45}$$

Assuming that the sensor bandwidth is five times the IPS pointing control loop bandwidth equation (10-45) can be written as

$$\overline{T_o^2(t)} = J^2\omega_n^3 K_g(20 - \sqrt{2}\pi) = 15.56J^2\omega_n^3 K_{R.G.} = 3.86\times10^3 J^2 f_n^3 K_{R.G.} \tag{10-46}$$

where a damping ratio of $\frac{1}{\sqrt{2}}$ was assumed.

$$T_o(t)\big|_{rms}=62.19Jf_n^{3/2}K_{R.G.}^{1/2} \tag{10-47}$$

Substituting equation (10-19) into equation (10-47) results in

$$T_o(t)\big|_{rms}=1.435x10^{-4}Jf_n^2 \ (n-m) \tag{10-48}$$

The rate gyro noise equivalent rate error assuming that the rate gyro loop bandwidth is five times larger than the IPS loop bandwidth is given by

$$\sigma_R^2=20\pi f_n K_{R.G.} \tag{10-49}$$

Substituting equation (10-47) into equation (10-49) gives

$$\sigma_R=\frac{0.1276}{Jf_n}\,T_o(t)\big|_{rms}\,\frac{rad}{sec}=\frac{2.631x10^4}{Jf_n}\,T_o(t)\big|_{rms}\,\frac{\widehat{sec}}{sec} \tag{10-50}$$

The rate gyro noise equivalent rate error without consideration of resultant torquer range utilized can be obtained from equation (10-19) as

$$\sigma_R'=1.829x10^{-5}f_n\,\frac{rad}{sec}=3.771f_n\,\frac{\widehat{sec}}{sec} \tag{10-51}$$

where the integration was performed over five times the IPS pointing control loop bandwidth.

The value of loop bandwidth for which the rate noise equivalent error is the same from both torque noise and pointing accuracy viewpoints is given by

$$f_n=83.53\left[\frac{T_o(t)\big|_{rms}}{J}\right]^{1/2} \tag{10-52}$$

Figures 10-5 through 10-10 summarize the results obtained in 10.1.1 through 10.1.5.

10.1.6 Computation of Optimum Pointing Control Loop Bandwidth for Separate Rate Plus Position Sensor Implementation - Using the results obtained in sections 10.1.1 through 10.1.3 the total mean squared error incurred from position, rate, and torquer noise can be written as

$$\overline{\theta_o^2(t)}\big|_{total}=\frac{\pi^2K_{p.s.}}{\zeta}\,f_n+\frac{\zeta K_{R.G.}}{4f_n}+\frac{K_{T.G.}}{16\pi^2J^2\zeta f_n^3} \tag{10-53}$$

Differentiating the above expression with respect to the IPS loop bandwidth f_n and setting the results equal to zero gives

$$\frac{\pi^2 K_{p.s.}}{\zeta} - \frac{\zeta K_{R.G.}}{4f_n^2} - \frac{3K_{T.G.}}{16\pi^2 J^2 \zeta f_n^4} = 0 \qquad (10\text{-}54)$$

Equation (10-54) can also be written as

$$f_n^4 - \frac{\zeta^2}{4\pi^2}\frac{K_{R.G.}}{K_{p.s.}} f_n^2 - \frac{3}{16\pi^4 J^2}\frac{K_{T.G.}}{K_{p.s.}} = 0 \qquad (10\text{-}55)$$

Solving the above equation for f_n results in

$$f_n = \frac{1}{\sqrt{2}}\left\{\frac{\zeta^2}{4\pi^2}\frac{K_{R.G.}}{K_{p.s.}} + \left[\left(\frac{\zeta^2}{4\pi^2}\frac{K_{R.G.}}{K_{p.s.}}\right)^2 + \frac{3}{4\pi^4 J^2}\frac{K_{T.G.}}{K_{p.s.}}\right]^{1/2}\right\}^{1/2} \qquad (10\text{-}56)$$

Equation (10-56) expresses the IPS loop bandwidth that would result in minimum pointing error in the presence of position, rate, and torquer noise for the separate rate plus position implementation as a function of these noise levels.

10.2 Rate Gyro Hold Sensor Implementation

10.2.1 Pointing Error Due to Rate Gyro and Position Noise - The simplified block diagram shown in figure (10-11) represents the rate gyro hold sensor implementation. The transfer function between rate gyro noise input and IPS angular error is given by

$$\frac{\theta_o}{N} = H(s) = \frac{-[K_R s + K_P]}{s[Js^2 + K_R s + K_P]} = -2\zeta\omega_n \frac{s + \frac{\omega_n}{2\zeta}}{s[s^2 + 2\zeta\omega_n s + \omega_n^2]} \qquad (10\text{-}57)$$

and

$$|H(j\omega)|^2 = 4\zeta^2\omega_n^2 \left[\frac{\omega^2 + \frac{\omega_n^2}{4\zeta^2}}{\omega^2[\zeta^2\omega_n^2 + (\omega+\omega_d)^2][\zeta^2\omega_n^2 + (\omega-\omega_d)^2]}\right] \qquad (10\text{-}58)$$

The power spectral density of the resultant pointing error can be written as

$$|\Phi_o(\omega)|^2 = 4\zeta^2\omega_n^2 K_{R.G.}\left[\frac{\omega^2 + \frac{\omega_n^2}{4\zeta^2}}{\omega^2[\zeta^2\omega_n^2+(\omega+\omega_d)^2][\zeta^2\omega_n^2+(\omega-\omega_d)^2]}\right] \qquad (10\text{-}59)$$

Examination of equation (10-59) indicates that there is a double pole at the origin implying that an infinitely large mean squared angular pointing error would result if the rate gyro hold mode were implemented as shown in figure 10-11. This result is not suprising since there is power around dc for the flat power spectral density of gyro rate noise that was assumed and hence the system will drift as time goes on resulting in ever increasing angular pointing error. It is therefore necessary that a gyro update scheme be employed in order to eliminate the effects of gyro drift thus keeping the angular pointing error finite. An analog update loop that can be employed for this function is shown in figure 10-12.

The position estimate power spectral density can be written as

$$|\hat{\theta}_o(\omega)|^2 = \frac{\omega_u^2 K_{p.s.}}{\omega^2+\omega_u^2} + \frac{K_{R.G.}}{\omega^2+\omega_u^2} \qquad (10\text{-}60)$$

The mean squared error of the position estimate can be written as

$$\overline{\hat{\theta}_o^2(t)} = \pi\omega_u K_{p.s.} + \frac{\pi_{R.G.}}{\omega_u} \qquad (10\text{-}61)$$

In order to find the optimum update frequency equation (10-61) can be differentiated with respect to ω_u and the results set equal to zero. This results in

$$\omega_u = \left(\frac{K_{R.G.}}{K_{p.s.}}\right)^{1/2} \qquad (10\text{-}62)$$

or

$$f_u = \frac{1}{2\pi}\left(\frac{K_{R.G.}}{K_{p.s.}}\right)^{1/2} \qquad (10\text{-}63)$$

The optimum mean squared error can be obtained by substituting equation (10-62) into equation (10-61) resulting in

$$\overline{\hat{\theta}_o^2(t)} = 2\pi(K_{p.s.}K_{R.G.})^{1/2} \qquad (10\text{-}64)$$

and the rms error in the position estimate is given by

$$\hat{\theta}_o(t)\big|_{rms} = \sqrt{2\pi}\,(K_{p.s.}K_{R.G.})^{1/4} \tag{10-65}$$

If the position sensor is truely updating the rate gyro then $\omega_u << \omega_n$. Therefore the mean squared error given in equations (10-61) and (10-64) is also the mean squared position error of the vehicle due to what can be thought of as an equivalent position sensor. However, the rate gyro still feeds the signal needed for rate damping into the system and to furnish the high frequency attitude information required for vehicle control. In order to obtain the gyro high frequency (i.e., $\omega_u < \omega < \omega_n$) error contribution, equation (10-59) will be integrated from $-\infty \leq \omega \leq +\infty$. However, contour integration cannot be immediately applied on equation (10-59) since there is a double pole located at the origin. Therefore equation (10-59) is written in the following form

$$|\Phi_o(\omega)|^2 = 4\zeta^2\omega_n^2 K_{R.G.}\left[\frac{A}{\omega^2} + \frac{B\omega+C}{\zeta^2\omega_n^2+(\omega+\omega_d)^2} + \frac{D\omega+E}{\zeta^2\omega_n^2+(\omega-\omega_d)^2}\right] \tag{10-66}$$

Upon evaluating constants A, B, C, and D the following results

$$A = \frac{1}{4\zeta^2\omega_n^2} \tag{10-67}$$

$$B = \frac{3}{16\zeta^2\omega_d\omega_n^2} \tag{10-68}$$

$$C = \frac{1}{4\zeta^2\omega_n^2} \tag{10-69}$$

$$D = -\frac{3}{16\zeta^2\omega_d\omega_n^2} \tag{10-70}$$

$$E = \frac{1}{4\zeta^2\omega_n^2} \tag{10-71}$$

Substituting equations (10-67) through (10-71) into equation (10-66) the following results

$$|\Phi_o(\omega)|^2 = K_{R.G.}\left[\frac{1}{\omega^2} + \frac{\frac{3}{4\omega_d}\omega + 1}{\omega^2 + 2\omega\omega_d + \omega_n^2} + \frac{1 - \frac{3}{4\omega_d}\omega}{\omega^2 - 2\omega\omega_d + \omega_n^2}\right] \qquad (10\text{-}72)$$

Examination of the first term in the brackets of equation (10-72) indicates that an infinitely large angular error will result when that term is integrated between $\pm\infty$. This is to be expected since as indicated above it reflects the fact that the gyro will cause a vehicle drift since there is energy in the flat rate power spectral density assumed for the rate gyro around dc. However, the gyro drift error is taken care of by the gyro update loop as outlined above. The high frequency noise contribution of the rate gyro can be obtained by integration of the second two terms in equation (10-72) over all of frequency. Performing the evaluation results in

$$\overline{\theta_o^2(t)}\Big|_{\text{high frequency}} = \frac{\pi K_{R.G.}}{2\zeta\omega_n} \qquad (10\text{-}73)$$

Therefore the total vehicle mean squared pointing error due to sensors can be written as the sum of the low frequency errors given in equations (10-61) and (10-64) and the high frequency error given in equation (10-73) which results in

$$\overline{\theta_o^2(t)}\Big|_{\substack{\text{total}\\ \text{sensor}}} = \pi\omega_u K_{p.s.} + \frac{\pi K_{R.G.}}{\omega_u} + \frac{\pi K_{R.G.}}{2\zeta\omega_n} \qquad (10\text{-}74)$$

Substituting the optimum update frequency value given in equation (10-62) results in

$$\overline{\theta_o^2(t)}\Big|_{\substack{\text{total}\\ \text{sensor}}} = 2\pi(K_{p.s.}K_{R.G.})^{1/2} + \frac{\pi K_{R.G.}}{2\zeta\omega_n} \qquad (10\text{-}75)$$

The overall mean squared pointing error due to both sensors and actuators is given by

$$\overline{\theta_o^2(t)}\Big|_{\text{total}} = 2\pi(K_{p.s.}K_{R.G.})^{1/2} + \frac{\pi K_{R.G.}}{2\zeta\omega_n} + \frac{\pi K_{T.G.}}{2J^2\zeta\omega_n^3} \qquad (10\text{-}76)$$

Examination of equation (10-76) indicates that there is no clear optimum loop bandwidth, for minimum pointing error, at which the rate gyro hold loop should operate. The noise error incurred will decrease with increasing loop bandwidth and will be asymptotic to

$$\overline{\theta_o^2(t)}\Big|_{\substack{\text{total}\\ \text{asump}}} = 2\pi(K_{p.s.}K_{R.G.})^{1/2} \tag{10-77}$$

These results have been verified on various LST simulations where rate gyro hold was employed.

Assuming that 20 percent of the allowable 1 sec pointing error would be budgeted for high frequency rate gyro noise the following results

$$K_{R.G.} = 4.236\text{x}10^{-13}\omega_n \frac{\left(\frac{\text{rad}}{\text{sec}}\right)^2}{\frac{\text{rad}}{\text{sec}}} \tag{10-78}$$

where a damping ratio of $\frac{1}{\sqrt{2}}$ was assumed.

Assuming that the position sensor and torquer noise power spectral density are those given in equations (10-15) and (10-19), respectively, the resultant mean squared pointing error for the rate gyro hold sensor implementation is given by

$$\overline{\theta_o^2(t)} = 2\pi(5.323\text{x}10^{-12}\text{x}4.235\text{x}10^{-13})^{1/2} + 2[.2(4.85\text{x}10^{-6})]^2 = 1.132\text{x}10^{-11}\ \text{rad}^2 \tag{10-79}$$

$$\theta_o(t)\Big|_{\substack{\text{total}\\ \text{rms}}} = 3.364\text{x}10^{-6}\ \text{rad} = .6936\ \text{sec} \tag{10-80}$$

It is therefore seen that the total rms IPS pointing error will be met with the numbers budgeted for the various error sources.

10.2.2 Torque Noise Due to Rate Gyro Noise for Rate Gyro Hold Sensor Implementation - Using the block diagram shown in figure (10-11) the transfer function between gyro noise input and the resultant torque noise is given by

$$\frac{T_o}{N} = H(s) = \frac{Js[K_R s + K_P]}{Js^2 + K_R s + K_P} \tag{10-81}$$

and

$$|H(j\omega)|^2 = \frac{J^2 4\zeta^2\omega_n^2\omega^2\left[\omega^2+\frac{\omega_n^2}{4\zeta^2}\right]}{[\zeta^2\omega_n^2+(\omega+\omega_d)^2][\zeta^2\omega_n^2+(\omega-\omega_d)^2]} \qquad (10\text{-}82)$$

Using the same techniques as outlined in sections 10.1.4 and 10.1.5 the mean squared torque noise resulting from rate gyro noise is given by

$$\overline{T_o^2(t)} = 8\zeta^2\omega_n^2 J^2\omega_c K_{R.G.} + \frac{\pi J^2\omega_n^3 K_{R.G.}}{2\zeta}[1+4\zeta^2-16\zeta^4] \qquad (10\text{-}83)$$

Assuming a rate gyro cutoff frequency of five times the IPS pointing control loop bandwidth the following results

$$\overline{T_o^2(t)} = 40\zeta^2\omega_n^3 J^2 K_{R.G.} + \frac{\pi J^2\omega_n^3}{2\zeta} K_{R.G.}[1+4\zeta^2-16\zeta^4] \qquad (10\text{-}84)$$

Assuming a loop damping of $\frac{1}{\sqrt{2}}$ the mean squared noise torque becomes

$$\overline{T_o^2(t)} = 17.78\omega_n^3 J^2 K_{R.G.} \qquad (10\text{-}85)$$

The gyro mean squared rate error assuming a cutoff of five times the loop bandwidth is given by

$$\sigma_R^2 = 10\omega_n K_{R.G.} \qquad (10\text{-}86)$$

Substituting equation (10-85) into equation (10-86), simplifying and taking the square root results in

$$\sigma_R = .1194\ \frac{T_o(t)|_{rms}}{Jf_n}\left(\frac{rad}{sec}\right) \qquad (10\text{-}87)$$

The rms rate error allowable from pointing considerations only is given by

$$\sigma_R' = 1.829\times10^{-5} f_n \qquad (10\text{-}88)$$

Therefore the loop bandwidth for which the allowable gyro mean squared rate error is equal from both pointing accuracy and torquer range utilization viewpoints is given by

$$f_n = 80.8\left(\frac{T_o(t)\big|_{rms}}{Jf_n}\right)^{1/2} \qquad (10\text{-}89)$$

These expressions are essentially equal to those shown in section 10.1.5 and hence the plots of those expressions also apply here.

10.2.3 Pointing Accuracies and Update Frequencies Involved When Using the LDG 540 Gyro in a Rate Gyro Hold Mode - Using the noise data for the LDG 540 gyro obtained by Martin Marietta Aerospace and presented at the Seventh Biennial Guidance Test Symposium at Holloman Air Force Base in a paper titled "Testing Technology for Fine Pointing Systems" by R. L. Gates, the low frequency power spectral density of the LDG 540 can be approximated as

$$|\phi(\omega)|^2 = \frac{2.211\times10^{-18}}{\omega^2}\ \frac{\text{rad}^2}{\frac{\text{rad}}{\text{sec}}} \qquad (10\text{-}90)$$

where adjustments were made to the data presented in the paper to obtain the units employed in this report, and to account for the double sided power spectral densities employed throughout this study. Since the data is presented in terms of an angular power spectral density referred to as table motion when it is controlled by the LDG 540 gyro operating in the attitude mode, the gyro update loop considered in section 10.2.1 can be revised in the following manner as shown in figure (10-13).

It should be noted that this formulation favors the LDG 540 gyro since the noise due to the electronics which would be present in the strapdown mode is not accounted for in equation (10-90). However, it is presently felt that the electronic noise contribution in the frequency range of interest is not substantial enough to grossly change the results obtained.

The transfer function between rate gyro noise input θ_{gn} and angular error output is given by

$$H(s) = \frac{s}{s+\omega_u} \qquad (10\text{-}91)$$

and

$$|H(j\omega)|^2 = \frac{\omega^2}{\omega^2+\omega_u^2} \qquad (10\text{-}92)$$

The power spectral density of the angular error in the position estimate due to rate gyro noise is given by

$$|\theta(\omega)|^2 = \frac{2.211\text{x}10^{-18}}{\omega^2+\omega_u^2} \qquad (10\text{-}93)$$

The mean squared angular error in the position estimate due to rate gyro noise is given by

$$\overline{\hat{\theta}_o^2(t)}\Big|_{R.G.} = \frac{\pi(2.211\text{x}10^{-18})}{\omega_u} \qquad (10\text{-}94)$$

The total mean squared error in the position estimate due to both rate gyro and position noise is given by

$$\overline{\hat{\theta}_o^2(t)}\Big|_{total} = \frac{\pi(2.211\text{x}10^{-18})}{\omega_u} + \pi\omega_u K_{p.s.} \qquad (10\text{-}95)$$

The optimum update loop bandwidth resulting in minimum error in the position estimate is given by

$$\omega_u = \left(\frac{2.211\text{x}10^{-18}}{K_{p.s}}\right)^{1/2} \qquad (10\text{-}96)$$

and the total mean squared error in the position estimate is given by

$$\overline{\hat{\theta}_o^2(t)}\Big|_{total} = 2\pi(2.211\text{x}10^{-18}\text{x}K_{p.s.})^{1/2} \qquad (10\text{-}97)$$

The total pointing error due to both rate gyro and position sensor noise can be written as [i.e., equation (76)]

$$\overline{\theta_o^2(t)}\Big|_{total} = 2\pi(2.211\text{x}10^{-18}K_{p.s.})^{1/2} + \frac{\pi(2.211\text{x}10^{-18})}{2\zeta\omega_n} + \frac{\pi(K_{T.G.})}{2J^2\zeta\omega_n^3} \qquad (10\text{-}98)$$

Using the value for position sensor noise given in equation (10-15) and assuming an IPS loop bandwidth of 2 Hz with a damping ratio of $\frac{\sqrt{2}}{2}$ the following results

$$\overline{\theta_o^2(t)}\Big|_{total} = 9.452\text{x}10^{-13}\ \text{rad}^2 \qquad (10\text{-}99)$$

$$\theta_o(t)\Big|_{\substack{\text{total}\\ \text{rms}}} = 9.722\text{x}10^{-7} \text{ rad} = .2005 \text{ sec} \qquad (10\text{-}100)$$

This value of rms pointing error is almost totally due to torque generator noise and the contribution of the position sensor noise has been virtually eliminated by the use of the LDG 540 in a rate gyro hold mode. The gyro update frequency is given by

$$f_u = 5.142\text{x}10^{-4} \text{ Hz} \qquad (10\text{-}101)$$

or

$$\tau_u = 1,945 \text{ sec} \qquad (10\text{-}102)$$

This calculation indicates the reduced sensitivity to position noise that can be obtained using a rate gyro in an update mode. However, it seems that the LDG 540 gyro is considerably better than that needed for the IOG.

10.3 Derived Rate Sensor Implementation

10.3.1 Angular Error Due to Position Noise for Derived Rate Sensor Implementation - A simplified block diagram of the IPS control loop using a derived rate sensor implementation is shown in figure 10-14. The transfer function between position noise input and the resultant angular error is given by

$$\frac{\theta_o}{N} = H(s) = \frac{K_R}{J}\left[\frac{s+\frac{K_P}{K_R}}{s^2+\frac{K_R}{J}s+\frac{K_P}{J}}\right] = 2\zeta\omega_n\left[\frac{s+\frac{\omega_n}{2\zeta}}{s^2+2\zeta\omega_n s+\omega_n^2}\right] \qquad (10\text{-}103)$$

and

$$|H(j\omega)|^2 = 4\zeta^2\omega_n^2\left[\frac{\omega^2+\frac{\omega_n^2}{4\zeta^2}}{(\omega^2+2\omega_d\omega+\omega_n^2)(\omega^2-2\omega\omega_d+\omega_n^2)}\right] \qquad (10\text{-}104)$$

Using the same method as outlined above the mean squared angular position error can be written as

$$\overline{\theta_o^2(t)} = \left(\frac{4\zeta^2+1}{\zeta}\right)\pi^2 K_{p.s.} f_n \qquad (10\text{-}105)$$

The ratio of the mean squared angular error due to position sensor noise using the derived rate sensor implementation to that incurred using the separate rate plus position sensor implementation is given by

$$\frac{\overline{\theta_o^2(t)}\Big|_{\substack{\text{derived}\\ \text{rate}}}}{\overline{\theta_o^2(t)}\Big|_{\substack{\text{separate}\\ \text{rate plus}\\ \text{position}}}} = 4\zeta^2+1 \qquad (10\text{-}106)$$

For a system damping of $\frac{1}{\sqrt{2}}$, this ratio is three or approximately 1.73 times the rms angular error due to position sensor noise results when the derived rate sensor implementation is used over that which would be incurred for the separate rate plus position sensor implementation.

10.3.2 Torque Noise Due to Position Noise for the Derived Rate Sensor Implementation - Using the block diagram shown in figure 10-14 the transfer function between position noise input and torque noise output is given by

$$\frac{T_o}{N} = H(s) = \frac{Js^2[K_P+K_R s]}{Js^2+K_R s+K_P} = \frac{J2\zeta\omega_n s^2\left[s+\frac{\omega_n}{2\zeta}\right]}{s^2+2\zeta\omega_n s+\omega_n^2} \qquad (10\text{-}107)$$

and

$$|H(j\omega)|^2 = \frac{J^2 4\zeta^2\omega_n^2\omega^4\left[\omega^2+\frac{\omega_n^2}{4\zeta}\right]}{\omega^4+(4\zeta^2-2)\omega_n^2\omega^2+\omega_n^4} \qquad (10\text{-}108)$$

Equation (10-108) can also be written as

$$|H(j\omega)|^2 = J^2 4\zeta^2\omega_n^2\left[\omega^2+\left(\frac{1+8\zeta^2-16\zeta^4}{4\zeta^2}\right)\omega_n^2\right] + J^2\omega_n^2\left[\frac{A\omega^2+B}{\omega^4+(4\zeta^2-2)\omega_n^2\omega^2+\omega_n^4}\right] \qquad (10\text{-}109)$$

where

$$A = [(2-4\zeta^2)(1+8\zeta^2-16\zeta^4)-4\zeta^2]\omega_n^4 \qquad (10\text{-}110)$$

$$B = [16\zeta^4-8\zeta^2-1]\omega_n^6 \qquad (10\text{-}111)$$

Using the same technique as outlined in section 10.1.4 the mean squared torque noise can be written as

$$\overline{T_o^2(t)} = 8J^2\zeta^2\omega_n^2\left[\frac{\omega_c^3}{3} + \frac{1+8\zeta^2-16\zeta^4}{4\zeta^2}\,\omega_n^2\omega_c\right]K_{p.s.} \qquad (10\text{-}112)$$

Assuming the position sensor cutoff is five times the IPS loop bandwidth equation (10-112) can be written as

$$\overline{T_o^2(t)} = 8J^2\zeta^2\omega_n^5 K_{p.s.}\left[\frac{125}{3} + \frac{5}{4}\,\frac{1+8\zeta^2-16\zeta^4}{\zeta^2}\right] + \frac{J^2\pi\omega_n^5 K_{p.s.}}{2\zeta}\left(1-48\zeta^4+64\zeta^6\right) \qquad (10\text{-}113)$$

The ratio of mean square torque noise for the derived rate to the separate rate plus position sensor implementation is given by

$$\frac{\overline{T_o^2(t)}\Big|_{\substack{\text{derived}\\ \text{rate}}}}{\overline{T_o^2(t)}\Big|_{\substack{\text{separate}\\ \text{rate plus}\\ \text{position}}}} = \frac{192\pi\zeta^6-960\zeta^5-144\pi\zeta^4+2.48\times10^3\zeta^3+60\zeta+3\pi}{3[20\zeta+\pi(1-4\zeta^2)]} \qquad (10\text{-}114)$$

Assuming a damping ratio of $\frac{1}{\sqrt{2}}$, equation (10-114) results in

$$\frac{\overline{T_o^2(t)}\Big|_{\substack{\text{derived}\\ \text{rate}}}}{\overline{T_o^2(t)}\Big|_{\substack{\text{separate}\\ \text{rate plus}\\ \text{position}}}} = 21.86 \qquad (10\text{-}115)$$

or approximately 4.7 times the rms torque noise will result in the derived rate sensor implementation as that which results for separate rate plus position sensor implementation.

Assuming a damping ratio of $\frac{1}{\sqrt{2}}$, the mean squared torque for the derived rate sensor implementation can be written as

$$\overline{T_o^2(t)} = 173.3J^2\omega_n^5 K_{p.s.} = 1.697\times10^6 J^2 f_n^5 K_{p.s.} \qquad (10\text{-}116)$$

The allowable position power spectral noise amplitude assuming that 20 percent of the allowable 1 sec pointing error would be budgeted for position noise is

$$K_{p.s.} = \frac{2.247 \times 10^{-14}}{f_n} \frac{rad^2}{\frac{rad}{sec}} \tag{10-117}$$

The star sensor noise equivalent angle as a function of allowable torquer range utilization can be obtained by assuming the star tracker bandwidth is five times that of the IPS pointing control loop. Hence

$$\sigma_R^2 = 20\pi f_n K_{p.s.} \ rad^2 \tag{10-118}$$

Substituting equation (10-116) into equation (10-118) and taking the square root gives

$$\sigma_R = 6.085 \times 10^{-3} \frac{T_o(t)\big|_{rms}}{Jf_n^2} \ rad = 1.255 \times 10^{3} \frac{T_o(t)\big|_{rms}}{Jf_n^2} \ \widehat{sec} \tag{10-119}$$

The allowable star sensor noise equivalent angle from a pointing stability viewpoint is given by

$$\sigma_R' = 1.188 \times 10^{-6} \ rad = 0.245 \ sec \tag{10-120}$$

The value of IPS loop bandwidth for which equal noise equivalent angle requirements result from both pointing stability and torquer utilization viewpoints is given by

$$f_n = 71.57 \left(\frac{T_o(t)\big|_{rms}}{J} \right)^{1/2} \tag{10-121}$$

10.3.3 Computation of Optimum Loop Bandwidth for Derived Rate Sensor Implementation - The total mean squared pointing error for the derived rate sensor implementation is given by

$$\overline{\theta_o^2(t)}\big|_{total} = \left(\frac{4\zeta^2+1}{\zeta} \right) \pi^2 K_{p.s.} f_n + \frac{K_{T.G.}}{16\pi^2 J^2 \zeta f_n^3} \tag{10-122}$$

Differentiating equation (10-122) with respect to f_n setting the results equal to zero and solving for f_n gives

$$f_n = \frac{1}{2\pi J^{1/2}}\left[\left(\frac{3}{4\zeta^2+1}\right)\frac{K_{T.G.}}{K_{p.s.}}\right]^{1/4} \tag{10-123}$$

which is the bandwidth for which minimum pointing error results.

10.3.4 Criteria for Choosing Between Derived Rate and Separate Rate Plus Position Sensor Implementations - The criteria for when one chooses between separate rate plus position and derived rate sensor implementations can be formulated by the following inequality

$$\overline{\theta_o^2(t)}\Big|_{S.R.P.} \leq \overline{\theta_o^2(t)}\Big|_{D.R.} \tag{10-124}$$

Substituting equations (10-53) and (10-122) into equation (10-124) gives

$$\frac{\pi^2 K_{p.s.}}{\zeta} f_n + \frac{\zeta K_{R.G.}}{4 f_n} \leq \left(\frac{4\zeta^2+1}{\zeta}\right)\pi^2 K_{p.s.} f_n \tag{10-125}$$

Simplifying equation (10-125) results in

$$K_{R.G.} \leq 16\pi^2 f_n^2 K_{p.s.} \tag{10-126}$$

When the rate gyro noise power spectral density meets the above inequality separate rate plus position sensor implementation should be employed.

Another way of viewing equation (10-126) is to write it in the following form

$$f_n \geq \frac{1}{4\pi}\left(\frac{K_{R.G.}}{K_{p.s.}}\right)^{1/2} \tag{10-127}$$

or separate rate plus position should be employed over derived rate when the IPS loop bandwidth meets the inequality given in equation (10-127).

10.3.5 Criteria for Choosing Between Rate Gyro Hold and Derived Rate Sensor Implementations - The criteria for choosing between derived rate and rate gyro hold sensor implementation can be formulated by the following inequality

$$\overline{\theta_o^2(t)}\Big|_{R.H.} \leq \overline{\theta_o^2(t)}\Big|_{D.R.} \tag{10-128}$$

Substituting equations (10-76) and (10-122) into equation (10-128) results in

$$2\,(K_{p.s.}K_{R.G.})^{1/2} + \frac{K_{R.G.}}{4\zeta f_n} \leq \left(\frac{4\zeta^2+1}{\zeta}\right)\pi^2 K_{p.s.} f_n \tag{10-129}$$

After some algebraic manipulations equation (10-127 can be written as

$$K_{p.s.} \leq \left[\frac{12\zeta^2+1+4\,(8\zeta^2+1)^{1/2}}{[(4\zeta^2+1)2\pi f_n]^2}\right] K_{R.G.} \tag{10-130}$$

If the position sensor noise power spectral density meets the inequality shown in equation (10-130), derived rate should be employed over rate gyro hold.

Another way to view the inequality shown in equation (10-130) is the followi g

$$f_n \leq \frac{[12\zeta^2+1+4\zeta(8\zeta^2+1)^{1/2}]^{1/2}}{2\pi(4\zeta^2+1)} \left(\frac{K_{R.G.}}{K_{p.s.}}\right)^{1/2} \tag{10-131}$$

If the IPS loop bandwidth meets the inequality constraint shown in equation (10-131) the. derived rate should be employed over the rate gyro hold sensor implementation.

10.4 Summary and Recommendations - The following are some of the results during this study phase:

a. The derived rate sensor implementation will give three times the rms pointing error as the separate rate plus position sensor implementation for the same value of position noise power spectral density for an IPS control loop damping ratio of $\frac{1}{\sqrt{2}}$. This is true regardless of IPS pointing control loop bandwidth.

b. The derived rate sensor implementation will use approximately five times the torquer range as the separate rate plus position sensor implementation for the same value of position noise power spectral density for an IPS control loop damping ratio of $\frac{1}{\sqrt{2}}$. This is true regardless of IPS pointing control loop bandwidth.

c. For the derived rate sensor implementation. If 2 n-m of torquer range is budgeted to be used by sensor noise, which would correspond to 10 percent of the gimbal torquer range for a 20 n-m torquer, the allowable sensor noise power spectral density would be governed by this requirement for IPS loop bandwidths of 2 Hz and above. For IPS loop bandwidths below 2 Hz the allowable sensor noise power spectral densities would be governed by pointing stability requirements.

It is recommended that a study be performed to determine the effects of sensor and actuator noise on overall IPS performance using the system three body performance model described above which were performed on a simplified linear second order model of the IPS using white noise spectra. Actual sensor and activator noise characteristics including the effects of sampling and quantization which would not be handled in an efficient manner analytically would be included, thus allowing an optimum choice of sensor implementation.

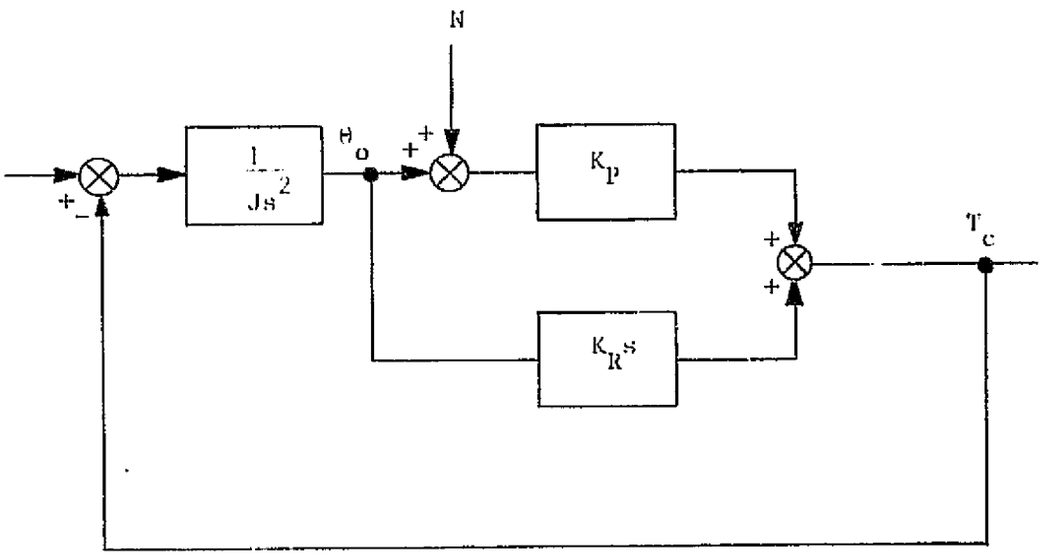

Figure 10-1. Simplified Block Diagram of the IPS for Separate Rate Plus Position Sensor Implementation

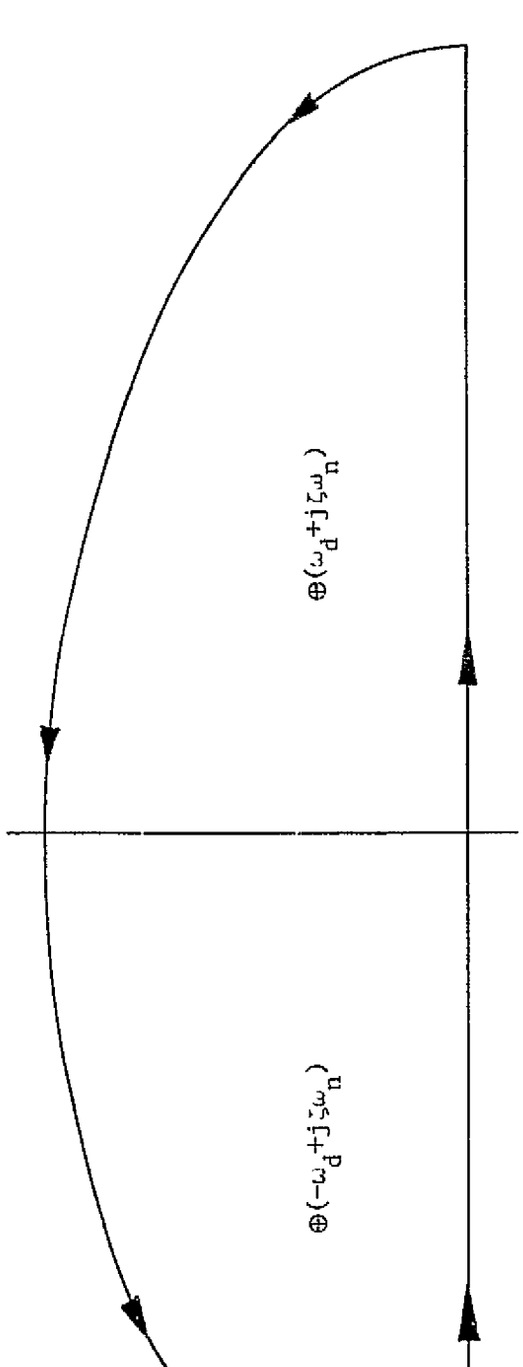

Figure 10-2. Contour for Noise Integral Evaluation

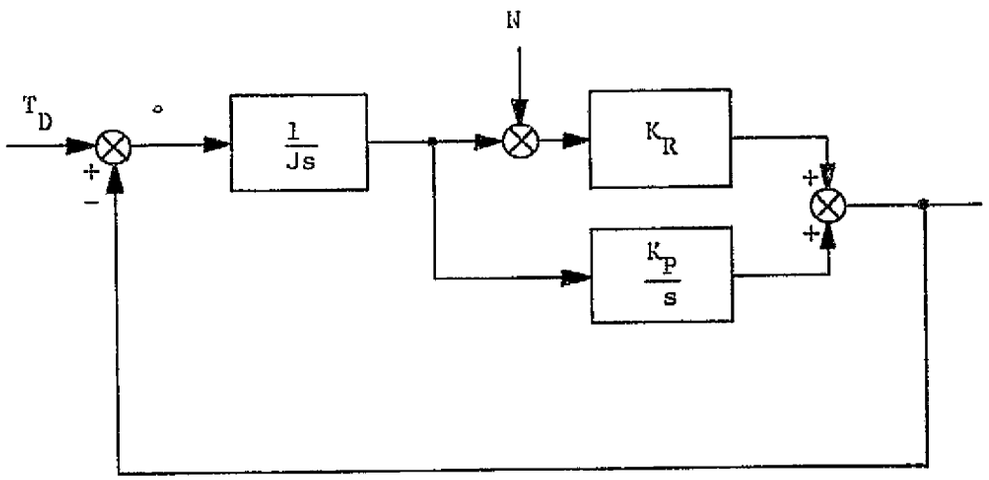

Figure 10-3. Simplified Block Diagram of the IPS with Rate Gyro Noise

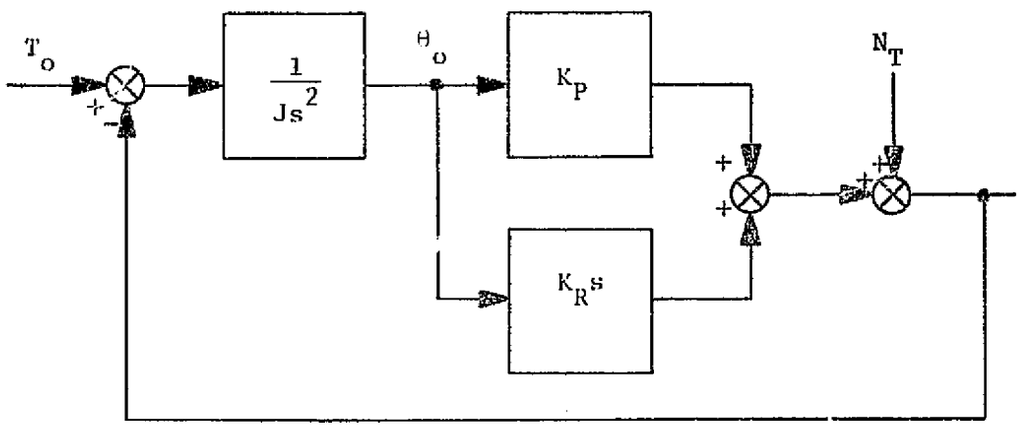

Figure 10-4. Simplified Block Diagram of the IPS with Torquer Noise Input

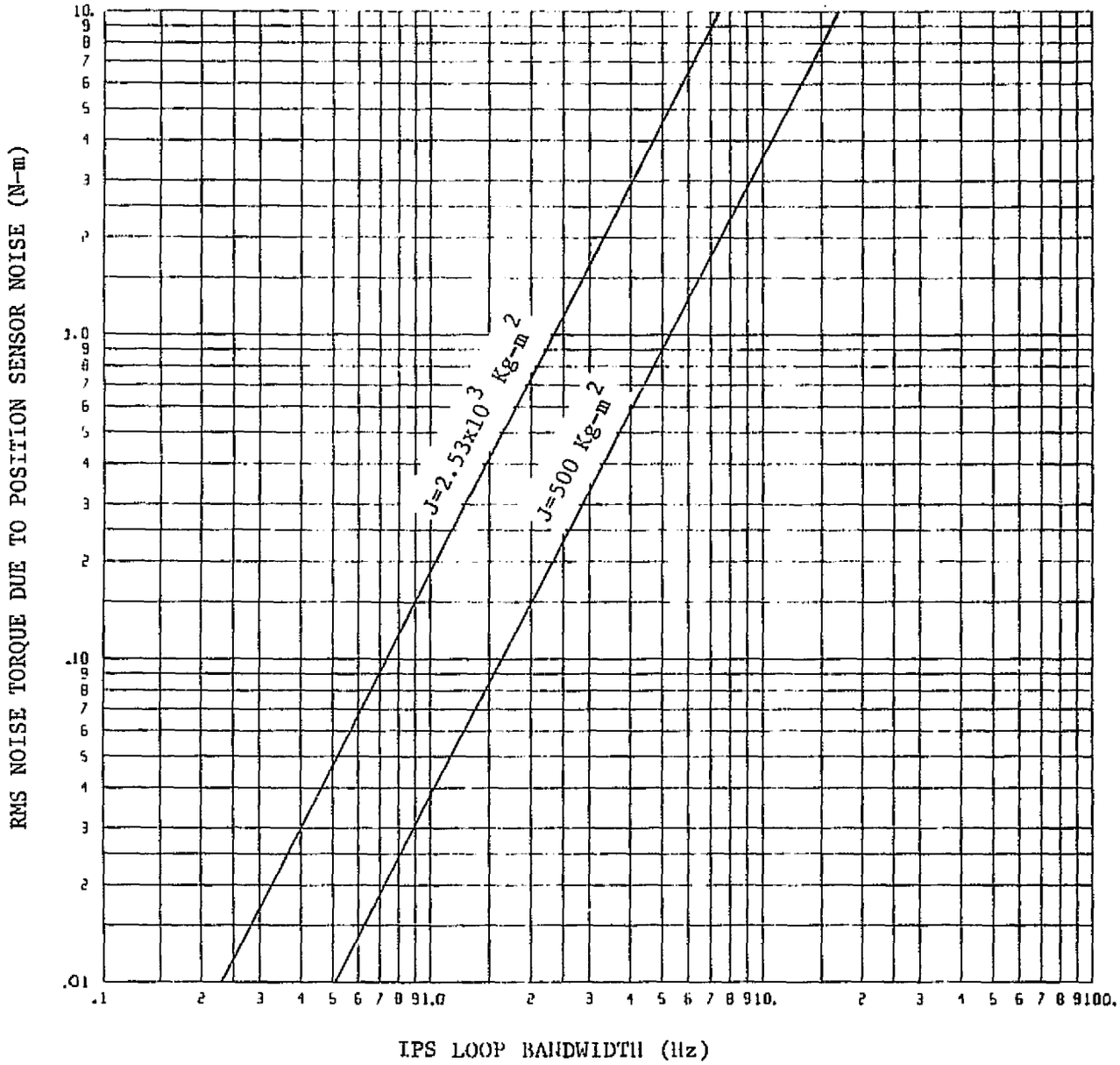

Figure 10-5. Noise Torque Due to Position Sensor Noise (Equation 10-38)

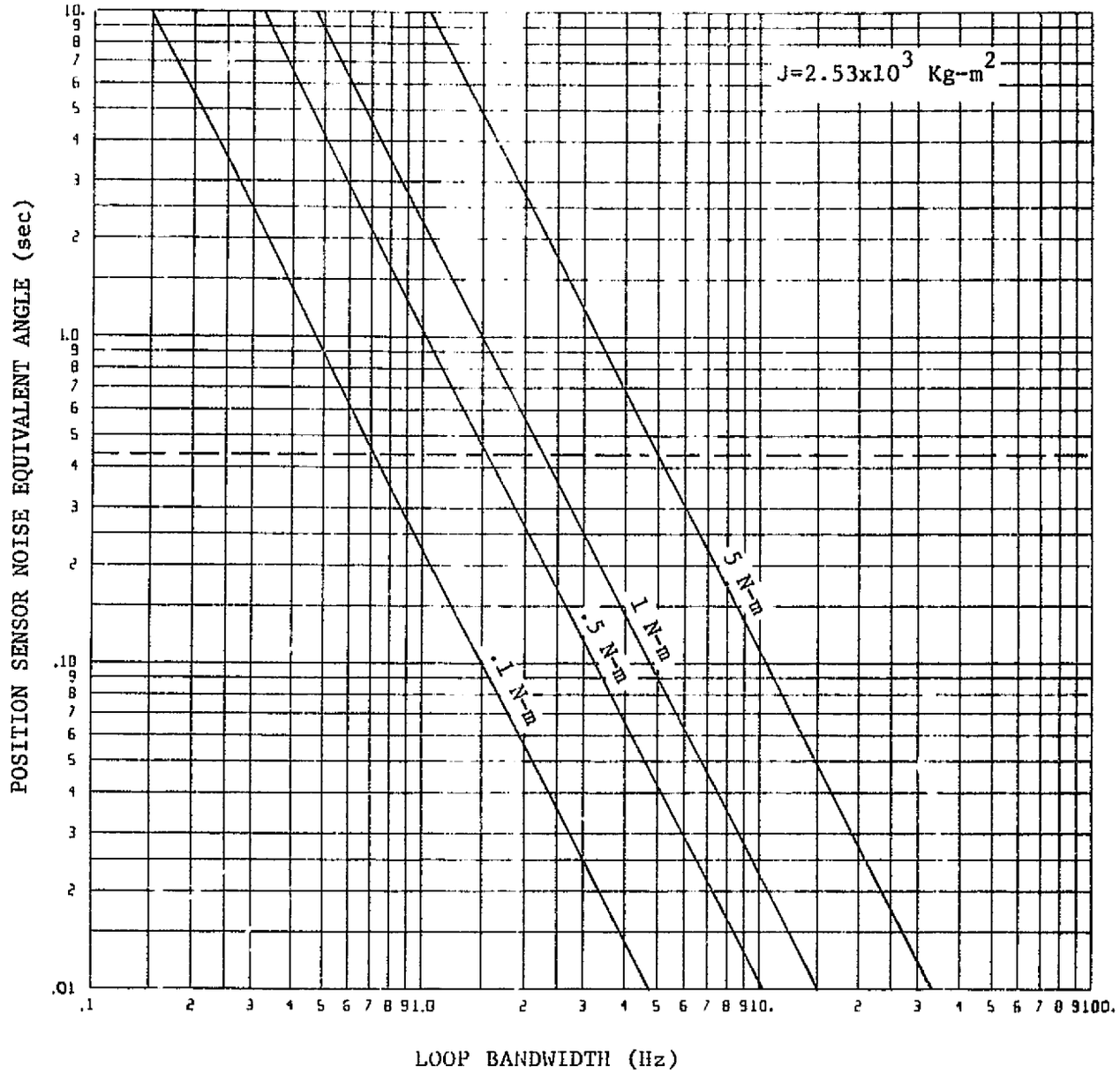

Figure 10-6. Comparison of Position Sensor Noise Equivalent Angle Requirements from Pointing Stability and Torque Noise Viewpoints (Equations 10-40, 10-41)

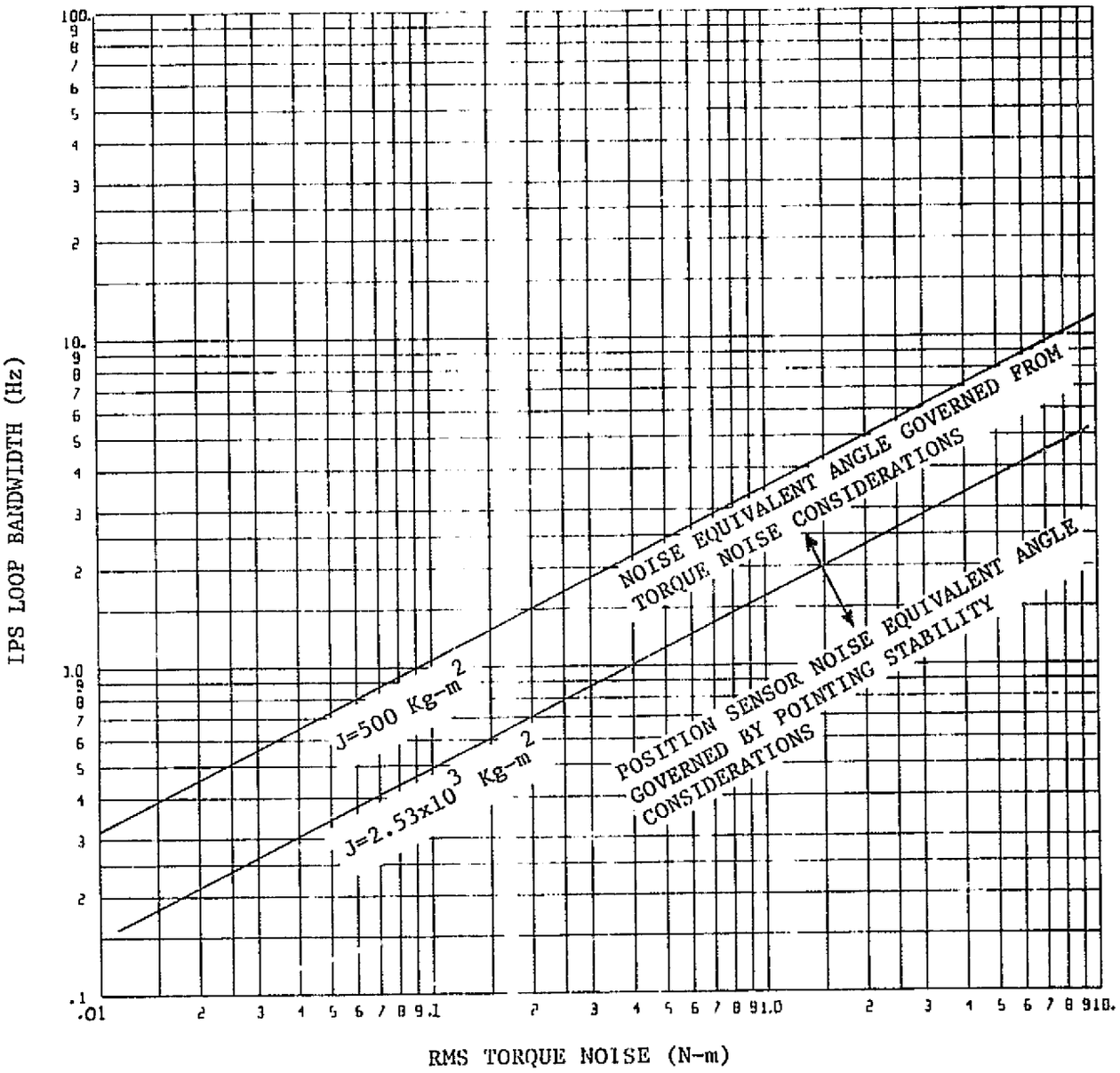

Figure 10-7. IPS Loop Bandwidth for Which Position Sensor Noise Equivalent Angle Requirements are Equal from Both Pointing Stability and Torquer Noise Viewpoints (Equation 10-42)

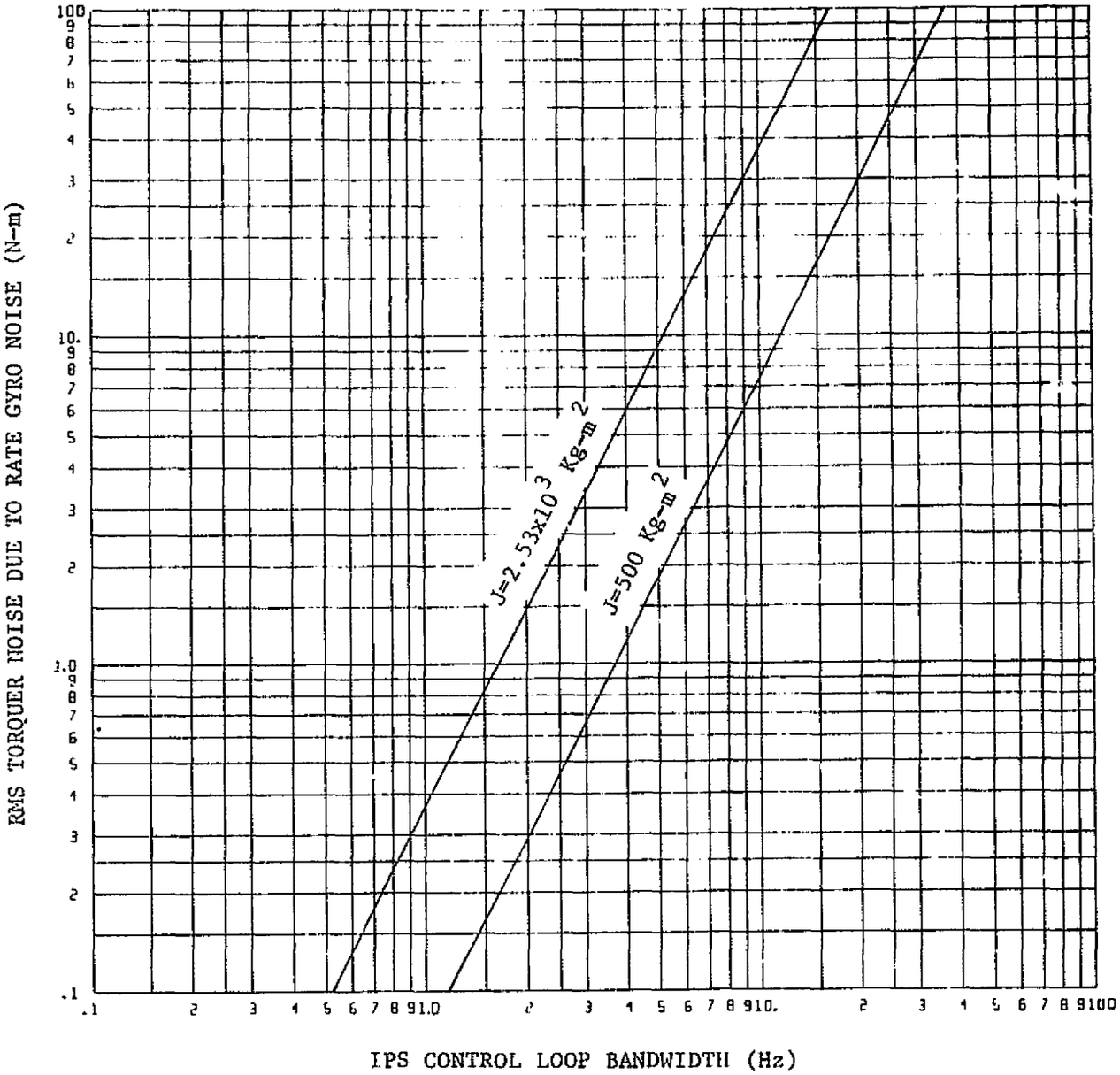

Figure 10-8. Torquer Noise Resulting from Allowable Rate Gyro Noise Considering Pointing Stability Only (Equation 10-48)

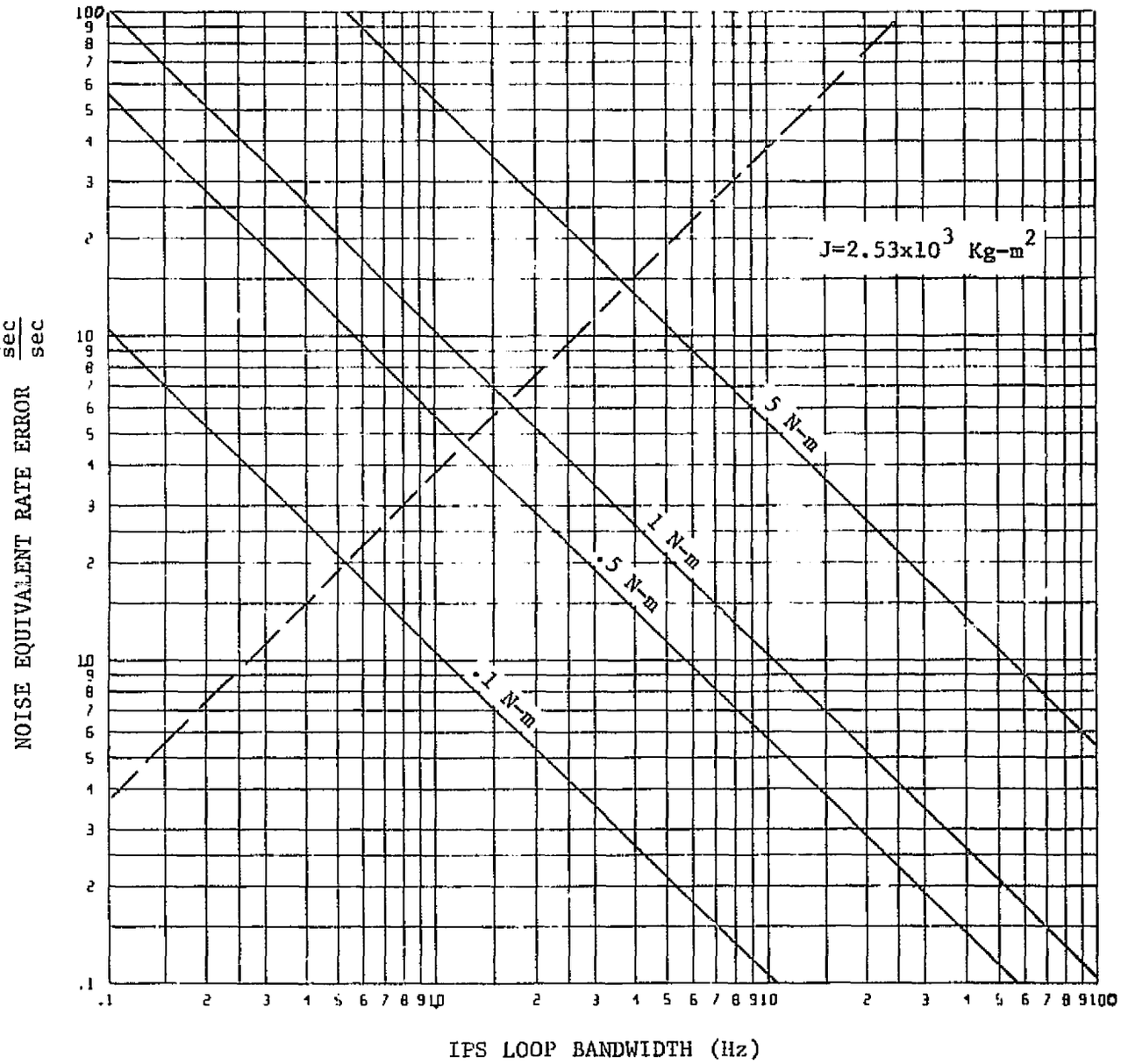

Figure 10-9. Comparison of Rate Sensor Noise Equivalent Rate Error Requirements from Pointing Stability and Torque Noise Viewpoints (Equations 10-50, 10-51)

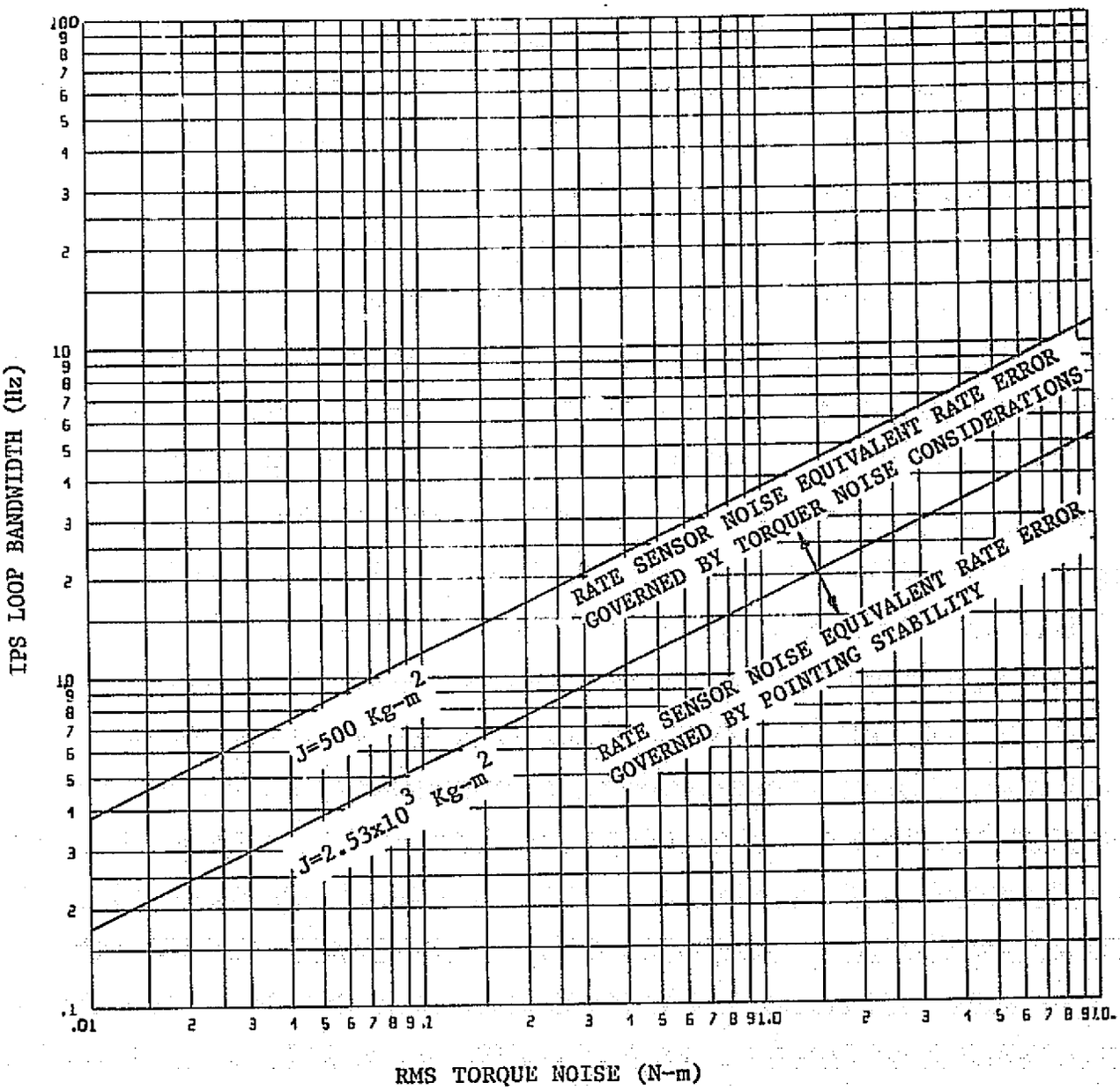

Figure 10-10. LPS Loop Bandwidth for Which Noise Equivalent Rate Error Requirements are Equal from Both Pointing Stability and Torquer Noise Viewpoints (Equation 10-52)

C.5

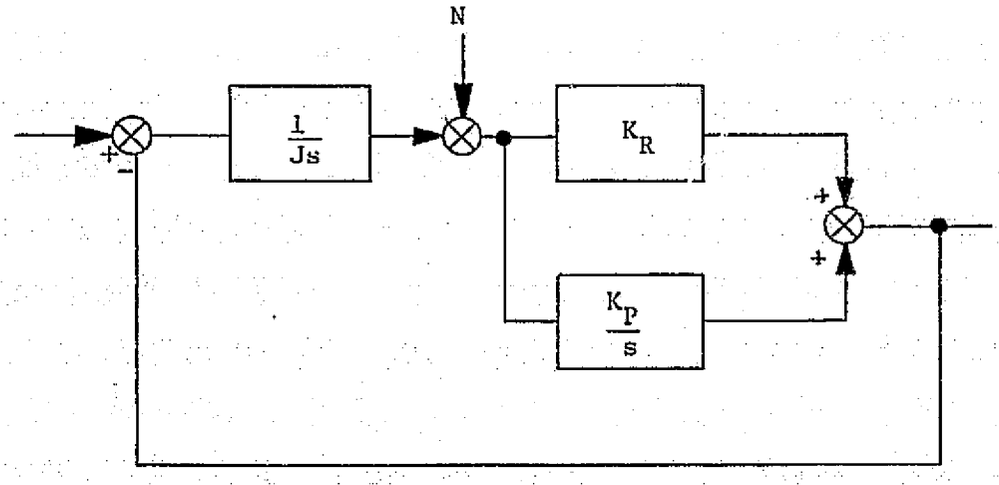

Figure 10-11. Simplified Block Diagram for Rate Gyro Hold Sensor Implementation

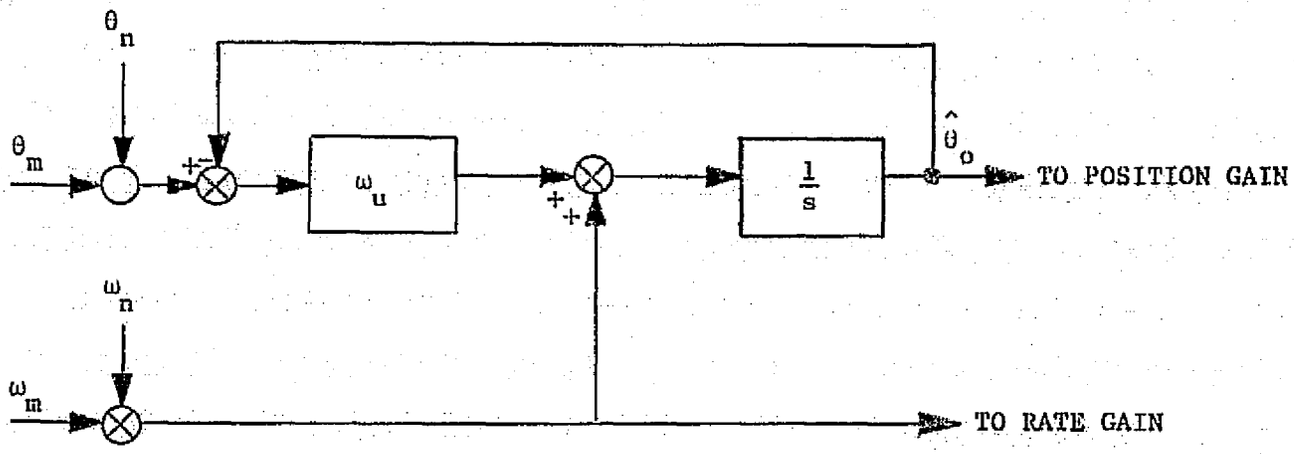

Figure 10-12. Analog Rate Gyro Update Loop

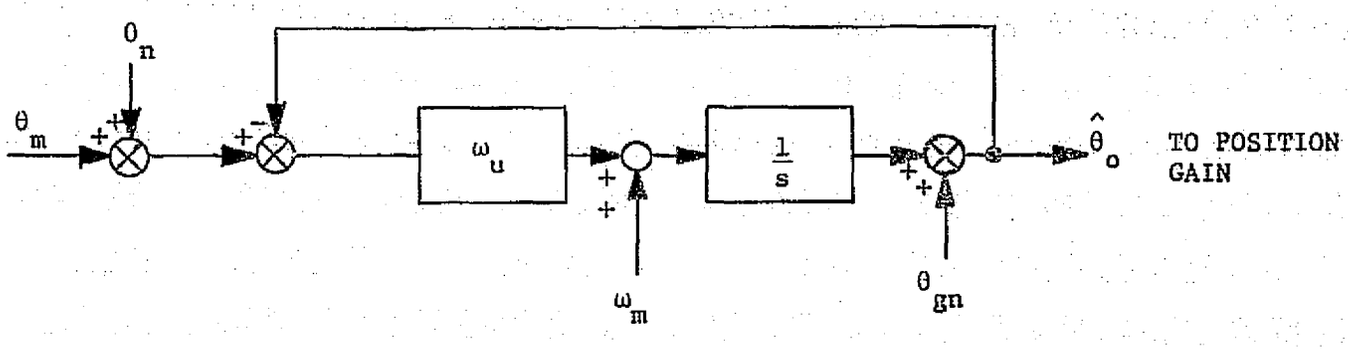

Figure 10-13. Modified Analog Rate Gyro Update Loop

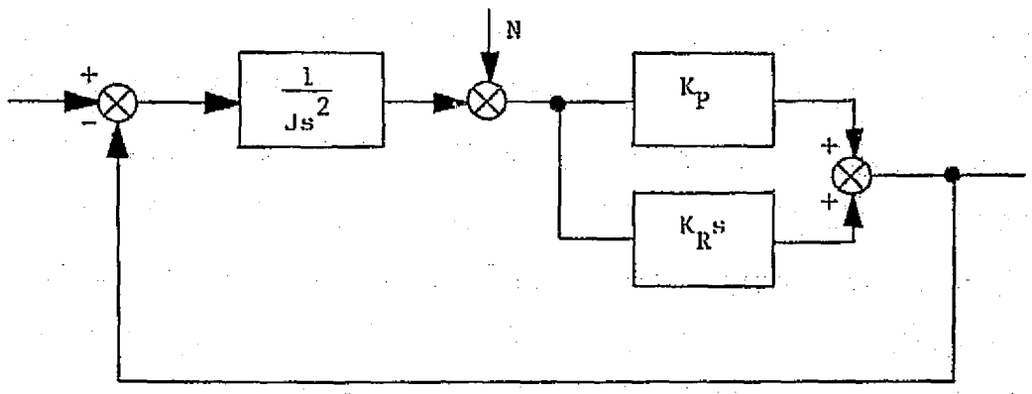

Figure 10-14. Simplified Block Diagram of IOG Control Loop Using Derived Rate Sensor Implementation

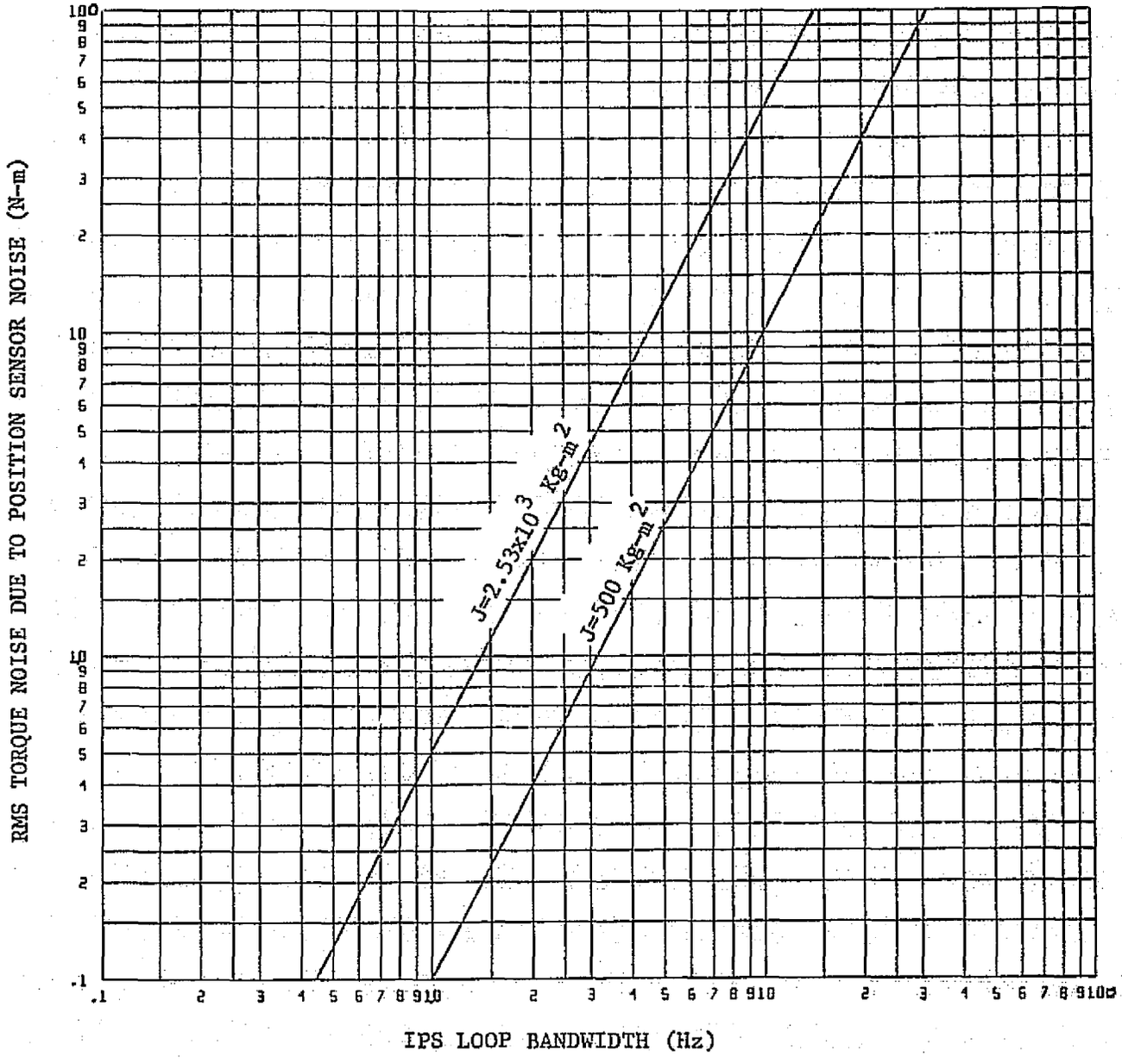

Figure 10-15. Noise Torque Due to Position Sensor Noise from Pointing Stability Viewpoint Only

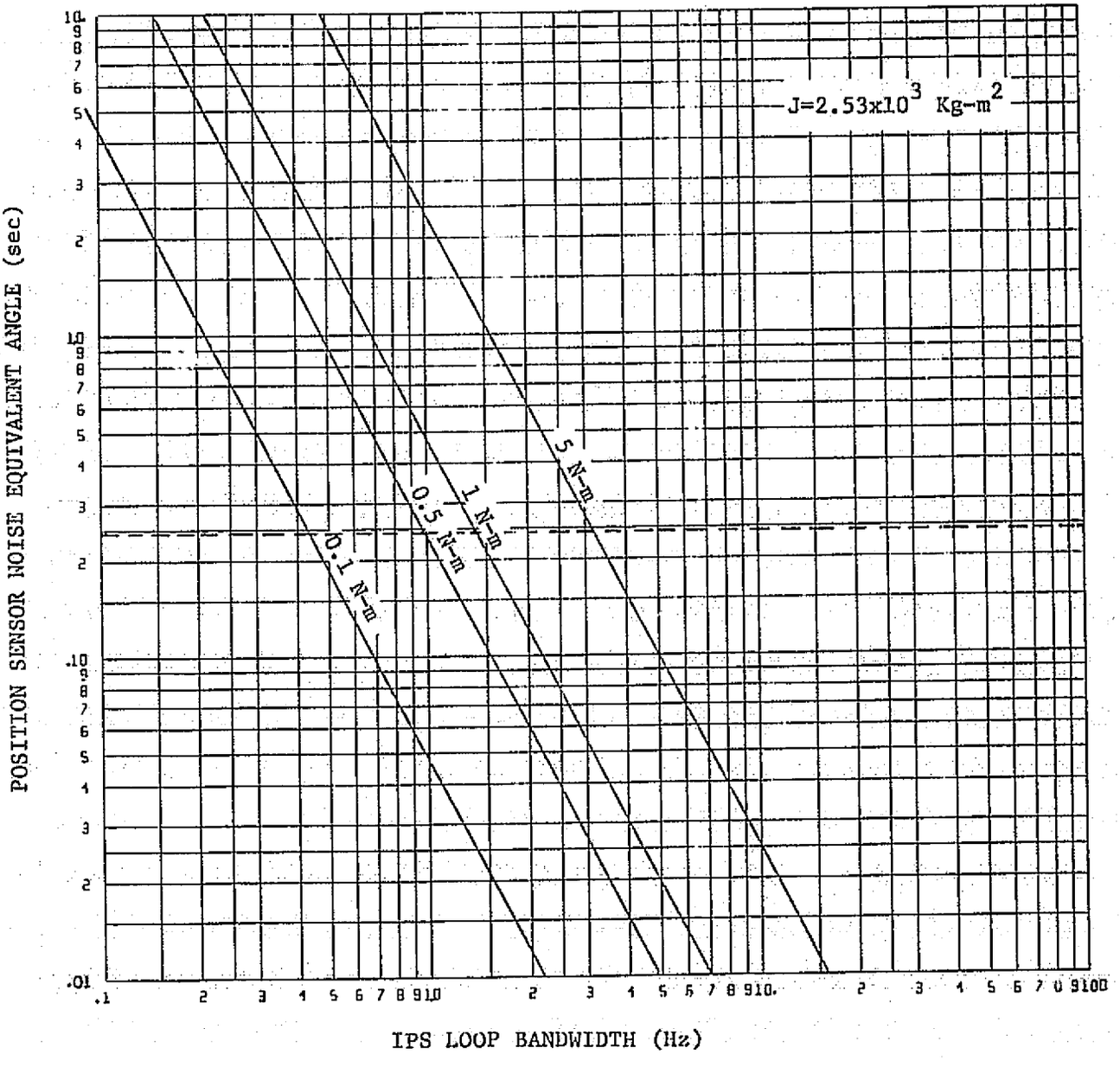

Figure 10-16. Comparison of Position Sensor Noise Equivalent Angle Requirements from Pointing Stability and Torque Noise Viewpoints (Equations 10-119, 10-120)

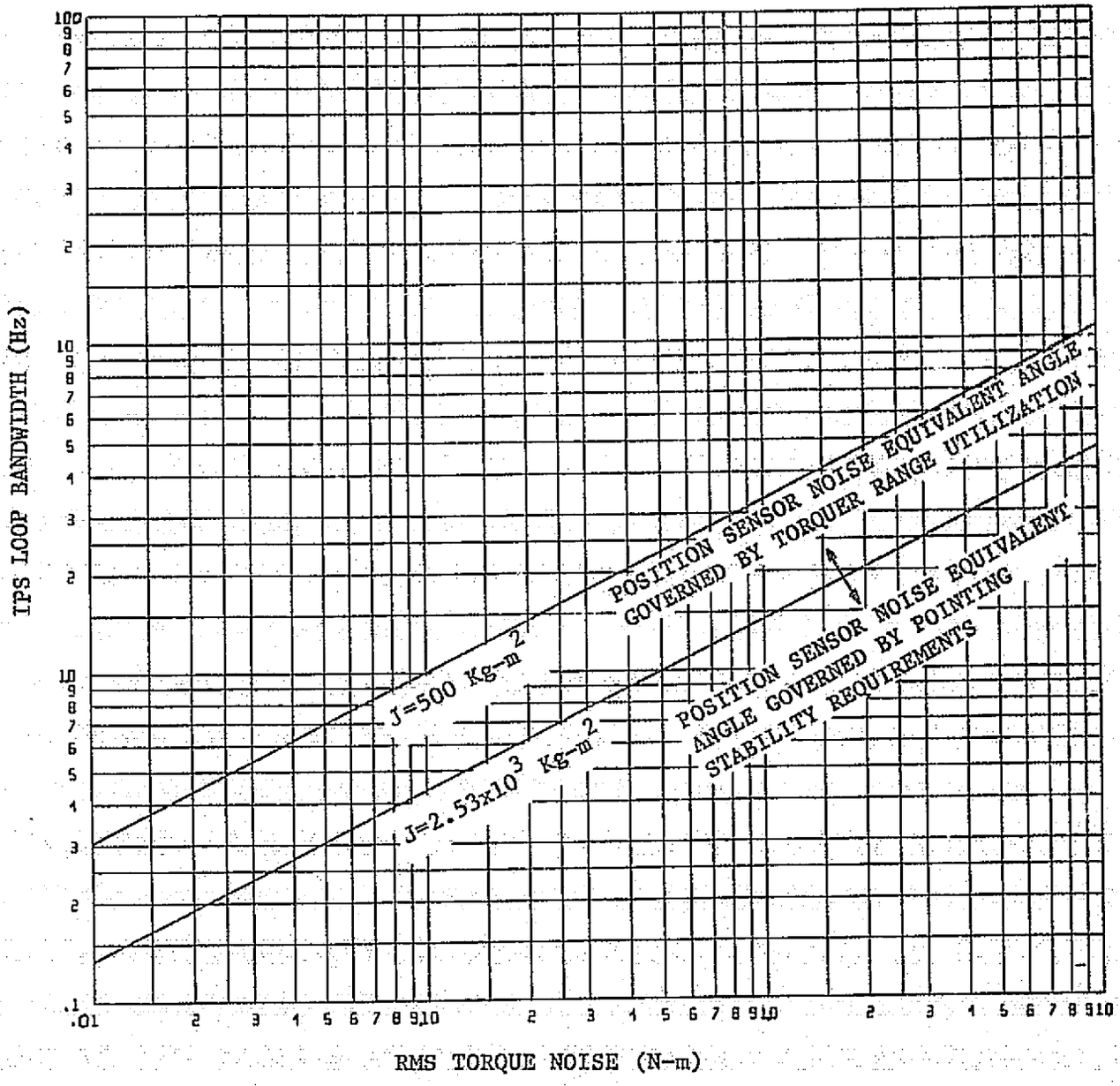

Figure 10-17. IPS Loop Bandwidth for Which Position Sensor Noise Equivalent Angle Requirements are Equal from Both Pointing Stability and Torquer Range Utilization Viewpoints

11. SUMMARY AND CONCLUSIONS

The major conclusions of the studies performed can be summarized as follows:

a. IPS stability and performance is not sensitive to suspension damping characteristics. Damping can be varied over wide ranges (i.e., reduced by an order of magnitude from a nominal damping ratio of 0.1) without any substantital change in system pointing performance.

b. IPS stability and performance is not sensitive to pedestal mass and inertia variations with pointing performance remaining essentially the same for pedestal mass and inertia variations of plus and minus an order of magnitude from nominal values.

c. IPS pointing performance is a function of telescope mass and inertia characteristics. A pointing error of approximately 2.6 arc-seconds was incurred for a pointing control loop bandwidth of 2 Hz in the presence of crew motion disturbances for the telescope mass characteristics listed below

$J_{3x} = 50$ Kg-m^2

$J_{3y} = 50$ Kg-m^2

$J_{3z} = 35$ Kg-m^2

$m_3 = 290$ Kg

If telescopes in this class are to be integrated with the IPS suspension system, modification would be required if $\pm$ 1 arc-second pointing stability is to be achieved.

d. A pointing error of 0.895 arc-second was incurred for a pointing control loop bandwidth of 2 Hz, in the presence of crew motion disturbances using the suspension system parameters specified by Dornier Systems for the Coincident Gimbal system configuration. This pointing error which is due to one source only is quite large and it is doubtful if $\pm$ 1 arc-second pointing stability could be realized once all the other contributing error sources (e.g., sensor and actuator noise, gimbal nonlinearities, sampling and quantization, etc.) are taken into consideration.

e. Isolator axial elongations of approximately 4.3 mm (1.7 in) result during earth point tracking from a 438 KM orbit for the suspension parameters specified by Dornier Systems for the Coincident Gimbal configuration. These elongations, which become worse as the orbital altitude decreases, are too large to be accommodated by reasonable suspension system designs.

f. It is recommended that the suspension system parameters for the Coincident Gimbal be modified from those specified by Dornier to the following:

$K_x = K_y = 2000$ n/m $\qquad k_x = k_y = 202.5$ n-m/rad

$K_z = 500$ n/m $\qquad k_z = 3.242 \times 10^3$ n-m/rad

$D_x = D_y = 475.2$ n-sec/m $\qquad d_x = d_y = 48.11$ n-m-sec

$D_z = 118.8$ n-sec/m $\qquad d_z = 769.8$ n-m-sec

The values for the suspension parameters listed above result in the following isolator design characteristics for the Coincident Gimbal suspension system designs:

$K = 750$ n/m

$D = 178.2$ n-sec/m

$\alpha = 19.47$ deg

$R = 0.9$ m

The modified suspension not only reduces isolator elongations incurred during earth point tracking but also improves pointing performance over that which resulted for the Dornier suspension specifications.

g. If the gimbal wire torque nonlinearity is accurately described by the characteristic shown in section 5, the jump in that wire torque characteristic would have to be 0.05 n-m or less for the nominal telescope and 0.01 n-m or less for the 290 Kg telescope discussed above in item c, if a pointing stability of $\pm$ 1 arc-second is to be achieved. These values will result in limit cycle amplitudes of 0.2 arc-second which is twenty percent of the total allowable error budget.

h. The maximum telescope inertia that could be accommodated during earth point tracking assuming that not more than 80 percent of the gimbal torque capability of 20 n-m be used, is proportional to the peak angular acceleration required to earth point track at a given orbital altitude. However, the actual torque required to earth point track considerably exceeds, particularly at lower orbital altitudes, the peak angular acceleration times the telescope inertia about the gimbal hinge point due to the action of pedestal dynamics. This effect can be reduced as the gimbal hinge point, pedestal CM, and suspension center of elasticity are brought closer together. These results are for the recommended Coincident Gimbal suspension parameters and do not take into account the isolator elongations incurred during earth point tracking but only considers the 16 n-m torque limitation.

i. The telescope tracking errors incurred are appreciably exceeding $\pm$ 1 arc-second for orbital altitudes below 420 KM for a pointing control loop bandwidth of 2 Hz when only angular rate and position commands are employed. It is clear that if $\pm$ 1 arc-second tracking accuracy is to be achieved during earth point tracking, a feed forward torque command would be required in addition to the angular rate and position commands presently being employed.

j. Telescope tracking error is proportional to the rate of change of angular acceleration required to earth point track and is essentially independent of telescope inertia provided that the pointing control loop bandwidth remains constant.

12. RECOMMENDED FUTURE EFFORT

The following tasks are recommended to continue and extend the results obtained in this study in order to better understand and aid ESA in the design of the IPS.

a. Determine the functional form of the command torque profile that would be required to improve system tracking accuracy as a function of command torque profile complexity with a $\pm$ 1 arc-second tracking accuracy for orbital altitudes between 160 and 480 KM being a design goal.

b. Determine the effect of parameterizing the distance between the gimbal hinge point, pedestal CM, and suspension center of elasticity, on system pointing and slewing performance. In particular, investigate the torque required, and isolator elongations incurred, to perform earth point tracking as a function of these distances taking into consideration the suspension modifications required to maintain $\pm$ 1 arc-second stability during stellar pointing as the distance between telescope hinge point, pedestal CM, and suspension system center of elasticity, decrease.

c. Determine the maximum telescope mass and inertia that could be accommodated as a function of allowable isolator elongation for various orbital altitudes.

d. Determine the effects of sensor and actuator noise on IPS pointing performance. Establish the allowable levels for these noise sources as a function of sensor implementation and specify recommended implementation update frequencies, etc. as a function of sensor and actuator noise characteristics.

e. Determine the effects of sampling and quantization on IPS pointing performance. Establish the sampling frequency and quantization levels that would result in satisfactory system performance without compensating for these effects. If these values result in excessive software utilization investigate use of compensation to reduce sampling frequency while still maintaining desired system performance characteristics. The effects of sampling and quantization on the errors incurred due to sensor and actuator noise characteristics should also be determined.

f. Determine the effect of telescope flexibility on overall IPS stability and pointing performance. Establish a meaningful technique by which telescope flexibility characteristics could be specified so that if adhered to by the payload designer would result in satisfactory system stability and pointing performance once integrated with the IPS.